Karsten König, Andreas Ostendorf (Eds.)
Optically Induced Nanostructures

Also of Interest

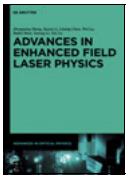

Advances in High Field Laser Physics
Zhengming Shen et al., 2016
ISBN 978-3-11-030426-8, e-ISBN (PDF) 978-3-11-030441-1,
e-ISBN (EPUB) 978-3-11-038800-8

Advances in Ultrafast Optics
Zhiyi Wei et al., 2016
ISBN 978-3-11-030436-7, e-ISBN (PDF) 978-3-11-030455-8,
e-ISBN (EPUB) 978-3-11-038283-9

Advanced Optical Technologies
Michael Pfeffer (Editor-in-Chief)
ISSN 2192-8576, e-ISSN 2192-8584

Biomedical Engineering
Olaf Dössel (Editor-in-Chief)
ISSN 0013-5585, e-ISSN 1862-278X

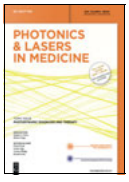

Photonics & Lasers in Medicine
Frank Frank, Lothar Lilge, Carsten m. Philipp, Ronald Sroka
(Editors-in-Chief)
ISSN 2193-0635, e-ISSN 2193-0643

Optically Induced Nanostructures

Biomedical and Technical Applications

Edited by
Karsten König and Andreas Ostendorf

DE GRUYTER

Physics and Astronomy Classification Scheme 2010
42, 68, 78, 81, 87

Editors
Prof. Dr. rer. nat. habil. Karsten König
Department of Biophotonics and Laser Technology
Saarland University
Campus A5.1
66123 Saarbrücken
Germany
k.koenig@blt.uni-saarland.de

Prof. Dr.-Ing. habil. Andreas Ostendorf
Applied Laser Technology
Ruhr University Bochum
Universitätsstr. 150
44780 Bochum
Germany
andreas.ostendorf@ruhr-uni-bochum.de

ISBN 978-3-11-033718-1
e-ISBN (PDF) 978-3-11-035432-4
e-ISBN (EPUB) 978-3-11-038350-8

Library of Congress Cataloging-in-Publication Data
A CIP catalog record for this book has been applied for at the Library of Congress.

Bibliographic information published by the Deutsche Nationalbibliothek
The Deutsche Nationalbibliothek lists this publication in the Deutsche Nationalbibliografie; detailed bibliographic data are available on the Internet at http://dnb.dnb.de.

Cover image: Femtosecond laser nanoprocessing of a blood cell nucleus using Bessel beams.
Typesetting: PTP-Berlin, Protago-TEX-Production GmbH
Printing and binding: CPI books GmbH, Leck
♾ Printed on acid-free paper
Printed in Germany

www.degruyter.com

Foreword 1

2015 is the year that the United Nations has declared as the *International Year of Light*. Light-based technologies change our economies and lifestyles. They become vital in our daily lives. Also the winners of the latest Nobel Prizes focus on photonics.

The Nobel Prize for physics had been awarded to Isamu Akasaki, Hiroshi Amano and Shuji Nakamura who developed the blue LED. Stefan Hell, Eric Betzig and William Moerner won the Nobel Prize for chemistry for super-resolved fluorescence microscopy with a resolution far beyond Abbe's diffraction limit of about half the wavelength (200 nanometers). Pushing optical microscopy into the nanodimension with certain fluorescent molecules, microscopy "turned" into *nanoscopy*. A resolution below 10 nm has been achieved in fluorescence nanoscopy using visible light.

But microscopes and nanoscopes are not just analytical tools. They can also operate as highly precise nanomaching tools with features sizes below 100 nanometers even when operating in the near infrared (NIR). Non-linear optics, in particular multiphoton effects, made that possible.

The PhD student and later Nobel Prize Winner Maria Göppert predicted multiphoton effects in the late twenties of the last century. It took about 30 years until the first laser was built to prove her hypothesis by the generation of second harmonic generation (SHG) and two-photon fluorescence in 1961. Again 30 years later the first two-photon laser microscope was built utilizing a femtosecond dye laser. One decade later, multiphoton tomographs became medical devices and the first stimulated emission depletion (STED) microscope was realized. Both systems were based on titanium:sapphire femtosecond laser technology.

With the new millennium, femtosecond NIR laser systems became novel micromachining tools in material production and in refractive eye surgery.

And within the last 10 years, femtosecond NIR laser technology "turned" micromachining into nanomachining. These novel nonlinear photonic nanoprocessing tools are based on two-photon and STED-lithography as well as on multiphoton ionization and plasma formation. In-bulk nanoprocessing became feasible when using non-ultraviolet (UV) laser radiation.

This book refers to the latest developments in laser-produced sub-100 nanometer features, typically with femtosecond NIR laser systems. 15 research groups consisting of engineers and natural scientists describe the basics of femtosecond laser – material interaction and the interior of the novel nanotools. Technical and biomedical applications such as STED-lithography to develop protein nanoanchors, production of ultrathin resists, biochemical sensors and scaffolds, laser-induced periodic nanostructures for friction control in titanium and steel as well as virus-free optical reprogramming of cells are demonstrated.

The editors and authors of this book wish to thank the *German Science Foundation* for the possibility to publish their latest results within this open access book and for long-term funding within the Key Project SPP 1327 (2008–2015).

May 2015

Karsten König
Biophotonics and Laser Technology
Saarland University
Germany

Andreas Ostendorf
Applied Laser Technology
Ruhr University Bochum
Germany

Foreword 2

The invention of lasers in 1960 marked the birth of an entirely new era of optical science and technology. The combination of a laser beam and an optical microscope offers a way to confine a laser beam to a region smaller than the wavelength of the beam. For a visible wavelength beam, the size of this small region can be down to 200–300 nm, determined by Abbe's diffraction law. Scanning this focused spot across a sample under illumination leads to the invention of laser scanning microscopy such as confocal microscopy which gives an optical sectioning property for three-dimensional (3D) imaging. Due to the strong confinement of the light beam, the intensity in the focal region can be used to induce the localized physical or chemical processes in a sample under illumination, which provides a powerful way to fabricate sub-wavelength structures in the sample.

The integration of ultrafast laser beams with an optical microscope was a milestone in optical microscopy as it allows for nonlinear excitation in the focal region. Nonlinear excitation such as two-photon excitation removes the necessity of using a confocal pinhole for 3D imaging. In the context of optically induced fabrication, two-photon excitation is a flexible tool for 3D micro-fabrication. Because of the threshold effect associated with the laser–material interaction, the 3D fabrication by a femtosecond laser beam usually results in a 3D structure with a feature size smaller than the diffraction limit.

The core of the stimulated emission depletion microscopy method, invented by the 2014 Nobel Laureate, Stefan Hell, is the use of two laser beams rather than one. In this case, the first laser beam is the induction of fluorescence while the second one is to terminate it. With an appropriate spatial overlapping arrangement of the two beams, one can break the diffraction limited resolution barrier, leading to nanoscopy. Inspired by this idea, over the last 5 years, many research groups have embarked on laser-induced fabrication by coupling two laser beams, one for photoinduction and the other for photo-inhibition, into a microscope. It is now possible to generate 3D nanostructures with a feature size down to 9 nm.

The current book timely presents the progress in laser-induced micro- and nano-fabrication. It will be a useful reference for scientists and students who wish to get involved in 3D laser direct writing for nano-science and nano-engineering.

May 2015

Min Gu
Centre of Micro-Photonics
Swinburne University of Technology
Australia

Satoshi Kawata
Photonics Advanced Research Center
Osaka University
Japan

Contents

Part II: **Biomedical applications**

Authors

Giulio Abagnale
Laser Technology
RWTH Aachen University
52074 Aachen
Germany

Maziar Afshar
Department of Micromechanics,
Microfluidics and Microactuators
Saarland University
Campus A5.1
66123 Saarbrücken
Germany

Ilya Alexeev
Institute of Photonic Technologies
University of Erlangen-Nuremberg
Konrad-Zuse-Straße 3
91052 Erlangen
Germany
and
Erlangen Graduate School
in Advanced Optical Technologies
Paul-Gordan-Straße 6
91052 Erlangen
Germany

Thomas S. Asche
Leibniz Universität Hannover
Institute of Inorganic Chemistry
Callinstraße 9
30167 Hannover
Germany

Caroline Augspurger
Department of Women's Health
Research Institute for Women's Health
University Hospital of the Eberhard Karls
University Tübingen
Silcherstr. 7/1
72076 Tübingen
Germany

Andreas Aumann
Helmholtz Institute for Biomedical Engineering,
Stem Cell Biology, and Cellular Engineering
Ruhr-University Bochum
Applied Laser Technologies
Universitätsstr. 150
44780 Bochum
Germany

Stephan Barcikowski
Technical Chemistry I and Center for Nano-
integration Duisburg-Essen (CENIDE)
University of Duisburg-Essen
Universitätsstr. 5–7
45141 Essen
Germany

Marcus Baum
Institute of Photonic Technologies
University of Erlangen-Nuremberg
Konrad-Zuse-Straße 3
91052 Erlangen
Germany
and
Erlangen Graduate School in Advanced Optical
Technologies
Paul-Gordan-Straße 6
91052 Erlangen
Germany

Thomas Baumert
University of Kassel
Institute of Physics and CINSaT
Heinrich-Plett-Str. 40
34132 Kassel
Germany

Carolin Beck
University Hospital Würzburg
Tissue Engineering and Regenerative Medicine
Roentgenring 11
97070 Würzburg
Germany

Peter Behrens
Leibniz Universität Hannover
Institute of Inorganic Chemistry
Callinstraße 9
30167 Hannover
Germany

Sabrina Berger
Institute for Inorganic Chemistry and Center
for Nanointegration Duisburg-Essen (CeNIDE)
University of Duisburg-Essen
Universitätsstr. 5–7
45117 Essen
Germany

Tobias Birr
Laser Zentrum Hannover
Hollerithallee 8
30419 Hannover
Germany

Jörn Bonse
BAM Bundesanstalt für Materialforschung
und -prüfung
Unter den Eichen 87
12205 Berlin
Germany

Elke Bremus-Köbberling
Laser Technology
RWTH Aachen University
52074 Aachen
Germany
and
Fraunhofer Institute for Laser Technology
52074 Aachen
Germany

Hans Georg Breunig
Department of Biophotonics
and Laser Technology
Saarland University
Campus A5.1
66123 Saarbrücken
Germany

Frank Burmeister
Friedrich-Schiller-Universität Jena
Abbe Center of Photonics
Institute of Applied Physics
Albert-Einstein-Straße 15
07745 Jena
Germany
and
Fraunhofer Institute for Applied Optics
and Precision Engineering
Albert-Einstein-Straße 7
07745 Jena
Germany

Robert Buschlinger
Institute of Optics, Information and Photonics
University of Erlangen-Nürnberg
Haberstraße 9a
90158 Erlangen
Germany

Boris Chichkov
Laser Zentrum Hannover
Hollerithallee 8
30419 Hannover
Germany

Vincent Coger
Department of Plastic, Hand-
and Reconstructive Surgery
Hannover Medical School
Carl-Neuberg-Str. 1
30625 Hannover
Germany

Sandro Eckert
Laser Technology
RWTH Aachen University
52074 Aachen
Germany

Lukas M. Eng
Institut für Angewandte Photophysik
Technische Universität Dresden
01062 Dresden
Germany

Lars Englert
University of Oldenburg
Institute of Physics
Carl-von-Ossietzky-Straße 9–11
26129 Oldenburg
Germany

Matthias Epple
Institute for Inorganic Chemistry and Center
for Nanointegration Duisburg-Essen (CeNIDE)
University of Duisburg-Essen
Universitätsstr. 5–7
45117 Essen
Germany

Dara Feili
Department of Micromechanics,
Microfluidics and Microactuators
Saarland University
Campus A5.1
66123 Saarbrücken
Germany

Valeriano Ferreras Paz
Institut für Technische Optik
Universität Stuttgart
Pfaffenwaldring 9
70569 Stuttgart
Germany

Sebastian Fessel
Leibniz Universität Hannover
Institute of Inorganic Chemistry
Callinstraße 9
30167 Hannover
Germany

Steffen Franzka
Department of Chemistry
University of Duisburg-Essen
Universitätsstr. 5
45141 Essen
Germany
and
CENIDE – Center for Nanointegration
Duisburg-Essen
NanoEnergieTechnikZentrum
Carl-Benz-Str. 199
47057 Duisburg
Germany

Karsten Frenner
Institut für Technische Optik
Universität Stuttgart
Pfaffenwaldring 9
70569 Stuttgart
Germany

Martin Garcia
Theoretical Physics and Center
for Interdisciplinary Nanostructure
Science and Technology (CINSAT)
Universität Kassel
Germany

Karl-Heinz Gärtner
University Hospital Würzburg
Tissue Engineering
and Regenerative Medicine
Roentgenring 11
97070 Würzburg
Germany

Ulrike Georgi
Leibniz-Institut für Polymerforschung
Dresden e. V.
Hohe Straße 6
01069 Dresden
Germany

Michael M. Gepp
Fraunhofer Institute for Biomedical
Engineering IBMT
Ensheimer Str. 48
66386 St. Ingbert
Germany

Arnold Gillner
Laser Technology
RWTH Aachen University
52074 Aachen
Germany

Nadine Götte
University of Kassel
Institute of Physics and CINSaT
Heinrich-Plett-Str. 40
34132 Kassel
Germany

Manfred Hartelt
BAM Bundesanstalt für Materialforschung
und -prüfung
Unter den Eichen 87
12205 Berlin
Germany

Nils Hartmann
Department of Chemistry
University of Duisburg-Essen
Universitätsstr. 5
45141 Essen
Germany
and
CENIDE – Center for Nanointegration
Duisburg-Essen
NanoEnergieTechnikZentrum
Carl-Benz-Str. 199
47057 Duisburg
Germany

Rainer Heintzmann
Institute of Physical Chemistry
Friedrich-Schiller-University Jena
Helmholtzweg 4
07743 Jena
Germany
and
Leibniz Institute of Photonic Technology
Albert-Einstein-Straße 9
07745 Jena
Germany
and
King's College London
Randall Division of Cell
and Molecular Biophysics
London
UK

Hartmut Hillmer
University of Kassel
Institute of Nanostructure Technologies
and Analytics and CINSaT
Heinrich-Plett-Str. 40
34132 Kassel
Germany

Sandra Höhm
Max-Born-Institut für Nichtlineare Optik
und Kurzzeitspektroskopie (MBI)
Max-Born-Straße 2A
12489 Berlin
Germany

Ruth Houbertz
Fraunhofer Institute for Silicate Research ISC
Neunerplatz 2
97082 Würzburg
Germany
and
Multiphoton Optics GmbH
Auweg 27
63920 Grossheubach
Germany

Dmitry Ivanov
Theoretical Physics and Center
for Interdisciplinary Nanostructure Science
and Technology (CINSAT)
Universität Kassel
Germany

Pascal Josten
Fraunhofer Institute for Silicate Research ISC
Neunerplatz 2
97082 Würzburg
Germany

Larissa Juschkin
Institute of Physics
EUV Sources and Applications and JARA – Fundamentals of Future Information Technologies
RWTH Aachen University
52056 Aachen
Germany

Thomas Kämpfe
Institut für Angewandte Photophysik
Technische Universität Dresden
01062 Dresden
Germany

Yousuf Khan
University of Kassel
Institute of Nanostructure Technologies and
Analytics and CINSaT
Heinrich-Plett-Str. 40
34132 Kassel
Germany

Thomas A. Klar
Institut für Angewandte Physik
Johannes Kepler Universität Linz
4040 Linz
Austria

Madlen Klötzer
Department of Biophotonics
and Laser Technology
Saarland University
Campus A5.1
66123 Saarbrücken
Germany

Karsten König
Department of Biophotonics
and Laser Technology
Saarland University
Campus A5.1
66123 Saarbrücken
Germany

Robert Koter
BAM Bundesanstalt für Materialforschung
und -prüfung
Unter den Eichen 87
12205 Berlin
Germany

Jörg Krüger
BAM Bundesanstalt für Materialforschung
und -prüfung
Unter den Eichen 87
12205 Berlin
Germany

Kestutis Kurselis
Laser Zentrum Hannover
Hollerithallee 8
30419 Hannover
Germany

Thomas Kusserow
University of Kassel
Institute of Nanostructure Technologies
and Analytics and CINSaT
Heinrich-Plett-Str. 40
34132 Kassel
Germany

Ronan Le Harzic
Fraunhofer Institute for Biomedical
Engineering IBMT
Ensheimer Str. 48
66386 St. Ingbert
Germany

Karl-Heinz Leitz
Institute of Photonic Technologies
University of Erlangen-Nuremberg
Konrad-Zuse-Straße 3
91052 Erlangen
Germany
and
Erlangen Graduate School
in Advanced Optical Technologies
Paul-Gordan-Straße 6
91052 Erlangen
Germany

Stephan Marschner
Max-Born-Institut für Nichtlineare Optik
und Kurzzeitspektroskopie (MBI)
Max-Born-Straße 2A
12489 Berlin
Germany

Tobias Maß
Institute of Physics (IA) and JARA – Fundamen-
tals of Future Information Technologies
RWTH Aachen University
52056 Aachen
Germany

Tamara Meinl
University of Kassel
Institute of Nanostructure Technologies
and Analytics and CINSaT
Heinrich-Plett-Str. 40
34132 Kassel
Germany

Nina Million
Technical Chemistry I and Center for Nano-
integration Duisburg-Essen (CENIDE)
University of Duisburg-Essen
Universitätsstr. 5–7
45141 Essen
Germany

Michael Monaghan
Department of Cell and Tissue Engineering
Fraunhofer IGB Stuttgart
Nobelstr. 12
70569 Stuttgart
Germany

Philipp Wilke
Interactive Materials Research
Institute for Macromolecular
and Technical Chemistry
RWTH Aachen University
Forckenbeckstr. 50
52074 Aachen
Germany

Julia C. Neubauer
Fraunhofer Institute for Biomedical
Engineering IBMT
Ensheimer Str. 48
66386 St. Ingbert
Germany

Joachim Nickel
University Hospital Würzburg
Chair Tissue Engineering
and Regenerative Medicine
Roentgenring 11
97070 Würzburg
Germany
and
Fraunhofer Institiute for Interfacial
Engineering and Biotechnology IGB
Project Group Regenerative Therapies
in Oncology
Roentgenring 11
97070 Würzburg
Germany

Bert Nitzsche
Max-Planck-Institut für Molekulare Zellbiologie
und Genetik
Photenhauerstraße 108
01307 Dresden
Germany

Stefan Nolte
Institute of Applied Physics
Abbe Center of Photonics
Friedrich-Schiller-University Jena
Max-Wien-Platz 1
07743 Jena
Germany
and
Fraunhofer Institute for Applied Optics
and Precision Engineering
Albert-Einstein-Straße 7
07745 Jena
Germany

Kerstin Obel
Fraunhofer Institute for Silicate Research ISC
Neunerplatz 2
97082 Würzburg
Germany

Ulrich Oertel
Leibniz-Institut für Polymerforschung
Dresden e. V.
Hohe Straße 6
01069 Dresden
Germany

Wolfgang Osten
Institut für Technische Optik
Universität Stuttgart
Pfaffenwaldring 9
70569 Stuttgart
Germany

Andreas Ostendorf
Ruhr University Bochum
Applied Laser Technologies
Universitätsstr. 150
44780 Bochum
Germany

Dirk Otto
University of Kassel
Institute of Physics and CINSaT
Heinrich-Plett-Str. 40
34132 Kassel
Germany

Simone Pentzien
BAM Bundesanstalt für Materialforschung
und -prüfung
Unter den Eichen 87
12205 Berlin
Germany

Ulf Peschel
Institute of Optics, Information and Photonics
University of Erlangen-Nürnberg
Haberstraße 9a
90158 Erlangen
Germany

Andrij Pich
Interactive Materials Research
Institute for Macromolecular
and Technical Chemistry
RWTH Aachen University
Forckenbeckstr. 50
52074 Aachen
Germany

Reinhart Poprawe
Laser Technology
RWTH Aachen University
52074 Aachen
Germany
and
Fraunhofer Institute for Laser Technology
52074 Aachen
Germany

Ulf Quentin
Institute of Photonic Technologies
University of Erlangen-Nuremberg
Konrad-Zuse-Straße 3
91052 Erlangen
Germany
and
Erlangen Graduate School
in Advanced Optical Technologies
Paul-Gordan-Straße 6
91052 Erlangen
Germany

Philipp Reichenbach
Institut für Angewandte Photophysik
Technische Universität Dresden
01062 Dresden
Germany

Kerstin Reimers
Department of Plastic, Hand-
and Reconstructive Surgery
Hannover Medical School
Carl-Neuberg-Str. 1
30625 Hannover
Germany

Carsten Reinhardt
Laser Zentrum Hannover
Hollerithallee 8
30419 Hannover
Germany

Martin Reininghaus
Laser Technology
RWTH Aachen University
52074 Aachen
Germany
and
Fraunhofer Institute for Laser Technology
52074 Aachen
Germany

Sören Richter
Institute of Applied Physics
Abbe Center of Photonics
Friedrich-Schiller-University Jena
Max-Wien-Platz 1
07743 Jena
Germany

Arkadi Rosenfeld
Max-Born-Institut für Nichtlineare Optik
und Kurzzeitspektroskopie (MBI)
Max-Born-Straße 2A
12489 Berlin
Germany

Cristian Sarpe
University of Kassel
Institute of Physics and CINSaT
Heinrich-Plett-Str. 40
34132 Kassel
Germany

Katja Schenke-Layland
Department of Women's Health
Research Institute for Women's Health
University Hospital of the Eberhard Karls
University Tübingen
Silcherstr. 7/1
72076 Tübingen
Germany

Michael Schmidt
Institute of Photonic Technologies
University of Erlangen-Nuremberg
Konrad-Zuse-Straße 3
91052 Erlangen
Germany
and
Erlangen Graduate School
in Advanced Optical Technologies
Paul-Gordan-Straße 6
91052 Erlangen
Germany

Andreas M. Schneider
Leibniz Universität Hannover
Institute of Inorganic Chemistry
Callinstraße 9
30167 Hannover
Germany

Anja Schröter
Department of Chemistry
University of Duisburg-Essen
Universitätsstr. 5
45141 Essen
Germany
and
CENIDE – Center for Nanointegration
Duisburg-Essen
NanoEnergieTechnikZentrum
Carl-Benz-Str. 199
47057 Duisburg
Germany

Helmut Seidel
Department of Micromechanics, Microfluidics
and Microactuators
Saarland University
Campus A5.1
66123 Saarbrücken
Germany

Arne Senftleben
University of Kassel
Institute of Physics and CINSaT
Heinrich-Plett-Str. 40
34132 Kassel
Germany

Sapna Shukla
Institute of Physical Chemistry
Friedrich-Schiller-University Jena
Helmholtzweg 4
07743 Jena
Germany
and
Leibniz Institute of Photonic Technology
Albert-Einstein-Straße 9
07745 Jena
Germany

Dirk Spaltmann
BAM Bundesanstalt für Materialforschung
und -prüfung
Unter den Eichen 87
12205 Berlin
Germany

Sönke Steenhusen
Fraunhofer Institute for Silicate Research ISC
Neunerplatz 2
97082 Würzburg
Germany

Michael Steger
Laser Technology
RWTH Aachen University
52074 Aachen
Germany
and
Fraunhofer Institute for Laser Technology
52074 Aachen
Germany

Florian Stelzle
Erlangen Graduate School in Advanced Optical
Technologies
Paul-Gordan-Straße 6
91052 Erlangen
Germany
and
Department of Oral and Maxillofacial Surgery
University Hospital Erlangen
Glückstraße 11
91054 Erlangen
Germany

Frank Stracke
Fraunhofer Institute for Biomedical
Engineering IBMT
Ensheimer Str. 48
66386 St. Ingbert
Germany

Martin Straub
Department of Biophotonics
and Laser Technology
Saarland University
Campus A5.1
66123 Saarbrücken
Germany

Johannes Strauß
Institute of Photonic Technologies
University of Erlangen-Nuremberg
Konrad-Zuse-Straße 3
91052 Erlangen
Germany
and
Erlangen Graduate School
in Advanced Optical Technologies
Paul-Gordan-Straße 6
91052 Erlangen
Germany

Thomas Taubner
Institute of Physics (IA) and JARA – Fundamentals of Future Information Technologies
RWTH Aachen University
52056 Aachen
Germany

Nico Tucher
Fraunhofer Institute for Silicate Research ISC
Neunerplatz 2
97082 Würzburg
Germany

Andreas Tünnermann
Friedrich-Schiller-Universität Jena
Abbe Center of Photonics
Institute of Applied Physics
Albert-Einstein-Straße 15
07745 Jena
Germany
and
Abbe School of Photonics
Friedrich-Schiller-Universität Jena
Max-Wien-Platz 1
07743 Jena
Germany
and

Fraunhofer Institute for Applied Optics
and Precision Engineering
Albert-Einstein-Straße 7
07745 Jena
Germany

Aisada Uchugonova
Saarland University
Department of Biophotonics
and Laser Technology
Campus A5.1
66123 Saarbrücken
Germany

Peter M. Vogt
Department of Plastic, Hand-
and Reconstructive Surgery
Hannover Medical School
Carl-Neuberg-Str. 1
30625 Hannover
Germany

Brigitte Voit
Leibniz-Institut für Polymerforschung
Dresden e. V.
Hohe Straße 6
01069 Dresden
Germany

Wolfgang Wagner
Helmholtz Institute for Biomedical Engineering,
Stem Cell Biology, and Cellular Engineering
Laser Technology
RWTH Aachen University
52074 Aachen
Germany

Kathrin Wallat
Institute for Inorganic Chemistry and Center
for Nanointegration Duisburg-Essen (CeNIDE)
University of Duisburg-Essen
Universitätsstr. 5–7
45117 Essen
Germany

Heike Walles
University Hospital Würzburg
Chair Tissue Engineering
and Regenerative Medicine
Roentgenring 11
97070 Würzburg
Germany
and
Fraunhofer Institiute for Interfacial Engineering
and Biotechnology IGB
Project Group Regenerative Therapies
in Oncology
Roentgenring 11
97070 Würzburg
Germany

Thomas Winkler
University of Kassel
Institute of Physics and CINSaT
Heinrich-Plett-Str. 40
34132 Kassel
Germany

Matthias Wollenhaupt
University of Oldenburg
Institute of Physics
Carl-von-Ossietzky-Straße 9–11
26129 Oldenburg
Germany

Herbert Wolter
Fraunhofer Institute for Silicate Research ISC
Neunerplatz 2
97082 Würzburg
Germany

Lei Zheng
Laser Zentrum Hannover
Hollerithallee 8
30419 Hannover
Germany

Bastian Zielinski
University of Kassel
Institute of Physics and CINSaT
Heinrich-Plett-Str. 40
34132 Kassel
Germany

Felix Zimmermann
Institute of Applied Physics
Abbe Center of Photonics
Friedrich-Schiller-University Jena
Max-Wien-Platz 1
07743 Jena
Germany

Heiko Zimmermann
Fraunhofer Institute for Biomedical
Engineering IBMT
Ensheimer Str. 48
66386 St. Ingbert
Germany
and
Department of Molecular
and Cellular Biotechnology
Saarland University
66123 Saarbrücken
Germany

Urs Zywietz
Laser Zentrum Hannover
Hollerithallee 8
30419 Hannover
Germany

A. Ostendorf and K. König

Tutorial

Laser in material nanoprocessing

1 Introduction

The American engineer and physicist Dr. Theodore "Ted" Harold Maiman invented the first working laser on May 16, 1960. The journal *Physical Review Letters* rejected his manuscript but *Nature* finally published the paper on August 6 the same year [1]. He received a US patent for his invention on Nov 14, 1967 [2].

The first laser was a ruby laser emitting in the red spectral region at 694.3 nm. This novel artificial light source, which provided intense coherent radiation, opened up completely new technologies and applications such as the introduction of nonlinear optics. The theoretical basis of two-photon technology was provided by the PhD student Maria Göppert in 1929 [3], but at that "pre-laser" time, there was no light source to prove her hypothesis of two-quantum transitions. In 1961, shortly after Maiman's invention, second harmonic generation (SHG) and two-photon excited fluorescence were demonstrated [4, 5]. Nonlinear optics was born. The simultaneous absorption of multiple photons resulted in multiphoton ionization, optical breakdown, and plasma formation.

Also in 1961, the first laser radiation effects on eyes were studied using live rabbits [6–8]. Somewhat later a ruby laser was employed to destroy a retinal eye tumor in humans. Goldman reported on the pathology of the effect of laser beams on skin [9, 10]. Laser medicine began.

In 1962, Brech and Cross achieved a ruby laser induced microemission of materials and introduced laser-induced breakdown spectroscopy (LIBS) [11]. In the same year, the LIBS instrument was commercialized as *Laser Microprobe* by the US company *Jarrell-Ash*. An advanced laser microscope, LMA 1 (laser micro analyzer), was developed by VEB Carl Zeiss Jena in 1964. One year later, Birnbaum observed laser-induced periodic surface structures (LIPSS) in semiconductors, also termed ripples, with a periodicity close to the exposure wavelength [12].

At that time, several other laser types had been invented. The first semiconductor laser was realized in 1961, the HeNe laser in 1962, the CO_2 laser (10.6 μm), the Nd:YAG laser (1064 nm), and the dye laser in 1964. The laser printer was invented in 1973. One year later, the barcode scanner was introduced.

A major step was the invention of the excimer laser. Now a powerful ultraviolet (UV) laser source with a wavelength of 308 nm and shorter became available. Nanoprocessing, meaning the fabrication of feature sizes below 100 nm, was now realistic. Two major applications of the excimer laser in the field of material processing

today are photolithography for the integrated circuit (IC) industry and the shaping of the human cornea for the treatment of shortsightedness, a technique called LASIK.

In addition to the availability of short wavelength laser sources, a further important technological step for the realization of material nanoprocessing occurred. In particular, bulk nanoprocessing became possible with the generation of ultrashort laser pulses. As shown in this book, even the use of long wavelength infrared radiation enables nanoprocessing when femtosecond lasers are employed.

"Conventional" lasers such as the ruby and excimer laser typically operate with nanosecond or even longer pulses. For the first time, pulses in the picosecond-range were generated by passive mode-locking of a ruby laser in 1965 [13].

The first femtosecond laser was realized in 1976 using dye lasers [14]. In 1981, the first sub-100 fs laser pulse was generated [15]. Using a mode-locked femtosecond dye laser, the first two-photon femtosecond laser scanning microscope was introduced in 1990 [16]. At that time, the solid state mode-locked Titanium:sapphire lasers with a spectral bandwidth of more than 200 nm began to replace the femtosecond dye laser systems [17].

Using ultrashort laser pulses can cause the ablation of the surface as well as in bulk areas of many kinds of materials, leading to very precise machining results with minimal damage to the micro-environment and even nano-environment. This includes even the nanomachining of delicate materials with high heat conductivities or comparatively low melting temperatures, such as metals, as well as optically transparent non-organic and organic materials such as cells and tissues. This book focuses mainly on the use of long wavelength ultrashort laser pulses for nanoprocessing.

2 Laser-material interactions

Most laser-material interactions are based on linear or nonlinear absorption. Exceptions are reflection, scattering, diffraction, and other forms of changes of the photon direction. In fact, these changes are employed in optical coherence tomography (OCT), SHG microscopy, and optical trapping, where the change of momentum results in optical forces. Depending on the interaction of photons with atoms or molecules of the materials, light can be scattered elastically or inelastically. In elastic light scattering processes, e.g. Rayleigh scattering, the scattered light exhibits the same wavelength as the incident light, whereas in inelastic scattering, e.g. in Raman scattering, the frequency of the scattered light is shifted towards a higher or lower value.

One-photon absorption takes place along the beam path depending on the spectral absorption behavior. Selective absorption of the spectrum is the origin of the color of many optical materials. If a crystal appears red, this can be attributed to the absorption of the complementary colors blue and green. All materials absorb UV light due to absorption by bound electrons. Typically, the UV laser beam has a low light penetration depth of some micrometers. Luminescence can be observed in many types

of materials along with absorption. Luminescence, which is a spontaneous emission process, occurs if a material is transferred prior to the emission to an excited state. Luminescence light can be emitted in all directions, its frequency is usually different from the excitation frequency. Depending on whether a spin change of the electronic state is involved, luminescence can occur either as fluorescence or phosphorescence, the latter accompanied by a change of the total spin.

In contrast to linear or single-photon absorption, multiphoton absorption depends strongly on the applied light intensity. For many transparent materials, the intensity of the visible or near infrared laser beam has to be on the order of GW/cm^2 (10^9 W/cm^2) in order to achieve multiphoton absorption. Therefore, nonlinear absorption is induced most efficiently only in the center of a small laser spot of a tightly focused laser beam. This allows for sub-100 nm processing even when the laser spot size is about half a micrometer.

Typically, small laser spots are required in single-photon and multiphoton nanoprocessing. According to Ernst Abbe's famous diffraction formula (Fig. 1), the spot size d of a "perfect" laser beam such as a Gaussian beam depends on the wavelength and numerical aperture (NA) of the focusing optics. NA is defined as the product of the refractive index of the environment, such as 1.00 for air, times the sinus of half the incident beam angle after transmission through the optics. This means that the typical minimum spot size d for non-UV radiation is about 200 nm.

$$d = \frac{\lambda}{2 \cdot \mathrm{NA}}$$

For a spatial profile of a laser beam with different TE-modes, the minimum spot size d can be calculated according to

$$d = \frac{2 \cdot M^2 \cdot \lambda}{\pi \cdot \mathrm{NA}} .$$

Different methods can therefore be applied in order to achieve a small laser spot size: A laser system with good spatial beam quality can be chosen (M^2 close to 1.0; M^2 is defined as the beam parameter product divided by the corresponding product for a diffraction-limited Gaussian beam, with the beam parameter product as the product of focal radius and far field divergence angle), but also a short wavelength λ or a high NA which can be as high as 1.5, when using special immersion oil objectives. High NA values imply a short working distance.

Recent developments in the field of laser sources have led to lasers with excellent beam quality, also in the UV spectral range. Besides spatial optimization, also temporal measures can be taken to influence the intensity of laser radiation and the duration of the interaction between laser and material. Using pulsed lasers, the peak power can reach multiple orders of magnitude higher values, than the average power.

An illustrative overview is provided in Fig. 2, where state-of-the-art laser systems are classified according to their pulse peak power and pulse duration.

Fig. 1: Photograph of a sculpture with Abbe's famous formula in the city of Jena, where Ernst Abbe worked as university professor and later as director of the ZEISS factory.

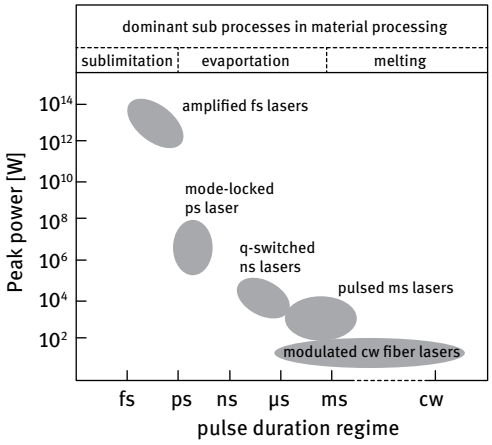

Fig. 2: Lasers for micro- and nanoprocessing classified according to their temporal pulse length and peak power.

3 UV laser nanoprocessing

According to conventional (linear) optics and Abbe's law, there are some established methods for shifting the diffraction limit to smaller structure sizes. A mature technology is optical lithography using UV laser radiation, i.e. making use of the linear scaling of the resolution limit with the exposure wavelength. Optical lithography is the standard manufacturing technology in the semiconductor industry and has been further developed during the last five decades to allow minimum structure sizes far below the micrometer range. This technology has been driven by the demand of higher transistor and integration density of microprocessors and storage components. Figure 3 depicts the development of microprocessors during the last 40 years. Gordon Moore, one of the founders of computer processor giant Intel®, postulated exponential growth (every

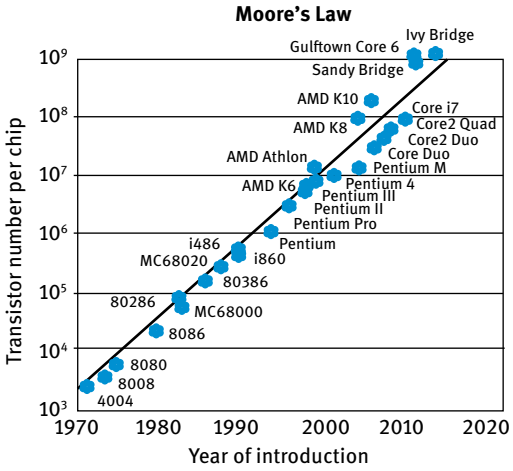

Fig. 3: "Moores' Law" was predicted by the co-founder of Intel®, Gordon Moore, in 1965 and slightly corrected in 1975. The graph shows its validity until today.

18 months the complexity of integrated circuits will be doubled) and his forecast has turned out to be pretty correct so far.

The common technology of optical lithography is based on the transfer of a mask pattern by an optical system onto a semiconductor substrate. Silicon substrates coated by a thin resin material are mostly employed in microelectronics. The resin is modified by UV radiation and acts as a resist material for etching processes, after it has been developed. The performance of optical lithography can be impressively demonstrated by the latest generation of nanoprocessors, where minimum structure sizes of 22 nm on wafer diameters of 300 mm are realized (Fig. 4). Additional optical and chemical effects have been explored in order to achieve such small structures when applying an ArF excimer laser at 193 nm. Figure 5 shows the different processing steps in the semiconductor industry.

The surface which is going to be structured, is initially coated by a radiation sensitive thin resin (photoresist). Different photoresists, based on either polymers or epoxy resins, can be used. In order to enhance the photochemical reaction, additional photosensitive molecules are mixed into the resin. In negative tone resist materials the solubility for the developer is decreased on illumination with UV-radiation. Weak π-bonds between the resist molecules are transferred into strong intermolecular σ-bonds. In contrast, in positive tone materials, the solubility is increased. In this case the resist material has been solidified during thermal pretreatment. The UV-radiation then breaks the bonds and, as a consequence, increases solubility in the subsequent development process. Positive resists are usually made up of three components: (i) a resin which is readily soluble in an alkaline developer (often novolak); (ii) a photoactive component (often diazonaphthoquinone, in short: DNQ), which ensures that the resin in the unexposed state is insoluble; and (iii) the solvent (often esters from alcohols and carboxylic acids), which makes the resin flowable.

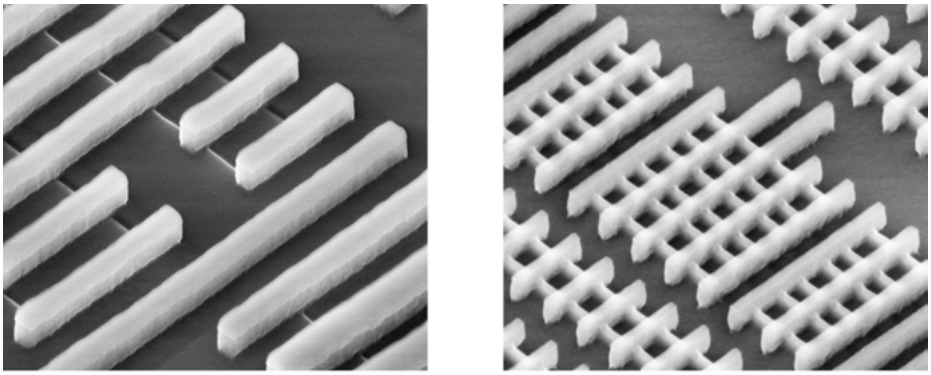

Fig. 4: 3D field effect transistors with 32 nm structure sizes (a) and 22 nm structure sizes (b) manufactured by double pattern UV immersion lithography. Source: Intel Inc. (left Sandy Bridge, right Ivy Bridge).

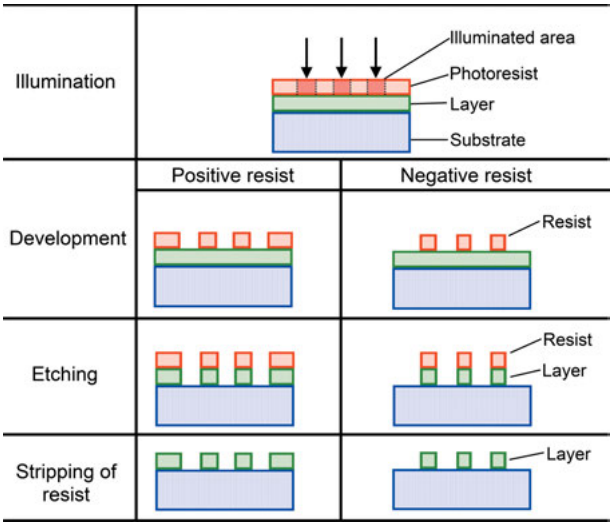

Fig. 5: Processing steps in optical lithography using negative and positive resists.

The exposure is typically realized by mask projection, while the mask is composed of a chrome-on-glass setup. The choice of positive or negative tone lithography is determined by the type of structure. The larger the area of the mask covered by chrome, the smaller the scattering will be in the beam guiding system. If only small single structures (e.g. micro-vias) have to be processed, positive tone materials are preferably used. On the contrary, if only single structures have to be generated, negative tone resists offer some advantages. After the essential processing step (etching for geometrical structures, doping for the generation of different semiconductor properties, coating of thin layer structures), the remaining photoresist material is finally stripped off.

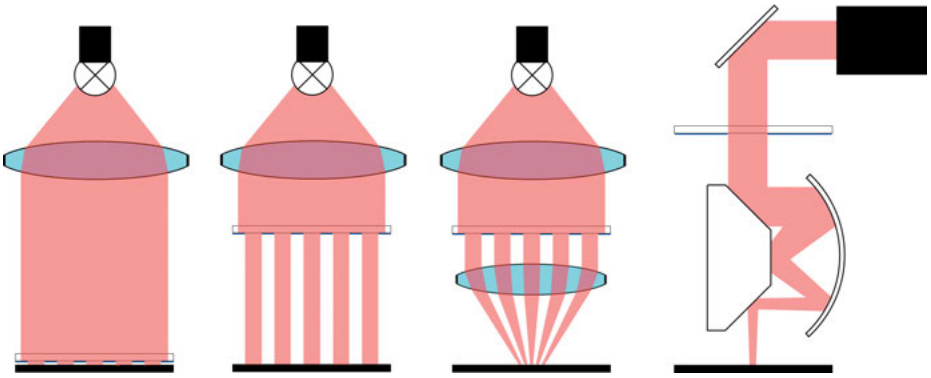

Fig. 6: Different illumination techniques in photolithography. From left to right: contact exposure, proximity illumination, projection patterning, and optimized projection patterning.

In addition to the resin properties and related chemical processes, the exposure setup is of crucial importance for the result. Ideal structures are obtained only at a controlled and uniform illumination. Basically, three exposure variations (Fig. 6) can be distinguished: contact exposure, proximity exposure, and projection exposure.

In the case of contact exposure, the mask is "pressed" by vacuum directly onto the coated wafers covering the entire wafer surface. During exposure, the structures are transferred to the photoresist by a scale of 1 : 1. Since both the chromium pattern on the mask substrate and the photoresist layer are very thin, near field diffraction of the light can occur on the edges of the chrome patterns. The contrast between exposed and unexposed areas is very high using this method. The problem with this form of exposure is the need to push the bottom of the mask with the chromium into the soft resist structure. This problem can be overcome by proximity exposure, in which the mask is placed at a small distance above the wafer surface. However, this decreases the resolution and contrast, since diffracted light can penetrate the gap between wafer and mask. The more complex and expensive mask projection is used for larger quantities and smaller structures. The lower the structure size, the more complex the production of 1 : 1 masks is. Even the slightest error in mask production is accurately transferred. In mask projection the masks are transferred for example on a scale of 5 : 1. This reduces mask production, costs significantly. Such illumination tools often operate in the step-and-repeat mode, i.e. not the entire wafer is uniformly illuminated but only a small field, which then, gradually strung together, covers the entire wafer. To minimize chromatic aberrations and absorption effects, small, modern mask projectors are often designed based on reflective optics. When using a UV laser with a narrow linewidth as an illumination device, perfectly crafted lenses can be used. Today, modern mask projection with an ArF laser at 193 nm is often used.

4 Femtosecond laser technology

Alternative to the use of UV laser radiation, very short pulses are able to effectively reduce structure sizes by their unique interaction with materials. The short interaction time in conjunction with extremely high intensities in the focal area, can induce nonlinear absorption for example. The general method for generating ultrashort laser pulses with pulse duration in the ps- to fs-range, is mode-locking. Pulses in the ps-range were generated for the first time by passive mode-locking of a ruby laser shortly after its discovery [13].

Mode-locking can be effectively realized for laser media with a relatively broad laser transition bandwidth and thus, for lasers with a broad amplification profile, in which numerous longitudinal modes can oscillate simultaneously. Assuming that $2N + 1$ modes oscillate with the same amplitude E_0 and a constant phase relation between the modes, the resultant field amplitude $E_{\text{tot}}(t)$ can be expressed as a function of the time t:

$$E_{\text{tot}} = E_0 \sum_{n=-N}^{N} e^{2\pi i\left[(\nu_0 + n\Delta\nu_{k,k+1})t + n\phi\right]},$$

with the central mode frequency ν_0 and the phase difference ϕ, while the frequency distance between two neighboring longitudinal modes $\Delta\nu_{n,n+1}$ is given by

$$\Delta\nu_{n,n+1} = \frac{c}{2L}$$

since the resonator length L must be an integer multiple of half the wavelength. It is assumed that at $t = 0$ all modes fulfil the phase condition. Due to their different frequencies, they leave the phase condition immediately after this point in time. However, constant phase relation occurs at periodic time intervals, where the frequency distance is an integer of the inverse cycle time of the resonator. At these points in time, all modes are at their field maximum, so that the superposition of the $2N + 1$ modes reaches its highest theoretical value $(2N + 1)E_0$. In the case of uncorrelated modes, this value would never be reached.

The resultant total irradiance $I_{\text{tot}}(t)$ is given by:

$$I_{\text{tot}}(t) = I_0 \left| \frac{\sin\left[(2N + 1) \cdot (2\pi\,\Delta\nu_{n,n+1}t + \phi)/2\right]}{\sin\left[(2\pi\,\Delta\nu_{n,n+1}t + \phi)/2\right]} \right|^2$$

The superposition of the single modes with a constant phase difference leads to laser pulses with a duration τ_p

$$\tau_p = \frac{1}{2N + 1}\frac{1}{\Delta\nu_{n,n+1}}$$

and a temporal distance between the laser pulses Δt_p

$$\Delta t_p = \frac{2L}{c}$$

The peak intensity I_p of the single pulses is given by:

$$I_p = (2N + 1)^2 I_0 .$$

Thus, the peak intensity is $(2N + 1)$ times the sum of the single intensities when the oscillating modes are statistically coupled. In order to achieve phase coupling between the oscillating modes, different methods can be applied within the laser resonator. They are subdivided into active and passive mode-locking techniques.

Active mode-locking

Active mode-locking implies that the resonator is equipped with a modulator close to one of the resonator mirrors. The modulator is triggered by an external signal in such a way that a sinusoidal modulation of the losses or the optical path in the optical resonator takes place with a frequency dv. The frequency dv is equal to the frequency difference $\Delta\, v_{n,n+1}$ of the longitudinal modes. Initially, this loss modulation represents an amplitude modulation AM with the frequency dv of the mode which starts to oscillate first at a maximum amplification at the frequency v_0. This modulation then induces the neighboring modes with the frequencies $v_0 \pm dv$, which experience an amplitude modulation as well. This process continues until all longitudinal modes within the amplification bandwidth of the laser are coupled and synchronized. The induction of the side bands automatically results in the constant phase relation.

When observing this phenomenon in the time domain instead of the frequency domain, the modulation frequency dv would correspond to the time period $T = 2L/c$, which in turn corresponds to a full cycle inside the resonator. Thus, from a temporal point of view, the electromagnetic waves passing inside the resonator keep coming across the same modulation cycle. This means that all parts of the wave are attenuated, except for the part which passes the modulator just in the exact moment in which the loss is just about 0. Therefore, short-pulsed radiation concentrates in the time regions with minimum modulation losses. A similar situation arises when modulation of the refractive index takes place instead of attenuation. By changing the refractive index, the optical path is modified. Active mode-locking can be used not only in pulsed lasers, but also in cw-lasers [18]. Generally, electro-optic and acousto-optic modulators can be used in both cases.

Passive mode-locking

Passive mode-locking is based on the same principle as active mode-locking, that is a temporal modulation of the resonator losses. In contrast to active mode-locking, the laser system itself determines the point in time at which the losses are at their minimum [19]. The loss modulation takes place either by means of an intensity dependent

absorption caused by a saturable absorber [20] or the use of the Kerr effect [21]. Due to the fact that many modes oscillate simultaneously in an oscillator with a broad amplification bandwidth, the intensity initially shows a statistic temporal behaviour. Such time dependent intensity automatically causes a temporal loss modulation in the absorber. This gradually leads to an arrangement with a constant phase relation between the individual longitudinal modes.

In passive mode-locking using saturable absorbers, mode-locking starts from normal noise fluctuations in the laser cavity. Once a noise spike exceeds the threshold of saturating an absorber, the losses decrease, and gain increases in the round trip. The thus initiated spike begins to grow, and becomes shorter, until a stable pulse width is obtained. The advantage of this setup is that the reflected front edge of the pulse and the approaching back edge of the pulse interfere inside the absorber, which results in saturation at lower intensities. For the generation of ultrashort laser pulses in solid-state lasers currently Kerr lens mode-locking is usually applied. This method uses the nonlinear Kerr effect, i.e. the dependency of the refractive index on incident intensity

$$n = n_0 + n_2 \cdot I\,.$$

If a laser beam with high intensity and Gaussian profile passes a Kerr medium, the refractive index is not spatially constant due to the intensity profile. According to the high intensities close to the center of the laser beam, the refractive index and, accordingly, the optical path is higher than in the outer regions. Consequently, the Kerr medium acts as a gradient index lens (Kerr lens). For Kerr lens mode-locking, an aperture is installed in the focal point of the Kerr lens. The focused pulsed beam passes through while most of the low intensity radiation (Fig. 7) is blocked. This intracavity aperture enables the mode-locked pulses with high intensities to pass through and blocks the modes with statistical phase relation and low intensity level until they get the right phase relation by accident.

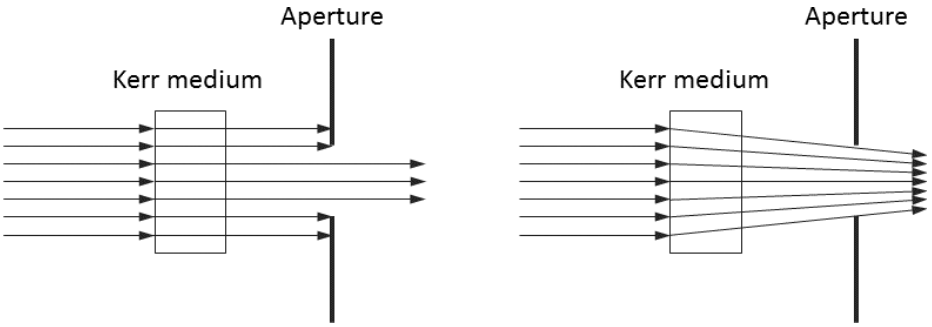

Fig. 7: Principle of Kerr lens mode-locking. The figure on the left represents the low intensity regime. The figure on the right becomes valid for high intensities.

5 Multiphoton effects

Multiphoton effects were predicted by the young PhD student and later Nobel Prize winner for physics, Maria Goeppert in 1929 [3]. Her theory was proven in 1961.

Figure 8 demonstrates the principles of two-photon excited fluorescence, two-photon photochemistry, and multiphoton ionization.

Two-photon fluorescence applies typically two NIR photons at twice the wavelength normally required to excite the visible fluorescence. Because two-photon absorption spectra are broad, the excitation with a fs laser beam at a certain wavelength in the range of 700 to 1200 nm results in the excitation of a variety of fluorophores. Note that a 10 fs laser beam covers a wavelength range of about 100 nm.

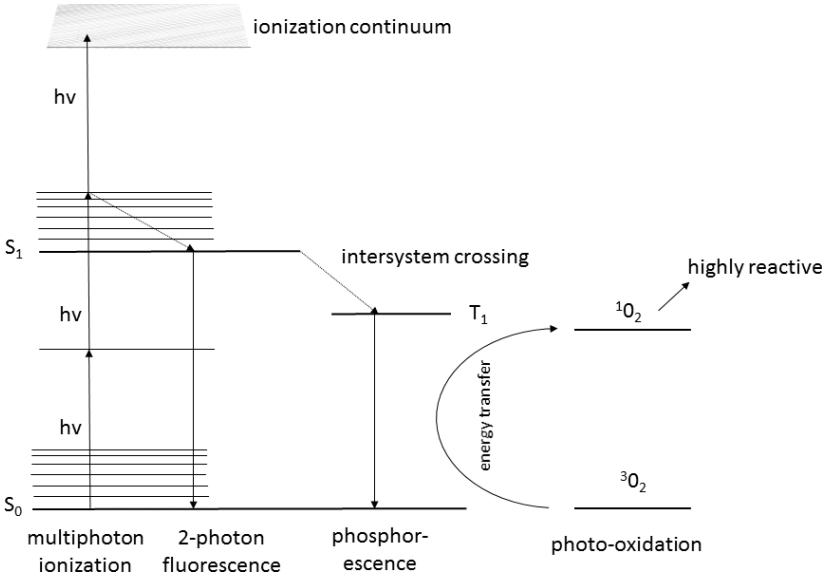

Fig. 8: Two-photon excited fluorescence, two-photon photochemistry, and multiphoton ionization.

Two-photon fluorescence is mainly employed in the laser microscopes of cell biologists and neurobiologists. Non-amplified 100-fs NIR laser resonators at a high repetition frequency of 80 MHz with mean *in situ* powers of 1–50 mW and transient GW/cm^2 light intensities at the sample, are typically employed.

Note that, in principle, two-photon effects can be generated even with highly focused cw-laser beams such as those used as optical traps with powers of some hundred milliwatts [22]. However, the use of femtosecond laser pulses is by far more efficient due to the high "transient" peak power and a typical low beam dwell time of some microseconds per pixel for fluorescence photon collection, in laser scanning microscopes.

With special long-working distance objectives, a long-wavelength NIR excitation, and clearing agents, deep-tissue imaging of several millimeters has been performed in the brains of live mice.

Two-photon and three-photon chemistry have been realized based on photooxidation processes from the long-lived triplet state to induce photodynamic reactions in biological tissues and cells. For photolithography, conventional photoresists such as SU-8 can be easily employed and "photoactivated" by intense visible and NIR laser beams.

When using high intensities such as TW/cm^2, four or more photons can be absorbed simultaneously, resulting in the generation of free electrons from the material. Multiphoton ionization occurs. When a certain density of free electrons is exceeded, plasma is generated. When using a liquid microenvironment, plasma-filled cavitation-bubbles can be observed. Furthermore, shock waves are generated. Destructive effects based on cavitation bubble dynamics and shock wave generation are termed photodisruptive effects. Photodisruptive effects scale with pulse energy. In order to avoid collateral effects, the lowest pulse energy possible should be employed for nanoprocessing.

6 Laser-matter interactions for ultrashort laser pulses

Laser ablation is the removal of material from a substrate by direct absorption of laser energy. The onset of ablation occurs above a threshold fluence, which depends on the absorption mechanism, particular material properties, surface structure, morphology, the presence of defects inside the material, and on laser parameters such as wavelength and pulse duration. Typical threshold fluences for metals are between 1 and $10\,J/cm^2$, for inorganic insulators between 0.5 and $2\,J/cm^2$ and for organic materials between 0.1 and $1\,J/cm^2$. The threshold may decrease with multiple pulses due to accumulations of defects. Above the ablation threshold, the thickness or volume of material removed per pulse, typically shows a logarithmic increase with fluence.

A variety of mechanisms for material removal may be involved in laser ablation processes, depending on the particular material system and laser processing parameters such as wavelength, fluence, and pulse length. At low fluences, photothermal mechanisms for ablation include material evaporation and sublimation. For multicomponent systems, the more volatile species may be depleted more rapidly by changing the chemical composition of the remaining material. With higher fluence, heterogeneous nucleation of vapor bubbles leads to normal boiling. If material heating is sufficiently rapid for the material to approach its thermodynamic critical temperature, rapid homogeneous nucleation and expansion of vapor bubbles lead to explosive boiling (phase explosion) removing solid and liquid material fragments.

When the excitation time is shorter than the thermalization time in the material, non-thermal, photochemical ablation mechanisms can occur. For instance, with ultra-

short pulses, direct ionization and the formation of a dense electron-hole plasma can lead to athermal phase transformations, direct bond-breaking and explosive disintegration of the lattice through electronic repulsion (Coulomb explosion).

In certain non-metals such as polymers and biological materials with relative long thermalization times, photochemical ablation can still occur with short-wavelength nanosecond lasers, producing well-defined ablation regions with small heat affected zones. In all cases, material removal is accompanied by a highly directed plume ejected from the irradiated zone. The dense vapor plume may contain solid and liquid clusters of material. Furthermore, the ionization of vapor during high laser intensity irradiation may lead to the generation of plasma due to the growing electron density. At this stage, the high-density plasma plume strongly absorbs the laser energy by free carrier absorption and attenuates the laser energy reaching the target. The plasma plume expansion could also lead to the generation of shockwaves. In addition, the laser-matter interactions are associated with mechanical stress due to thermal expansion or the propagation of shockwaves, which can cause another kind of ablation by spallation if the amplitude exceeds the binding strength of the lattice within the target.

7 Biomedical applications of nanoprocessing

Femtosecond NIR lasers have been employed as a medical treatment on millions of short-sighted people to optically generate the required tissue flap of several millimeters in diameter for LASIK procedures [23]. These femtosecond laser systems replace current micromechanical tools for flap generation, so-called microkeratomes. Furthermore, fs lasers are employed in ophthalmology to process the ocular lens. Relatively high pulse energies and focusing optics with a relatively low NA are employed, which enables micromachining but not nanomachining.

Medical femtosecond laser systems, such as multiphoton tomographs, have been employed for diagnostic purposes, such as early diagnosis of the skin cancer malignant melanoma [24]. The lateral resolution of these innovative high-resolution medical imaging tools is about 300 nm and the axial resolution is about 1–2 μm. Therefore, this medical imaging device is not a "real" nanotechnology device even if it is possible to image sub-100 nm single elastin fibers deep in the skin, single intratissue ZnO sunscreen particles, and tattoo nanoparticles.

The same submicron resolution applies to two-photon microscopes as the major imaging tool of cell biologists studying living cells and the brains of live transgenic mice.

Femtosecond laser nanoprocessing in living cells is feasible. Cutting and drilling with feature sizes below 100 nanometers were first demonstrated by König et al. in 1999 [25]. The group was able to nanodissect a single chromosome within a live PTK

cell without collateral effects. The cell survived and divided. The authors called this procedure nanosurgery.

Targeted transfection has become a major application of nanoprocessing of living cells, where a single foreign DNA plasmid is introduced to a cell by transient opening of the cell's membrane, called optoporation [26]. Typically, the membrane is closed within 5 seconds due to self-repair processes.

One of the chapters of this book reports for the first time on the use of femtosecond laser transfection to introduce a cocktail of 4 plasmids into live skin cells with the purpose to realize virus-free optical reprogramming [27]. Interestingly, an extremely low mean power of some milliwatts is sufficient to realize drilling, cutting, and ablation of biological targets when using very ultrashort NIR picojoule laser pulses of 10 femtosecond pulse width and 85 MHz repetition frequency. The journal *Nature Photonics* termed this novel nanoprocessing technique "low-power nanosurgery" [28].

8 Technical applications

Similar to biological applications, high intensity laser pulses can be used to structure surfaces with nanometer accuracy or to use nonlinear absorption in order to induce modifications inside the bulk of a work piece. The latter is limited to materials which are transparent for the fundamental wavelength.

In surface patterning, a laser beam is scanned over a surface in a defined scheme while modifying the surface. Depending on the pulse energy, the focusing conditions and the type of material, the energy melts or ablates the material. For very high intensities, the material is sublimated directly from the solid phase. If the energy of a femtosecond laser pulse is just above the melting threshold, hydrodynamic forces can generate melt pool dynamics, which result in nanojets, i.e. very small metal peaks on the surface which exhibit quite high reproducibility. Reducing the energy by a small amount will result in polarization ripples. These kinds of regular structures have been observed in different types of materials. Their orientation is highly dependent on the orientation of the electric field vector of the incident light. Their origin is still debated by different research groups and so far, consistent models are only available for some cases. A more detailed description of the formation of low-spatial frequency and high-spatial frequency laser-induced periodic surface structures (LIPSS) will be presented in this book. A commercial application is the use of ripple formation to change the light absorption on silicon surfaces. If ripples are generated by multi-pulse exposure in SF_6 atmosphere on silicon surfaces, the reactive gas supports efficient etching. The resulting cone-like structures allow multiple reflection and absorption processes on the surfaces, increasing the total absorbance in a large spectral window. Further applications of highly oriented ripples are in microfluidic channels in order to control the fluid flow on channel or chamber surfaces. Higher laser pulse energies allow ablation of the material, directly generating holes, grooves or cuts. Another commercial appli-

cation of ultrashort laser cutting can be found in dicing of ultrathin semiconductor wafers.

Transparent media can be modified, by depositing the energy in the bulk of the material. Glass materials can be modified, for example by nonlinear absorption. Low energy femtosecond pulses, which are tightly focused below the surface, cause material changes in the vicinity of the focal point, resulting in local modifications of the refractive index. If lines are written by placing pulses next to each other, 3D waveguide structures are generated. Another often noted technique is the production of fiber Bragg gratings (FBG) in optical fibers, which are used in fiber lasers, optical telecommunication systems, and sensor applications. The standard fabrication techniques for FBG are based on the exposure to cw or long pulsed UV laser sources to induce a periodic variation of the refractive index in the fiber core. Therefore, the core is doped with germanium or hydrogen loading.

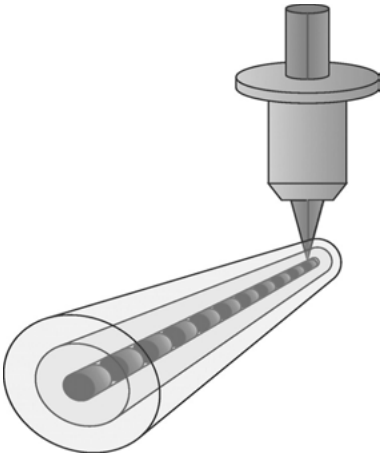

Fig. 9: Principle of FBG generation via laser-induced volume modification of transparent materials.

Another highly interesting field of investigation is the focusing of ultrashort laser pulses inside transparent polymers, inorganic crystals, and glasses, leading to local modifications of the properties of the irradiated sample without co-doping of photosensitive materials. Figure 9 shows the principle of FBG generation in fibers. Photosensitization is difficult in rare earth doped fibers, which are used in fiber lasers with FBGs as internal high reflective mirrors. The main application field here is direct writing of waveguide structures, based on a controlled change of the refractive index in laser-modified zones. The presence of ultrashort pulsed lasers has expanded the field of material processing in 3D laser micro- and nanofabrication.

To provide crack-free laser writing of permanent structures with positive refractive index changes for waveguiding applications, laser irradiation should be applied gently in an accumulative manner avoiding conditions of material failure. Several accumulation mechanisms are responsible for gentle modification of transparent ma-

terials towards waveguiding properties. At high repetition rates, the energy absorbed at the focal volume from each pulse, has no time to diffuse out before the subsequent pulse arrives, forming a point source of heat. The process of heat accumulation upon waveguide writing can be controlled by several means, including variations of pulse energy, pulse repetition rate, scanning speed, and focusing conditions.

Under intermediate irradiation conditions between the nonthermal and thermal regimes of modification of transparent materials, an intriguing phenomenon of self-assembled volume nanograting formation becomes possible. This has attracted strong interest for studies of fundamental physical mechanisms as well as for potential applications. Different research groups all over the world have demonstrated that self-organized volume nanogratings (NG) can be produced in a controlled manner, erased, and rewritten in fused silica glass. They are formed as a result of the accumulative action of several thousand linearly polarized laser pulses focused inside the material bulk and the NG layers, which are always perpendicular to the light polarization vector. It is intriguing that only three materials, fused silica, sapphire, and TeO_2, allow the inscription of the NG structures in their bulk. Nevertheless, the mechanism of NG formation is still debated and intrinsically unclear.

The generation of plasma standing waves excited by the polarized light, nanoplasm self-organization, or defect formations, are discussed as possible mechanisms. Many important applications of these amazing structures have been proposed for the development of various integrated optical and microfluidic devices and rewritable 3D optical memory storage. The grating period, usually in the range of 100 to 300 nm, decreases with laser exposure time at a fixed pulse energy, whilst increasing with pulse energy for a fixed number of applied laser pulses. NG exhibit extremely large temperature stability up to 1150 °C. The high degree of control of the structural parameters allows the fabrication of integrated highly precise phase elements, such as quarter- and half-wave plates.

In specific types of glass, a modification of the material is generated after illumination. This physical-chemical modification allows subsequent selective etching by KOH or HF. When writing a line or a certain volume, the material can then be removed by etching. Microchannels with extreme aspect ratios (up to 100) can be produced in glass or sapphire using selective laser-induced etching (SLE). Microvalves and micropumps have also been produced. The same technique has been extended to fabricate free-space optics, such as micromirrors and micro-optical lenses in glass materials.

9 Summary and outlook

UV nanosecond lasers are the major nanoprocessing tools in today's Integrated Circuit industry. Future extreme ultraviolet technology will employ radiation at a wavelength of 13 nm. However, ultrashort laser pulses in the femtosecond range can also realize nanoprocessing, even when operating at higher wavelengths. Feature sizes one

order of magnitude smaller than the laser wavelength or less, are feasible. Furthermore, 3D nanomachining can easily be performed, such as 3D two-photon lithography and STED lithography for rapid prototyping. In-bulk nanomachining in transparent materials can be performed in contrast to standard UV nanoprocessing. Deep sub-diffraction optical two-beam lithography with 9 nm feature size and 52 nm two-line resolution has been reported based on two-photon polymerization and single-photon inhibition [29].

All-diode-based, low-cost, compact turn-key femtosecond lasers will become available within the next years. This will significantly change the market for industrial nanomachining and non-linear imaging.

References

[1] T. H. Maiman: Stimulated optical radiation in ruby. *Nature* 187 (1960) 493–494.
[2] C. Townes: Theodore H. Maiman (1927–2007). Maker of the first laser. *Nature* 447 (2007) 654.
[3] M. Göppert: Über die Wahrscheinlichkeit des Zusammenwirkens zweier Lichtquanten in einem Elementarakt, *Naturwissenschaften* 17 (1929) 932.
[4] P. A. Franken, A. E. Hill, C. W. Peters, G. Weinreich: Generation of Optical Harmonics, *Phys. Rev. Lett.* 7 (1961) 118–119.
[5] W. Kaiser, C. G. B. Garrett: Two-photon excitation in CaF2:Eu2+, *Phys. Rev. Lett.* 7 (1961) 229–231.
[6] M. M. Zaret, M. Milton, G. M. Breinin, H. Schmidt, H. Ripps, I. M. Siegel, L. R. Jolon: Ocular lesions produced by an optical maser (Laser), *Science* 134 (1961) 1525–1526.
[7] L. Solon, R. Aronson, G. Gould: Physiological implications of laser beams, *Science* 134 (1961) 1506–1508.
[8] M. M. Zaret, H. Ripps, I. M. Siegel, G. M. Breinin: Laser Photocoagulation of the Eye, *Arch. Ophthalmology* 69 (1963) 97–104.
[9] L. Goldman, D. J. Blaney, D. J. Jr. Kindel, D. Richfield, E. K. Franke: Pathology of the effect on laser beams on skin, *Nature* 197 (1963) 912–913.
[10] L. Goldman, D. J. Blaney, D. J. Jr. Kindel, E. K. Franke: Effect of the Laser Beam on the Skin. *The Journal of Investigative Dermatology* 40 (1963) 121–122.
[11] F. Brech, L. Cross: Optical microemission stimulated by a ruby MASER, *Appl. Spectroscopy* 16 (1962) 59.
[12] M. Birnbaum: Semiconductor surface damage produced by ruby lasers, *J. Appl. Phys.* 36 (1965) 3688–3689.
[13] H. W. Mocker, R. J. Collins: Mode-competition and self-locking effects in a Q-switched ruby laser, *Appl. Phys. Lett.* 7 (1965) 270–273.
[14] I. S. Ruddock, D. J. Bradley: Bandwidth-limited subpicosecond pulse generation in modelocked cw dye lasers, *Appl. Phys. Lett.* 29 (1976) 296–297.
[15] R. L. Fork, B. I. Greene, C. V. Shank: Generation of optical pulses shorter than 0.1 ps by colliding pulse modelocking, *Appl. Phys. Lett.* 38 (1981) 617–619.
[16] W. Denk, J. Strickler W. Webb: Two-photon laser scanning fluorescence microscopy, *Science* 248 (1990) 73–76.
[17] P Moulton: Ti-doped sapphire: tunable solid-state laser, *Optics News* 8 (1982) 9–13.
[18] S. E. Harris, R. Targ: FM oscillation of the He-Ne laser, *Appl. Phys. Lett.* 5 (1964) 202–204.

[19] F. Krausz, T. Brabec, C. Spielmann: Self-starting passive mode locking, *Opt. Lett.* 16 (1991) 235–237.
[20] A. J. DeMaria, D. A. Stetser, H. Heynau: Self mode-locking of lasers with saturable absorbers, *Appl. Phys. Lett.* 8 (1966) 174–176.
[21] D. E. Spence, P. N. Kean, W. Sibbett: 60-fsec pulse generation from a self-mode-locked Ti:sapphire laser, *Opt. Lett.* 16 (1991) 42–44.
[22] K. König, H. Liang, MW. Berns, B. Tromberg: Cell damage by near-IR microbeams. *Nature* 377 (1995) 20–21.
[23] I. Ratkay-Traub et al.: Ultra-short pulse (femtosecond) laser surgery: initial use in LASIK flap creation. *Ophtalmol. Clin. North Am.* 14 (2001) 347–355.
[24] K. König: Clinical multiphoton tomography. J Biophot. 1 (2008) 13–23.
[25] K. König, I. Riemann, P. Fischer, KJ. Halbhuber: Intracellular nanosurgery with near infrared femtosecond laser pulses. *Cell. Mol. Biol.* 45 (1999) 195–201.
[26] U. K. Tirlapur, K. König: Targeted transfection by femtosecond laser. *Nature* 18 (2002) 290–291.
[27] A. Uchugonova, H. G. Breunig, C. Augsburger, M. Monaghan, K. Schenke-Layland, K. König: Optical Reprogramming and optical characterization of cells using femtosecond lasers. This book, chapter 5.1.
[28] J. Baxter: Research highlights: Low-power nanosurgery. *Nature Photonics* 6 (2012) 573.
[29] Z. Gan, Y. Cao, R. A. Evans, and M. Gu. Three-dimensional deep sub-diffraction optical beam lithography with 9 nm feature size. *Nature Communications* 4 (2013) 2061.

Part I: **Technical applications**

K. König, H. Seidel, M. Afshar, M. Klötzer, D. Feili, and M. Straub

1 Nanoprocessing using near-infrared sub-15 femtosecond laser microscopes

Abstract: Tightly focused 85 MHz repetition rate sub-15 femtosecond pulsed laser light of a central wavelength at 800 nm facilitates submicron and nanoscale processing of a large variety of materials. Three-dimensional polymer structures were generated by two-photon lithography and applied as cell culture substrates. Conically shaped capillaries with sub-100 nm edges were produced in SU-8 for electrospray ionization. Indium tin oxide (ITO) nanowires resulted from recrystallization on sub-ablation threshold exposure and subsequent etching in hydrochloric acid. Nanowires on glass were applied as gas sensors, whereas free-standing nanowires acted as resonators with resonance frequencies in the megahertz range. Laser-induced periodic surface structures (LIPSS) were generated on crystalline silicon surfaces and in thin ITO films at periodicities below 200 nm. Periodic nanocuts produced on-chip increased the effective area of ITO multi-electrode arrays. ITO thin-film electrodes for liquid crystal (LC) applications were patterned by sub-15 fs LIPSS in order to facilitate LC alignment. The properties of the structures and the performance of the devices were investigated using the finite-element method.

1.1 Laser microscopes – universal tools for imaging, manipulation, material characterization, and micro- and nanoprocessing

Laser microscopes have existed for more than 50 years. In 1962, just two years after the invention of the laser, Bessis et al. reported on the use of a ruby laser microscope applied to expose cell organelles [1]. In the same year, Brech and Cross achieved a microemission of materials and introduced laser-induced breakdown spectroscopy (LIBS) [2]. Moreover, the LIBS instrument was commercialized by the company Jarrell-Ash. An advanced laser microscope LMA 1 was developed by VEB Carl Zeiss Jena in 1964 and presented in 1965 at the Leipzig Spring Fair.

In contrast, most of the applications of today's microscopes focus on non-destructive 3D imaging of materials and biological specimens. The first laser scanning imaging microscope, a further development of a Minsky confocal microscope, was built by Davidovits and Egger in 1969 using a 5 mW helium-neon laser [3]. Conventional laser microscopes such as confocal laser scanning microscopes employ ultraviolet (UV) and visible (VIS) laser radiation. Laser microscopes have also been used as optical manipulation tools such as laser tweezers [4, 5].

UV laser microscopes have been widely employed as microsurgery tools using excimer lasers, nitrogen lasers and solid state lasers. Excimer laser operation microscopes have been used for refractive eye surgery ("LASIK") on millions of patients. However, disadvantages of UV microscopes are the limitation to 2D micromachining (no "in-bulk" processing) due to low light penetration depth as well as the intense one-photon absorption resulting in phototoxic effects when studying living specimens.

An alternative method is the usage of tightly focused near-infrared (NIR) femtosecond laser radiation which can induce multiphoton effects in the focal volume. Most materials such as polymers, glass as well as biological cells and tissues have low absorption and scattering coefficients and appear nearly transparent when using NIR laser radiation in the spectral range of 700–1100 nm; i.e. the "optical window". Nonlinear absorption occurs at high transient light intensities within the range of GW/cm^2, which can be achieved with low mean power lasers (kW peak power) through a tight focus using high numerical aperture (NA) objectives. Two-photon effects occur in a 0.1 femtoliter volume corresponding to a focal spot of 0.3 µm (radial) and 0.7 µm (axial) in diameter. Higher-order multiphoton effects such as plasma formation occur within an even smaller volume. The spatially confined multiphoton effects make surface processing and in-bulk 3D laser nanoprocessing possible. Figure 1.1 illustrates the two- and multiphoton excitation scheme with various deactivation pathways exploited for imaging and material processing.

Multiphoton effects were predicted by the PhD student and later Nobel Prize winner Maria Göppert more than 80 years ago in Göttingen, Germany [6]. However, as no intense light sources existed at that time, it took 30 years for Kaiser and Garrett to prove her theory using lasers [7]. A further three decades were required for Denk et al. to apply this technology to cell biology and develop the first two-photon laser scanning microscope in 1990 using femtosecond dye lasers [8]. Ten years later, JenLab's certified multiphoton tomographs made the transition from the lab to the clinical bedside. In vivo histology became a reality with the use of titanium:sapphire femtosecond laser-based multiphoton tomographs [9]. These recently certified clinical imaging tools can provide rapid, scar-free and label-free optical biopsies with superior subcellular submicron resolution based on two-photon fluorescence, second harmonic generation (SHG), and Coherent Anti-Stokes Raman Spectroscopy (CARS) [10, 11]. Applications include early skin cancer detection, the testing of sunscreen nanoparticles and anti-ageing cosmetics, guidance during brain tumor surgery, as well as the evaluation of skin problems experienced by astronauts during space lab work [12].

In addition to non-destructive multiphoton imaging with microscopes and tomographs, femtosecond laser microscope devices have also been employed for 3D micro- and nanolithography. Two-photon lithography was demonstrated by Maruo et al. as early as 1997 [13]. In 1999 Cumpston et al. performed two-photon polymerization with photoinitiators of high two-photon absorption cross section [14]. Kawata et al. fabricated microdevices at a minimum feature size of 120 nm [15], and Straub et al. produced photonic crystal devices [16] as well as other sophisticated 3D structures

[17]. The first sub-100 nm features by two-photon lithography were manufactured by Juodkazis et al., who fashioned 30 nm thick rod structures in 2005 [18]. Later on, 20 nm rods in SCR500 [19] and woodpile structures with 60 nm features were generated [20].

Interestingly, femtosecond laser microscopes also produce laser-induced periodic surface structures (LIPSS) with a very low sub-wavelength lateral period termed 'high spatial frequency LIPSS' (HSFL). LIPSS were discovered by Birnbaum in 1965 using millisecond-pulsed ruby laser light [21]. However, such structures have always been periodic within the range of the wavelength (low spatial frequency LIPSS, LSFL). Only the application of ultrashort laser pulses results in sub-wavelength LIPSS. The first sub-100 nm HSFL generated with NIR femtosecond laser pulses (shorter than the laser wavelength by a factor of ten) were observed by the group of König. They observed periodicities as low as 70 nm on crystalline silicon using a 90 MHz Ti:sapphire resonator [22].

If the NIR laser intensity is significantly increased, typically to the range of TW/cm^2, four or more photons may be absorbed simultaneously. Such non-resonant absorption can induce multiphoton ionization, optical breakdown and plasma formation. The destructive multiphoton effects are used for micro- and nanomachining without significant thermal side effects. For example, NIR femtosecond lasers at high peak power are employed in operation microscopes to create a tissue flap in hundreds of thousands of shortsighted people during refractive eye surgery (Femtosecond LASIK) [23–25]. Typically, amplified laser systems at a kHz repetition frequency and a sub-μJ pulse energy are used. Nowadays, modern cataract surgery also applies femtosecond lasers. Commercial femtosecond laser surgery microscopes are provided by companies such as IntraLase, ZEISS, and Alcon. However, even low-energy NIR laser pulses at high repetition frequency from laser oscillators can be used for plasma-mediated material processing when using high-NA focusing optics. Therefore, femtosecond laser scanning microscopes can be used both as nano- and microprocessing multiphoton tools.

In 1999, König and coworkers realized the first femtosecond laser nanoprocessing microscope [26]. Intracellular nanosurgery within living cells was performed with 80 MHz laser pulses of 1 nJ pulse energy. Subsequently, intratissue nanoprocessing was realized in plants [27, 28] and in ocular tissue [25] using nJ femtosecond NIR laser microscopes. Nanodissection of chromosomes was reported in 2001 [29]. DNA nanosurgery as precise as 40 nm was realized in combination with nanoparticles as 'light antennas' [30]. One major application of these novel nanotools in life sciences is targeted transfection [31, 32], as well as the optical injection of substances into living cells by the generation of transient nanopores in the cellular membrane [33]. In addition to a variety of lab microscopes, a first commercial femtosecond laser nanoprocessing microscope FemtOgene (JenLab GmbH, Germany) was realized.

Femtosecond NIR laser microscopes have developed into nonlinear analytical tools in cell biology, medicine and material investigation, as well as a micro- and

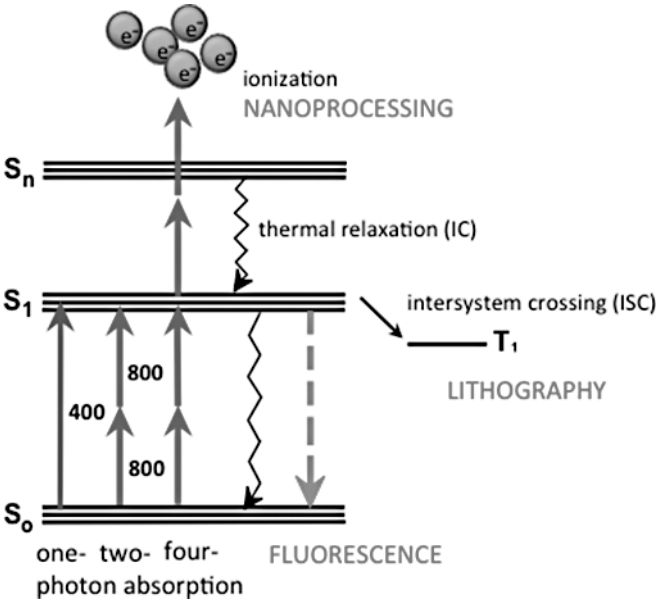

Fig. 1.1: Multiphoton effects in femtosecond laser microscopes include two-photon fluorescence and SHG for nonlinear imaging, ionization, and plasma formation for direct nanoprocessing as well as non-linear photochemical reactions for two-photon or three-photon lithography.

nanoprocessing tool based on 3D lithography, LIPSS formation, laser-induced material modification, and multiphoton-mediated plasma formation. In contrast to UV microscopes, they can be used in bulk nanomachining.

1.2 Sub-20 femtosecond laser scanning microscopes

A variety of commercial laser producers provide lasers with a pulse width τ shorter than 20 femtoseconds. The nanoprocessing efficiency can be enhanced by a shorter pulse width, as two-photon excitation follows a P^2/τ function, the three-photon effect a P^3/τ^2 relation. Therefore, the threshold for material ablation can be overcome with low-power laser systems if extremely short laser pulses are used. Importantly, two-photon 3D nanolithography and imaging can be performed with sub-mW mean laser powers when using a MHz femtosecond laser oscillator. Hole drilling and cutting are possible in a variety of materials with 1 mW mean power. This opens up possibilities for novel nanomachining tools using ultracompact femtosecond laser sources in the near future. In order to avoid pulse broadening in the optical system due to group velocity dispersion effects, chirped mirror technology is employed to maintain the ultrashort laser pulse width nearly within the focal plane of the microscope.

Figure 1.2 demonstrates the nanoprocessing microscope with a 10 fs laser, a step-motor driven stage, a galvo-scanning x/y-unit, and piezo-driven z-focusing optics. After transmission through the microscope including the 40× objective (NA 1.3), the in-situ pulse width is in the picosecond range. However, when employing a dispersion pre-compensation chirped mirror unit, a pulse width of 12 fs can be achieved on the target. At a central wavelength of 800 nm, a pulse width of 12 fs, and a laser spot diameter of $0.61\lambda/\mathrm{NA} = 375$ nm with an exposure area of $0.11\,\mu m^2$, respectively, 1 mW mean power is equivalent to 1 kW transient power, 11.8 pJ pulse energy, $0.9\,TW/cm^2$ peak intensity, and $10.8\,mJ/cm^2$ fluence per pulse [34]. The maximum scanning area was 512×512 pixels covering $450 \times 450\,\mu m^2$.

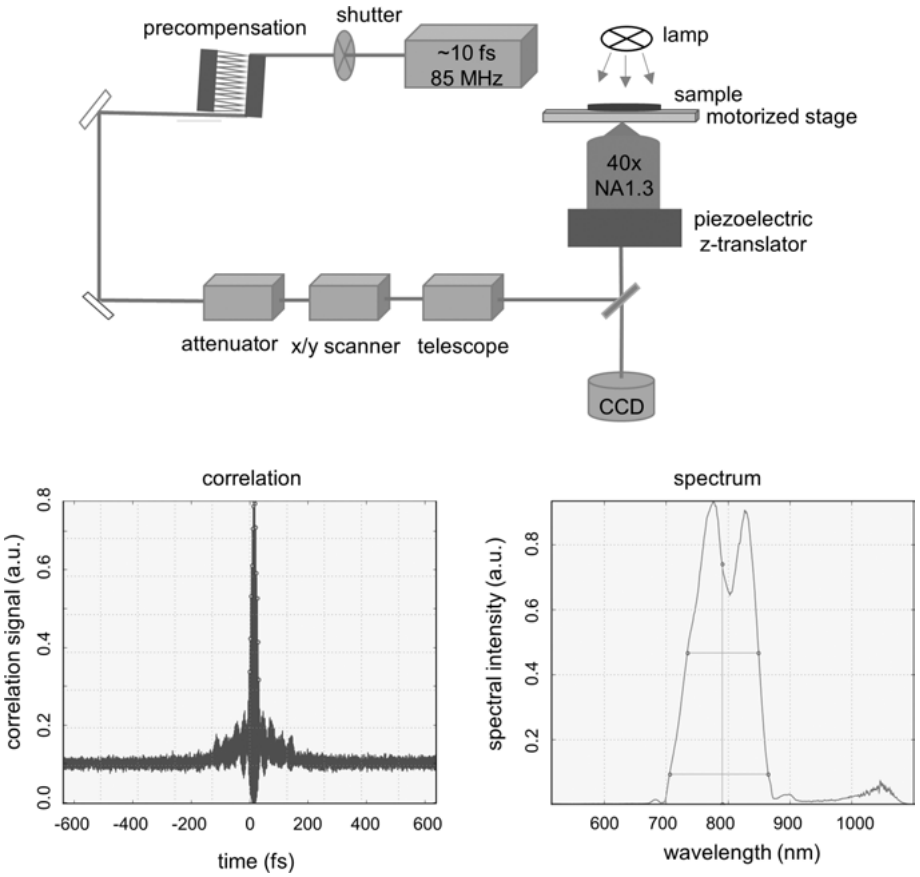

Fig. 1.2: Scheme of a 12-fs laser scanning microscope for nonlinear imaging, lithography, and direct nanoprocessing. The 80 MHz laser pulses feature an M-shaped broadband spectrum. An in-situ pulse width of 12 fs can be achieved with chirped mirrors for pre-compensation as demonstrated with a second-order interferometric scanning autocorrelator using a nonlinear photodiode at the focus.

Using galvoscanners, nanoprocessing was performed in three exposure modes: (i) scanning of a region of interest (ROI) for ablation and photoresist exposure; (ii) single point illumination for hole drilling; and (iii) cutting and photoresist illumination in which the galvoscanners performed a line scan. A CCD camera attached to the side port enabled on-site monitoring of the target during nanoprocessing, and a photomultiplier (PMT) was employed to detect two-photon fluorescence, SHG, and plasma luminescence.

1.3 Two-photon lithography with broadband pulses

Two-photon 3D nanolithography was performed in a variety of photoresists which could all be excited with the 120 nm broad spectrum of the 10 fs laser. They were spin-coated on 170 µm cover slips, baked and laser-exposed. The post-exposure bake and wet chemistry was performed in a class 100 cleanroom. Figure 1.3 shows examples of two-photon lithography in the well-established negative photoresist SU-8 (MicroChem Corp.). In some of the structures the aspect ratio exceeded 50 : 1 [35]. Stable microstructures were generated in an upright orientation with a width of 95 nm. Figure 1.3 (a, b) shows vertical walls of $8 \times 6.5\ \mu m^2$, which were produced within 6 s (0.7 mm/s line speed using 0.3 mW). Figure 1.3 (c, d) presents a 3D cell container of 20 µm in length featuring nanotopographical features on walls and bottom. The bottom pattern consists of straight lines of 175 nm in lateral diameter which were built up in vertical increments of 20 nm (0.4 mm/s with 0.6 mW).vadjust The artificially

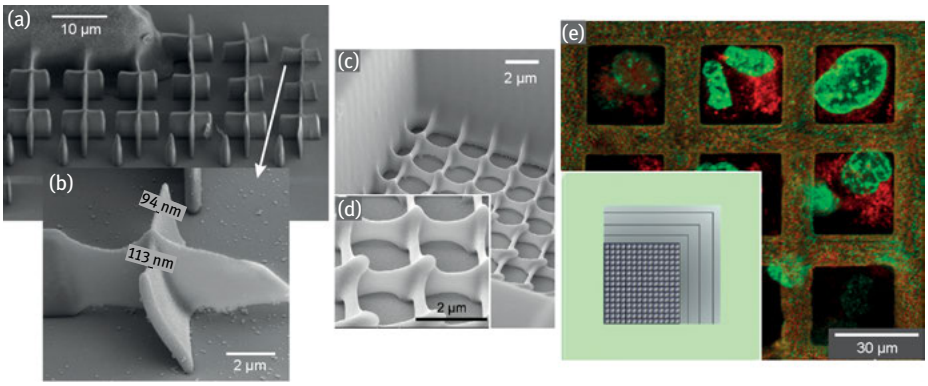

Fig. 1.3: Multiphoton lithography of 3D structures in SU-8 photoresist. (a) Assembly of stable vertical walls. (b) At the minimum thickness of 95 nm substantial distortions are observed. (c) Cell cage with bottom pattern of straight lines of 175 nm in lateral diameter. (d) Magnified section of the cell cage floor. (e) Array of cell containers hosting PC-3 cells with GFP-fluorescent nuclei and dsRed-fluorescent cytoplasm. The inset illustrates the bottom topography.

generated environment exerted an influence on cell aggregation compared to adjacent planar glass surface regions. PC-3 cells accumulated in a 3×3 array of cages with their floor patterned by orthogonal sets of 850 nm thick lines; see Fig. 1.3 (e) [36].

1.4 Generation of ITO-nanowires and nanoresonators

Laser processing of transparent conducting oxides (TCOs) is one of the most popular applications of laser micro- and nanostructuring, since it often turns out to be more convenient and economical in comparison to chemical processes. This is particularly the case for applications of TCOs in smartphone touchscreens and displays as well as in solar cells. Thanks to the development of pulsed lasers, maskless patterning by ablation of indium tin oxide (ITO), the most widely used TCO layer material, became technically feasible, with less thermal defects such as edge walls and cracks in the layer and substrate. Many studies were performed with Nd:YLF, Nd:YAG, and excimer lasers in the 90s, all with kHz repetition rates and ns pulse lengths [37–40]. Ablation processes with ns-pulses are dominated by thermal vaporization, whereby thermal effects propagate over a long distance in the film. Later, achieving better optoelectrical properties by laser annealing of ITO became an issue [41–44]. With pulse lengths below the electron–phonon interaction time (~ 10 ps), structuring becomes more efficient and thermal effects are minimized [45–47].

We performed submicron laser structuring of ITO in the form of both ablation and annealing. Using intensities above and below the ablation threshold, nanostructures were generated in 150 nm thick polycrystalline ITO layers sputter-deposited on glass; see Fig. 1.4 (a, b). At a mean power of 23 mW, cuts of sub-20 nm width were produced at periodicities of 50–250 nm. In contrast, at mean powers of less than 20 mW no direct material ablation was observed. However, due to laser-induced changes in the crystallographic morphology, post-processing by etching in 37 % HCl resulted in nanostructures, as illuminated regions were more resistant against HCl and hence persisted, whereas the rest of the ITO layer was removed. In particular, sub-100 nm ITO nanowires were generated by line scanning [35, 48]. In order to provide fully operable structures, laser processing was combined with a standard microsystem technology process for connecting the wires electrically with metallic pads.

Nanowires are simple and useful elements for many applications. They can be physically modeled to simulate their behavior. We used our laser-generated nanowires on glass substrates to realize gas sensors with low power self-heating capability which can detect oxidizing gases in the ppm and even down to the ppb range [48]. With the help of a transparent sacrificial layer which can be etched selectively with respect to ITO, we were able to realize free hanging nanowires as shown in Fig. 1.4 (c). ITO nanowires can also be employed as resonators able to detect very small mass changes (e.g. of biological objects) as a change in the resonance frequency.

The free-standing wires were fabricated on glass substrates by layer illumination through the substrate. We used aluminum nitride (AlN) as nonconductive transparent sacrificial layer (SL) beneath the ITO layer. It can be sputtered with very low surface roughness and etched selectively. The substrates were alkali-free 150 µm Schott glass wafers. After a standard cleaning process with acetone and isopropanol in an ultrasonic bath, we sputtered a 500 nm AlN layer. Afterwards a 100 nm thick conductive ITO layer was reactively sputtered from a metallic In/Sn target with a mass fraction of 90 : 10 in an oxygen plasma. Standard lithography was used to define dog-bone-shaped ITO microstructures, the gold pads and wire positions which we opened in the SL by etching the AlN in phosphoric acid at 85 °C. Afterwards, we deposited all of the gold pads and wires in a lift-off process by DC-sputtering in argon plasma. Finally, the wafers were diced to obtain single chips for laser processing.

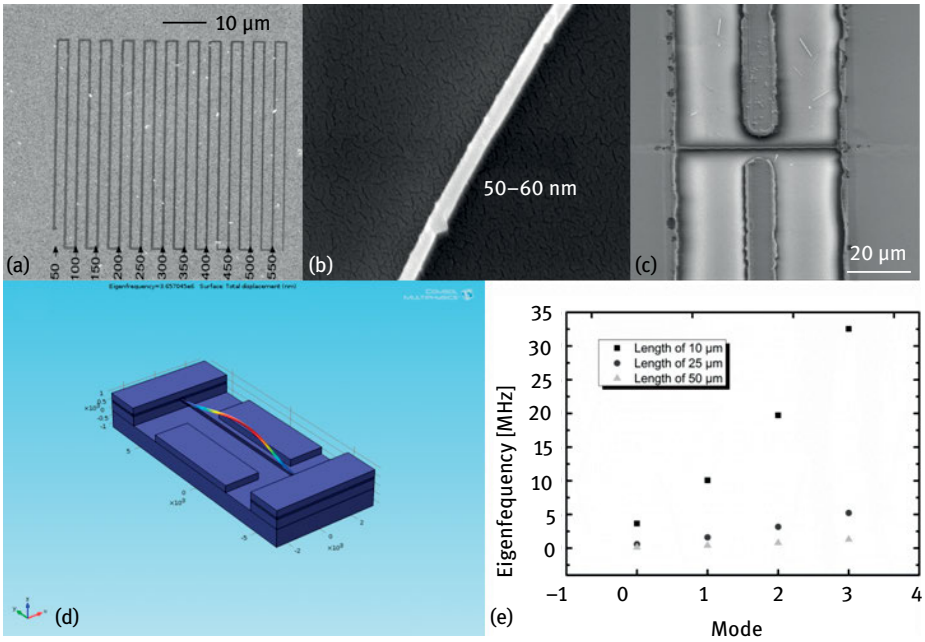

Fig. 1.4: (a) SEM image of laser-fabricated ITO line patterns after HCl etching. The wire widths decrease with increasing scanning speed. (b) SEM image of a 60 nm ITO wire. (c) SEM micrograph of a fabricated 300 nm nanoresonator with a length of 40 µm suspended between two side and two bottom gold electrodes. (d) Simulated displacement by the fundamental resonance mode (f_0) of a 10 µm resonator with 100 nm width and 100 nm thickness. (e) Simulation results of resonance frequencies of a 100 nm x 100 nm resonator with lengths of 10, 25, and 50 µm for the first four modes. The lowest frequency of the 50 µm resonator is 146 kHz.

On the chips we generated an ITO bridge between two gold pads on top of AlN as sacrificial layer. Its position can easily be found in the laser microscope so that we were able to write a nanowire with the desired parameters within this field [48]. This step also defines the lateral dimension of the nanowire after etching. The chip was then etched in phosphoric acid and in hydrochloric acid to release a free-standing element on the chip.

COMSOL simulations were performed to find out the eigenfrequencies of the resonator and the appropriate design dimensions of the sensor. Fig. 1.4 (d) shows a simulation for a nanoresonator with a length of 10 µm and a square cross section with 100 nm edges. A fundamental eigenfrequency of 3.6 MHz was calculated with a thermal time constant of about 20 µs. The resonance detection can be done by an impedance measurement due to the change of resistance in the nanowire and/or by using the change of capacitance between nearby electrodes and the nanowire. Due to their very small dimensions the power consumption is in the µW range. These features are very attractive, e.g. in gas sensor applications or for small mass change detection.

1.5 Generation of sub-wavelength LIPSS

LIPSS, frequently simply termed “ripples”, with periodicity in the micrometer range were first discovered on exposure of semiconductor surfaces to millisecond-pulsed ruby laser light [21] and have since been intensely investigated. Such ripples with a lateral period close to the wavelength (LSFL) are generally explained in an over-simplified model by interference between a surface scattered wave with the incident laser beam, which results in a periodic dissipation pattern [49]. A thorough theoretical treatment was provided by Sipe and coworkers, who applied Maxwell’s equations to rough surfaces [50]. Typically, LSFL are produced with nanosecond UV and VIS lasers at fluences close to the ablation threshold.

In contrast, femtosecond lasers facilitate the generation of subwavelength-period ripples (HSFL). For instance, ripples of period 50–100 nm were observed on diamond surfaces with 380-fs UV laser pulses at 248 nm for near-threshold irradiance [51]. On titanium nitride films [52] and on gallium arsenide surfaces [53], 170-nm LIPSS were induced by 130-fs Ti:sapphire lasers at 800 nm, whereas under the same conditions sapphire surfaces revealed a periodicity of 260 nm [53]. Sub-wavelength LIPSS on crystalline silicon were examined most intensely. The ripple period observed was 200 nm in ultrahigh vacuum [54], 130 nm in air [55], 100 nm [56] and 130–150 nm in water [57, 58], and 70–100 nm in oil [22]. Most studies referred to LIPSS oriented perpendicular to the laser polarization, but alignment of ripples parallel to the electric field also occurred [54, 59, 60]. Both parallel and perpendicular sub-wavelength LIPSS were observed on lithium niobate surfaces subsequent to multipulse 800 nm sub-15 fs irradiation [61].

Figure 1.5 (a) shows a scanning electron microscope image of nanoripples generated at a period of 152 ± 5 nm on a heavily boron-doped Si(100) surface using our experimental setup. The pattern is part of a 120 μm × 120 μm size area exposed to 8 mW for 15 min. This corresponds to a pulse fluence of 90 mJ/cm^2, a pulse peak intensity of 7 TW/cm^2 and a total number of 6×10^5 pulses acting per site. Laser processing was performed with the silicon surface immersed in water. Thereafter, silicon oxide debris was removed by hydrofluoric acid etching (3 % HF for 3 min.). Ripple crests feature a typical width of 20–40 nm and a height of 70 nm [57]. Figure 1.5 (b) presents laser-induced nanocuts of period 100 ± 2 nm in a 150 nm thick ITO film sputtered on glass. The cuts are typically 20 nm in width and penetrate the entire film [48]. Isolated sub-20 nm cuts were generated approaching the ablation threshold extremely closely.

An extension of the Sipe model involving transient changes of optical properties was proposed as a mechanism of nanoripple formation [59]. Generation of sub-wavelength LIPSS was also attributed to SHG [62] and self-organization following a laser-induced surface instability [63]. However, in recent years explanations in terms of micro- and nanoplasmonics have been increasingly favored. Interference of bulk plasma waves in the laser-induced transient microplasma with incident laser light was suggested for periodic in-bulk modifications [64]. Surface nanoripples were explained by accumulation of transiently excited in-bulk plasma nanobubbles, which on multi-pulse exposure turn into periodic plasma planes and finally extend to the surface [65]. Nanoripples perpendicular to the laser polarization were attributed to longitudinal surface plasmons. Periodic field enhancement at defect sites located in the amplitude maxima of propagating transient surface and interface plasma waves provided such an interpretation [66]. As shown recently by a Drude-like surface plasmon polariton model, standing surface plasma waves of the electron-hole plasma generated transiently in the tight focus of a high-numerical aperture objective may also result in a periodic pattern of dissipation and ablation [58].

Plasmon excitation in a dense electron-hole plasma transiently excited in a silicon surface by an ultrashort laser pulse was studied in detail with the finite-element method (FEM). The simulation was performed in a 2D focusing geometry using the software COMSOL Multiphysics. The calculations were run with the optical (RF) module using a transient solver. Light propagation in the continuously changing material and generation of photocarriers were simulated at full coupling of their partial differential equations with nanometer-sized mesh in time periods of one sixteenth of a light cycle. The concentration of photoexcited electrons was governed by a partial differential equation which included linear and two-photon absorption, electron diffusion as well as recombination in line with references [58] and [67]. Through a cylindrical aperture of half-angle 60° centered on the silicon surface with radius 15 μm a p-polarized harmonic pulse of amplitude 2×10^9 V/m and average wavelength 800 nm featuring a Gaussian intensity profile of 12 fs full width at half maximum was launched and propagated towards the diffraction limited focal spot. Figure 1.5 (c) shows the magnitude of the electric field 5.9 fs after the pulse peak hit the surface. The corresponding

concentration of excited electrons is plotted in Fig. 1.5 (d). During the earlier stages of pulse propagation in the focal region a carrier concentration well beyond the critical concentration of 5×10^{21} cm^{-3}, which marks the onset of metallic behavior, was built up within a 20 nm thick surface layer. The electric field distribution reveals excitation of a longitudinal surface plasma wave with two maxima at a distance of 130 nm in fair agreement with the period of nanoripples observed experimentally. As shortly afterwards the magnitude of the electric fields diverges at these places, lattice destabilization and ablation are expected to follow. In order to confirm the plasmonic nature of excitation, the FEM calculation was also performed with s-polarized light. However, under these conditions plasma waves were not excited.

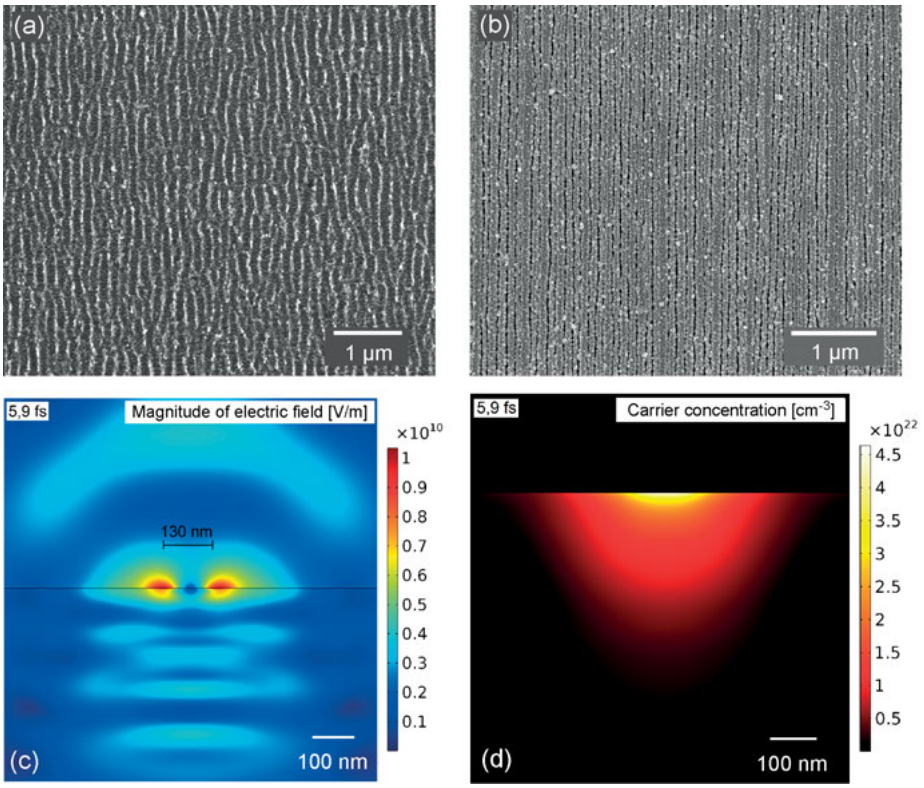

Fig. 1.5: (a) Nanoripples of period 152 nm on a heavily p-doped Si(100) surface, and (b) nanocuts of period 100 nm in a 150 nm ITO film. (c) Finite-element simulation of transient electron-hole plasma generation and plasma wave excitation at a silicon surface by a p-polarized 12-fs pulse of central wavelength 800 nm. In the diffraction-limited focal spot a standing plasma wave with two intensity maxima at a distance of 130 nm is excited. Note the strong localization of the plasma wave at the surface 5.9 fs after the arrival of the pulse peak. (d) At the silicon surface the calculated concentration of electrons excited by the front end of the laser pulse exceeds the critical concentration. Hence, the surface transiently features a metallic character.

1.6 On-chip laser nanoprocessing

An electrolyte measurement cell sealed by a glass cup was assembled with ITO-based multi-electrode arrays (MEAs) of various radii; – Fig. 1.6 (a) – fabricated on glass substrates and covered by an SU-8 passivation layer. The electrical interconnections were made of gold, and the chips were connected to a board with SMD technology; see Fig. 1.6 (e). Laser nanocutting of the ITO film was performed homogeneously on the sealed chip [35, 48]. The 20 nm wide cuts at a period of 100–140 nm [Fig. 1.6 (b, c)] increased the effective electrode area, which is in contact with the electrolyte solution. Impedance spectroscopy revealed a decrease in the electrode impedance, as the cell was immersed with the counter and the reference electrode (diameter 70 µm) in an isotonic saline solution; see Fig. 1.6 (d). COMSOL simulations (not shown) demonstrated that nanostructuring increased the effective electrode surface by more than a factor of four. However, the high aspect ratio (15 : 2) of the nanocuts prevented penetration of the electric field. Therefore, the reduction of impedance, which improves the signal-to-noise ratio [68], must be attributed to an increase in surface roughness due to redeposited ITO.

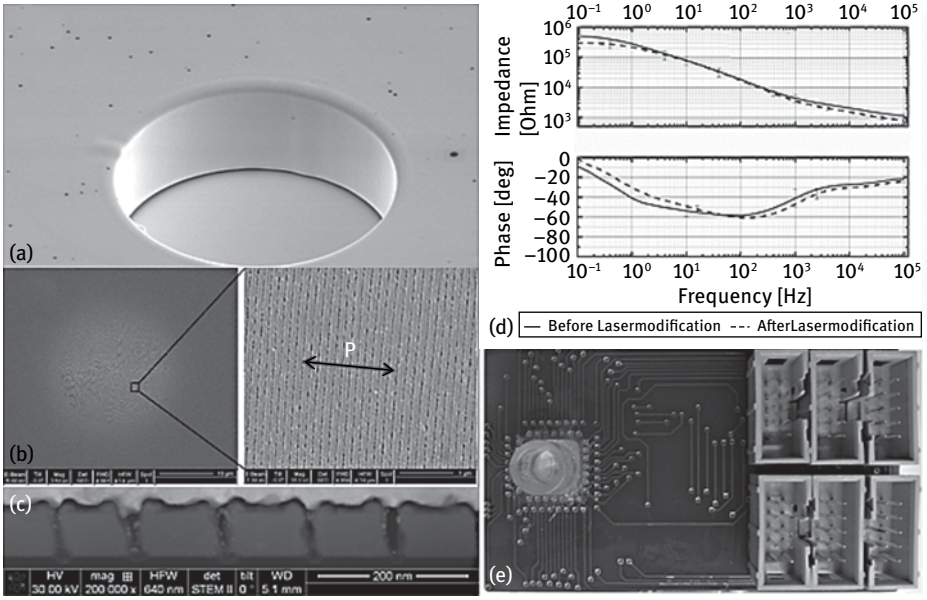

Fig. 1.6: (a) SEM image of a ⌀ 70 µm ITO electrode fabricated on glass substrate, passivated with SU-8 photoresist; (b) SEM micrograph of the processed area with 73.5 % of the whole surface of the electrode modified by nanocuts perpendicular to the laser beam polarization (arrow); (c) TEM image of the nanocuts with sub-20 nm width; (d) impedance diagrams of the electrode before and after laser processing; (e) photograph of a fabricated cell connected with SMD technique and passivated with resin with a glass cup on top.

1.7 Femtosecond laser-generated liquid crystal filters

Starting with small segment-type displays for calculators and watches in the early seventies, liquid crystal devices have found widespread application in measurement instruments, digital cameras, video projectors, car navigation systems and mobile phones [69]. High-resolution active-matrix displays exceeding 25 cm in size are used in portable computers and television sets. Most liquid crystal devices are operated in the twisted-nematic mode, in which the orientation of the liquid crystal molecules is twisted by 90° due to alignment layers on glass slides on both sides of the liquid crystal cell. The liquid crystal molecules can be redirected by low voltages with low power consumption and high optical contrast [70]. Figure 1.7 (a) illustrates such an arrangement schematically. The voltage is applied by transparent thin-film ITO electrodes. The alignment layers are usually made of polyimide because of its stability and favorable electrical characteristics. They maintain an in-plane orientation of the liquid crystal molecules in their immediate vicinity typically due to directional rubbing by a cloth with short fibers, which establishes nanometer-sized grooves and results in polymer reorientation [71]. Unfortunately, the rubbing process suffers from a general lack of controllability. For instance, unevenness causes alignment defects, which deteriorate the optical properties of the liquid crystal cell. Non-rubbing alignment procedures include stretching of polymer films [72], columnar growth of silicon oxide by oblique deposition [73] as well as photolithographic submicrometer patterning of photoresist followed by reactive ion etching into silicon dioxide [74]. Photoalignment of liquid crystal molecules by polarized laser light, which persisted after exposure, was demonstrated in an azobenzene-mixed polyimide [75]. However, it is desirable to align the liquid crystal molecules without adding a specific alignment layer. A nematic liquid crystal cell with walls of fused silica patterned by femtosecond laser-induced nanoripples allowed switching with an extinction ratio of 21 dB, but it was operated with four copper electrodes a distance of 100 µm away from the cell walls [76].

Here, we demonstrate a novel concept and major steps of an approach to construct a nematic liquid crystal cell with micrometer-sized pixels, which does not require an alignment layer but incorporates nanostructured ITO electrodes on 3 mm × 3 mm glass substrates of 0.17 mm thickness in direct contact to the liquid crystal. The cell is assembled as depicted in Fig. 1.7 (a). The scanning electron microscope images (Figs. 1.7 (b–d)) show such a laser-structured ITO thin-film electrode of thickness 150 nm, which features 30 µm × 30 µm large areas patterned by approximately 20 nm wide nanocuts of period 120–140 nm which allow for liquid crystal alignment. The laser scan was performed within 16 s at a mean focal power of 21 mW. In order to ensure electrical isolation the patterned area was bounded by submicrometer-wide laser cuts carried out at higher irradiance. Spacers were generated in UV-sensitive ma-N 2400 negative photoresist (micro resist technology GmbH, Berlin) by multiphoton lithography in order to maintain a vertical distance of about 2 µm between the two opposite cell electrodes. They appear as dark hollow squares in Figs. 1.7 (b, c). The spacers were

polymerized with a focal power of 5 mW at a scan speed of 40 µm/s. After careful alignment of the electrodes with a dedicated microscopic mounting setup and their electrical connection to a DC power supply by thin copper leads, the cell is filled by a small droplet of the nematic liquid crystal MDA-98-1602 (Merck) with ordinary refractive index $n_o = 1.51$ and extraordinary refractive index $n_e = 1.78$. Using visible cw laser light or incoherent illumination it will be operated in the twisted-nematic mode between two polarizers and is expected to feature a strong change in transmission on electrical switching.

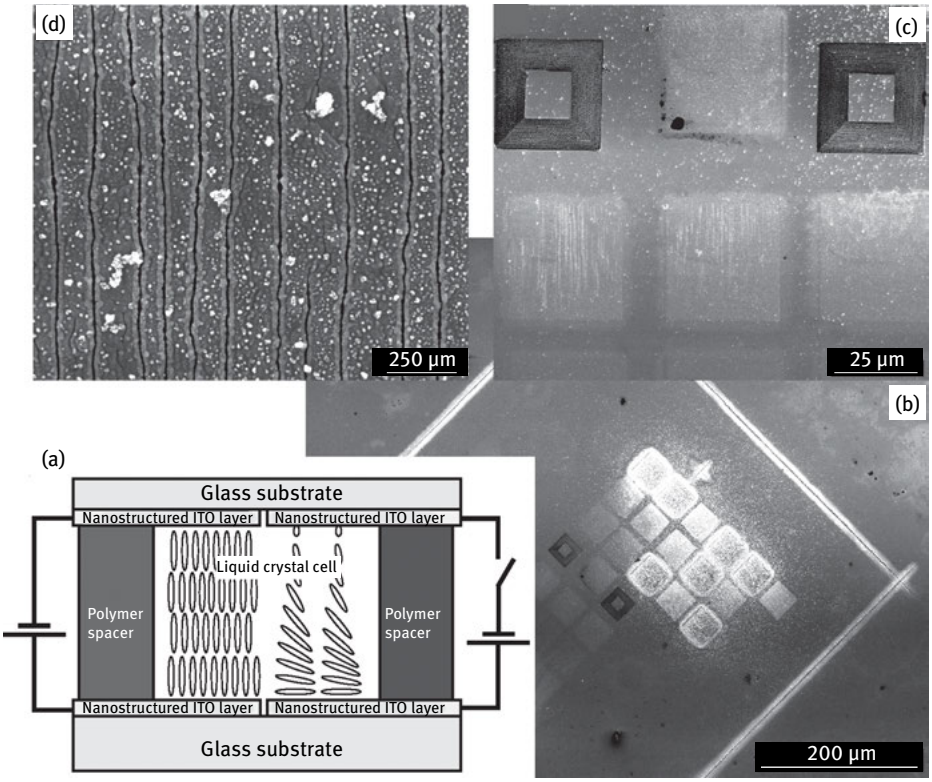

Fig. 1.7: Twisted nematic liquid crystal cell with laser-nanostructured ITO thin film electrodes. (a) Sketch of the liquid crystal cell setup with biased (left) and unbiased pixels (right). (b) Scanning electron microscope image of an electrode with square-shaped nanopatterned areas. Straight long laser cuts mark the edge of the electrode. The distance to the counterelectrode is adjusted by hollow square polymer spacers. (c) Magnified section with laser-structured areas (light grey) and spacers (dark). (d) Periodic laser-induced nanocuts ensure alignment of the liquid crystal molecules at the electrode surfaces.

1.8 Micro/nanojets for electrospray ionization

Electrospray ionization (ESI) is an electrohydrodynamic process in which a strong electric field converts a liquid into tiny charged droplets. Figure 1.8 (a) illustrates this process. An electrically conductive liquid passes through a capillary tube. A high electric field of about 10^6 V/m is needed between the capillary tip and the counter electrode to induce charge separation in the liquid. Deformation of the meniscus into a Taylor cone results from the interaction of Coulomb repulsion and surface tension [77]. Starting from a threshold voltage V_{th} [78], a jet of liquid is emitted from the Taylor cone, which transforms into charged droplets. The size of the droplets produced by the atomization depends primarily on the flow rate and the properties of the liquid as well as on the capillary geometry and on the applied voltage

$$V_{th} = \sqrt{\frac{\gamma R_c \cos\theta}{2\varepsilon_0}} \ln\left(\frac{4d}{R_c}\right), \tag{1.1}$$

where R_c is the capillary radius, γ the surface tension, d the electrode gap, ε_0 the dielectric constant and θ the contact angle. The most important emission mode is the cone-jet mode, which is characterized by a stable spray and a nearly monodisperse distribution of droplets [79, 80]. According to the Charge Residue Model, the Rayleigh-limit of the charge carrier density is reached in the droplet evaporation process. Beyond this limit the electrostatic forces can overcome the surface tension in the droplets, causing them to collapse into smaller droplets. This chain reaction can end up with single ions which can even be emitted from droplets as in the ion emission model [78]; see Fig. 1.8 (a).

The most important application of electrospray is the ionization of macromolecules for mass spectrometric analysis. This gentle ionization method is particularly important for biomolecules, since prior to the introduction of ESI it was not possible to transform fragile macromolecules into ions without destroying them. ESI allows the ionization of biomolecules at atmospheric pressure and room temperature with little or no fragmentation [81]. This can be used for detecting traces of explosives, drugs or toxic materials. ESI can also be used for the realization of electric propulsion and in colloid microthrusters (CMT) [80, 82] to generate thrusts in the µN- to mN-range with a resolution of sub-µN. For this purpose, the ESI system must be complemented by an additional acceleration electrode and a counter electrode. Multiple capillaries are arranged into an array in order to achieve significant thrusts.

The electric field strength is a key parameter for generating and influencing the electrospray process. Applying newer technologies to reduce the size of the capillary and its radius could reduce V_{th} considerably from 5 kV down to 1 kV and even lower [83]. Here, we report on manufacturing conically shaped capillaries with a sub-100 nm capillary edge to implement a very high field strength at the tip of the capillary. We used Si (100) wafers as substrate with a 300 nm silicon nitride passivation layer deposited on both sides by a plasma CVD process. Using standard lithography and an

anisotropic wet etching process we realized cavities with 1900 µm edges from one side in silicon leaving a membrane with a thickness of 30–50 µm. A connecting path to these cavities is opened as holes with 5 µm radii by a dry etching process. After dicing the wafer in 7 mm chips, each chip is ready to be processed individually in a spin coating step and by the laser system.

A commercial SU-8 2000 from MicroChem Corp. with a thickness of about 100 µm was used to cover the holes and obtain a homogeneous layer. The chip was mounted on the microscope with the SU-8 side toward the objective. A cover glass and a thin film of water protected the SU-8 from the immersion oil and provided a convenient sequence of refractive indexes through the layers. The pre-etched holes were centrically aligned to the laser spot. Completed conical nozzles are shown in Fig. 1.8 (b).

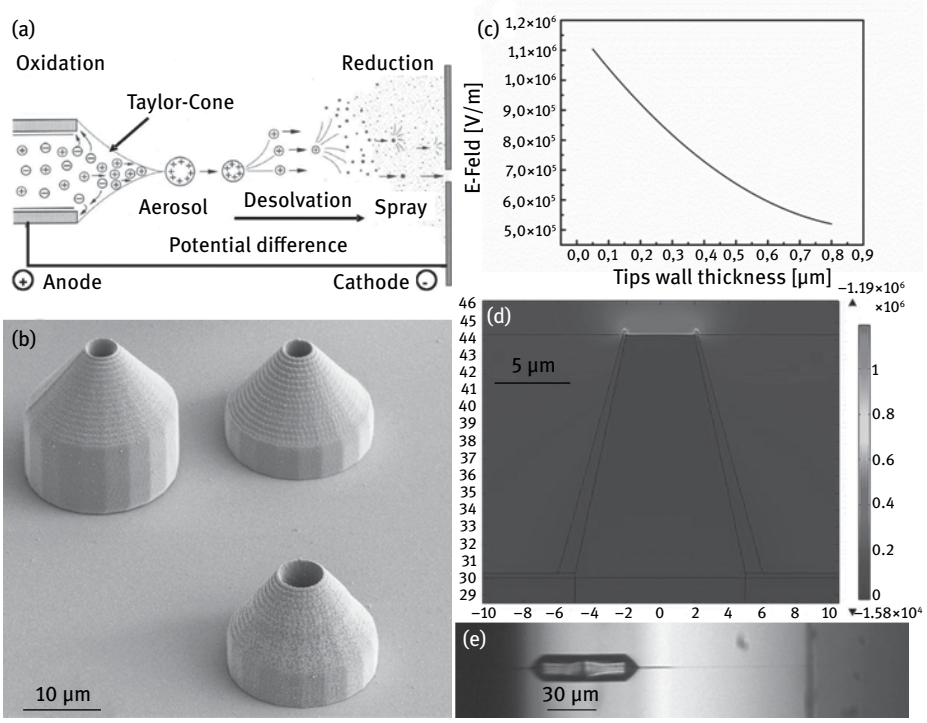

Fig. 1.8: (a) Schematic diagram of the modular concept of an electrospray nozzle; (b) SEM image of three different conic nozzles with tip thicknesses of about 100–150 nm made of SU-8 with two-photon lithography; (c) diagram of the simulated E-field depending on the wall thickness of the tip; (d) FEM-simulated E-field with 100 V at the tip of a nozzle of 15 µm height and with a permittivity of 80 of the fluid; (e) microscopic image of an ethylene glycol jet out of a cylindrical SU-8 micro-nozzle in air.

COMSOL Multiphysics was used to model the electric field distribution between the emitter and the counter electrode. A study was made to determine how the nozzle geometry affects the field strength at the tip of the emitter; see Fig. 1.8 (c). Because of the rotational symmetry of the problem, the simulation could be simplified to a 2D geometry; see Fig. 1.8 (d). The emitter length, the emitter radius and the angles of the cone were varied as well as the wall thickness at the tip down toward 100 nm. After setting the emitter length to 15 µm, the hole radius to 5 µm, and the emitter-extractor distance to 1000 µm we found an optimum value of 60° for the cone angle. The results indicate that the conical outside of the capillary doubles the electric field strength in comparison to a cylindrical shape. By adding an extra conical shape to the inside of the capillary, a further 35 % increase of the electric field was obtained. With a constant tip wall thickness of 200 nm, an applied voltage of 100 V, and a water/ethanol mixture with a permittivity of 74 we simulated a high electric field of more than 1×10^6 V/m at the tip which can easily start the emission process. Fig. 1.8 (e) shows an actual spray of ethylene glycol with a cylindrical cone structure.

1.9 Outlook

Multiphoton effects induced by VIS or NIR femtoseond laser pulses can be employed to perform sub-100 nm processing of biological and non-biological materials. Low mean powers of less than 10 mW are sufficient to perform 3D nanoprocessing in a variety of materials when employing 10-fs NIR 85-MHz high-NA laser microscopes. Sub-100 nm features without collateral thermal or mechanical effects can be generated at picojoule pulse energies. A very interesting feature of this technology is the ability to induce morphological crystallographic changes in some materials (e.g. ITO), rendering the illuminated areas resistant against subsequent attack of chemical etchants. Thus, nanostructures such as nanowires can be generated directly, without the need of a more complicated lithographic process requiring the deposition, illumination, development, and removal of a photoresist layer on top of the material plus a subsequent highly anisotropic etching step. Using sub-mW mean powers, two-photon 3D nanolithography and two-photon imaging can be performed. The 3D capability is unique to this approach and cannot be reached even with the most advanced, extremely expensive lithography systems of microelectronics reaching down to feature sizes below 40 nm in planar structural arrangements.

These results may influence the future production of small, low cost femtosecond lasers for biophotonics and material processing. Ultracompact chiller-free femtosecond laser resonators may be directly attached to a microscope. Ultrafast fiber lasers may become the most important femtosecond laser sources due to their low cost, versatility, liability, and the less complex architecture. When using microscopes with a sub-20 fs source, the broad laser emission spectrum may facilitate the excitation of multiple fluorophores and photoresists without the need of wavelength tuning.

It is also an ideal source for optical coherence microscopy (OCM), optical coherence tomography (OCT), and multiphoton tomography (MPT).

In the future, femtosecond laser nanoprocessing will influence ophthalmic surgery significantly. Furthermore, 3D nanolithography opens up the possibility of generating complex non-planar 3D nanostructures and nanoelectromechanical systems (e.g. conical jets, lenses, resonators) with applications in many areas, including optical data communication, fluidic systems for microthrusters in space technology, and trace detection of hazardous materials. The laser-induced fabrication of nanowires is extremely attractive for biological and chemical analysis and for gaining new physical insight into the quantum behavior of such structures. All these capabilities taken together may impact the field of optical storage, rapid prototyping in particular for tissue implants (cardiovascuar stents, intraocular lenses, catheters, teeth material, and prosthetics), optical communication, and nanomachining. With novel commercial low cost femtosecond lasers, material processing and medical diagnostics will be revolutionized in the years to come.

References

[1] M. Bessis, F. Gires, G. Mayer and G. Nomarski, "Irradiation des organites cellulaires a l'aide d'un laser a rubis," *Compte Rendus de l'Academie des Sciences* 1962, 255, 1010–1012.
[2] F. Brech and L. Cross, "Optical microemission stimulated by a ruby MASER," *Applied Spectroscopy* 1962, 16, 59.
[3] P. Davidovits and M. D. Egger, "Scanning laser microscope," *Nature* 1969, 223, 831.
[4] A. Ashkin, "Optical trapping and manipulation of neutral particles using lasers," *Proceedings of the National Academy of Sciences of the United States of America* 1997, 94, 4853–4860.
[5] A. Ashkin, J. M. Dziedzic and T. Yamane, "Optical trapping and manipulation of single cells using infrared-laser beams," *Nature* 1987, 330, 769–771.
[6] M. Göppert, "Über die Wahrscheinlichkeit des Zusammenwirkens zweier Lichtquanten in einem Elementarakt," *Naturwissenschaften* 1929, 17, 932.
[7] W. Kaiser and C. G. B. Garrett, "Two-photon excitation in CaF2:Eu2+," *Physical Review Letters* 1961, 7, 229–231.
[8] W. Denk, J. Strickler and W. Webb, "Two-photon laser scanning fluorescence microscopy," *Science* 1990, 248, 73–76.
[9] K. König and I. Riemann, "High-resolution multiphoton tomography of human skin with subcellular spatial resolution and picosecond time resolution," *Journal of Biomedical Optics* 2003, 8, 432–439.
[10] K. König, "Clinical multiphoton tomography," *Journal of Biophotonics* 2008, 1, 13–23.
[11] M. Weinigel, H.-G. Breunig, J. Lademann and K. König, "In vivo histology: optical biopsies with chemical contrast using multiphoton/CARS tomography," *Laser Physics Letters* 2014, 11, 055601.
[12] K. König, "Skin problems in outer space," *The New Economy*, Spring 2015.
[13] S. Maruo, O. Nakamura and S. Kawata, "Three-dimensional microfabrication with two-photon-absorbed photopolymerization," *Optics Letters* 1997, 22, 132–134.
[14] B. H. Cumpston, S. P. Ananthavel, S. Barlow, D. L. Dyer, J. E. Ehrlich, L. L. Erskine, A. A. Heikal, S. M. Kuebler, I.-Y. S. Lee, D. McCord-Maughon, J. Qin, H. Röckel, M. Rumi, X.-L. Wu,

S. R. Marder and J. W. Perry, "Two-photon polymerization initiators for three dimensional storage and microfabrication," *Nature* 1999, 398, 51–54.
[15] S. Kawata, H.-B. Sun, T. Tanaka and K. Takada, "Finer features for functional microdevices," *Nature* 2001, 412, 687–688.
[16] M. Straub and M. Gu, "Near-infrared photonic crystals with higher-order bandgaps generated by two-photon photopolymerization," *Optics Letters* 2002, 27, 1824–1826.
[17] M. Straub, L. H. Nguyen, A. Fazlic and M. Gu, "Complex-shaped three-dimensional microstructures and photonic crystals generated in a polysiloxane polymer by two-photon microstereolithography," *Optical Materials* 2004, 27, 359–364.
[18] S. Juodkazis, V. Mizeikis, K. K. Seet, M. Miwa and H. Misawa, "Two-photon lithography of nanorods in SU-8 photoresist," *Nanotechnology* 2005, 16, 846–849.
[19] D. Tan, Y. Li, F. Qi, H. Yang, Q. Gong, X. Dong and X. Duan, "Reduction in feature size of two-photon polymerization using SCR500," *Applied Physics Letters* 2007, 90, 071106.
[20] W. Haske, V. Chen, J. Hales, S. Barlow, S. Marder and J. Perry, "65 nm feature sizes using visible wavelength 3-D multiphoton lithography," *Optics Express* 2007, 15, 3426–3436.
[21] M. Birnbaum, "Semiconductor surface damage produced by ruby lasers," *Journal of Applied Physics* 1965, 36, 3688–3689.
[22] R. Le Harzic, H. Schuck, D. Sauer, T. Anhut, I. Riemann and K. König, "Sub-100 nm nanostructuring of silicon by ultrashort laser pulses," *Optics Express* 2005, 13, 6651–6656.
[23] T. Juhasz, H. Frieder, R. Kurtz, C. Horvath, J. Bille and G. Mourou, "Corneal refractive surgery with femtosecond lasers," *IEEE Journal of Selected Topics in Quantum Electronics* 1999, 5, 902–910.
[24] A. Sugar, "Ultrafast (femtosecond) laser refractive surgery," *Current Opinion in Ophthalmology* 2002, 13, 246–249.
[25] K. König, "High-resolution multiphoton imaging and nanosurgery of the cornea using femtosecond laser pulses," in *Lasers in ophthalmology. Basics, diagnostic and surgical aspects.*, F. Fankhauser and S. Kwasniewska, Eds., Kugler Publications, 2003.
[26] K. König, I. Riemann, P. Fischer and K. Halbhuber, "Intracellular nanosurgery with near infrared femtosecond laser pulses," *Cellular and Molecular Biology* 1999, 45, 195–201.
[27] U. Tirlapur and K. König, "Near-infrared femtosecond laser pulses as a novel means for dye permeation and 3D imaging of localized dye-coupling in the Arabidopsis root meristem," *The Plant Journal* 1999, 20, 363– 370.
[28] U. Tirlapur and K. König, "Femtosecond near-infrared laser pulses as a versatile non-invasive tool for intratissue nanoproccessing in plants without compromising viability," *The Plant Journal* 2002, 31, 365–374.
[29] K. König, I. Riemann and W. Fritzsche, "Nanodissection of human chromosomes with near-infrared femtosecond laser pulses," *Optics Letters* 2001, 26, 819–821.
[30] A. Csaki, F. Garwe, A. Steinbrück, G. Maubach, G. Festag, A. Weise, I. Riemann, K. König and W. Fritzsche, "A parallel approach for sub-wavelength molecular surgery using gene-specific positioned metal nanoparticles as light antennas," *Nano Letters* 2007, 7, 247–253.
[31] U. Tirlapur and K. König, "Targeted transfection of cells by femtosecond near-infrared laser pulses," *Nature* 2002, 418, 290–291.
[32] A. Uchugonova, K. König, R. Bückle, A. Isemann and G. Tempea, "Targeted transfection of stem cells with sub-20 femtosecond laser pulses," *Optics Express* 2008, 16, 9357–9364.
[33] Z. Földes-Zapp, K. König, H. Studier, R. Bückle, H.-G. Breunig, A. Uchugonova and G. Kostner, "Trafficking of mature miRNA-122 into the nucleus of live liver cells," *Current Pharmaceutical Biotechnology* 2009, 10, 569–578.

[34] K. König, A. Uchugonova, M. Straub, H. Zhang, M. Licht, M. Afshar, D. Feili and H. Seidel, "Sub-100 nm material processing and imaging with a sub-15 femtosecond laser scanning microscope," *Journal of Laser Applications* 2012, 24, 042009.
[35] M. Afshar, S. Saremi, H. Völlm, D. Feili, H. Seidel, M. Straub, H. Zhang and K. König, "Multiphoton lithography and ITO structuring by high repetition-rate sub-15 femtosecond laser pulses," *Proceedings of the Society of Photo-Optical Instrumentation Engineers (SPIE)* 2001, 7920, 792015.
[36] M. Licht, A. Uchugonova, K. König and M. Straub, "Sub-15 fs multiphoton lithography of three-dimensional structures for live cell applications," *Journal of Optics* 2012, 14, 065601.
[37] M. Takai, D. Bollmann and K. Haberger, "Maskless patterning of indium tin oxide layer for flat-panel displays by diode-pumped Nd:YLF laser irradiation," *Applied Physics Letters* 1994, 64, 2560–2562.
[38] T. Szörenyi, L. D. Laude, I. Bertoti, Z. Kantor and Z. Geretovszky, "Excimer-laser processing of indium-tin-oxide films – an optical investigation," *Journal of Applied Physics* 1995, 78, 6211–6219.
[39] O. Yavas and M. Takai, "High-speed maskless laser patterning of indium tin oxide thin films," *Applied Physics Letters* 1998, 73, 2558–2560.
[40] O. Yavas and M. Takai, "Effect of substrate absorption on the efficiency of laser patterning of indium tin oxide thin films," *Journal of Applied Physics* 1999, 85, 4207–4212.
[41] H. Hosono, M. Kurita and H. Kawazoe, "Excimer laser crystallization of amorphous indium-tin oxide thin films and application to fabrication of Bragg gratings," *Thin Solid Films* 1999, 351, 137–140.
[42] F. O. Adurodija, H. Izumi, T. Ishihara, H. Yoshioka, M. Motoyama and K. Murai, "Effect of laser irradiation on the properties of indium tin oxide films deposited by pulsed laser deposition," *Applied Surface Science* 2001, 177, 114–121.
[43] F. O. Adurodija, H. Izumi, T. Ishihara, H. Yoshioka, M. Motoyama and K. Murai, "Effect of laser irradiation on the properties of indium tin oxide films deposited at room temperature by pulsed laser deposition," *Vacuum* 2002, 67, 209–216.
[44] W. Chung, M. O. Thompson, P. Wickboldt, D. Toet and P. G. Carey, "Room temperature indium tin oxide by XeCl excimer laser annealing for flexible display," *Thin Solid Films* 2004, 460, 291–294.
[45] M. Park, B. H. Chon, H. S. Kim, S. C. Jeoung, D. Kim, J. I. Lee and H. Y. Chu, "Ultrafast laser ablation of indium tin oxide thin films for organic light-emitting diode application," *Optics and Lasers in Engineering* 2006, 44, 138–146.
[46] A. De Bonis, A. Galasso, V. Marotta, S. Orlando, A. Santagata, R. Teghil, S. Veronesi, P. Villani and A. Giardini, "Pulsed laser ablation of indium tin oxide in the nano and femtosecond regime: Characterization of transient species," *Applied Surface Science* 2006, 252, 4632–4636.
[47] C. W. Cheng, C. Y. Lin, W. C. Shen, Y. J. Lee and J. S. Chen, "Patterning crystalline indium tin oxide by high repetition rate femtosecond laser-induced crystallization," *Thin Solid Films* 2010, 518, 7138–7142.
[48] M. Afshar, M. Straub, H. Voellm, D. Feili, K. Koenig and H. Seidel, "Sub-100 nm structuring of indium-tin-oxide thin films by sub-15 femtosecond pulsed near-infrared laser light," *Optics Letters* 2012, 37, 563–565.
[49] P. M. Fauchet and A. E. Siegman, "Surface ripples on silicon and gallium arsenide under picosecond laser illumination," *Applied Physics Letters* 1982, 40, 824–826.
[50] J. E. Sipe, J. F. Young, J. S. Preston and H. M. van Driel, "Laser-induced periodic surface structure. I. Theory," *Physical Review B* 1983, 27, 1141–1154.

[51] A. M. Ozkan, A. P. Malshe, T. A. Railkar, W. D. Brown, M. D. Shirk and P. A. Molian, "Femtosecond laser-induced periodic structure writing on diamond crystals and microclusters," *Applied Physics Letters* 1999, 75, 3716–3718.
[52] J. Bonse, H. Sturm, D. Schmidt and W. Kautek, "Chemical, morphological and accumulation phenomena in ultrashort-pulse laser ablation of TiN in air," *Applied Physics A: Materials Science & Processing* 2000, 71, 657–665.
[53] A. Borowiec and H. K. Haugen, "Subwavelength ripple formation on the surfaces of compound semiconductors irradiated with femtosecond laser pulses," *Applied Physics Letters* 2003, 82, 4462–4464.
[54] F. Costache, S. Kouteva-Arguirova and J. Reif, "Sub–damage–threshold femtosecond laser ablation from crystalline Si: surface nanostructures and phase transformation," *Applied Physics A: Materials Science & Processing* 2004, 79, 1429–1432.
[55] R. Le Harzic, D. Dörr, D. Sauer, M. Neumeier, M. Epple, H. Zimmermann and F. Stracke, "Large-area, uniform, high-spatial-frequency ripples generated on silicon using a nanojoule-femtosecond laser at high repetition rate," *Optics Letters* 2011, 32, 229–231.
[56] G. Daminelli, J. Krüger and W. Kautek, "Femtosecond laser interaction with silicon under water confinement," *Thin Solid Films* 2004, 467, 334–341.
[57] M. Straub, M. Afshar, D. Feili, H. Seidel and K. König, "Periodic nanostructures on Si(100) surfaces generated by high-repetition rate sub-15 fs pulsed near-infrared laser light," *Optics Letters* 2012, 37, 190–192.
[58] M. Straub, M. Afshar, D. Feili, H. Seidel and K. König, "Surface plasmon polariton model of high-spatial frequency laser-induced periodic surface structure generation in silicon," *Journal of Applied Physics* 2012, 111, 124315.
[59] Q. Wu, Y. Ma, R. Fang, Y. Liao, Q. Yu, X. Chen and K. Wang, "Femtosecond laser-induced periodic surface structure on diamond film," *Applied Physics Letters* 2003, 82, 1703–1705.
[60] R. Böhme, C. Vass, B. Hopp and K. Zimmer, "Sub-wavelength ripples in fused silica after irradiation of the solid/liquid interface with ultrashort laser pulses," *Nanotechnology* 2008, 19, 495301.
[61] M. Straub, B. Weigand, M. Afshar, D. Feili, H. Seidel and K. König, "Periodic subwavelength ripples on lithium niobate surfaces generated by tightly focused sub-15 femtosecond sub-nanojoule pulsed near-infrared laser light," *Journal of Optics* 2013, 15, 055601.
[62] A. Dufft, A. Rosenfeld, S. K. Das, R. Grunwald and J. Bonse, "Femtosecond laser-induced periodic surface structures revisited: A comparative study on ZnO," *Journal of Applied Physics* 2009, 105, 034908.
[63] J. Reif, F. Costache, M. Henyk and S. V. Pandelov, "Ripples revisited: non-classical morphology at the bottom of femtosecond laser ablation craters in transparent dielectrics," *Applied Surface Science* 2002, 197–198, 891–895.
[64] Y. Shimotsuma, P. G. Kazansky, J. Qiu and K. Hirao, "Self-organized nanogratings in glass irradiated by ultrashort light pulses," *Physical Review Letters* 2003, 91, 247404.
[65] R. Buividas, L. Rosa, R. Sliupas, T. Kudrius, G. Slekys, V. Datsyuk and S. Juodkazis, "Mechanism of fine ripple formation on surfaces of (semi)transparent materials via a half-wavelength cavity feedback," *Nanotechnology* 2011, 22, 055304.
[66] G. Miyaji and K. Miyazaki, "Origin of periodicity in nanostructuring on thin film surfaces ablated with femtosecond laser pulses," *Optics Express* 2008, 16, 16265–16271.
[67] K. Sokolowski-Tinten and D. von der Linde, "Generation of dense electron-hole plasmas in silicon," *Physical Review B* 2000, 61, 2643–2650.
[68] W. Franks, I. Schenker, P. Schmutz and A. Hierlemann, "Impedance characterization and modeling of electrodes for biomedical applications," *IEEE Transactions on Biomedical Engineering* 2005, 52, 1295–1302.

[69] K. Takatoh, M. Hasegawa, M. Koden, N. Itoh, R. Hasegawa and M. Sakamoto, Alignment Technologies of Liquid Crystal Devices, 1 ed., Abingdon, New York: Taylor & Francis, 2005.
[70] D.-K. Yang and S.-T. Wu, Fundamentals of Liquid Crystal Devices, 1 ed., Chichester: John Wiley & Sons, 2006.
[71] A. J. Pidduck, G. P. Bryan-Brown, S. Haslam, R. Bannister, I. Kitely, T. J. McMaster and L. Boogaard, "Atomic force microscopy studies of rubbed polyimide surfaces used for liquid crystal alignment," *Journal of Vacuum Science & Technology A: Vacuum Surfaces and Films* 1996, 14, 1723–1728.
[72] H. Aoyama, Y. Yamazaki, N. Matsuura, H. Mada and S. Kobayashi, "Alignment of liquid crystals on the stretched polymer films," *Molecular Crystals and Liquid Crystals* 1981, 72, 127–132.
[73] J. L. Janning, "Thin film surface orientation for liquid crystals," *Applied Physics Letters* 1972, 21, 173–174.
[74] A. Sugimura, N. Yamamoto and T. Kawamura, "High surface ordering of nematic liquid crystal using periodicity grating," *Japanese Journal of Applied Physics* 1981, 20, 1343–1344.
[75] W. M. Gibbons, P. J. Shannon, S.-T. Sun and B. J. Swetlin, "Surface-mediated alignment of nematic liquid crystals with polaized light," *Nature* 1991, 351, 49–50.
[76] Y. Liao, L. Qiao, Z. Wang, M. Wang, L. Liu, K. Sugioka and Y. Cheng, "Fabrication of a liquid crystal light modulator by use of femtosecond-laser-induced nanoripples," *Optical Materials Express* 2013, 3, 1698–1704.
[77] "QSTAR-QqTOF Tandem Hybrid System, ESI-QqTOF," Maiman Institute for Proteome Research, George S. Wise Faculty of Life Sciences, Tel Aviv University, Israel, 2014. [Online]. Available: http://www.tau.ac.il/lifesci/units/proteomics/qstar.html.
[78] R. B. Cole, Ed., Electrospray Ionization Mass Spectroscopy; Fundamentals, Instrumentation and Application, New York: John Wiley & Sons, Inc., 1997.
[79] F. Schulz, Deposition ligandfreier Metall-Nanopartikel mittels Elektrospray und pneumatischer Zerstäubungsmethode zur Änderung von Grenzflächeneigenschaften; Dissertation, Fachbereich Chemie, Universität Essen, 2002.
[80] L. E. Stillwagon, R. G. Larson and G. N. Taylor, "Planarization of substrate topography by spin coating," *Journal of the Electrochemical Society: Solid State Science and Technology* 1987, 134, 2030–2037.
[81] J. B. Fenn, „Elektrospray: Molekulare Elefanten lernen das Fliegen (Nobel-Vortrag)", *Angewandte Chemie* 2003, 115, 3999–4024.
[82] L. F. Velasquez-Garcia, A. I. Akinwande and M. Martinez-Sanchez, "A planar array of microfabricated electrospray emitters for thruster applications", *Journal of Microelectromechanical Systems* 2006, 15, 1272–1280.
[83] B. Gassend, L. F. Velasquez-Garcia, A. I. Akinwande and M. Martinez-Sanchez, "A microfabricated planar electrospray array ionic liquid ion source with integrated extractor", *Journal of Microelectromechanical Systems* 2009, 18, 679–694.

M. Reininghaus, D. Ivanov, T. W. W. Maß, S. Eckert, L. Juschkin,
M. E. Garcia, T. Taubner, and R. Poprawe

2 Nanophotonic applications of fs-laser radiation induced nanostructures and their theoretical description

Abstract: We present the analysis of the optical properties of two different fs-laser-induced nanostructures which possess great potential for near-field applications due to their sub-100 nm features. The first structures are standing gold nanojets generated by irradiation of thin gold films with single pulses of fs-laser radiation. Due to their upright standing orientation, the characteristic extinction resonances of these nanojets are studied by grazing incidence infrared spectroscopy with p-polarized radiation. The resonance wavelength strongly depends on the lateral extent of the nanojet and can be tailored by adjusting the focusing numerical aperture and the applied pulse energy. The observed correlation between the lateral extent of the nanojet and the resonance wavelength is described by the monopole model of a linear antenna. The second type of structures under investigation are fs-laser-induced sub-wavelength ripples on silicon. Ripple structures of different geometrical shape are generated and coated with a thin gold film. Here, the metallic cover layer allows for the excitation of surface plasmons. Based on the generated surface profiles, the corresponding plasmonic resonances are simulated. Angle-resolved UV-VIS spectroscopy measurements are performed and the resulting plasmonic dispersion relation of these structures is compared to the calculated resonance conditions. The plasmonic resonances and additional experiments of the surface structures reveal insights into the localized or propagation nature of the plasmonic modes excited on generated surface profiles.

2.1 Introduction

The field of nanophotonics or nano-optics comprises the study of light on a nanometer, i.e. a subwavelength scale. In particular plasmonics, or in other words, optics with metallic nanostructures in the visible but also in the near and mid-IR spectral range, has been studied extensively during the last few decades [1–3]. Since nanostructures are able to affect light and control it on a nanometer scale, they have given rise to a variety of applications: e.g. surface enhanced spectroscopy [4], plasmonic sensors [5, 6], solar cells [7], superlenses [8], plasmonic beam shaping and collimation [9], chiral metamaterials [10, 11], and medical applications [12–14].

A key point of plasmonics with nanostructures is that nanostructures can be used as nanoantennas which can couple the energy of free space radiation to a confined

region of subwavelength size. In these so-called “hot spots”, electromagnetic fields can be enhanced by several orders of magnitude as compared to free space radiation [15]. As the strength of molecular vibrational signals characterized by Raman- and IR-spectroscopy strongly depends on the local field amplitude, near-field enhancing nanostructures can be used to increase the sensitivity for an analyte. These surface-sensitive techniques are then called Surface Enhanced Raman Spectroscopy (SERS) [16, 17], or Surface Enhanced Infrared Absorption Spectroscopy (SEIRAS) [18]. In the case of metallic nanoantennas, the local field enhancement is especially high if the localized surface plasmons are excited resonantly. Whereby the resonance condition and thus the field enhancement depend on the geometry and arrangement of nanostructures, their environment, as well as the wavelength and incident angle of the exciting light. Thus, a precise tailoring of these nanostructures or nanostructure arrays is required in order to control their properties and match them to specific applications. In this contribution, we present the generation, optical properties and potential applications of fs-laser radiation generated nanostructures, which can be varied in size and geometry and show tiny subwavelength features down to 20 nm.

The first structures are so-called “nanojets” or “standing antennas”, which are referred to as “gold nanoantennas” since their long axis is oriented perpendicularly to the substrate surface. Nanojets of different lengths and geometries, and thus different resonance conditions, can be produced with single fs-laser pulses [19]. An array of such nanojets is shown in Fig. 2.1 (a), with the inset showing an enlarged exemplary single nanojet. The width of a nanojet (several tens of nanometers), and its length (from a few hundred nanometers up to a few micrometers), determine the high aspect ratio of the structure. Furthermore, the tip size of these nanojets is around 20 nm in diameter. An excitation with grazing incident light leads to highly confined and enhanced fields at the nanojets’ tip. Importantly, due to the upright orientation of the nanojets, the volume in which the high fields emerge can easily be accessed. This is advantageous when compared to antennas oriented alongside the substrate surface. For the latter, high fields partly extend into the substrate and are therefore inappropriate for near-field based analytical applications [20]. Fs-laser pulse generated nanojets are highly reproducible and enable patterning of arbitrary antenna arrangements over large areas with high spatial accuracy and high processing speed. Therefore, a collective excitation of a tailored nanojet array becomes possible, which can also increase the near-field enhancement. These advantages make nanojet arrays particularly suitable for sensor applications and surface-enhanced spectroscopy.

The second structure is ripples on silicon. Under the applied experimental conditions, these periodic surface structures are oriented perpendicularly to the polarization of the incident laser radiation and can be generated with periodicities slightly smaller than the wavelength of the incident laser radiation. Figure 2.1 (b) shows a typical cross-section of a sinusoidal 2D ripple field generated on a silicon surface. When these ripples are coated with a thin gold film, the surface structures are conserved and the metallic properties of the thin gold film permit an angle-dependent light-

plasmon coupling. Furthermore, a variation of process parameters results in shallow or deeper ripples showing more or less pronounced subwavelength features. Consequently, these different features and geometries lead to a change in the optical response, enabling a tailoring of the optical properties of these structures for various applications. Deep ripple structures lead to more localized plasmonic modes with large near-fields in the sub-100 nm grooves and enable possible applications for plasmonic sensors and surface-enhanced spectroscopy. Periodic nanostructures can also be used for beam shaping [21] and plasmonic collimation [9, 22]. In particular, the shallow ripples, which enable propagating modes, could be generated on a laser-facet in order to decrease beam divergence [22, 23]. Generally, the ripple structures are capable of launching as well as out-coupling surface plasmon polaritons (SPP). This enables applications such as nanoscale detectors, SEIRA substrates, or plasmonic collimators. Fs-laser radiation is a promising tool for the production of inexpensive large-area plasmonic devices.

Besides their use for analytical applications, near-fields can also be applied to perform material modification in very tightly localized areas, as demonstrated for nanostructuring by the enhanced local field in the vicinity of a probe tip [24–27]. The use of nanostructures for the localized deposition of laser energy complements approaches to generate material modifications on the submicrometer scale [28–31].

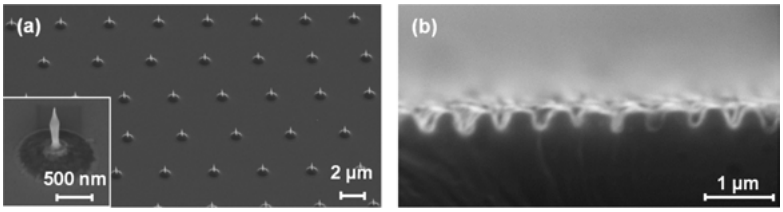

Fig. 2.1: (a) SEM image of gold nanojets generated by single ultrashort laser pulses. (b) SEM image shows cross-section of an extended ripple field on a silicon substrate generated by multiple ultrashort laser pulses.

2.2 Theoretical description of nanostructure generation with an ultrashort laser pulse

It has been demonstrated in a number of publications [32–35] that ordered arrays of hollow bumps, jet, and nanobarrier-like structures can be directly written onto metal films of different thicknesses by means of focusing an ultrashort laser pulse onto a material's surface at the fluence peak close to the material modification threshold; see Figs. 2.1 (a) and 2.2 (a). However, while experimental applications of material nanostructuring have made significant progress, especially in bio-technologies [36], the mechanisms of surface restructuring after short laser pulse excitation are still controversially discussed. In the particular case of thin metal films, possible mechanisms

discussed in the literature include Marangoni convection [32], peeling and expansion of the film due to the pressure of evaporating material [34], as well as thermo-elastic and plastic deformations of the film [37]. Significant efforts were also made in [33, 35] to elucidate the mechanism responsible for nanostructuring, where a combination of the mechanisms mentioned above was proposed.

Due to its complexity and significant difficulties of implementation, the experimental analysis of nanofeature formation mechanisms is commonly limited to a posteriori observations of the final, laser generated structures. However, they do not reveal the complete kinetics of the process. An a priori theoretical modeling of the nanostructuring processes, on the other hand, is also not a straightforward task. The essential difficulty here is dictated by the necessity of describing several transient concurrent processes occurring on wide time and spatial scales in a single computational cell. Not surprisingly, under the extreme conditions reached in the solid during ultrashort laser pulse exposure, the applicability of the continuum methods, such as the two temperature model (TTM) [38] is questionable [39–42]. An attractive alternative to continuum computational methods is provided by the combined atomistic-continuum MD-TTM method (molecular dynamics (MD) coupled with TTM). This method can account for both the kinetics of fast non-equilibrium phase transition processes at the atomic scale with MD, and the effect of free carrier dynamics in the continuum with TTM [43].

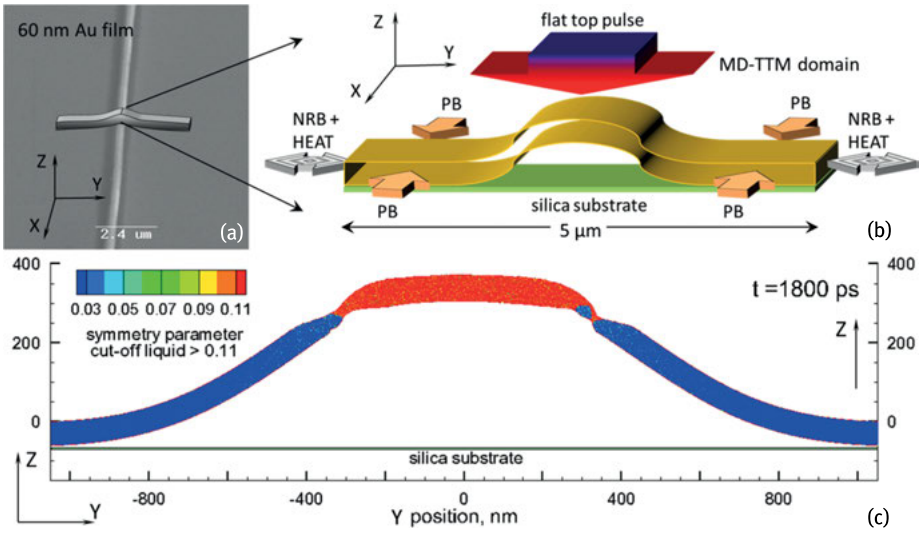

Fig. 2.2: (a) Nanobarrier generated on the surface of a gold film [33]. (b) Schematic of the computational cell used for super large scale modeling of the formation dynamics [44]. (c) A 0.5 nm thin slice of the atomic configuration of the MD domain in the YZ plane. The atoms are colored according to the central symmetry parameter (CSP), which quantitatively shows the matter of state. The parameter distinguishes between the crystalline (CSP $<$ 0.11, blue) and liquid (CSP $>$ 0.11, red) state of the gold film.

Recently, with the help of the MD-TTM model implemented in the optimized multiprocessing algorithm, the super large-scale simulation of the short laser pulse surface nanostructuring process was performed on an experimental scale [44, 45]. For a direct comparison of the theoretical model and the experimental results, we applied the experimental symmetry in the direction of the pulse elongation (Fig. 2.2 (a)). To simulate the generation of a nanobarrier kind of structure on a 60 nm thin gold film (Fig. 2.2 (a), vertical line) by a 30 fs flat-top laser pulse [33], we selected the computational cell, as schematically shown in Fig. 2.2 (b). The MD cell consists of 1.5×10^8 atoms with dimensions of $10 \times 5000 \times 60$ nm along the x, y, and z axes. In the y direction, the gold film ends with nonreflective boundaries (NRB) [44, 46]. In the x direction we applied periodic boundary (PB) conditions, and free boundaries (FB) were implemented at the top, where the material was irradiated with the laser pulse. At the bottom, the gold sample interacts with an immobile silica substrate on the xy plane. The direct comparison of model and experiment is also reinforced by the implementation of a realistic interatomic potential optimized for gold by Zhakhovskii [47]. The model also accounts for the complexity of the dependences of the free carrier system parameters, as well as for the thermoreflectance model by Hopkins [48]. The complete model and computational setup description is given elsewhere [44].

The incident fluence of 275 mJ/cm^2 (corresponding to the absorbed value of 30.2 mJ/cm^2) is taken slightly higher than in the experiments 125–250 mJ/cm^2. The onset of a spallation process leading to the generation of nanodroplets was also observed in the experiments [49–51]. The resulting nanobarrier-like structure obtained in our simulation can be seen in Fig. 2.2 (c) at the time of 1.8 ns. By considering how pressure, lift-off velocity, and the electron/lattice temperatures evolve over time, we can reconstruct the physical mechanisms involved in nanostructure formation. The relaxation of compressive stresses generated under confinement conditions [50] is identified as the main driving force responsible for accelerating a transiently melted region of the film, which results in nanostructure formation. On the other hand, fast electron heat conduction in 3D provides the ultrafast cooling of the molten material and enables rapid solidification of the surface features generated by the hydrodynamic motion of liquid material. Modeling on an experimental scale reveals the full complexity of the dynamics of thermo-physical quantities due to competing laser-induced processes involved in the mechanism of nanostructuring [45]. The characteristic time of nanostructure formation (~ 10 ns), size of the structures (~ 1 μm), lift-off velocity (~ 100 m/s) during the formation process [44] and finally the nanocrystalline character of the generated structure [49] obtained from our simulations were found to be in very good agreement with experimental results [32, 33, 35, 36]. To conclude, it is necessary to mention that for other experimental conditions other mechanisms like Marangoni convection, ablation processes, or laser beam interference with the surface plasmons [52] may play a significant role in nanostructuring.

2.3 Tailored resonances of upright gold nanoantennas

The following section deals with upright, infrared active gold antennas generated by single femtosecond laser pulses. We present two different approaches to tune the resonance wavelength of these nanojets in a graduated manner. An accurate adjustment of the resonance wavelength is essential to receive a maximized near-field enhanced signal in sensor applications and to enhance the sensitivity of infrared analysis and specificity. The tuning steps presented here allow for the adjustment of the resonance wavelength in the range of several micrometers down to several hundreds of nanometers.

2.3.1 Tailoring infrared resonances of upright gold nanoantennas

Throughout this study, a Ti:Sapphire CPA (chirped pulse amplification) laser system (Coherent, Libra) was used to generate tailored surface structures for near-field applications. To generate spiky nanojets on thin gold films, a variety of different microscope objectives with numerical apertures (NA) from 0.4 to 0.15 were used to focus the ultrashort pulsed laser radiation with a central wavelength of $\lambda = 800\,\text{nm}$ and a pulse duration of $\tau = 500\,\text{fs}$. The resulting focus diameter of 1.5 to 4 µm of the spatial Gaussian beam profile and the pulse energy of the single laser pulses determine the size of the generated nanojets; see Fig. 2.3 (a). Depending on the focal diameter, the applied pulse energies range from approximately 12 to 57 nJ and were adjusted by a combination of a $\lambda/2$-waveplate and a linear polarizing beam splitter.

A silicon substrate was coated with a 50 nm thin gold film by magnetron sputtering and mounted on an x, y translation stage. Separation of adjacent nanojets was controlled by the feed rate of a translation stage and the repetition rate of the pulsed laser radiation. To avoid any incubation effects on the formation dynamics of two neighboring structures, the distance between adjacent single pulses should be larger than twice the focal diameter of the laser beam.

The nanojet length was calculated from SEM images recorded under a tilting angle of 45°. Besides the lengths of the nanojets, the SEM images of the nanojets reveal a high aspect ratio larger than 10 : 1 and tip radii of less than 20 nm. Both features are essential for potential near-field applications. On the one hand, the high aspect ratio results in a spectral separation of the resonant frequencies of the long and short axes of the nanojet. For electromagnetic excitation of the nanojets in the near-infrared wavelength regime, we only have to consider the long axis of the nanojet. Additionally, the resonance properties can be approximated by a linear antenna. On the other hand, the spiky tip of the nanojets causes high near-field enhancement factors crucial for sensor applications.

We now present two methods which allow a gradual adjustment of the nanojet length l and the corresponding resonance wavelength λ_0. The length of the nanojets

can be varied by several micrometers with the coarse tuning step and by several hundred nanometers with the fine tuning step.

The coarse tuning step consists of applying different numerical apertures to focus the single ultrashort laser pulses onto the surface of the thin gold film. The selection of the numerical aperture determines the lateral extent of the irradiated spot on the gold surface, and hence the extent of the induced melt pool. Larger melt pools comprise an extended volume of gold which can potentially be ejected to form the nanojet. This tuning step can thereby be used to form nanojets with a length of up to three micrometers. As the size of the irradiated surface increases, properties such as morphology, crystallinity, grain sizes and imperfections of the thin gold film constitute limiting factors of the fragile stress-based formation dynamics. Due to decreasing reproducibility with increasing size, we confine our experiments to nanojet lengths of 0.42 to 1.61 µm, resulting in characteristic resonance wavelengths of 2.46 to 6.51 µm; see Fig. 2.3 (a).

The fine tuning step allows for an adjustment of the nanojet resonance wavelength in the range of several hundreds of nanometers. It is based on the exact control of gold volume ejected from the melt pool. The ejected volume can be accurately controlled by adjusting the pulse energy under constant focusing conditions. To generate a nanojet of 0.73 µm in length and a corresponding resonance wavelength of 3.33 µm, we applied a focal diameter of 1.5 µm and a pulse energy of 12.3 nJ; see Fig. 2.3 (b). A further increase in the pulse energy leads to an additional ejection of gold from the melt pool. The additionally ejected gold forms a gold sphere, which can be ablated.

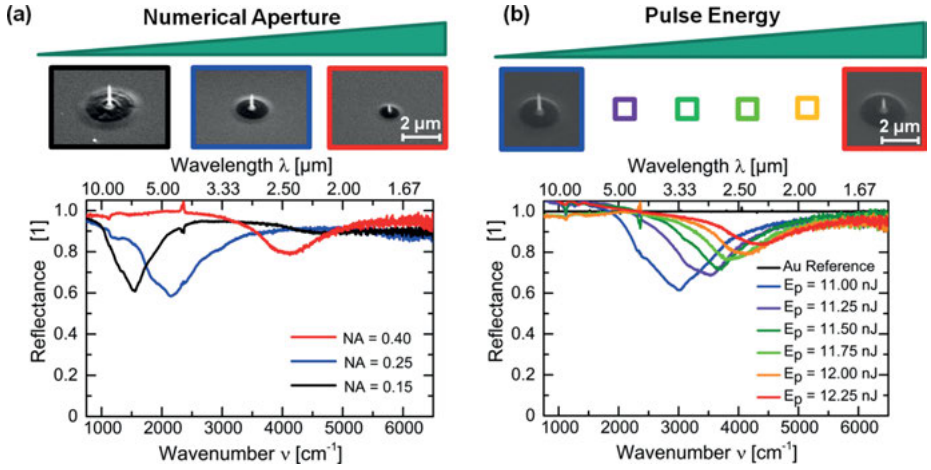

Fig. 2.3: Two approaches to tune the resonance wavelength of the nanojets. (a) A coarse tuning step is based on applying different numerical apertures to tune the resonance wavelength in the range of several µm. (b) The adjustment of the pulse energy allows for the fine tuning of the resonance wavelength by several hundreds of nanometers.

In consequence, the effective mass of gold remaining available to form the nanojet is reduced, the nanojet length decreased and the corresponding resonance wavelength shifted to smaller wavelengths.

A reproducible formation process is necessary to generate a field of approximately 300 identical nanojets (Fig. 2.1 (a)), which can be characterized by means of Fourier transformed infrared spectroscopy (FTIR) to determine the resonance wavelength of the corresponding nanojets; see Fig. 2.3 (a). Because of their orientation, the reflectance spectra of the upright nanojets are recorded under a grazing incidence angle of 83°. Additionally, the polarization of the incident electromagnetic field is oriented almost parallel to the long axis of the nanojets to obtain an optimized, enhanced resonance signal.

2.3.2 Correlation of resonance wavelength and nanojet length

We applied a monopole model to theoretically describe the correlation of nanojet length and the observed resonance wavelength [53, 54]. For this purpose, we define the nanojet length l as the vertical extent from the base of the bump-like structure to the tip of the nanojet, as depicted in Fig. 2.4 (a). When the nanojet is irradiated with p-polarized light under grazing incidence, the electromagnetic field causes a separation of opposite charges within the nanojet as shown in Fig. 2.4 (b). Due to the metallic nature of the substrate, a distribution of the free charge carrier arises, which nullifies all tangential field vectors at the surface of the conductor. In this case, the resulting electric field distribution can be described by introducing a mirror plane and image charges as depicted in Fig. 2.4 (c). The resulting effective dipole antenna exhibits a vertical extent that is twice the length of the original nanojet length l. With respect to the resonance wavelength of a dipole, the expected dependence of the resonance wavelength and the length of the nanojet should obey the linear correlation of

$$l = \frac{\lambda_0}{4}. \tag{2.1}$$

Figure 2.4 (d) shows a compilation of different nanojets generated with various focusing optics and pulse energies. The resulting nanojet lengths extracted from the SEM images are plotted versus the experimentally determined resonance wavelengths so as to validate the assumed model represented by the solid line. Apart from a slight trend to redshift, the observed resonance wavelengths match the theoretically expected resonance wavelengths of the $\lambda_0/4$-model.

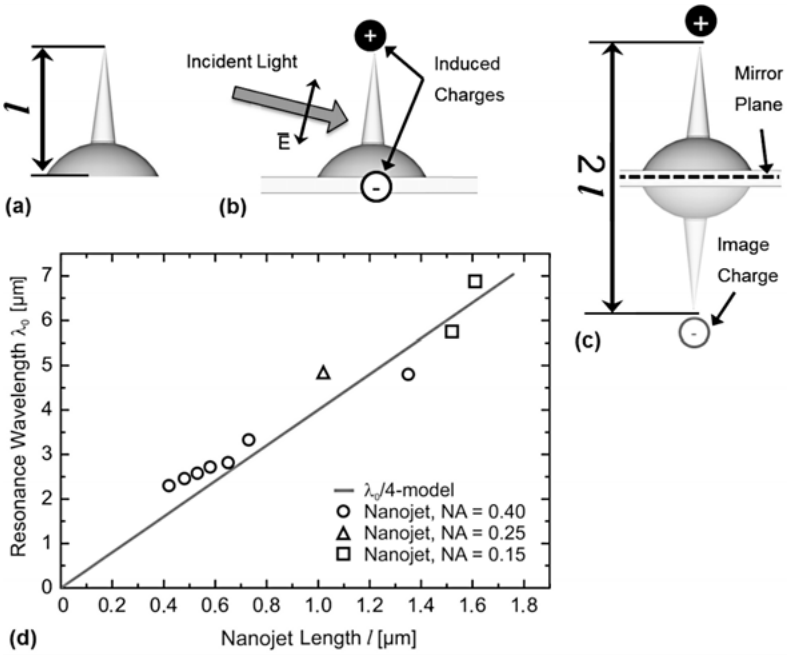

Fig. 2.4: (a) Schematic of a spiky nanojet and the definition of the nanojet length *l*. (b) Illumination of the nanojet with an electromagnetic wave, polarized almost parallel to the long axis of the nanojet causes the illustrated charge distribution. (c) As the nanojet is generated on a conductive substrate, the charge distribution shown in (b) can be described by introducing image charges resulting in a resonance wavelength that equals four times the nanojet length *l*. (d) Comparison of experimental data and theoretical model. The experimentally observed dependence of the nanojet length and the corresponding resonance wavelength validates the assumptions of the $\lambda_0/4$-model.

2.4 Plasmonic excitation of ripple structures generated by fs-laser radiation

In the following section, we evaluate how well ripple structures generated by ultrashort pulsed laser radiation can be applied to excite propagating surface plasmons. The controlled excitation of these optical surface modes is a central aspect to generate tailored functional surfaces for plasmonic applications such as biosensors [5] or the integrated collimation of laser diodes [55].

To enable the plasmonic excitation, we generated extended areas of ripples and coated these structures with a thin metallic film. Based on these structures, we calculated excitation conditions for different plasmonic resonances. In a second step, we present two possible pathways for experimental validation of the calculated resonances. On the one hand, we estimate the plasmonic dispersion relation of the generated structures and assign the character of the occurring resonances to located and

propagating plasmonic modes. On the other hand, we generate different ripple geometries to prove the localized or propagating nature of the identified plasmonic excitation as a function of the geometrical shape of the ripple structures.

2.4.1 Generation of ripple structures

Alongside beads, spikes and others, ripple structures belong to laser-induced periodic surface structures (LIPSS). They were discovered in the mid-1960s, and since then various types of ripple structures have been observed on almost every laser irradiated material [56]. Even for a distinct type of ripple, so-called low spatial frequency LIPSS (LSFL), scientists still do not agree upon the underlying physics of the formation process. These ripples are generated at near ablation threshold conditions when a substrate is irradiated with multiple linearly polarized fs-laser pulses. Their period is slightly smaller than the wavelength of the applied laser radiation. The minor deviation is explained by an efficiency factor, which accounts for inhomogeneous absorption of the incident laser radiation due to surface roughness [57]. In accordance with the latter publication, a widely accepted approach to describe the formation of LSFL is based on the interference of electromagnetic surface waves or so-called surface plasmons with the incident laser radiation [58]. To meet the coupling conditions of the incident light with surface plasmons, an initial surface roughness amplitude of 8 nm or impurities is necessary [59]. For every following pulse the nascent impurities or defects generated by the previous pulse or pulses ensure fulfillment of the resonance conditions.

To explain the decreasing period of the observed structures with increasing number of pulses per area, so-called feedback mechanisms have been developed. The different approaches assume angle-dependent effects [60], dependencies on optically generated free carrier concentrations [61], or inherent regulating mechanisms. The latter approach describes the change of the ripple period as a consequence of the ripple structures deepening during the ongoing ablation process. This deepening shifts the resonance conditions to lower frequencies. To continue to match the resonance conditions for the constant excitation wavelength, the ripple period readjusts itself to maintain the resonant excitation of surface plasmons [62].

As was shown previously, the applied fluence and the number of pulses per area are the most crucial parameters to manipulate the period of the ripple structures while the wavelength of the incident ultrashort pulsed laser radiation is kept constant. Since our goal is to characterize possible plasmon resonances on extended ripple fields, we also have to take profile, groove depth and the progressive evolution of the generated ripple structures on a large area into account.

In order to structure ripple fields of cm^2 in size, the pulsed laser radiation is focused by the use of a 50 mm plano-convex lens onto a native silicon surface, resulting in a focus diameter of $2w_0 = 13\,\mu m$. The polarization and the pulse energy of the

ultrashort pulsed laser radiation are adjusted by a combination of a $\lambda/2$-waveplate and a linear polarizing beam splitter. To increase the intensity and, in consequence, the non-linear absorption of the ultrashort pulsed laser radiation, we apply the shortest possible pulse duration of the laser system of $\tau = 100$ fs.

In accordance with previous analysis, the single pulse ablation threshold of the native silicon target is experimentally determined to be 265 mJ/cm^2 [63]. With respect to this ablation threshold, all investigated structures are generated at sub-threshold fluences. In detail, the investigated process window includes peak fluences of 75 to 220 mJ/cm^2, corresponding to pulse energies of 100 to 265 nJ, respectively. The pulse-to-pulse stability of more than 99.7 % enables an advantageously precise control of the deposited energy density, which is essential to generate large, homogeneously extended ripple fields.

The silicon sample is mounted on an x, y translation stage and the repetition rate is kept at a constant value of $f = 1$ kHz. Thus, the pulse overlap in the direction of the translation is varied only by adjusting the speed of the sample movement. The number of pulses per area N is defined by the adjacent pulses within the same line in combination with the corresponding pulses of the neighboring lines. To reduce the number of possible parameter sets, we use a symmetric meander shaped scan strategy. In this context, 'symmetric' denotes an identical pulse overlap between adjacent pulses in the same line and pulses of neighboring lines. Besides the pulse energy, the polarization and the number of pulses per area basically determine the structural properties of the local ripple structures, whereas the scan strategy is of crucial importance with regard to the progressive evolution of coherent ripple structures on large fields up to several cm^2. In all experiments we carried out, the scan strategy did not affect the geometry of the locally generated structures, but the progressive evolution of ripple structures. In general, the progressive evolution of ripple structures is most favorable when the feed direction of the sample is oriented perpendicularly to the polarization of the laser radiation. In this case, the grooves of the ripple structures are oriented parallel to the feed direction of the sample, and the laser radiation progressively generates ripple structures along their grooves.

In the aforementioned process window, we observe three types of ripple structures. The smallest observed periodic structure occurs at a peak fluence of 176 mJ/cm^2 and 208 pulses per area. It is 10 to 20 nm in height and shows a u-shaped cross-section; see Fig. 2.5 (a). Apart from the reduced length of this structure, the shape is comparable to a directly structured line consisting of a groove that is bordered by a wall of redeposited material on each side. The distance between the two walls is in the region of 100 nm and the period of neighboring grooves is 700 nm. With respect to potential applications, this structure can be progressively propagated. At a peak fluence of 200 mJ/cm^2 and 52 pulses per area, the latter structure co-exists, but is locally superimposed by holes with a depth of 50 to 100 nm. These holes are arranged in 1 µm thin lines oriented parallel to the polarization. Within these lines the holes possess a periodicity slightly smaller than 700 nm. Because of the random transition between

the first and this second structure, the latter structure is not applicable for large extended ripple fields; see Fig. 2.5 (b). An increase in the number of pulses per area leads to another significant deepening of the holes. The resulting ripple structures of this third regime appear to be approximately 300 nm; see Fig. 2.5 (c), and very uniform periodic gratings with a lateral extent of several centimeters can be achieved for these ripple structures [20, 64]. Compared to the 50–100 nm flat ripple structures, these structures occur with a more plateau-like profile (Fig. 2.6 (a)) and narrow grooves in the sub-100 nm regime. In particular, these narrow and 300 nm deep grooves cause high near-field intensities when irradiated by a laser pulse [65], which is essential for potential sensor applications. Besides the ripple profile, the period of the ripple structures shifts to a smaller value of 620 nm, which is consistent with the aforementioned feedback mechanisms [61, 62].

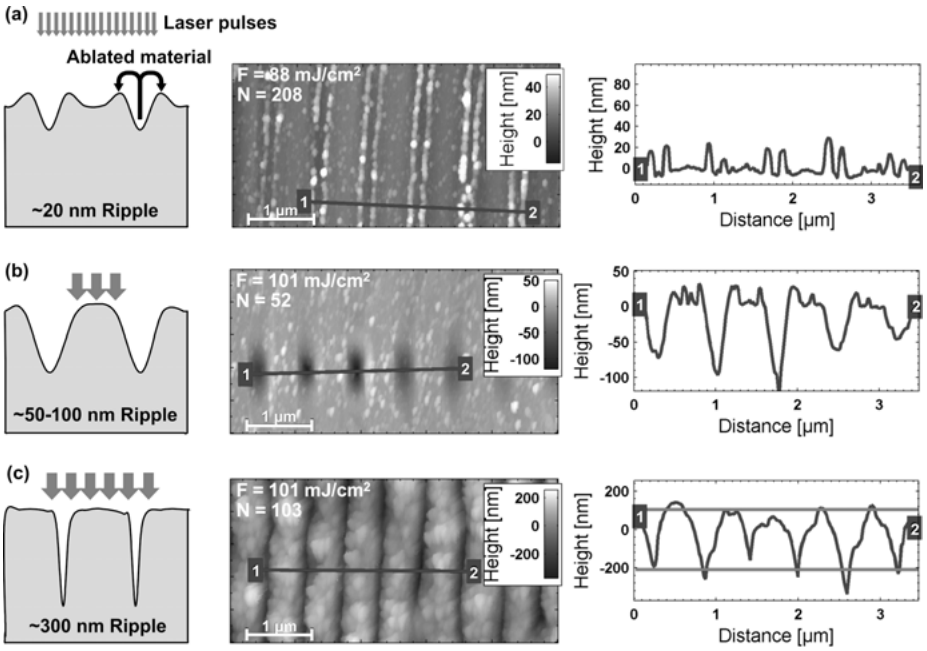

Fig. 2.5: Different types of ripple structures generated by ultrashort pulsed laser radiation. The schematics on the left illustrate the observed formation of ripples depending on the applied fluence F and the number of pulses per area N. The center column shows AFM images of the generated ripple structures and the corresponding profile on the right. (a) At fluences of 88 mJ/cm^2 and 208 pulses per area, u-shaped structures with a height of 20 nm are observed. (b) At higher fluences and 52 pulses per area, the evolution of 50 to 100 nm deep grooves is observed. (c) Compared to (b), the groove depth significantly increases from 50 nm to 300 nm by slightly increasing the number of pulses per area. Additionally, a reduced ripple period reveals the presence of a feedback mechanism as proposed in [61, 62, 66, 67].

2.4.2 Simulation of plasmon resonances

In the following section we calculated possible plasmonic resonances based on the profile of the generated ripple structures. The applied numerical simulation has been developed and extended by various authors over the last 30 years and enables the theoretical description of resonances of periodic metal gratings [68, 69].

Central to this numerical approach, the coordinate system is transformed into a nonorthogonal system determined by the periodic morphology of the irradiated surface. Subsequently, the Maxwell equations are formulated in the corresponding coordinates and the electromagnetic field distributions or plasmonic resonances are calculated in Fourier space. For the excitation of plasmons, free charge carriers at the metal/dielectric interface are necessary. Therefore, we cover the surface of the laser generated ripple structures with a thin gold film of 550 nm thickness. SEM (Fig. 2.6 (a) and (b)) and AFM measurements demonstrate how the morphology was successfully transferred from the rippled silicon surface to the sputter deposited thin gold film. This is of great importance, as in particular the groove depth, general profile, period and groove width impact the resonances of the plasmonic excitation substantially. Next, we calculate the spectral reflectivity or plasmonic resonances of a sinusoidal grating profile as a function of the groove depth. In the context of plasmonic excitation, reduced reflectivity corresponds to an enhanced coupling of the incident light to the plasmonic modes. This is the case whenever the in-plane momentum of the diffracted orders of the incident light matches the momentum of the plasmons at the metal/dielectric interface [70]. Figure 2.6 (c) shows the plasmonic resonances calculated for a constant wavelength of 800 nm and an incident angle close to zero degrees. The vertical dashed lines represent the pseudocritical edges, where a diffraction order becomes evanescent. In total, three plasmonic resonances between 740 and 840 nm occur, which will be discussed in detail.

For a ripple depth of a few nanometers, no plasmonic resonance is observed. At ripple depths of 10 to 100 nm, two significant plasmonic resonances are observed which are attributed to the diffraction order of the first two Bragg planes $m = \pm 1$ at 755 and 780 nm, respectively. These two modes show no significant wavelength dependence. For ripple depths between 70 and 120 nm, the energy transfer of incident light to the surface plasmons is reduced. A further increase in the depth of the ripple structures up to 300 nm leads to a third plasmonic mode. This mode shifts to longer wavelengths with increasing depths, which is in accordance with the different feedback mechanisms mentioned above. Under the assumption of the plasmonic feedback mechanism predicted by Huang [62], the plasmonic resonances shift to lower frequencies or longer wavelengths as a consequence of the deepening of the ripple structure. As a consequence of the lower resonance frequencies, the period of the ripple structure has to be reduced in order to maintain the resonance conditions for a constant excitation wavelength. For this reason, the calculated plasmon resonances

validate the theoretically predicted change in the ripple period and the experimental observations presented in Fig. 2.5.

The reflectance of 40 and 300 nm deep ripples is shown in Fig. 2.6 (d) to emphasize the drop of reflectivity due to plasmonic excitation at a certain resonance wavelength. To evaluate the applicability of these structures for sensors or optical collimators, we investigate the optical properties of these ripple structures.

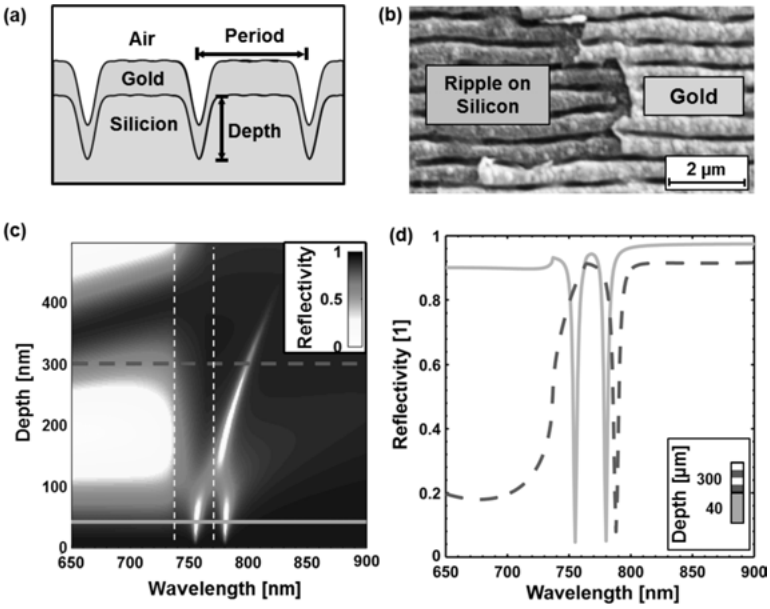

Fig. 2.6: (a) Schematic of the gold coated ripple sample produced to investigate the plasmon resonances and plasmon propagation at the gold/air interface. (b) Ripples on silicon partially covered with a 500 nm thin goldfilm. The sample demonstrates the successful transfer of the rippled surface strucures from the silicon surface onto the surface of the evaporated thin gold film. (c) Calculated plasmon resonances of an extended, sinusoidal ripple field in dependence on the groove depth and the excitation wavelength. (d) Two selected groove depths are extracted from (c) to emphasize the occurrence of the pseudocritical edge at 740 nm (vertical dashed line in (c)), and the three possible plasmon resonances for a grating with a groove depth of 40 (solid line) or 300 nm (dashed line), respectively.

2.4.3 Optical properties of ripple structures

To validate the assumption of a plasmonic excitation of ripple structured surfaces and to evaluate the localized or propagating nature of the excited modes, we perform angle-resolved reflectivity measurements as a function of the incident wavelength and determine the plasmonic dispersion relation. Due to the spot diameter of 5 mm of the spectrometer utilized, the samples we applied consist of progressively extended ripple

fields with an edge length of 1 cm. The ripple structures under investigation possess a period of 640 nm, a groove depth of 300 nm and a profile comparable to the one shown in Fig. 2.5 (c). Due to the calculations (Fig. 2.6 (b)), we expect the plasmonic resonance to appear around 800 nm. Figure 2.7 (a) shows the angle-resolved reflectivity from 10° to 60° in 10° steps. In the wavelength interval of interest from 700 to 1300 nm, two distinct reflectivity dips or resonances are observed when the polarization of the incident radiation of the applied thermal light source is oriented perpendicularly to the ripple structures (transverse magnetic (TM)). The surface plasmon (SP2) resonance occurring at a smaller wavelength of approximately 800 nm reveals an angle dependency, while the wavelength of the other resonance at 1200 nm (SP1) is not affected by the angle of incidence. As expected for plasmonic origin of the observed resonances, the recorded spectrum of the reflectivity excited by a transverse electric (TE) plane wave shows no resonances; see Fig. 2.7 (b). In this case, the incident electric field is oriented completely parallel to the ripple structures and, therefore is not affected by the periodical ripple structures. On the contrary, the TE-polarized radiation is reflected as if it were reflected by a planar surface. For comparison, we plot the angle-dependent SP2 resonance with the theoretically expected angle dependency of an SPP of a planar surface [71], which obeys

$$\sin(\theta) = -\frac{m\lambda}{n_d d} \pm \frac{1}{n_d}\sqrt{\frac{\varepsilon'_m}{\varepsilon_d + \varepsilon'_m}} \tag{2.2}$$

Here, θ and λ denote the polar angle and the wavelength of the incident electromagnetic wave respectively. The influence of the grating is represented by the period of the grating d and the integer multiples of the grating wave vector in reciprocal space m. The specific material properties are accounted for by the refractive index in air $n_d = 1$, the dielectric constants $\varepsilon_d \approx 1$ in air, and the real part of the dielectric constant of the gold film $\varepsilon'_m \approx -15$ [72]. For incident angles of 15° to 40°, the experimentally determined resonance wavelength is in agreement with the SPP resonance. In contrast, for smaller incident angles the resonance wavelength approximates a constant value of 810 nm and the deviation between experimental data and the theoretical expectation increases. This observation implies the pronounced localized character of the excited plasmons due to a flat plasmonic band structure. To illustrate the latter interpretation, additional reflectivity measurements with an accuracy of 2° were performed. The resulting dispersion relation includes the seven selected measurements seen in Fig. 2.7 (a), highlighted as colored lines. The two observed resonances at 390 and 260 THz correspond to a resonance wavelength of 810 and 1160 nm, respectively. The absence of a nonzero slope in the plasmonic band structure for the SP1 mode and a vanishing small dispersion of the SP2 mode support the assumption of localized plasmonic modes.

The experimental proof of the propagating nature of plasmonic modes is implied by the optical observation of a plasmonic energy transfer between spatially separated structures. Therefore, we generate one sample with 50 nm and another with 300 nm

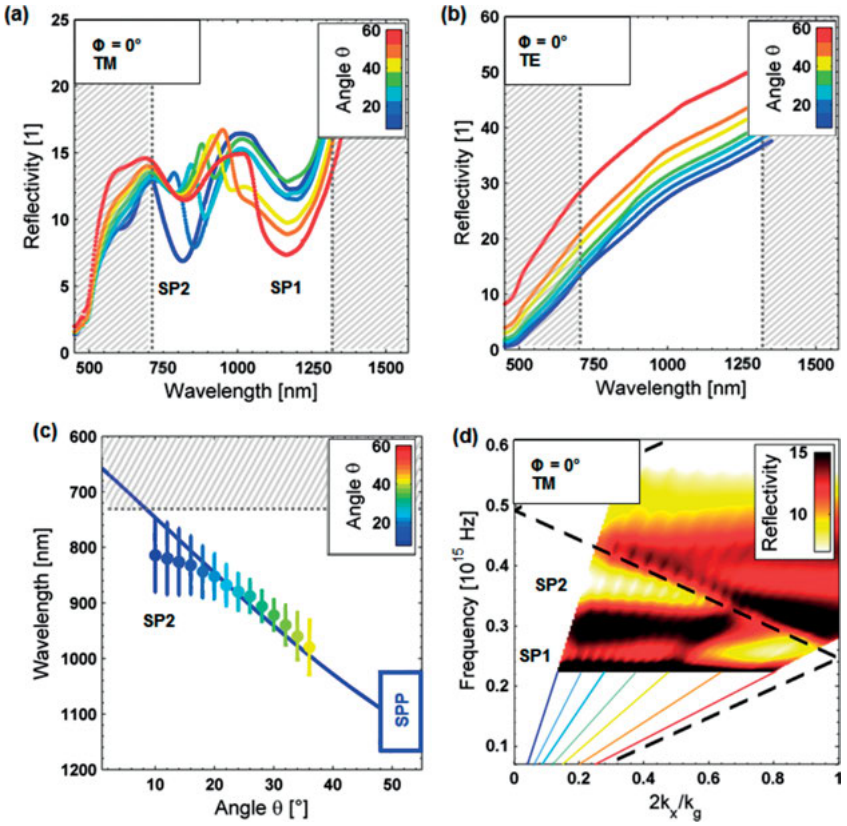

Fig. 2.7: (a) Angle- and wavelength-dependent reflectivity measurements of ripple structures (sample presented in Fig. 2.6) with TM-polarized radiation. (b) For a TE-polarized plane wave the observed resonances vanishes, which confirms the assumption of the plasmonic origin of the resonances observed in (a). (c) The angle-dependent position of the plasmon resonance around 800 nm is extracted from (a) and compared to the theoretically predicted angle-dependent plasmon resonance described by equation (2.2). (d) Experimentally determined dispersion relation of an extended ripple field. Colored lines represent the selected spectra illustrated in (a).

deep ripple structures (Fig. 2.5 (b) and (c)). On each sample two smaller fields with identical ripple structures are separated by an unmodified area. A coaxial microscope setup (Fig. 2.8 (a)) is utilized to excite one of the ripple fields and to observe the plasmonic energy transfer to the separated non-irradiated ripple field. Figure 2.8 (b) shows the corresponding light microscope image, in which the laser generated ripple structures occur as dark structures, while the light area shows the unmodified area which separates the opposing ripple structures by approximately 50 µm. Consistent with the vanishing propagating nature of the SP2 mode of the 300 nm deep ripple structures described above, the plasmonic energy transfer between the generated ripple fields is only observed for the 50 nm flat ripple structures. As shown in Fig. 2.8 (c), the ripple

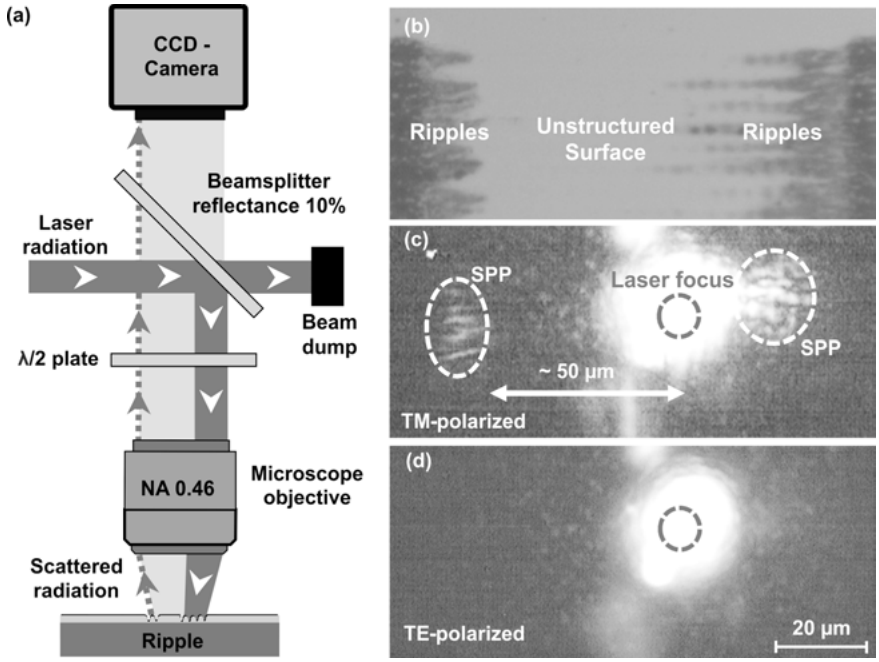

Fig. 2.8: (a) Schematic of the coaxial microscope setup applied to visualize the propagation of surface plasmons. (b) Microscope image of the ripple structures (appear as dark structures) separated by approximately 50 µm of unstructured surface (light area). (c) 50 nm flat ripple structures are irradiated by TM-polarized laser radiation under plasmon resonance conditions. Therefore, energy can propagate to the non-irradiated, neighboring ripple field at a distance of 50 µm. At this field the surface plasmons are scattered and can be detected as luminescent spots. (d) Illumination of the same ripple structures under TE-polarized laser radiation.

structures on the right are irradiated by focused laser radiation with a wavelength of 800 nm. The applied pulse energy of less than 10 nJ and a focus diameter of 2 µm result in a fluence below the ablation threshold. The excitation of surface plasmons enables energy transfer from the irradiated ripples on the right to the ripple field on the left. Since the photon-plasmon coupling conditions are identical for excitation and scattering, the transferred energy is reemitted at the ripple structures on the left and can be detected as bright spots (marked as SPP). To validate the plasmonic origin of the detected emission and to exclude any undesirable irradiation which may result from reflections, the setup includes a $\lambda/2$-waveplate which allows switching between TM and TE oriented excitation, respectively. As can be seen from the direct comparison of Fig. 2.8 (c) and Fig. 2.8 (d), the successful energy transfer is only present for the valid resonance conditions of TM-polarized excitation. The effective excitation of SPPs is observed for almost normal incidence. Based on the ripple period of 720 nm and the aforementioned values of the refractive index, this agrees with the theoretically expected incident angle of 4.4°, calculated using equation (2.2). In conclusion, the

experimental results imply an energy transfer by propagating surface plasmons on flat laser-generated ripple structures and reveal their potential for optical couplers or optical beam shaping.

2.5 Conclusion

In conclusion, we have presented theoretical and experimental aspects of femtosecond laser-generated nanostructures for near-field applications. In the theoretical section we introduced a simulation for laser materials processing in consideration of molecular dynamics and the two temperature model on wide time and spatial scales. The resulting time scales and feature sizes of the formation process of the applied simulation are in good agreement with experimental results and support the valid description of the stress-based formation of metallic nanostructures with respect to free carrier dynamics as well as nonequilibrium phase transformations at atomic scales.

Experimentally, we applied single ultrashort pulses to generate upright gold nanojets. These nanojets exhibit a large aspect ratio of 10 : 1 and tip radii of approximately 20 nm. Due to their geometrical dimensions, these nanojets induce highly localized electromagnetic fields and have great potential for analytical applications based on near-field enhancement in the near-infrared wavelength regime. As the adjustment of the resonance frequency is of crucial importance for such applications, we presented two possible ways of tailoring the nanojet length and the corresponding resonance wavelength in a gradual manner.

In addition to nanojets, we generated extended ripple fields on silicon and coated the occurring ripple structures with a thin gold film; subsequently, surface plasmons were excited at the gold/air interface. Two different experimental approaches are presented to distinguish between propagating and localized plasmonic modes. The small features of the observed deep ripple structures reveal high electromagnetic near-fields, which make them promising for sensor applications. On the other hand, the 50 nm flat ripple structures preferentially tend to exhibit propagating plasmonic modes which match the requirements of applications such as optical beam shaping.

References

[1] Fang Z, Zhu X. Plasmonics in Nanostructures, Adv Mater 2013, 25, 3840.
[2] Zeng S, Baillargeat D, Ho H, Yong K. Nanomaterials enhanced surface plasmon resonance for biological and chemical sensing applications, Chem Soc Rev 2014, 43, 3426.
[3] Law S, Podolskiy V, Wasserman D. Towards nano-scale photonics with micro-scale photons: the opportunities and challenges of mid-infrared plasmonics, Nanophotonics 2013, 2, 103–130.
[4] Aroca R. Surface-Enhanced Vibrational Spectroscopy. Southern Gate, Chichester, West Sussex, England, John Wiley & Sons Ltd, 2007.
[5] Chen Y, Ming H. Review of surface plasmon resonance and localized surface plasmon resonance sensor, Photonic Sens 2012, 2, 37.
[6] Willets KA, Van Duyne, RP. Localized Surface Plasmon Resonance Spectroscopy and Sensing, Annu Rev Phys Chem 2007, 58, 267.
[7] Atwater HA, Polman A. Plasmonics for improved photovoltaic devices, Nat Mater 2010, 9, 205.
[8] Kawata S, Inouye Y, Verma P. Plasmonics for near-field nano-imaging and superlensing, Nat Photonics 2009, 3, 388.
[9] Yu N, Fan J, Wang QJ, Pflügl C, Diehl L, Edamura T, Yamanishi M, Kan H, Capasso F. Small-divergence semiconductor lasers by plasmonic collimation, Nat Photonics 2008, 2, 564.
[10] Li Z, Mutlu M, Özbay E. Chiral metamaterials: from optical activity and negative refractive index to asymmetric transmission, J Opt 2013, 15, 23001.
[11] Mackay TG, Lakhtakia A. Negatively refracting chiral metamaterials: a review, J Photon Energy 2010, 18003.
[12] Ayala-Orozco C, Urban C, Bishnoi S, Urban A, Charron H, Mitchell T, Shea M, Nanda S, Schiff R, Halas N, Joshi A. Sub-100nm gold nanomatryoshkas improve photo-thermal therapy efficacy in large and highly aggressive triple negative breast tumors, J Control Release 2014, 191, 90.
[13] Garwe F, Czaki A, Maubach G, Steinbrück G, Weise A, König K, Fritzsche W. Laser pulse energy conversion on sequence-specifically bound metal nanoparticles and its application for DNA manipulation, Med. Laser Appl. 2005, 20, 201–206.
[14] Czaki A, Garwe F, Steinbrück A, Maubach G, Festag G, Weise A, Riemann I, König K, Fritzsche W. A parallel approach for sub-wavelength molecular surgery using gene-specific positioned metal nanoparticles as laser light antennas, Nanoletters 2007, 2, 247–253.
[15] Wei H, Xu H. Hot spots in different metal nanostructures for plasmon-enhanced Raman spectroscopy, Nanoscale 2013, 5, 10794.
[16] McNay G, Eustace D, Smith WE, Faulds K, Graham D. Surface-Enhanced Raman Scattering (SERS) and Surface-Enhanced Resonance Raman Scattering (SERRS): A Review of Applications, Appl Spectrosc 2011, 65, 825.
[17] Schlücker S. Surface-Enhanced Raman Spectroscopy: Concepts and Chemical Applications, Angew Chem Int Ed 2014, 53, 4756.
[18] Aroca RF, Ross DJ. Surface-Enhanced Infrared Spectroscopy, Appl Spectrosc 2004, 58, 324–338.
[19] Reininghaus M, Wortmann D, Cao Z, Hoffmann JM, Taubner T. Fabrication and spectral tuning of standing gold infrared antennas using single fs-laser pulses, Opt Express 2013, 21, 32176.
[20] Adato R, Yanik AA, Wu C, Shvets G, Altug H. Radiative engineering of plasmon lifetimes in embedded nanoantenna arrays, Opt Express 2010, 18, 4526.
[21] Lin D, Fan P, Hasman E, Brongersma ML. Dielectric gradient metasurface optical elements, Science 2014, 345, 298.
[22] Yu N, Wang Q, Capasso F. Beam engineering of quantum cascade lasers, Laser & Photon Rev 2012, 6, 24.

[23] Yu N, Blanchard R, Fan J, Wang QJ, Pflügl C, Diehl L, Edamura T, Yamanishi M, Kan H, Capasso F. Quantum cascade lasers with integrated plasmonic antenna-array collimators, Opt Express 2008, 16, 19447.
[24] Boneberg J, Münzer H, Tresp M, Ochmann M, Leiderer P. The mechanism of nanostructuring upon nanosecond laser irradiation of a STM tip, Appl Phys A 1998, 67, 381.
[25] Chimmalgi A, Choi TY, Grigoropoulos CP, Komvopoulos K. Femtosecond laser aperture less near-field nanomachining of metals assisted by scanning probe microscopy, Appl Phys Lett 2003, 82, 1146.
[26] Huang SM, Hong MH, Luk'yanchuk BS, Zheng YW, Song WD, Lu YF, Chong TC. Pulsed laser-assisted surface structuring with optical near-field enhanced effects, J Appl Phys 2002, 92, 2495.
[27] Jersch J, Demming F, Hildenhagen J, Dickmann K. Nano-material processing with laser radiation in the near field of a scanning probe tip, Opt Laser Technol 1998, 29, 433.
[28] Korte F, Serbin J, Koch J, Egbert A, Fallnich C, Ostendorf A, Chichkov BN. Towards nanostructuring with femtosecond laser pulses, Appl Phys A 2003, 77, 229.
[29] Pronko PP, Dutta SK, Squier J, Rudd JV, Du D, Mourou G. Machining of sub-micron holes using a femtosecond laser at 800 nm, Opt Commun 1995, 114, 106.
[30] Dahotre NB, Harimkar SP. Laser Fabrication and Machining of Materials, New York, USA, Springer Science+Business Media, 2008.
[31] Simon P, Ihlemann J. Machining of submicron structures on metals and semiconductors by ultrashort UV-laser pulses, Appl Phys A 1996, 63, 505.
[32] Korte F, Koch J, Chichkov BN. Formation of microbumps and nanojets on gold targets by femtosecond laser pulses, Appl Phys A 2004, 79, 879.
[33] Kuznetsov AI, Koch J, Chichkov BN. Nanostructuring of thin gold films by femtosecond lasers, Appl Phys A 2009, 94, 221.
[34] Nakata Y, Okada T, Maeda M. Nano-sized hollow bump array generated by single femtosecond laser pulse, Jpn J Appl Phys 2003, 42, L1452.
[35] Wortmann D, Koch J, Reininghaus M, Unger C, Hulverscheidt C, Ivanov D, Chichkov BN. Experimental and theoretical investigation on fs-laser-induced nanostructure formation on thin gold films, J Laser Appl 2012, 24, 42017.
[36] Fadeeva E, Truong VK, Stiesch M, Chichkov BN, Crawford RJ, Wang J, Ivanova EP. Bacterial retention on superhydrophobic titanium surfaces fabricated by femtosecond laser ablation, Langmuir 2011, 27, 3012.
[37] Meshcheryakov YP, Bulgakova NM. Thermoelastic modeling of microbump and nanojet formation on nanosize gold films under femtosecond laser irradiation, Appl Phys A 2006, 82, 363.
[38] Anisimov SI, Kapeliovich BL, Perel'man TL. Electron emission from metal surfaces exposed to ultrashort laser pulses, Soviet Physics JETP 1974, 39, 365.
[39] Agranat MB, Ashitkov SI, Fortov VE, Kirillin AV, Kostanovskii AV, Anisimov SI, Kondratenko PS. Use of optical anisotropy for study of ultrafast phase transformations at solid surfaces, Appl Phys A 1999, 69, 637.
[40] Lu K, Li Y. Homogeneous nucleation catastrophe as a kinetic stability limit for superheated crystal, Phys Rev Lett 1998, 80, 4474.
[41] Rethfeld B, Sokolowski-Tinten K, Von der Linde D, Anisimov SI. Ultrafast thermal melting of laser-excited solids by homogeneous nucleation, Phys Rev B 2002, 65, 92103.
[42] Sokolowski-Tinten K, Bialkowski J, Boing M, Cavalleri A, Von der Linde D. Thermal and nonthermal melting of gallium arsenide after femtosecond laser excitation, Phys Rev B 1998, 58, R11805.
[43] Ivanov DS, Zhigilei LV. Combined atomistic-continuum modeling of short-pulse laser melting and disintegration of metal films, Phys Rev B 2003, 68, 64114.

[44] Ivanov DS, Rethfeld B, O'Connor GM, Glynn TJ, Volkov AN, Zhigilei LV. The mechanism of nanobump formation in femtosecond pulse laser nanostructuring of thin metal films, Appl Phys A 2008, 92, 791.
[45] Ivanov DS, Kuznetsov AI, Lipp VP, Rethfeld B, Chichkov BN, Garcia ME, Schulz W. Short laser pulse nanostructuring of metals: direct comparison of molecular dynamics modeling and experiment, Appl Phys A 2013, 111, 675.
[46] Schäfer C, Urbassek HM, Zhigilei LV, Garrison BJ. Pressure-transmitting boundary conditions for molecular-dynamics simulations, Comp Mat Sci 2002, 24, 421.
[47] Zhakhovskii VV, Inogamov NA, Petrov YV, Ashitkov SI, Nishihara K. Molecular dynamics simulation of femtosecond ablation and spallation with different interatomic potentials, Appl Surf Sci 2009, 255, 9592.
[48] Hopkins PE. Influence of electron-boundary scattering on thermoreflectance calculations after intra-and interband transitions induced by short-pulsed laser absorption, Phys Rev B 2010, 81, 35413.
[49] Ivanov DS, Lin Z, Rethfeld B, O'Connor GM, Glynn TJ, Zhigilei LV. Nanocrystalline structure of nanobump generated by localized photoexcitation of metal film, J Appl Phys 2010, 107, 13519.
[50] Ivanov DS, Zhigilei LV. Effect of pressure relaxation on the mechanisms of short-pulse laser melting, Phys Rev Lett 2003, 91, 105701.
[51] Unger C, Gruene M, Koch L, Koch J, Chichkov B. Time-resolved imaging of hydrogel printing via laser-induced forward transfer, Appl Phys A 2011, 103, 271–277.
[52] Wagner R, Gottmann J. Sub-wavelength ripple formation on various materials induced by tightly focused femtosecond laser radiation, J Phys: Conf Ser 2007, 59, 333.
[53] Taminiau TH, Moerland RJ, Segerink FB, Kuipers L, van Hulst, Niek F. $\lambda/4$-Resonance of an Optical Monopole Antenna Probed by Single Molecule Fluorescence, Nano Lett 2007, 7, 28.
[54] Çetin AE, Yanik AA, Yilmaz C, Somu S, Busnaina A, Altug H. Monopole antenna arrays for optical trapping, spectroscopy, and sensing, Appl Phys Lett 2011, 98, 111110.
[55] Yi J, Cuche A, Devaux E, Genet C, Ebbesen TW. Beaming Visible Light with a Plasmonic Aperture Antenna, ACS Photonics 2014, 1, 365.
[56] Birnbaum M. Semiconductor Surface Damage Produced by Ruby Lasers, J Appl Phys 1965, 36, 3688.
[57] Bonse J, Rosenfeld A, Krüger J. On the role of surface plasmon polaritons in the formation of laser-induced periodic surface structures upon irradiation of silicon by femtosecond-laser pulses, J Appl Phys 2009, 106, 104910–104915.
[58] Sipe JE, Young JF, Preston JS, van Driel HM. Laser-induced periodic surface structure, I. Theory, Phys Rev B 1983, 27, 1141.
[59] Derrien TJ, Itina TE, Torres R, Sarnet T, Sentis M. Possible surface plasmon polariton excitation under femtosecond laser irradiation of silicon, J Appl Phys 2013, 114, 83104.
[60] Bonse J, Munz M, Sturm H. Structure formation on the surface of indium phosphide irradiated by femtosecond laser pulses, J Appl Phys 2005, 97, 13538.
[61] Bonse J, Krüger J. Pulse number dependence of laser-induced periodic surface structures for femtosecond laser irradiation of silicon, J Appl Phys 2010, 108, 34903.
[62] Huang M, Zhao F, Cheng Y, Xu N, Xu Z. Origin of Laser-Induced Near-Subwavelength Ripples: Interference between Surface Plasmons and Incident Laser, ACS Nano 2009, 3, 4062.
[63] Bonse J, Baudach S, Krüger J, Kautek W, Lenzner M. Femtosecond laser ablation of silicon-modification thresholds and morphology, Appl Phys A 2002, 74, 19.
[64] Hong L, Rusli, Wang XC, Zheng HY, Wang H, Yu HY. Femtosecond laser fabrication of large-area periodic surface ripple structure on Si substrate, Appl Surf Sci 2014, 297, 134.
[65] Huang M, Zhao F, Cheng Y, Xu N, Xu Z. Mechanisms of ultrafast laser-induced deep-subwavelength gratings on graphite and diamond, Phys Rev B 2009, 79.

[66] Huang M, Cheng Y, Zhao F, Xu Z. The significant role of plasmonic effects in femtosecond laser-induced grating fabrication on the nanoscale, Ann Phys (Berlin) 2013, 525, 74.
[67] Bonse J, Rosenfeld A, Krüger J. Implications of transient changes of optical and surface properties of solids during femtosecond laser pulse irradiation to the formation of laser-induced periodic surface structures, Appl Surf Sci 2011, 257, 5420.
[68] Chandezon J, Dupuis MT, Cornet G. Multicoated gratings: a differential formalism applicable in entire optical region, J Opt Soc Am 1981, 72, 839.
[69] Chandezon J, Maystre D, Raoult G. A new theoretical method for diffraction gratings and its numerical application, J Optics, 1980, 11, 235.
[70] Kreiter M, Mittler S, Knoll W, Sambles J. Surface plasmon-related resonances on deep and asymmetric gold gratings, Phys Rev B 2002, 65, 125415.
[71] Sarid D, Challener WA. Modern introduction to surface plasmons: Theory, Mathematica modeling, and applications, Cambridge, New York, USA, Cambridge University Press, 2010.
[72] Rakic AD, Djurišic AB, Elazar JM, Majewski ML. Optical Properties of Metallic Films for Vertical-Cavity Optoelectronic Devices, Appl Opt 1998, 37, 5271.

N. Götte, T. Kusserow, T. Winkler, C. Sarpe, L. Englert, D. Otto,
T. Meinl, Y. Khan, B. Zielinski, A. Senftleben, M. Wollenhaupt,
H. Hillmer, and T. Baumert

3 Temporally shaped femtosecond laser pulses for creation of functional sub-100 nm structures in dielectrics

Abstract: Material processing of dielectrics by temporally shaped femtosecond laser pulses will be presented in this chapter. Structures with feature sizes in the sub-100 nm range are created and the motivation for their application in optical devices is given. The properties of our processing method are discussed with respect to the ionization effects of the light-matter interaction and the implemented tailored pulse shapes to address these individually. Experimental results of structures created in dielectric solids are shown. Electron densities in a water jet were studied numerically and by spectral interferometry to confirm a model for light-matter interaction. The application and characterization of fabricated patterns with regard to the implementation of an optical filter element were studied by numerical simulations and experimental methods.

3.1 Application and processing of dielectric materials for optical devices

A large variety of optical elements are made from dielectric materials. For example, lenses and prisms for free space optics, as well as optical fibers and of course thin-film coatings or optical MEMS (Microelectromechanical systems) – are all based on the distinctive properties of dielectrics [1]. The main advantage is their low absorption over a wide spectral range, which makes them applicable in most cases from the UV to the near-IR. Processing technologies to produce, deposit or structure these materials are well-established and low cost when compared to other optical materials, such as III/V semiconductors. Optical properties and other important parameters can be varied by choosing the appropriate group of dielectric materials. Fluorides, such as MgF_2 and CaF_2, are highly transparent far into the UV range and have very low refractive indices, but are often hygroscopic and show low mechanical stability. Nitrides, like Si_3N_4 or AlN, are more stable and have a higher refractive index of around $n = 2$, but become absorbent for UV wavelengths. The most common group of dielectrics in optical applications are oxides, which can have low refractive indices around $n = 1.5$, such as SiO_2, or are located in a medium range below $n = 2$, like Al_2O_3, but also reach higher indices, like ZrO_2, Nb_2O_5, or TiO_2. Generally, oxides are mechanically and chemically stable and can hence be applied when long-term durability is required. For our investigation on processing of dielectrics by temporally shaped fs-laser pulses

we focused only on amorphous or polycrystalline oxides, as these feature most beneficial properties.

The optical properties of a dielectric material are mainly defined by the bandgap energy, which ranges at least from $E_{gap} = 5$ eV to 10 eV, and a Fermi level well below the lowest energy of the conduction band. Due to the high bandgap energies, light in the near-IR, visible or even UV range is not absorbed, as the energy of single photons is not sufficient. Since the conduction band is not occupied by electrons, the materials are also electrically insulating, which actually defines the term "dielectric" [2].

Optical elements with nanostructures

The interaction of waves with a structure shows the strongest effects if the feature size of the structure is of the same order as the wavelength or below. For the optical spectral range between $\lambda = 200$ nm and 2000 nm, structures with sub-µm dimensions or nanostructures are hence required. Feature sizes between approx. $\lambda/4$ and a few λ lead to superposition of waves. This effect can be enhanced if a periodic pattern of the structure is implemented, resulting in constructive, destructive, or resonant behavior, respectively. Patterns with 1D periodicity are, for example, diffraction gratings or multi-stacks of thin-films. By extending the periodic properties to 2D or 3D, photonic crystals are obtained which can be described analogous to the behavior of electrons in a crystalline structure [3]. Photonic crystal devices are commonly fabricated in semiconductor materials, which have excellent properties but limit their use to the near-IR. Similar structures have been reported in dielectrics with promising results [4] and will be the subject of the first test of our material processing method using fs-laser pulses.

When nanostructures with feature sizes far below the target wavelength are considered, rather different interaction effects will occur. First, scattering of light can be observed and tailored by appropriate structures [1]. A second approach is the generation of artificial refractive index materials by use of the spatial averaging properties of the incident wave [5]. Finally, the near field of optical waves can be accessed, analyzed and manipulated, leading to an entirely new type of optics [6]. These effects are mainly observable for feature sizes between $\lambda/100$ and $\lambda/10$, shifting structures even for applications in the near-IR range to the sub-100 nm range. Thus, creating such structures by temporally shaped fs-laser pulses is a promising method for future applications.

Fabrication of nanostructures in dielectric materials

Creation of nanostructures in dielectric materials can be rather challenging for various reasons. The most conventional methods are based on serial lithography by exposure of a resist material (e.g. PMMA) to an electron beam or direct ion milling of the dielectric with the help of a focused Ga^+ ion beam. Both methods are well-established, commercially available and applicable for feature sizes as small as a few tens of nanometers [7, 8]. In the case of electron beam lithography, further processing steps

are required to transfer the pattern to the dielectric material. The main disadvantage of these methods, when dielectrics are considered, is the accumulation of charges at the sample surface. As the beams interact with the material, charged particles of the beam and secondary charged particles appear due to inelastic scattering. For a conducting sample they discharge via the sample stage which is electrically grounded. As dielectric materials are by definition insulating, no charge transfer can take place and surface charging occurs, which deteriorates the incident focused beam and makes high-quality patterning unfeasible. A common workaround when structuring dielectric materials is to coat the surface with a thin conductive layer, for example sputtering or evaporating Pt or Au with a thickness of 10 nm. Aside from the additional processing steps of deposition and removal, the surface roughness of these thin metal films is likely to reduce the achievable pattern quality if feature sizes in the sub-100 nm range are desired. Another option is to implement active charge compensation, by either installing a source of inversely charged particles that are exposed to the sample surface during lithography, or by increasing the pressure in the vacuum chamber and exploiting charge transport and compensation by residual gas molecules. Both methods require additional complex components in the lithography system and add other undesired effects. Furthermore, the lithography processes discussed require high vacuum conditions to provide sufficient free mean path lengths for the particle beams. This can become problematic if samples with pores or closed cavities are considered as well as for samples which contain outgassing materials.

Optical lithography can overcome the problems of charging and does not depend on vacuum conditions. Serial laser beam exposure of a photoresist, however, cannot reach resolutions in the sub-100 nm range due to the diffraction limit. Making use of stimulated emission depletion however has the potential to overcome this barrier [9]. In commercial photo-lithography, mask projection is employed for mass production and feature sizes of a few tens of nanometers are state of the art [10]. The use of deep UV, vacuum UV or even extreme UV light and the extremely high complexity of the related processing make this approach economically not justifiable for smaller batches or research however. In recent years nanoimprint technology has become more and more competitive for reproduction of nanostructures and may be a good option for the applications discussed. However, as a master template for the imprint needs to be fabricated, the demand for a primary structuring method remains.

Our approach of using temporally shaped fs-laser pulses ($\lambda = 800\,\text{nm}$) for sub-100 nm material processing combines the advantages of optical lithography with direct structuring techniques and the resolution of focused charged particle beams. Since photons are used, no charging effects occur and no vacuum conditions are required. By employing nonlinear optical ionization effects and addressing them individually by tailored pulse shapes, material ablation far below the diffraction limit has been achieved [11]. Complex patterns of nanostructures are generated with the help of a piezo stage, scanning the sample in relation to the laser focus. Lateral dimensions and depth of the structures can be controlled by adjusting the exposure dose.

Different experiments have shown that laser-induced damage thresholds are strongly dependent on the laser pulse duration [12–14] and its temporal shape [11], respectively. An exemplary pulse selection is shown in Fig. 3.3. This can be attributed to the influence of the pulse characteristics on the ionization processes and temporal evolution of free electron density [15, 16], as will be discussed in Section 3.2. Furthermore, it has been demonstrated that direct structuring of dielectric materials with temporally shaped femtosecond laser pulses [11, 17, 18] and double pulses generates reproducible structures with dimensions down to one order of magnitude below the diffraction limit (sub-100 nm structures; compare Fig. 3.1). Femtosecond pulse manipulation techniques play a major role in many applications [19–21].

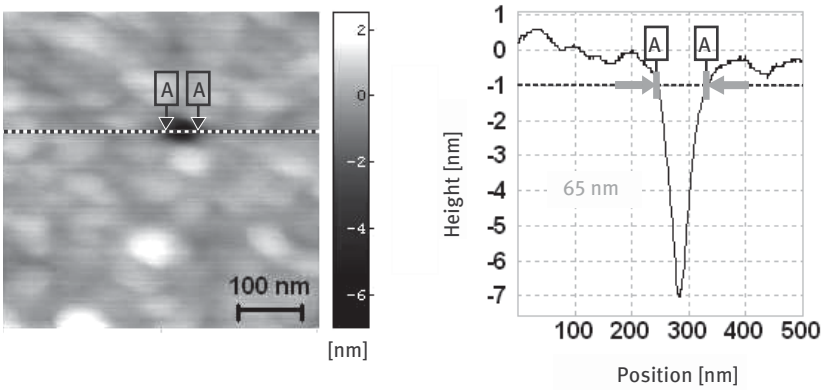

Fig. 3.1: Exemplary sub-100 nm hole in fused silica generated via a single double pulse with an interpulse delay of 3.0 ps and a total pulse energy of E = 122 nJ. The surface diameter of d = 65 nm was measured via atomic force microscopy (resolution 1 pixel/nm) [22] (unpublished).

3.2 Laser material processing of dielectrics via short and ultrashort laser pulses

As mentioned before, most advantages of the conventional primary structuring processes are combined in the alternative approach with fs-laser. For goal-oriented material processing comprehensive knowledge of the material, in this case the dielectric and its interaction with the laser, is necessary. The following section will therefore give a short summary of the current state of research.

3.2.1 Fundamentals: light-matter interaction of dielectrics and pulse shaping

Transparent dielectric materials, e.g. glasses, become highly absorbing on application of ultrashort laser pulses with sufficient intensities [23, 24]. As soon as the laser pulse

exceeds a certain intensity it is able to generate small numbers of free electrons. In turn, the plasma thus produced is highly absorbing for the later parts of the laser pulse [11, 25]. The first step is accomplished by multiphoton ionization[1] (MPI), which is related to the wide bandgap of the dielectric in relation to the photon energy. It is well known that the probability of MPI is proportional to I^n, where I is the intensity of the laser pulse, and n the number of photons required to overcome the bandgap. These first few electrons can be considered as seed-electrons for avalanche ionization (AI). AI is a two-step process, where an electron in the conduction band gains kinetic energy by free carrier absorption (inverse Bremsstrahlung) and impact ionizes another electron from the valance band (compare Fig. 3.2). Please note that in laser material processing the expressions "ionization" and "free electrons" are commonly equivalent to "excitation" and "conduction band electrons", respectively [24].

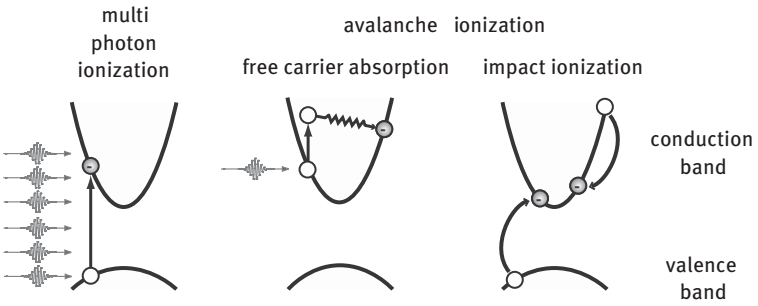

Fig. 3.2: Generation of a high density of free electrons in dielectrics. Left: Six photons are simultaneously absorbed by the electron from the highly intense laser pulse to overcome the bandgap. Right: The combination of free carrier absorption and impact ionization is known as Avalanche ionization. An existing electron in the conduction band can absorb single photons to increase its energy. Since the electron has sufficient energy it can impact ionize a valence band electron.

The relevance of the different ionization channels is strongly related to the temporal shape of the ultrashort laser pulses, as will be discussed in detail later. But first we want to expand on the pulse shapes typically employed, by giving the basic mathematical description and examples. An overview of the four basic classes of pulse shapes typically applied is given in in Fig. 3.3.

1 In general, strong field ionization contains MPI and tunnel ionization. Due to the relatively low intensities in the experiments tunnel ionization only contributes in a minor fashion and can be neglected.

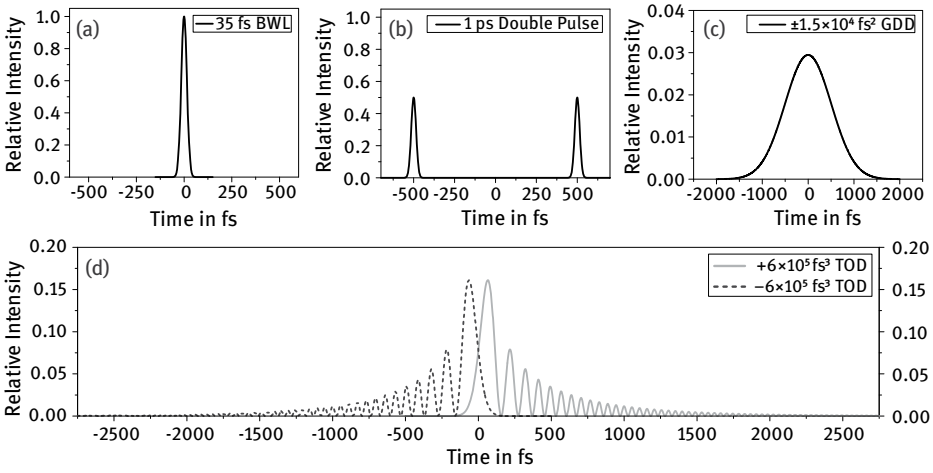

Fig. 3.3: All pulses are simulated with the same total pulse energy and are intensity normalized to the bandwidth-limited pulse (BWL) with a FWHM pulse duration of $\tau = 35$ fs (a). BWL pulse with a FWHM pulse duration of $\tau = 35$ fs (a), double pulses (each pulse $\tau = 35$ fs) with an inter-pulse delay of $\Delta\tau = 1$ ps and an intensity ratio of 1 : 1 (b). BWL pulse subjected to a second order dispersion (GDD) of $\phi_2 = \pm 1.5 \cdot 10^4$ fs^2 (c) and BWL pulse subjected to a third order dispersion (TOD) of $\phi_3 = +6 \cdot 10^5$ fs^3 (d) leading to a pulse duration of $\tau \approx 1$ ps, respectively.

A more detailed representation – comprising pulse shaping technique via spectral phase modulation – can be found for example in the following references: [17, 26, 27].

(a) Bandwidth-limited ultrashort laser pulses

The first class of pulses are ultrashort bandwidth-limited pulses (BWL) with Gaussian temporal pulse envelope (Fig. 3.3 (a)) and a full width at half maximum (FWHM) pulse duration of $\tau = 35$ fs. Since MPI requires a highly intense laser pulse and no initial free electrons, it has the highest efficiency for the generation of a high free electron density for pulses shorter than approx. 50 fs. In contrast, due to the shortness of the pulse, there is no time for AI to establish and AI can therefore be neglected. The BWL pulse has the lowest energy threshold for material ablation and the according pulse envelope of such an unmodulated pulse can be mathematically described as

$$E(t) = \frac{E_0}{2} \cdot \exp\left[-\ln(4)\left(\frac{t}{\tau}\right)^2\right]$$

With an amplitude E_0 of the pulse and τ is the unmodulated pulse duration. The instantaneous frequency is constant throughout the unmodulated pulse and the spectral phases are constant (in contrast to parabolic and cubic phase for GDD and TOD; see below).

(b) Chirped laser pulses by group delay dispersion (GDD)

The second class is represented by linearly chirped pulses with varying instantaneous frequency $\omega(t)$ (Fig. 3.3 (c)). Their spectrum and the symmetric, Gaussian temporal pulse envelope are identical to those of BWL pulses, but in comparison the peak intensity is reduced due to temporal broadening of the pulse (energy conservation). Group delay dispersion (GDD) is introduced by applying a parabolic spectral phase function $\varphi(\omega) = \frac{\phi_2}{2} \cdot \omega^2$ to the spectrum $\tilde{E}(\omega)$ ($\tilde{E}_{\mathrm{mod}}(\omega) = \tilde{E}(\omega) \cdot e^{-i\varphi(\omega)}$); ϕ_2 is the so-called chirp parameter. A positive value of ϕ_2 leads to an up-chirped pulse characterized by a linear increase of the instantaneous frequency in time, whereas a negative value of ϕ_2 implies a decrease of the instantaneous frequency, known as down-chirp. The modulated FWHM pulse duration for a chirped Gaussian pulse is

$$\tau_{\mathrm{GDD}} = \sqrt{\tau^2 + 16 \cdot [\ln(2)]^2 \left(\frac{\phi_2}{\tau}\right)^2}.$$

Wherein τ denotes the unmodulated pulse duration and ϕ_2 the chirp parameter. The higher ϕ_2 the more pronounced is the temporal broadening. When the pulse duration exceeds 50 fs the avalanche ionization can no longer be neglected for free electron generation.

(c) Temporally asymmetric shaped laser pulses by third order dispersion (TOD)

The third class of pulses is characterized by an elongated pulse duration and an asymmetric pulse envelope. The instantaneous frequency – and therefore the photon energy provided by the pulse – is constant over the course of the whole pulse. Third order dispersion (TOD) is introduced by applying a cubic spectral phase function $\varphi(\omega) = \frac{\phi_3}{6} \cdot \omega^3$ to the spectrum $\tilde{E}(\omega)$, and ϕ_3 is the dispersion parameter of third order. This leads to a modulated pulse shape, which is characterized by an intense initial pulse followed by a sequence of pulses with decaying amplitudes. The sign of ϕ_3 controls the temporal direction of the pulse shape: positive values of ϕ_3 lead to a series of post-pulses, whereas negative values of ϕ_3 result in a series of pre-pulses (Fig. 3.3 (d)).

Since TOD pulses are asymmetrically broadened in time, the temporal FWHM is no longer a suitable property to describe pulse duration. Therefore, we use the statistical pulse duration[2] $2\sigma = \tau / \sqrt{2 \ln 2}$ [26] to describe the pulse duration. Since the statistical pulse duration 2σ delivers shorter values for an unmodulated Gaussian pulse compared to the FWHM, we define the modulated pulse duration by $\tau_{\mathrm{mod}} = \sqrt{8 \cdot \ln(2)} \cdot \sigma$

2 The statistical definition of the pulse duration derived with the help of the second moment of the intensity distribution uses twice the standard deviation σ to characterize pulse duration.

to obtain a quantitative measure of pulse duration

$$\tau_{\mathrm{TOD}} = \sqrt{\tau^2 + 16 \cdot [\ln(2)]^3 \left(\frac{\phi_3}{\tau^2}\right)^2},$$

[27] which agrees with the FWHM of the unmodulated pulse.

(d) Bandwidth-limited double pulses with 1 : 1 ratio

The last class of laser pulse shapes that was applied in our studies for material processing are BWL, Gaussian-shaped double pulses with varying inter-pulse delay and an intensity ratio of 1 : 1 (Fig. 3.3 (b)). The generation with a polarization pulse shaper of such pulse shapes is described in detail in [28].

3.3 Experimental results in dielectrics

3.3.1 Fused silica SiO2

The results obtained from our earlier experiments [11, 29] are summarized in Fig. 3.4. Systematic studies with phase-shaped laser pulses based on TOD leading to asymmetric temporally shaped laser pulses revealed a change in the damage threshold depending on whether the direct (positive ϕ_3) pulse shape or the time inverted profile (negative ϕ_3) was used; see Fig. 3.4 (a). Theoretical simulations based on a multiple rate equation (MRE) model described in [15] show that it is the timing of an intense photo-ionizing sub-pulse which can turn on AI or not. The observed nanoscale structures are an order of magnitude below the diffraction limit and remarkably stable with respect to variations in laser fluence (Fig. 3.4 (c)). Applying pure second order dispersion at the threshold, sub-diffraction structures are also created; however, no substructure which was stable with respect to laser fluence variations was observed [27].

In Fig. 3.5, the morphologies observed for BWL pulses and TOD shaped pulses are summarized. Our original data were analyzed mainly via SEM (scanning electron microscopy) and AFM (atomic force microscopy). Recently, we turned to FIB (focused ion beam) characterization in combination with SEM in addition. The maximum depth of the generated structures may be limited by the shape of the high aspect ratio tip used. The shape of the high aspect ratio tip is also responsible for the asymmetry in the profile seen in Fig. 3.5 (b). At threshold, the structures are a few 10 nm in depth.

The intriguing observation in Fig. 3.5 is that the observed substructure for unshaped pulses occurs only for high intensities and is embedded in a large area defined by the inner structure, whereas for the TOD shaped pulses, this substructure starts to appear already at threshold. On first glance, the substructure might be attributed to filamentation processes as observed in bulk fused silica under similar excitation conditions [30], as well as on surfaces of dielectrics [31, 32] and reviewed in [33]. However,

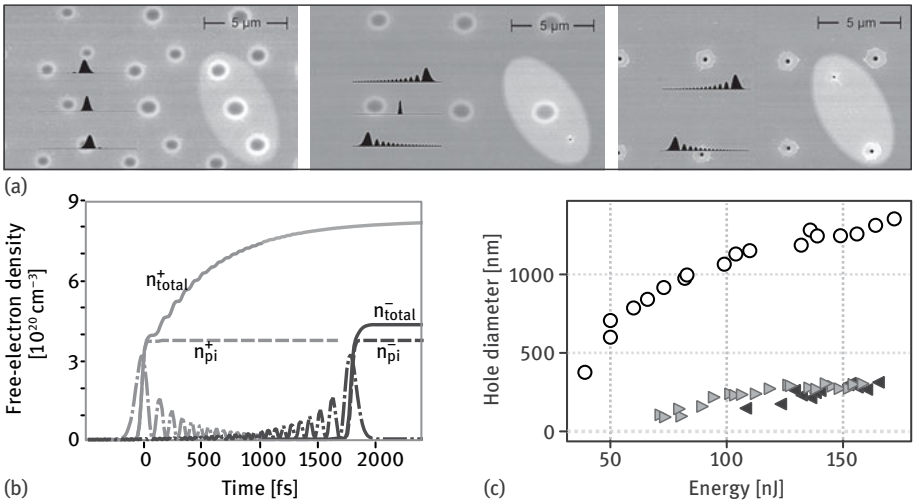

Fig. 3.4: (a) SEM micrographs of a measurement pattern on fused silica: For an applied energy E and focal position, a triplet of applied laser pulses is highlighted by the ellipse. Negative, zero, and positive TODs were used where the corresponding normalized temporal intensity profiles are sketched in black for different TODs. Left: low TOD ($\phi_3 = \pm 2.5 \cdot 10^4$ fs^3, statistic pulse duration of $2\sigma = 50$ fs, $E = 77$ nJ) results in negligible differences between created structures. Middle: high positive TOD ($\phi_3 = +6 \cdot 10^5$ fs^3, statistic pulse duration of $2\sigma = 960$ fs, $E = 71$ nJ) results in a change of structure size and threshold energy. Right: the threshold energy for ablation with high negative TOD ($\phi_3 = -6 \cdot 10^5$ fs^3) is reached with $E = 110$ nJ. Here, the unshaped pulse is suppressed in order not to mask structures with TOD. (b) Transient free electron density n_{total} (solid lines) as calculated with help of the MRE, together with the density of electrons provided by photoionization n_{PI} (dashed lines), and the corresponding transient intensities (dashed-dotted lines) of the pulse with positive TOD (index +) and negative TOD (index –), respectively. (c) Inner diameters (compare Fig. 3.5) of ablation structures as a function of pulse energy for unshaped pulses (circles). For (+) shaped pulses (triangles pointing right) and for (–) shaped pulses (triangles pointing left), the diameter of the substructure is displayed. Without changing the focus spot diameter, substructures below 300 nm are obtained over a large energy range, thus providing a large process window for the creation of nanostructures. The smallest structures are about 100 nm in diameter.

as filamentation usually needs propagation to occur, the lack of observed propagation structures, especially for the TOD shaped pulses, may rule out filamentation as the only explanation. Note that no plasma in air was observed at the applied laser energies, i.e. the used pulse energies for TOD are well below (factor of approx. 10) the critical power for self-focusing and filamentation processes. In order to investigate to what extent the seed and heat model explaining the differences in observed ablation threshold for temporally asymmetric pulse shapes may be extended to explain the spatial observations, we started simulations. The motivation stems from the simple picture that an initial part of the temporal pulse structure may create a free electron density well below the damage threshold via MPI in a spatially very confined region, and the remaining pulse also initializes AI to reach the critical energy in a

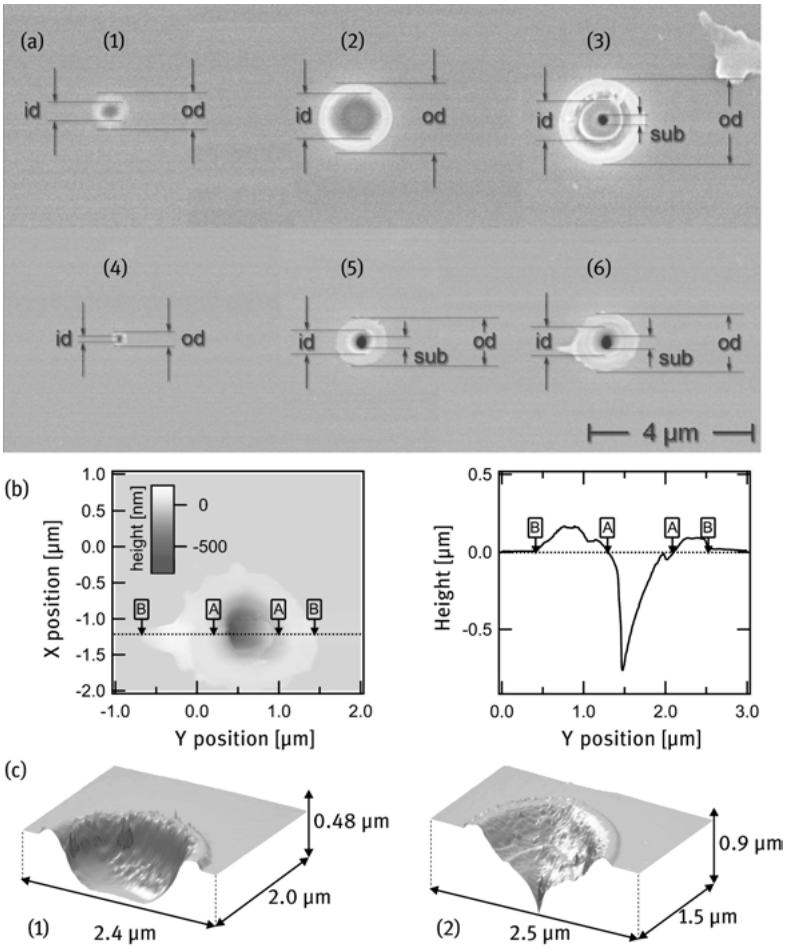

Fig. 3.5: (a) SEM micrographs for selected structures of Fig. 3.4 (c). *od* = outer diameter, *id* = inner diameter, and *sub* = diameter of substructure. For unshaped pulses at threshold for material processing (40 nJ) (1); at intermediate energy (140 nJ) (2); and at high energy (240 nJ) (3). Structures for high positive TOD ($\phi_3 = +6 \cdot 10^5$ fs^3) at threshold (4); at intermediate energy (120 nJ) (5); and at high energy (150 nJ) (6). At threshold, the substructure merges into the inner structure. For unshaped pulses, the substructure occurs only for high intensities and is embedded in a large area defined by the inner structure. (b) AFM image of structure (a) (6). The distance BB defines the outer diameter *od*, and AA defines the inner diameter *id*. Note the high aspect ratio of the 800 nm deep structure. As a general trend, the depth of the structures increased approximately linearly from the threshold up to 50 nJ above threshold in a range from several 10 s to several 100 nm for positive and negative phase masks. (c) Typical AFM structures for the unshaped laser pulse. In the energy range up to 140 nJ, a shallow crater is observed (1), whereas in the energy range from 150 to 250 nJ, the additional small substructure appears (2).

very restricted area. In those simulations, we solve rate equations for a Gaussian spatial beam profile taking MPI, AI, and trapping into account as a function of various temporal profiles. So far we did not get a conclusive picture from these simulations: in the calculations, the threshold of material ablation was set by reaching a certain electron density. This criterion allowed description of the threshold for material ablation correctly for various temporal profiles, the structure diameter (inner structure) as a function of fluence was sometimes overestimated and sometimes underestimated compared to the measured ones, however. The substructure behavior was never reproduced in this approach. Currently we are extending this approach to take propagation effects into account. Dedicated double pulse experiments up to 10 ps are currently being performed in our labs with the help of our latest pulse shaping setup [28] in order to study early stage material modifications (Fig. 3.1). An extension of the experiments to materials with different orders of MPI process also appears to be a promising route for a better understanding.

3.3.2 Experimental realization for fused silica

In our experiments, we combine femtosecond pulse shaping techniques [19] (which can nowadays reach zeptosecond precision) [28] with a microscope setup for material processing [11, 34]. Linearly polarized laser pulses with 35 fs FWHM pulse duration and a central wavelength of 790 nm are provided by an amplified Ti:Sapphire laser system. After passing a calibrated home built spectral phase modulator [35], the pulses are focused via a Zeiss LD Epiplan 50×/0.5 NA objective to a spot diameter of 1.4 µm ($1/e^2$ value of intensity profile). The dispersion of the objective was constantly compensated prior to the experiments. The pulse shaper is properly operated in a parameter regime far away from space time coupling effects [36], as verified also via quantum optical measurements with the same setup [37, 38]. Shaped pulses are characterized in the interaction region via second order cross correlation. The sample is translated by a 3-axis piezo stage to a new position for each shot (a single laser pulse). A typical measurement pattern consists of an array of points where we vary the pulse shapes, energy, and focal z-position. After laser processing, the samples are analyzed via SEM and AFM.

3.3.3 Spectral interferometry: motivation and setup

Usually the influence of the temporal duration of laser pulses on the laser material processing is investigated via different post mortem techniques, such as AFM, SEM, or optical microscopy. However, this has the disadvantage that between the excitation of the electrons and the final material ablation a large number of processes take place which can't be directly observed this way. That is why we chose an in situ measurement

approach to directly observe the excitation of water in real time with femtosecond resolution from the initial excitation up to 6.5 ps later. Water can be treated as an amorphous semiconductor with a reported energy bandgap ranging from 6.5 eV [39] to 8.3 eV and 12.4 eV [40] sharing the main ionization processes like solid dielectrics.

In our experiments, the laser pulses interact with a free flowing water jet, which ensures a new and fresh area of the sample for each laser pulse at repetition rate of 1 kHz.

Due to the fact that the optical breakdown process[3] is a general one, our findings can well be expanded to the behavior of solid dielectrics. In either case, the first step in the ablation process is the optical breakdown in which a high density of free electrons (around 10^{20}–10^{22} cm^{-3}) is generated by the abovementioned nonlinear ionization processes. The free electrons absorb energy from the laser pulse, transfer it to the ions, atoms, and molecules and, on a significantly longer time scale (several ps to ns), ablation can take place. The final features of the ablation process are strongly dependent on the primary processes involved in the laser-matter interaction.

We set up a common-path spectral interferometer to investigate the free electron density in real time of the transient plasma produced by temporally asymmetric shaped ultrashort laser pulses in a thin water jet [25]. Spectral [41–44] and spatial [45, 46] interferometry techniques are well established methods [47] to investigate the early time dynamics of laser excited dielectrics. In spectral interferometry a pair of probe and reference pulses, usually created in a Michelson line interferometer, is sent to an imaging spectrometer and frequency domain interference is produced. From the spectral interference data the phase shift – a reduction of the temporal separation of the probe pulse pair – and the transmission coefficient of the probe pulse can, for example, be obtained by inverse Fourier transformation [41]. Both quantities are directly dependent on the real and imaginary part of the complex refractive index of the excited sample, as seen by the probe pulse.

Inspired by [48], we made use of a common-path interferometer in which a pair of frequency doubled 400 nm reference and probe pulses (τ_{SHG} = 50 fs) are generated as ordinary and extraordinary beams when the light propagates through a birefringent crystal (Fig. 3.6). The time delay between the pulses is defined by the thickness of the crystal. A second, thinner birefringent crystal, oriented 90 degrees with respect to the first one, is used to decrease the delay between the interfering pulses just before entering an analyzing spectrometer. This common-path approach leads to a much higher stability than in conventional interferometers.

3 Optical breakdown describes the case when a transparent dielectric becomes highly absorbent due to high free electron density.

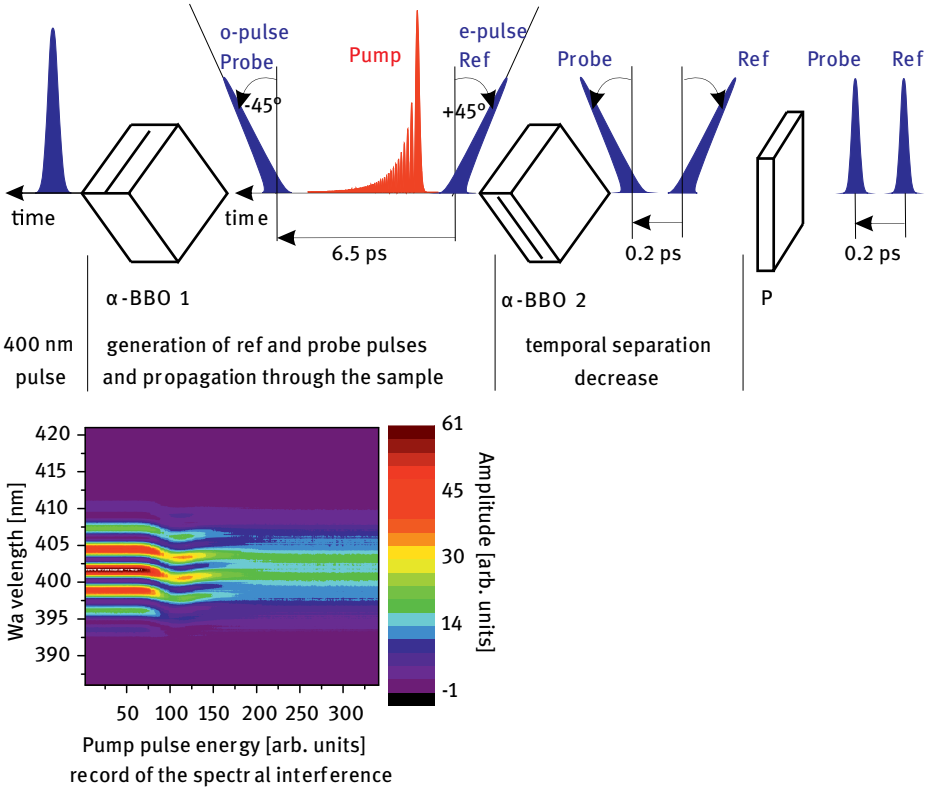

Fig. 3.6: From left to right: A time delayed pulse is frequency-doubled to 400 nm (blue pulses) and passes through a birefringent crystal (α-BBO 1). This creates a pair of orthogonally polarized pulses with a temporal separation of 6.5 ps. The reference and probe pulses propagate through the interaction area, together with the pump pulse (red pulse) in between, probing the changes in the optical properties. A second birefringent crystal (α-BBO 2) decreases the temporal separation between the blue pulses to 0.2 ps. After passing through a polarizer (P), the frequency-domain interference pattern is recorded in a spectrometer, containing the optical properties of the excited sample. An example (raw-data) for a pump pulse energy dependent scan is shown below.

An 800 nm shaped pump pulse is adjusted in such a way that it creates the free carriers within the thin water jet inside the 6.5 ps time window between the reference and probe pulse (Fig. 3.6). The resulting phase difference and contrast of the interference fringes contains direct information about the optical properties of the plasma. This common-path setup for the probe pulses was hitherto not used in combination with spectral interference. We demonstrated that it is a powerful tool to investigate the early and medium time dynamics of ultrafast processes [25].

3.3.4 Spectral interferometry: results on water jet

Our experimental realization of the spectral interferometry gives access to two main parameters of the resulting spectra: the phase shift $\Delta\Phi$ contains information about the real part of the refractive index of the water jet and the optical density, *OD*, about the free electron plasma absorption. From the combined data, the electron density and electron collision time τ_c can be evaluated by the well-known Drude formalism [49]. However, this is only directly possible as long as the sample is excited homogenously along the propagation direction of the laser pulse [46, 50], which can be assumed for low pump pulse intensities; compare Fig. 3.8 (b). Within this range the phase shift is directly proportional to electron density.

Below the results of two investigations are presented. The first section deals with the dependence of $\Delta\Phi$ and *OD* on the peak intensity of a BWL pump pulse. Subsequently, the effect of positive and negative temporal asymmetrically shaped TOD pulses is investigated.

Please note that here we only present the pump pulse energy dependent excitation of water right after the BWL or TOD pump pulse has passed through the water jet. Time-sensitive measurements over the whole 6.5 ps time window have been performed as well and are extensively discussed in [25].

Bandwidth-limited femtosecond pulses

Figure 3.7 presents the dependence of the absolute phase shift and the optical density on the peak pump laser intensity. For low intensities, the dependence follows a power law indicated by the solid lines in Fig. 3.7, with an exponent of 5.1 ± 0.2 for the phase shift and 5.2 ± 0.2 for the optical density. This hints at a five-photon ionization process in the range of 0.1–0.8 rad, as also expected from the bandgap of 6.5 eV mentioned in the introduction section. With increasing pump intensity, the absolute phase shift also increases, but the assumption of a longitudinal homogeneous distribution is not valid anymore and the deviation from the straight line is evident.

The phase shift reaches a maximum at pump peak intensity of $4.8 \cdot 10^{12}\,\mathrm{W\,cm^{-2}}$ and starts to decrease for higher values. This behavior was also observed for solid dielectrics [23, 46] and attributed to a strong inhomogeneous distribution of free electron density in longitudinal direction (in contrast to the assumption of homogenous excitation made above). This can be substantiated by the observation of visible localized plasma sparks in the water at $9.6 \cdot 10^{12}\,\mathrm{W\,cm^{-2}}$. Also, previous studies reported an average threshold intensity of $6.6 \cdot 10^{12}\,\mathrm{W\,cm^{-2}}$, for which the longitudinal distribution of high density free electron plasma is of the order of 1 µm [50], and thus much smaller than the sample thickness of our water jet.

The optical density shows roughly the same dependence on the pump laser intensity as the phase shift. The Drude collision time can be extracted from the two curves; the value was measured to be $\tau_c = (1.6 \pm 0.3)$ fs [25] for the intensity range indicated in

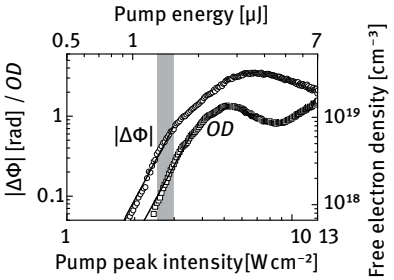

Fig. 3.7: Measured absolute phase shift and optical density *OD* as a function of the peak pump laser intensity for 35 fs BWL pulses together with a fit taking a 5-photon ionization process into account (solid lines). On the right scale the calculated free electron density, assuming a homogeneous distribution (realistic only for low laser intensities) is also shown. The light gray window represents the intensity in which an electron collision time of (1.6 ± 0.3) fs was determined. In this intensity regime, both the *OD* and the phase shift follow the power law I^5.

Fig. 3.7, where the assumption of a homogeneous distribution is reasonable. This value is in good agreement with values presented in the literature, ranging from 1.2 [50] to 1.7 fs [51].

Third order dispersion shaped pulses

Temporally asymmetric laser pulses and their temporal inverted counterparts show quite different effects to bandwidth-limited pulses of the same pulse energy. The measured dependence of phase shift on pump pulse energy can be seen in Fig. 3.8. The threshold value for TOD shaped pulses is higher than for the BWL pulse due to the decreased peak laser intensity (compare Fig. 3.3 in Section 3.3). It can also be seen that for identical pump pulse energy the absolute phase shift induced by positive TOD shaped pulses is higher than that corresponding to the negative TOD.

Furthermore, the maximum phase shift produced by positive TOD is considerably higher than for negative TOD or BWL pulses. Seeing that the trend of phase shift continuously falls in each case after the maximum has been reached, even the bandwidth-limited pulse with its high peak intensity is at no pulse energy as effective as the positive TOD pulse. This is a strong indication that temporally shaped pulses can be used to optimize the transfer of laser pulse energy into the transparent dielectric and merits further investigation.

In addition to the abovementioned experiments, a basic rate equation model was employed to simulate laser excitation and optical properties in the range of homogeneous excitation [25]. By applying the different pulse shapes (namely BWL and $\pm 6 \cdot 10^5$ fs^3 TOD) we were able to extract, the multiphoton and avalanche ionization coefficients of water for the first time. The simulated and measured curves showed a very good agreement, as seen in Fig. 3.8 (b).

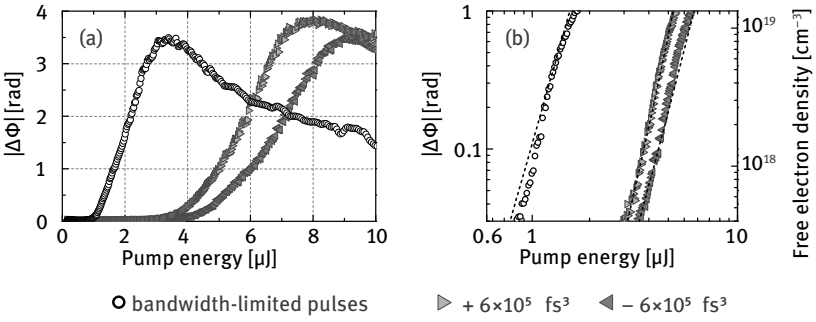

Fig. 3.8: Dependence of the absolute phase shift on the pulse laser energy for BWL 35 fs pulses and $\pm 6 \cdot 10^5$ fs^3 third order dispersion shaped pulses in linear representation. Positive cubic pulses produce a higher phase shift than negative ones for the same total energy (tilt of triangles indicates sign of dispersion) (a). Excerpt of (a) in double logarithmic representation from region of homogeneous excitation. Black dashed lines show simulation based on a generic rate equation model (b).

The interaction of highly intense laser pulses with large bandgap dielectric materials was shown, and how the selective manipulation of the temporal intensity distribution can control ionization processes. With this powerful tool, it was demonstrated that the creation of sustainable material modification of fused silica one order below the diffraction limit is possible.

Below a useful application of this tool and its advantages compared to conventional methods in the creation of photonic structures is presented.

3.4 Fabrication of a photonic crystal based filter device by temporally shaped fs-laser pulses

As a demonstration of the potential that material processing by temporally shaped fs-laser pulses bears for optical applications, the fabrication of a typical device structure is investigated. The structure consists of a dielectric thin-film with a 2D photonic crystal pattern, employing the excitation of Fano resonances for a narrow-band spectral filter element.

Fano resonances are observed when a resonant state is superposed to a continuous state [52, 53]. In an optical implementation, a thin-film with higher refractive index than the surrounding medium acts as a slab waveguide. Waves with normal incident to the layer cannot couple to a waveguide mode due to their orthogonal properties. By structuring the slab waveguide with a periodic pattern, the incident wave can couple resonantly to a waveguide mode if the matching conditions are fulfilled [54]. Since the coupling takes place in both directions, the mode is not truly guided by the slab, but is considered a leaky mode. Thus the resonant mode couples out of the slab again and

superposes with free-space modes of directly transmitted or reflected waves. Fano resonances often show asymmetric spectral behavior, stemming from the phase change in the resonance of the coupled leaky mode. Spectral position, width, strength, and shape of the Fano resonance can be tailored by designing the slab waveguide and periodic structure accordingly. In our device we implement a 2D photonic crystal pattern with a square lattice and circular base elements to obtain a polarization-independent narrow-band filter. The advantage of such an element is the very compact design, which consists of only one structured dielectric layer on a substrate material. Comparable filter elements are based on a Fabry-Pérot configuration, consisting of numerous layers surrounding a cavity. Additionally, polarization dependency can be introduced to a Fano filter by designing the periodic structure with a broken symmetry. All these properties are beneficial for application in e.g. MEMS devices or on the tip of an optical fiber [55, 56].

Impact of fs-laser pulse processing on the implementation of photonic crystals

The fabrication of a Fano filter structure using conventional technologies is based mainly on three processing steps. First, a single layer or multiple thin-films are deposited and form the slab waveguide. Subsequently, the photonic crystal pattern is generated by lithography and transferred to the slab waveguide via anisotropic dry etching.

If ablation by temporally shaped fs-laser pulses is employed for the fabrication of Fano resonant structures, several constraints have to be considered and investigated. Due to the relation of the ionization processes to the bandgap energy, a clear material dependency exists. In the first approach structures are therefore solely created in a single material. For our experiments we chose SiO_2, which was already studied in our previous investigation on the fs-laser induced ablation process (compare Section 3.3). Since we receive a periodic pattern in a low-index material by this method, a high-index layer has to be coated on top to obtain the required slab waveguide. During the deposition of this layer the high-index material also partly fills the ablated hole structures, leading to a periodic modulation of the waveguide core as well. Another important parameter which affects the performance of the Fano filters is the shape and profile of the laser-generated base elements. Characterization of ablated structures generated by TOD fs-laser pulses shows a funnel shape in the top section with a small rim at the surface. The deeper section of the hole forms a narrow and parallel channel which can exhibit rather high aspect ratios (Fig. 3.10 (a)). A final remark must be made on the refractive indices of the available materials. Since SiO_2 is used as a substrate and high-index thin-films are restricted to indices below $n = 2.3$, only a low index contrast of approx. $\Delta n = 0.8$ can be exploited. This is a further challenge when designing the Fano filter. Air-bridged elements, which could increase the index contrast, are not implemented due to the commonly observed bending problems based on high mechanical stresses.

Material processing of a thin-film on top of the substrate material is very promising for further investigations. This would not only provide a method to fabricate Fano filters and similar devices directly in the target material, but could also be used for generation of structured hard masks for further etching steps. If the ablation process in thin-films can be controlled to be sufficiently material dependent, selective structuring of one material without damaging other materials becomes possible.

Theoretical model calculations of realistic filter devices

Fundamental investigations into the particular properties of photonic crystal structures generated by fs-laser pulse processing and optimized design parameters for Fano filter devices were obtained by numerical simulations. We utilize the 3D finite-difference time-domain method (FDTD) [57], which provides the distribution and propagation of fields in the time domain and spectral properties by applying a harmonic inversion. Three main base models were implemented in order to address the complexity of different problems efficiently. (1) The principle characteristics of photonic crystal structures can be calculated using a unit cell of the periodic pattern and applying periodic boundary conditions. If the device and source can be assumed to be uniform, this model delivers very good results with reasonable numerical efforts. (2) Finite samples and sources with defined profiles can be simulated using a slice, one or only a few unit cells thick, of the real device as model domain. For the other spatial directions the structure is defined with the true parameters and periodic boundary conditions are implemented only in the direction of the slice thickness. (3) Full information on the behavior of devices with certain 3D shapes and source properties, such as exact spot profiles, were investigated by applying a true 3D model of the full structure. This approach clearly delivers the best results, but is restricted by its very high demand on computing capacities.

First numerical calculations were performed to analyze the possible parameter regime for Fano resonances in material systems with low refractive index contrast. Various parameters were tested, such as refractive index combinations, layer thicknesses, hole depth and diameter, as well as lattice geometries. Fano resonances with different strengths and spectral widths can be excited for symmetric slab waveguides with a low index material on top and for asymmetric configurations with a direct core-to-air interface on top. These results were used as a basis for further implementations of Fano filters.

Models concerning a deposited layer on top of a previously structured photonic crystal array were investigated next. The variation of the pre-existing hole structures and the amount of high-index layer material reaching into it showed that for this technological approach good quality Fano resonances are still obtainable.

Finally, the particular shape of the ablated structures – the funnel-like entrance, the narrow channel with high aspect ratio in the lower part and the rim forming at the surface – were defined by considering the characterization of the actual results

of fs-laser pulse ablation (Fig. 3.9 (a)). It was demonstrated that the rim and funnel-like shape in the top section does not affect the potential to excite Fano resonances or even limit their quality (Fig. 3.9 (b)). The high aspect ratio of the narrow channel becomes rather beneficial as this section is only partly filled with the high index-layer material and stays void below. This results in a reduced effective index of the substrate material, increasing the index contrast to the waveguide core considerably.

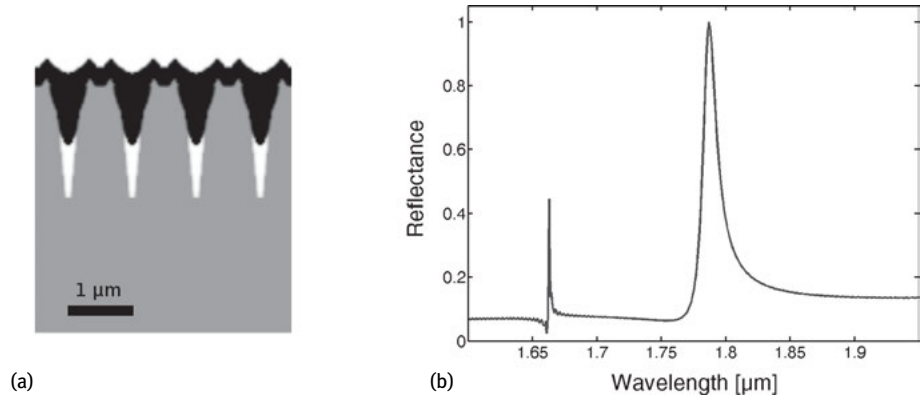

(a) (b)

Fig. 3.9: Simulation model of a photonic crystal structure with realistic structure profile, including the rim formation and funnel-like top section (a). Numerical result of a filter spectrum which has been obtained from the simulation model (a) and exhibits a strong Fano resonance at 1.78 µm wavelength (b).

In summary, numerical calculations indicate that photonic crystal structures in low-index dielectric materials can be designed to exhibit strong Fano resonances. The fabrication of such devices by temporally shaped fs-laser pulses proves to be feasible, as neither the deposition of the high-index layer on the hole arrays nor the actual hole profiles render a serious problem in the design process. The high aspect ratio of the structures created by TOD pulses even improves the performance of photonic crystal devices due to a lowered effective index of the substrate material.

Investigation of the reduction and avoidance of rim formation

One current drawback of the ablated structures is the formation of a rim around the hole created at the surface. This property may be an obstacle if a very high quality of densely placed array structures is desired, as the rim areas can overlap and influence the optical performance or even the ablation process at neighboring positions (Fig. 3.10 (b)). We therefore propose different strategies to either avoid, reduce, or remove the rim.

Our first approach is to remove the rim after structuring the sample by either dry or wet chemical etching processes. The idea is to make use of different etch rates in the rim area and substrate. Although both originally consist of the same material, the ablation process may damage the material in the rim to weaken its etch resistivity. Additionally, elevated or isolated small features often show faster etching due to the surface/volume ratio and tip effects. In the experiments, however, the removal of the rim was always accompanied by severe damage to the generated hole structure, making this method unfeasible.

In the next tests we deposited a thin layer of a material with the same or similar bandgap energy on top of the substrate prior to fs-laser pulse processing. If the light matter interaction is not influenced by the additional layer, the rim forms on top of this extra layer. Afterwards, selective etching can be used to remove the top "sacrificial" coating and a clean hole array is obtained. Results of this investigation still exhibited the undesired degradation of the fabricated structures, although the occurrence of etching defects is clearly reduced.

The third method investigated is based on an additional top layer which reduces or avoids the formation of a rim. In previous experiments different substrate materials revealed different behavior regarding the rim. For Al_2O_3 for example, the rim is barely noticeable, whereas for SiO_2 a strong formation is observable. Experiments with various top-layer materials and thicknesses were therefore carried out, showing that a reduction of rim formation can be obtained if appropriate combinations of layer material, thickness and pulse energy are applied.

3.5 Characterization of ablation channels by focused ion beam milling

The experimental results of fs-laser pulse structuring have previously been characterized by two techniques: SEM and AFM. Both methods are very capable of providing high resolution surface information but struggle to give information about the depth and shape of the generated holes. Even with a high aspect ratio tip, the AFM measurements of sub-100 nm structures are still limited to a depth of several tens of nanometers.

A very powerful technique to gain insight into the inner volume of samples is the preparation by focused ion meam milling (FIB) (Fig. 3.10 (a)). Typically, an ion optical system with liquid Ga^+ metal source is attached to an electron optical system. In this two beam configuration alignment and processing of samples can be carried out by direct inspection and images acquired during and after the preparation. The highly accelerated ions are focused on the sample surface and can sputter the material directly with resolutions as low as to the nanometer range. If the ion current or acceleration voltage is reduced, the sputtering process turns from deep milling towards high quality polishing. A gas injection system, which locally emits gas precursors in

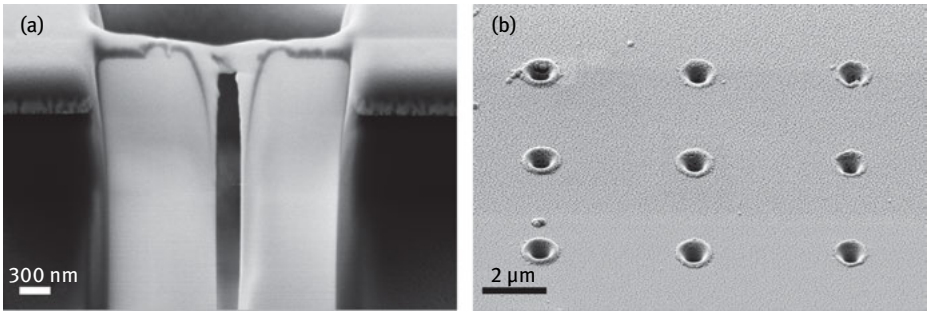

Fig. 3.10: SEM micrograph of an FIB cross-section showing the top section of a hole structure ablated by temporally shaped (TOD) fs-laser pulses in SiO_2 (a). Top view of a photonic crystal array fabricated using the fs-laser structuring method presented. The formation of the rim around each hole element at the sample surface can be clearly observed (b).

the focus region, offers the option of ion beam induced deposition of materials or gas enhanced ion milling for higher yield and quality [7].

For the preparation of fs-laser pulse generated hole structures, the high local resolution and precise alignment, the quality of polished surfaces, and the possibility of utilizing different detectors of the SEM system are the main advantages. On the other hand, surface charging has again to be addressed, e.g. by coating a thin conductive layer on top of the sample. Also the geometric fidelity of the measured structure parameters needs to be verified accurately, since deviations during processing, such as a tilt in the final polishing step, may affect the visible projection of the structure. It has to be mentioned of course, that FIB preparation by milling and polishing is a destructive process and cannot be reverted. Depending on the technique applied, the process can also be rather time consuming, limiting the number of samples to inspect. Three different approaches were used in our investigation.

(1) Preparation of cross-sections by ion beam milling and subsequent surface polishing. First a protective layer is deposited locally with the gas injection system. A rough gap is milled in the vicinity of the target structure to provide visible access to the depth profile of the hole. Low current polishing is applied until the center of the target structure is reached. This method is comparably fast and offers insight into most geometric parameters, like depth, width and shape.
(2) Milling and polishing from both sides results in a thin lamella structure of less than 100 nm thickness. The procedure is analogous to the preparation of cross-sections, but provides a sample with better contrast, as scattering is reduced and back-scattered and secondary electrons can be detected with good selectivity. Additionally, the lamella can be transferred to a copper grid by a lift-out process step and investigated in a TEM or STEM to obtain information on the morphology.
(3) Full 3D information of the target structure by FIB tomography. The procedure is similar to the preparation of cross-sections, but after polishing for approx. 10 nm

the process is interrupted and an SEM image acquired. Polishing and image acquisition are repeatedly carried out in a loop, starting in front of the target structure and ending after fully removing it. The single images each represent a slice of the structure and a stack of all slices can be compiled by software to reconstruct a 3D model of the ablation channel. However, this preparation technique destroys the investigated structure completely and is by far the most time consuming approach.

3.6 Summary

We demonstrated a sustainable method which made use of temporally shaped femtosecond laser pulses to create structures down to the sub-100 nm scale in dielectrics. Our investigations showed that the approach is suitable for creation of optical elements for the visible wavelength range by direct laser writing. Due to the diffraction limit and charging effects in dielectric materials, it is difficult to reach structures in the sub-100 nm range by conventional production methods.

References

[1] E. Hecht, Optik, 6., verb. Aufl. ed., München: De Gruyter, 2014, pp. XVII, 1125 S..
[2] S. Kasap and P. Capper, Springer Handbook of Electronic and Photonic Materials, S. Kasap and P. Capper, Eds., Berlin: SPRINGER, 2006, pp. V–1306.
[3] J. D. Joannopoulos, S. G. Johnson, J. N. Winn and R. D. Meade, Photonic Crystals, vol. 2, Princeton University Press, 2008, pp. i-286.
[4] K. B. Crozier, V. Lousse, O. Kilic, S. Kim, S. H. Fan and O. Solgaard, "Air-bridged photonic crystal slabs at visible and near-infrared wavelengths," *Phys.Rev.B*, vol. 73, no. 11, p. 115126, 2006.
[5] G. A. Niklasson, C. G. Granqvist and O. Hunderi, "Effective Medium Models for the Optical-Properties of Inhomogeneous Materials," *Appl.Opt.*, vol. 20, no. 1, pp. 26–30, 1981.
[6] L. Novotny and B. Hecht, Principles of Nano-Optics, vol. 2, Cambridge University Press, 2012.
[7] L. A. Giannuzzi and F. A. Stevie, Introduction to Focused Ion Beams Instrumentation, Theory, Techniques and Practice, Springer New York, 2005, pp. V–357.
[8] T. Djenizian and P. Schmuki, "Electron beam lithographic techniques and electrochemical reactions for the micro- and nanostructuring of surfaces under extreme conditions," *J.Electroceram*, vol. 16, no. 1, pp. 9–14, 2006.
[9] R. Wollhofen, J. Katzmann, C. Hrelescu, J. Jacak and T. A. Klar, "120 nm resolution and 55 nm structure size in STED-lithography," *Optics Express*, vol. 21, no. 9, pp. 10831–10840, 2013.
[10] P. van Zant, Microchip fabrication, vol. 6, McGraw-Hill, 2014.
[11] L. Englert, B. Rethfeld, L. Haag, M. Wollenhaupt, C. Sarpe-Tudoran and T. Baumert, "Control of ionization processes in high bandgap materials via tailored femtosecond pulses," *Optics Express*, vol. 15, no. 26, p. 17855, 2007.

[12] M. Lenzner, J. Krüger, S. Sartania, Z. Cheng, C. Spielmann, G. Mourou, W. Kautek and F. Krausz, "Femtosecond Optical Breakdown in Dielectrics," *Physical Review Letters*, vol. 80, no. 18, pp. 4076–4079, 1998.
[13] B. C. Stuart, M. D. Feit, A. M. Rubenchik, B. W. Shore and M. D. Perry, "Laser-Induced Damage in Dielectrics with Nanosecond to Subpicosecond Pulses," *Physical Review Letters*, vol. 74, no. 12, pp. 2248–2251, 1995.
[14] A. C. Tien, S. Backus, H. Kapteyn, M. Murnane and G. Mourou, "Short-pulse laser damage in transparent materials as a function of pulse duration," *Physical Review Letters*, vol. 82, no. 19, pp. 3883–3886, 1999.
[15] B. Rethfeld, "Unified model for the free-electron avalanche in laser-irradiated dielectrics," *Physical Review Letters*, vol. 92, no. 18, p. 187401, 2004.
[16] B. Rethfeld, "Free-electron generation in laser-irradiated dielectrics," *Physical Review B*, vol. 73, no. 3, p. 035101, 2006.
[17] M. Wollenhaupt, L. Englert, A. Horn and T. Baumert, "Control of Ionization Processes in High Band Gap Materials," *Journal of Laser Micro/Nanoengineering*, vol. 4, pp. 144–151, 2009.
[18] L. Englert, M. Wollenhaupt, C. Sarpe, D. Otto and T. Baumert, "Morphology of nanoscale structures on fused silica surfaces from interaction with temporally tailored femtosecond pulses," *Journal of Laser Applications*, vol. 24, no. 4, p. 042002, 2012.
[19] A. M. Weiner, "Femtosecond pulse shaping using spatial light modulators," *Rev.Sci.Instr.*, vol. 71, no. 5, pp. 1929–1960, 2000.
[20] M. Wollenhaupt, A. Assion and T. Baumert, "Femtosecond Laser Pulses: Linear Properties, Manipulation, Generation and Measurement," in *Springer Handbook of Lasers and Optics*, Springer New York, 2007, pp. 937–983.
[21] M. Krug, T. Bayer, M. Wollenhaupt, C. Sarpe-Tudoran, T. Baumert, S. S. Ivanov and N. V. Vitanov, "Coherent strong-field control of multiple states by a single chirped femtosecond laser pulse," *New J.Phys.*, vol. 11, p. 105051, 2009.
[22] D. Otto, "Sub-100 Nanometer-Strukturen via Femtosekunden-Doppelpulse," Master Thesis, Universität Kassel, 2014.
[23] S. S. Mao, F. Quéré, S. Guizard, X. Mao, R. E. Russo, G. Petite and P. Martin, "Dynamics of femtosecond laser interactions with dielectrics," *Applied Physics A*, vol. 79, no. 7, pp. 1695–1709, 2004.
[24] P. Balling and J. Schou, "Femtosecond-laser ablation dynamics of dielectrics: basics and applications for thin-films," *Reports on Progress in Physics*, vol. 76, no. 3, p. 036502, 2013.
[25] C. Sarpe, J. Köhler, T. Winkler, M. Wollenhaupt and T. Baumert, "Real-time observation of transient electron density in water irradiated with tailored femtosecond laser pulses," *New Journal of Physics*, vol. 14, p. 075021, 2012.
[26] M. Wollenhaupt, A. Assion and T. Baumert, "Chap. 12," in *Springer Handbook of Lasers and Optics*, Springer New York, 2012, pp. 1047–1094.
[27] M. Wollenhaupt, L. Englert, A. Horn, T. Baumert, J.-J. Song, K.-T. Tsen, M. Betz and A. Y. Elezzabi, "Temporal femtosecond pulse tailoring for nanoscale laser processing of wide-bandgap materials," *Proc. SPIE*, vol. 7600, pp. 76000X–76000X-11, 2010.
[28] J. Köhler, M. Wollenhaupt, T. Bayer, C. Sarpe and T. Baumert, "Zeptosecond precision pulse shaping," *Optics Express*, vol. 19, no. 12, pp. 11638–11653, 2011.
[29] L. Englert, M. Wollenhaupt, L. Haag, C. Sarpe-Tudoran, B. Rethfeld and T. Baumert, "Material processing of dielectrics with temporally asymmetric shaped femtosecond laser pulses on the nanometer scale," *Applied Physics A*, vol. 92, no. 4, pp. 749–753, 2008.
[30] A. Couairon, L. Sudrie, M. Franco, B. Prade and A. Mysyrowicz, "Filamentation and damage in fused silica induced by tightly focused femtosecond laser pulses," *Phys.Rev.B*, vol. 71, no. 12, pp. 125435–125435-11, 2005.

[31] Y. V. White, X. Li, Z. Sikorski, L. M. Davis and W. Hofmeister, "Single-pulse ultrafast-laser machining of high aspect nano-holes at the surface of SiO_2," *Optics Express*, vol. 16, no. 19, p. 14411, 2008.
[32] B. Delobelle, F. Courvoisier and P. Delobelle, "Morphology study of femtosecond laser nano-structured borosilicate glass using atomic force microscopy and scanning electron microscopy," *Optics and Lasers in Engineering*, vol. 48, pp. 616–625, 2009.
[33] A. Couairon and A. Mysyrowicz, "Femtosecond filamentation in transparent media," *Physics Reports*, vol. 441, no. 2–4, pp. 47–189, 2007.
[34] A. Assion, M. Wollenhaupt, L. Haag, F. Mayorov, C. Sarpe-Tudoran, M. Winter, U. Kutschera and T. Baumert, "Femtosecond laser-induced breakdown spectrometry for Ca2+ analysis of biological samples with high spatial resolution," *Appl.Phys.B*, vol. 77, no. 4, pp. 391–397, 2003.
[35] A. Präkelt, M. Wollenhaupt, A. Assion, C. Horn, C. Sarpe-Tudoran, M. Winter and T. Baumert, "Compact, robust and flexible setup for femtosecond pulse shaping," *Rev.Sci.Instr.*, vol. 74, no. 11, pp. 4950–4953, 2003.
[36] B. J. Sussman, R. Lautsen and A. Stolow, "Focusing of light following a 4-f pulse shaper: Considerations for quantum control," *Phys.Rev.A*, vol. 77, pp. 043416–043416-11, 2008.
[37] T. Bayer, M. Wollenhaupt and T. Baumert, "Strong-field control landscapes of coherent electronic excitation," *J.Phys.B*, vol. 41, pp. 074007–074007-13, 2008.
[38] T. Bayer, M. Wollenhaupt, C. Sarpe-Tudoran and T. Baumert, "Robust Photon Locking," *Physical Review Letters*, vol. 102, pp. 023004-1-023004-4, 2009.
[39] C. A. Sacchi, "Laser-induced electric breakdown in water," *J. Opt. Soc. Am. B*, vol. 8, no. 2, pp. 337–345, 1991.
[40] C. G. Elles, A. E. Jailaubekov, R. A. Crowell and S. E. Bradforth, "Excitation-energy dependence of the mechanism for two-photon ionization of liquid H2O and D2O from 8.3 to 12.4 eV," *J.Chem.Phys.*, vol. 125, pp. 044515-1-044515-12, 2006.
[41] E. Tokunaga, A. Terasaki and T. Kobayashi, "Frequency-domain interferometer for femtosecond time-resolved phase spectroscopy," *Opt.Lett.*, vol. 17, no. 16, pp. 1131–1133, 1992.
[42] P. Martin, S. Guizard, P. Daguzan, G. Petite, P. D'Oliveira, P. Meynadier and M. Perdix, "Subpicosecond study of carrier trapping dynamics in wide-band-gap crystals," *Phys.Rev.B*, vol. 55, no. 9, pp. 5799–5810, 1997.
[43] P. Audebert, P. Daguzan, A. Dos Santos, J. C. Gauthier, J. P. Geindre, S. Guizard, G. Hamoniaux, K. Krastev, P. Martin, G. Petite and A. Antonetti, "Space-Time Observation of an Electron-Gas in SiO2," *Physical Review Letters*, vol. 73, no. 14, pp. 1990–1993, 1994.
[44] F. Quéré, S. Guizard and P. Martin, "Time-resolved study of laser-induced breakdown in dielectrics," *Europhys.Lett.*, vol. 56, no. 1, pp. 138–144, 2001.
[45] V. V. Temnov, K. Sokolowski-Tinten, P. Zhou and D. Linde, "Femtosecond time-resolved interferometric microscopy," *Appl.Phys.A*, vol. 78, no. 4, pp. 483–489, 2004.
[46] V. V. Temnov, K. Sokolowski-Tinten, P. Zhou, A. El-Khamhawy and D. Linde, "Multiphoton Ionization in Dielectrics: Comparison of Circular and Linear Polarization," *Physical Review Letters*, vol. 97, p. 237403, 2006.
[47] J. Siegel and J. Solis, "Chap. 2," in *Femtosecond Laser Micromachining*, Springer-Verlag Berlin Heidelberg, 2012, pp. 19–41.
[48] M. A. van Dijk, M. Lippitz, D. Stolwijk and M. Orrit, "A common-path interferometer for time-resolved and shot-noise-limited detection of single nanoparticles," *Optics Express*, vol. 15, no. 5, pp. 2273–2287, 2007.
[49] M. Born and E. Wolf, Principles of optics -electromagnetic theory of propagation, interference and diffraction of light, vol. 7th (exp.), Cambridge University Press, 1999, pp. 1–952.

[50] C. Sarpe-Tudoran, A. Assion, M. Wollenhaupt, M. Winter and T. Baumert, "Plasma dynamics of water breakdown at a water surface induced by femtosecond laser pulses," *Applied Physics Letters*, vol. 88, no. 26, p. 261109, 2006.
[51] A. Vogel, J. Noack, G. Huttman and G. Paltauf, "Mechanisms of femtosecond laser nanosurgery of cells and tissues," *Applied Physics B: Lasers and Optics*, vol. 81, no. 8, pp. 1015–1047, 2005.
[52] U. Fano, "Effects of Configuration Interaction on Intensities and Phase Shifts," *Physical Review*, vol. 124, no. 6, pp. 1866–1878, 1961.
[53] A. E. Miroshnichenko, S. Flach and Y. S. Kivshar, "Fano resonances in nanoscale structures," *Reviews of Modern Physics*, vol. 82, no. 3, pp. 2257–2298, 2010.
[54] A. Hessel and A. A. Oliner, "A New Theory of Wood's Anomalies on Optical Gratings," *Applied Optics*, vol. 4, no. 10, p. 1275, 1965.
[55] A. Gellineau, Y.-P. Wong, A. Wang, M. J. Butte and O. Solgaard, "Miniature Fiber Facet Atomic Force Mircoscope Using Photonic Crystal Sensors," *International Conference on Optical MEMS and Nanophotonics*, pp. 3–4, 2014.
[56] T. Kusserow, Yousuf Khan, R. Zamora, F. Messow and H. Hillmer, "Guided-mode resonances in dielectric photonic crystal slabs with low index contrast," 2012, pp. 170–171.
[57] A. F. Oskooi, D. Roundy, M. Ibanescu, P. Bermel, J. D. Joannopoulos and S. G. Johnson, "Meep: A flexible free-software package for electromagnetic simulations by the FDTD method," *Computer Physics Communications*, vol. 181, no. 3, pp. 687–702, 2010.

C. Reinhardt, V. Ferreras Paz, L. Zheng, K. Kurselis, T. Birr,
U. Zywietz, B. Chichkov, K. Frenner, and W. Osten

4 Design and fabrication of near- to far-field transformers by sub-100 nm two-photon polymerization

Abstract: In recent years, technological progress in nanotechnology has pushed structure sizes to its limits. As an example, in the semiconductor industry, structures well below 100 nm are routinely produced. The characterization of such structures is a demanding and very important task. Classical microscopy methods do not allow direct imaging in this regime because of the Abbe diffraction limit. Nevertheless, characterization of sub-wavelength structures in the far-field is possible using interferometric Fourier transform scatterometry (IFTS) combined with numerical simulation in a feedback loop. Here, we show that the resolution of this method can be considerably enhanced by use of additional plasmonic nanoantennae structures which transform scattering near-field information into the optical far-field. These structures were realized using different photofabrication approaches.

4.1 Introduction

An electromagnetic near-field around metallic nanostructures is associated with the excitation of localized surface plasmons. The realization of plasmonic near-field to far-field transformers in the optical region between 400 and 800 nm requires structures of sub-wavelength dimensions with a pronounced optical near-field and a strong light scattering ability. When the size of the objects is smaller than the optical wavelength λ, the structures start to scatter the localized plasmonic excitations into the far-field. The enhanced information, now available in the far-field, enables detection of structural feature sizes of sub-wavelength critical dimensions with optical methods. The principle idea of this sub-wavelength far-field characterization of groove and grating structures, providing nanometric resolution, is shown in Fig. 4.1 (a). Additional light scattering from optical near-fields, carrying information about sub-wavelength structural features, into the far-field is accomplished by rod-like nanoantennae.

Fabrication and far-field characterization of sub-wavelength grating structures are presented in this work. Measurements of the scattered light with and without rod nanoantennae from gold-covered samples have been performed and compared with numerical results. Sensitivities to structural dimension of 50 nm have been obtained, using light with a wavelength of 632.8 nm. The fabrication approach for both the sub-wavelength grating structures and the near-to-far-field (NTFF) transformation nanoantennae is based on high-resolution two-photon polymerization (2PP). Repeatable realization of line and dot structures with dimensions down to 50 nm is presented.

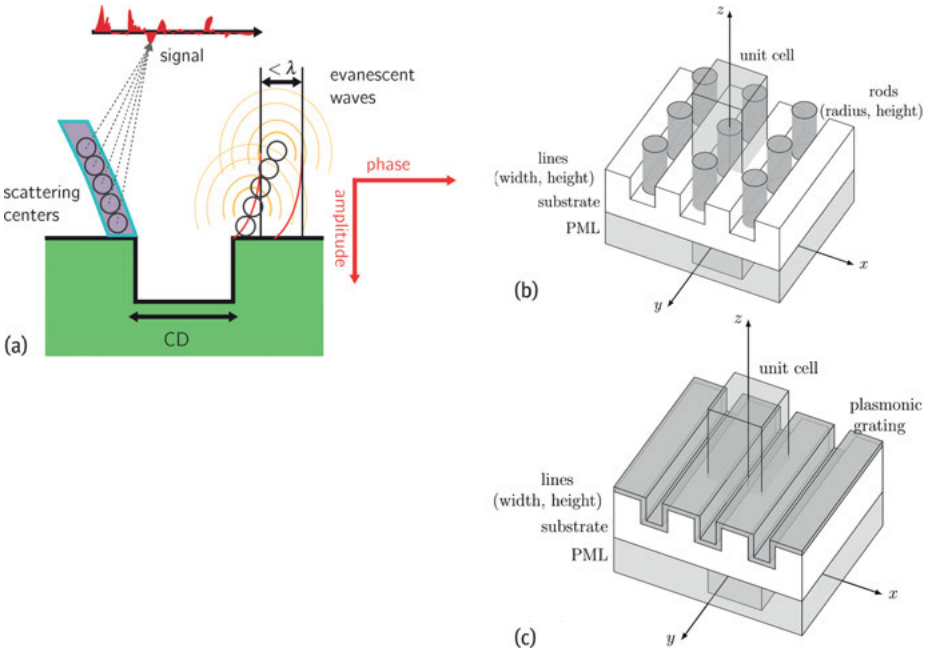

Fig. 4.1: Principle idea of near-field to far-field transforming plasmonic structures (a). Schematics structures with added plasmonic features as a plasmonic grating (c) or scattering near-field nano-antennae (b).

4.2 Fabrication approaches for near- to far-field transformation optics

For a demonstration of enhanced optical imaging below the diffraction limit, high-resolution grating structures (see Fig. 4.1 (b & c)), consisting of periodic sequences of lines of different widths have been fabricated with and without NTFF structures. These structures are described in detail in Section 4.3. Examples of test structures with minimum line widths down to 230 nm fabricated in a positive tone photo resist S1805 by microscopic projection photolithography (MPP) [1] are shown in Fig. 4.2.

The NTFF transforming structures consist of nanoantennas with dimensions of less than 100–300 nm. In order to achieve high flexibility in the realization of the structures and high resolutions down to the sub-100 nm range for both the fabrication of grating NTFF structures, the process of two-photon polymerization (2PP) was applied. Especially for the creation of high aspect ratio NTFF structures, the potential of real 3D structuring using 2PP was exploited.

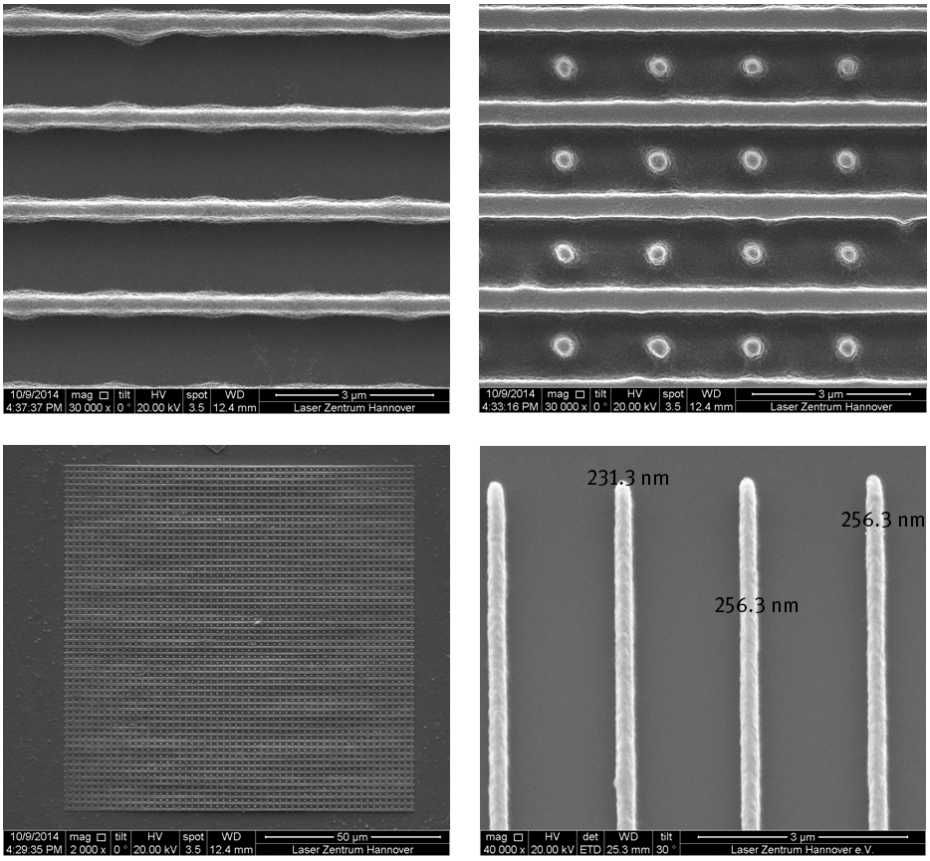

Fig. 4.2: Structures under consideration for near-field to far-field transformation of plasmonic structures. Upper left: grating structure with sub-wavelength ridge widths of 350 nm fabricated by MPP. Upper right: grating with polymer pillars between the grating ridges as NTFF structures. Bottom left: image of the complete 100 µm × 100 µm structure. Bottom right: achievable line width of 230 to 250 nm by MPP.

4.2.1 Two-photon fabrication

Growing interest in downscaling optical components, photonic and plasmonic devices, as well as metamaterial structures together with the demand for their integration has pushed the development of micro- and nanofabrication methods [2, 3]. One method for the generation of 3D structures in rapid prototyping is UV stereolithography, developed in 1986 by Hull [4]. This technology, although flexible and cost-efficient, is limited in resolution to several micrometers and in fabrication speed [5]. To overcome these limitations, nonlinear light-matter interactions can be used in true 3D structuring. The method of nonlinear laser structuring has been demonstrated

to be a promising candidate regarding flexibility, cost efficiency, and the ability to generate arbitrary complex 3D structures.

The process of nonlinear laser writing, as used in this study, is based on two-photon absorption (TPA). TPA was theoretically investigated by Göppert-Mayer in 1930 and 1931 [6, 7]. Kaiser and Garret demonstrated it experimentally in 1961 after the invention of the laser by two-photon excitation of CaF2:Eu2+ [8]. These investigations of nonlinear optical and especially two-photon processes became possible with the advent of the laser. But only since the development of commercially available ultrashort pulsed titanium:sapphire lasers in the 1990s have two-photon absorption processes been routinely applied in microscopy and microfabrication.

The potential of TPA for 3D laser structuring was suggested in 1992 by Wu et al. with the idea for applications in microelectronics [9]. 3D microstructures with a resolution down to 500 nm have already been demonstrated. Three-dimensional microfabrication was later introduced by Maruo et al. in 1997, using a standard polymer SCR-500 [10]. The potential for subwavelength resolution has been pointed out. Since laser radiation can be focused directly into the material volume and is only absorbed in the focal region of the beam, the process speed can be much faster compared to conventional 3D stereolithography, and the fabricated structures can have a much higher complexity. The term two-photon polymerization (2PP), which has been given to this technology, was introduced in 2003, when this technique was applied to radical polymerization of a new class of organic-inorganic hybrid materials [11]. This method was used independently one year later in 2004 by Deubel [12] and Serbin [13] to realize 3D photonic crystals. Today, TPA is also used with polymer systems which can be cationically polymerized (such as the epoxy-based SU8 polymer), or which undergo chemical bond cleavage, like the commercial photoresists used in microelectronics. A detailed overview of this technology up to 2004 is given in [14]. The developments of 2PP technology within the last 10 years are reviewed in [15].

In the following section, the focus is on radical polymerization. The radicals that lead to polymerization are formed in the triplet state of certain photoinitiator molecules upon single- or multiphoton excitation. Typical radical photoinitiators undergo intersystem crossing from the excited singlet to the triplet state on a time scale of the order of 100 ps [16], whereas a direct decay of the excited state to the ground state would lead to fluorescence. In 2PP, the photoinitiator in a (pre-)polymer resin is excited by the simultaneous absorption of two photons. The absorption probability thus depends on the square of the laser intensity. As a consequence, ultrafast laser systems have commonly been used to provide high peak intensities at low average power. The ultrashort laser pulses are focused through a microscope objective such that the photons are confined in space and time. The laser power in 2PP applications is set to a level that the intensity of the light is only high enough in a small region of the focal volume of the beam. In most implementations of 2PP, TPA initiates crosslinking of polymer molecules. By moving the laser focus through the volume of the resin,

arbitrary complex, computer generated three dimensional (3D) polymeric [17–22] and high resolution 2D plasmonic structures can be created [23–26].

Due to the optical nonlinearity of TPA, an intensity threshold exists for 2PP. 2PP can thus create volume elements (voxels) which are considerably smaller than the wavelength of the laser beam, e.g. 800 nm for titanium:sapphire lasers. Although intrinsically capable of producing arbitrary narrow line widths and heights, the 2PP process has encountered a persistent limit of about 100 nm due to potential instabilities of the laser beam power, the positioning systems used, and radical diffusion [15]. Different strategies have been followed to overcome this limit. The first approach was based on radical quenchers to avoid the diffusion of radicals out of the focal volume where the laser intensity is above the 2PP threshold [27]. A further step was the use of more efficient photoinitiators which lead to local crosslinking of the polymer faster than the created radicals can diffuse into the surrounding material regions [28]. With these two strategies, lateral widths of laser-written polymer lines on glass substrate surfaces of 100 nm and 80 nm respectively were obtained. Recently, processes based on the principle of stimulated emission depletion (STED) of fluorophore molecules have been applied [29–31]. Here, the widths of laser-written lines on glass surfaces have been reduced by efficient de-excitation of the excited photoinitiator molecules using a second laser beam with ring-shaped intensity distribution and either similar [29] or different [30, 31] wavelengths. Feature sizes of 40 nm [29] and 65 nm [31], respectively, have been demonstrated.

In the bulk volume, however, this approach has also been limited thus far to 100 nm lateral line width realized in photonic crystals [31]. A drawback of this technological approach is its sensitivity to misalignments. The smallest reliable 3D line widths of 65 nm in photonic crystals [32] and of 45 nm for supported single lines [33] to date were obtained using either highly efficient specialized photoinitiators or ultrashort pulse durations down to 10 fs respectively. To this date, there is no common simple recipe for the reliable generation of 3D structures with dimensional features in the sub-100 nm range. One reason for this is the decreasing stability of the polymerized structures.

Two approaches have been taken to overcome the persistent limitations for the production of sub-100 nm structures inside the resin volume and on dielectric (glass) surfaces: the use of additional crosslinking molecules to increase the stability of fabricated 3D structures in zirconium-based inorganic-organic hybrid polymer, and careful investigation of the actually achievable resolution in the commercially available small molecule acrylate resin E-Shell 300 using the 2PP technique without further specialized ingredients.

4.2.2 3D two-photon polymerization with additional crosslinker

The influence of the crosslinker dipentaerythritol penta-methacrylate (DPMA) on the achievable dimensions of supported isolated polymer lines was investigated in the experiments.

4.2.2.1 Materials

A zirconium-based inorganic-organic hybrid polymer (Zr-Hypo) was used as basis material for the investigations. The material has been demonstrated to exhibit only minor volume shrinkage, which is favorable for high resolution structuring [34]. Synthesis of the zirconium-based inorganic-organic hybrid polymer was carried out by a sol-gel-process [35]. The commonly available radical photoinitiator 4,4′-bis(dimethylamino)benzophenone (Bis) was used for initiation of the polymerization process. A diagram of the synthesis protocol is shown in Fig. 4.3.

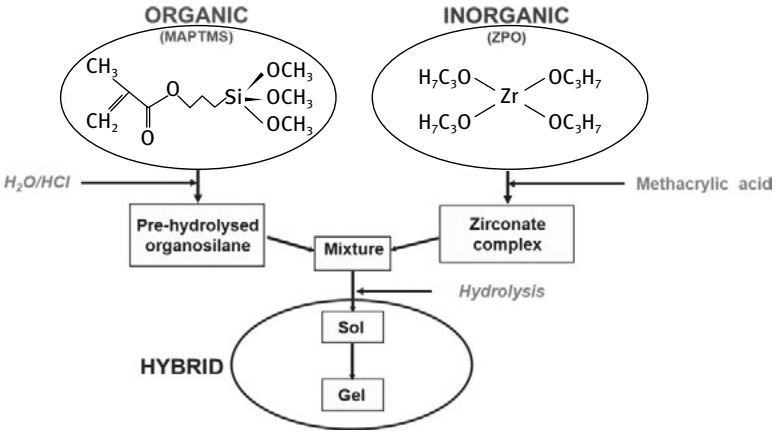

Fig. 4.3: Synthesis of zirconium-based inorganic-organic hybrid polymer.

Methacryloxypropyltrimethoxysilane (MAPTMS, Sigma-Aldrich) was hydrolyzed with 0.1 M hydrochloric acid (HCl, Sigma-Aldrich). Methacrylic acid and zirconium isopropoxide were mixed separately in a molar ratio of 4 : 1 and stirred for 30 min.

The chelated zirconium isopropoxide was subsequently added to the hydrolyzed silane precursor, and a small amount of water added. The molecular ratio of MAPTMS to ZPO was set to 5 : 1 (20 %). The mixture was stirred for another 30 min. At the end, 0.5 wt % of the photoinitiator was added. Before structuring, the pre-polymer was drop-casted onto a microscope cover glass slide with a thickness of 150 µm and heated for 1 h to 100 °C. A mixture of 50 vol % isopropanol (Iso, Sigma Aldrich) and 50 vol % 4-methyl-2-pentanone (methyl isobutylketone, MIBK, Sigma Aldrich) was

used to develop the realized structures, i.e. to dissolve the non-polymerized portion of the material. The samples were immersed in this mixture for 1 h. Line widths in woodpile crystal structures of 320 nm have been demonstrated with this material [34].

The performance of this material was compared to the same material with an addition of 15 % crosslinker DPMA for the realization of sub-100 nm structures. The simple change in the synthesis protocol is shown in Fig. 4.4. The amount of DPMA was added to the basis material described above just before addition of the photoinitiator, which again was 0.5 wt % Bis.

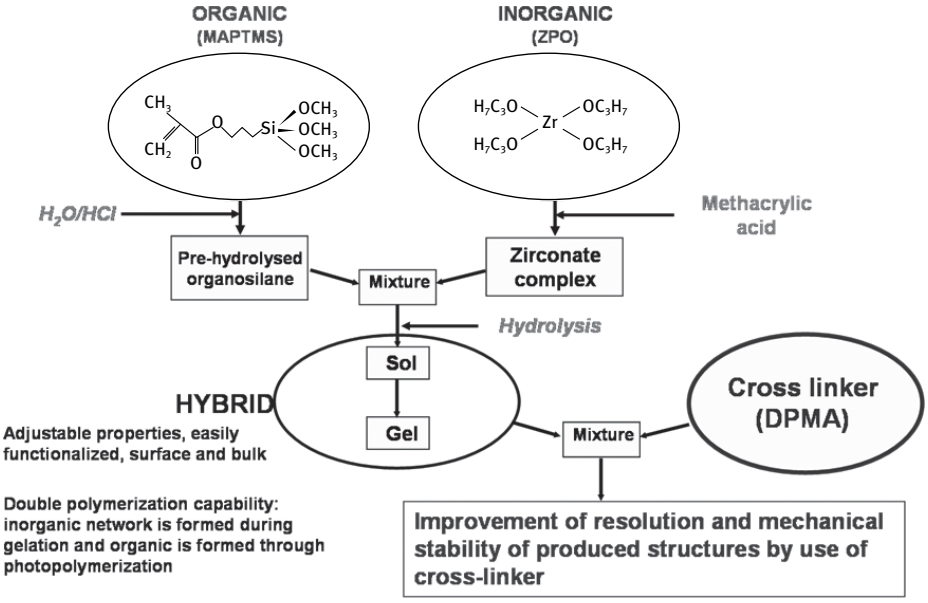

Fig. 4.4: Synthesis of DPMA-amplified Zr-Hypo.

2PP of these two materials was initiated using the Ti:Sapphire based high-peak power femtosecond laser oscillator Femtosource scientific XL500 (Femtolasers) with a repetition rate of 5 MHz, a central wavelength of 800 nm, and a pulse width smaller than 50 fs. The laser pulses were spatially focused into the bulk volume of the photosensitive material by a microscope objective lens. A 100× immersion oil microscope objective with a numerical aperture of 1.4 was used to obtain the best focus. The laser beam was focused from the back of the cover glass plate. In order to generate the test structures, the focus was scanned through the polymer volume by moving the sample with a computer controlled positioning system (Physik Instrumente PI, 3x M-126.DG for *x*-, *y*-, and *z*-axes). The scanning speed of the laser beam was kept at 1 mm/s. The laser beam focusing in this configuration is fixed.

For the development of the realized structures, i.e. to dissolve the non-polymerized portion of the material, a mixture of 50 vol % isopropanol (Iso, Sigma Aldrich) with 50 vol % 4-methyl-2-pentanone (methyl isobutylketone, MIBK, Sigma Aldrich) was used. The samples were immersed in this mixture for 1 h.

4.2.2.2 Experimental results

The writing speed was fixed at 1 mm/s. The applied average laser power varied within the range of 0.1–10 mW. The line widths and heights were measured depending on the applied average laser power using high resolution SEM images. The line widths and heights measured for the two materials Zr-Hypo and DPMA-Zr-Hypo are shown in Fig. 4.5. Note that the applied average laser power in the case of the non-amplified Zr-Hypo has to be multiplied by a factor of 10. At first glance it is obvious that there is an abrupt cut-off for the achievable widths and heights towards low laser powers in all cases. This cut-off is due to the stability of the materials. Below a certain laser power, and thus a certain achieved polymerized material strength, the structures do not withstand the development process. The structures are destroyed by the evaporating solvent mixture. Further, it can be seen that the smallest lines can indeed be achieved with amplified DPMA-Zr-Hypo for a minimum applicable average laser power of 0.5 mW, whereas the smallest lines were realized for the Zr-Hypo for an average laser power of 1 mW.

The results and the achieved minimum line widths and heights for Zr-Hypo and DPMA-Zr-Hypo are summarized in Fig. 4.6. In the non-amplified material, the smallest reproducible line width achieved was around 150 nm. Smaller polymerized structures have principally been observed in the online process observation, but were washed away during development.

The reproducible smallest line width achieved in the amplified polymer containing 15 % DPMA was measured to be 82.5 nm according to the SEM images. It should be noted that the structures had been isotropically covered with a gold layer of at least 10 nm thick by sputtering in a gas discharge with a background gas pressure of 10 mbar for SEM inspection [36]. Under these conditions the achieved minimum line width can be estimated to be smaller than 62 nm. In further experiments, free-standing polymer structures with high aspect ratios of 10 : 1 were also obtained. The smallest diameter of a rod-like nanoantenna has been measured to be 40 nm.

4.2.3 2D two-photon polymerization of E-Shell 300 on dielectric surfaces

2PP has also been investigated with materials which are cheap and easily available commercially. One of those materials is E-Shell 300, which is commonly used for 3D printing and hearing aid fabrication. The material has a high flexural strength up to 88.4 MPa and is suitable for the fabrication of structures with dimensions

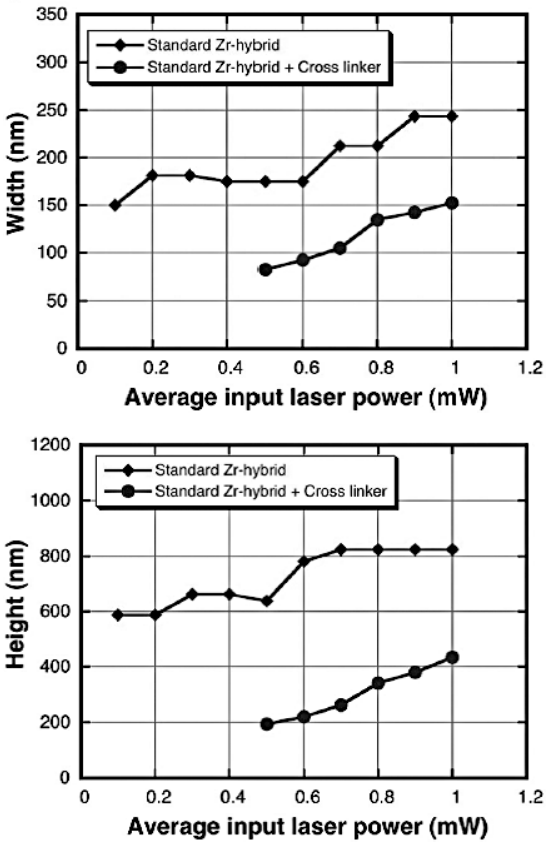

Fig. 4.5: Supported line widths (left) and heights (right) achieved for the two polymers Zr-Hypo (diamonds) and DPMA-Zr-Hypo (circles).

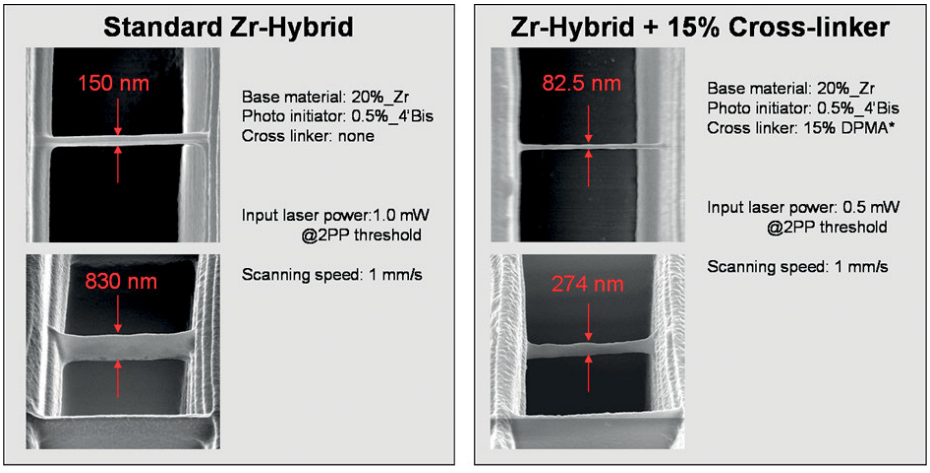

Fig. 4.6: Summary of the structuring of Zr-Hypo and amplified DPMA-Zr-Hypo. Lines of less than 82.5 nm in width were reproducibly fabricated under the influence of an additional crosslinker.

below 100 nm. The photoinitiator used in the commercial product is Irgacure 127, at a concentration of 5 wt %. Initial experiments have shown that the material can directly be structured by 2PP using frequency doubled ytterbium:potassium-gadolinium-tungstate laser radiation with 200 fs pulse duration. A laser power variation was performed to quantify the material properties and the structural sizes obtainable with 2PP. The exposure time for the fabrication of single voxels was fixed to 20 ms. A typical result is shown in Fig. 4.7. In the first test of the material variable voxel sizes ranging from 200 nm down to 50 nm were obtained.

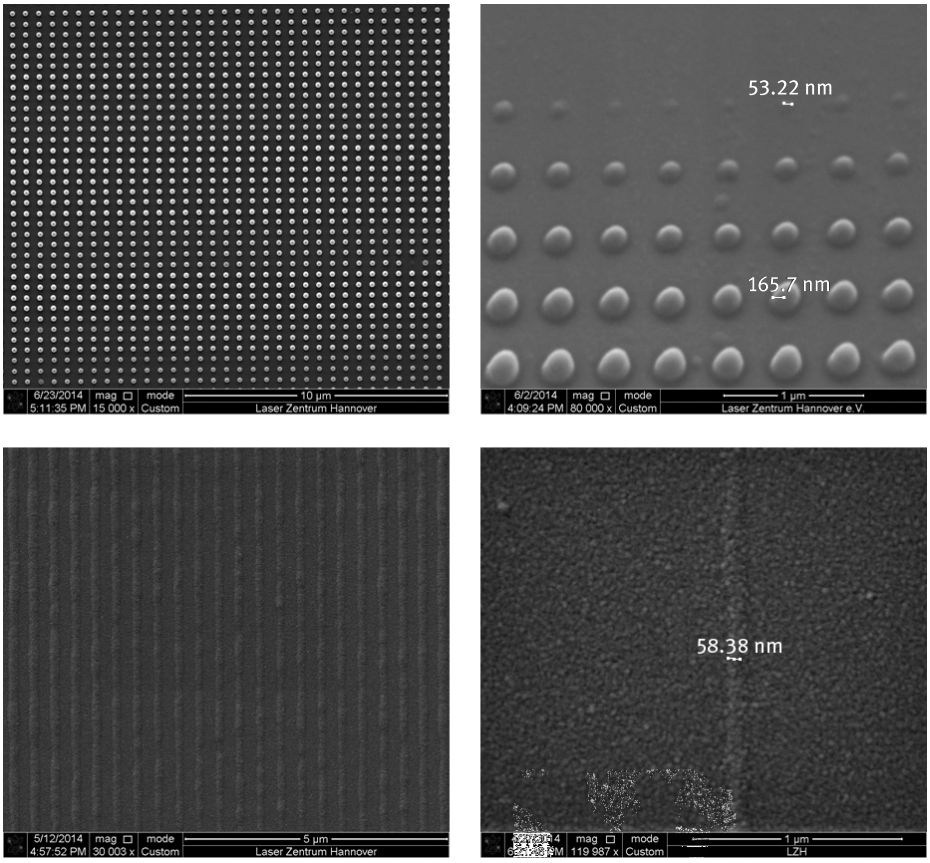

Fig. 4.7: 2PP with E-Shell 300: fabrication of voxels for material characterization. Upper left: large array of pillar structures. Upper right: power variation for a fixed exposure time of 20 ms. Minimum voxel diameters of 53 nm have been measured. A grating structure with 100 nm line width and 350 nm period is shown bottom left. By careful slow scanning and low laser powers of 1 mW, line widths of 58 down to as low as 50 nm respectively (bottom right) were obtained.

Line structures have also been fabricated with the same material. Gratings consisting of polymer lines with diameters of 100 nm and below have been realized, as demonstrated in Fig. 4.7. The writing speed was set to 10 µm/s and the laser power adjusted to 2 mW.

By carefully adjusting the laser focus with respect to the substrate surface, line widths of 58 nm down to 50 nm were obtained for applied laser powers of 1 mW, and slow scanning speeds of 5 µm/s and 7 µm/s respectively. At these dimensions, even very small fluctuations in the laser beam power and the positioning stages have huge influences on the structuring results. These fluctuations are slightly visible in the images in Fig. 4.7. They have no influence on structures with a critical dimension greater than 100 nm however.

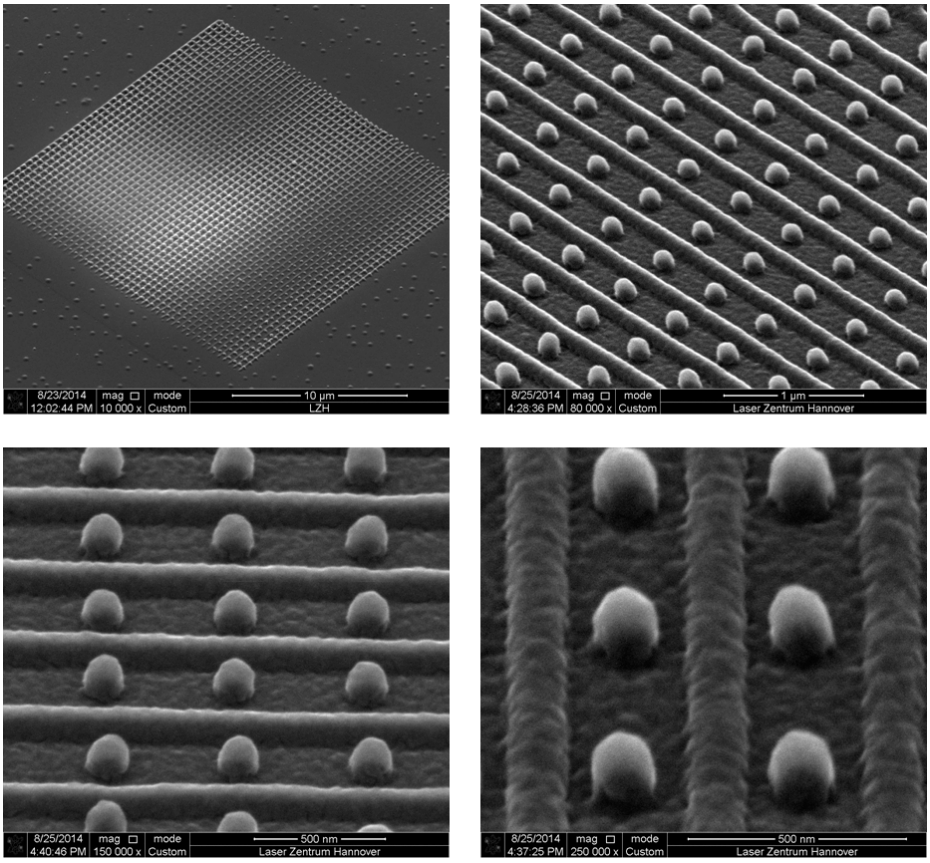

Fig. 4.8: Grating and NTFF structures fabricated by high-resolution 2PP. Upper left: overview image of an exemplary 20 µm × 20 µm grating with nanorod antennae. Upper right: magnified image showing the regularity of the structure. Bottom left: side view, period of NTFF nanoantennae is 500 nm. Bottom right: front view, line width is 95 nm, line height is 70 nm. The diameter of the NTFF structures is 110 nm and height 150 nm.

Gratings with and without NTFF nanoantennae have been realized from E-Shell 300. The results are shown in Fig. 4.8. The period of the grating was chosen to be 450 nm. A line width of 95 nm and a height of 70 nm for the grating ridges were obtained for a scanning speed of 7 μm/s and a laser power of 2 mW in front of the focusing microscope objective. The NTFF nanoantennae with 500 nm period are cylindrical pillars with a rounded top of 110 nm diameter and a height of 150 nm.

4.3 Fourier scatterometry on gratings with designed near-field structures

The characterization of sub-lambda structures with a fast non-destructive optical method is a common metrology task.

One of the most widely used techniques for these tasks is the scatterometry method [37]. Scatterometry is a method for analysis of the diffraction spectrum from a periodic arrangement of nanostructures. It is used to reconstruct the unknown structure parameters by comparison of measured and simulated spectra, which is why it belongs to the field of so-called model-based metrology methods [38].

There have been various attempts to improve scatterometric sensitivity, mainly by increasing the illumination wavelength range used, variation of the incidence angle or a high numerical aperture illumination, as well as combinations with other measurement methods, such as for example white light interferometry [38]. While all of these methods increase the sensitivity of the measurements by increasing the information content of the measurement itself, a different approach was taken in the work presented. The simulation branch needed for all scatterometric measurements can itself be exploited to design an optimized scatterometric sensitivity inherent to the structure. While this may not be generally applicable due to practical constraints, it is conceivable for alignment, testing or calibration targets.

While we have already shown some promising results based on simulations [39], we now want to verify these results with experimental data. We apply the so-called Fourier scatterometry method [38] to detect the backscattered light of polymer test line gratings fabricated as described in Section 4.2. We then analyze the influence of added near-field structures on sensitivity to line width. In contrast to the simulation study mentioned, we used a brightfield illumination with a broad range of incident directions containing much more information. In addition to new adapted simulations we show a first experimental implementation and verification of the result obtained previously.

4.3.1 Simulation method

Simulations of the Fourier scatterometry technique are performed with our simulation tool, MicroSim [40]. It is based on the rigorous coupled wave analysis method [41] for diffraction from arbitrary three-dimensional structures and includes some improved convergence methods [42].

The extended illumination pupil is modeled by planar waves emerging from a quadratic grid, which is sampled with equidistant points corresponding to the different incident angles. Due to the symmetry of the structure studied, only one-quarter of the pupil was simulated. This quarter was sampled by a 99×99 grid. The points are defined by their NA coordinates, NA_x and NA_y. For each of these points, the diffracted spectrum from the sample is calculated. This high sampling is needed due to the very fine features which can be found in the pupil images caused by higher diffraction orders of the illuminated gratings. A wavelength of 617 nm was assumed.

Finally, the calculated fields for every incidence angle were coherently superposed to obtain the resulting pupil images. The analyzed periodic grating was modeled with a staircase approximation. The width of the lines (CD) was varied and the sensitivity towards those changes was obtained from the difference in the corresponding pupil images. These sensitivities were compared to the ones calculated after the introduction of near-field structures (nanorods) between the lines of the gratings.

4.3.2 Experimental setup

We built a Fourier scatterometry setup which will be explained in the following section. It was completely redesigned and based on a setup used in previous works [39]

We start with the illumination path. A red LED with a wavelength of 617 nm is used as light source. We use a microscope objective (10×) to magnify and depict the end of the polished fiber on the back focal plane of the microscope objective used to illuminate the sample. A polarizer allows selection of s or p polarized illumination. The image of the fiber covers the complete aperture of the backfocal plane of the objective, producing a homogenous intensity distribution. We use a microscope objective with a NA of 0.95 (250× magnification); this means that the sample is illuminated with plane waves covering the angles from 0 to 72°. The backscattered light from the analysed sample is again collected by the same objective, as our microscope works in reflection mode. A beamsplitter is used to image the backfocal plane of the objective and the image plane of the sample at the same time. The backfocal plane is imaged with the help of a Bertrand lens on a CCD camera, while the image plane is imaged with help of a matched tube lens. Both lenses are specially designed and aberration -corrected for the microscope objective used.

Besides the illumination and imaging path of the Fourier scatterometry microscope, a reference arm for a Linnik type setup is also included in the setup. It includes

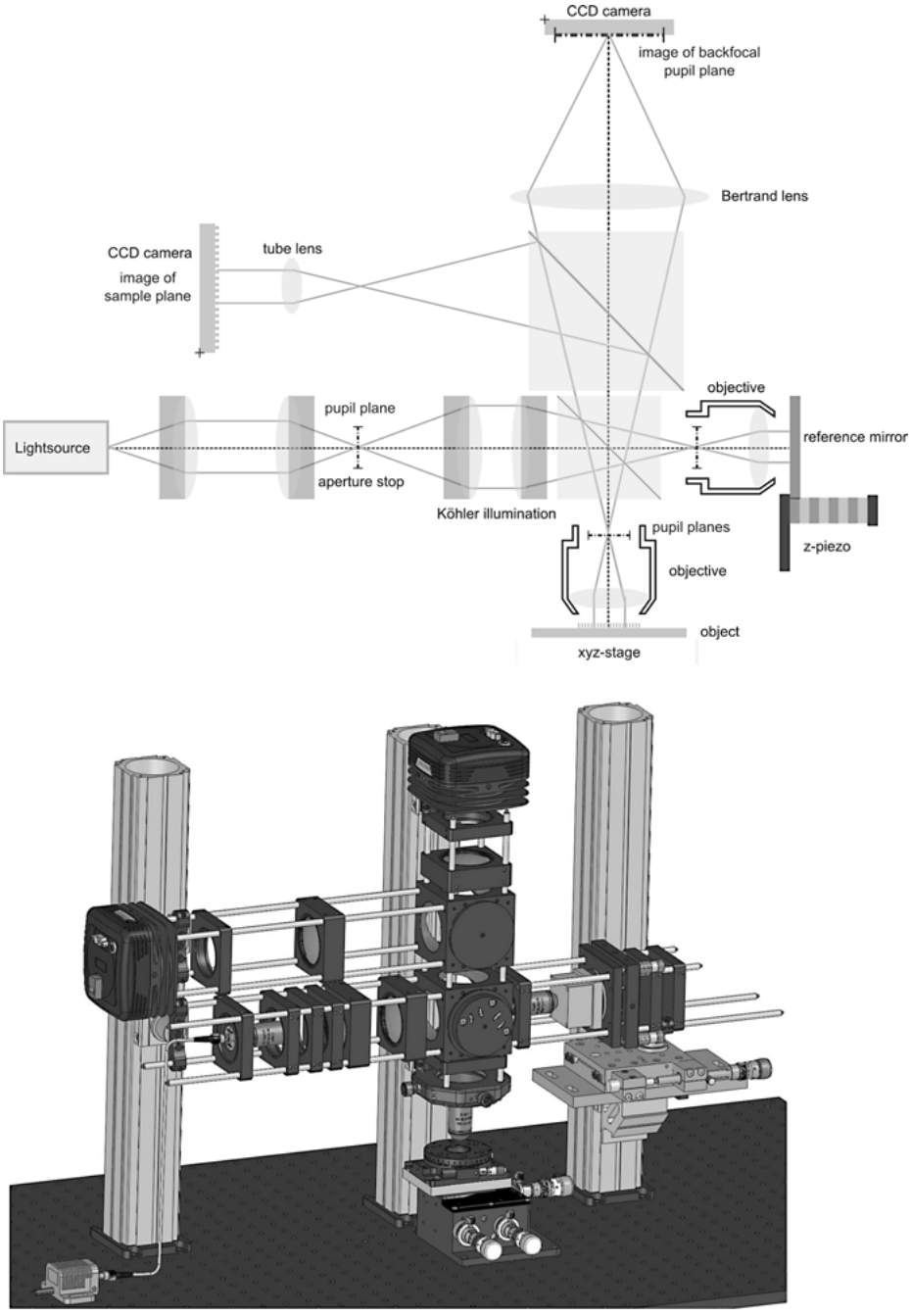

Fig. 4.9: CAD design of the setup (top) and scheme of the experimental setup showing the different beam paths (bottom).

a matched objective with identical NA as the imaging objective and allows imaging of the interfering backfocal planes of both objectives. This type of measurement is detailed in [39] but will not be used in this setup. The reference path is blocked with an absorbing plate. The CAD construction of the setup as well as the schematic setup showing the detailed light paths can be found in Fig. 4.9.

A typical measurement consists of searching the grating to be analyzed on the sample using classical imaging microscopy and focusing directly on top of the structure and then recording the pupil plane images for both polarizations (s and p). Using structures which only vary in width and comparing the images allows extraction of the sensitivity of the signal towards changes of the line width.

4.4 Experimental results

First the structures are characterized with an electron microscope to get an impression of the different structure parameters. The images are shown in Section 4.2. This data is used for the modelling of the structure to be used by the simulations. We define the sensitivity towards a parameter as the change in the pupil plane intensity compared to the absolute changes of the parameter.

The analyzed structures consist of polymer test line gratings fabricated as described in Section 4.2. The period of the lines is 1800 nm, while the height is 500 nm. There are gratings with different line widths (250 and 350 nm). The complete grating is covered with a 20 nm layer of gold.

Pupil images for these structures were taken for both s- and p-polarization. The resulting images and the difference in pupil plane intensity can be found in Fig. 4.10 together with the results of the same measurements and simulations with added nanorods between the lines. In the case with rods, the linewidths are 380 nm and 420 nm, meaning that the difference is smaller than for the lines without the rods (250 to 350 nm). The rod itself has a radius of approx. 175 nm and a height of 500 nm. Again the structures are covered with 20 nm of gold.

Differences between measured and simulated pupil images can have different reasons. The most important is the simplified simulation model which had to be used due to the very large calculation times. The grating was modelled with perfectly steep walls; neither roundings nor line edge roughness was taken into account. The SEM pictures and microscope pictures show that this is a very rough assumption. Additionally, till now we have not taken any aberrations of the optical elements used in the setup into account. The LED light source is modelled as perfectly homogenous and with a very narrow band of only 1 nm wavelength range, while realistically 20 nm should be assumed. Each wavelength would need one simulation and the global simulation time for that would increase drastically. Additionally, the agreement between simulation and experiment is worse in the case of added nanorods. This could indicate that a more

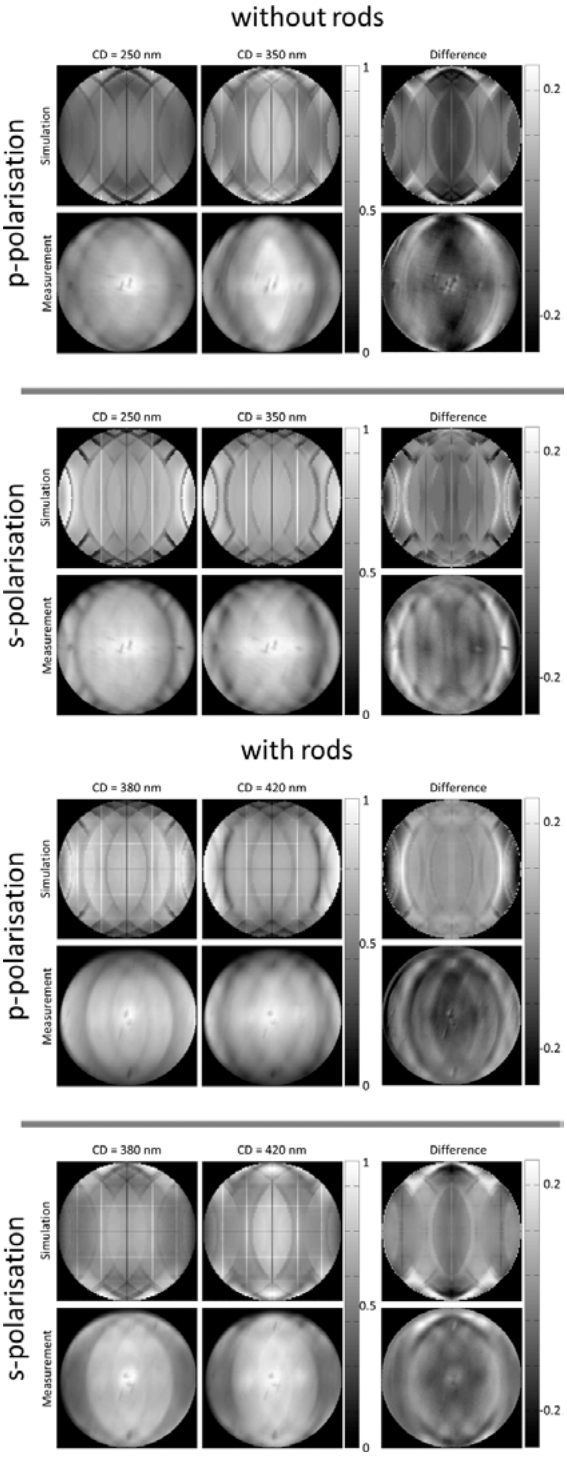

Fig. 4.10: Resulting pupil images (simulated and measured) for s- and p-polarization for gratings with and without nanorods between the lines, as well as the corresponding differences when the CD of the gratings is varied. For the lines without nanorods the compared CD values are 250 and 350 nm. For the lines with nanorods the values are 380 and 420 nm. The radius of the rods is 175 nm. The difference in intensity is a direct indication of the sensitivity towards the change in line width (CD).

sophisticated modelling of the nanorods is needed, which would lead to significantly increased computation time.

The measured and simulated results show comparable absolute differences in pupil intensity for the gratings both with and without rods. It must be noted, however, that the line widths analyzed do not agree for both cases. In the case of the lines without rods, the line width differs from approx. 250 to 350 nm, a difference of 100 nm. While the widths for the lines with rods are much closer; 380 compared to 420 nm, a difference of only 40 nm. The results show almost identical differences in intensity. For that the system is much more sensitive for the case of a grating with rods. This proves the improved sensitivity obtained by adding scattering near-field structures.

4.5 Conclusions

Based on the assumption of higher scatterometric sensitivity of structures with added near- to far-field transformers designed by previous simulation-based studies, we have now provided a first experimental verification for measuring critical dimensions of gratings with resolutions as low as 50 nm. 2PP methods have been developed, improved, and successfully applied for the fabrication of sub-wavelength structures. The experimental results supported by corresponding rigorous simulations show the expected sensitivity gain in the scatterometric signatures.

Acknowledgments

The authors acknowledge contributing work by Tim Fischer and Ayman El-Tamer for the preparation of 3D sub-100 nm structures.

References

[1] J. C. Love, D. B. Wolfe, H. O. Jacobs, G. M. Whitesides, Microscope Projection Photolithography for Rapid Prototyping of Masters with Micron-Scale Features for Use in Soft Lithography, Langmuir 17, pp. 6005–6012 (2001)
[2] M. Köhler, W. Fritzsche, Nanotechnology, 2nd Edition Wiley (2007)
[3] M. Madou, Fundamentals of Microfabrication and Nanotechnology, Boca Raton, CRC Press (2012)
[4] C. W. Hull, Apparatus for Production of Three-Dimensional Objects by Stereolithography, U.S. Patent 4,575,330 (1982)
[5] J.-W. Choi, E. MacDonald, R. Wicker, Multi-material microstereolithography, International Journal of Advanced Manufacturing Technology 49, pp. 543–551 (2010)
[6] M. Göppert Mayer, Über Elementarakte mit zwei Quantensprüngen, Dissertation, Univ. Göttingen (1930)

[7] M. Göppert Mayer, Über Elementarakte mit zwei Quantensprüngen, Annalen der Physik 9, p. 273–294 (1931)
[8] W. Kaiser and C. G. B. Garrett, Two-photon excitation in CaF2:Eu2+, Phys. Rev. Lett. 7, pp. 229–231 (1961)
[9] E.-S. Wu, J. H. Strickler, W. R. Harrell, W. W. Webb, Two-photon lithography for microelectronic application, Proceedings Article, Proc. SPIE 1674, p. 776–782 (1992)
[10] S. Maruo, O. Nakamura, S. Kawata, Three-dimensional microfabrication with twophoton-absorbed photopolymerization, Optics Letters 22, pp. 132–134 (1997)
[11] J. Serbin, A. Egbert, A. Ostendorf, B. N. Chichkov, R. Houbertz, G. Domann, J. Schulz, C. Cronauer, L. Fröhlich, M. Popall, Femtosecond laser-induced two-photon polymerization of inorganic organic hybrid materials for applications in photonics, Optics Letters 28, pp. 301–303 (2003)
[12] M. Deubel, G. von Freymann, M. Wegener, S. Pereira, K. Busch, C. M. Soukoulis, Direct laser writing of three-dimensional photonic-crystal templates for telecommunications, Nature Materials 3, pp. 444–447 (2004)
[13] J. Serbin. A. Ovsianikov, B. N. Chichkov, Fabrication of woodpile structures by two-photon polymerization and investigation of their optical properties, Optics Express 12, pp. 5221–5228 (2004)
[14] H.-B. Sun, S. Kawata, Two-Photon Photopolymerization and 3D Lithographic Microfabrication, Advances in Polymer Science 170, pp. 169–273 (2004)
[15] M. Malinauskas, M. Farsari, A. Piskarskas, S. Juodkazis, Ultrafast laser nanostructuring of photopolymers: a decade of advances, Physics Reports 533, pp. 1–31 (2013)
[16] C. S. Colley, D. C. Grills, N. A. Besley, S. Jockusch, P. Matousek, A. W. Parker, M. l. Towrie, N. J. Turro, P. M. W. Gill, M. W. George, Probing the reactivity of photoinitiators for free radical polymerization: time-resolved infrared spectroscopic study of benzoyl radicals, Journal of the American Chemical Society 124, pp. 14952–14958 (2002)
[17] C. Schizas, V. Melissinaki, A. Gaidukeviciute, C. Reinhardt, C. Ohrt, V. Dedoussis, B. N. Chichkov, C. Fotakis, M. Farsari, D. Karalekas, On the design and fabrication by two-photon polymerization of a readily assembled micro-valve, International Journal of Advanced Manufacturing Technology 48, pp. 435–441 (2010)
[18] J. Koch, T. Bauer, C. Reinhardt, B. N. Chichkov, Recent progress in direct write 2D and 3D photofabrication technique with femtosecond laser pulses, in Recent Advances in Laser Material Processing, Chapter 8, Elsevier, pp. 472–495 (2006)
[19] F. Claeyssens, E. A. Hasan, A. Gaidukeviciute, D. S. Achilleos, A. Ranella, C. Reinhardt, A. Ovsianikov, X. Shizhou, C. Fotakis, M. Vamvakaki, B. N. Chichkov, M. Farsari, Three-Dimensional Biodegradable Structures Fabricated by Two-Photon Polymerization, Langmuir 25, pp. 3219–3223 (2009)
[20] S. Passinger, M. S. Saifullah, C. Reinhardt, K. R. V. Subramanian, B. N. Chichkov, M. E. Welland, Direct 3D Patterning of TiO2 Using Femtosecond Laser Pulses, Advanced Materials 19, pp. 1218–1221 (2007)
[21] I. Sakellari, A. Gaidukeviciute, A. Giakoumaki, D. Gray, C. Fotakis, M. Farsari, M. Vamvakaki, C. Reinhardt, A. Ovsianikov, B. N. Chichkov, Two-photon polymerization of titanium-containing sol-gel composites for three-dimensional structure fabrication, Applied Physics A 100, pp. 359–364 (2010)
[22] K. Terzaki, N. Vasilantonakis, A. Gaidukeviciute, C. Reinhardt, C. Fotakis, M. Vamvakaki, M. Farsari, 3D conducting nanostructures fabricated using direct laser writing, Optical Materials Express 1, pp. 58–597 (2011)
[23] C. Reinhardt, R. Kiyan, S. Passinger, A. L. Stepanov, A. Ostendorf, and B. N. Chichkov, Rapid laser prototyping of plasmonic components, Applied Physics A 89, pp. 321–325 (2007)

[24] C. Reinhardt, A. Seidel, A. B. Evlyukhin, W. Cheng, R. Kiyan, B. N. Chichkov, Direct laser-writing of dielectric-loaded surface plasmon-polariton waveguides for the visible and near infrared, Appl. Phys. A 100, pp. 347–352 (2010)
[25] C. Reinhardt, A. B. Evlyukhin, W. Cheng, T. Birr, A. Markov, B. Ung, M. Skorobogatiy, B. N. Chichkov, Bandgap-confined large-mode waveguides for surface plasmon-polaritons, Journal of the Optical Society of America B 30, pp. 2898–2905 (2013)
[26] C. Reinhardt, A. Seidel, A. B. Evlyukhin, W. Cheng, B. N. Chichkov, Mode selective excitation of laser-written dielectric-loaded surface plasmon polariton waveguides, Journal of the Optical Society of America B 26, pp. B55 – B60 (2009)
[27] K. Takada, H.-B. Sun, and S. Kawata, Improved spatial resolution and surface roughness in photopolymerization-based nanowriting, Applied Physics Letters 86, 071122 (2005)
[28] J.-F. Xing, X.-Z. Dong, W.-Q. Chen, X.-M. Duana, N. Takeyasu, T. Tanaka, S. Kawata, Improving spatial resolution of two-photon microfabrication by using photoinitiator with high initiating efficiency, Applied Physics Letters 90, 131106 (2007)
[29] L. Li, R. R. Gattass, E. Gershgoren, H. Hwang, J. T. Fourkas, Achieving $\lambda/20$ Resolution by One-Color Initiation and Deactivation of Polymerization, Science 324, pp. 910–913 (2009)
[30] J. Fischer, M. Wegener, Three-dimensional direct laser writing inspired by stimulated-emission-depletion microscopy, Optical Materials Express 1, pp. 614–624 (2011)
[31] J. Fischer, M. Wegener, Three-dimensional optical laser lithography beyond the diffraction limit, Laser Photonics Review 7, pp. 22–44 (2013)
[32] W. Haske, V. W. Chen, J. M. Hales, W. Dong, S. Barlow, S. R. Marder, J. W. Perry, 65 nm feature sizes using visible wavelength 3-D multiphoton lithography, Optics Express 15, pp. 3426–3436 (2007)
[33] M. Emons, K. Obata, T. Binhammer, A. Ovsianikov, B. N. Chichkov, U. Morgner, Two-photon polymerization technique with sub-50 nm resolution by sub-10 fs laser pulses, Optical Materials Express 2, pp. 942–947 (2012)
[34] A. Ovsianikov, X. Shizhou, B. N. Chichkov, M. Farsari, M. Vamvakaki and C. Fotakis, Optics Express 17, pp. 2143–2148 (2009)
[35] B. Bhuian, R. J. Winfield, S. O'Brien, G. M. Crean, Applied Surface Science 252, pp. 4845–4849 (2006)
[36] V. Ferreras Paz, M. Emons, K. Obata, A. Ovsianikov, S. Peterhänsel, K. Frenner, C. Reinhardt, B. Chichkov, U. Morgner, W. Osten, Development of functional sub-100 nm structures with 3D two-photon polymerization technique and optical methods for characterization, Journal of Laser Application 24, 042004 (2012)
[37] C. J. Raymond, Scatterometry for Semiconductor Metrology. In A. C. Diebold (Ed.), Handbook of silicon semiconductor metrology (pp. 477–513). CRC Press (2001)
[38] V. Ferreras Paz, S. Peterhänsel, K. Frenner, W. Osten, Solving the inverse grating problem by white light interference Fourier scatterometry, Nature Light: Science & Applications, 1(11), e36. (2012)
[39] V. Ferreras Paz, K. Frenner, W. Osten, Increasing Scatterometric Sensitivity by Simulation Based Optimization of Structure Design. In W. Osten (Ed.), Fringe 2013 - 7th International Workshop on Advanced Optical Imaging and Metrology (pp. 345–348). Springer Berlin Heidelberg (2014)
[40] M. Totzeck, Numerical simulation of high-NA quantitative polarization microscopy and corresponding near-fields. Optik - International Journal for Light and Electron Optics, 112(9), 399–406. (2001)
[41] M. G Moharam, T. K. Gaylord, Rigorous coupled-wave analysis of planar-grating diffraction. Journal of the Optical Society of America, 71(7), 811. (1981)

[42] T. Schuster, J. Ruoff, N. Kerwien, S. Rafler, W. Osten, Normal vector method for convergence improvement using the RCWA for crossed gratings. Journal of the Optical Society of America A, 24(9), 2880. (2007)

F. Zimmermann, S. Richter, R. Buschlinger, S. Shukla,
R. Heintzmann, U. Peschel, and S. Nolte

5 Ultrashort pulse-induced periodic nanostructures in bulk glass: from fundamentals to applications in high-resolution microscopy

Abstract: We investigated sub-wavelength structures, so-called nanogratings, induced by ultrashort laser pulses in the bulk of transparent materials. By using small angle x-ray scattering and focused ion beam milling we were able to show that nanogratings consist of sheet-like cavities with dimensions of $(280 \times 25 \times 380)\,\mathrm{nm}^3$ and $(30 \times 25 \times 75)\,\mathrm{nm}^3$. Their size remains constant with an increasing number of laser pulses while the number of sheets increases. This is in agreement with the continuously decreasing period obtained by diffraction measurements and SEM images. Furthermore, nanogratings were inscribed on different types of glass, such as ULE™ or borosilicate glasses. Different nanograting features, such as sheet thickness and periodicity, were obtained in borosilicate.
Theoretical studies reveal that wavelength-scale plasma structures form during the interaction of laser light with glass. Their competition leads to the formation of periodic plasma patterns, which show the same orientation and period as nanogratings in glass (at low pulse numbers).
Finally, nanograting-based waveplates have been successfully implemented in single shot optical sectioning analysis using the polarized-illumination-coded structured illumination microscopy (picoSIM) method.

5.1 Introduction

The ultrashort pulse laser has been established as a universal tool for micromachining of transparent materials and fabrication of various photonic devices in recent years [1, 2]. Due to the short pulse duration in the femtosecond regime, high intensities in the focal region (typically in the range of 10^{13} W/cm^2) trigger nonlinear absorption mechanisms which allow precise deposition of the pulse energy. This enables local modification of transparent materials within the bulk volume. Fused silica in particular has turned out to be a versatile platform. Here, three kinds of modifications can be induced. Low laser pulse energies lead to an isotropic refractive index increase in the focal volume which, by translating the sample during irradiation, can serve as a waveguide and hence allow the fabrication of complex photonic networks [3, 4]. In contrast, high laser pulse energies provoke an expanding plasma wave leaving a void with typical diameters of several hundreds of nanometers surrounded by a shell of densified material [5, 49].

In 1999, Kazansky et al. [6] reported on anisotropic light scattering in Ge-doped silica glass when using an intermediate regime of pulse energies. Sudrie et al. also observed birefringent material modifications in the bulk of fused silica [7]. It turned out that self-assembled nanogratings with a sub-wavelength periodicity cause this local birefringence [8]. Further studies discovered that the orientation of the grating planes is always perpendicular to the laser polarization, while the degree of birefringence can be tuned by setting the laser parameters adequately [9, 10]. Moreover, on combination with the direct writing technique using a high precision translation stage, the three spatial degrees of freedom (x, y, z), and the possibility of locally tailoring the birefringence enable the fabrication of various photonic functionalities. These range from wave plates for generating almost arbitrary polarization states [10, 11], computer generated holograms [12] up to microscopic applications [13]. The latter will be covered in Section 5.4.

Although a number of theories have been put forward to explain the formation of nanogratings [8, 9], there is still no complete model capable of describing all effects associated with the self-organization process. The following section covers experimental investigations to gain new insights into the formation and evolution of nanogratings, and subsequently Section 5.3 addresses theoretical aspects.

5.2 Experimental analysis of nanograting formation and evolution

5.2.1 Formation of ultrashort pulse-induced nanogratings

In order to explore the formation and evolution of nanogratings in the bulk of fused silica, the relevant process parameters first need to be identified. Nanogratings were therefore inscribed into the bulk of fused silica using a femtosecond oscillator (Amplitude t-pulse 500) at a wavelength of 515 nm (frequency doubled oscillator output) and pulse duration of 450 fs. Figure 5.1 (a) depicts the inscription process and Fig. 5.1 (b) is an exemplary SEM micrograph of nanogratings after polishing and etching.

As mentioned in the introductory section, pulse energy plays a major role in the observation of birefringent material modifications. However, since the formation of the self-assembled nanogratings requires the action of several hundreds of laser pulses [31], the pulse overlap in terms of the number of laser pulses incident on one laser spot (N) has to be set correspondingly. This can be expressed as $N = 2\omega_0 R/v$, with ω_0 denoting the beam waist radius, v the speed of the sample movement, and R the laser repetition rate. The latter strongly influences the formation itself, as Fig. 5.1 (c) shows.

The formation of nanogratings occurs in a well-defined parameter window (green area). No modification was observed at small average powers (e.g. pulse energies of 40 nJ and 100 kHz repetition rate). In contrast, large repetition rates (> 1 MHz) lead to heat accumulation of successive pulses, resulting in melting and the destruction of

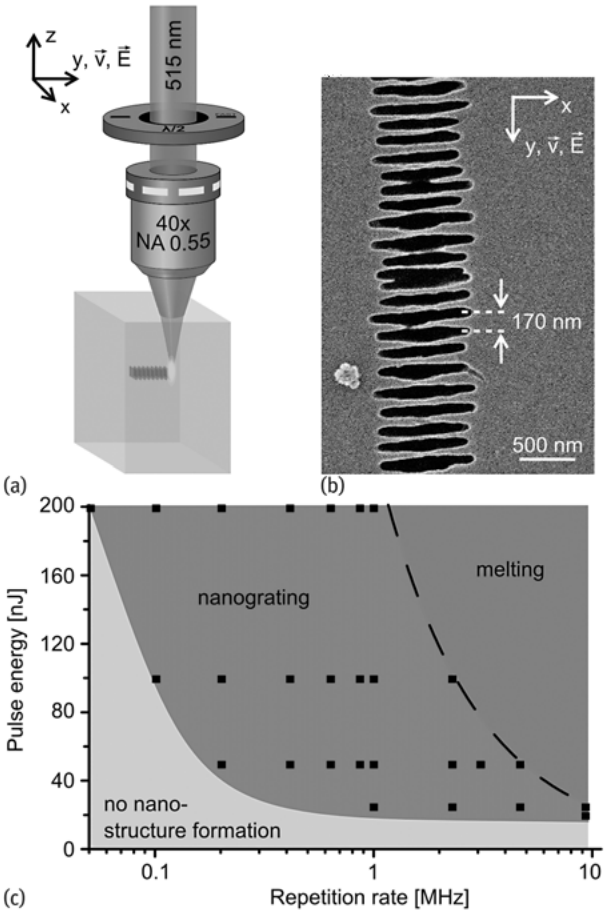

Fig. 5.1: (a) Principle of the nanograting inscription. (b) Exemplary SEM image of nanogratings after polishing and etching. (c) Parameter window for the inscription of nanogratings; from [31].

nanostructures. This upper threshold is determined by the average power delivered, thus the usable pulse energy is inversely proportional to the repetition rate (dashed graph in Fig. 5.1 (c)). Consequently, the available parameter region shrinks at higher repetition rates. However, nanostructures up to 9.4 MHz could even be observed, allowing for fast inscription of local birefringence.

In order to gain a better understanding of the self-organization process we investigated the influence of the number of laser pulses applied. Figure 5.2 (a) shows different nanostructures obtained by varying the speed of the sample movement for fixed repetition rate (2.3 MHz) and pulse energy (50 nJ). Isolated modifications which are already aligned perpendicular to the laser polarization can be observed after a number of of laser pulses. However, the nanostructures exhibit no visible periodicity and contain a high fraction of non-modified regions in the trace of the focus. Periodic structures emerge with ongoing illumination while the vacancies between the isolated modifications start to vanish. A homogeneous grating shows up after several hundred

laser pulses while the period continuously decreases with an increasing number of applied pulses. Saturation of the period can be observed at high numbers of laser pulses. As Fig. 5.2 (b) indicates, the grating period scales approximately half of the wavelength of the inscribing laser in the glass ($\lambda/2n$).

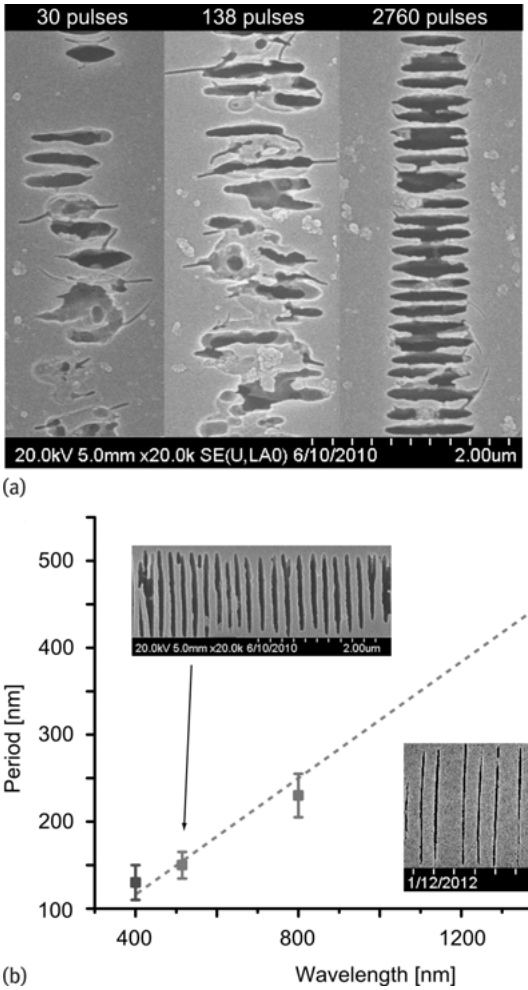

Fig. 5.2: (a) Evolution of nanogratings with increasing number of laser pulses; from [31]. (b) Minimal nanograting period in dependence of the inscribing laser wavelength; from [50]. SEM micrographs of nanogratings inscribed with 515 and 1550 nm are shown as inset.

5.2.2 Characterization of nanogratings

Laser-induced nanogratings can be typically characterized by measuring the induced birefringence. However, such measurements do not provide structural information. Thus, most studies explore the formation of nanogratings by polishing and subsequent etching of nanograting samples (see also Fig. 5.2). However, this leads to blurring and erasing of fine structure details. In contrast, diffraction of light provides a noninvasive and simple approach to mapping the formation and evolution of nanogratings. In this case, short wavelengths are required due to the fine periods.

An ultrashort laser source (Smart Light 50, Raydiance) emitting pulses at 1550 nm wavelength (pulse duration of 800 fs) was used for the inscription of nanogratings. The long wavelength and correspondingly large grating period facilitate the inspection by diffraction. The pulse energy was 900 nJ and a microscope objective with a numerical aperture of 0.35 (beam waist $\omega_0 = 1.4\,\mu m$) served to focus the pulses in shallow material depths. The inscribed nanogratings were subsequently analyzed by diffraction of visible light (wavelength 473 nm). Figure 5.3 shows the corresponding nanograting period measured by diffraction as well as by SEM after polishing and

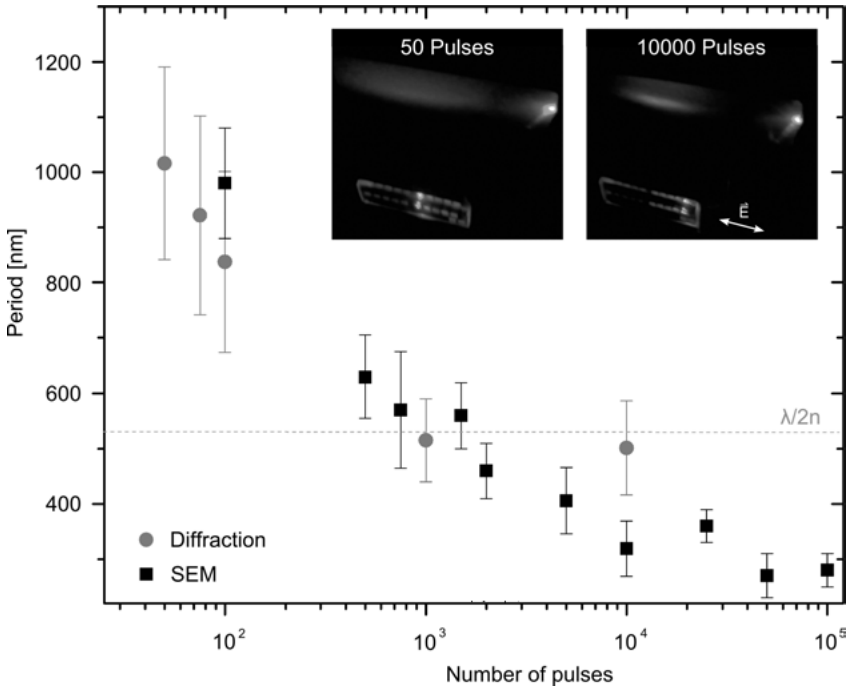

Fig. 5.3: Periods of nanogratings measured by diffraction and SEM, respectively. The inset shows an example of the first order diffraction of nanogratings inscribed with 50 and 104 laser pulses per spot respectively.

etching. The periods obtained by both methods agree very well and decrease with an increasing number of incident pulses. At the same time, the corresponding error bars, which indicate the standard deviation of the measured period in the SEM images and the width of the diffraction peak, respectively, shrinks. This is also noticeable by the first order diffraction peak in the inset of Fig. 5.3, which is much more pronounced in the case of large pulse numbers. In SEM images, a trend from isolated nanomodifications after few pulses to a homogeneous grating after several hundred incident pulses, analogue to Fig. 5.2 (a), laser wavelength of 515 nm, can be observed. Interestingly, at large numbers of incident pulses ($\gtrsim 5000$), periods smaller than the predicted value from the nanoplasmonic model ($\lambda/2n$) [9] (see also Section 5.3) are measured, as has also been reported by other groups [33].

5.2.3 Underlying structure of nanogratings

Using small-angle x-ray scattering (SAXS) also facilitates non-invasive exploration of the fine and sensitive structural features of nanogratings. As this technique maps the local density contrast, porous structures embedded within an isotropic material background can be treated equivalently to suspended nanoparticles which are typically investigated by SAXS [36].

The SAXS measurements of nanogratings were performed at the cSAXS beamline of the Swiss Light Source (PSI Villigen, CH). Figure 5.4 (a) depicts the measurement setup. The nanograting sample was illuminated with an 11.2 keV x-ray beam while the central transmitted beam was blocked. The scattered light was recorded by a pixelated direct converting detector (Pilatus 2M). Due to the experimental setup used and the high beam brilliance, maximum feature sizes up to 400 nm could be directly measured. Details of the measurements can be found in [37]. After standard image corrections were applied and the background from the pristine material was subtracted, the recorded two-dimensional scattering signal was integrated along the main axes (x, y) to observe the scattered intensity $I(q)$ (q-scattering vector). This was analyzed in terms of a unified scattering intensity model [38, 39], revealing feature sizes of the underlying scattering ensemble. As a useful quantity the so called Porod invariant, $P = \int I(q)q^2\,dq = \phi(1-\phi)$ was determined. For a diluted system, as empty pores in an isotropic glass matrix, P only depends on the volume filling fraction ϕ. For a porous material with a filling fraction of $\phi \ll 1$, the Porod invariant reflects the total pore volume and hence corresponds to the total scattering strength within the probed volume. Thus, P serves as a crucial quantity for the evolution of the total pore volume of nanogratings [35, 40]. Since this analysis can be performed for different azimuthal orientations relative to the laser polarization, the directions x and z (see Fig. 5.4 (a)) can be studied independently. By rotating the nanograting sample within the setup with respect to the z-axis, feature sizes along the remaining direction (y) could be measured.

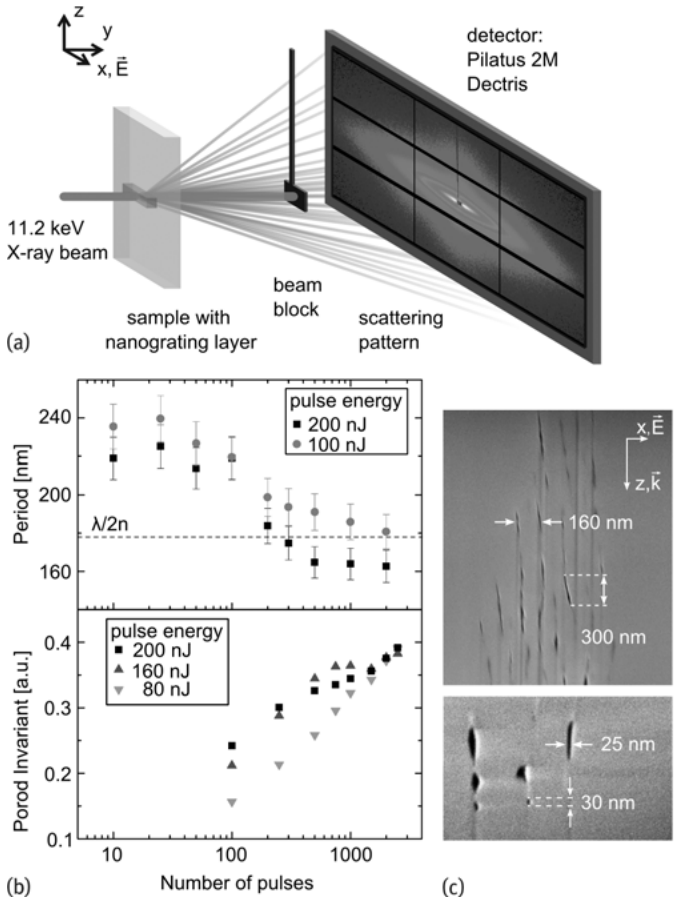

Fig. 5.4: (a) Sketch of the SAXS setup. (b) Results of the SAXS measurements. (c) FIB-SEM images of nanogratings inscribed with a pulse energy of 200 nJ: after 500 (upper) and 10 (lower) pulses per spot in the *x*-*z* plane, where *x* is the laser polarization direction, and *z* the direction of the inscribing laser; from [37].

The evaluation of the SAXS data revealed that two distinct populations with different diameters exist. First, a small population with diameters of (z = 30, x = 25, y = 75) nm, and a larger one with typical feature sizes of (z = 280, x = 25, y = 380) nm were measured [37]. Remarkably, for different numbers of applied pulses as well as for various laser pulse energies, the feature sizes remain constant. For comparison, SEM images of nanogratings prepared by FIB slicing [41] were acquired. This allows for etch-free excavation of nanometric features making them accessible for the SEM. Figure 5.4 (c) shows two FIB-SEM images of nanogratings (inscribed with 200 nJ pulse energy and 500 (upper) or 10 (lower) pulses per spot) in the *x*-*z* plane. The images depict nanometric hollow pores with pronounced elongation along the inscribing laser

direction. Typical feature sizes match the diameters measured by SAXS. Moreover, the periodic arrangement of sheets is clearly visible in the FIB-SEM images.

In the SAXS data, a certain correlation of scattering features shows up as modulation of the total scattering intensity. These diffraction peaks directly correspond to the period of the grating which is shown in the upper graph of Fig. 5.4 (b). The period decreases with an increasing number of applied pulses. This trend agrees well with the period evolution measured by diffraction in the visible range (see Section 5.2.2). The reduction of the grating period is accompanied by an increase in total scattering volume which is mapped by the Porod Invariant (see Fig. 5.4 (b), bottom). This indicates a rising number of scattering features within the probed volume, i.e. nanometric pores and cracks with ongoing illumination.

The results give an explanation for various aspects of nanogratings. The large index contrast between hollow sheets and the surrounding glass accounts for the large birefringence despite the small size of the nanograting constituents. Moreover, the grating planes typically obtained in etched samples appear due to small linked pores. In contrast, the material in between is devoid of nanometric pores and hence more resilient. This gives rise to the extremely anisotropic etching behavior which has been reported by other groups [42].

5.2.4 Nanogratings in different glasses

Since the discovery of nanogratings, fused silica has been the main platform to study the principal effects [9, 17]. In contrast, only a few reports exist of nanogratings in the bulk of other transparent materials, e.g., crystals [43] or doped glasses [44]. Hence we investigated the formation of nanogratings in various types of glass, such as the borosilicate glass BK7 (Schott) and Borofloat 33 (Schott) as well as ULE (Corning), which is a silica glass with a high fraction of TiO_2 to provide a low thermal expansion coefficient. We studied the influence of the pulse duration since it is a crucial parameter for nanograting formation in fused silica [42]. Thus a tunable ultrashort pulse oscillator (Femtosource XL 500, Femtolasers GmbH) emitting pulses at a wavelength of 800 nm and a pulse energy of 500 nJ was used to inscribe nanogratings. By tuning the position of the compressor prisms, the pulse duration was varied from 50 fs up to 450 fs proven by FROG (Grenouille, Swamp Optics) measurements. An aspheric lens with a focal length of 4.51 mm (Thorlabs C230 TME-B) served to focus 400 nJ pulses in shallow material depths (150 µm). A sample translation velocity of 10 mm/min and a pulse repetition rate of 100 kHz resulting in an exposure of 800 pulses per irradiated focal spot were used for the experiments.

Figure 5.5 (a) shows the measured retardation at a wavelength of 633 nm resulting from the nanogratings in the different types of glass. The error bars account for the standard deviations of the measurements of different lines inscribed with identical parameters. An increasing birefringence with rising pulse duration is measured for fused

silica, corresponding to the studies by Poumellec et al. [45] and Hnatovsky et al. [42]. In contrast, ULE shows only a weak pulse duration dependence. For pulse durations $\gtrsim 150$ fs, nanogratings in ULE and fused silica exhibit almost the same retardation. However, significantly smaller values are measured for the borosilicate glasses (BK7, Borofloat 33). Both glasses show their maximum retardation for pulse durations from 130–200 fs, which is approximately 10 % of that of fused silica and ULE, while for larger pulse durations the retardation is about 50 times smaller than in fused silica. The SEM images of nanogratings in ULE (pulse energy 200 nJ, pulse duration 120 fs)

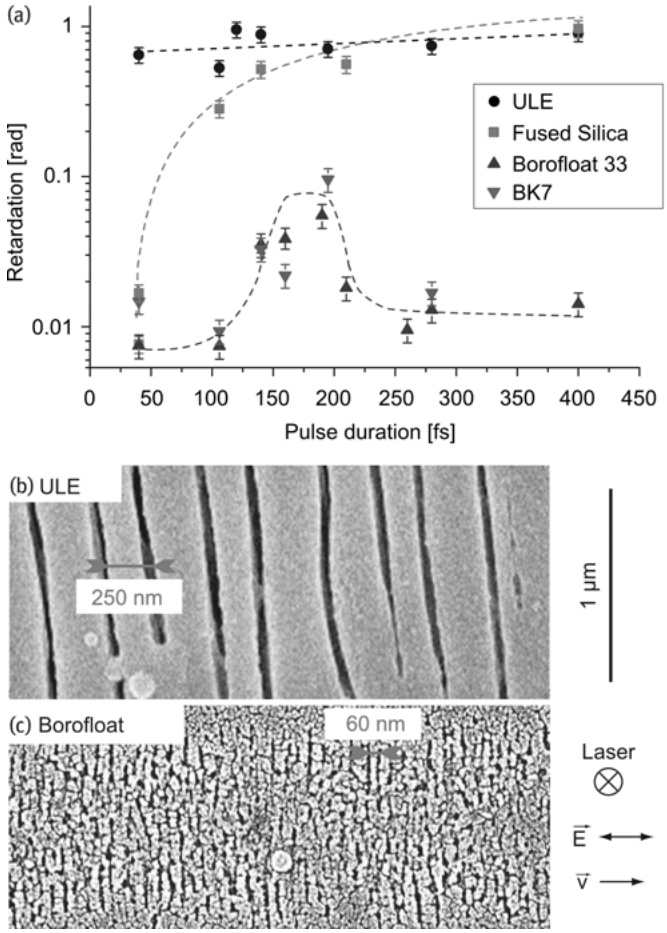

Fig. 5.5: (a) Measured optical retardation for nanogratings in different glasses dependent on the pulse duration (pulse energy of 400 nJ). (b)/(c) SEM images of nanogratings in ULE (pulse energy 200 nJ, pulse duration 120 fs) and Borofloat (pulse energy 400 nJ, pulse duration 400 fs); from [55]. The samples were gold coated before inspection in the SEM to prevent charge accumulation.

and Borofloat (pulse energy 400 nJ, pulse duration 400 fs) after polishing and etching give an explanation for this behavior; see Fig. 5.5 (b).

ULE shows distinct grating planes with a mean distance of about 250 nm which agrees well to the predicted period $\lambda/2n$ ($n = 1.48$) and the results obtained in fused silica. Remarkably, the observed period in Borofloat is only about 60 nm. In addition, the grating planes are not fully established, indicating a reduced number of nanostructures while the width of the grating planes is significantly smaller. Both issues influence the filling fraction between grating planes and surrounding material and hence lead to a reduced optical birefringence.

A closer look at the nanometric structure of nanogratings in borosilicate is provided in [46]. While the grating planes consist of empty sheets with diameters of 10 nm, their number is strongly reduced in contrast to fused silica nanogratings. This is attributed to the thermo-mechanical properties of borosilicate. The low viscosity and weak contraction during fast cooling leads to pronounced reflow of glass melt during the re-solidification process [47, 48]. Thus the formation of nanopores and larger cracks is prevented. Correspondingly, the SEM image after polishing and etching illustrates the fissured nanograting structure; see Fig. 5.5 (b).

5.3 Theoretical aspects of nanograting formation in the bulk of transparent materials

A first model for nanograting formation was proposed with the initial observation of the grating structure in 2003 [8]. The so-called plasma interference theory describes the inherent periodicity in terms of an imprinted density modulation due to the interference of the laser field with the laser-induced plasma wave. However, the prediction of a strong pulse energy dependence of the nanograting period could not hold with the experimental observations as well as the threshold for the nanograting formation. Another approach was made by Taylor et al. in 2008 [9]. This nanoplasmonic model explains the formation starting from defects which lead, due to the absorption of focused ultrashort laser pulses, to inhomogeneous plasma spots. These grow due to field enhancement and finally arrange periodically via quasi-metallic waveguiding, which leads to the imprinting of a grating period corresponding to $\lambda/2n$ (n – refractive index, λ – laser wavelength). In contrast, for example, the experimentally observed continuous decreasing period with an increasing number of laser pulses (see Fig. 5.3) cannot be explained by this model. Moreover, Beresna et al. report on longitudinal periodicity of nanogratings explained by interference of short-living exciton-polaritons [14], while the formation of the transverse period remains open.

Most previous modelling efforts concerning laser energy deposition in dielectrics have concentrated on the temporal and spatial evolution of laser pulses, while treating the material as homogeneous [15–18]. However, as far as nonlinear self-organization is concerned, a certain seed is required to start the process. Therefore, we take a different

approach and investigate the interaction of laser light with nanometer-sized inhomogeneities [19]. In order to understand the potential of purely optical self-organization processes we limit our scope to continuous illumination, which can be viewed both as a limiting case of single-pulse excitation and as an extrapolation of multiple pulses.

5.3.1 Theoretical model

For our model, we use a nonlinear finite-difference time-domain (FDTD) approach, which has previously been applied to the modelling of ionization and void formation in silica [18, 20]. Maxwell's equations

$$\frac{\partial}{\partial t}\vec{D} = \frac{1}{\mu_0}\nabla \times \vec{B} - \vec{J} \tag{5.1}$$

$$\frac{\partial}{\partial t}\vec{B} = -\nabla \times \vec{E}, \tag{5.2}$$

with $\vec{D} = \varepsilon\vec{E} + \vec{P}$ are solved using the standard FDTD algorithm [21, 22]. The response of the unexcited medium is included in the background permittivity $\varepsilon = n^2\varepsilon_0$, using a linear refractive index $n = 1.45$. The remaining contributions to the material response are included via the current density $\vec{J} = \vec{J}_\mathrm{d} + \vec{J}_\mathrm{mpi}$, where $\vec{J}_\mathrm{mpi}$ is used to model the energy loss due to multiphoton ionization, while $\vec{J}_\mathrm{d}$ describes the optical response of the newly generated conduction band electrons based on a Drude model

$$\frac{\partial}{\partial t}\vec{J}_\mathrm{d} = -\nu_e\vec{J}_\mathrm{d} + \frac{e^2}{m_e}\rho\vec{E}. \tag{5.3}$$

We assume the electron collision frequency to have a constant value $\nu_e = 10^{14}\,\mathrm{s}^{-1}$ within the range of reported values [17, 23, 24]. The conduction band carrier density ρ is described with a rate equation taking multiphoton ionization and recombination into account

$$\frac{\partial}{\partial t}\rho = (\rho_0 - \rho)\,\nu_\mathrm{mpi} - \frac{\rho}{\tau_\mathrm{rec}}. \tag{5.4}$$

In this model, the free carrier density reaches saturation at a value of $\rho_0 = 2\times10^{28}\,\mathrm{m}^{-3}$ [20]. The electron recombination time is $\tau_\mathrm{rec} = 150\times10^{-15}\,\mathrm{s}$ [25]. For an excitation wavelength of $\lambda = 800\,\mathrm{nm}$, and a fused silica target with a band gap of $W_\mathrm{ion} = 9\,\mathrm{eV}$, 6 photons are needed to promote an electron to the conduction band, resulting in an ionization rate

$$\nu_\mathrm{mpi} = \frac{\sigma_6 I^6}{\rho_0} \tag{5.5}$$

with a cross-section of $\sigma_6 = 2\times10^{-65}\,\mathrm{m}^9\,\mathrm{W}^{-6}\,\mathrm{s}^{-1}$ [26]. An expression for $\vec{J}_\mathrm{mpi}$ can be derived by equating the energy gain of electrons $\frac{\partial}{\partial t}W = W_\mathrm{ion}\nu_\mathrm{mpi}(\rho_0 - \rho)$ due to multiphoton ionization to the energy loss of the electric field $\vec{J}_\mathrm{mpi}\vec{E}$, yielding

$$\vec{J}_\mathrm{mpi} = \frac{\sigma_6}{\rho_0}W_\mathrm{ion}I^5\vec{E}(\rho_0 - \rho). \tag{5.6}$$

Additional attention has to be paid to the modelling of inhomogeneities. According to the literature, voids in conventional silica take up a mere 3% of the material volume [27], and have an average size of $d = 0.6\,\mathrm{nm}$ [28], resulting in a mean spacing below 20 nm. We consider such typical inhomogeneities as well as stronger inhomogeneities, which allow for the exploration of self-organization in single-shot simulations.

5.3.2 Numerical results

In order to understand the initial stages of the ionization process, we first consider a single sub-wavelength sphere, in which plasma generation can occur due to a non-vanishing ionization cross-section. Plasma generated inside the sphere according to equation (5.4) causes a decrease of the dielectric constant according to equation (5.3). The fields can be calculated in a quasi-static approximation [29, 30]. Due to scattering on the nanoplasma, the intensity inside the sphere is increased, leading to positive feedback between the local electric field and the carrier density. Eventually, the plasma reaches the resonant density, where $\varepsilon_{\mathrm{plasma}}(\rho_{\mathrm{Mie}}, \omega_{\mathrm{source}}) = -2\varepsilon_{\mathrm{background}}$. Now carrier densities increase almost exponentially even until the maximum carrier density $\rho = \rho_0$ is reached and saturation sets in. Pronounced intensity maxima now lie at the poles of the nanoplasma. If ionization in the surrounding medium is taken into account, this field enhancement leads to the formation of an ionized region growing into the direction of the electric field. Since scattering is now mostly caused by the induced nanoplasma, the final structure is invariant concerning shape, size and chemical nature of the seed inhomogeneity. This has been verified both for regions with an enhanced ionization cross-section as well as for voids with different diameters using the full FDTD model from Section 5.3.1 [19].

As the structure size leaves the sub-wavelength domain, the plasma acts as a nanoantenna causing strong back-reflection (Fig. 5.6 (a)). Further ionization is stimulated along the negative propagation direction (Fig. 5.6 (b)), and a new structure is formed in front of the old one, inhibiting further growth in the direction of polarization. In this way, a periodic plasma chain with wavelength dimensions growing backwards against the propagation direction is formed (Fig. 5.6 (c)).

We now turn to the study of randomly distributed inhomogeneities in a three-dimensional volume. Now a large number of plasma structures compete in the growth process, resulting in an onset of self-organization. In order to explore such effects, we allow for stronger ionization-enhancement inside the inhomogeneities.

In such systems the structures also expand into the third direction not covered by our previous two-dimensional simulations until they merge with their neighbors to form extended plasma planes oriented perpendicularly to the polarization direction (Fig. 5.7 (a)). Ionization is suppressed directly adjacent to each plasma plane and enhanced at a distance of approximately $\frac{\lambda}{n}$. This effect leads to an interaction between separate structures. As a result, order emerges during growth and a periodic pattern

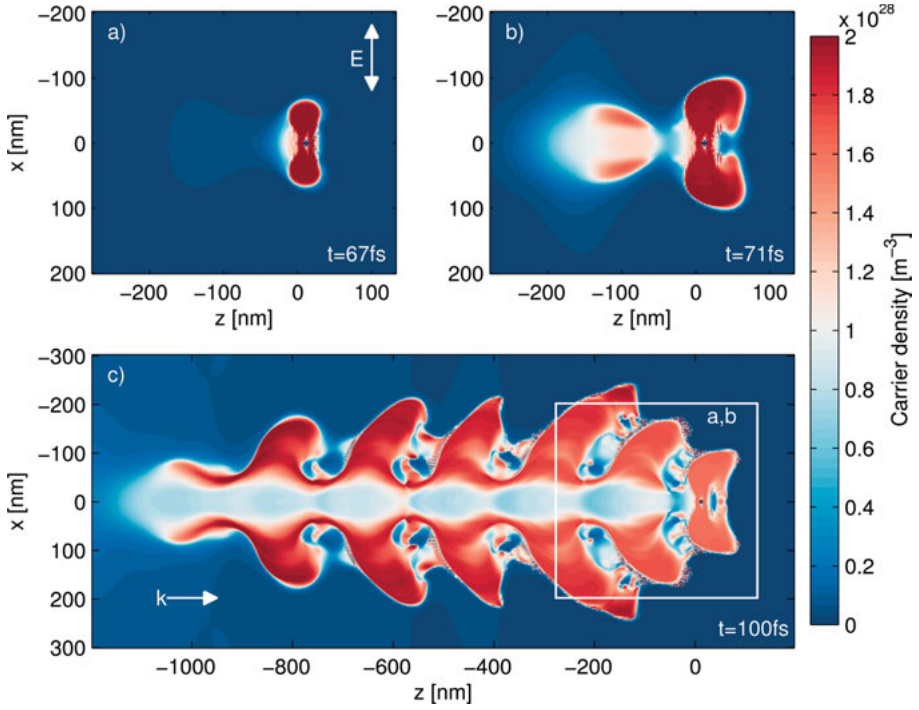

Fig. 5.6: Carrier density (2D FDTD) around a single void ($\sigma_6 = 0$, $n = 1.0$, $d = 7$ nm) embedded in fused silica at the coordinate origin for several stages of structure growth. (a) Plasma growth in the direction of polarization. (b) Saturation of growth and initiation of a second structure. (c) Periodic plasma structure formed by subsequent growth. Illumination is a cw plane wave with amplitude $E_0 = 1.7 \times 10^{10}\,\mathrm{V\,m^{-1}}$ incident from the left.

is formed (Fig. 5.7 (b)). The resulting plasma structures exhibit strong similarities to experimentally observed volume nanogratings [31]. However, most publications focus on high pulse numbers and report on thin planes with a period of $\frac{\lambda}{2n}$. Our model only reproduces the limit of low pulse numbers, where larger periods around $\frac{\lambda}{n}$ [32] and thicker grating planes [9] have been observed. Our results further reproduce the increasing self-organization towards the back of nanogratings [9] and their large size in propagation direction. Both observations can be explained by the near-field-driven growth of plasma structures, which continues well out of the focal region.

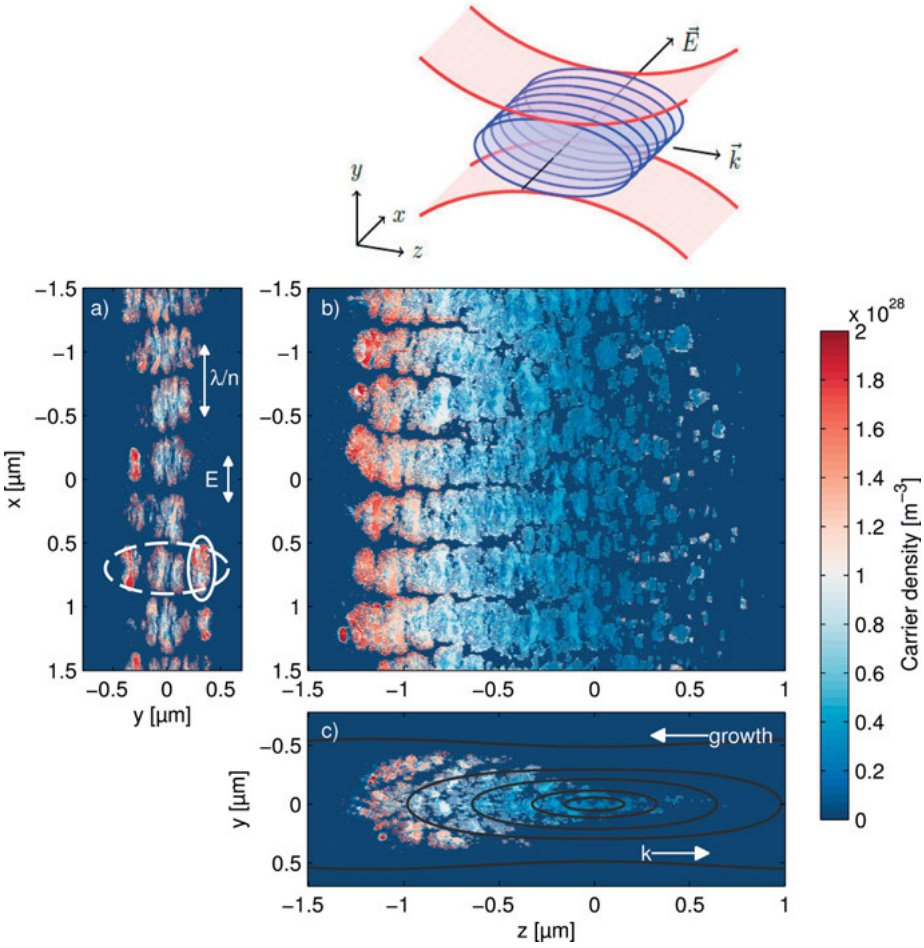

Fig. 5.7: Carrier density (3D FDTD) within an inhomogeneous volume (inhomogeneities have an enhanced ionization cross-section $\sigma_{6,\mathrm{inh}} = 40 \times \sigma_6$ and occupy a percentage of $p_{\mathrm{inh}} = 0.01$ of the material volume) illuminated with a beam (maximum field strength in the homogeneous case $E_0 = 1.9 \times 10^{10}\,\mathrm{V\,m^{-1}}$, NA = 0.8) focused in the y-direction, polarized in the x-direction and propagating in the z-direction. The linear focus is located at $z = 0$ (see overlay of lines of equal field strength $|E|^2$ in panel (c)). The sketch shows the focusing geometry and orientation of periodic structures.

5.4 Application of nanograting-based devices for high resolution microscopy

Tailoring the local birefringence by inscribing nanogratings enables many new applications. Here, we outline some possible practical applications of nanograting-based devices in the field of high resolution microscopy.

5.4.1 Polarized-illumination-coded structured illumination microscopy (picoSIM)

Conventional wide-field microscopy, although a great technique for biological and material imaging, is significantly restricted in its performance. Sample features in the focal plane are illuminated uniformly along with out-of-focus features. This leads to contributions from these non-focal planes to the image of the focal plane, resulting in poor image quality, thanks to a blurring effect and low signal-to-noise ratio. Optical sectioning methods like structured illumination microscopy (SIM) aim to eliminate these out-of-focus contributions and exclusively retain the focal plane information, besides providing resolution enhancement in all directions [51]. However, the need to move the grating electronically or mechanically in order to acquire at least three images with a different grating position for each sample slice limits the acquisition speed.

Polarized-illumination-coded SIM (picoSIM) is a modified version of classical optical sectioning SIM which performs optical sectioning in a single exposure, yielding high temporal and spatial resolution [13]. The speed of this technique is limited by the acquisition rate of the camera. picoSIM requires the illumination of the sample with a polarization-coded grating pattern, unlike the intensity grating pattern employed in classical SIM. In this polarization-coded illumination pattern, the orientation of the polarization vector for each grating line changes periodically, producing a uniform intensity distribution with linearly varying polarization. This polarized grating pattern is only present in the focal plane and its contrast vanishes in the out-of-focus region. Therefore, only the polarization in the focal plane is selectively modulated, while the out-of-focus regions remain unmodulated.

A tailored nanograting is inscribed in order to realize this pattern, where the nanopores are arranged in such a fashion that the polarization vector of the pores rotates by a certain angle periodically. By adjusting the strength of the birefringence this device acts like a quarter-wave plates (when illuminated with circularly polarized light) with varying orientation. This results in a variable polarization distribution in the grating as described above (see also Fig. 5.8 (a)). In the conventional picoSIM system [13], the ±1 diffraction orders are respectively left- and right-circularly polarized using two $\lambda/4$ waveplates so that they interfere in the focal plane to form the required polarization pattern. A clear separation of orders is crucial to block the unwanted zero diffraction order, which is difficult to achieve with incoherent light. However,

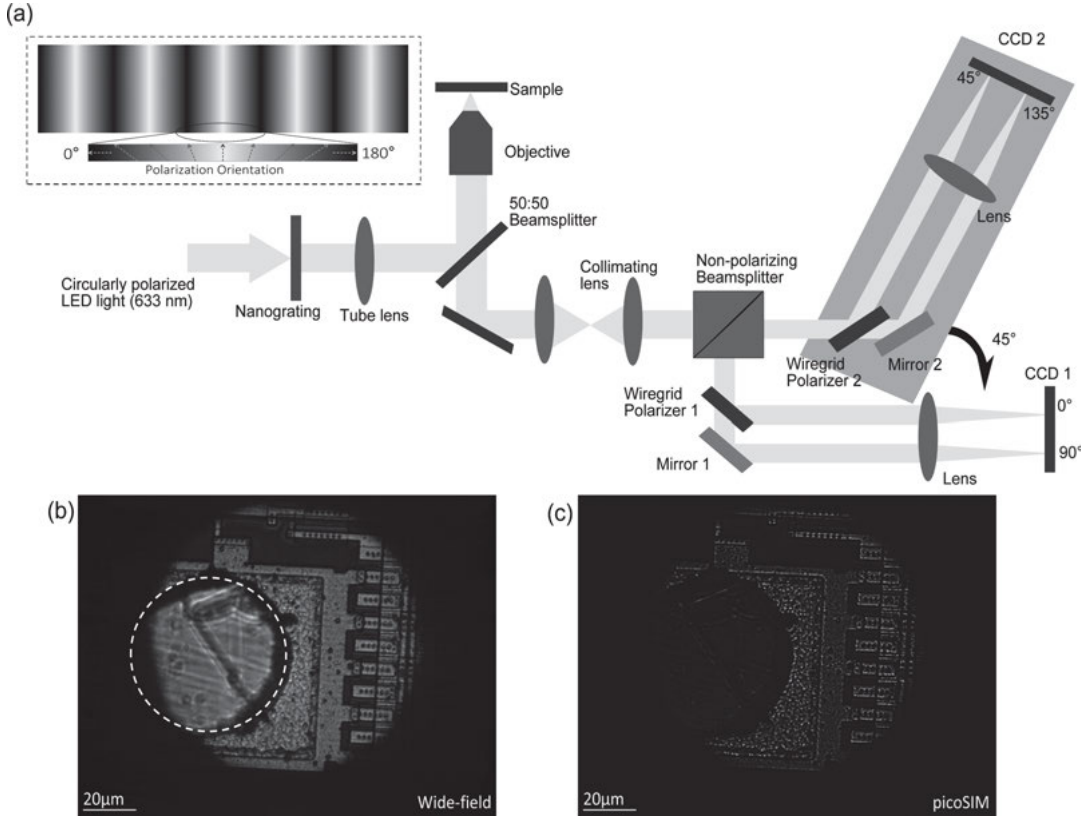

Fig. 5.8: (a) Schematic diagram of the picoSIM setup with the nanograting. Also shown in the inset is the polarization grating pattern formed in the sample plane. (b) Wide-field image of a ceramic chip sample with out-of-focus region marked with yellow dashed line. (c) picoSIM reconstructed image of the same sample showing a significant suppression of out-of-focus blur.

the use of the nanograting instead of the diffraction grating not only reduces the complexity of the setup, but also enables the use of incoherent illumination, as the zero diffraction order is suppressed by design and extends the application of picoSIM to reflective samples like metallic surfaces.

As shown in the schematics in Fig. 5.8 (a), the grating is illuminated using a circularly-polarized red LED source and is imaged onto the sample using an objective and tube lens combination. The emission light from the sample retains the polarization to (at least) a certain degree. The detection sub-unit has two identical arms at a 45° angle to each other. The light from the sample is first split by a 50 : 50 non-polarizing beam splitter into two halves, and then further split into two orthogonal polarization components in each arm by a polarizing beam splitter and mirror combination. As a result, we simultaneously obtain four images with grating positions corresponding to 0°, 90° and 45°, 135° from the two arms respectively, which can now be reconstructed to produce an optically sectioned image with suppressed out-of-focus blur.

This proof-of-concept setup has demonstrated that picoSIM in combination with nanogratings can perform efficient optical sectioning in material samples in a single shot. When compared with the wide-field image (Fig. 5.8 (b)), the reconstructed image of a ceramic chip sample (Fig. 5.8 (c)) has suppressed out-of-focus blur and improved lateral resolution with a single exposure of 1 ms. This method can also be successfully applied to fluorescence microscopy of biological samples and can be used to image fast cellular or mechanical processes.

5.4.2 Quasi-Bessel beams with large depth-of-focus

Another interesting application for nanogratings being investigated is to generate very narrow beams with large depth-of-focus for light sheet microscopy, secondary harmonic generation, Raman spectroscopy etc. Such a beam would ideally be longitudinally polarized in free space with a sub-diffraction size which is uniform along the optical axis – similar to the non-diffractive behavior exhibited by Bessel beams. These contradictory requirements, along with the infinite energy required to propagate a Bessel beam, make the design very complicated. However, a simple approach for a longitudinally polarized, long-focus beam has been described in [52] and consists of three optical elements, namely: a radial polarization converter, a binary-phase optical element, and a high numerical aperture (NA) lens (Fig. 5.9 (a)).

The design of a radial polarization converter is rather straightforward, as described in [53]. Although several methods of birefringence manipulation to create a radial polarization converter have been tested, the use of sub-wavelength gratings has emerged as the preferred fabrication method [11]. These converters can additionally create a polarization vortex where the beam has an orbital angular momentum whose sign depends on the handedness of the incident circular polarization (producing

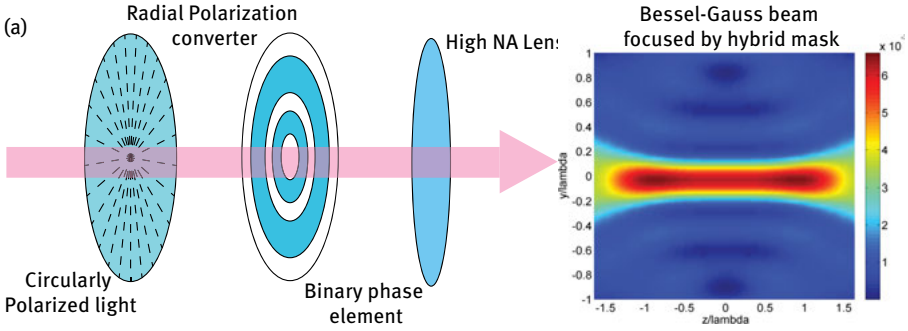
(a)
Radial Polarization converter
High NA Lens
Bessel-Gauss beam focused by hybrid mask
Circularly Polarized light
Binary phase element
y/lambda
z/lambda
x 10^4

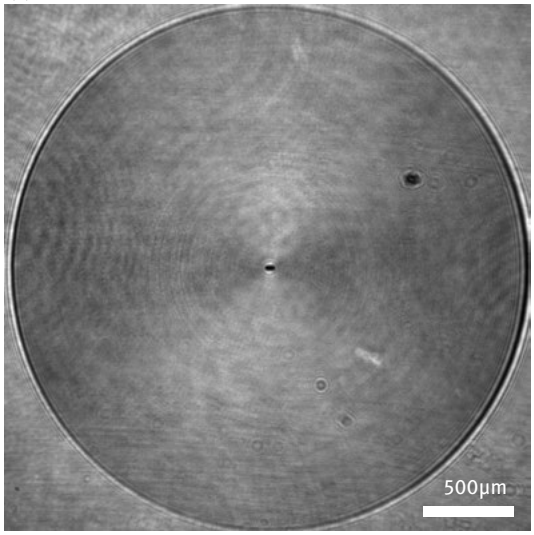
(b)
500µm

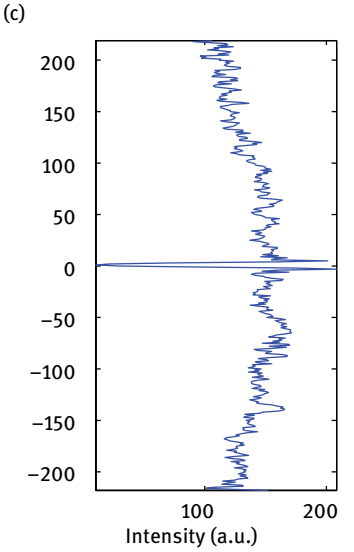
(c)
Intensity (a.u.)

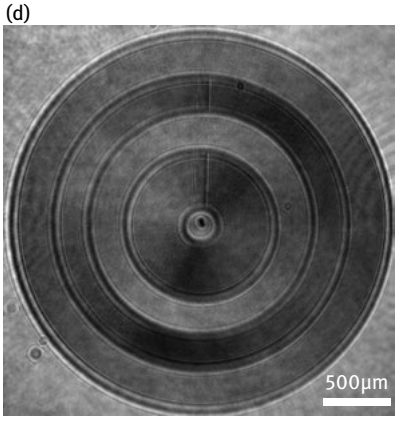
(d)
500µm

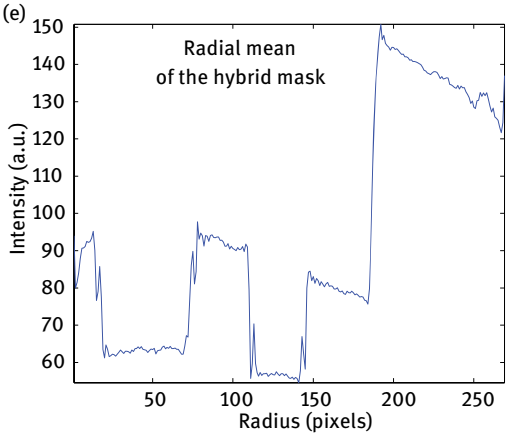
(e)
Radial mean of the hybrid mask
Intensity (a.u.)
Radius (pixels)

both radially and azimuthally polarized beams). On the other hand, the design of the binary-phase optical element is non-trivial and highly dependent on the NA of the lenses used in the system. The binary element consists of a series of concentric rings of optimized widths and relative phases alternating between 0 and π to introduce a phase modulation in the beam such that the axial extent of intensity of the beam is maximized.

Due to very precise control of polarization and ease of manufacturing, the nanograting is ideal for practically realizing both the radial polarization converter and the binary-phase optical element. An image of the radial polarization converter is shown in Fig. 5.9 (b), along with its Y cross-section in Fig. 5.9 (c). Ideally, this converter should have a uniform intensity with a central dip showing the point of singularity, when illuminated with circularly polarized light. This dip is visible in Fig. 5.9 (c). This intensity variation in Fig. 5.9 (b) may be due to residual elliptical polarization of the illumination or a mismatch between the retardation of the design and the experimental wavelength. For ease of alignment, the radial polarization converter and the binary element were fabricated on a single substrate as shown in Fig. 5.9 (d). The minima of the radial mean of this hybrid mask, shown in Fig. 5.9 (e), correspond to the rings of the binary-phase element. This mask also shows similar effects of intensity variation as seen in the radial polarization converter. The resultant Bessel beam from this hybrid mask can now be recorded in a microscope setup with a high NA objective.

Although it is a promising start, the binary element design itself has certain drawbacks and can benefit from further optimization. First, the proposed approach assumes a Bessel-Gaussian input beam to yield an even longer focus which is not easy to achieve experimentally. Moreover, the axial intensity of the beam shows a small dip, which may be due to the incorrect compensation of phases or pixelation of the simulated mask. The design is also highly sensitive to the numerical aperture of the imaging system. A more robust solution for the design of binary-phase optical elements can be described using 'maximally-flat filters' [54]. Although this method involves rigorous numerical calculation of the binary-phase element based on the power series expansion of the axial intensity, it results in a much flatter and longer Bessel-like beam. Henceforth, this scheme will be used to improve the binary-phase element design and produce better quality long-focus beams.

◂ **Fig. 5.9:** (a) Generation of a narrow, long-focus Bessel beam using a radial polarization converter and a binary-phase optical element [52], which can be fabricated based on nanogratings. Also shown on the right is the simulated axial intensity distribution of the Bessel beam with a focal width of 0.43λ and a length of 4λ. (b) and (c) Image and cross-section of the radial polarization convertor. A dip in the center of (c) shows the point of singularity. (d) and (e) Image and radial mean of the hybrid mask. The minima in (d) signify the effect of the binary phase element on the mask.

5.5 Summary

To inscribe artificial form birefringence due to self-assembled nanogratings in bulk glass is one of the key findings of ultrashort pulse processing of transparent materials in recent years. By utilizing small angle x-ray scattering and focused ion beam milling we were able to show that these nanogratings consist of sheet-like cavities with dimensions of $(280 \times 25 \times 380)\,\mathrm{nm}^3$ and $(30 \times 25 \times 75)\,\mathrm{nm}^3$. Due to the cumulative action of numerous laser pulses, these cavities form and arrange in periodic grating planes while their size remains constant. With an increasing number of pulses the period continuously decreases, as diffraction measurements of nanograting samples reveal. For high numbers of incident pulses smaller periods than the predicted value of $\lambda/2n$ were measured. Furthermore we found that nanogratings can be inscribed in various types of glass, such as ULE™ or borosilicate glass. However, the latter show a small parameter window for the nanograting inscription, while the induced birefringence is about one order of magnitude smaller than in fused silica. This is due to the different thermomechanical properties of borosilicate leading to a smaller number of induced voids, as well as the smaller width of these voids. Remarkably, the period of nanogratings in borosilicate is strongly reduced and does not match the predicted value of $\lambda/2n$ at all.

Our theoretical studies of the interaction of laser light with media containing small seed inhomogeneities show how ionization hotspots positioned at individual inhomogeneity sites lead to the formation of wavelength-scale plasma structures growing into the negative propagation direction. We were able to demonstrate that the competition between these structures leads to periodic ionization patterns which have the same orientation and period as nanogratings in glass at low pulse numbers. We conclude that the assumption of growing and interacting nanoplasmas leads to a good description of the self-organization processes taking place during the early stages of bulk nanograting formation in glass.

Nanograting technology opens up a whole new range of promising applications, e.g. in the field of high resolution microscopy. A proof-of-concept setup has experimentally demonstrated the successful use of nanogratings for single shot optical sectioning using the polarized-illumination-coded structured illumination microscopy (picoSIM) method. The implementation of nanogratings leads to several advantages for the picoSIM method such as simplification of the setup and use of incoherent light for reflective microscopy. Using the combination of nanogratings and picoSIM, fast processes like cellular dynamics and MEMS sensor movements can be studied. Furthermore, devices fabricated using nanogratings like a radial polarization converter and a binary-phase optical element can be combined in a single mask to form a hybrid mask to generate thin, long-focus beams. A prototype of this hybrid mask has been fabricated and the preliminary test is in accordance with the theory. This hybrid mask will now be used to produce a narrow Bessel-like beam and promises to improve the scanning performance of light sheet microscopy and several other imaging methods.

References

[1] Gattass RR, Mazur E. Femtosecond laser micromachining in transparent materials. Nat Photon 2008, 2, 219–225.

[2] Itoh K, Watanabe W, Nolte S, Schaffer CB. Ultrafast processes for bulk modification of transparent materials. MRS Bulletin 2006, 31, 620–625.

[3] Szameit A, Nolte S. Discrete optics in femtosecond-laser-written photonic structures. J Phys B – At Mol Opt 2010, 43, 163001.

[4] Davis KM, Miura K, Sugimoto N, Hirao K. Writing waveguides in glass with a femtosecond laser. Opt Lett 1996, 21, 1729–1731.

[5] Glezer EN, Mazur E. Ultrafast-laser driven micro-explosions in transparent materials. Appl Phys Lett 1997, 71, 882–884.

[6] Kazansky P, Inouye H, Mitsuyu T, Miura K, Qiu J, Hirao K, Starrost F. Anomalous anisotropic light scattering in Ge-doped silica glass. Phys Rev Lett 1999, 82, 2199–2202.

[7] Sudrie L, Franco M, Prade B, Mysyrowicz A. Writing of permanent birefringent microlayers in bulk fused silica with femtosecond laser pulses. Opt Commun 1999, 171, 279–284.

[8] Shimotsuma Y, Kazansky PG, Qiu J, Hirao K. Self-organized nanogratings in glass irradiated by ultrashort light pulses. Phys Rev Lett 2003, 91, 247405.

[9] Taylor R, Hnatovsky C, Simova E. Applications of femtosecond laser induced self-organized planar nanocracks inside fused silica glass. Laser Photonics Rev 2008, 2, 26–46.

[10] Ramirez L, Heinrich M, Richter S, Dreisow F, Keil R, Korovin A, Peschel U, Nolte S, Tünnermann A. Tuning the structural properties of femtosecond-laser-induced nanogratings. Appl Phys A – Mater 2010, 100, 1–6.

[11] Beresna M, Gecevicius M, Kazansky PG. Polarization sensitive elements fabricated by femtosecond laser nanostructuring of glass. Opt Mater Express 2011, 1, 783–795.

[12] Cai W, Libertun AR, Piestun R. Polarization selective computer-generated holograms realized in glass by femtosecond laser induced nanogratings. Opt Express 2006, 14, 3785–3791.

[13] Wicker K, Heintzmann R. Single-shot optical sectioning using polarization-coded structured illumination. J Opt A – Pure Appl Op 2010, 12, 084010.

[14] Beresna M, Gecevicius M, Kazansky PG, Taylor T, Kavokin AV. Exciton mediated self-organization in glass driven by ultrashort light pulses. Appl Phys Lett 2012, 101, 053120.

[15] Petrov GM, Davis J. Interaction of intense ultra-short laser pulses with dielectrics. J Phys B – At Mol Opt Phys 2008, 41, 025601.

[16] Bourgeade A, Mézel C, Saut O. Modeling the early ionization of dielectrics by ultrashort laser pulses. J. Sci. Comput. 2010, 44, 170–190.

[17] Bulgakova NM, Zhukov VP, Meshcheryakov YP. Theoretical treatments of ultrashort pulse laser processing of transparent materials: toward understanding the volume nanograting formation and 'quill' writing effect. Appl Phys B 2013, 113, 437–449.

[18] Mezel C, Hallo L, Bourgeade A, Hebert D, Tikhonchuk VT, Chimier B, Nkonga B, Schurtz G, Travaille G. Formation of nanocavities in dielectrics: A self-consistent modeling. Phys Plasmas 2008, 15, 093504.

[19] Buschlinger R, Nolte S, Peschel U. Self-organized pattern formation in laser-induced multiphoton ionization. Phys Rev B 2014, 89, 184306.

[20] Peñano JR, Sprangle P, Hafizi B, Manheimer W, Zigler A. Transmission of intense femtosecond laser pulses into dielectrics. Phys Rev E 2005, 72, 036412.

[21] Yee KS. Numerical solution of initial boundary value problems involving Maxwell's equations in isotropic media. IEEE Trans. Antennas and Propagation 1966, 302–307.

[22] Taflove A, Hagness SC. Computational Electrodynamics: The Finite-Difference Time-Domain Method. Artech House, 3rd edition, 2005.

[23] Sudrie L, Couairon A, Franco M, Lamouroux B, Prade B, Tzortzakis S, Mysyrowicz A. Femtosecond laser-induced damage and filamentary propagation in fused silica. Phys Rev Lett 2002, 89, 186601.
[24] Mao X, Mao SS, Russo RE. Imaging femtosecond laser-induced electronic excitation in glass. Appl Phys Lett 2003, 82, 697–699.
[25] Audebert P, Daguzan PH, Dos Santos A, Gauthier JC, Geindre JP, Guizard S, Hamoniaux G, Krastev K, Martin P, Petite G, Antonetti A. Space-time observation of an electron gas in SiO_2. Phys Rev Lett 1994, 73, 1990–1993.
[26] Gamaly EG, Juodkazis S, Nishimura K, Misawa H, Luther-Davies B, Hallo L, Nicolai P, Tikhonchuk VT. Laser-matter interaction in the bulk of a transparent solid: Confined microexplosion and void formation. Phys Rev B 2006, 73, 214101.
[27] Doremus RH. Physical solubility of gases in fused silica. J Am Ceram Soc 1966, 49, 461–462.
[28] Hasegawa M, Saneyasu M, Tabata M, Tang Z, Nagai Y, Chiba T, Ito Y. Positron and positronium studies of irradiation-induced defects and microvoids in vitreous metamict silica. Nucl Instrum Meth B 2000, 166–167:431–439.
[29] Bohren CF, Huffman DR. Absorption and scattering of light by small particles. Wiley, volume 1, 1983.
[30] Jackson JD. Classical electrodynamics. Wiley, New York, NY, 3rd edition, 1999.
[31] Richter S, Heinrich M, Döring S, Tünnermann A, Nolte S. Formation of femtosecond laser-induced nanogratings at high repetition rates. Appl Phys A – Mater 2011, 104, 503–507.
[32] Mishchik K, Cheng G, Huo G, Burakov IM, Mauclair C, Mermillod-Blondin A, Rosenfeld A, Ouerdane Y, Boukenter A, Parriaux O, Stoian R. Nanosize structural modifications with polarization functions in ultrafast laser irradiated bulk fused silica. Opt Express 2010, 18, 24809–24824.
[33] Mauclair C, Zamfirescu M, Colombier JP, Cheng G, Mishchik K, Audouard E, Stoian R. Control of ultrafast laser-induced bulk nanogratings in fused silica via pulse time envelopes. Opt Express 2012, 20, 12997–13005.
[34] Lancry M, Brisset F, Poumellec B. In the heart of nanogratings made up during femtosecond laser irradiation. Proc of Bragg gratings, photosensitivity, and poling in glass waveguides (BGPP) 2010, BWC3.
[35] Richter S, Plech A, Steinert M, Heinrich M, Döring S, Zimmermann F, Peschel U, Kley EB, Tünnermann A, Nolte S. On the fundamental structure of femtosecond laser-induced nanogratings. Laser & Photonics Rev 2012, 6, 787–792.
[36] Plech A, Leiderer P, Boneberg J. Femtosecond laser near field ablation. Laser & Photonics Rev 2009, 3, 435–451.
[37] Zimmermann F, Plech A, Richter S, Döring S, Tünnermann A, Nolte S. Structural evolution of nanopores and cracks as fundamental constituents of ultrashort pulse-induced nanogratings. Appl Phys A – Mater 2014, 114, 75–79.
[38] Beaucage G. Approximations Leading to a Unified Exponential / Power-Law Approach to Small-Angle Scattering. J Appl Crystallogr 1995, 28, 717–728.
[39] Sztucki M, Narayanan T, Beaucage G. In situ study of aggregation of soot particles in an acetylene flame by small-angle x-ray scattering. J Appl Phys 2007, 101, 114304.
[40] Kammler HK, Beaucage G, Kohls DJ, Agashe N, Ilavsky J. Monitoring simultaneously the growth of nanoparticles and aggregates by in situ ultra-small-angle x-ray scattering. J Appl Phys 2005, 97, 054309.
[41] Mackenzie RAD, Smith GDW. Focused ion beam technology: a bibliography. Nanotechnology 1990, 1, 163.
[42] Hnatovsky C, Taylor RS, Simova E, Bhardwaj VR, Rayner DM, Corkum PB. Polarization-selective etching in femtosecond laser-assisted microfluidic channel fabrication in fused silica. Opt Lett 2005, 30, 1867–1869.

[43] Gottmann J, Wortmann D, Hörstmann-Jungemann M. Fabrication of sub-wavelength surface ripples and in-volume nanostructures by fs-laser induced selective etching. Appl Surf Sci 2009, 255, 5641–5646.
[44] Lancry M, Poumellec B, Chahid-Erraji A, Beresna M, Kazansky PG. Dependence of the femtosecond laser refractive index change thresholds on the chemical composition of doped-silica glasses. Opt Mater Express 2011, 1, 711–723.
[45] Poumellec B, Lancry M, Chahid-Erraji A, Kazansky PG. Modification thresholds in femtosecond laser processing of pure silica: review of dependencies on laser parameters. Opt Mater Express 2011, 1, 766–782.
[46] Zimmermann F, Plech A, Richter S, Tünnermann A, Nolte S. Ultrashort laser pulse induced nanogratings in borosilicate glass. Appl Phys Lett 2014, 104, 211107.
[47] Hayasaki Y, Isaka M, Takita A, Juodkazis S. Time-resolved interferometry of femtosecond-laser-induced processes under tight focusing and close-to-optical breakdown inside borosilicate glass. Opt Express 2011, 19, 5725–5734.
[48] Richter S, Döring S, Burmeister F, Zimmermann F, Tünnermann A, Nolte S. Formation of periodic disruptions induced by heat accumulation of femtosecond laser pulses. Opt Express 2013, 21, 15452–15463.
[49] Williams RJ, Krämer RG, Nolte S, Withford MJ, Steel MJ. Detuning if apodized point-by-point fiber Bragg gratings: insighs into the grating morphology. Opt Express 2013, 21, 26854.
[50] Richter S, Heinrich M, Döring S, Tünnermann A, Peschel U, Nolte S. Nanogratings in fused silica: Formation, control, and applications. J. Laser Appl. 2012, 24, 042008.
[51] Neil MA, Juskaitis R, Wilson T. Method of obtaining optical sectioning by using structured light in a conventional microscope. Opt. Lett. 1997, 22, 1905–1907.
[52] Wang H, Shi L, Lukyanchuk B, Sheppard C, Chong CT. Creation of a needle of longitudinally polarized light in vacuum using binary optics. Nat. Photonics 2008, 2, 501–505.
[53] Beresna M, Gecevičius M, Kazansky PG, Gertus T. Radially polarized optical vortex converter created by femtosecond laser nanostructuring of glass. Appl Phys Lett 2011, 98, 201101.
[54] Sheppard CJR. Binary phase filters with a maximally-flat response. Opt Lett 2011, 36, 1386–1388.
[55] Richter S, Miese C, Döring S, Zimmermann F, Withford MJ, Tünnermann A, Nolte S. Laser induced nanogratings beyond fused silica – periodic nanostructures in borosilicate glasses and ULE. Opt Mat Express 2013, 3, 1161.

N. Hartmann, S. Franzka, A. Schröter, A. Aumann, and A. Ostendorf

6 Nonlinear processing and multiphoton ablation of self-assembled monolayers for application as ultrathin resists and in biochemical sensors

6.1 Preface

Self-assembled monolayers (SAMs) addressed in this chapter are monomolecular organic coatings, which allow one to adjust a variety of surface properties of solid materials including bioaffinity and chemical resistance [1–3]. In view of these opportunities, such organic coatings are widely used as ultrathin resists and functional films in micro- and nanofabrication [1–5]. Nonlinear laser processing has evolved as a powerful and versatile means for nanopatterning of SAMs [6, 7]. Generally, laser processing is a maskless and flexible noncontact technique. Also, rapid processing over areas ranging from square centimeters to square decimeters can be carried out on essentially all kinds of support materials at high pressures and in liquids. In recent years femtosecond (fs) lasers have been proven to provide specific perspectives in nonlinear processing and sub-100 nm patterning of organic monolayers [7]. In particular, finely tuned photothermal reactions and multiphoton absorption processes introduce high nonlinearities [8, 9]. In addition, the ultrathin nature of these coatings allows single pulse processing, thus ensuring short processing times [7]. The molecular thickness also ensures well-defined irradiation and burr-free patterning and avoids the formation of bubbles and particles [8, 9]. All these issues represent common problems in ablative fs-laser processing [10, 11]. This chapter reviews recent progress in nonlinear fs-laser processing of organic monolayers, i.e. results from references [7–9, 12–15]. Particular emphasis is placed on prospects of tunable fs-laser sources in resonant laser processing of organic monolayers and the application of such coatings as ultrathin resists and functional platforms for fabrication of protein micro- and nanoarrays [12–15].

6.2 Introduction

6.2.1 Self-assembled monolayers

Self-assembled monolayers consist of densely packed elongated organic molecules which are tethered on the surface of a material in tilted or vertical orientation [1–3]. The general chemical structure of SAMs is shown in Fig. 6.1 (a) [6, 7]. The thickness of these coatings is in the range of 1–2 nm. The molecules exhibit three functional parts: (1) The head group, which is bound to the surface and classifies the type of SAM.

Prominent examples are thiol-based SAMs on Au [1], silane-based SAMs on oxides or surface-oxidized substrates [2, 4], and SAMs which are built on semiconducting materials using olefinic precursors [3]. (2) The backbone, e.g. an aliphatic hydrocarbon chain or an aromatic system; and (3) the end group, e.g. standard functionalities such as amine or carboxyl groups, polyethylene glycol (PEG) or more complicated chemical and biochemical structures. The chemical reactivity and resistance of the coatings can be adjusted to specific needs by varying these functional parts [1–3]. For this reason, SAMs are widely used as ultrathin resists and functional platforms [1–5]. Aliphatic thiol-based SAMs, such as dodecanethiolate (DDT), hexadecanethiolate (HDT) SAMs and octadecanethiolate (ODT) SAMs may act as ultrathin positive-tone resists [1, 16, 17]. In contrast, thiol-based SAMs containing biphenyl groups, such as biphenylthiolate (BPT) SAMs and nitrobiphenylthiolate (NBPT) SAMs represent ultrathin negative-tone resists [17–19]. Similarly, the end groups are known to determine the chemical and biochemical affinity of SAMs [1–5]. PEG-terminated SAMs, for example, serve as protein-repellent coatings [20–22]. Precursor molecules such as $CH_3O(CH_2CH_2O)_{6-9}(CH_2)_3SiCl_3$ (PEGCl) and $CH_3O(CH_2CH_2O)_{6-9}(CH_2)_3Si(OCH_3)_3$ (PEGMeO) can be used to build up PEG-terminated SAMs [21-22]. The adsorption of proteins, e.g. bovine serum albumine (BSA) and streptavidin (STV) is significantly reduced on PEG-terminated surfaces [20]. Other end groups allow the coupling of nanoparticles, biomolecules and other nanoscopic components to the surface [1–5]. Amine groups, for example, are known to bind citrate-stabilized Au nanoparticles [23]. Also, biotin groups selectively couple STV via formation of a biotin-streptavidin complex [24]. Generally, the functionality of the SAMs strongly depends on the packing density of the molecular entities, and hence on the quality and degree of order of the monolayer [1–3]. The optimization of the preparation procedure is therefore a key step in all applications [1–5].

Patterning techniques can be exploited in order to fabricate micro- and nanostructured SAMs, i.e. chemical templates, which expose domains of defined size, geometry and chemical functionality [5]. A common approach considers patterning of a primary monolayer and subsequent backfilling of the depleted areas with a secondary monolayer or other functional entities [5, 25]. Alternatively, post functionalization routines and direct chemical patterning can be exploited [26–28].

Chemical templates allow the selective coupling of nanoscopic components at predefined surface positions and build up functional surface architectures [5]. An example of a laser-fabricated nanostructured chemical template is shown in Fig. 6.2 [6]. Dense line patterns have been fabricated via photothermal processing of octadecylsiloxane monolayers (ODS monolayers) using a microfocused continuous-wave laser (CW-laser) operated at $\lambda = 514\,\text{nm}$ [26, 27]. In photothermal processing, laser irradiation induces a local temperature increase and initiates thermal reactions, e.g. decomposition of the monolayer [6, 27]. Because of the temperature-dependent reaction rate, highly activated processes introduce high nonlinearities, which allows for sub-wavelength patterning [26, 27]. After laser processing, amination of the pat-

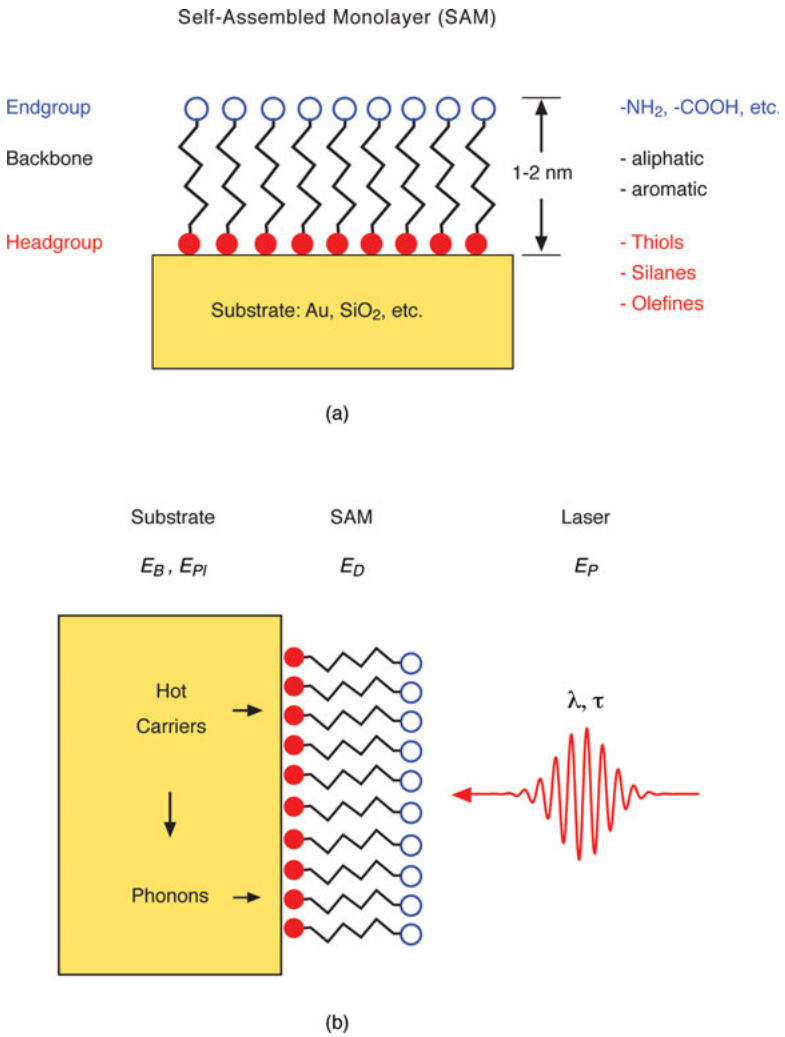

Fig. 6.1: (a) Schematic presentation of the structure of self-assembled monolayers. (b) Schematic presentation of fundamental processes during fs-laser processing of self-assembled monolayers. Notations correspond to photon energy E_P, the linear photodissociation threshold E_D, the bandgap E_B, and plasmon energy E_{Pl}. Adapted and reproduced with permission from [6]. Copyright IOP Publishing & Deutsche Physikalische Gesellschaft. CC BY-NC-SA. See also [7].

terns and self-assembly of citrate-stabilized Au nanoparticles is carried out [6, 27]. Single nanoparticle chains with an average width of 50 nm are formed on narrow stripes, which corresponds to a value equal to $\lambda/10$ [27]. This example demonstrates the prospects of nonlinear laser processing in nanofabrication of chemical surface structures. As outlined below, fs-lasers offer particular perspectives in nonlinear processing via multiple photon absorption and other processes [7].

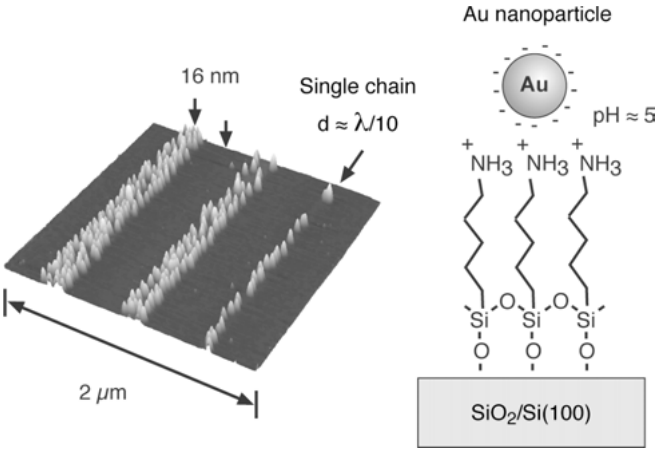

Fig. 6.2: Topographic image of Au nanoparticle structures on a laser fabricated chemical template (left). Single nanoparticle chains are formed on narrow aminated stripes of a photothermally patterned ODS monolayer. These structures exhibit a width of $d \approx 50$ nm corresponding to $\lambda/10$ of the laser light at $\lambda = 514$ nm. The schematic presentation displays the structure of the aminated stripes with an Au nanoparticle on top (right). Adapted and reproduced with permission from [6]. Copyright IOP Publishing & Deutsche Physikalische Gesellschaft. CC BY-NC-SA. See also [7].

6.2.2 Femtosecond laser processing

Laser processing represents a simple and versatile means for direct patterning of organic monolayers [6, 7]. As far as lateral resolution is concerned, the optical diffraction limit of course poses a significant constraint [29–31]. If highly focusing optics with a numerical aperture (NA) close to one are used, the minimum structure size is about equal to the wavelength λ of the laser light [29].

Nonlinear effects provide an opportunity to increase the lateral resolution of laser techniques and fabricate structures with lateral dimensions in the sub-wavelength range [11, 29–31]. In view of the complexity of photoexcited processes at surfaces [32–34], a huge variety of nonlinearities can be exploited [6, 7]. Generally, direct and indirect excitation mechanisms are distinguished [35]. Direct mechanisms refer to an immediate excitation of the molecular entities within the organic monolayer. This includes single or multiphoton excitation processes as well as field-induced processes. Indirect mechanisms begin with excitation processes which are initiated in the substrate. At first, laser light is absorbed in the substrate and generates excited charge carriers, i.e. hot electrons. These electrons interact with the adsorbed molecules within the monolayer via photochemical or photoelectrochemical pathways and initiate reactions. In contrast, in photothermal processes hot electrons eventually scatter inelastically with the substrate lattice and excite phonons. Hence a certain temperature rise is induced at the surface, which opens up thermal reaction channels.

All these laser-induced processes take place on material-specific time, length and energy scales, which vary over several orders of magnitude. For this reason, laser patterning is a rich and complex process [29]. Hence, the proper choice of all laser parameters is a key requirement in order to selectively initiate the desired reactions and avoid unwanted processes, e.g. laser ablation or modification of the substrate [6, 7].

Important energetic parameters are shown in Fig. 6.1 (b) [6, 7]: the photon energy E_P, the linear photodissociation threshold E_D of the monolayer, and substrate-specific parameters, such as the bandgap E_B or plasmonic energy E_{Pl}. In order to ensure nonlinear laser processing, photon energies well below the photodissociation threshold are chosen, that is $E_P < E_D$. Processing with fs-lasers provides particularly promising perspectives [7–9]. On metals, for example, multiple electronic excitations or photothermal reactions can be initiated [8]. Note, fs-laser processing is commonly chosen in order to avoid or minimize heat generation, however it can also be used in order to finely tune energy deposition and heat generation. In addition, plasmonic materials allow exploitation of near-field effects [36]. On dielectric and semiconducting materials, multiphoton absorption processes can be initiated for $E_B > E_P$. All these processes introduce strong nonlinearities and hence open up avenues for laser patterning with sub-100 nm resolution [7].

Resonant processing with tunable fs-lasers appears particularly promising [12, 13]. Excitation of surface plasmon resonances at $E_P = E_{Pl}$, for example, provides a means to optimize energy deposition and exploit near-field effects on nanostructured metallic surfaces. Also, matching the photon energy and the bandgap in n-photon absorption processes, $n \times E_P = E_B$, may reduce the overall thermal impact.

Irrespective of the specific mechanism, the size of the fabricated structures in nonlinear fs-laser processing strongly depends on the laser fluence F via [7–9]:

$$d = d_{1/e}\sqrt{\ln\left(F/F_{\text{th}}\right)}, \tag{6.1}$$

where F_{th} is a critical threshold of the considered process, e.g. the critical thresholds $F_{\text{th}}^{\text{SAM}}$ and F_{th}^{S} for monolayer decomposition or substrate ablation. Analysis of the experimental data on the basis of equation (6.1) allows determination of the corresponding critical threshold values $F_{\text{th}}^{\text{SAM}}$, F_{th}^{S} and the $1/e$ spot diameter $d_{1/e}$.

6.3 Femtosecond laser patterning of self-assembled monolayers

As outlined above, fs-laser patterning of self-assembled monolayers opens up avenues for distinct applications. Depending on the targeted application, a specific strategy is required in order to achieve the desired functionality. Figure 6.3 shows distinct strategies which are detailed below. Alkanethiolate SAMs on thin Au films can be used as ultrathin resists (Fig. 6.3 (a)) [8, 12, 13]. Laser processing removes the coating. Subsequent wet-chemical etching in a ferri-ferrocyanide solution allows transfer of the pattern into the underlying Au film [8, 12, 13, 37].

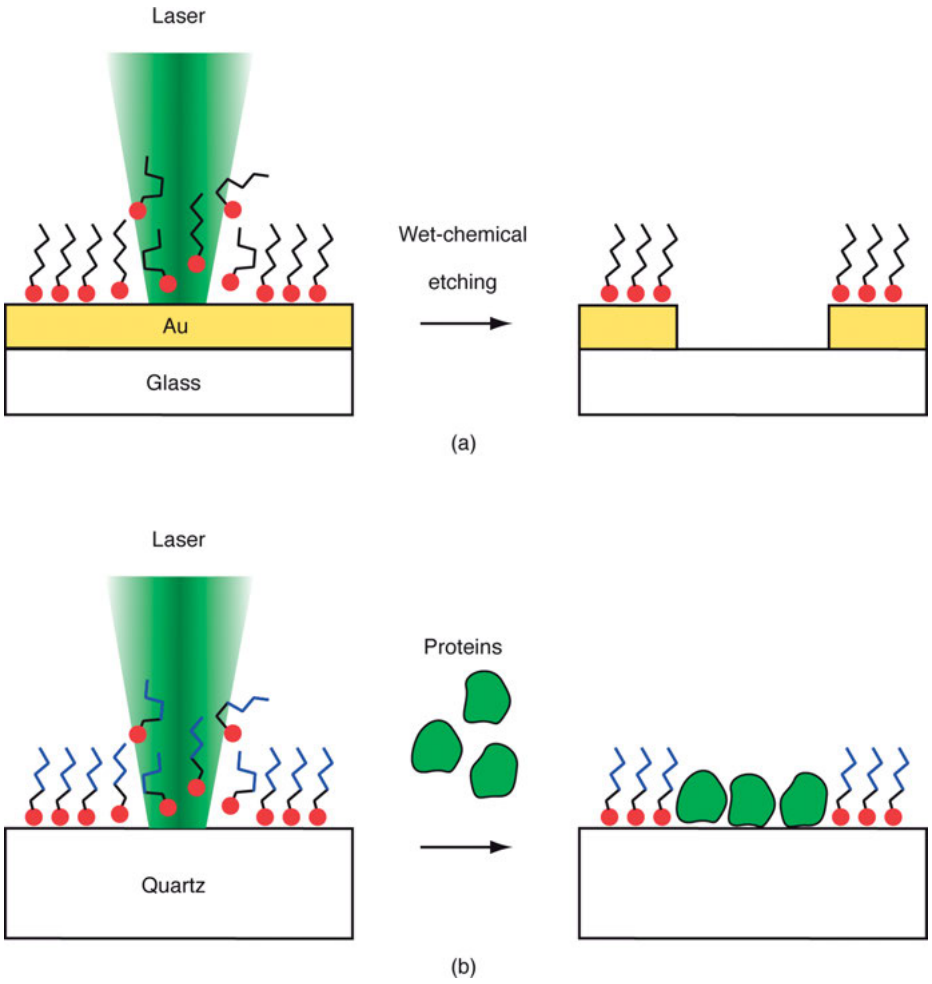

Fig. 6.3: Schematic presentations of fs-laser patterning strategies: (a) patterning of alkanethiolate SAMs on Au/glass platforms and subsequent pattern transfer into the Au film via wet-chemical etching in a ferri-/ferrocyanide solution. (b) Patterning of PEG-terminated SAMs on quartz glass followed by selective protein adsorption.

A strategy for fabrication of protein micro- and nanoarrays is based on laser processing of PEG-terminated monolayers (Fig. 6.3 (b)) [15]. PEG-terminated monolayers are protein-repellent coatings [20–22]. Laser processing initiates monolayer decomposition. This allows for local protein adsorption in predefined domains via unspecific interactions [15]. In addition, a variety of chemical strategies can be used in order to introduce functionalities for a specific protein binding [15, 24, 38].

6.3.1 Self-assembled monolayers as ultrathin resists

Various studies have addressed the application of alkanethiolate monolayers such as DDT, HDT or ODT on thin Au films as ultrathin positive-tone resists [8, 12, 13, 39–41]. Typically, the thickness of the Au films in these studies is in the range of 30–100 nm. Silicon wafers and glass plates are used as supports and patterning is commonly carried out in air using standard fs-laser sources such as microfocused Ti:sapphire-lasers at $\lambda = 800\,\text{nm}$ and $E_P = 1.6\,\text{eV}$, respectively. At this photon energy alkanethiolate SAMs are highly transparent, whereas Au exhibits a $1/e$ penetration depth of 14 nm [8]. Considering a linear photodissociation threshold $E_D \approx 5\,\text{eV}$, photochemical processing with continuous light sources requires wavelengths in the deep ultraviolet range, i.e. $\lambda \leq 250\,\text{nm}$ [42]. Hence, nonlinear fs-laser processing of alkanethiolate monolayers at $\lambda = 800\,\text{nm}$ via indirect mechanisms appears feasible (cf. Section 2.2).

Chang et al. carried out experiments with a microfocused Ti:sapphire-laser at $\lambda = 800\,\text{nm}$ and $\tau = 220\,\text{fs}$ [39]. Patterning was performed via multiple-pulse processing with a highly focusing microscope objective at a numerical aperture of NA = 0.8, yielding a nominal laser spot size of $d_{1/e} \approx 1.6\,\mu\text{m}$. Line widths are in the range of few microns. In addition, the authors demonstrated fabrication of submicron-sized structures via near-field optical lithography with a quartz pipette with an apex diameter of 200 nm [40]. Using the fundamental and the second harmonic of a Ti:sapphire-laser, $\lambda = 790\,\text{nm}$ and 395 nm, multiple-pulse processing at $\tau = 130\,\text{fs}$ yields line widths in the range of 250–400 nm. In contrast to far-field processing, scanning near-field optical lithography is very slow and restricted to small areas. Kirkwood et al. reported nonlinear processing in multiple-pulse experiments using a Ti:sapphire-laser at $\lambda = 800\,\text{nm}$ and $\tau = 118\,\text{fs}$ [41]. At a 1/e laser spot diameter of $d_{1/e} = 17.5\,\mu\text{m}$, minimum line widths of $4\,\mu\text{m}$ are obtained. Mathieu et al. provided first single-pulse experiments with a microfocused Ti:sapphire-laser at $\lambda = 800\,\text{nm}$, $\tau < 30\,\text{fs}$ and $d_{1/e} = 1.8\,\mu\text{m}$ [8]. In contrast to multiple-pulse processing, single-pulse processing ensures short processing times and allows for rapid large-area patterning. The authors reported minimum structure sizes of 160 nm, i.e. structure sizes in the sub-wavelength range $< \lambda/5$, indicative of a highly nonlinear process. An analysis of the data on the basis of equation (6.1) yields a modification threshold of the monolayer of $F_{\text{th}}^{\text{SAM}} = 0.53\,\text{J/cm}^2$. Very similar values have been reported for ablation of thin Au films, i.e. $F_{\text{th}}^{S} = 0.55\,\text{J/cm}^2$ [41]. Hence, selective monolayer processing appears to take place in a very narrow parameter range. This limits the application of such fs-laser procedures in the fabrication of flat chemical templates [5, 8]. Defined pattern transfer via etching, though, has been demonstrated up to fluences of $2.0\,\text{J/cm}^2$ [8]. Some conflicting results have been reported regarding the laser-induced chemical mechanism [8, 39–41]. In principle, both photothermal and photochemical mechanisms appear possible [8]. Chang et al. suggested that the process involves oxidation of the alkanethiolates to alkanesulfonates [39]. This is the widely accepted mechanism during photooxidation with continuous light sources in the ultraviolet wavelength range [1, 42]. Comparative

experiments in air and in nitrogen by Kirkwood et al., however, revealed no difference [41]. Also, as outlined above, the modification threshold for patterning of alkanethiolate monolayers on Au is very close to the ablation threshold for Au [8]. On the basis of these experiments, substrate ablation has been suggested to be the dominant mechanism [41]. The study by Mathieu et al. clearly reveals two regions [8]. The authors used atomic force microscopy (AFM) for characterization of laser-fabricated surface structures prior to and after wet-chemical etching. In the inner region a fine tip structure indicative of substrate melting is observed [43]. In the outer region removal of the monolayer is apparent [8]. These data suggest a mechanism based on photothermal desorption and decomposition of the monolayer [8].

Most recently, Aumann et al. and Maragkaki et al. reported on sub-wavelength patterning of alkanethiolate SAMs using a sophisticated tunable fs-laser system [12, 13]. The system consists of a non-collinear optical parametric amplifier pumped by an fs-laser operating at $\lambda = 1030$ nm, a prism compressor, an autocorrelator, an autofocus sensor, and a microscope objective, NA = 0.55, for focusing. This setup provides Gaussian laser pulses with a selectable wavelength in the range of $\lambda = 480–950$ nm and a pulse length of $\tau < 35$ fs. At a $1/e$ laser spot size of about 2 µm, structures with a diameter d down to 400 nm and below have been fabricated [12, 13]. Characterization was carried out using AFM. Figure 6.4 shows an optical micrograph and AFM data of structures created at $\lambda = 645$ nm [12]. Widths are measured at half-depth and are not corrected for tip size effects. Note, complete pattern transfer requires full removal of the Au film in the laser-depleted surface areas [8]. Because of the isotropic process, the diameter of the laser-depleted areas increases during etching. Hence, the immersion time has to be adjusted in order to achieve complete pattern transfer but minimize widening of the structures [16]. Total widening at half-depth of fully depleted structures is about equal to the Au film thickness. At a film thickness of 30 nm, widening corresponds to less than 10 % of the smallest structure size in Fig. 6.4. Most notably, further experiments reveal a wavelength-dependent modification threshold [12, 13]. Respective data at $\lambda = 645$ nm, $\lambda = 743$ nm and $\lambda = 840$ nm yield $F_{\mathrm{th}}^{\mathrm{SAM}} = 0.09\,\mathrm{J/cm^2}$, $F_{\mathrm{th}}^{\mathrm{SAM}} = 0.24\,\mathrm{J/cm^2}$, and $F_{\mathrm{th}}^{\mathrm{SAM}} = 0.34\,\mathrm{J/cm^2}$, respectively and are shown in Fig. 6.5 [13]. Noteworthily, the linear optical properties of the underlying Au/glass substrates only slightly change in this wavelength range [44]. In particular, the $1/e$ penetration depth varies between 13 and 15 nm. On this account, the observations have been tentatively attributed to nonlinear plasmonic effects because of the inherent nanoroughness of the Au layer [12].

In addition to alkanethiolate SAMs, SAMs containing biphenyl groups have also been investigated [14], and in contrast are known to act as negative-tone resists [17–19]. Exposure to electrons and extreme ultraviolet radiation (EUV) results in dehydrogenation and crosslinking of the molecules [17–19]. This increases the chemical resistance of the processed monolayer during etching. The process is expected to follow an indirect mechanism, i.e. to be induced by hot electrons, which are excited in the substrate [19]. Excitation energies above 5 eV are required for dehydrogenation [19, 45].

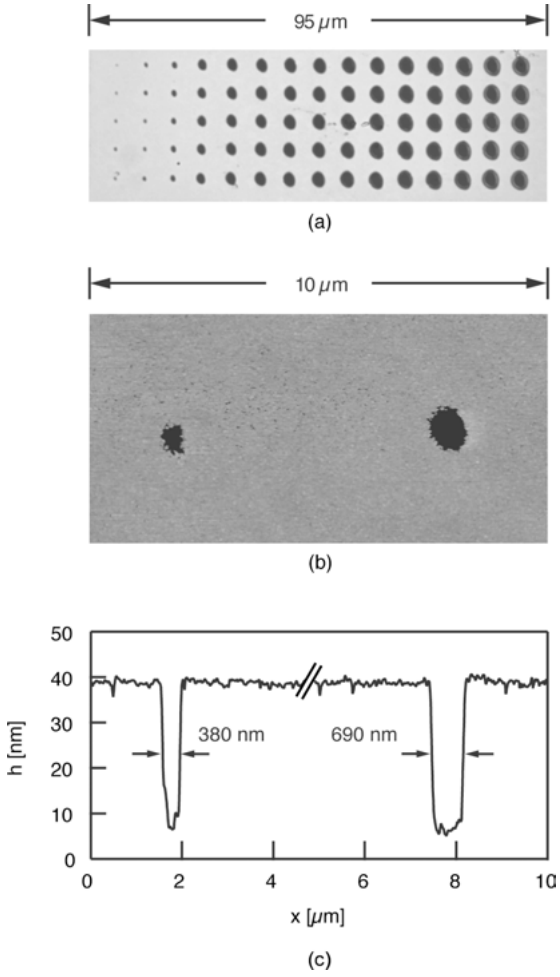

Fig. 6.4: Data from laser patterning experiments on HDT SAMs on Au/glass supports: (a) optical micrograph; (b) topographic AFM image; and (c) height profile. The Au film on top of the glass substrates exhibits a thickness of 30 nm. Laser processing was carried out with single pulses at $\lambda = 645$ nm, $\tau < 35$ fs and $d_{1/e} = 1.8$ μm and distinct fluences: (a) $F = 0.04$–3.93 J/cm^2 (left to right); (b) and (c) $F = 0.04$–0.08 J/cm^2 (left to right). Adapted and reproduced with permission from [12]. Copyright 2013, Laser Institute of America, Orlando, Florida.

Such energies are accessible in fs-laser processing, e.g. via multiphoton absorption processes or multiple electronic excitations [29]. This motivated recent experiments by Schröter and coworkers [14]. The authors studied single-pulse fs-laser processing of NBPT SAMs with a microfocused Ti:sapphire-laser at $\lambda = 800$ nm and $\tau < 30$ fs and $d_{1/e} = 1$ μm. Minimum structure sizes of 300 nm were achieved, indicative of a highly nonlinear process. Noteworthy, though, NBPT SAMs do not act as a negative-

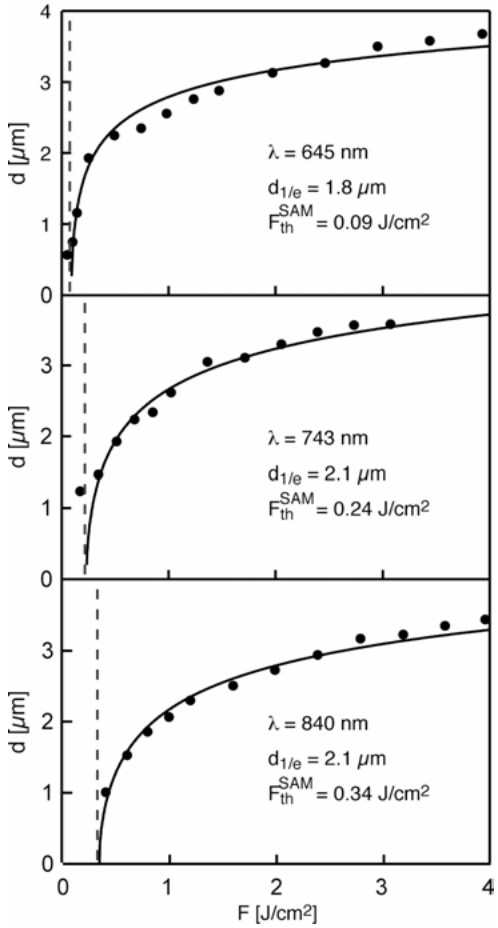

Fig. 6.5: Data from laser patterning experiments on HDT SAMs on Au/glass supports. The Au film on top of the glass substrates exhibits a thickness of 30 nm. Laser processing was carried out with single pulses at $\tau < 35$ fs. After laser processing the patterns are transferred into the Au film via wet-chemical etching. The diagrams show the dependence of the diameter d on the fluence F at distinct wavelengths λ as given in the diagrams. Full lines are fits on the basis of equation (6.1). Critical modification thresholds F_{th}^{SAM} and $1/e$ laser spot diameters $d_{1/e}$ from these fits are given in the diagrams. Adapted and reproduced with permission from [13]. Copyright 2014, SPIE.

tone resist. During wet-chemical etching the Au film is completely removed in the irradiated areas, whereas the native SAM in the surrounding areas impedes etching. These data suggest that fs-laser irradiation results in desorption and decomposition rather than dehydrogenation and crosslinking. Pitting is observed with longer etching times and also observed at low fluences, i.e. in those areas where no decomposition and desorption of the SAM takes place. Apparently, crosslinking between the biphenyl groups is marginal, irrespective of the fluence and the etching time.

Upon exposure of NBPT SAMs to electrons or EUV radiation chemical transformation of the nitro end groups into amine functionalities also takes place [18, 19]. This can be used for chemical patterning. In the study by Schröter et al. no chemical transformation of the nitro group was observed. In particular, the authors report on labeling experiments with citrate-stabilized Au nanoparticles [14]. Citrate-stabilized Au nanoparticles are known to selectively bind to amine functionalities [23]. AFM measurements, however, show that no selective adsorption of Au nanoparticles takes place in laser-processed areas [14].

In general, crosslinking and chemical transformation of the nitro groups are expected to depend on the packing density and the degree of order of the BPT SAMs. IR data suggest a well-ordered monolayer [14]. This is supported by the etching experiments, which demonstrate the good performance of unprocessed NBPT SAMs as positive-tone resists. Apparently, processing with standard fs-laser sources does not induce these peculiar chemical transformations even though hot electrons with excitation energies well above the threshold are generated [29, 45]. Photothermal reaction pathways, for example, open up shortly after irradiation with fs-laser pulses [7]. This could well result in decomposition or desorption of the coating prior to or after crosslinking and reduction of the nitro groups [14]. The work by Schröter et al. reveals a modification threshold of $F_{\mathrm{th}}^{\mathrm{SAM}} = 1.0\,\mathrm{J/cm^2}$. In contrast, crosslinking and end group transformation of NBPT SAMs on EUV irradiation requires fluences $\gg 1.0\,\mathrm{J/cm^2}$ [19]. This suggests that fs-laser induced crosslinking and chemical patterning necessitates adjustment of other laser parameters in order to initiate these processes and minimize heat generation [14]. Here, processing with tunable fs-lasers appears particularly promising [12, 13]. Processing with fs-lasers at wavelengths in the UV range, of course, should allow triggering of crosslinking; see [19]. In addition, excitation of surface plasmon resonances in the visible and near-infrared wavelength range represents a promising means of addressing near-field effects on nanostructured Au surfaces; see [36].

6.3.2 Fabrication of micro- and nanostructured bioarrays

Fabrication of micro- and nanostructured chemical templates for directed adsorption of biomolecules necessitates the proper choice of the SAM/substrate system as well as optimization of the laser patterning procedure [15]. In addition, distinct analytical methods and labeling techniques are required for detailed characterization of biofunctionalized micro- and nanosized domains.

Transparent substrates, such as glass or quartz, are preferred platforms for many biomedical and biotechnical applications, most notably in biosensor applications [2, 4]. Such platforms combine nicely with silane-based SAMs [2]. Only a few techniques, however, allow direct nanopatterning of silane-based monolayers on glass or quartz [5]. EUV lithography, of course, can be used. Investment and operating costs,

however, are high. In addition, the whole process flow, of course, is adapted to the geometric constraints and specific materials considered in microchip fabrication. Dip pen nanolithography and micro contact printing, in turn, are complicated because of the intricate silane chemistry, and surface charging hampers electron beam lithography. Femtosecond lasers represent an efficient and versatile means for processing quartz and glass [11]. In order to selectively pattern silane-based SAMs on such substrates, Hartmann et al. investigated fs-laser processing of alkylsiloxane monolayers on quartz glass platforms using a Ti:Sapphire laser at $\lambda = 800\,\text{nm}$, $\tau < 30\,\text{fs}$ and $d_{1/e} = 1.8\,\mu\text{m}$ [9]. Photochemical patterning of these coatings requires wavelengths in the UV range, typically at $\lambda < 200\,\text{nm}$ [46]. This corresponds to a linear photodissociation energy of $E_D \approx 6\,\text{eV}$. The bandgap of quartz glass is $E_B = 9\,\text{eV}$. In view of these energetic constraints, nonlinear processing via multiphoton absorption processes at a photon energy of $E_P = 1.6\,\text{eV}$ has been addressed [9]. Moreover, selective patterning of the monolayer has been anticipated well below the ablation threshold of the quartz substrate.

AFM data from experiments in which ODS monolayers on quartz glass substrates are patterned with single laser pulses are displayed in Fig. 6.6 [7, 9]. Laser processing results in circular spots with fluence-dependent morphology and size. At high laser fluences, two regions are distinguished (Fig. 6.6 (a)–(d)). In the inner region substrate ablation takes place. Depths reach deep into the bulk (Fig. 6.6 (c)). In contrast, depths in the outer region are below 2 nm, suggesting selective decomposition of the SAM. The outer and inner regions are also visible in the friction contrast image (Fig. 6.6 (b)). The diameters of the regions where monolayer decomposition and substrate ablation take place are referred to as d_{SAM} and d_S (Fig. 6.6 (d)).

At lower laser fluences, no substrate ablation takes place (Fig. 6.6 (e)–(h)). Monolayer decomposition, though, is observed down to very low fluences. In Fig. 6.7 the dependence of the diameters d_{SAM} and d_S on the laser fluence is shown. Using equation (6.1) a data fit gives critical thresholds for monolayer decomposition of $F_{\text{th}}^{\text{SAM}} = 3.1\,\text{J/cm}^2$ and substrate ablation of $F_{\text{th}}^{S} = 4.2\,\text{J/cm}^2$. Hence, selective processing of the SAMs can be carried out in a large parameter window. Most notably, selective patterning with a lateral resolution in the sub-wavelength range below $\lambda/3$ is feasible. The inset in Fig. 6.7, for example, shows a structure with a lateral dimension of 250 nm [7]. In these experiments a Schwarzschild objective with NA = 0.5 has been used for focusing. Hence, the optical setup leaves enough room for further improvements. In addition, resonant fs-laser processing may reduce the overall thermal impact in direct proximity of the structures, thus increasing the lateral resolution. This provides a method of fabricating chemical templates with sub-100 nm sized functional domains on transparent substrates. Such platforms could be used for protein chips or other bioarrays. In addition, processing at higher fluences opens up an avenue toward combined chemical/topographic structures, e.g. for microfluidic applications.

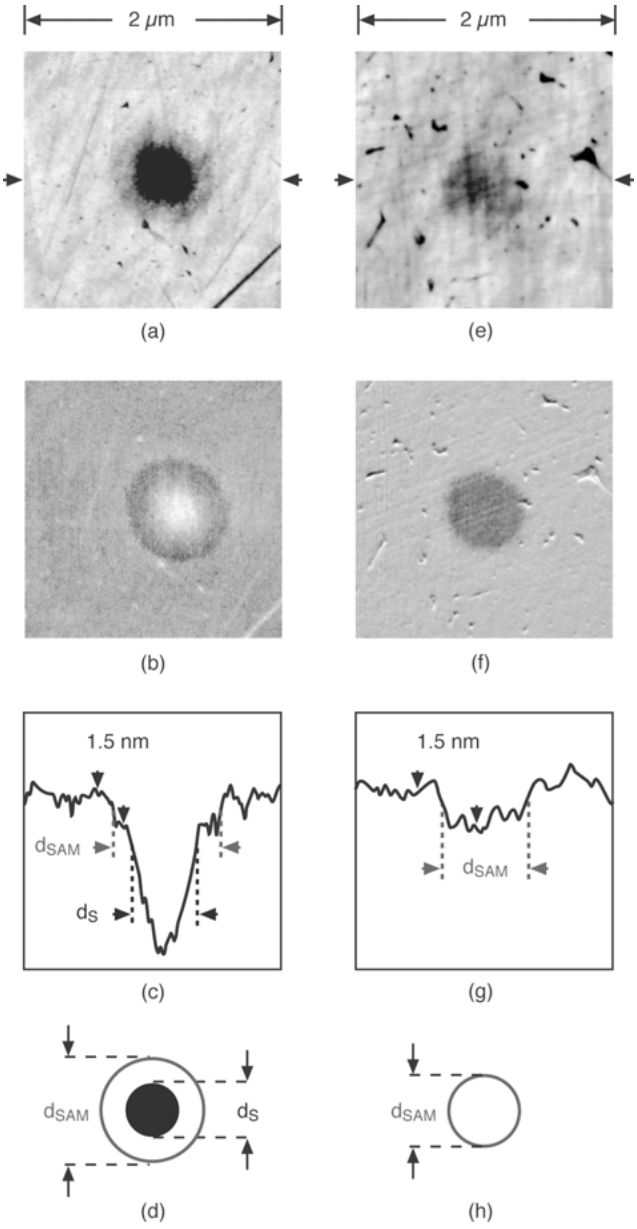

Fig. 6.6: AFM data from laser patterning experiments on ODS monolayers on quartz glass supports: (a) and (e) topographic AFM images; (b) and (f) friction contrast images; (c) and (g) height profiles across the structures; (d) and (h) schematic presentation of the structures. Laser processing was carried out with single pulses at $\lambda = 800$ nm, $\tau < 30$ fs and $d_{1/e} = 1.8$ µm and distinct fluences: (a)–(d) $F = 4.2\,\mathrm{J/cm^2}$ and (e)–(h) $F = 3.1\,\mathrm{J/cm^2}$. The notations d_{SAM} and d_S refer to the diameters of the region where monolayer decomposition and substrate ablation are observed. Adapted and reproduced with permission from [9]. Copyright 2008, AIP Publishing LLC.

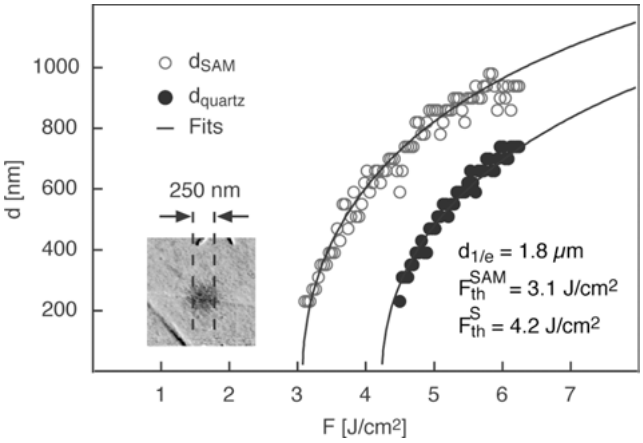

Fig. 6.7: Data from laser patterning experiments on ODS monolayers on quartz glass supports. Laser processing was carried out with single pulses at $\lambda = 800$ nm and $\tau < 30$ fs. The diagram shows the dependence of the diameters d of the structures on the fluence F. d_{SAM} and d_S denote the regions where monolayer decomposition and substrate ablation are observed, respectively. Full lines are fits on the basis of equation (6.1). Critical modification thresholds F_{th}^{SAM} and F_{th}^{S} and the $1/e$ laser spot diameter $d_{1/e}$ from these fits are given in the diagram. The inset shows a structure with a diameter of 250 nm demonstrating selective sub-wavelength patterning of the ODS SAMs below $\lambda/3$. Adapted and reproduced with permission from [9]. Copyright 2008, AIP Publishing LLC.

In view of these opportunities, Schröter et al. addressed fs-laser processing of PEG-terminated SAMs on quartz platforms in order to fabricate protein micro- and nanopatterns (Fig. 6.3 (b)). Along this path distinct coating routines and analytical characterization methods have been employed (Figs. 6.8–6.10) [15]. The fabrication of protein micro- and nanopatterns at first requires the preparation of optimized protein-repellent coatings in order to avoid unspecific protein adsorption in the background [20]. Generally, the preparation of silane-based SAMs sensitively depends on the particular silane precursor [2]. For each precursor the coating routine and all experimental parameters have to be optimized for proper performance of the coating. Figure 6.8 displays data from coating experiments on oxidized silicon substrates with two PEG functionalized precursors with trichloro- and trimethoxysilane end groups, PEGCl and PEGMeO [15]. Fluorescence microscopy, AFM, and contact angle goniometry were used for characterization. Fluorescence microscopy represents a simple method for investigation of the protein repellency of the coating. Labeled proteins with fluorescence markers are required for detection. Alexa Fluor 555-labeld BSA was used in the study by Schröter et al. After coating with PEG-terminated SAMs, the samples are covered with a drop of protein solution and subsequently thoroughly cleaned. Note, because of interference effects, the fluorescence intensity on thermally oxidized silicon substrates with an oxide layer thickness of about 100 nm is significantly increased [15]. These substrates are therefore ideal platforms for sensitive fluores-

cence microscopy studies. Figures 6.8 (a) and 6.8 (c) compare fluorescence images on PEGMeO- and PEGCl-coated substrates. In order to allow for easy identification of protein adsorption, the contrast of the fluorescence micrographs has been inverted. Thus, dark spots in these micrographs point to fluorescent radiation from the labeled proteins. A closer look reveals a nearly uniform size and intensity of these spots. This observation is attributed to the adsorption of single proteins. A quantitative analysis yields $\approx 2 \times 10^4$ proteins/mm^2 on substrates coated with PEGMeO SAMs versus $\approx 9 \times 10^5$ proteins/mm^2 on substrates coated with PEGCl SAMs. These results demonstrate the higher protein repellency of PEGMeO SAMs when compared with PEGCl SAMs. Incomplete monolayers, of course, show lower protein repellency. Thus a high packing density is required for optimal functionality of these SAMs. Fundamental studies, however, suggest that the protein repellency of PEG-terminated SAMs involves the penetration of water in the monolayer [47]. Hence, either a rather relaxed lateral packing density or some disorder or defects of the monolayer are required in order to achieve optimal protein repellency. For this reason, the data in Fig. 6.8 provides no information on the relative packing density and order of these SAMs [15].

Complementary AFM data on PEG-terminated SAMs on native silicon substrates with an oxide layer thickness of 1–2 nm are shown in Fig. 6.8 (b) and (d). Prior to characterization, the coatings in the center are removed via photothermal laser patterning (see below) [15]. This allows for determination of the film thickness via height profiles across these line structures. As evident, the thickness of both SAMs is about 1 nm. Further characterization via water contact angle goniometry yields static water contact angles of 38° and 33° for PEGCl and PEGMeO SAMs, respectively. These thicknesses and contact angles are in good agreement with data reported in the literature [21, 22].

CW- and fs-laser processing has been carried out for the fabrication of protein micro- and nanopatterns on PEG-terminated SAMs. Respective data are shown in Fig. 6.9 [15]. In first experiments, Schröter et al. used a photothermal routine which employs a microfocused CW-laser beam at $\lambda = 532$ nm and $d_{1/e} = 2.8$ µm and distinct laser powers P and irradiation times τ [15]. This allows for fabrication of micro- and nanosized protein-binding domains on surface-oxidized silicon wafers. During laser processing the PEG-terminated SAM is decomposed, leaving a reactive substrate surface behind. Proteins attach to such laser-depleted surface areas via unspecific interactions. Detection of protein adsorption in domains with diameters ≥ 1 µm can conveniently be carried out using fluorescence microscopy (Fig. 6.9 (a)). The lateral resolution of standard fluorescence microscopy, however, is limited by optical diffraction. Hence, for analysis of domains with diameters < 1 µm other analytical techniques are required. Scanning electron microscopy, for example, represents a simple technique if labeled proteins with Au nanoclusters are employed (Fig. 6.9 (c)). In addition, AFM offers a high lateral resolution (Fig. 6.9 (d)). These techniques are used for characterization of protein domains with diameters down to 300 nm (Fig. 6.9 (e)).

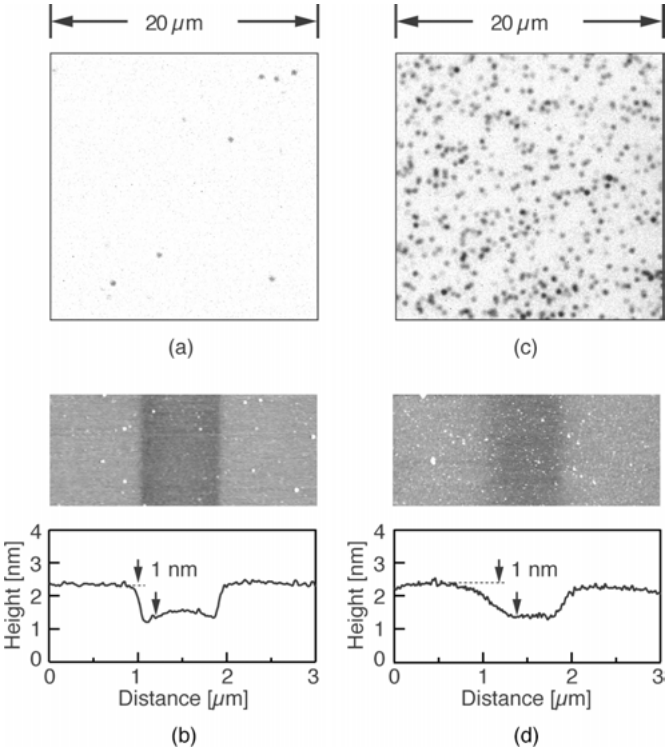

Fig. 6.8: PEG-terminated silane-based SAMs on surface-oxidized silicon substrates: (a)–(b) PEGMeO SAMs and (c)–(d) PEGCl SAMs. (a) and (c) display inverted fluorescence micrographs of the SAMs after wetting with Alexa Fluor 555-labled BSA solution and subsequent cleaning. In these experiments thermally oxidized silicon substrates with an oxide layer of $d_{Ox} = 100$ nm are used. (b) and (d) show topographic images and height profiles of PEGMeO and PEGCl SAMs on silicon substrates with a native oxide layer of $d_{Ox} = 1–2$ nm. Photothermal laser patterning was carried out prior to the measurements in order to remove the SAMs along a center line and determine the thickness of the monolayers. Adapted and reproduced with permission from [15]. Copyright 2014, American Chemical Society.

Photothermal processing with CW-lasers, of course, requires non-transparent substrates [6]. Hence, this technique cannot be used for patterning of PEG-terminated SAMs on quartz or glass substrates. The silane coating routine and the general patterning strategy, however, is fully compatible with transparent platforms such as quartz and glass [7, 9]. Schröter et al. used a microfocused Ti:sapphire-laser at $\lambda = 800$ nm, $\tau < 30$ fs to pattern PEG-terminated SAMs. A water immersion objective with NA = 0.75 provided a nominal spot diameter of $d_{1/e} \approx 1$ µm. A fluorescence microscopy image of micro- and nanosized protein patterns is shown in Fig. 6.9 (b). Minimum structure sizes of 650 nm were fabricated in these experiments. The experimental setup, however, was not optimized.

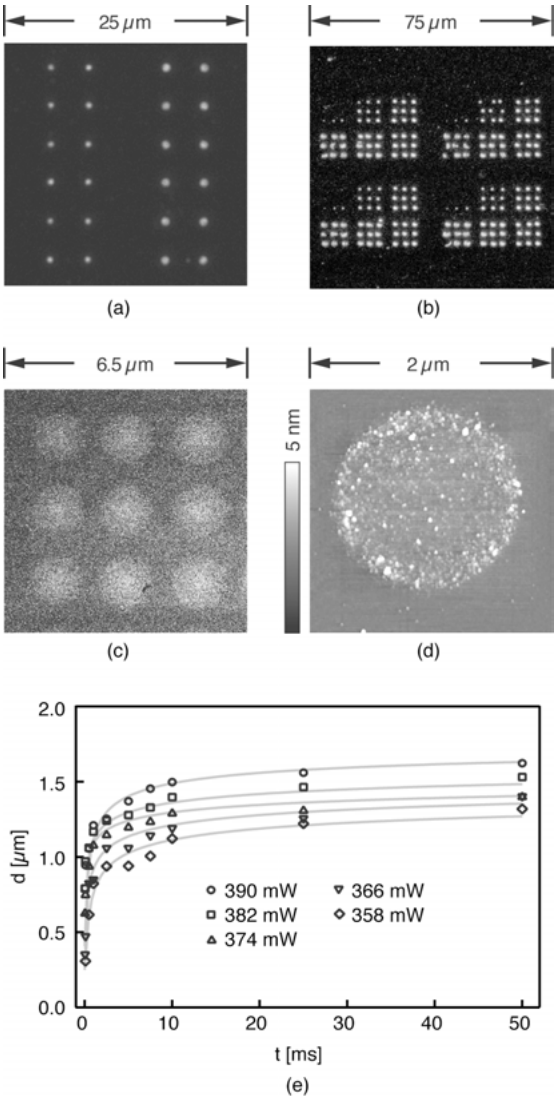

Fig. 6.9: Data from laser patterning experiments of PEGMeO SAMs on (a) thermally oxidized silicon substrates with an oxide layer of d_{Ox} = 100 nm; (b) quartz glass supports; and (c)–(e) silicon substrates with a native oxide layer of d_{Ox} = 1–2 nm. In (a) and (c)–(e) a microfocused CW-laser at λ = 532 nm and $d_{1/e}$ = 2.0 µm is used for patterning at distinct laser powers P and irradiation times t. In (b) a microfocused fs-laser at λ = 800 nm, τ < 30 fs and a nominal laser spot diameter of $d_{1/e} \approx$ 1 µm is used for processing with single pulses. The images in (a)–(b) display fluorescence micrographs of protein micro- and nanopatterns after wetting with Alexa Fluor 555-labeled BSA solution and subsequent cleaning. In (c)–(e) data from respective experiments with nanogold-labeled BSA are shown: (c) SEM image; (d) topographic AFM image; and (e) dependence of the protein domain diameter d on the laser power P and irradiation time t. Adapted and reproduced with permission from [15]. Copyright 2014, American Chemical Society.

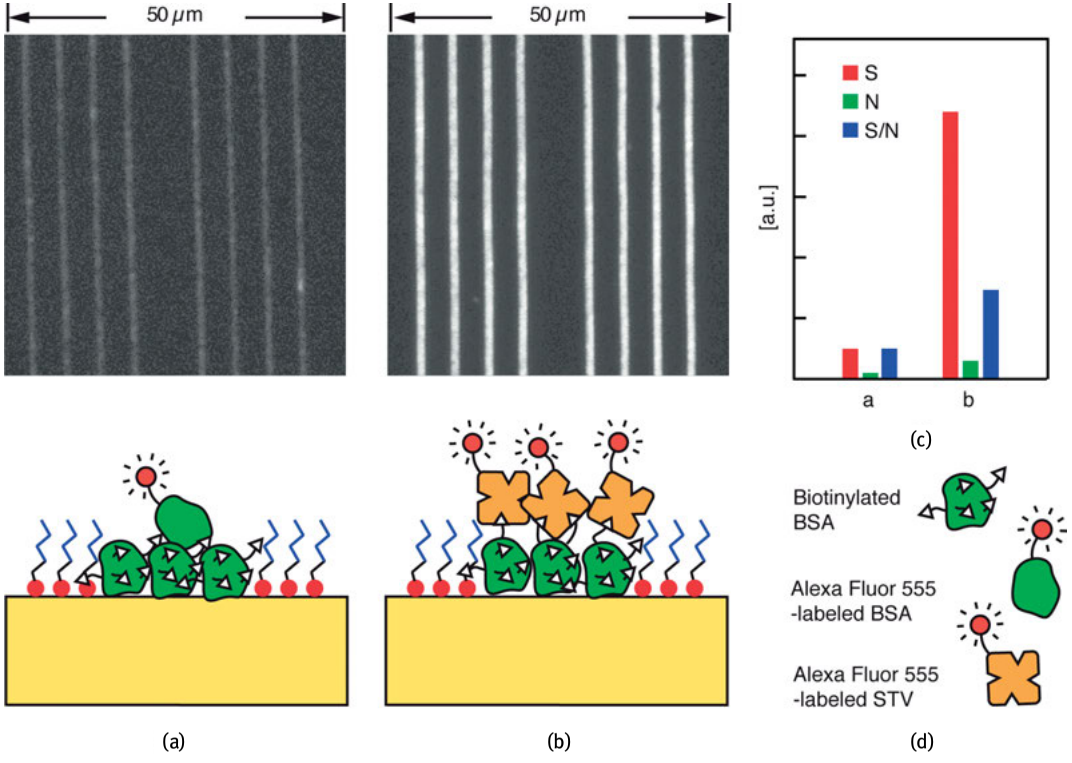

Fig. 6.10: Fluorescence micrographs of protein micropatterns on laser patterned PEGMeO SAMs: (a) after subsequent wetting with biotinylated BSA and Alexa Fluor 555-labled BSA. (b) After subsequent wetting with biotinylated BSA and Alexa Fluor 555-labled STV. (c) Average relative fluorescence signals and noise levels measured on the fluorescent line patterns and in the background in (a) and (b), respectively. (d) Legend of the schemes at the bottom of (a) and (b). Thermally oxidized silicon substrates with an oxide layer thickness of d_{Ox} = 100 nm are used as supports. Laser patterning was carried out using a microfocused CW-laser at λ = 532 nm and $d_{1/e}$ = 2.0 µm. Adapted and reproduced with permission from [15]. Copyright 2014, American Chemical Society.

Laser-fabricated domains on PEG-terminated substrates expose no specific binding sites for protein coupling, i.e. protein adsorption takes place via nonspecific interactions. Such interactions may result in protein denaturation and affect the biofunctionality of adsorbed proteins [48]. Furthermore, the fabrication of multiplexed protein arrays is hampered [49–51]. This limits the range of applications of such protein patterns [49–51]. Specific binding sites are required to couple intact proteins [24, 38]. Schröter et al. exploited the biotin-streptavidin complex for specific coupling of proteins [15]. Figure 6.10 shows data from an analysis via fluorescence microscopy [15]. In these experiments laser-fabricated PEG-terminated line patterns are coated with biotinylated BSA. BSA blocks further protein adsorption [38, 48]. For this reason, subsequent adsorption of Alexa Fluor 555-labeled BSA is strongly reduced (Fig. 6.10a). Only weak adsorption via nonspecific interactions is observed. In contrast, STV exhibits specific binding sites for biotin. Hence, significantly enhanced protein adsorption is observed using Alexa Fluor 555-labeled STV (Fig. 6.10 (b)). For comparison, relative signal intensities S on the line pattern, relative noise levels N, i.e. the intensities in surrounding surface areas, and the S/N ratios in Fig. 6.10 (a) and (b) are determined (Fig. 6.10 (c)). The ratio of the relative signal intensities S after adsorption of Alexa Fluor 555-labeled BSA and Alexa Fluor 555-labeled STV is ≈ 10. Also, the S/N ratio in Fig. 6.10 (b) is higher by a factor of about 3, exploiting the high selectivity of the biotin-streptavidin complex.

6.4 Summary

In conclusion, progress in nonlinear processing of self-assembled monolayers with microfocused fs-laser sources is reviewed. Generally, the patterning results strongly depend on the chemical and electronic structure of the monolayer/substrate interface [7]. The proper choice of all laser parameters is a key requirement in order to selectively initiate monolayer decomposition or specific chemical transformations and avoid substrate damage.

Results from patterning experiments suggest that processing of thiol-based monolayers on Au-coated supports such as glass or silicon using standard Ti:sapphire lasers at $\lambda = 800\,\text{nm}$ and $\tau < 30\,\text{fs}$ proceeds via indirect mechanisms, most likely via photothermal pathways [8, 14].

Alkanethiolate SAMs, such as HDT SAMs, show great promise as ultrathin positive-tone resists in rapid fs-laser patterning of thin Au films. Selective processing of the monolayer is limited to a narrow range of fluences. Defined pattern transfer into the Au film, however, is feasible up to high fluences via wet-chemical etching in ferri-ferrocyanide solution. Minimum structures at $\lambda = 800\,\text{nm}$ and $\tau < 30\,\text{fs}$ exhibit a width of 160 nm corresponding to sub-wavelength structure sizes of $\lambda/5$, indicative for a highly nonlinear process [8]. Further experiments reveal a wavelength-dependent

modification threshold, which could point to nonlinear plasmonic effects because of the inherent nanoroughness of the Au layer [12, 13].

Femtosecond laser processing of SAMs containing biphenyl groups, i.e. NBPT SAMs, at $\lambda = 800\,\text{nm}$ and $\tau < 30\,\text{fs}$ reveals no indications for crosslinking [14]. In particular, these SAMs do not act as negative-tone resists. Furthermore, no chemical transformation of the nitro end groups into amine groups is observed. Processing with fs-lasers at wavelengths in the UV range is expected to trigger these chemical processes. In addition, excitation of surface plasmon resonances in the visible and near-infrared wavelength range represents a promising method.

Silane-based SAMs on transparent supports such as quartz or glass allow for exploitation of multiphoton absorption processes [9]. Femtosecond laser processing of alkylsiloxane monolayers on quartz glass has been investigated at $\lambda = 800\,\text{nm}$ and $\tau < 30\,\text{fs}$ [9]. Selective patterning of ODS monolayers can be carried out in a fairly large fluence range. Sub-wavelength patterning down to $\lambda/3$ and below is also demonstrated. This approach has been extended to PEG-terminated SAMs, i.e. to SAMs with polyethylene glycol end groups, in order to build up protein arrays [15]. Considering tighter focusing optics and shorter wavelength, sub-100 nm patterning appears feasible. In addition, resonant processing with tunable fs-lasers provides a promising means of reducing the overall thermal impact in direct proximity of the structures and pushing the lateral resolution into the sub-100 nm range.

Acknowledgments

Financial support from the German Science Foundation (DFG, grant OS-188/30 and HA 2769/5-1 within the Priority Program SPP 1327) is gratefully acknowledged. The authors thank Jürgen Koch and Boris Chichkov from the Laser Zentrum Hannover (LZH) for fruitful collaborations.

References

[1] Love JC, Estroff LA, Kriebel JK, Nuzzo RG, Whitesides GM. Self-assembled monolayers of thiolates on metals as a form of nanotechnology. Chem Rev 2005, 105, 1103–1170.
[2] Onclin S, Ravoo BJ, Reinhoudt DN. Engineering silicon oxide surfaces using self-assembled monolayers. Angew Chem Int Ed 2005, 44, 6282–6304.
[3] Buriak JM. Organometallic chemistry on silicon and germanium surfaces. Chem Rev 2002, 102, 1271–1308.
[4] Pujari SP, Scheres L, Marcelis ATM, Zuilhof H. Covalent surface modification of oxide surfaces. Angew Chem Int Ed 2014, 53, 6322–6356.
[5] Woodson M, Liu J. Functional nanostructures from surface chemistry patterning. Phys Chem Chem Phys 2007, 9, 207–225.

[6] Mathieu M, Hartmann N. Sub-wavelength patterning of organic monolayers via nonlinear processing with continuous-wave lasers. New J Phys 2010, 12, 125017-1–21.
[7] Hartmann N. Sub-wavelength patterning of organic monolayers via nonlinear processing with femtosecond laser pulses. In: Duarte FJ, ed. Coherence and ultrashort pulse laser emission. Rijeka, Croatia, InTech, 2010, 629–44. ISBN: 978-953-307-242-5, open access: http://intechopen.com.
[8] Mathieu M, Franzka S, Koch J, Chichkov BN, Hartmann N. Self-assembled organic monolayers as ultrafast high-resolution resists in nonlinear femtosecond laser processing. Appl Phys A 2010, 101, 461–466.
[9] Hartmann N, Franzka S, Koch J, Ostendorf A, Chichkov BN. Subwavelength patterning of alkylsiloxane monolayers via nonlinear processing with single femtosecond laser pulses. Appl Phys Lett 2008, 92, 223111-1–3.
[10] Koch J, Fadeeva E, Engelbrecht M, Ruffert C, Gatzen HH, Ostendorf A, Chichkov BN. Maskless nonlinear lithography with femtosecond laser pulses. Appl Phys A 2006, 82, 23–26.
[11] Koch J, Korte F, Fallnich C, Ostendorf A, Chichkov BN. Direct-write sub-wavelength structuring with femtosecond laser pulses. Opt Eng 2005, 44, 051103-1–5.
[12] Aumann A, Maragkaki S, Schulz F, Schröter A, Schöps B, Franzka S, Hartmann N, Ostendorf A. Sub-wavelength patterning of self-assembled organic monolayers via non-collinear optical parametric amplifier. Paper N202. Proc ICALEO 2013.
[13] Maragkaki S, Aumann A, Schulz F, Schröter A, Schöps B, Franzka S, Hartmann N, Ostendorf A. Micro-patterning of self-assembled organic monolayers by using tunable ultrafast laser pulses. Proc SPIE 2014, 897213-1-7, doi:10.1117/12.2037716.
[14] Schröter A, Franzka S, Koch J, Chichkov BN, Ostendorf A, Hartmann N. Femtosecond-laser processing of nitrobiphenylthiol self-assembled monolayers. Appl Surf Sci 2013, 278, 43–46.
[15] Schröter A, Franzka S, Hartmann N. Photothermal laser fabrication of micro- and nanostructured chemical templates for directed protein immobilization. Langmuir 2014, 30, 14841–14848.
[16] Schröter A, Kalus M, Hartmann N. Substrate mediated effects in photothermal patterning of alkanethiol self-assembled monolayers with microfocused continuous-wave lasers. Beilstein J Nanotechnol 2012, 3, 65–74.
[17] Gölzhäuser A, Geyer W, Stadler V, Eck W, Grunze M, Edinger K, Weimann T, Hinze P. Nanoscale patterning of self-assembled monolayers with electrons. J Vac Sci Technol 2000, 18, 3414–3418.
[18] Eck W, Stadler V, Greyer W, Zharnikov M, Gölzhäuser A, Grunze M. Generation of surface amino groups on aromatic self-assembled monolayers by low energy electron beams – a first step towards chemical lithography. Adv Mater 2000, 12, 805–808.
[19] Turchanin A, Schnietz M, El-Desawy M, Solak HH, David C, Gölzhäuser A. Fabrication of molecular nanotemplates in self-assembled monolayers by extreme-ultraviolet-induced chemical lithography. Small 2007, 3, 2114–2119.
[20] Banerjee I, Pangule RC, Kane RS. Antifouling coatings: recent developments in the design of surfaces that prevent fouling by proteins, bacteria and marine organisms. Adv Mater 2011, 23, 690–718.
[21] Cecchet F, De Meersman B, Demoustier-Champagne S, Nysten B, Jonas AM. One step growth of protein antifouling surfaces: monolayers of poly(ethylene oxide) (PEO) derivatives on oxidized and hydrogen-passivated silicon surfaces. Langmuir 2006, 22, 1173–1181.
[22] Papra A, Gadegaard N, Larsen NB. Characterization of ultrathin poly(ethylene glycol) monolayers on silicon substrates. Langmuir 2001, 17, 1457–1460.
[23] Hartmann N, Dahlhaus D, Franzka S. Self-assembled organic templates for the selective adsorption of gold nanoparticles into confined domains. Surf Sci 2007, 601, 3916–3920.

[24] Ballav N, Thomas H, Winkler T, Terfort A, Zharnikov M. Making protein patterns by writing in a protein-repelling matrix. Angew Chem Int Ed 2009, 48, 5833–5836.
[25] Schröter A, Mathieu M, Franzka S, Feydt J, Irsen S, Hartmann N. Fabrication of chemical templates via selective laser-induced desorption of hexadecanethiol self-assembled monolayers. Appl Surf Sci 2013, 278, 57–61.
[26] Balgar T, Franzka S, Hartmann N. Laser-assisted decomposition of alkylsiloxane monolayers at ambient conditions: Rapid patterning below the diffraction limit. Applied Physics A: Materials Science & Processing 2006, 82, 4, 689–695.
[27] Dahlhaus D, Franzka S, Hasselbrink E, Hartmann N. 1D nanofabrication with a micrometer-sized laser spot. Nano Letters 2006, 6, 2358–2361.
[28] Klingebiel B, Scheres L, Franzka S, Zuilhof H, Hartmann N. Photothermal micro- and nanopatterning of organic/silicon interfaces. Langmuir 2010, 26, 6826–6831.
[29] Bäuerle D. Laser processing and chemistry. Berlin, Germany, Springer, 2000.
[30] Ali M, Wagner T, Shakoor M, Molian PAJ. Review of laser nanomachining. J Laser Appl 2008, 20, 169–184.
[31] Chong TC, Hong MH, Shi LP. Laser precision engineering: from microfabrication to nanoprocessing. Laser & Photon 2010, 4, 123–143.
[32] Richter LJ, Cavanagh RR. Mechanistic studies of photoinduced reactions at semiconductor surfaces. Prog Surf Sci 1992, 39, 155–226.
[33] Zhou XL, Zhu XY, White JM. Photochemistry at adsorbate/metal interfaces. Surf Sci Rep 1991, 13, 73–220.
[34] Zimmermann FM, Ho W. State resolved studies of photochemical dynamics at surfaces. Surf Sci Rep 1995, 22, 127–247.
[35] Hartmann N, Balgar T, Bautista R, Franzka S. Direct laser patterning of octadecylsiloxane monolayers on surface-oxidized silicon substrates: indications for a photothermal excitation mechanism. Surf Sci 2006, 600, 4034–4038.
[36] Álvarez M, Best A, Pradhan-Kadam S, Koynov K, Jonas U, Kreiter M. Single-photon and two-photon induced photocleavage for monolayers of an alkyltriethoxysilane with a photoprotected carboxylic ester. Adv Mater 2008, 20, 4563–4567.
[37] Xia Y, Zhao XM, Kim E, Whitesides GM. A selective etching solution for use with patterned self-assembled monolayers of alkanethiolates on gold. Chem Mater 1995, 7, 2332–2337.
[38] Jonkheijm P, Weinrich D, Schröder H, Niemeyer CM, Waldmann H. Chemical strategies for generating protein biochips. Angew Chem Int Ed 2008, 47, 9618–9647.
[39] Chang W, Choi M, Kim J, Cho S, Whang K. Sub-micron scale patterning using femtosecond laser and self-assembled monolayers interaction. Appl Surf Sci 2005, 240, 296–304.
[40] Chang W, Kim J, Cho S, Whang K. Femtosecond-laser-coupled near-field scanning optical microscopy patterning using self-assembled monolayers. Jpn J Appl Phys 2006, 45, 2082–2086.
[41] Kirkwood SE, Shadnam MR, Amirfazli A, Fedosejevs R. Mechanism for femtosecond laser pulse patterning of self-assembled monolayers on gold-coated substrates. J Phys Conf Series 2007, 59, 428–431.
[42] Ryan D, Parviz BA, Linder V, Semetey V, Sia SK, Su J, Mrksich M, Whitesides GM. Patterning multiple aligned self-assembled monolayers using light. Langmuir 2004, 20, 9080–9088.
[43] Koch J, Korte F, Bauer T, Fallnich C, Ostendorf A, Chichkov BN. Nanotexturing of gold films by femtosecond laser-induced melt dynamics. Appl Phys A 2005, 81, 325–328.
[44] Lide DR. CRC Handbook of Chemistry and Physics. Bocca Raton, Florida, USA, Taylor & Francis, 2009.

[45] Olsen C, Rowntree PA. Bond-selective dissociation of alkanethiol based self-assembled monolayers adsorbed on gold substrates using low-energy electron beams. J Chem Phys 1998, 108, 3750–3764.
[46] Sugimura H, Ushiyama K, Hozumi A, Takai O. Micropatterning of alkyl- and fluoroalkylsilane self-assembled monolayers using vacuum ultraviolet light. Langmuir 2000, 16, 885–888.
[47] Herrwerth S, Eck W, Reinhardt S, Grunze M. Factors that determine the protein resistance of oligoether self-assembled monolayers – internal hydrophilicity, terminal hydrophilicity, and lateral packing density. J Am Chem Soc 2003, 125, 9359–9366.
[48] Cretich M, Damin F, Pirri G, Chiari M. Protein and peptide arrays: recent trends and new directions. Biomol Engineering 2006, 23, 77–88.
[49] Mendes PM, Yeung CL, Preece JA. Bio-nanopatterning of surfaces. Nanoscale Res Lett 2007, 2, 373–384.
[50] Wu CC, Reinhoudt DN, Otto C, Subramaniam V, Velders AH. Strategies for patterning biomolecules with dip-pen nanolithography. Small 2011, 7, 989–1002.
[51] Hynes, MJ, Maurer JA. Lighting the path: photopatternable substrates for biological applications. Mol BioSyst 2013, 9, 559–564.

J. Bonse, S. Höhm, M. Hartelt, D. Spaltmann, S. Pentzien, R. Koter, S. Marschner, A. Rosenfeld, and J. Krüger

7 Femtosecond laser-induced surface nanostructures for tribological applications

Abstract: Laser-induced periodic surface structures (LIPSS) were generated on two types of steel (100Cr6, X30CrMoN15-1) and two types of titanium (Ti, Ti6Al4V) surfaces upon irradiation with multiple linear polarized femtosecond laser pulses in air environment (pulse duration 30 fs, central wavelength 790 nm, pulse repetition rate 1 kHz, Gaussian beam shape). The conditions (laser fluence, spatial spot overlap) were optimized in a sample-scanning geometry for the processing of large surface areas covered homogeneously by two different types of LIPSS – either near wavelength or sub-100 nm structures. The tribological performance of the nanostructured surfaces was characterized under reciprocating sliding at 1 Hz against a ball of hardened steel using different lubricants and normal forces. After 1000 cycles the corresponding wear tracks were characterized by optical and scanning electron microscopy. For specific conditions, the wear was strongly reduced and the laser-generated nanostructures endured the tribological treatment. Simultaneously, a significant reduction of the friction coefficient was observed in the laser-irradiated LIPSS-covered areas, indicating the benefit of laser surface structuring for tribological applications. The spatially Gaussian shaped beam used for the laser processing was transformed via beam shaping into a top hat distribution at the surface of the samples for optimization. The tribological performance of the laser-induced nanostructures is discussed on the basis of different physical and chemical mechanisms.

7.1 Introduction

Since the first observation of *laser-induced periodic surface structures* (LIPSS), also termed *ripples*, on semiconductors by Birnbaum [1], such structures have been found on almost every material. The generation of LIPSS on laser irradiation is a universal phenomenon [2], although their occurrence, structural size, and formation mechanism depend on the material and irradiation parameters. LIPSS have attracted remarkable interest over the past decades, as their generation is possible in a single-process step. This provides a simple way of surface nanostructuring towards a control of optical, mechanical, or chemical surface properties [3].

7.1.1 Femtosecond laser-induced periodic surface structures (fs-LIPSS)

Since the turn of the new millennium, a remarkable amount of research has been devoted to the formation mechanisms of LIPSS after irradiation by ultrashort laser pulses (see [4–10] and references therein). Typically, two distinct types of LIPSS are observed on irradiation of solids with linearly polarized fs-laser pulses. For strongly absorbing materials (metals and semiconductors) so-called *low-spatial-frequency LIPSS* (LSFL) are observed with a period Λ_{LSFL} close to the irradiation wavelength λ and an orientation perpendicular to the laser beam polarization [11–14]. It is generally accepted that these LSFL are generated by interaction of the incident laser beam with a surface electromagnetic wave (SEW) generated at the rough surface [5, 14–16].

The second LIPSS type are the so-called *high-spatial-frequency LIPSS* (HSFL). With periods Λ_{HSFL} significantly smaller than the incident wavelength, these structures are observed predominantly for laser pulse durations in the fs- to ps-range. Their origin is still discussed controversially in the literature. Second harmonic generation [11, 17], the involvement of specific types of plasmon modes [18–20] or self-organization [4] have been proposed as possible formation mechanisms.

7.1.2 fs-LIPSS on metals

Several groups have already studied the generation of fs-LIPSS on metals [3, 13, 21, 22]. Steel and titanium belong to the most relevant materials used in industrial applications involving tribological demands. Using Ti:sapphire laser pulses, on steel LSFL were mostly reported with spatial periods in the range of 500–700 nm [3, 22–25]. Titanium and its alloys provide high corrosion and temperature resistance along with an extraordinary strength-to-weight ratio, which makes it interesting for many industrial, aeronautical or medical applications. Near-infrared fs-laser processing experiments on titanium revealed both types of LIPSS with LSFL periods between 400 and 800 nm, and HSFL periods of 65 to 95 nm only (for a literature survey refer to Table 1 in [26]).

7.1.3 Technical applications of LIPSS

Different technical applications of LIPSS have recently been proposed and studied, such as surface colorization [21, 22], control of surface wetting behavior [27] or friction management [28–36]. However, the tribological methods and specific test conditions vary strongly among the latter studies, thereby complicating a direct comparison of the results. Mizuno et al. used an atomic force microscopic technique under controlled atmospheric conditions. They reported a reduction of the friction coefficient of fs-LIPSS covered diamond-like-carbon (DLC) films for low normal loads in the nN range [28]. Later, the same group used a ball-on-disk friction test for study-

ing the influence of additional overlayers and hardcoatings, and by complementary geometrical surface patterns [29, 30]. Pfeiffer and co-workers qualified the friction and wear behavior of fs-LIPSS on super-hard tetrahedral amorphous carbon films [31]. Employing a pin-on-disk tribometer under unlubricated conditions, they also found a significant reduction of the friction coefficient and the corresponding wear rate. Eichstädt et al. used a tribometer with a linear reciprocating module in a ball-on-flat configuration. This group presented results of an increased friction coefficient of fs-LIPSS covered silicon for normal loads in the mN range [32]. Chen et al. demonstrated the low friction characteristics of fs-LIPSS-covered microscale stripes on silicon carbide seals in air and water contact by using a ring-on-disk tribometer [33].

In the following chapter, the tribological characteristics of large area fs-LIPSS covered surfaces are systematically qualified. They are compared for four different metals in two different lubricating oils under identical conditions. These results were already partly reported in [34] and [36].

7.2 Experimental details

7.2.1 Materials

Commercial grade-1 titanium (Ti, 99.5 % purity, DIN 3.7025) and grade-5 titanium alloy (Ti6Al4V, DIN 3.7165) were purchased from Schumacher Titan GmbH (Solingen, Germany) as 25 mm diameter rods. These rods were cut into circular slabs of 8 mm thickness and mechanically polished, resulting in mirror-like surface finish with an average roughness $R_a < 10$ nm. Cylindrical slabs of hardened 100Cr6 steel were supplied by Optimol Instruments Prüftechnik GmbH (München, Germany) with 24 mm diameter, 8 mm thickness (DIN 1.3505) and a polished surface ($R_a \sim 35$ nm). Similar sized slabs were acquired from Energietechnik Essen GmbH (Essen, Germany), made of a hardened, nitrogen enriched, high toughness bearing steel (X30CrMoN15-1, DIN 1.4108) with a lapped surface ($R_a \sim 190$ nm).

7.2.2 Laser processing technology

A Ti:sapphire laser amplifier system (Femtolasers, Compact Pro) was used to generate linearly polarized laser pulses of $\tau = 30$ fs duration and $\lambda = 790$ nm central wavelength at a pulse repetition rate of $f = 1$ kHz. The laser pulse energies E were measured with a pyroelectric detector. The pulses were focused by a spherical dielectric mirror (500 mm focal length).

The samples were mounted on a motorized x-y-z linear translation stage and placed normal to the incident laser beam a few millimeters in front of the geometrical laser focus. At this sample position, a Gaussian-like beam profile was measured

with a radius $w_0(1/e^2) \sim 140\,\mu m$. The corresponding peak fluence in front of the sample surface was calculated via $\phi_0 = 2E/(\pi w_0^2)$ [37]. The sample was moved in a meandering motion under the focused laser beam at a constant scan velocity v_x and with a line offset of Δy. This led to the processing of a square-shaped area of $5 \times 5\,mm^2$. Under these conditions, the effective number of laser pulses per focused laser spot diameter $D = 2w_0$ (for a single laser processing pass) accounts in the x-direction to $N_{eff} = (D \times f)/v_x$ [37]. In some cases, an additional pass with identical processing parameters was performed at the same sample area. Subsequent to laser processing in ambient air, the samples were cleaned in acetone for five minutes using an ultrasonic bath and stored in a desiccator to avoid long-term chemical reactions with the ambient air atmosphere.

7.2.3 Sample characterization

The laser-processed surface regions were characterized by optical microscopy (OM, Nikon Eclipse L200), white light interference microscopy (WLIM, Zygo NewView 5020), and scanning electron microscopy (SEM, Carl Zeiss Gemini Supra 40).

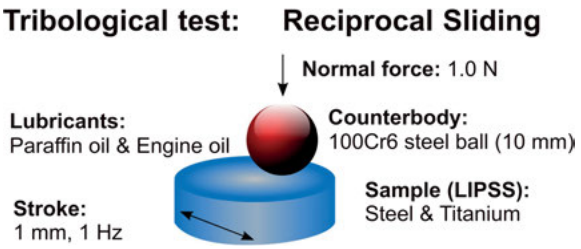

Fig. 7.1: Scheme of the reciprocal sliding tribological test (RSTT).

Reciprocal sliding tribological tests (RSTT) were performed in a home-made tribometer by sliding the laser-processed samples at a normal force of $F_N = 1.0\,N$ against a hardened and polished steel ball (100Cr6, 10 mm diameter, $R_a \sim 6\,nm$) as counterbody (see the scheme in Fig. 7.1). The velocity between sample and ball is a sine function with its maximum value in the middle of the stroke distance of 1 mm total length. During the movement, the frictional forces acting on the sample are recorded. From this information and the known normal force, the friction coefficient can be quantified [38]. A 100Cr6 ball as counterbody is our "standard" in RSTT and allows comparison with previous experiments.

The radius of the ball-sample contact was estimated using a Hertzian deformation model (HDM) of a sphere in contact with a flat sample. At this normal force, the contact radius lies between 30 and 40 µm for all materials tested, i.e., it is about 2–3 orders of magnitude larger than the LIPSS periods. Moreover, for the given conditions, the HDM predicts material (hardness) dependent sample-ball deformations between 200

and 300 nm, i.e., values of the order of the expected modulation depths of the LSFL (see Section 7.3.1). In previous studies [39, 40] it was shown that RSTT experiments with balls of 10 mm diameter and normal forces between 0.1 and 1.0 N are sensitive to surface grooves with a depth of ~ 160 nm and widths down to 100 nm only, i.e., groove widths of less than 1/500 of the Hertzian diameter of the contact area [40]. In the RSTT experiments, 1000 cycles were performed at a frequency of 1 Hz in a synthetic paraffin oil (free of additives) as well as in a fully formulated engine oil with additives (Castrol VP-1). The range of uncertainty in the friction coefficient measurements is ± 0.02. After the tribological tests, the samples were cleaned in petroleum ether for five minutes using an ultrasonic bath in order to remove the residual lubricants. Subsequently, the corresponding wear tracks were inspected by OM and SEM.

7.3 Tribological performance of LIPSS

In a first step, suitable laser processing conditions were identified and optimized for the generation of large surface areas (several tens of mm^2) covered homogeneously by LIPSS on all four metals (Ti, Ti6Al4V, 100Cr6, X30CrMoN15-1). As an example, Section 7.3.1 presents the optimized processing conditions for the titanium alloy covered by near-wavelength (LSFL) and sub-100 nm LIPSS (HSFL), both generated with a spatial Gaussian beam profile. In a second step, the tribological performance of the different types of LIPSS was systematically tested for all materials in the two different lubricating oils – exemplified for LSFL and HSFL in Section 7.3.2. The process optimization is demonstrated in Section 7.3.3. Here, spatial beam shaping is used to transform the Gaussian beam into a top hat distribution.

7.3.1 Large area surface processing of LIPSS

By choosing a peak fluence of $\phi_0 = 0.11\ J/cm^2$, a scan velocity of $v_x = 5$ mm/s ($N_{eff} \sim 56$) and a line offset of $\Delta y = 0.1$ mm at the given focusing conditions, a common set of parameters was identified which allowed the generation of LSFL structures on all four different metals with a single laser processing pass [34, 36]. As an example, Fig. 7.2 (a) shows the WLIM topography of the central $1.40 \times 1.05\ mm^2$ laser processed surface area in a 3D view (left). The periodic pattern observed here is formed by the arrangement of adjacent ablation lines. A cross-sectional surface line profile is given below the corresponding topography and reveals comb-like height variations of $\Delta z = \pm 150$ nm. Note that the spatial resolution of the WLIM is not sufficient here to resolve the LSFL. Scanning electron microscopy confirmed the simultaneous existence of the LSFL at the top and bottom of the surface topography [36]. As seen on the right hand side of Fig. 7.2 (a), LSFL are formed with periodicities of (620 ± 80) nm and an orientation

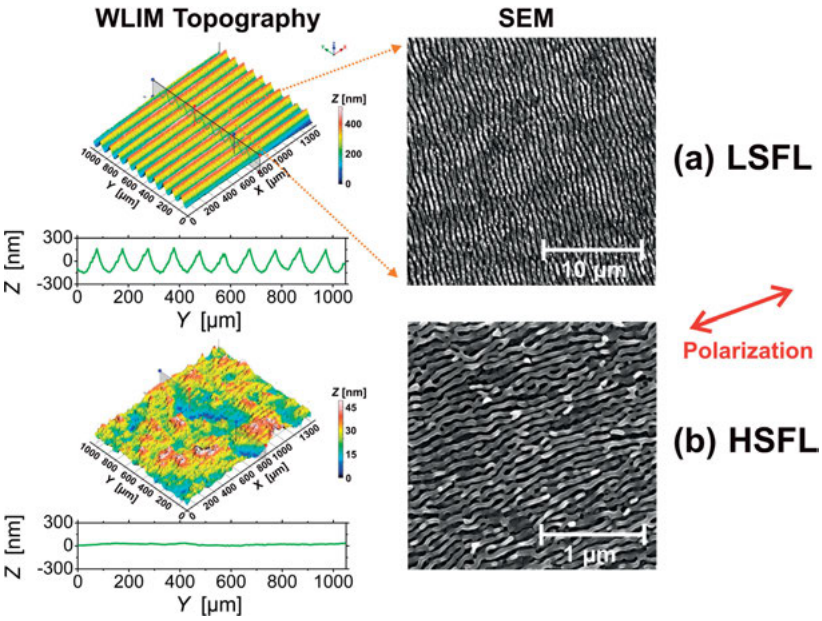

Fig. 7.2: White light interference microscopic topography (left) and scanning electron micrographs (right) from the centre of the fs-laser processed Ti6Al4V titanium alloy surface area (τ = 30 fs, λ = 800 nm, ν = 1 kHz). The processing conditions in (a) were optimized for the generation of LSFL (ϕ_0 = 0.11 J/cm^2, N_{eff} ~ 56, one pass) and in (b) for the generation of HSFL (ϕ_0 = 0.08 J/cm^2, N_{eff} ~ 280, two passes). The red double arrows indicate the direction of laser beam polarization. Note the different magnifications of the SEM images.

perpendicular to the polarization. Typical LSFL modulation depths were estimated by atomic force microscopy measurements to be (110 ± 20) nm.

On titanium surfaces (Ti, Ti6Al4V) HSFL were successfully generated with two processing passes at a lowered peak fluence of ϕ_0 = 0.08 J/cm^2 with a decreased scan velocity of v_x = 1 mm/s (N_{eff} ~ 280) and a reduced line offset of Δy = 0.05 mm. The corresponding WLIM topography (Fig. 7.2 (b), left) exhibits surface height variations of Δz = ±15 nm which are similar to those of the non-irradiated surface. However, the high-resolution SEM micrograph in the right part of the figure indicates HSFL with periodicities of (80±20) nm and an orientation parallel to the laser beam polarization. Atomic force microscopy measurements revealed typical HSFL modulation depths of (25 ± 10) nm.

It is instructive to evaluate the "photonic costs" (PC) for fs-laser nanostructuring in order to compare them to those of alternative industrial techniques. An estimation of the PC for the large area fs-laser fabrication of LIPSS using current state-of-the-art processing technology yields a typical value of 0.1 €/cm^2 for LSFL on metal surfaces [36].

7.3.2 Tribological characterization of LIPSS

On all four metals, the tribological performance of the LIPSS was evaluated by RSTT using paraffin oil (free of additives) and fully formulated engine oil as lubricants [34, 36]. The friction coefficient and the resulting wear tracks were characterized for sliding directions parallel and perpendicular to the ablation lines. No significant differences were found for sliding both directions, indicating that the directional effect due to the LIPSS is smaller than the uncertainty of the measurements. Hence, below we only present data for the sliding direction parallel to the laser processing lines.

The LIPSS (LSFL) covered steel samples (100Cr6, X30CrMoN15-1) generally showed an almost constant friction coefficient ranging between 0.11 and 0.17 in both lubricants (100Cr6: see [34]; X30CrMoN15-1: see [36]). These values were always very similar to the behavior of the non-processed surfaces and are typical for the regime between "mixed friction" (where both solid body friction and fluid friction appear; including solid asperity interaction) and "boundary friction" (where a direct contact between the sliding bodies is present) [41]. The wear tracks generated in engine oil were somewhat smaller than those obtained in paraffin oil. On 100Cr6 steel the LIPSS partly endured the RSTT [36].

The tribological performance of the two different LIPSS covered titanium materials (Ti, Ti6Al4V) was very similar but disparate from that of the steel materials. These findings are exemplified in detail for LSFL and HSFL in the following two sub-sections for the titanium alloy Ti6Al4V, complemented by a summary of the tribological performance of all four materials.

LSFL

Figure 7.3 contrasts the tribological performance of LSFL covered titanium alloy surfaces tested in paraffin oil [Fig. 7.3 (a), upper part] and in engine oil [Fig. 7.3 (b), lower part]. For each lubricant, the friction coefficient is shown vs. the number of sliding cycles (left). The corresponding wear tracks were imaged by OM (middle) and SEM (right). Additionally, the results of a non-irradiated reference sample location are provided for comparison.

In paraffin oil (Fig. 7.3 (a)), the friction coefficient of the LSFL covered titanium alloy surface and the reference area both exhibit large oscillations between 0.15 and 0.6. The inspection of the wear tracks by OM and SEM reveals severe damage in both tribologically tested regions (LSFL: lower row, reference: upper row). The LSFL were completely destroyed during the RSTT procedure.

In engine oil (Fig. 7.3 (b)), the friction coefficient of the reference area also shows rather large variations between ~ 0.3 and ~ 0.5, associated with a damaged surface region (see the OM and SEM images). Interestingly, on the LSFL covered surface, the friction coefficient is reduced by a factor of more than two and lies in the range of 0.11

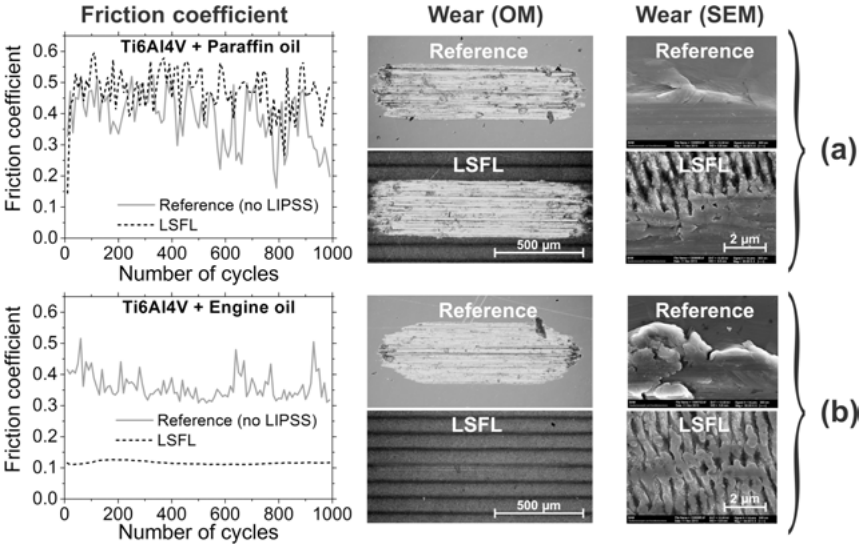

Fig. 7.3: Friction coefficient vs. number of sliding cycles (left) and the corresponding wear tracks of the LSFL covered Ti6Al4V titanium alloy surface tested in paraffin oil (a) and in engine oil (b). The middle column provides low-resolution optical micrographs, while the right column indicates high-resolution scanning electron micrographs. A reference measurement on the non-irradiated surface is provided for comparison.

to 0.13, without any oscillations. The complementing high-resolution SEM images reveal that the LSFL endured the tribological test (see lower right part of Fig. 7.3 (b)).

This very positive effect of the engine oil on the tribological performance of LSFL covered titanium surfaces was first reported in [34]. As the main differences between the two lubricants are the additives contained in the engine oil, the effect has been attributed to the presence of the additives. These additives efficiently cover and bond to the laser-generated surface structures and reduce friction and wear by forming a gliding intermediate layer which protects the sample from a direct intermetallic contact [36]. A chemical analysis of the additives contained in the engine oil used here revealed the presence of the elements calcium (3538 ppm), zinc (883 ppm), and phosphorous (836 ppm). The beneficial tribological influence of the additives might additionally be promoted by laser-induced oxidation in the ambient atmosphere at the highly reactive titanium surface. This laser-induced surface oxidation was indicated in preliminary energy dispersive x-ray analyses (EDX). However, it must be underlined that the positive tribological effect is observed only for the joint action of laser processing (LSFL) and in the presence of the engine oil additives. Simple laser-induced surface hardening or oxidation effects can be ruled out here, as the effect was not observed in paraffin oil (free of additives).

HSFL

Analogous tribological tests were performed on titanium alloy surfaces covered by sub-100 nm laser-induced nanostructures (HSFL). The results are compiled in Fig. 7.4. In both lubricants large friction coefficients were observed, oscillating between 0.15 and 0.6, along with significant damage of the surface within the wear tracks (see the OM and SEM images). The HSFL do not improve the tribological performance (in contrast to the LSFL with engine oil). Supposedly, this is related to the reduced laser processing fluence which affects the superficial oxidation. Moreover, the HSFL modulation depth of a few tens of nanometers is significantly smaller than the elastic deformation depth of ~ 300 nm estimated by the HDM for titanium. Hence, we assume that the HSFL are less beneficial for the tribological performance (in both lubricants).

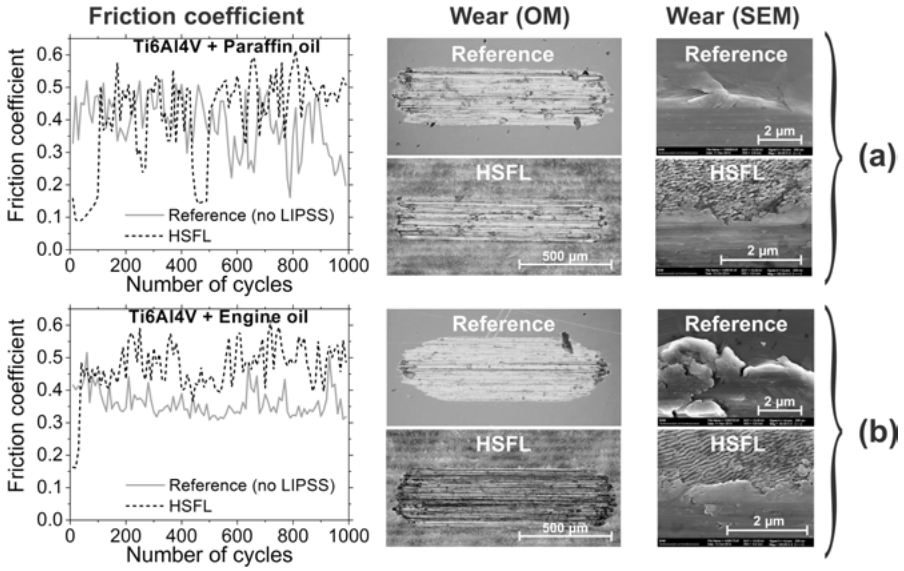

Fig. 7.4: Friction coefficient vs. number of sliding cycles (left) and the corresponding wear tracks of the HSFL covered Ti6Al4V titanium alloy surface tested in paraffin oil (a) and in engine oil (b). The middle column provides low-resolution optical micrographs, while the right column indicates high-resolution scanning electron micrographs. A reference measurement on the non-irradiated surface is provided for comparison.

Comparison of the materials

Table 7.1 summarizes the results of the RSTT performed for all four materials in paraffin oil and engine oil. The third column unites the measurements of the friction coefficient and indicates the upper and lower limits during the 1000 sliding cycles. The fourth column qualifies the wear behavior of the laser-nanostructured surfaces in comparison to the non-irradiated reference surface.

Tab. 7.1: Summary of the friction coefficient range and the wear behavior for the RSTT on four different materials and in two different lubricants. The wear column compares the wear track appearance with the corresponding reference track. Symbols and abbreviations: "–": more wear; "0", similar wear; "+": less wear; "++": significantly less wear.

Material	Lubricant	Friction coefficient [during 1000 cycles]	Wear [after 1000 cycles]	Literature
100Cr6	Paraffin oil	LSFL: 0.13–0.17	0	[34]
		HSFL not observed		
		Reference: 0.13–0.17		[34]
	Engine oil	LSFL: 0.13–0.17	0/+	[34]
		HSFL not observed		
		Reference: 0.13–0.17		[34]
X30CrMoN15-1	Paraffin oil	LSFL: 0.13–0.17	0	[36]
		HSFL not observed		
		Reference: 0.13–0.17		[36]
	Engine oil	LSFL: 0.11–0.14	0/+	[36]
		HSFL not observed		
		Reference: 0.11–0.14		[36]
Ti	Paraffin oil	LSFL: 0.12–0.65	–	[36]
		HSFL: 0.13–0.73	–	
		Reference: 0.12–0.55		[36]
	Engine oil	LSFL: 0.12–0.14	++	[36], this work
		HSFL: 0.15–0.75	–	
		Reference: 0.32–0.61		[36], this work
Ti6Al4V	Paraffin oil	LSFL: 0.14–0.6	–	[34], this work
		HSFL: 0.1–0.6	–	This work
		Reference: 0.16–0.6		[34], this work
	Engine oil	LSFL: 0.11–0.13	++	[34], this work
		HSFL: 0.15–0.6	–	This work
		Reference: 0.32–0.52		[34], this work

For both titanium materials (Ti and Ti6Al4V), the tribological performance of the surfaces with LSFL is superior in engine oil as lubricant (compared to paraffin oil). Hence, the alloying elements Al and V have no significant influence on the RSTT. They cannot account for the beneficial tribological behavior.

Although the roughness of both steel materials (100Cr6 and X30CrMoN15-1) was very different (factor 5) there is no significant impact on the tribological behavior in engine oil when compared to the paraffin oil (see Tab. 7.1). The positive tribological influence of the LSFL (as observed for the titanium materials) is much less pronounced on steel surfaces.

The same set of RSTT experiments (four metals, two lubricating oils) was repeated at a reduced normal force of 0.5 N, i.e., at the lower force limit of the home-made tribometer. Those measurements confirmed the results obtained at 1.0 N and are thus not listed here.

7.3.3 Optimization by laser beam shaping

Using a spatially Gaussian laser beam in the ablative regime, the linewise sample processing typically leads to a comb-like micrometer-sized surface structure which is superimposed onto the LIPSS topography (see WLIM topography shown in Fig. 7.2 (a)). This microstructure can easily provide height variations of a few hundred nanometers, which may even exceed the typical LIPSS modulation depths.

One way to reduce the height variations due to linear laser scanning is via *spatial beam shaping*, transforming the Gaussian laser beam into a top hat distribution. The impact on the laser ablation result is illustrated in Fig. 7.5. When strongly absorbing materials (such as metals) are processed by a Gaussian laser beam, in regions where the ablation threshold (ϕ_{th}) is locally surpassed, the topography typically follows a parabolic profile [42]. As a result, height variations are caused across the ablation region (see Figs. 7.5 (a) and 7.2 (a)). This effect can be significantly reduced when using a top hat beam (see Fig. 7.5 (b)).

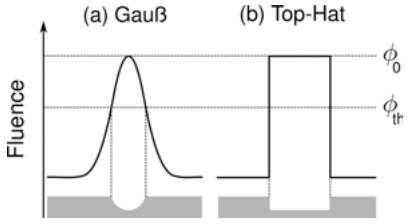

Fig. 7.5: Scheme of the laser processing with different spatially shaped beams (fluence profile and corresponding ablation topography). Gaussian laser beam (a), top hat laser beam (b).

In order to realize the spatial beam shaping experimentally (see setup illustrated in Fig. 7.6), the Ti:sapphire fs-laser pulses (800 nm, 80 fs, 100 Hz) were selected by an electromechanical shutter before passing through a programmable *spatial light modulator* (SLM) operated in reflection geometry (HOLOEYE PLUTO SLM, Berlin, Germany). The phase modulated (shaped) laser beam was then redirected by a mirror (M) and focused onto the sample surface by a spherical lens (L) with a focal length of 300 mm. A dielectric beam splitter (BS) and a CCD camera allowed the in situ monitoring of the laser beam profile in the focal region (sample surface). Using an adaptive beam shaping algorithm (Gerchberg-Saxton) [43, 44], the SLM was utilized to generate a top hat profile in the sample processing plane (see the example of the shaped beam profile in Fig. 7.6). The top hat-shaped beam profile is formed at the sample processing plane under optimized conditions by superposition and constructive interference of

the phase modulated partial waves. These waves are spatially selected and manipulated by beam shaping. In contrast to amplitude modulation techniques, laser pulse energy losses are reduced here. Upon meandering movement of the sample (motorized) under the spatially shaped top hat laser beam at a constant scan velocity and with an optimized line offset, square-shaped areas of $5 \times 5\,\mathrm{mm}^2$ covered homogeneously by LIPSS were again processed in a single pass in air environment.

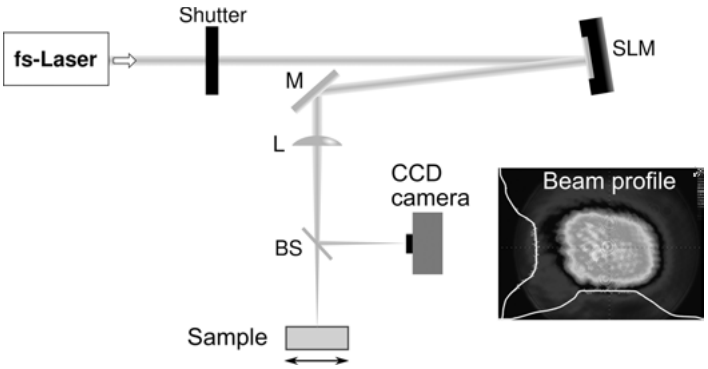

Fig. 7.6: Scheme of the experimental setup for laser processing with a top hat-shaped fs-laser beam. Abbreviations: SLM: spatial light modulator; M: mirror; L: lens; BS: beam splitter.

Figure 7.7 compares the WLIM surface topographies of a titanium surface processed with a Gaussian laser beam (a) and with a spatially shaped top hat beam (b), both with individually optimized processing conditions for the generation of LSFL. In both cases, SEM was used to confirm the homogeneous coverage of the surface by LSFL with periods around 600 nm. The laser treatment with a Gaussian beam shows periodic arrangement of individual ablation lines separated by 100 µm with height variations of ± 120 nm (see the cross-sectional line profile in the lower part of the Fig. 7.7 (a)). The residual surface height variations are reduced by a factor of 2–3 for processing with a spatially shaped top hat beam profile and account for less than ± 50 nm (see Fig. 7.7 (b)).

The tribological performance of the two titanium samples already shown in Fig. 7.7 was characterized by RSTT in engine oil. The results for the friction coefficient measured as function of the number of cycles are presented in Fig. 7.8 (a) for the sample processed with the Gaussian beam and in Fig. 7.8 (b) for the top hat-shaped beam treated specimen. In both cases, a reference measurement of the non-processed (polished) sample surface is added, which shows large friction coefficients between 0.3 and 0.6. In contrast, both fs-laser treated samples show very similar and almost constant friction coefficient values around 0.13 ± 0.01. However, direct comparison of the results indicates that the residual micrometer sized ablation line structures are not detrimental for the tribological performance here.

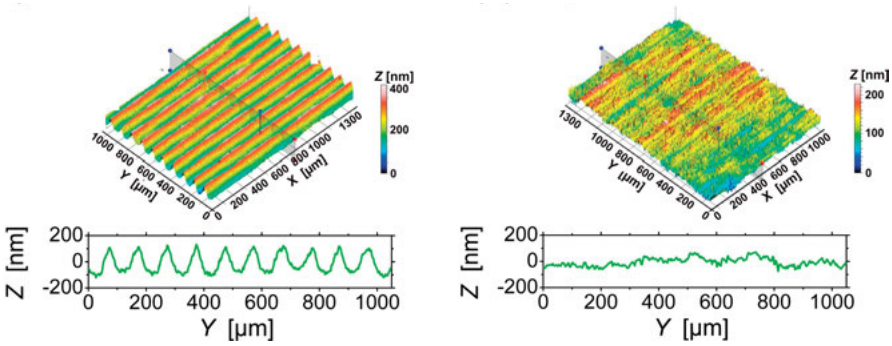

(a) Gauss (b) Top-Hat

Fig. 7.7: WLIM topography of the LSFL covered Ti surface processed under optimized conditions by a spatially Gaussian beam (a) and by a top hat laser beam (b).

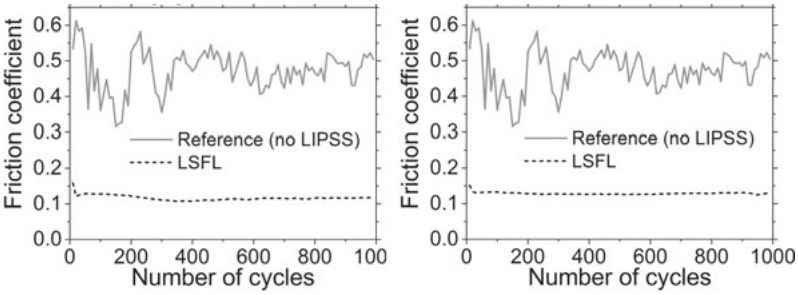

(a) Gauss (b) Top-Hat

Fig. 7.8: Friction coefficient vs. number of sliding cycles of the LSFL covered Ti surfaces previously characterized in Fig. 7.7 for a Gaussian (a) and a top hat laser beam (b). Both measurements were performed in engine oil.

7.4 Summary

Different types of LIPSS were homogeneously processed on $5 \times 5\,mm^2$ large surface areas on four different metals (two types of steel & two types of titanium materials). The respective surfaces were tribologically tested (reciprocal sliding against a 10 mm-100Cr6 ball: 1.0 N normal force, 1 mm stroke length, 1 Hz frequency, 1000 cycles) in two different lubricants (additive-free paraffin oil, and fully formulated engine oil) and the wear tracks were subsequently inspected. Under specific conditions (titanium material, engine oil), the nanostructures (LSFL) endured the tribological test and provided significantly reduced friction coefficients and almost no wear when compared to the non-irradiated (polished) surfaces. The effect in the nanostructured areas was attributed to additives contained in the engine oil forming a gliding interlayer preventing intermetallic contact, and might additionally be promoted by laser-induced

superficial oxidation. The presence of individual ablation lines after processing with a spatially Gaussian laser beam did not significantly affect the tribological performance. Sub-100 nm structures (HSFL) did not show a reduction of the friction coefficient. On steel surfaces the positive tribological impact of the LSFL is much less pronounced.

Acknowlegments

The authors would like to thank N. Slachciak (BAM 6.3) for help with the tribological tests, S. Benemann (BAM 6.8) and M. Tischer (MBI) for SEM characterizations, M. Weise (BAM 6.7) for WLIM measurements, and S. Binkowski and M. Scheibe (both BAM 6.3) for polishing titanium samples. The help of Dr. A. Mermillod-Blondin (MBI) in setting up the SLM is gratefully acknowledged. This work was supported by the German Science Foundation (DFG) under grant nos. RO 2074/7-2 and KR 3638/1-2.

References

[1] Birnbaum M. Semiconductor surface damage produced by ruby lasers. J Appl Phys 1965, 36, 3688–3689.
[2] van Driel HM, Sipe JE, Young JF. Laser-induced periodic surface-structure on solids – a universal phenomenon. Phys Rev Lett 1982, 49, 1955–1958.
[3] Bonse J, Krüger J, Höhm S, Rosenfeld A. Femtosecond laser-induced periodic surface structures. J Laser Appl 2012, 24, 042006.
[4] Costache F, Henyk M, Reif J. Surface patterning on insulators upon femtosecond laser ablation. Appl Surf Sci 2003, 208–209, 486–491.
[5] Huang M, Zhao F, Cheng Y, Xu N, Xu Z. Origin of laser-induced near-subwavelength ripples: interference between surface plasmons and incident laser. ACS Nano 2009, 3, 4062–4070.
[6] Obara G, Maeda N, Miyanishi T, Terakawa M, Nedyalkov NN, Obara M. Plasmonic and Mie scattering control of far-field interference for regular ripple formation on various material substrates. Opt Express 2011, 19, 19093–19103.
[7] Skolski JZP, Römer GRBE, Obona JV, Ocelik V, Huis in't Veld AJ, De Hosson JTM. Laser-induced periodic surface structures: fingerprints of light localization. Phys Rev B 2012, 85, 075320.
[8] Tsibidis GD, Barberoglou M, Loukakos PA, Stratakis E, Fotakis C. Dynamics of ripple formation on silicon surfaces by ultrashort laser pulses in subablation conditions. Phys Rev B 2012, 86, 115316.
[9] Höhm S, Rosenfeld A, Krüger J, Bonse J. Femtosecond diffraction dynamics of laser-induced periodic surface structures on fused silica. Appl Phys Lett 2013, 102, 054102.
[10] Derrien TJY, Krüger J, Itina TE, Höhm S, Rosenfeld A, Bonse J. Rippled area formed by surface plasmon polaritons upon femtosecond double-pulse irradiation of silicon: the role of carrier generation and relaxation processes. Appl Phys A 2014, 117, 77–81.
[11] Borowiec A, Haugen HK. Subwavelength ripple formation on the surfaces of compound semiconductors irradiated with femtosecond laser pulses. Appl Phys Lett 2003, 82, 4462.
[12] Bonse J, Munz M, Sturm H. Structure formation on the surface of indium phosphide irradiated by femtosecond laser pulses. J Appl Phys 2005, 97, 013538.

[13] Vorobyev AY, Makin VS, Guo C. Periodic ordering of random surface nanostructures induced by femtosecond laser pulses on metals. J Appl Phys 2007, 101, 034903.
[14] Bonse J, Rosenfeld A, Krüger J. On the role of surface plasmon polaritons in the formation of laser-induced periodic surface structures upon irradiation of silicon by femtosecond-laser pulses. J Appl Phys 2009, 106, 104910.
[15] Sipe JE, Young JF, Preston JS, van Driel HM. Laser-induced periodic surface structure. I. Theory. Phys Rev B 1983, 27, 1141–1154.
[16] Bonch-Bruevich AM, Libenson MN, Makin VS, Trubaev VV. Surface electromagnetic-waves in optics. Opt Eng 1982, 31, 718–730.
[17] Dufft D, Rosenfeld A, Das SK, Grunwald R, Bonse J. Femtosecond laser-induced periodic surface structures revisited: A comparative study on ZnO. J Appl Phys 2009, 105, 034908.
[18] Martsinowskii GA, Shandybina GD, Smirnov DS, Zabotnov SV et al. Ultrashort excitations of surface polaritons and waveguide modes in semiconductors. Opt Spectroscop 2008, 105, 67–72.
[19] Straub M, Afshar M, Feili D, Seidel H, König K. Surface plasmon polariton model of high-spatial frequency laser-induced periodic surface structure generation in silicon. J Appl Phys 2012, 111, 124315.
[20] Derrien TJY, Koter R, Krüger J, Höhm S, Rosenfeld A, Bonse J. Plasmonic formation mechanism of periodic 100-nm-structures upon femtosecond laser irradiation of silicon in water. J Appl Phys 2014, 116, 074902.
[21] Vorobyev AY, Guo C. Colorizing metals with femtosecond laser pulses. Appl Phys Lett 2008, 92, 041914.
[22] Dusser B, Sagan Z, Soder H, Faure N, Colombier JP, Jourlin M, Audouard E. Controlled nanostructures formation by ultrafast laser pulses for color marking applications. Opt Express 2010, 18, 2913–2924.
[23] Groenendijk MNW, Meijer J. Surface microstructures obtained by femtosecond laser pulses. CIRP Annals 2006, 55, 183–186.
[24] Qi L, Nishii K, Namba Y. Regular subwavelength surface structures induced by femtosecond laser pulses on stainless steel. Opt Lett 2009, 34, 1846–1848.
[25] Hou S, Huo Y, Xiong P et al. Formation of long- and short-periodic nanoripples on stainless steel irradiated by femtosecond laser pulses. J Phys D: Appl Phys 2011, 44, 505401.
[26] Bonse J, Höhm S, Rosenfeld A, Krüger J. Sub-100 nm laser-induced periodic surface structures upon irradiation of titanium by Ti:sapphire femtosecond laser pulses in air. Appl Phys A 2013, 110, 547–551.
[27] Zorba V, Stratakis E, Barberoglou M, Spanakis E, Tzanetakis P, Fotakis C. Tailoring the wetting response of silicon surfaces via fs structuring. Appl Phys A 2008, 93, 819–825.
[28] Mizuno A, Honda T, Kiuchi J, Iwai Y, Yasumaru N, Miyazaki K. Friction properties of the DLC film with periodic structures in nano-scale. Tribol Online 2006, 1, 44–48.
[29] Yasumaru N, Miyazaki K, Kiuchi J. Control of tribological properties of diamond-like carbon films with femtosecond-laser-induced nanostructuring. Appl Surf Sci 2008, 254, 2364–2368.
[30] Yasumaru N, Miyazaki K, Kiuchi J, Sentoku E. Frictional properties of diamond-like carbon, glassy carbon and nitrides with femtoseond-laser-induced nanostructure. Diamond Relat Mater 2011, 20, 542–545.
[31] Pfeiffer M, Engel A, Gruettner H, Guenther K, Marquardt F, Reisse G, Weissmantel S. Ripple formation in various metals and super-hard tetrahedral amorphous carbon films in consequence of femtosecond laser irradiation. Appl Phys A, 2013, 110, 655–659.
[32] Eichstädt J, Römer GRBE, Huis in't Veld AJ. Towards friction control using laser-induced periodic surface structures. Phys Procedia 2012, 12, 7–15.

[33] Chen CY, Chung CJ, Wu BH et al. Microstructure and lubricating property of ultra-fast laser pulse textured silicon carbide seals. Appl Phys A 2012, 107, 345–350.
[34] Bonse J, Koter R, Hartelt M, Spaltmann D, Pentzien S, Höhm S, Rosenfeld A, Krüger J. Femtosecond laser-induced periodic surface structures on steel and titanium alloy for tribological applications. Appl Phys A 2014, 117, 103–110.
[35] Sawada Y, Sawada H, Hirayama T, Tomita N. Tribological performance of femtosecond laser-induced periodic surface structures, J Bone Joint Surg Br 2012, 94-B, 161
[36] Bonse J, Koter R, Hartelt M, Spaltmann D, Pentzien S, Höhm S, Rosenfeld A, Krüger J. Femtosecond laser-induced periodic surface structures on titanium and a high toughness bearing steel. Appl Surf Sci 2014, http://dx.doi.org.10.1016./j.apsusc.2014.08.111, in press.
[37] Bonse J, Mann G, Krüger J, Marcinkowski M, Eberstein M. Femtosecond laser-induced removal of silicon nitride layers from doped and textured silicon wafers used in photovoltaics. Thin Solid Films 2013, 542, 420–425.
[38] Fouvry S, Paulin C. An effective friction energy density approach to predict solid lubricant friction endurance: Application to fretting wear. Wear 2014, 319, 211–226.
[39] Meine K, Schneider T, Spaltmann D, Santner E. The influence of roughness on friction – Part I: The influence of a single step. Wear 2002, 253, 725–732.
[40] Meine K, Schneider T, Spaltmann D, Santner E. The influence of roughness on friction – Part II: The influence of multiple steps. Wear 2002, 253, 733–738.
[41] Czichos H, Habig KH. Tribologie-Handbuch: Tribometrie, Tribomaterialien, Tribotechnik. 3rd ed. Wiesbaden, Germany, Teubner-Vieweg Verlag, 2010.
[42] Bonse J. All-optical characterization of single femtosecond laser-pulse-induced amorphization in silicon. Appl Phys A 2006, 84, 63–66.
[43] Gerchberg RW, Saxton WO. A practical algorithm for the determination of phase from image and diffraction plane pictures. Optik 1972, 35, 237–241.
[44] Sanner N, Hout N, Audouard E, Larat C, Huignard JP, Loiseaux B. Programmable focal spot shaping of amplified femtosecond laser pulses. Opt Lett 2005, 30, 1479–1481.

Part II: **Biomedical applications**

A. Uchugonova, H. G. Breunig, C. Augspurger, M. Monaghan,
K. Schenke-Layland, and K. König

1 Optical reprogramming and optical characterization of cells using femtosecond lasers

Abstract: Stem cell research attracts considerable attention in developmental biology, nanobiotechnology, and medicine. Since Maksimow's landmark hypothesis on stem cells in 1909, hundreds of thousands of reports have been published in biology, medicine and biotechnology regarding stem cells, evidence of their considerable worth as a major research subject.
Artificial stem cells such as 'induced pluripotent stem cells' (iPS cells), which morphologically and functionally resemble embryonic stem cells have been generated through the reprogramming of somatic cells for research purposes. Typically, optical techniques such as light microscopy in combination with fluorescent markers are applied, sometimes accompanied with fluorescence-activated cell sorting (FACS), to characterize and isolate both tissue-specific stem and iPS cells. To date, modern laser-based techniques such as nonlinear multiphoton microscopy and optical transfection using femtosecond lasers are only used in a few laboratories. The application of innovative femtosecond laser techniques in stem cell research shall be the subject of this chapter. Of particular focus is the application of femtosecond laser microscopy (i) for imaging and characterization of stem cells with high spatial sub-cellular resolution; (ii) as a nanoscalpel for optical cleaning; and (iii) for transfection and optical reprogramming of cells.

1.1 Stem cells and iPS cells

Stem cells are now considered significantly potent in terms of their adaptability in the generation of cells and tissues for the purpose of transplantation therapies. Stem cell research also furthers the understanding of mammalian development, the onset of diseases, and the development of pharmaceuticals.

Stem cells were first discovered within fully developed tissues or organs in the adult body, and became known as either adult, somatic, or tissue-specific stem cells.

These uncommitted cells have been found to be capable of self-renewal and can give rise to specialized cell lineage under defined conditions. Hematopoietic stem cells can be isolated from peripheral and umbilical cord blood, and also within bone marrow [1]. A number of different tissues such as bone, skin, muscle, adipose, and cartilage, are all abundant sources of mesenchymal stem cells [2–7]. Neural stem cells have successfully been isolated from different parts of the brain. Stem cells have also been found in human hair, the retina, teeth, skin, lungs, the liver [8, 9], and glands such as the thyroid, salivary, and pancreas [10–12]. Regardless of their presence in numerous

anatomical locations, adult stem cells are scarce in tissues, so their use is limited to the application of replacement therapies.

Being 'multipotent', adult stem cells are capable of differentiating into specific cells within isolated tissues. Under laboratory conditions, directed differentiation can be achieved by stimulation with certain factors and cytokines. Successfully differentiated cells can be evaluated by their morphology, function, and gene profiles.

Differentiation of cells may be induced by diverse biological, chemical, and physical factors, for example nano-/microstructuring of culture devices, mechanical stress, vibration, temperature, light, pressure, and electrical fields [13–18]. It is also hypothesized that laser-induced differentiation is possible, but not yet proven.

The discoverers of embryonic stem cells (ES cells) were awarded the Nobel Prize in 2007. Embryonic stem cells were first isolated in 1981 from mice [19, 20] and human embryonic stem cells in 1998 [21] from an *in vitro* fertilized blastocyst. These stem cells are "pluripotent", and can generate differentiated cells from all three germ layers: meso-, endo- and ectoderm. However, only the fertilized egg is known as a totipotent cell and therefore able to generate all of the cells/tissues of the developing embryo. Since ES cell research or even the use of ES cells for therapies consumes embryos, this approach is ethically highly controversial. An additional problem of ES-based therapies is the necessity for immunogenetic compatibility which limits the use of ES cells.

An alternative to ES cells are induced pluripotent stem cells (iPS), generated by Yamanaka and Takahashi in 2006, who received the Nobel Prize in 2012 for this achievement [22]. They demonstrated that the introduction of the transcription factors Oct4, Sox2, c-Myc, and Klf4 stimulated fibroblasts into becoming iPS cells. This breakthrough event has taken stem cell research to the next level, where generated iPS cells can be unrestrictedly used to produce differentiated cells. Currently, iPS cells have been generated from different somatic cells such as peripheral blood cells [23, 24], hepatocytes, keratinocytes, oral mucosa, umbilical cord blood as well as dental pulp cells from different species such as mice, rats, monkeys, pigs, dogs, rabbits, and humans, although levels of generation efficiency vary.

Typically, retro/lenti viruses are used to deliver and facilitate the integration of transcription factors into the host genome. In order to avoid the random integration of genes and subsequent mutations induced by the virus, attempts in reprogramming via proteins, mRNA, DNA, episomal plasmids, and various small molecules have also been tested. The low efficiency and toxicity of the approaches implemented are still the biggest concerns.

Here, we report on a new alternative to conventional reprogramming approaches: optical reprogramming based on femtosecond lasers (Fig. 1.1).

Adult stem cells and ES/iPS cells have been tested on both human and animal models for therapeutic purposes. Notably, tumorigenicity of ES/iPS cells has been reported on transplantation [25, 26]. Controlling and monitoring the growth, proliferation, and differentiation of stem cells before and on transplantation is of great importance and would necessitate non-invasive imaging techniques. Multiphoton tech-

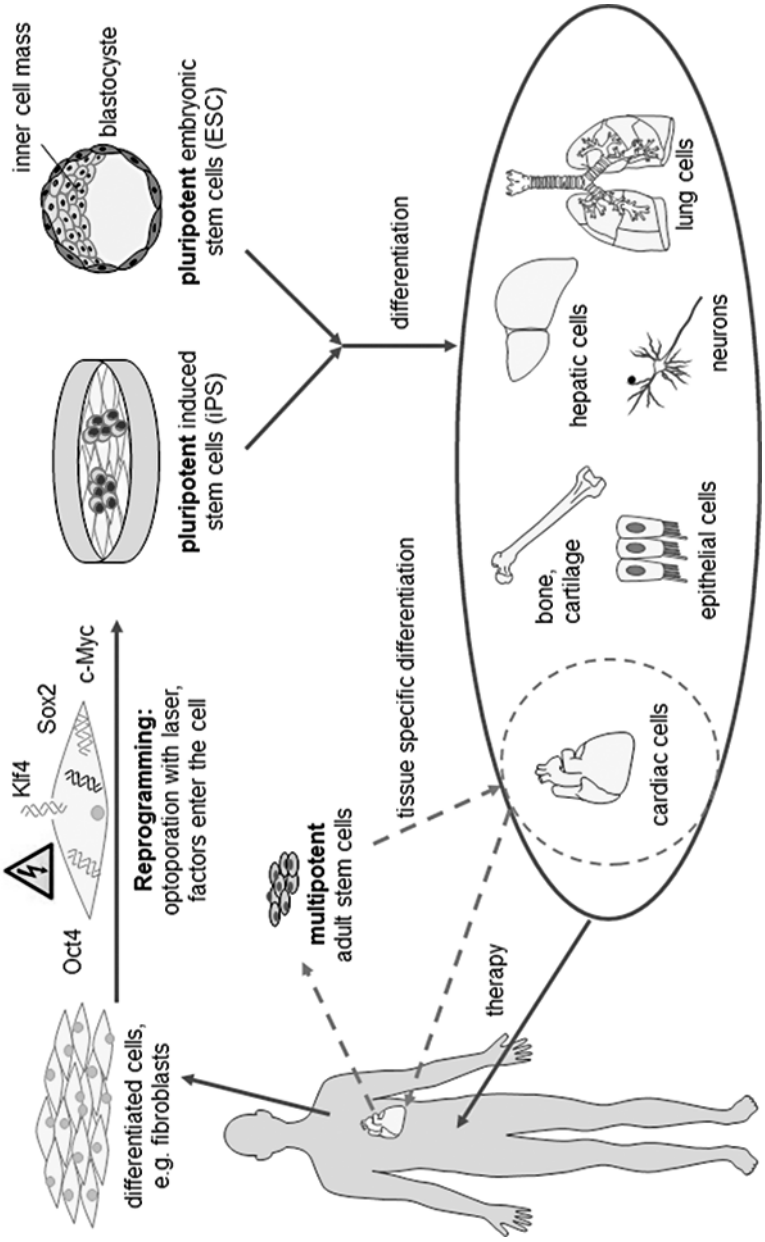

Fig. 1.1: Schematic presentation of reprogramming by optoporation to generate stem cell sources for regenerative therapies.

niques allow the monitoring of cells in physiological conditions for longer periods of time.

Furthermore, optical micro- and nanoprocessing techniques are of high interest if they can be applied for selective destruction of undesired cells (optical cleaning), as well as for virus-free transfection/reprogramming.

1.2 5D two-photon imaging and nanoprocessing microscopes

Multiphoton microscopy which uses nonlinear absorption to excite fluorophores has become an indispensable tool in biological and medical research including stem cells as a means of non-invasive imaging technology [27]. Multiphoton microscopy currently employs near-infrared light (NIR) femtosecond lasers. The principle on which multiphoton excitation is based is the simultaneous absorption of multiple low energy NIR photons. Excitation only occurs in the focal region due to the high GW/cm^2 light intensity which results in neither photobleaching nor damage in out-of-focus regions. High-resolution optical sectioning can be performed at high penetration depths due to the low scattering and absorption of near-infrared light in the range of 670–1300 nm, where most unstained cells/tissues appear transparent. Merging a stack of subsequent images can produce a 3D image. Multicolor imaging can also be realized due to the broad multiphoton absorption bands of multiple fluorophores. Multiphoton microscopy has been used for *in vivo* stem cell tracking, particularly hair follicle stem cells within the hair shaft [28]. Multiphoton microscopy in combination with spectral (4D) and fluorescence lifetime (5D) imaging (FLIM), has been used to study metabolic heterogeneity of mice as well as human stem cells while keeping samples under physiologically sustainable conditions without any additional labeling [29–32]. Natural fluorophores such as NADH, flavins/flavoproteins can be utilized as contrast agents and labeling of therapeutically valuable cells can be avoided. In addition to multiphoton fluorescence, multiphoton microscopy enables second harmonic generation (SHG) imaging, whereby two photons interact simultaneously with non-centrosymmetrical structures and generate coherent radiation at exactly half of the excitation wavelength. In this case, photobleaching and photodamage are avoided due to the absence of light absorption. Collagen-producing stem cells have been monitored during differentiation without any external labeling [30]. The organization and development of the extracellular matrix protein, i.e. collagen, can be investigated within a 3D natural environment due to SHG formation. Artifacts resulting from staining and fixation procedures can be avoided. Taking advantage of the marker-free NIR multiphoton microscopy technique, the stem cells can be imaged over long periods of time without photo-destructive effects. However, certain laser exposure parameters are important for the safe and non-destructive observation of living specimens which are mainly defined through light intensity thresholds and the wavelength of the NIR laser light [33–35].

Furthermore, highly focused multiphoton absorption can also be used as a nanoprocessing tool when increasing light intensity (4–5 photon absorption) which ultimately results in the optical breakdown following the formation of plasma.

Both cuts with incisions and holes with diameters of less than 100 nm were achieved within white blood cells while using the same ultrashort femtosecond laser pulses (Fig. 1.2).

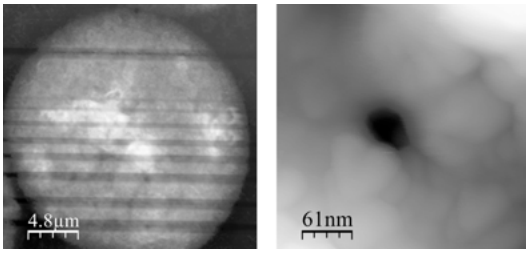

Fig. 1.2: AFM images of white blood cells after laser nanosurgery. Cuts with incisions as well as holes with diameters of sub-100 nm can be realized with the ultrashort fs laser pulses.

In this chapter, the aim shall be to cover current applications of multiphoton microscopy in combination with FLIM (Fluorescence Lifetime Imaging Microscopy), which is used to characterize stem cells. Moreover, additional roles of femtosecond microscopes in optoporation, optical cleaning, and single cell isolation are reported on.

1.2.1 Setup of 5D femtosecond laser microscopes

In most laboratories, tunable solid state 80/90 MHz titanium:sapphire lasers as "turnkey" laser sources (670–1060 nm; *Chameleon* from Coherent, USA, *MaiTai* from Newport/Spectra Physics, USA), or lasers with a fixed wavelength of 800 or 760 nm are used (*Integral Pro* from Femtolasers, *Vitesse* from Coherent). The laser is combined with an *x*-*y* scanning module, which is used to scan the target with the aforementioned highly focused laser beam. In addition, beam expander, attenuator, trigger supply, shutter control unit, and highly sensitive photomultipliers for the detection of fluorescence/SHG signals are applied. A CCD camera attached to the side port enables on-line monitoring of the cells and the laser beam especially during optical cleaning and transfection procedures.

In this chapter, we focus on an extremely ultrashort femtosecond laser (< 10 fs; Femtolasers Produktions GmbH, Vienna, Austria) microscope (JenLab GmbH, Jena, Germany; detailed description of the 12 fs laser microscope can be found in Chapter I.1) equipped with a motorized stage and a piezosystem (MIPOS 5, Piezosystems Jena, Germany) in order to change x, y focal plane and z, respectively (Fig. 1.3).

The microscope was used in the two-photon fluorescence excitation mode at mean powers in the microwatt range for nondestructive imaging of stem cells of interest as well as in the milliwatt range for nanoprocessing. Three exposure modes are available:

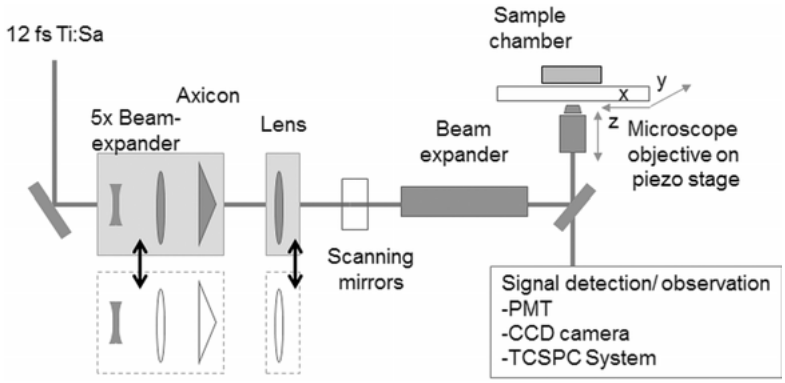

Fig. 1.3: Schematic overview of the 5D 12 fs microscope for nanoprocessing and two-photon imaging.

(i) frame mode used for imaging; (ii) scanning of a region of interest (ROI), mostly used for optical cleaning; and (iii) single point illumination used for transfection.

A 16-channel photomultiplier module (Becker & Hickl GmbH) with fast rise time attached to the front port was employed for spectral and fluorescence lifetime imaging (spectral-FLIM) in 5D (Fig. 1.4). Time-correlated single photon counting (TCSPC) was performed to obtain photon numbers as well as information on the arrival time of fluorescence photons. The temporal resolution was 250 ps. The beam splitter HFT KP 640 DCXRSP and the short pass filter KP 680SP were employed for two-photon imaging. Additionally, a quasi-Bessel beam, enabling automation of this technique for transfection, can be generated through the integration of an axicon lens into the laser scanning microscope system (Section 1.2.2).

1.2.2 Bessel beam setup

The number of cells addressable by optical cell transfection is limited because every single cell has to be individually targeted and the laser focus height adjusted to the position of the cell membrane. One method of making the height adjustment unnecessary is to exploit extended focal geometries by generating a quasi-Bessel beam, where the lateral intensity pattern is described by a Bessel function of the first kind, i.e. by concentric rings, and the axial focus range is elongated compared to a Gaussian focal volume [36]. We integrated an axicon lens into our laser scanning microscope system to generate such a quasi-Bessel beam behind the microscope objective. A schematic overview of the experimental setup is given in Fig. 1.3. To generate the quasi-Bessel beam shape, the laser beam diameter was expanded 5× and subsequently focused by an axicon lens (Thorlabs, opening angle 0.05°). A Fourier lens was placed behind the axicon such that in combination with a further beam expander, the beam diameter

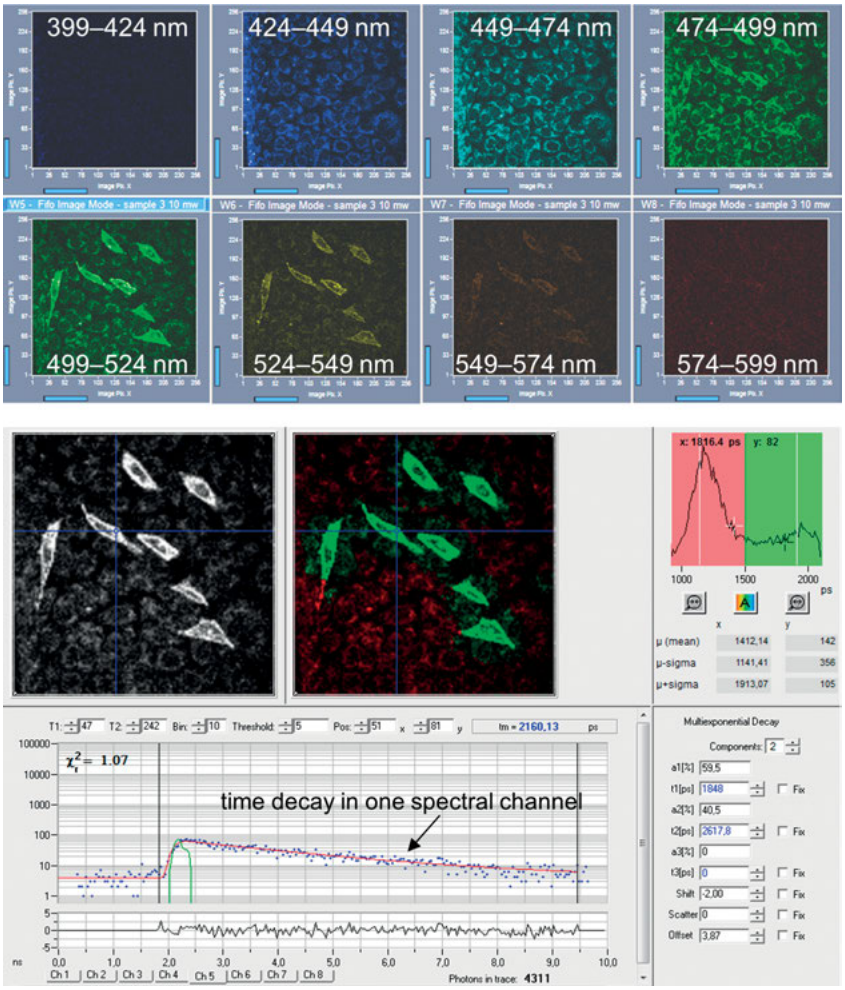

Fig. 1.4: Spectral-FLIM image obtained from single transfected cells (bright green: GFP-cells). Non-transfected cells imaged by autofluorescence. Optical sections can be acquired with spectral information (above) and fluorescence lifetimes (below).

matched the entrance aperture of the objective (40×, 1.3 NA). All optical components for the generation of the quasi-Bessel beam shape were placed onto a motorized linear translation stage to enable fast switching between Gaussian and Bessel beam shapes. Fluorescent sub-resolution 50 nm spheres (Fluoresbrite, Polysciences Inc.) were used to determine point spread functions (PSF) by evaluating fluorescence intensity profiles. The focal beam shape was directly characterized by optical drilling into cell nuclei samples, which were measured by atomic force microscope (AFM) afterwards.

To illustrate the extent of the focal regions of Gaussian and Bessel shaped beams, two-photon fluorescence of fluorescein solution was imaged at an angle of 90° from the side with a CCD camera (Fig 1.5 (a)). The intensity profiles along the beam axis can be derived from the images shown in Fig. 1.5 (b). The two-photon focal region of the Bessel shaped beam is about 250 µm long for a laser power of 230 mW behind the objective. The inset in (a) shows the region of the maximum intensity, which indicates an intensity change of < 20 % over ~ 150 µm along the axis. Note that the intensity profile of the Gaussian beam shape does not accurately represent the two-photon excitation volume due to the limited camera resolution. The minimal PSF in radial direction of the focal volumes with quasi-Bessel beam and Gaussian shape (0.66 µm and 0.50 µm, respectively) are shown in Fig. 1.5 (c). The PSFs were determined from line profiles two-photon images of a sub-resolution 50 nm nanosphere and fitted with Gaussians fitting curves. From Fig. 1.5 (a) it is also apparent that the FWHM of the radial PSF is almost constant over a range of several tens of µm (although an axial dependence exists). To exemplify imaging by laser scanning imaging in the extended focal region, two-photon fluorescence images from a single 50 nm nanosphere for different positions along the beam axis (*z* axis) are shown in Fig. 1.5 (d) An example for the direct determination of the radial *in situ* beam extension is shown in Fig. 1.5 (e), which depicts an AFM image of a fixed cell nucleus which was drilled by a quasi-Bessel shape beam incident from below.

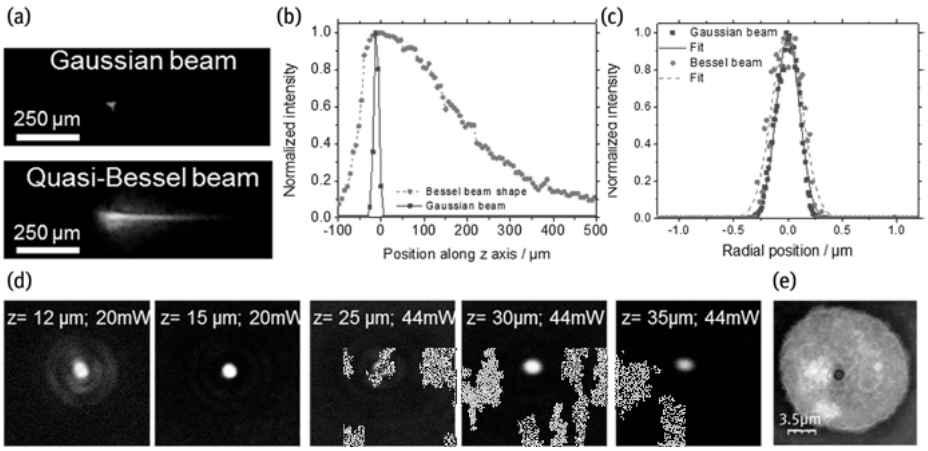

Fig. 1.5: Two-photon fluorescence of fluorescein excited by laser beams with Gaussian and Bessel shaped focal regions. The laser pulses were incident from the left side. (b) Intensity profiles along the beam direction. (c) PSF of a fluorescent 50 nm nanosphere. (d) Two-photon fluorescence images of a single 50 nm nanosphere for different z positions along the beam axis. (e) AFM image of a cell nucleus with a hole drilled by a quasi-Bessel shaped beam.

1.3 Femtosecond laser transfection

High differentiation efficiency of stem cells and reprogramming of somatic cells can be achieved via insertion of a combination of appropriate genes into the genome. Since non-viral gene vectors (pDNA, siRNA) are repelled by the cell membrane, the delivery of non-viral vectors is a key area of research. Different approaches have been applied to permeate the cell membrane transiently, so as to assist penetration of the genes into the cytoplasm and further into the nucleus. A variety of methods have been applied such as chemical (DEAE-dextran, calcium phosphate, and liposome-mediated transfection), physical (electroporation, magnet-assisted transfection, DNA guns, ultrasound, and microinjection), as well as biological methods involving viruses [37]. However, the issue of cytotoxicity associated with chemical substances is problematic. Electrical fields, ultrasound waves, DNA guns, and microinjections may all cause irreversible damage which terminates cell life. Transfection efficiency and gene expression following integration vary, depending on the transfection methods used. The delivery of genes through viruses is one of the most efficient methods. However viruses can only carry limited DNA sequences and there are concerns regarding immunogenicity and potential mutagenicity.

An alternative method, optical transfection, was demonstrated by several groups. Both UV and visible lasers have been applied, allowing for the diffusion of extracellular foreign genes into cytoplasm [38–41]. However, laser beams within these wavelength ranges cause problems due to heating effects, DNA strand damage, and destructive photochemical UV effects [42, 43]. The first targeted femtosecond laser transfection of adherent cells was demonstrated by Tirlapur and König [44]. Due to the cell's innate self-repair mechanism, transient pores in the cell membrane of the targeted cell of interest can be created by highly focused femtosecond laser beams in the NIR range. Genes or vectors can then enter the cell. Femtosecond laser transfection provides a sterile and non-toxic transfection. Furthermore, a high post-transfection efficiency was reported [45, 46]. Highly focused femtosecond laser radiation delivers extremely high light intensities which are able to create micro- and nanoholes without any collateral damage [47]. Femtosecond ablation occurs only within the high focal volume; therefore it demands high expertise and precision. Bessel beams with elongated focus can circumvent problems related to focusing. Concurrently, a single cell approach is highly selective but very time consuming. Recently our group developed semi-automated software systems which yield transfection of up to 200 cells per minute [48]. Figure 1.6 demonstrates Bessel-beam transfected cells.

A high cell flow femtosecond transfection system has also been realized. This system allows for a significantly larger amount of non-adherent cells to be transfected in cell suspensions [49].

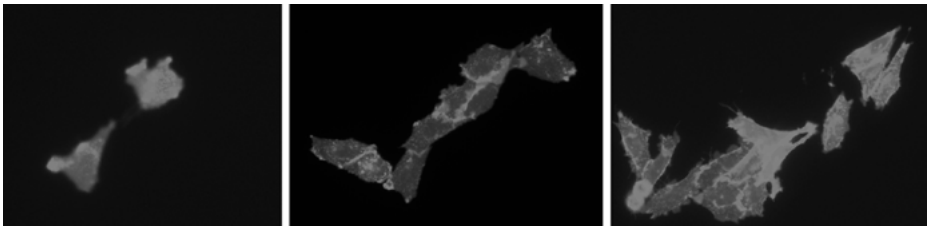

Fig. 1.6: Cell transfection with femtosecond laser pulses. The transfection was carried out with a plasmid vector of pAcGFP1-MEM applied directly into the medium. A laser radiation exposure time of 100 ms was applied. The GFP expression was monitored in several cell generations (up to 1 week), indicating the successful fs laser transfection. Cell proliferation and growth was also stable.

1.4 Optical reprogramming of murine cells

Here, we describe the application of femtosecond laser nanoprocessing for reprogramming of murine cells. We aimed for direct reprogramming (also known as transdifferentiation). Direct reprogramming means the transformation of a differentiated cell into another cell type without generating pluripotent iPS cells. This reprogramming method is a fast way to generate functional cell types without the risk of generating potentially tumorigenic induced pluripotent stem cells.

Mouse embryonic fibroblasts (MEFs) were isolated from C57/BL6 mouse embryos of gestational age E12.5 and cultured on gelatin-coated glass-bottom dishes with grid lines for easier relocalization at later points in time. Reprogramming medium was used according to Efe et al. [50]. A defined low glucose DMEM was used as cardiomyogenic medium. Single cells were selected and assigned to their grid location and treated with laser pulses in order to permeabilize the cell membrane. A cocktail of plasmids (TBX5, GATA4, and Mef2C) was utilized to realize direct reprogramming of genetically-engineered MEFs with an intrinsic GFP-gene coupled to the alpha-myosin heavy-chain gene (αGFP-MEF). Therefore, these cells show GFP expression and green fluorescence upon expression of α-myosin heavy-chain, which then indicates successful reprogramming towards a cardiomyocyte like state. As control for each group we used non-transfected αGFP-MEFs which were treated with the same media, as well as cells that were transfected non-optically with the chemical reagent lipofectamine.

As demonstrated in Fig. 1.7, lipofectamine-transfected cells showed a weak green fluorescence in all cells. However, laser-transfected cells resulted in a strong GFP emission of some laser-exposed cells as a result of targeted transfection and reprogramming towards a cardiomyocyte-like state.

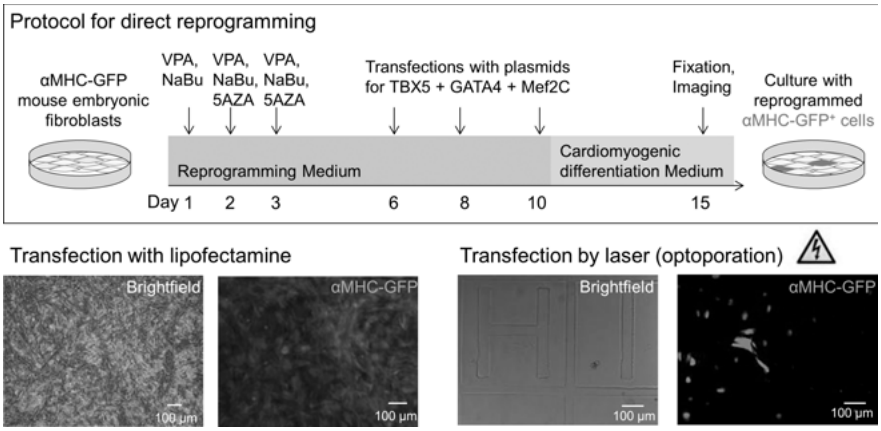

Fig. 1.7: Direct reprogramming of murine cells. Reprogrammed αGFP-MEF cells treated with different media (reprogramming medium I and II) and transfected with lipofectamine and laser.

1.5 Optical reprogramming of human cells

The artificial generation of human iPS cells with a similar differentiation potential to human embryonic stem cells offers the possibility of using the patient's own cells for replacement therapies, thus minimizing problems associated with immune compatibility [51, 52].

The initial iPS generation was realized through viral transduction of the four transcriptional factors OCT4, Sox2, Klf4, and c-Myc [53]. However, the use of viruses may result in insertional mutations, caused by the random integration of genes and therefore this may limit the use in clinical applications due to the risk of cancer formation. Recent studies have shown that iPS cells generated by means of retroviral viruses generate teratomas [54]. Meanwhile non-viral, non-optical transfection methods such as lipofectamine administration and electroporation have been applied to introduce micro-RNA, episomal plasmids as well as minicircle DNA plasmids into the cell so as to generate iPS cells. Typically, serial transfections (between three and twenty) should be done to achieve the sustained expression of genes required for the iPS cell generation. Therefore, the efficient transfection approach for reprogramming is one of the key issues apart from culture conditions (medium, O_2 tension, small molecules), transgenes, and donor cells.

We demonstrate an optical method of realizing the non-viral delivery of reprogramming factors. Ultrashort femtosecond laser transfection is a contamination-free non-contact method and enables a high post-transfection survivability [55]. The controllable delivery of exogenous plasmids into cells can be realized, and in doing so ultrashort femtosecond laser transfection is a potential method to reprogram cells.

We demonstrated the delivery of a plasmid cocktail consisting of the transcription factors Oct4, Sox2, Nanog, and Lin28 as well as a GFP plasmid (minicircle DNA, [56]) into human dermal fibroblasts (hDF) using 12 fs laser pulses at 80 MHz repetition rate. Cells were exposed to laser radiation by focusing the light onto the cell's membrane. After laser exposure, cells were placed in an incubator and checked daily for the occurrence of GFP fluorescence. Figure 1.8 shows human dermal fibroblasts generated GFP-expressing, dome-shaped iPS cell-like colonies with ~ 100 µm diameter from 5 days post-exposure following an optical transfection procedure.

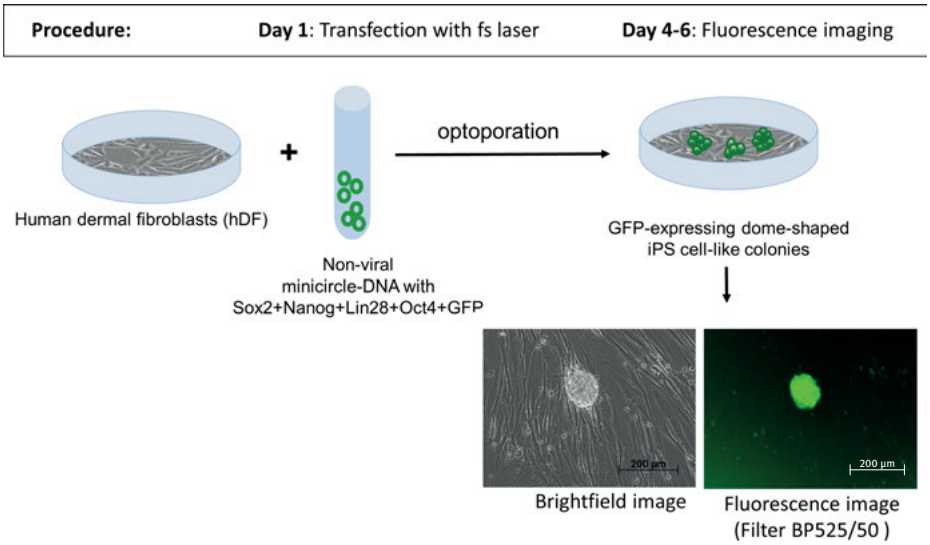

Fig. 1.8: Transfected cells expressed GFP and formed dome-shaped colonies on days 4–6 following laser transfection.

1.6 Fluorescence lifetime imaging

Fluorescence lifetime imaging microscopy (FLIM) was introduced to the life sciences 20 years ago [57] and became an indispensable tool for the study of cellular metabolic processes and protein-protein interactions [58–61].

Fluorescence lifetime is a signature of a molecule and refers to the time a fluorophore spends in the excited state before returning to the ground state by emitting a photon following excitation. The fluorescence lifetime depends strongly on the microenvironment and binding sites of molecules, but is ultimately independent of the fluorophore concentration and the illumination intensity [62]. The fluorescence lifetime may change as a result of the interaction with other molecules and therefore allows for the study of the binding status of fluorophores. Multiphoton excitation is suit-

able for the excitation of natural fluorophores (autofluorescence) with an absorption band in the UV/blue range. Important metabolic coenzymes nicotinamide adenine dinucleotide (NADH) and flavin adenine dinucleotide (FAD), which are involved in cellular respiration processes, possess autofluorescence. Two distinct lifetimes for NADH and FAD can be measured in the picosecond and nanosecond ranges, depending on whether the molecules are bound to protein or not. The ratio of bound to free NADH or FAD is indicative of the metabolic state and can be used to discriminate between healthy and diseased tissue [63].

Fluorescence lifetime studies based on autofluorescence have been used to assess the metabolic state of stem cells prior to and post differentiation, without affecting the integrity of the cell [32]. An increase in fluorescence lifetimes of NAD(P)H and bound/free NAD(P)H ratios during stem cell differentiation into mature cells [32, 64] was detected. Such metabolic changes indicate the reconfiguration of metabolic states from glycolysis into oxidative phosphorylation during differentiation [31]. FLIM has recently been utilized to differentiate mouse embryonic fibroblasts from iPS originating from mouse embryonic fibroblasts and from non-proliferative (gamma-irradiated) mouse embryonic fibroblasts [65]. Significant differences were detected in fluorescence lifetime fingerprints between non-proliferative and high proliferative mouse embryonic fibroblasts and iPS cells. Furthermore, increased lifetime values were detected in spontaneous differentiating iPS colonies in comparison with non-proliferative colonies [65].

We also used this non-invasive technique to analyze differences in the FLIM fingerprints of pluripotent mouse embryonic stem cells (mESC). FLIM data from a specific mESC colony were compared with data from conventional immunocytochemistry for the same colony to check for correlations.

Cells were seeded on gelatin coated (0.1 % gelatin from porcine skin, Sigma) glass bottom dishes with 500 µm grids (Ibidi) and incubated for 24 hours (37 °C, 5 % CO_2) to adhere. FLIM measurements were then performed using TCSPC and NIR laser excitation at 760 nm. The cells were fixed in 4 % paraformaldehyde after the FLIM measurement and immunocytochemical analyses were performed by conventional labelling techniques using fluorescent antibodies. Cells were briefly blocked with serum, incubated with the first antibody against surface markers (4 °C, overnight) and then incubated with secondary antibody (room temperature, 30 min). Thereafter intracellular markers were stained: cells were fixed again, permeabilized with 0.05 % TritonX-100, blocked with serum, incubated with the first antibody against intracellular markers (4 °C, overnight) and then incubated with a secondary antibody (room temperature, 30 min). After each step, the cells were washed three times with phosphate buffered saline (PBS). Finally, the cells were counterstained with DAPI and embedded with ProLong Gold (Life Technologies). Fluorescence imaging of exactly the same colonies which were analyzed by FLIM was performed with a confocal laser scanning microscope (LSM 710, Zeiss, Germany).

In our experiment, we observed heterogeneous pluripotent colonies with cells expressing SSEA1 but not always OCT4. SSEA1 and OCT4 are both cellular markers for pluripotency although not expressed synchronously in time. Their expression timelines also differ during reprogramming processes [66]. FLIM revealed that mESC cells expressing SSEA1$^+$ and OCT4$^+$ have a larger full width at half maximum (FWHM) and a shorter mean decay time than cells not expressing SSEA1$^-$ (Fig. 1.9). FLIM can be used to discriminate between different cell populations, even between different pluripotent populations.

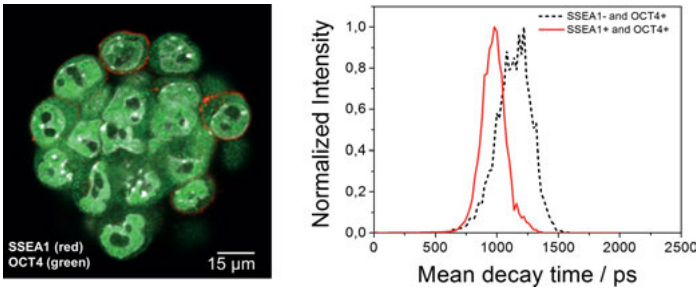

Fig. 1.9: FLIM analyses of murine embryonic stem cells (mESC) and correlation with conventional immunocytochemical staining analyses. Immunocytochemical labelling (left) and FLIM histogram distributions with mean decay times (right) of mESCs with different marker expression profiles: SSEA1$^+$/OCT4$^+$ cells and SSEA1$^-$/OCT4$^+$ cells.

1.7 Optical cleaning

Multiphoton microscopy utilizing femtosecond lasers is increasingly advancing towards use as a nanosurgery tool. Femtosecond lasers make it possible to perform nanosurgery within entire cells. Focused femtosecond laser pulses have been successfully used to manipulate intracellular structures such as single dendrites and cytoskeletons, microtubulus and intracellular mitochondria without causing collateral damage to the cell [67]. Human chromosomes have been dissected with incisions smaller than 100 nm [68]. Precise membrane surgery (nano/micro-optoporation) has become a useful application for cell transfection, as discussed in the previous chapters. The use of extremely ultrashort laser pulses such as sub 20 fs particularly enhances nanoprocessing and reduces collateral damage [69]. Femtosecond lasers can also be used to perform optical cell sorting or cleaning by destroying unwanted cells, causing no or only minimal damage to their surroundings. However, it must be considered that two-photon absorption may provoke UV-like photochemical reactions, including the formation of reactive oxygen species (ROS), and may result in DNA strand breaks and apoptosis. When high TW/cm^2 intensities are applied, multiphoton ionization results in free electrons and plasma formation which induces photodisruptive effects such as shockwaves and destructive bubble formation [70]. This can cause

immediate cell death. Only the choice of appropriate laser parameters enables safe and precise damage without collateral photochemical or photomechanical effects.

Here, we report on optical cleaning with 12 fs laser pulses without any collateral effect. The method has the potential to be used to control the purity of a stem cell population by knocking out undesired cell types in stem cell cultures aiming for an efficient and specific cell differentiation. Single non-differentiated cells within clearly differentiated tissues can also be destroyed so as to avoid unregulated growth. Optical cleaning can also be performed in cell clusters or 3D-iPS/ES cell colonies. Figure 1.10 demonstrates optical cleaning of cell clusters through the ablation of cells in the ROI without any evidence for apoptosis in the neighboring cells, as examined by Annexin V probe.

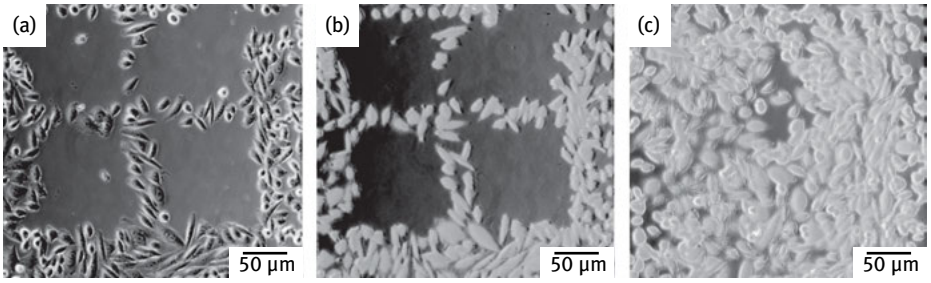

Fig. 1.10: Optical cleaning. Cells within the ROI (4 frames) are destroyed by multiphoton-induced plasma formation. No apoptotic cells were detected in the out-of-focus areas as examined by Annexin V (a). Calcein indicates (green) living cells (b). Cells migrated into the laser exposed ROI on the following day (c).

1.8 Conclusion and outlook

The application of femtosecond lasers has a huge potential in stem cell research and tissue engineering for regenerative medicine. While most transfection techniques (such as liposomal transfection) affect global populations, femtosecond laser induced optoporation offers the advantage of being capable of selecting specific cells [71]. With the use of femtosecond lasers it will soon be possible to direct the cell fate while monitoring in real time without any adverse effect on cellular viability.

Another more recent avenue is that of directly reprogrammed cells, i.e. cells which are transduced from one cell type to another, obviating the pluripotent cell stage [72–74]. Such a method permits attainment of valuable cell types from an otherwise plentiful source. Mouse fibroblasts, for example, have been reprogrammed to cardiomyocytes, a promising method with respect to therapies after cardiac infarction [50]. The direct reprogramming of cells entails the use of various small molecules, media regimes, and the delivery of transcription factors or genes to enable genome

editing of the cell in order to reprogram it into another cell type. Considering that such transcription factors and genes can be encoded by plasmid DNAs, optoporation facilitated by femtosecond lasers could take on a significant role in direct reprogramming of cells.

It will probably be possible to engineer functional tissue using femtosecond manipulation soon. One could reprogram specific cell phenotypes in a spatio-temporal manner and use FLIM/multiphoton/SHG microscopy to monitor tissue development. Optical cleaning and laser microdissection could then be used to shape this tissue's development.

The acceptance of femtosecond lasers in the clinic will become more widespread as soon as NIR femtosecond lasers become integrated into an endoscopy system. In the future not only analysis and diagnosis but also direct manipulation of patient tissue could be performed on internal organs. One scenario might be the manipulation of diseased infracted heart tissue, first through laser micro-dissection and optical cleaning, and then *in vivo* transfection of tissue to program its regeneration. Achieving such a transition would make today's science fiction a reality in the future.

References

[1] Till JE, McCulloch EA. Hematopoietic stem cell differentiation. Biochim Biophys Acta. 1980 Nov 26; 605(4): 431–459.

[2] Gimble JM, Guilak F. Differentiation potential of adipose derived adult stem (ADAS) cells. Curr Top Dev Biol. 2003; 58: 137–160.

[3] Friedenstein AJ, Petrakova KV, Kurolesova AI, Frolova GP. Heterotopic of bone marrow. Analysis of precursor cells for osteogenic and hematopoietic tissues. Transplantation. 1968 Mar; 6(2): 230–247.

[4] Loncar D. Ultrastructural analysis of differentiation of rat endoderm in vitro. Adipose vascular-stromal cells induce endoderm differentiation, which in turn induces differentiation of the vascular-stromal cells into chondrocytes. J Submicrosc Cytol Pathol. 1992 Oct; 24(4): 509–519.

[5] Zuk PA, Zhu M, Mizuno H, Huang J, Futrell JW, Katz AJ, et al. Multilineage cells from human adipose tissue: implications for cell-based therapies. Tissue Eng. 2001 Apr; 7(2): 211–228.

[6] Young HE, Steele TA, Bray RA, Hudson J, Floyd JA, Hawkins K, et al. Human reserve pluripotent mesenchymal stem cells are present in the connective tissues of skeletal muscle and dermis derived from fetal, adult, and geriatric donors. Anat Rec. 2001 Sep 1; 264(1): 51–62.

[7] Gimble J, Guilak F. Adipose-derived adult stem cells: isolation, characterization, and differentiation potential. Cytotherapy. 2003; 5(5): 362–369.

[8] Hoffman RM. The pluripotency of hair follicle stem cells. Cell Cycle. 2006 Feb; 5(3): 232–233.

[9] in 't Anker PS, Noort WA, Scherjon SA, Kleijburg-van der Keur C, Kruisselbrink AB, van Bezooijen RL, et al. Mesenchymal stem cells in human second-trimester bone marrow, liver, lung, and spleen exhibit a similar immunophenotype but a heterogeneous multilineage differentiation potential. Haematologica. 2003 Aug; 88(8): 845–852.

[10] Thomas T, Nowka K, Lan L, Derwahl M. Expression of endoderm stem cell markers: evidence for the presence of adult stem cells in human thyroid glands. Thyroid. 2006 Jun; 16(6): 537–544.

[11] Hisatomi Y, Okumura K, Nakamura K, Matsumoto S, Satoh A, Nagano K, et al. Flow cytometric isolation of endodermal progenitors from mouse salivary gland differentiate into hepatic and pancreatic lineages. Hepatology. 2004 Mar; 39(3): 667–675.
[12] Seaberg RM, Smukler SR, Kieffer TJ, Enikolopov G, Asghar Z, Wheeler MB, et al. Clonal identification of multipotent precursors from adult mouse pancreas that generate neural and pancreatic lineages. Nat Biotechnol. 2004 Sep; 22(9): 1115–1124.
[13] Wagner DR, Lindsey DP, Li KW, Tummala P, Chandran SE, Smith RL, et al. Hydrostatic pressure enhances chondrogenic differentiation of human bone marrow stromal cells in osteochondrogenic medium. Annals of Biomedical Engineering. 2008 May; 36(5): 813–820.
[14] Cecchini M, Bumma G, Serresi M, Beltram F. PC12 differentiation on biopolymer nanostructures. Nanotechnology. 2007 Dec 19; 18(50).
[15] Yim EK, Pang SW, Leong KW. Synthetic nanostructures inducing differentiation of human mesenchymal stem cells into neuronal lineage. Exp Cell Res. 2007 May 15; 313(9): 1820–1829.
[16] Neeley WL, Redenti S, Klassen H, Tao S, Desai T, Young MJ, et al. A microfabricated scaffold for retinal progenitor cell grafting. Biomaterials. 2008 Feb; 29(4): 418–426.
[17] Zou GM, Chen JJ, Ni J. LIGHT induces differentiation of mouse embryonic stem cells associated with activation of ERK5. Oncogene. 2006 Jan; 25(3): 463–9.
[18] Ge DX, Liu XJ, Li L, Wu J, Tu QF, Shi YK, et al. Chemical and physical stimuli induce cardiomyocyte differentiation from stem cells. Biochemical and Biophysical Research Communications. 2009 Apr 10; 381(3): 317–321.
[19] Martin GR. Isolation of a pluripotent cell line from early mouse embryos cultured in medium conditioned by teratocarcinoma stem cells. Proc Natl Acad Sci U S A. 1981 Dec; 78(12): 7634–7638.
[20] Evans MJ, Kaufman MH. Establishment in culture of pluripotential cells from mouse embryos. Nature. 1981 Jul 9; 292(5819): 154–156.
[21] Thomson JA, Itskovitz-Eldor J, Shapiro SS, Waknitz MA, Swiergiel JJ, Marshall VS, et al. Embryonic stem cell lines derived from human blastocysts. Science. 1998 Nov 6; 282(5391): 1145–1147.
[22] Nobelprize.org. The Nobel Prize in Physiology or Medicine 2012. Accessed 11 Dec 2014; Available from: http://www.nobelprize.org/nobel_prizes/medicine/laureates/2012/
[23] Loh YH, Hartung O, Li H, Guo C, Sahalie JM, Manos PD, et al. Reprogramming of T cells from human peripheral blood. Cell Stem Cell. 2010 Jul 2; 7(1): 15–19.
[24] Higashi N, Mita H, Ono E, Fukutomi Y, Yamaguchi H, Kajiwara K, et al. Profile of eicosanoid generation in aspirin-intolerant asthma and anaphylaxis assessed by new biomarkers. J Allergy Clin Immunol. May; 125(5): 1084–1091 e6.
[25] Ben-David U, Benvenisty N. The tumorigenicity of human embryonic and induced pluripotent stem cells. Nat Rev Cancer. Apr; 11(4): 268–277.
[26] Kooreman NG, Wu JC. Tumorigenicity of pluripotent stem cells: biological insights from molecular imaging. J R Soc Interface. Dec 6; 7 Suppl 6: S753-763.
[27] Denk W, Strickler JH, Webb WW. Two-photon laser scanning fluorescence microscopy. Science. 1990 Apr 6; 248(4951): 73–76.
[28] Uchugonova A, Hoffman RM, Weinigel M, König K. Watching stem cells in the skin of living mice non-invasively. Cell Cycle. 2011 Jun 15; 10(12): 2017–2020.
[29] Wright BK, Andrews LM, Jones MR, Stringari C, Digman MA, Gratton E. Phasor-FLIM analysis of NADH distribution and localization in the nucleus of live progenitor myoblast cells. Microsc Res Tech. Dec; 75(12): 1717–1722.
[30] Uchugonova A, König K. Two-photon autofluorescence and second-harmonic imaging of adult stem cells. Journal of Biomedical Optics. 2008 Sep–Oct; 13(5).

[31] Stringari C, Edwards RA, Pate KT, Waterman ML, Donovan PJ, Gratton E. Metabolic trajectory of cellular differentiation in small intestine by Phasor Fluorescence Lifetime Microscopy of NADH. Sci Rep. 2: 568.
[32] König K, Uchugonova A, Gorjup E. Multiphoton Fluorescence Lifetime Imaging of 3D-Stem Cell Spheroids During Differentiation. Microscopy Research and Technique. 2011 Jan; 74(1): 9–17.
[33] König K, Liang H, Berns MW, Tromberg BJ. Cell damage in near-infrared multimode optical traps as a result of multiphoton absorption. Opt Lett. 1996 Jul 15; 21(14): 1090–1092.
[34] König K. Multiphoton microscopy in life sciences. J Microsc. 2000 Nov; 200(Pt 2): 83–104.
[35] König K. Multiphoton-induced cell damage. In: Master BR, and So, P.T.C, ed.: Oxford University Press, Inc., 2008: 334–347.
[36] D. McGloin KD. Bessel beams: Diffraction in a new light. Contemporary Physics. 2005; 46(1): 15–28.
[37] Kim TK, Eberwine JH. Mammalian cell transfection: the present and the future. Anal Bioanal Chem. Aug; 397(8): 3173–3178.
[38] Schneckenburger H, Hendinger A, Sailer R, Strauss WSL, Schmitt M. Laser-assisted optoporation of single cells. Journal of Biomedical Optics. 2002 Jul; 7(3): 410–416.
[39] Palumbo G, Caruso M, Crescenzi E, Tecce MF, Roberti G, Colasanti A. Targeted gene transfer in eucaryotic cells by dye-assisted laser optoporation. J Photochem Photobiol B. 1996 Oct; 36(1): 41–46.
[40] Shirahata Y, Ohkohchi N, Itagak H, Satomi S. New technique for gene transfection using laser irradiation. J Investig Med. 2001 Mar; 49(2): 184–190.
[41] Paterson L, Agate B, Comrie M, Ferguson R, Lake T, Morris J, et al. Photoporation and cell transfection using a violet diode laser. Opt Express. 2005 Jan 24; 13(2): 595–600.
[42] Tyrrell RM, Keyse SM. New trends in photobiology. The interaction of UVA radiation with cultured cells. J Photochem Photobiol B. 1990 Mar; 4(4): 349–361.
[43] König K, Krasieva TB, Bauer E, Fiedler U, Berns MW, Tromberg BJ, et al. Cell damage by UVA radiation of a mercury microscopy lamp probed by autofluorescence modifications, cloning assay, and comet assay. Journal of Biomedical Optics. 1996; 1(2): 217–222.
[44] Tirlapur UK, König K. Cell biology - Targeted transfection by femtosecond laser. Nature. 2002 Jul 18; 418(6895): 290–291.
[45] Uchugonova A, König K, Bueckle R, Isemann A, Tempea G. Targeted transfection of stem cells with sub-20 femtosecond laser pulses. Optics Express. 2008 Jun 23; 16(13): 9357–9364.
[46] Stevenson DJ, Gunn-Moore FJ, Campbell P, Dholakia K. Single cell optical transfection. J R Soc Interface. Jun 6; 7(47): 863–871.
[47] Uchugonova A, Lessel M, Nietzsche S, Zeitz C, Jacobs K, Lemke C, et al. Nanosurgery of cells and chromosomes using near-infrared twelve-femtosecond laser pulses. J Biomed Opt. Oct; 17(10): 101502.
[48] Breunig HG, Uchugonova A, Batista A, König K. Software-aided automatic cell optoporation with femtosecond laser pulses. Submitted.
[49] Breunig HG, Uchugonova A, Batista A, König K. High-throughput continuous flow femtosecond laser-assisted cell optoporation and transfection. Microsc Res Tech. Dec; 77(12): 974–979.
[50] Efe JA, Hilcove S, Kim J, Zhou H, Ouyang K, Wang G, et al. Conversion of mouse fibroblasts into cardiomyocytes using a direct reprogramming strategy. Nature cell biology. 2011 Mar; 13(3): 215–222.
[51] Araki R, Uda M, Hoki Y, Sunayama M, Nakamura M, Ando S, et al. Negligible immunogenicity of terminally differentiated cells derived from induced pluripotent or embryonic stem cells. Nature. Feb 7; 494(7435): 100–104.

[52] Guha P, Morgan JW, Mostoslavsky G, Rodrigues NP, Boyd AS. Lack of immune response to differentiated cells derived from syngeneic induced pluripotent stem cells. Cell Stem Cell. Apr 4; 12(4): 407–412.
[53] Takahashi K, Yamanaka S. Induction of pluripotent stem cells from mouse embryonic and adult fibroblast cultures by defined factors. Cell. 2006 Aug 25; 126(4): 663–676.
[54] Yu JY, Hu KJ, Smuga-Otto K, Tian SL, Stewart R, Slukvin II, et al. Human Induced Pluripotent Stem Cells Free of Vector and Transgene Sequences. Science. 2009 May 8; 324(5928): 797–801.
[55] Uchugonova A, König K, Bückle R, Isemann A, Tempea G. Targeted transfection of stem cells with sub-20 femtosecond laser pulses. Opt Express. 2008 Jun 23; 16(13): 9357–9364.
[56] Narsinh KH, Jia F, Robbins RC, Kay MA, Longaker MT, Wu JC. Generation of adult human induced pluripotent stem cells using nonviral minicircle DNA vectors. Nat Protoc. Jan; 6(1): 78–88.
[57] Bugiel I, König K, Wabnitz H. Investigation of cells by fluorescence laser scanning microscopy with subnanosecond time resolution. Lasers Life Sciences. 1989; 3: 1–7.
[58] Periasamy A. Fluorescence resonance energy transfer microscopy: a mini review. J Biomed Opt. 2001 Jul; 6(3): 287–291.
[59] Day RN, Periasamy A, Schaufele F. Fluorescence resonance energy transfer microscopy of localized protein interactions in the living cell nucleus. Methods. 2001 Sep; 25(1): 4–18.
[60] König K. Clinical multiphoton tomography. J Biophotonics. 2008 Mar; 1(1): 13–23.
[61] König K, Uchugonova A. Multiphoton Fluorescence Lifetime Imaging at the Dawn of Clinical Application. In: Periasamy A, Clegg RM, eds. *FLIM in Biology and Medicine*. Boca Raton London New York: Taylor & Francis (CRC Group) 2009: 165–187.
[62] Becker W. Advanced Time-Correlated Single Photon Counting Techniques: Springer Berlin Heidelberg 2005.
[63] Skala MC, Riching KM, Gendron-Fitzpatrick A, Eickhoff J, Eliceiri KW, White JG, et al. In vivo multiphoton microscopy of NADH and FAD redox states, fluorescence lifetimes, and cellular morphology in precancerous epithelia. Proceedings of the National Academy of Sciences of the United States of America. 2007 Dec 4; 104(49): 19494–19499.
[64] Stringari C, Nourse JL, Flanagan LA, Gratton E. Phasor fluorescence lifetime microscopy of free and protein-bound NADH reveals neural stem cell differentiation potential. PLoS One. 7(11): e48014.
[65] Uchugonova A, Batista A, König K. Fluorescence lifetime imaging of induced pluripotent stem cells. Proceedings of SPIE. 2014: 8948–8952.
[66] Brambrink T, Foreman R, Welstead GG, Lengner CJ, Wernig M, Suh H, et al. Sequential expression of pluripotency markers during direct reprogramming of mouse somatic cells. Cell Stem Cell. 2008 Feb; 2(2): 151–159.
[67] Shimada T, Watanabe W, Matsunaga S, Higashi T, Ishii H, Fukui K, et al. Intracellular disruption of mitochondria in a living HeLa cell with a 76-MHz femtosecond laser oscillator. Optics Express. 2005 Nov 28; 13(24): 9869–9880.
[68] König K, Riemann I, Fritzsche W. Nanodissection of human chromosomes with near-infrared femtosecond laser pulses. Optics Letters. 2001 Jun 1; 26(11): 819–821.
[69] Uchugonova A, Lessel M, Nietzsche S, Zeitz C, Jacobs K, Lemke C, et al. Nanosurgery of cells and chromosomes using near-infrared twelve-femtosecond laser pulses. Journal of Biomedical Optics. 2012 Oct; 17(10).
[70] König K. Cell Damage During Multi-Photon Microscopy. In: Pawley J, ed. *Handbook of Biological Confocal Microscopy*. 3rd ed: Springer Science Business Media, NY, USA 2006: 680–689.
[71] Stevenson D, Agate B, Tsampoula X, Fischer P, Brown CT, Sibbett W, et al. Femtosecond optical transfection of cells: viability and efficiency. Optics express. 2006 Aug 7; 14(16): 7125–7133.

[72] Lujan E, Chanda S, Ahlenius H, Südhof TC, Wernig M. Direct conversion of mouse fibroblasts to self-renewing, tripotent neural precursor cells. Proceedings of the National Academy of Sciences. 2012 February 14, 2012; 109(7): 2527–2532.
[73] Wapinski Orly L, Vierbuchen T, Qu K, Lee Qian Y, Chanda S, Fuentes Daniel R, et al. Hierarchical Mechanisms for Direct Reprogramming of Fibroblasts to Neurons. Cell. 155(3): 621–635.
[74] Muraoka N, Yamakawa H, Miyamoto K, Sadahiro T, Umei T, Isomi M, et al. MiR-133 promotes cardiac reprogramming by directly repressing Snai1 and silencing fibroblast signatures. The EMBO Journal. 2014; 33(14): 1565–1581.

M. Steger, G. Abagnale, E. Bremus-Köbberling, W. Wagner, and A. Gillner

2 Nanoscale biofunctionalization of polymer surfaces by laser treatment for controlled cellular differentiation

Abstract: In this chapter we will discuss how nanostructures can interact with stem cells. After an introduction regarding the basic concepts of stem cells, their properties, and their uses in the medical field, we will then examine how stem cells can recognize physical forces and how this can be reproduced in vitro using materials produced in micro- and nanofabrication processes. Afterwards we will describe the principles and applications of a novel direct laser ablation technique, multibeam interference, and how patterns produced with such a method can be employed in stem cell research.

2.1 Nanostructuring and mesenchymal stem cells

2.1.1 Introduction to stem cells

The heterogeneity of human cells is extremely broad; nonetheless, all cells can be roughly divided into two categories: differentiated cells which perform specific, defined functions, and stem cells which represent the undifferentiated, unspecialized progenitors whence all somatic cells originate. During intrauterine life stem cells are responsible for the development of the human being from zygote to completely formed fetus, whereas in the adult individual they control wound repair and the general homeostasis of tissues, e.g. the regrowth of hair and nails [1–3].

2.1.1.1 Definition of stemness

Stem cells are generally characterized by two key features: their differentiation potential and their self-renewal ability [4, 5]. The broadness of somatic cell types which can originate from stem cells is indicative of their potency. The more a stem cell is committed toward a defined fate, the less its potency (Fig. 2.1 (a)). Additionally, stem cells must possess self-renewal capacity to keep their number constant. When stem cells undergo cell division, the process can be either symmetric or asymmetric (Fig. 2.1 (b)). The balance between symmetric and asymmetric division affects self-renewal and differentiation of stem cells [6]. This complicated decision is regulated by an intricate network of biochemical and physical stimuli present in the milieu in which such cells are embedded: the stem cell niche [7].

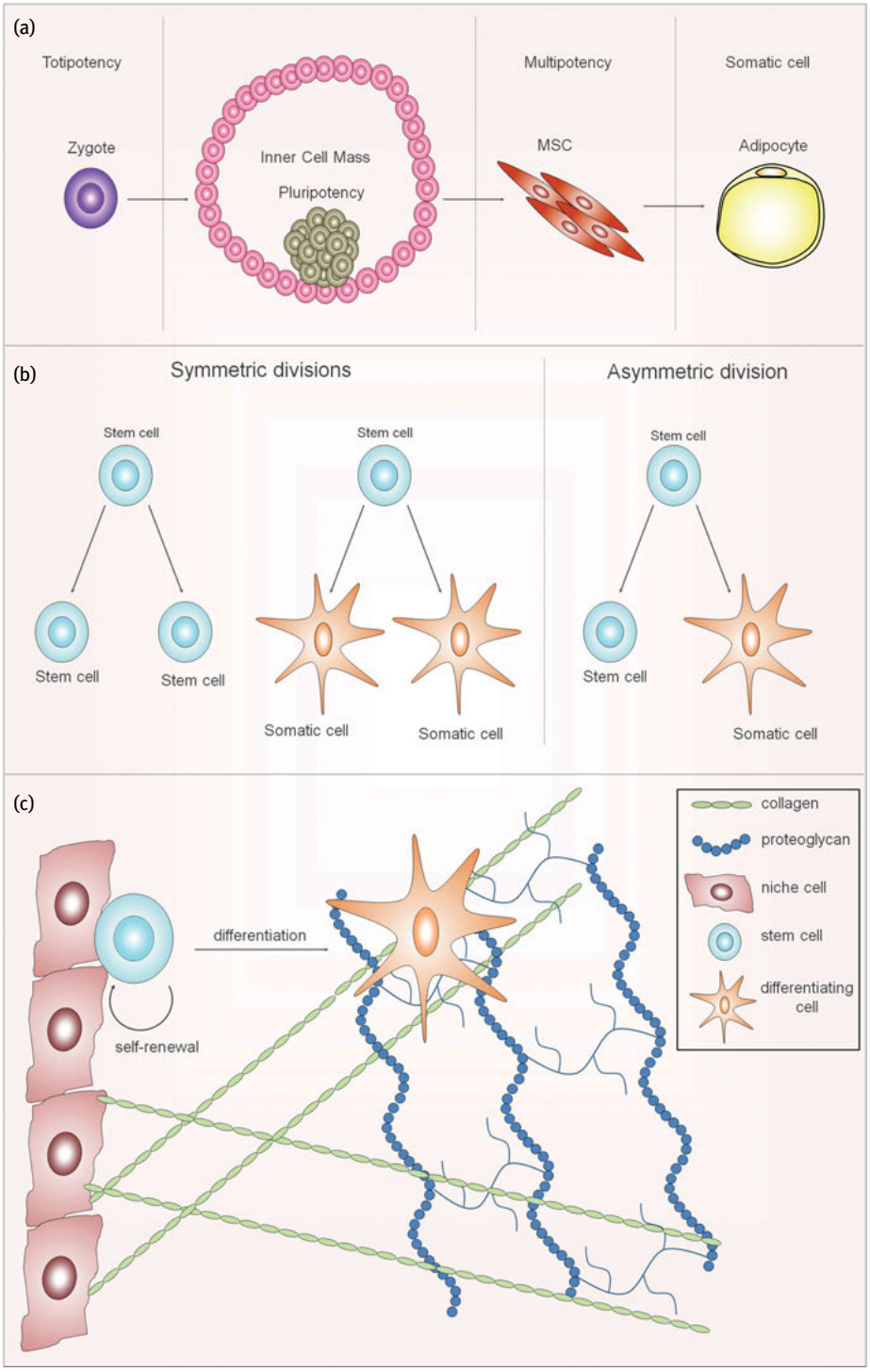
(a)
Totipotency
Zygote
Inner Cell Mass
Pluripotency
Multipotency
MSC
Somatic cell
Adipocyte
(b)
Symmetric divisions
Asymmetric division
Stem cell
Stem cell
Stem cell
Stem cell
Stem cell
Stem cell
Somatic cell
Somatic cell
Somatic cell
(c)
differentiation
self-renewal
collagen
proteoglycan
niche cell
stem cell
differentiating cell

2.1.1.2 The stem cell niche

The stem cell niche is the microenvironment which supports stem cell survival and self-renewal [8]. This niche can be composed of both cellular and non-cellular elements as extracellular matrix proteins or the basement membrane. Cell-cell and cell-matrix interactions in combination with soluble cytokines and growth factors contribute to the interplay between stem cells and their niche (Fig. 2.1 (c)). This tight signaling and the physical support provided by the niche modulate processes such as tissue regeneration and cellular turnover [9].

2.1.2 Mesenchymal stem cells

2.1.2.1 Introduction to MSCs

Mesenchymal stem cells (MSCs) can be found in several anatomical locations, though they are more abundant in bone marrow and adipose tissue [10, 11]. MSC preparations differ consistently depending on the site of origin, age, and sex of the donor [12, 13]. Nonetheless, MSCs are characterized by some common features: (1) they display good adherence to tissue culture plastic, exhibit a fibroblast-like morphology and can form colonies in vitro. (2) MSCs are usually positive for the surface antigens STRO-1 and CD73, while they do not normally express the lymphoid marker CD45 and the hematopoietic marker CD34. (3) MSCs are believed to be multipotent since they can differentiate into cell types deriving from a single embryonic layer, the mesoderm [14–16].

2.1.2.2 Functions of MSCs

One of the crucial functions of MSCs is to maintain homeostasis in tissues of mesodermal derivation. In fact, it has been demonstrated that MSCs can give rise in vitro to osteocytes, adipocytes, chondrocytes, fibroblasts, tenocytes, endothelial cells, smooth muscle cells, myoblasts, and cardiomyocytes [17, 18]. Another important function of MSCs is their immunomodulatory ability. Many studies have shown that MSCs can regulate the immune effectors through secretion of cytokines and direct interaction with immunocompetent cells. In detail, MSCs are able to dampen both adaptive and innate responses, and hence shift the balance of immune system activation toward an anti-inflammatory and immunotolerant state [19].

◂ **Fig. 2.1:** Schematic presentation of stem cell function. (a) The differentiation potential of a stem cell determines its potency. (b) The balance between symmetric and asymmetric cell divisions regulates stem cell self-renewal. (c) Schematic representation of a putative niche for stem cells comprising cellular (stromal cells) and noncellular elements (extracellular matrix proteins).

2.1.2.3 Clinical relevance of MSCs

MSCs can be used in clinical practice, e.g. their immunomodulatory properties could be exploited to improve transplant engraftment or treat chronic inflammatory diseases. Moreover, the ability of MSCs to differentiate into cells of mesodermal lineage makes them the perfect candidate for tissue engineering applications. MSCs have been used to repair cartilage or bone defects, either by applying the cells to the site of injury directly or after culture on biomimetic scaffolds to facilitate regeneration and integration into the surrounding tissue [20]. Most efforts to improve MSC-based regenerative therapies have focused on coordinating chemical and biological signals to achieve controlled cellular differentiation. An increasing number of studies have recently indicated that the effects of physical forces on cell dynamics might be the missing link in achieving this aim [21].

2.1.3 Mechanobiology of MSCs

2.1.3.1 Mechanical stimuli in the stem cell niche

Mechanobiology is the area of cellular biology which focuses on how cells recognize mechanical forces and then transduce them into a biological response [22]. Inside their niche MSCs are subjected to several types of physical stimuli: (1) shear stress generated by the blood flow, which is particularly relevant for perivascular MSCs [23, 24]; (2) mechanical strain associated with the traction of muscles and bone [25, 26]; (3) substrate stiffness, which has a deep impact on MSC behavior [27, 28]. Interestingly substrate stiffness also has an effect on MSC motility, since it has been shown that cells migrate from softer to stiffer areas in a process called durotaxis [29]. (4) Surface topography. In fact, the stem cell niche is a 3D microenvironment which includes structures of different sizes, shapes, and spatial disposition [30]. Following the physical interaction with their substrate, cells are able to first “sense” and distinguish diverse topographic cues and then integrate them into a specific biological response [31].

2.1.3.2 The mechanotransducer machinery of the cell

Integrins are a family of receptor proteins found on the cellular membrane and responsible for the mechanical anchorage of a cell to its substrate [32]. ECM proteins are the main ligand of integrin receptors.The binding of an integrin to its ligand elicits a complex response which leads to the formation of focal adhesions [33–36]. Focal adhesions recognize mechanical forces generated either by an external source or by the cell itself, and then translate them into a biological response (Fig. 2.2). Following the binding of their extracellular portions to the ECM, the cytoplasmic tails of the integrins recruit the protein talin, which functions as bridge between the site of adhesion and the cytoskeleton since it binds actin fibers both directly and through the protein vinculin. Anchorage of the actin filaments to the site of adhesion generates

internal mechanical forces and triggers integrin clustering, a fundamental event in the genesis of focal adhesions. Clustered integrins recruit more actin filaments to the site of adhesion, thus leading to the formation of contractile structures composed of actin microfilaments connected by myosin II molecules called stress fibers. This initial integrin/cytoskeleton complex evolves into a mature focal adhesion after the recruitment of various additional proteins including paxillin, zyxin, and the tyrosine kinase FAK. The signaling cascades downstream of focal adhesions include the activation

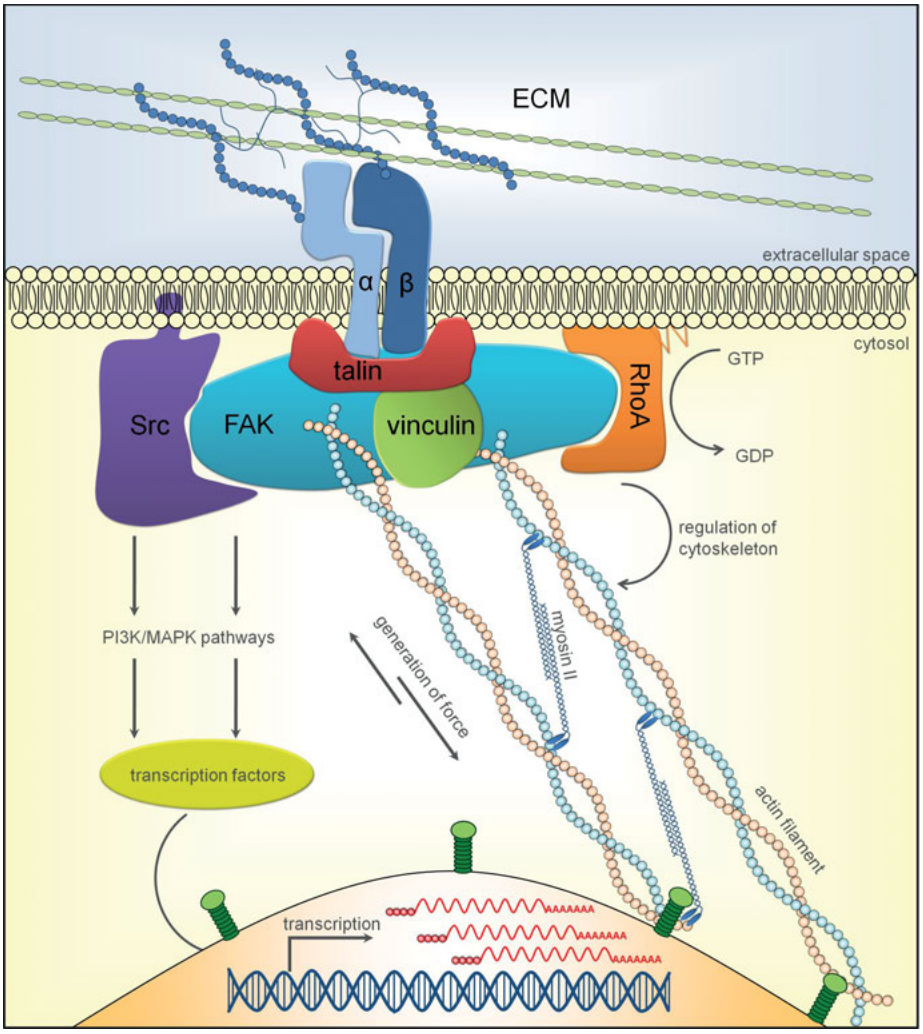

Fig. 2.2: Integrin-mediated recognition of extracellular matrix components leads to the formation of focal adhesion complexes able to connect the cytoskeleton with the adhesion site and moreover triggers downstream signaling pathways.

of the MAPK/ERK pathway, resulting in transcriptional regulation of cell cycle and differentiation, and the phosphorylation of the small GTPases of the Rho family, which regulate cytoskeletal dynamics and cell motility [37].

2.1.3.3 Interaction of MSCs with micro and nanostructures

Biomaterials are the ideal tool for studying the effects of substrate stiffness and surface topography on MSCs [38, 39]. Defined micro- and nanostructures have been shown to have a prominent role in keeping MSCs in a quiescent multipotent state or in directing their differentiation towards specific fates [40–43]. Fibrils, pillars, pits, grooves, and ridges are the features which better resemble the topographical landscape found in the stem cell niche; nonetheless the variety of cues which can be studied is much broader. In fact, it should be considered that scale size and the symmetric disposition of the structures contribute to increasing the combination of conceivable theoretical patterns [44, 45]. In this scenario the only limit to the number of cues which we can analyze is presented by our technological progress. In this regard, the ideal patterning process should allow generation of high resolution structures in a fast, cost-efficient, and reproducible fashion.

2.2 Nanostructuring of materials

2.2.1 Direct nanostructuring of surfaces with multibeam-interference

The most commonly used method for nanostructuring of surfaces is lithography. For more than three decades lithography has been the key enabling technology to decrease the structure size in semiconductors manufacturing to fulfill Moore's law [46] and sub 100 nm structuring by lithographic had its industrial breakthrough around 2005. The drawback of high resolution lithography is its high price, due to the many complex process steps and high precision photo masks. Therefore a crucial aim in ongoing research is not only the further reduction of structure size, but also cost reduction. Besides the reduction of the necessary steps involving lithography, in nanoimprinting, for example, multibeam interference lithography (MBI-L) is a promising approach as a flexible substitute for expansive photo masks. The periodic interferences pattern created by two or more coherent laser beams is used to expose the photo resist in MBI-L and parallel to further research the first commercial applications are beginning to emerge. MBI-L also makes fabrication of 3D structures possible. Multibeam interference (MBI) is not, however, limited to the low energy illumination necessary for the chemical modification of photoresists, it can also be used for direct photoablation of many materials [47].

The direct nanostructuring of surfaces with multibeam interference therefore has several advantages. Structuring is carried out in a single step process and a whole surface area is structured simultaneously. The size of the area depends mainly on beam diameter and ablation threshold of the material. Periodicity and geometry of the structures generated can easily be adapted by changing alignment or polarization of beams [48]. Depending on the wavelength of the laser source, the size of the generated structures can range from the sub 100 nm up to several µm. Many materials can also be processed with MBI, especially with use of ultra-short pulse (USP) laser sources. Its ability to structure surfaces cost-efficiently in a single step and its easy adaption of the pattern generated make MBI a very promising tool for cheap nanostructuring with periodic patterns, not only for research purposes, but also for industrial applications. Additionally, its inherent ability to structure nonplane surfaces is an interesting feature compared to standard lithography [49].

2.2.1.1 Theoretical background

The capacity for structuring by multibeam interference is based on the intensity modulation caused by the interference of two or more intercepting coherent laser beams. This intensity modulation is present in the whole volume where the beams intercept and the total time independent intensity modulation $I(\boldsymbol{r})$ inside this volume of the number of j plane waves can be described as follows [50]:

$$I(\boldsymbol{r}) = \sum_j I_j(\boldsymbol{r}) + 2\sum_{i<j} \sqrt{I_i(\boldsymbol{r})I_j(\boldsymbol{r})}\cos(\theta_{ij})\cos\left((\boldsymbol{K}_i - \boldsymbol{K}_j)\boldsymbol{r} + \phi_i - \phi_j\right), \tag{2.1}$$

where I_j is the intensity of beam j, θ_{ij} is the angle between the unit vectors of beam i and j in its polarization direction, $\boldsymbol{K}_j$ is the wave vector of beam j and the phase of beam i. The first sum of equation (2.1) describes the total intensity of all beams without interference, while the second sum defines the modulation around due to the interference. For a two-beam interference setup the expression can be written as:

$$I_{2B}(\boldsymbol{r}) = I_1 + I_2 + 2\sqrt{I_1 I_2}\cos(\theta_{12})\cos\left((\boldsymbol{K}_1 - \boldsymbol{K}_2)\boldsymbol{r} + \phi_i - \phi_j\right), \tag{2.2}$$

where ω is the beam radius. Further simplified for identical amplitude, polarization, and initial phase of both beams with λ as wavelength of the laser and α the half intersection angle of both beams, equation (2.2) can be simplified to:

$$I_{2B}(\boldsymbol{x}) = 2I_1\left(1 + \cos(x\frac{2\pi}{\lambda}\sin\alpha)\right). \tag{2.3}$$

The intensity pattern generated is in the shape of cosine in the direction of the x-axis, while the pattern is constant in y-z plane. As visible in equation (2.3), the periodicity of this modulation can be controlled by the wavelength λ and the intersection angle α. This correlation is shown in Fig. 2.3 (a) and 2.3 (b). The ideal modulated intensity reaches twice the intensity I_0 in its maxima $I_{\max}$, and zero intensity in its minima $I_{\min}$.

The depth of modulation compared to the ideal modulation depends on the coherence of the beams and their ability to interfere, and can be described by the interference contrast as:

$$\text{Contrast} = \frac{I_{\max} - I_{\min}}{I_{\max} + I_{\min}} \tag{2.4}$$

It ranges from 1 for an ideal modulation and 0 for an unmodulated signal (compare Fig. 2.3 (c) and 2.3 (d)). A measuring method for the interference contrast was developed and tested as part of this project [51]. High contrast is important for the optimization of direct surface structuring by MBI, because its value is directly linked to the quality of the ablation process. Reduced contrast means a decrease of $I_{\max}$ and an increase of $I_{\min}$, and therefore leads to a shift in intensity distribution from the ablation areas to the areas where no material alteration is desired. As a result of this shift, a reduced ablation depth is reached for a fixed total intensity and increased heating, ablation, or even destruction of the whole pattern occurs by the higher intensity of $I_{\min}$. For these reasons, the maximal ablation depth, structure size, and periodicity of the generated patterns is closely coupled to the interference contrast.

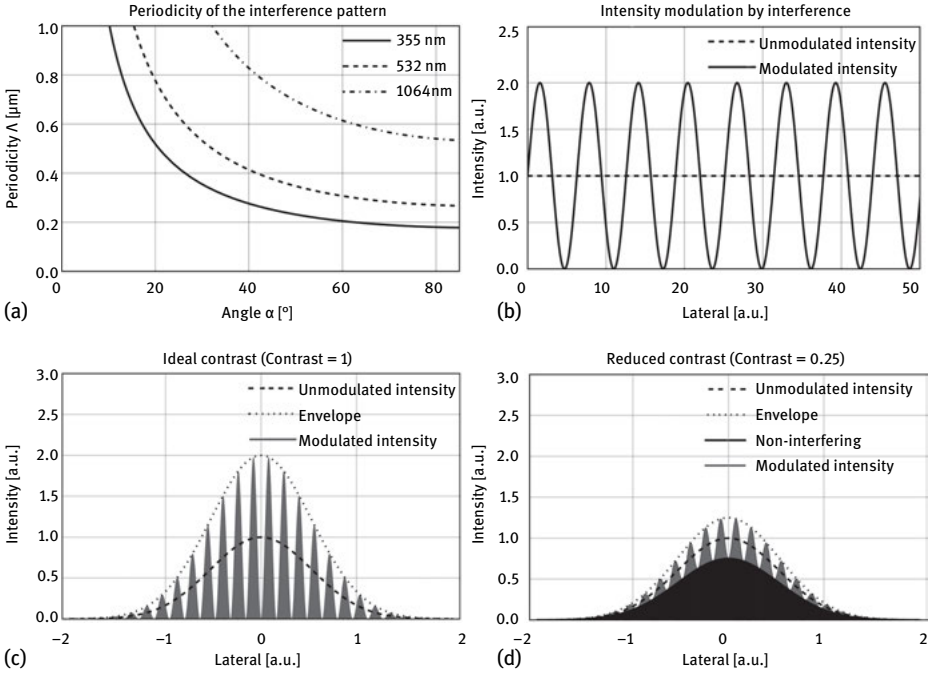

Fig. 2.3: Characteristics of 2-beam interference: (a) periodicity of a 2-beam interference pattern depending on the intercepting angle for 3 different wavelengths; (b) intensity modulation created by the interference of two beams compared to unmodulated signal; (c) intensity modulation of a Gaussian beam shape for an ideal contrast; (d) intensity modulation of a Gaussian beam shape for a reduced contrast.

2.2.1.2 Experimental setup & methods

The laser source is a diode pumped Nd:YAG laser (Q301-HD, JDSU) which operates at a wavelength of 355 nm with a pulse duration of 38 ns and a coherence length of 5.4 mm. The polarization of the laser beam is turned to a perpendicular polarization by a half-wave plate in relation to the plane of the optical table. Afterwards the beam is refined through a spatial room filter and split into two parts. Two different setups were used as beam splitters: first a reflective 50 : 50 beam splitter and second a transmissive diffractive grating. The diffractive grating has an efficiency of 78 % in the 1/−1 order used for the experiments. All other orders were blocked. Afterwards the partial beams are directed by mirrors to superpose at the sample surface. The intersection angle can be adjusted to control the periodicity of the applied pattern. The sample material is polyimide foil (Upilex), 50 µm thick. The output of the laser is measured by an energy detector (QE12LP-S-MP, Gentec) and a beam profiler (Spiricon, Ophir) at the intersection plane of the beams. A typical beam diameter is ~ 900 µm with maximum pulse energy of 1.2 mJ. The samples are structured by a single pulse. The diameter of the area ablated by one pulse is about 600 µm. Larger areas of structured surfaces for cell seeding are stitched together in a close package. The geometry of the structures generated is measured by an atomic force microscope (Rados N8, Bruker) and a scanning electron microscope (LEO, Zeiss).

2.2.1.3 Structuring results of multibeam interference

The structures generated by a two-beam interference for a single step process is a 1D line with geometry as shown in Fig. 2.4. The periodicity of the line pattern can easily be controlled by adjusting the intersection angle between 210 nm and several µm. The main structure size respective of the width of line generated depends on the fluence of the laser beam, the ablation threshold of the material, and the heat conductivity of the material. The width of the line can be varied in the wide regime for fixed periodicity of the interference pattern; see Fig. 2.4.

The interaction of the cells with the topography seems to be primarily at the elevated part of the structure and therefore not at the ablated surface area. As visible in the AFM scan in Figs. 2.4 and 2.5, an additional bulging at the edges of the generated grooves occurs. These bulges have a significant height and their size is only a fraction of the periodicity of the pattern. Due to their position they act as an additional divider between the elevated part of the surface and the ablated grooves.

A close package of the functional structure elements is necessary for to optimize the effect of cell guiding by surface topography. Therefore, even if sub 100 nm structures are reachable with a periodicity of 1000 nm, the low density of the structures is problematic and reduces the relative influence on the growth and differentiation process of the stem cells. To increase the density it is necessary to decrease the periodicity and therefore raise the package density of the functional structure elements. In contrast, we observed that with a reduction of periodicity two kinds of problems occur,

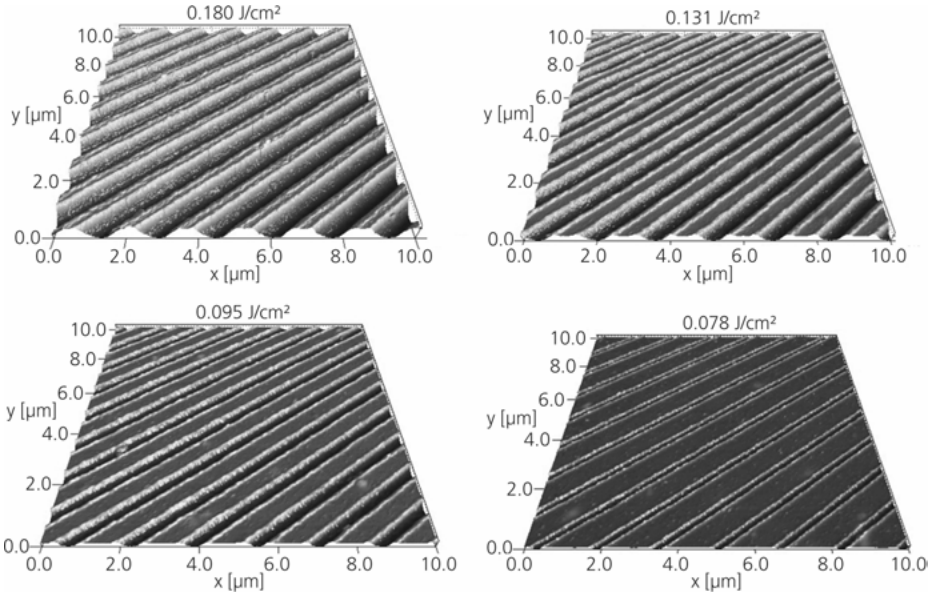

Fig. 2.4: AFM measurements of structured PI samples with different fluence. While the periodicity is constant with 1 µm, the geometry of generated grooves varies depending on the fluence.

or at least their influence on the structuring result increases: stability of structures and the homogeneity of the pattern. The stability of structures limits their maximal depth, which also has an important influence on cell growth and the homogeneity of pattern influences the structure deviations inside the pattern. Apart from this consideration we reached a minimal periodicity of 220 nm for the line pattern which leads to ridge width of less than 100 nm and bulges around 50 nm wide. An example for the structuring results is shown in Fig. 2.5.

2.3 Impact of laser-ablated nanogrooves on cell biology

2.3.1 Cell guidance along nanogrooves

The impact of laser-generated nanogrooves in the range of several hundred nanometers on neuronal cells has been shown in previous studies [52, 53]. Cellular extensions of neuronal B35 cells preferentially orient themselves parallel (i.e. within angles of 0 to 30°) to nanogrooves prepared via interference patterning. Our findings indicate that feature width is less crucial for alignment. Cells align along grooves which are 250 nm wide as well as along grooves 500 nm wide, but structure depth plays a crucial role. A depth to width (aspect) ratio greater than 0.6 induces a significantly higher degree of alignment compared to the shallower grooves.

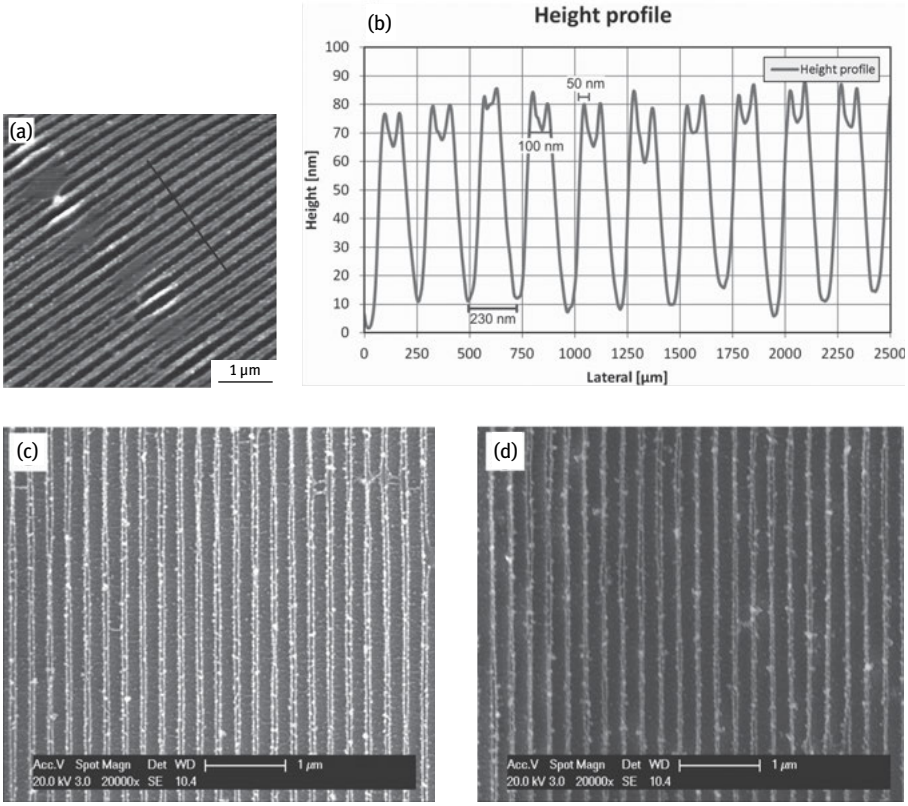

Fig. 2.5: (a) AFM measurements of structured PI samples with a periodicity of 230 nm; (b) corresponding height profile extracted from subfigure (a); (c), (d) REM measurements of structured PI samples with a periodicity of 230 nm.

In recent studies we examined the influence of three different nano patterns on orientation and length of cellular extensions. The nano patterns investigated were grooves, dots, and a mixture of both features called "dotted grooves" (compare Fig. 2.6) generated via interference patterning of polyimide (PI) and subsequent casting with polydimethylsiloxane (PDMS). PDMS casting was performed once to obtain a negative structure of the PI master and a second cast yielded the positive structure in PDMS. A loss in feature depth occurs due to the casting process. Casted groove structures are approx. 60 to 50 % of original feature depth of PI master (e.g. 382 nm in PI and 244/194 nm in PDS cast one/two; cf. Fig. 2.7: AFM/SEM pictures). The samples were incubated with B 35 neuronal cells (3000 cells per cm^2) and cell extensions were measured after two days of culture, followed by fixation with 4 % formalin and actin/DAPI staining. No alignment of cellular extensions could be detected on the dotted samples (b) and (c) (Fig. 2.6). Due to the lower degree of regularity on these samples, dendrites orient right or left around the dots leading to a random distribution

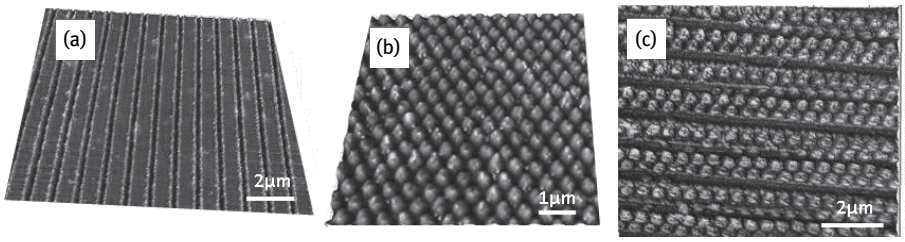

Fig. 2.6: AFM measurements of different nanopatterns: (a) grooves with 900 nm plateau and 200 nm groove width; (b) dots with 200 nm diameter and 200 nm pitch; (c) dotted grooves with two lines of dots per 900 nm plateau and 200 nm groove.

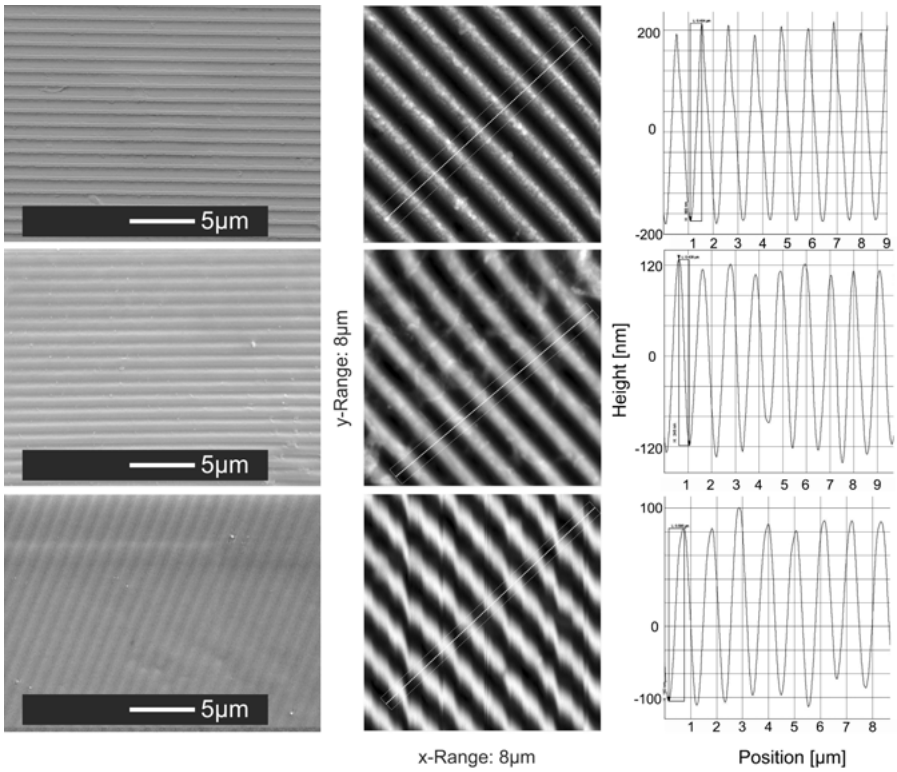

Fig. 2.7: AFM/SEM of nanogrooves. PI directly structured, PDMS-nL: cast one, negative structure of PI and PDMS-pL: cast two, shallow positive structure.

of cell extensions. The following observations were made regarding cell numbers and lengths of dendrites (Fig. 2.8):

- less cells on unstructured polymer surfaces than on glass positive reference
- longest cell extensions on glass positive reference (maximum length on glass 40–60 µm, maximum length on polymers 20–40 µm)

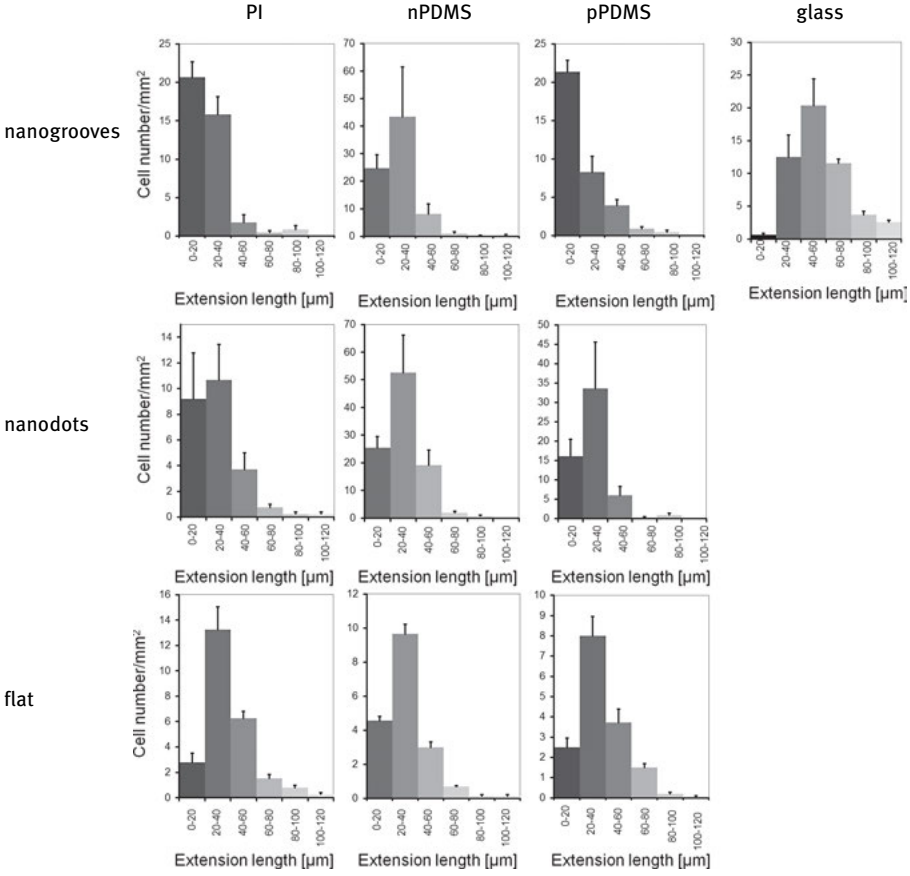

Fig. 2.8: Summary of cell numbers and length of cell extensions on nanogrooved and dotted polymer surfaces.

- increased cell numbers on nano patterned polymer surfaces compared to the unstructured polymer samples
- slightly decreased length of extensions on nanogrooved polymers (PI and positive PDMS cast) compared to unstructured polymer surfaces
- similar length distribution of extensions on nanodotted polymer surfaces compared to unstructured polymer samples, but increased length of extensions compared to grooved samples
- no clear effect of nanodotted lines on cell numbers and length of extensions.

These findings indicate that there is an influence of nanopatterns in the range of some hundred nanometers on cell numbers of neuronal cells as well as on orientation and length of cellular extensions. Further investigations are conducted with more sensitive cell types (MSCs).

2.3.2 Effect of nanotopography on MSC behavior

MSCs isolated from the adipose tissue of healthy donors have been seeded on a polyimide foil patterned with grooves with a structure size of ca 300 nm obtained using multibeam interference (Fig. 2.9 (a)). Polyimide is a biocompatible, inert plastic polymer which has been used for neuronal and sub-retinal implants. This material is also endowed with excellent mechanical properties such as low friction, high textile strength, resistance to wear and high flexibility [54–56]. No protein coating was used prior to the cell seeding in order to exclude the topographic influence of structures different to the nanogrooves and to improve the reproducibility of the experiments. Regarding cell adhesion there was no difference between the conventional tissue culture plastic, the non-structured PI used as control, and the nanogrooved PI; furthermore, this material also showed very low cytotoxicity since no relevant cell detachment or apoptosis was detected on any of the substrates. Interestingly, surface topography had a profound impact on cell shape: optical microscopy revealed that MSCs on the nanopatterned PI aligned parallel to the direction of the grooves and had an elongated morphology. Conversely, MSCs on the flat PI and on TCP displayed a random arrangement and no signs of elongation (Fig. 2.9 (b)). MSCs on the nanogrooved PI retained their alignment and elongated morphology even after having been successfully differentiated into adipocytes using an induction medium supplemented with specific chemicals and hormones (Fig. 2.9 (c)). Scanning electronic microscopy images showed that cells developed nice filopodia and tightly interacted with the periodic nanogrooves (Fig. 2.9 (d)).

2.4 Conclusion and outlook

Multibeam interference represents a novel technology for surface nanostructuring applications. Compared to other techniques, MBI can directly ablate a substrate to generate smaller structures over a larger area at lower cost. Interestingly, nanostructures can have a deep impact on cellular biology and be integrated into biomedical devices. Neuronal cells have been reported to elongate along nanogrooves but not on nanodots or dotted nanogrooves. The results indicated that groove depth was more relevant than groove width in stimulating cell elongation. Furthermore, when interacting with primary MSCs, periodical nanogrooves supported their growth and allowed their differentiation towards adipocytes in addition to eliciting cell elongation. In conclusion, MBI represents a straightforward and flexible technique with a broad range of applications, particularly in life sciences, e.g. for the generation of smart biomaterials able to control complex cellular functions through specific surface patterns.

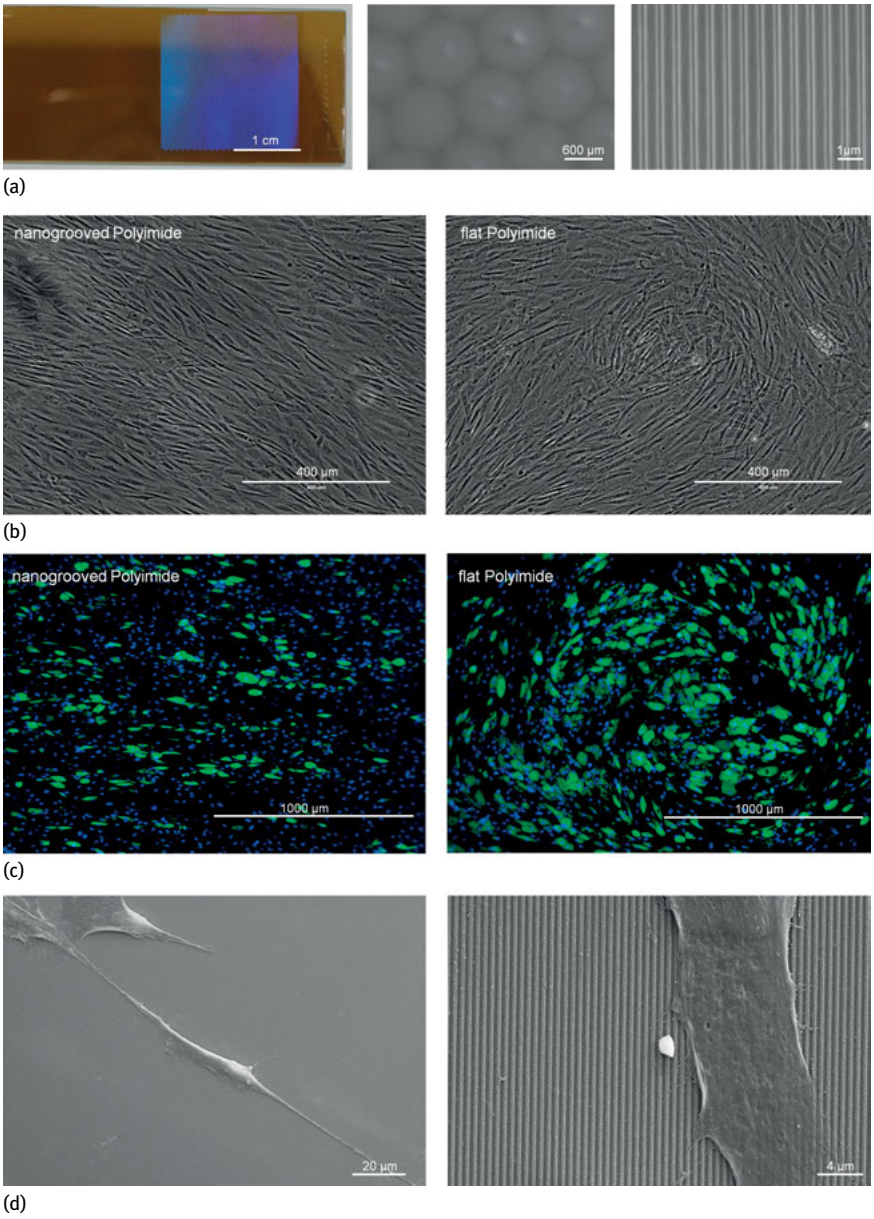

Fig. 2.9: (a) Photography of the nanogrooved polyimide foil with the structures depicted in blue due to the iridescence phenomenon (left), and SEM details of the nanogrooved areas (center and right). (b) Adipose tissue derived mesenchymal stem cells align parallel to the nanogrooves while displaying a random alignment on the non-structured surfaces. (c) Upon differentiation into adipocytes. MSCs retained their alignment. Fat droplets of the adipocytes are stained green with BODIPY while the nuclei are stained blue with DAPI. (d) Scanning electronic microscopy pictures of MSCs on the nanogrooved PI.

References

[1] Schellenberg A, Joussen S, Moser, K, Hampe, N, Hersch N, Hemeda H, Schnitker J, Denecke B, Lin, Q, Pallua N, Zenke M, Merke R, Hoffmann B, Wagner W. Matrix elasticity, replicative senescence and DNA methylation patterns of mesenchymal stem cells. Biomaterials, Issue 35, 2014, 6351–6358
[2] Laird DJ, von Andrian UH, Wagers AJ. Stem Cell Trafficking in Tissue Development, Growth, and Disease. Cell, Volume 132, Issue 4, 22 February 2008, 612–630
[3] Blau HM, Brazelton TR, Weimann JM. The Evolving Concept of a Stem Cell: Entity or Function? Cell, Volume 105, Issue 7, 29 June 2001, 829–841
[4] Weissman IL, Stem Cells: Units of Development, Units of Regeneration, and Units in Evolution. Cell, Volume 100, Issue 1, 7 January 2000, 157–168
[5] Morrison SJ, Shah NM, Anderson DJ. Regulatory Mechanisms in Stem Cell Biology. Cell, Volume 88, Issue 3, 7 February 1997, 287–298
[6] Knoblich JA. Mechanisms of Asymmetric Stem Cell Division. Cell, Volume 132, Issue 4, 22 February 2008, 583–597
[7] Jones L. Stem cells: So what's in a niche? Current Biology, Volume 11, Issue 12, 26 June 2001, R484–R486
[8] Morrison SJ, Spradling AC. Stem Cells and Niches: Mechanisms That Promote Stem Cell Maintenance throughout Life. Cell, Volume 132, Issue 4, 22 February 2008, 598–611
[9] Fuchs E, Tumbar T, Guasch G. Socializing with the Neighbors: Stem Cells and Their Niche. Cell, Volume 116, Issue 6, 19 March 2004, 769–778
[10] Caplan AI. Mesenchymal stem cells. Journal of Orthopaedic Research, Volume 9, Issue 5, 1991, 641–650
[11] da Silva ML, Chagastelles PC, Nardi NB. Mesenchymal stem cells reside in virtually all post-natal organs and tissues. Journal of Cell Science, Volume 119, Issue 11, June 2006, 2204–2213
[12] Phinney DG. Functional heterogeneity of mesenchymal stem cells: implications for cell therapy. Journal of Cell Biochem, Volume 113, Issue 9, September 2012, 2806–2812
[13] Ho AD, Wagner W, Franke W. Heterogeneity of mesenchymal stromal cell Preparations. Cytotherapy, Volume 10, Issue 4, 2008, 320–330
[14] Bianco P, Robey PG, Simmons PJ. Mesenchymal Stem Cells: Revisiting History, Concepts, and Assays. Cell Stem Cell, Volume 2, Issue 4, 10 April 2008, 313–319
[15] Dominici M, Le Blanc K, Mueller I, Slaper-Cortenbach I, Marini F, Krause D, Deans R, Keating A, Prockop DJ, Horwitz E. Minimal criteria for defining multipotent mesenchymal stromal cells. The International Society for Cellular Therapy position statement. Cytotherapy, Volume 8, Issue 4 August 2006, 315–317
[16] Nombela-Arrieta C, Ritz J, Silberstein LE. The elusive nature and function of mesenchymal stem cells. Nature Reviews Molecular Cell Biology, Volume 12, Issue 2, February 2011, 126–131
[17] Anguille S, Smits EL, Lion E, van Tendeloo VF, Berneman ZN. Clinical use of dendritic cells for cancer therapy. The Lancet Oncology, Volume 15, Issue 7, June 2014, e257–e267
[18] Pittenger MF, Mackay AM, Beck SC, Jaiswal RK, Douglas R, Mosca JD, Moorman MA, Simonetti DW, Craig S, Marshak DR. Multilineage Potential of Adult Human Mesenchymal Stem Cells. Science, Volume 284, Issue 5411, 2 April 1999, 143–147
[19] Uccelli A, Moretta L, Pistoia V. Mesenchymal stem cells in health and disease. Nature Reviews Immunology 8, September 2008, 726–736
[20] Macchiarini P, Jungebluth P, Go T, Asnaghi MA, Rees LE, Cogan TA, Dodson A, Martorell J, Bellini S, Parnigotto PP, Dickinson SC, Hollander AP, Mantero S, Conconi MT, Birchall MA. Clinical transplantation of a tissue-engineered airway. The Lancet, 13 December 2008, Vol. 372, Issue 9655, 2023–2030

[21] Schellenberg A, Joussen S, Moser K, Hampe N, Hersch N, Hemeda H, Schnitker J, Denecke B, Lin Q, Pallua N, Zenke M, Merkel R, Hoffmann B, Wagner W. Matrix elasticity, replicative senescence and DNA methylation patterns of mesenchymal stem cells. Biomaterials, Volume 35, Issue 24, August 2014, 6351–6358
[22] Eyckmans J, Boudou T, Yu X, Chen CS. A Hitchhiker's Guide to Mechanobiology. Developmental Cell, Volume 21, Issue 1, 19 July 2011, 35–47
[23] Kim KM, Choi YJ, Hwang JH, Kim AR, Cho HJ, Hwang ES, Park JY, Lee SH, Hong JH- Shear stress induced by an interstitial level of slow flow increases the osteogenic differentiation of mesenchymal stem cells through TAZ activation. PLoS One, Volume 9, Issue 3, 21 March 2014, Article Number e92427
[24] Ballotta V, Smits AIPM, Driessen-Mol A, Bouten CVC, Baaijens FPT. Synergistic protein secretion by mesenchymal stromal cells seeded in 3D scaffolds and circulating leukocytes in physiological flow. Biomaterials, Volume 35, Issue 33, November 2014, 9100–9113
[25] De Lisio M, Jensen T, Sukiennik RA, Huntsman HD, Boppart MD. Substrate and strain alter the muscle-derived mesenchymal stem cell secretome to promote myogenesis. Stem Cell Research & Therapy, 6 June 2014, Volume 5, Article 74
[26] Friedl G, Schmidt H, Rehak I, Kostner, G, Schauenstein K, Windhager R. Undifferentiated human mesenchymal stem cells (hMSCs) are highly sensitive to mechanical strain: transcriptionally controlled early osteo-chondrogenic response in vitro. Osteoarthritis and Cartilage, Volume 15, Issue 11, November 2007, 1293–1300
[27] Engler AJ, Sen S, Lee Sweeney H, Discher DE. Matrix Elasticity Directs Stem Cell Lineage Specification. Cell, Volume 126, Issue, 4, 25 August 2006, 677–689
[28] Lo CM, Wang HB, Dembo M, Wang YL. Cell movement is guided by the rigidity of the substrate. Biophysical Journey, Volume 79, Issue 1, July 2000, 144–152
[29] Conway A, Schaffer DV. Biophysical regulation of stem cell behavior within the niche. Stem Cell Research & Therapy, Volume 3, 14 December 2012, Article 50
[30] Curtis A, Riehle M. Tissue engineering: the biophysical background. Physics in Medicine and Biology, Volume 46, Issue 4, April 2001, R47–R65.
[31] Humphries MJ. Integrin Structure. Biochemical Society Transactions, Volume 28, Part 4, August 2000, 311–340
[32] Giancotti FG, Ruoslahti E. Integrin Signaling. Science, Volume 285, Issue 5430, 13 August 1999, 1028–1033
[33] Tanentzapf G, Martin-Bermudo MD, Hicks MS, Brown NH. Multiple factors contribute to integrin–talin interactions in vivo. Journal of Cell Science, Volume 119, Issue 8, 15 April 2006, 1632–1644
[34] Geiger B, Spatz JP, Bershadsky AD. Environmental sensing through focal adhesions. Nature Reviews Molecular Cell Biology, Volume 10, Issue 1, January 2006, 21–33
[35] Scales TME, Parsons MP. Spatial and temporal regulation of integrin signalling during cell migration. Current Opinion in Cell Biology, Volume 23, Issue 5, October 2011, 562–568
[36] McBeath R, Pirone DM, Nelson CM, Bhadriraju K, Chen CS. Cell Shape, Cytoskeletal Tension, and RhoA Regulate Stem Cell Lineage Commitment. Developmental Cell, Volume 6, Issue 4, April 2004, 483–495
[37] Murphy WL, McDevitt TC, Engler AJ. Materials as stem cell regulators. Nature Materials, Volume 13, Issue 6, June 2014, 547–55
[38] Dalby MJ, Gadegaard N, Oreffo ROC. Harnessing nanotopography and integrin matrix interactions to influence stem cell fate. Nature Materials, Volume 13, Issue 6, June 2014, 558–569

[39] McMurray RJ, Gadegaard N, Tsimbouri PM, Burgess KV, McNamara LE, Tare R, Murawski K, Kingham E, Oreffo ROC, Dalby MJ. Nanoscale surfaces for the long term maintenance of mesenchymal stem cell phenotype and multipotency. Nature Materials, Volume 10, Issue 8, 2010, 637–644
[40] Fiedler J, Özdemir B, Bartholomä J, Plettl A, Brenner RE, Ziemann P. The effect of substrate surface nanotopography on the behavior of multipotnent mesenchymal stromal cells and osteoblasts. Biomaterials, Volume 34, Issue 35, November 2013, 8851–8859
[41] Wang PY, Li WT, Yu J, Tsai WB. Modulation of osteogenic, adipogenic and myogenic differentiation of mesenchymal stem cells by submicron grooved topography. Journal of Materials Science: Materials in Medicine, Volume 23, Issue 12, December 2012, 3015–3028
[42] Wu YN, Law JBK, He AY, Low HY, Hui JHP, Lim CT, Zheng Yang Z, Lee EH. Substrate topography determines the fate of chondrogenesis from human mesenchymal stem cells resulting in specific cartilage phenotype formation. Nanomedicine: Nanotechnology, Biology and Medicine, Volume 10, Issue 7, October 2014, 1507–1516
[43] Nikkhah M, Edalat F, Manoucheri S, Khademhosseini A. Engineering microscale topographies to control the cell–substrate interface, Biomaterials, Volume 33, Issue 21, July 2012, 5230–5246
[44] Unadkat HV, Hulsman M, Cornelissen K, Papenburg BJ, Truckenmul¨ler RK, Post GF, Uetz M, Reinders MJT, Stamatialis D, Van Blitterswijk CA, De Boer J. An algorithm-based topographical biomaterials library to instruct cell fate. Proceedings of the National Academy of Sciences of the United States of America, Volume 108, Issue 40, 2011, 16565–16570
[45] Ghaemi SR, Harding FJ, Delalat B, Gronthos S, Voelcker NH. Exploring the mesenchymal stem cell niche using high throughput screening. Biomaterials, Volume 34, Issue 31, October 2013, 7601–7615
[46] Robison RA. Moore's Law: Predictor and Driver of the Silicon Era. World Neurosurgery, Volume 78, Issue 5, November 2012, 399–403
[47] Burrow GM, Gaylord TK. Multi-Beam Interference Advances and Applications: Nano-Electronics, Photonic Crystals, Metamaterials, Subwavelength Structures, Optical Trapping, and Biomedical Structures. Micromachines, Volume 2, Issue 2, June 2011, 221–257
[48] Beckemper S, Huang JT, Gillner A, Wang KY. Generation of Periodic Micro- and Nano-structures by Parameter-Controlled Three-beam Laser Interference Technique. JOURNAL OF LASER MICRO NANOENGINEERING, Volume 6, Issue 1, March 2011, 49–53
[49] Steger M, Hartmann C, Beckemper S, Holtkamp J, Gillner A. Fabrication of Hierarchical Structures by Direct Laser Writing and Multi-Beam-Interference. JOURNAL OF LASER MICRO NANOENGINEERING, Volume 8, Issue 3, December 2011, 210–215
[50] Hecht E. Optik. Oldenbourg, Munich, 2005, 624
[51] Steger M, Boes S, Thilker S, Gillner A. Measuring Method for the Interference Contrast of Multi-Beam-Interference. JOURNAL OF LASER MICRO NANOENGINEERING, Volume 9, Issue 3. 2014
[52] Bremus-Koebberling E A, Beckemper S, Koch B, Seiler N. Laser Functionalization of Polymers to Create Bio-inspired Surfaces. International Bionic Engineering Conference 2011, 18–20 Sept. 2011, Boston, MA, USA.
[53] Bremus-Koebberling EA, Beckemper S, Koch B, Gillner A. Nano structures via laser interference patterning for guided cell growth of neuronal cells. Journal of Laser Applications 2012, 042013-1–6.
[54] Klinge PM, Vafa MA, Brinker T, Brandis A, Walter GF, Stieglitz T, Samii M, Wewetzer K. Immunohistochemical characterization of axonal sprouting and reactive tissue changes after long-term implantation of a polyimide sieve electrode to the transected adult rat sciatic nerve. Biomaterials, Volume 22, Issue 17, September 2001, 2333–2343

[55] Julien S, Peters T, Ziemssen F, Arango-Gonzalez B, Beck S, Thielecke H, Büth H, Van Vlierberghe S, Sirova M, Rossmann P, Rihova B, Schacht E, Dubruel P, Eberhart Zrenner E, Schraermeyer U. Implantation of ultrathin, biofunctionalized polyimide membranes into the subretinal space of rats. Biomaterials, Volume 32, Issue 16, June 2011, 3890–3898
[56] Rubehn B, Stieglitz T. In vitro evaluation of the long-term stability of polyimide as a material for neural implants. Biomaterials, Volume 31, Issue 13, May 2010, 3449–3458

V. Coger, N. Million, P. Wilke, A. Pich, P. M. Vogt, K. Reimers, and S. Barcikowski

3 Laser-generated bioactive hydrogels as ion-release systems for burn wound therapy

Abstract: Here, we investigated the fabrication of bioactive metal nanoparticle-loaded hydrogels, their immobilization into non-woven electrospun microfibers and their biocompatibility. For this purpose, zinc and iron nanoparticles were synthesized by pulsed laser ablation of corresponding metal targets in an aqueous monomer solution. This solution was simultaneously and consecutively polymerized yielding loaded hydrogels. The laser ablation process was investigated concerning the influence of different laser parameters on the ablation efficiency, including the determination of the cavitation bubble dynamics. The *in situ* fabrication of stable nanoparticle polymer composites, namely nanoparticle-loaded microgels, using the laser ablation method was established. The microgels described were immobilized by electrospinning in order to achieve surface modified microfibers. Electron microscopy and inductively coupled plasma mass spectrometry were used to characterize the suitability of the zinc nanoparticle-loaded microgels immobilized in microfibers for a zinc ion release over a period of five days without release of the nanoparticles. The amounts of ions and the release rates were regulated by variations of the composites used for the electrospinning process. Parallely, *in vitro* indirect biocompatibility and bioresponse tests showed no cytotoxicity not from the hydrogels nor from the microfibers. Cell proliferation was increased for both systems separately and for their combination. The ion releases of the iron and zinc nanoparticle-loaded microgels were too low to induce any subsequent effect on cell culture.

3.1 Introduction

Severe burn injuries are wounds with a number of potential harmful consequences. For the patient deep and/or large burns often result in painful and difficult wound healing, unappealing scar formation and long-term sequelae. Due to the impairment of skin function, protection against outside aggressors such as microbes, difficulties maintaining homeostasis, acute infections or dehydration may occur. Therefore, restoration of integument integrity is an important first measure in any acute burn treatment.

Healing of a wound due to burns, abrasion, laceration or contusion always follows three main phases which overlap in time: inflammation, proliferation and remodeling. The inflammation phase is the healing initiation. A clot is formed by combination of vasoconstriction, aggregation of platelets, and thrombogenesis which enables maintenance of hemostasis. The recruitment of neutrophils and macrophages enable the

phagocytosis of infective particles, foreign substances cellular residue and extracellular matrix (ECM) debris. Neutrophil activity was shown *in vitro* to be stimulated by zinc ions at concentrations from 6 to 50 μM [1]. Parallely, macrophages, involved in the degradation of the damaged ECM, secrete proteases such as MMP-2, -9 or interstitial collagenase, three enzymes known to have zinc dependent activity [2–4]. Parallel to the end of the inflammatory phase, the proliferation phase starts during which ECM is rebuilt to form granulation tissue. It implies major collagen type III production, which is known to rely on procollagen-lysine 5-dioxygenase, an iron dependent enzyme [5]. During this phase, reepithelialisation occurs. Keratinocytes proliferate, migrate, and differentiate to cover the wound. Keratinocyte differentiation can be induced by local application of zinc, as shown by Inoue et al [6]. Finally, maturation begins by remodeling ECM from collagen type III into type I. Therefore once again zinc dependent MMPs [3, 7–9] play a major role in ECM degradation, while iron dependent production of collagen type I [5] occurs. Hence, the process of wound healing can greatly benefit from the release of zinc and iron ions, particularly when the dose is adapted to the corresponding wound healing phase.

Therefore several approaches have been taken to test the effects of metals like iron and zinc in wound healing, mainly aiming at a modification of cell activity or antimicrobial effects. It is known that topical or local application of metal particles or ions induces cell stimulation and that combinations of different metals can have synergetic effects [10]. But this raises the following problem concerning nanoparticle interactions with the different dermal cell populations: Vania et al. showed that zinc oxide nanoparticles do not penetrate further than the epidermis when applied topically onto healthy skin [11] although it had been proven that keratinocytes can uptake nanoparticles by endocytosis [12]. Furthermore, their application to wounded dermis is questionable due to their toxicity towards underlying cells deriving from different pathways well summarized by Roy et al. [13]. Therefore our approach focusses on zinc and iron for the development of an ion delivery system where metal nanoparticles are embedded into a hydrogel, itself immobilized onto microfibers. This allows safety, efficiency and long-term reliability, which are important features for drug-release systems in the treatment of large burns. We chose an ion release system based on nanoparticle carriers, because due to their high surface to volume ratio they can release more bioactive ions than micro-sized particles of the same mass [14]. Inspired by Hahn et al., who reported 80 days of ion release from nanoparticle silicon composites [15], nanoparticle-polymer composites could be applicable as long-term treatment systems.

Nanocomposites may be produced by a variety of methods. A chemical preparation method requires chemical precursors, several process steps and post-processing cleaning steps. Pulsed laser ablation in liquids (PLAL) [16] is a promising alternative. In brief, nanoparticles are obtained by ablating a solid metal plate in the desired liquid by a focused pulsed laser beam. When the liquid chosen is a polymer solution this setup describes an easy and fast *in situ* preparation of nanoparticle-polymer composites [17]. Due to the absence of salts, additional surfactants or reagents, subsequent

cleaning steps are not required. In contrast to chemical methods the laser ablation of metal targets offers a great variety of materials, which means it is not necessary to establish new synthesis routes for each metal, a simple exchange of the target plate is sufficient to generate nanoparticles of each desired material.

When using PLAL it has to be taken into consideration that various process parameters have an influence on the ablation process efficiency, e.g. the repetition rate, the liquid layer above the target and the characteristics of the liquid itself [16, 18, 19]. These interactions therefore have to be studied to understand the laser ablation process. The preparation of nanoparticle polymer composites also has to be investigated before microgel fixation onto electrospun microfibers is established.

Electrospinning is a technique aiming at the production of fibers with diameters on the micrometer-scale or even lower. Electrospinning is therefore used for applications where surfaces play a major role, e.g. sensors [20–23], photocatalytic properties [24–27], antibacterial properties [28–30], UV-protection [31] and humidity sensing [32]. Electrospinning is applied by introducing a polymer solution or a polymer melt into an electric field. Since only solution-spinning is relevant for this work, this approach will be described briefly in the following paragraph. Usually, the polymer containing reservoir will be charged, negatively or positively, while a target collector is connected grounded, or vice versa. This will be done until the solution exhibits an electric force sufficient to overcome the surface tension. Voltage acts as the driving force while at the same time, thanks to application of an additional feed pump, the solution is mechanically driven out of a capillary, forming a droplet at the tip of the outlet. Electrically charged polymer solutions are then ejected from the surface of droplets forming a characteristic cone-shaped structure [33]. Ejected fibers are targeted onto a collector which exhibits the opposite charge to the polymer solution. If only flat surfaces are used, the fibers are randomly oriented on the surface forming non-wovens. In principle, it is possible to apply additional devices to achieve orientation of the fibers, e.g. rotating drums, parallel ordered collectors and so on. For the preparation of wound dressings non-oriented fibers – i.e. non-wovens – are satisfactory and simple to prepare. Hence, the dressings discussed in this work, solely consist of non-wovens. In the case of wound dressings it is important that open channels exist between wound and environment in order to ensure a controlled wound atmosphere. This prevents accumulation of wound secretions and ensures the optimal humidity level required for each wound healing phase. Otherwise, bacterial contamination, wound maceration or drying out may have consequences such as wound closure delay or worse.

Poly(ε-caprolactone) (PCL) has been proven to be well-suitable for electrospinning processes and biomedical applications due to its biocompatibility and biodegradability [34–36]. The first property is a prerequisite for topical application as a wound dressing that will be in direct contact with wounds. If it is possible that low amounts of PCL are released and accumulate within the wound environment, biodegradability ensures that residues will be removed by degradation over time and the absence of long term toxic effects.

In this project *in situ* preparation of nanoparticle-loaded microgels using laser ablation technique will be presented. In this context several aspects of the laser ablation process will be investigated. To ensure that no hydrogels remain in the healed skin, we immobilized prepared nanoparticle-loaded hydrogels on electrospun fibers.

To ensure the biocompatibility of our system, we performed cell-based assays for cell metabolism and lactate dehydrogenase (LDH) activity with elution of either microgels and zinc or iron containing microgels, as well as eluates of microfibers and microgel covered microfibers onto L929 fibroblast cell line cultures.

3.2 Results and discussion

3.2.1 Microgels containing laser-generated nanoparticles

Within this DFG priority program 1327 we have examined the fundamentals of the laser ablation process and applied the received knowledge to fabricate functional nanocomposites for biological applications which were tested for their activity and biocompatibility in medically relevant setups.

First of all, the laser ablation process for the fabrication of laser-generated nanoparticles should be understood. Therefore, several investigations had been conducted in order to understand the fundamental processes occurring during the laser irradiation of pure metal plates in a liquid environment and how certain process parameters influence nanoparticle productivity.

As mentioned before, the laser ablation process is influenced by several parameters. For example a variation of the pulse energy, the fluence and the wavelength was found to alter nanoparticle productivity.

Previous experiments could show that with a picosecond laser system, the highest nanoparticle productivity could be reached using the fundamental wavelength (1030 nm, 250 µJ) (see Fig. 3.1). The fundamental wavelength reaches a higher pulse energy and therefore a higher laser fluence, resulting in the higher nanoparticle productivity compared to the second harmonic (515 nm, 125 µJ) [37].

The most important parameter which determines the laser ablation efficiency, defined as ablation per pulse, is the focus position of the laser beam. It has to be considered that while using ultra-short laser pulses in liquid environment non-linear effects like self-focusing and filamentation lead to a shift of the optimal focus [38, 39]. To avoid time consuming experiments to find the focus for each experimental system, a semi-empirical method which allows calculation of the focal position for each system was established [16].

The ablation efficiency is also dependent on the temporal interpulse distance, which is defined as the reciprocal value of the repetition rate. Wagener et al. could show that up to 5 kHz the ablation efficiency remains constant, while an exponential decrease is found at higher repetition rates [40]. The explanation for this phenomenon

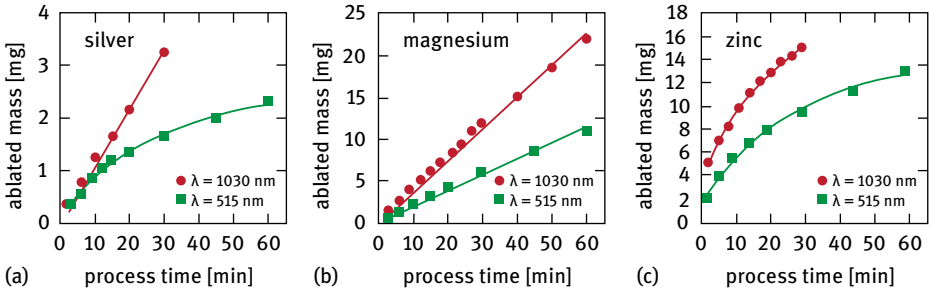

Fig. 3.1: Effect of wavelength and material on nanoparticle productivity; cumulative ablated mass over processing time of silver (a), magnesium (b) and zinc (c) for ablation in THF using fundamental (1030 nm; 250 µJ) and second harmonic (515 nm; 125 µJ) laser wavelengths. [37]

is founded on the dynamic behavior of the cavitation bubble. Each laser pulse induces a cavitation bubble with a defined lifetime. At higher repetition rates the cavitation bubble of the first pulse is still present when the next pulse is directed towards the target. Consequently, the cavitation bubble induces a shielding effect for the following pulse by scattering and absorption, resulting in a reduced ablation efficiency of the following pulse. For lower repetition rates the bubble generated by the first pulse is already collapsed when the next pulse hits the target surface. No interactions between bubble and pulse take place [40].

Beside the temporal pulse distance, a crucial aspect to influence the ablation efficiency is the spatial pulse to pulse distance which can be adjusted by the repetition rate and the scanning speed. An interpulse distance larger than 100 µm allows avoidance of the shielding effect of the cavitation bubble leading to high ablation efficiency [40]. However, it should be noted that with a further increase of the distance, the efficiency decreases due to the reduced or totally missing heating effect of the target by the previous laser pulse before, which normally support the ablation process [40].

Based on findings illustrated in the previous paragraph, it is obvious that the cavitation bubble plays an important role in the nanoparticle generation process. Accordingly it was required to study the cavitation bubble dynamics and particularly how it coincides with nanoparticle formation. Parallel to the work of De Giacomo et al., who investigated the temporal evolution of the bubble [41], we did small-angle X-ray scattering (SAXS) measurements to be able to look inside the cavitation bubble and track the nanoparticle distribution. The first results from SAXS determined a maximum bubble height of 1.15 mm above the gold target which was ablated by nanosecond laser pulses [42]. After 230 µs a second bubble, the rebound, could be detected [42]. By evaluating the data, two different gold nanoparticle species could be differentiated inside the cavitation bubble. With an average diameter of 8–10 nm small primary particles could be found and also secondary particles with a diameter of 45 nm are present inside the bubble [42]. The small ones are located in the whole bubble volume, whereas secondary particles are accumulated in the middle [42]. This

primary work only analyze the cavitation bubble at the maximum bubble extension. In order to get an idea of the nanoparticle formation process during the whole cavitation bubble lifetime, further examinations had been done using SAXS. The cavitation bubble lifetime could be determined to be 350 µs, while the maximum height was reached after 80 µs [43]. These studies could confirm the presence of two particle populations with diameters of 8–10 nm and 40–60 nm inside the bubble [43]. In addition, these experiments could show that the nanoparticle distribution inside the bubble is time dependent. When the bubble reaches its maximum height, primary particles are located all over the bubble, whereas only a few agglomerates could be found. During the first collapse, small particles seem to form agglomerates and both, small particles and agglomerates, accumulate near the target surface. The particles stay close to the target surface during the bubble rebound, agglomerate and are released into the surrounding liquid after the final collapse [43]. These experiments give spatial and temporal information on the initial stages of nanoparticle generation process during laser ablation in liquids.

After the investigation of the fundamentals of the laser ablation process the fabrication of nanoparticle-polymer composites of different metals will be discussed.

To fabricate desired nanoparticle-polymer composites an *in situ* conjugation approach was used. In first experiments zinc, silver and magnesium nanoparticles were generated in thermoplastic Polyurethane (TPU) dissolved in tetrahydrofuran (THF) by picosecond laser ablation [37]. In case of zinc, mono-crystalline fully oxidized nanoparticles with an average diameter of 6.5 nm surrounded by a polymer shell were formed. The formation of ZnO was validated by X-ray diffraction (XRD) while photoluminescence measurements revealed oxygen defects inside the crystal structure [44]. The conjugation of nanoparticles with polymers influences the dispersion of the particles, which could be shown for systems consisting of silver or copper nanoparticles [45]. By adjusting the polymer (TPU) concentration, the agglomeration could be minimized resulting in a homogeneous composite with embedded nanoparticles at average sizes of 5 nm [45]. The optimal stabilization concentration of TPU for the observed system was determined to be 0.3 wt % [45]. Furthermore, these nanocomposites could be post processed by injection molding, while the ideal dispersion of the nanoparticles in the polymer matrix was retained [45].

Another approach was to carry out the ablation process in a monomer solution consisting of ε-Caprolactone (CL), polymerizing into of Poly(ε-caprolactone) (PCL), and the solvent THF. PCL was chosen as a basic matrix material for nanocomposites applicable in burn wound treatment. In first experiments, polymerization was meant to be initiated by zinc oxide nanoparticles. However, it could be shown, that at room temperature the polymerization was incomplete leading to the formation of oligomers [46]. To accomplish full polymerization, the laser ablation process was done at elevated temperatures. At 140 °C full polymerization could be achieved while the absence of any remaining oligomers was verified by Fourier Transform Infrared Spectroscopy (FTIR) [46].

However, in order to synthesize nanocomposites for biological and medical applications organic solvents should be avoided. Hence, water soluble monomers like *N*-Vinylcaprolactam (VCL) and Acetoacetoxyethyl methacrylate (AAEM), crosslinked by *N*,*N*′-Methylenebis(acrylamide) (BIS), and 2,2-Azobis(2-methylpropyonamidine) dihydrochloride (AMPA) as polymerization initiator were further examined as a suitable matrix material for nanocomposites [47]. It could be verified that this system is highly suitable for the fabrication of nanoparticle-loaded microgels, while laser synthesis of nanoparticles occurred parallel to the microgel formation. It was shown that the nanoparticles are located inside these gels [47]. As these composites were fabricated via a purely water-based and hence potentially biocompatible synthesis route they are ideally suited as ion-release systems in for medical applications. Hence *in vitro* evaluations were performed in order to determine their biocompatibility.

3.2.2 Microgel biotesting

We performed indirect *in vitro* testing on NCTC clone 929 cell line with CytoTox-One™ for cytotoxicity and CellTiter-Blue® for cell proliferation (Fig. 3.2 (a), (b) and (f)). Several concentrations of empty microgels and microgels containing iron or zinc nanoparticles were eluted. The solutions obtained remained microparticle free as we tested them via absorption spectrophotometry and dynamic light scattering.

The indirect cytotoxicity tests (Fig. 3.2 (a)) performed with elutions of microgels showed no differences between the control cultures and those exposed to three types of microgels tested at varying concentrations. Therefore we concluded that the microgel itself as well as those loaded with metal nanoparticles were non-toxic.

Concerning cell proliferation (Fig. 3.2 (b)), we were able to observe an improvement of the measured cell activity for microgels eluates at a concentration of 400 µg/ml, which was up to 1.3 times higher than in the control culture. We could therefore define our microgel as non-cytotoxic, and it can be seen as a proliferation enhancer for the tested L929 cell line. Concerning the loading of metals into microgels, no significant differences were found between the empty microgel and the microgels with embedded iron nanoparticles at the same concentration. On the other hand, a statistical improvement was found at elution concentration of 400 µg/ml when zinc nanoparticles are embedded in hydrogels. If we refer to the ion release potential, at a microgel concentration of 400 µg/ml, zinc ion concentration is estimated to be 2 µg/ml or 150 µM. No statistical differences in cell proliferation were found at this concentration of zinc salts (Fig. 3.2 (b)).

As we defined the microgel's content at 1 % (w/w) and the release after 24 hours of incubation in aqueous solution about 50 % (data not shown), we concluded that we had a maximum metal ion released concentration around 20 µg/ml (corresponding to 450 µM and 300 µM for iron and zinc respectively). Comparing these concentrations with the literature, the LD50 of zinc on L929 fibroblasts is shown at concentration of

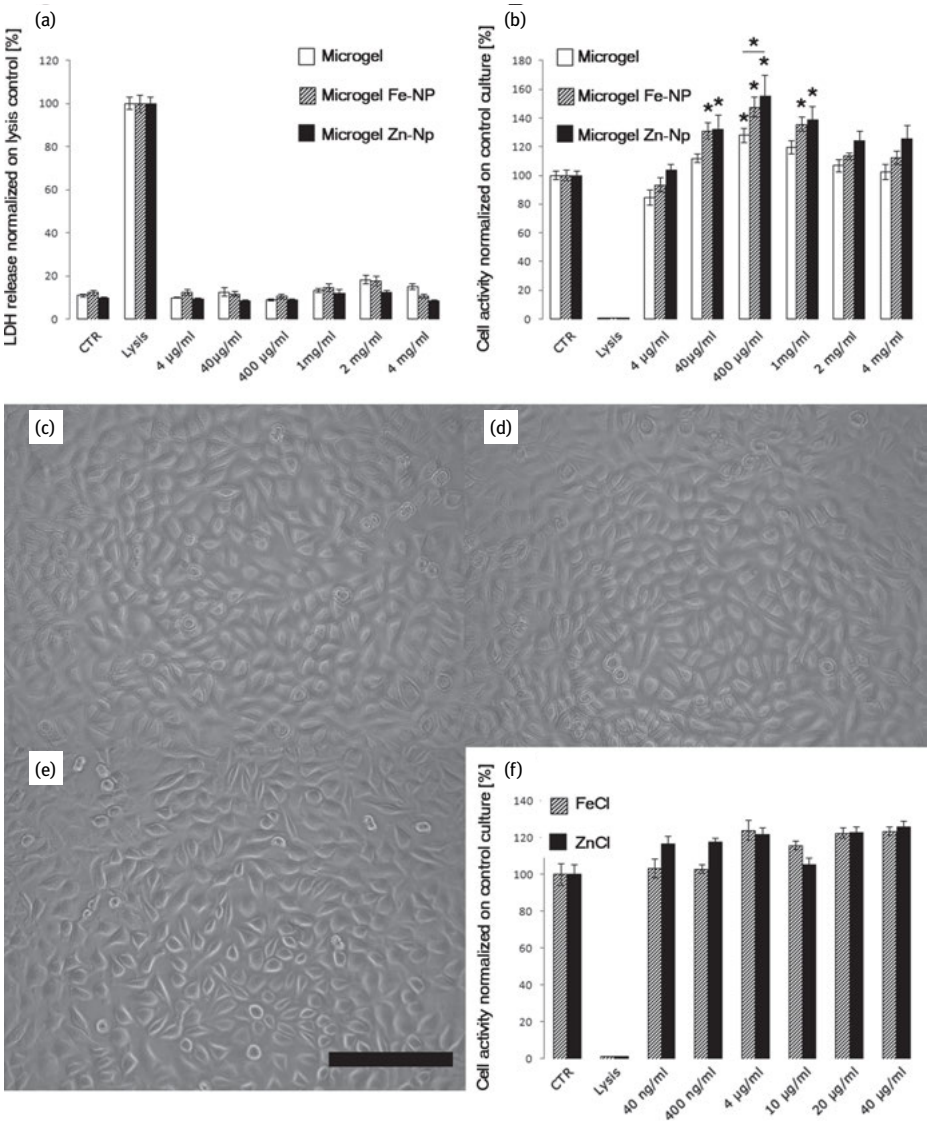

Fig. 3.2: Effect of different microgel eluate concentrations and contents on L929 cell line culture. (a) cytotoxicity assay and (b) proliferation assay performed with elutions of the different microgels. Microscopy observations were performed with elutions of iron chloride (c) and zinc chloride (d) 40 µg/ml and compared to control culture (e), before testing the proliferation under metal salt elutions at equivalent concentrations released by the microgels. (c), (d) and (e) are representative of three independent reproductions; scale bar represents 200 µm. Values are normalized on lysis control for (a) and control culture (CTR) for (b) and (f); results are expressed as means of three independent experiments ± standard error of the mean; Bonferroni analysis of variance, * $p < 0.05$.

335 µM [48]. Additionally, Wataha et al. showed that culture conditions could affect the appearing cytotoxicity [49]. In order to evaluate cytotoxicity of zinc and iron ions under our chosen conditions, we also tested iron (in ferric form) and zinc as chloride salts diluted in culture medium (Fig. 3.2 (c)–(f)). This confirmed iron to be non-cytotoxic at the administered concentrations as previously described [50]. Surprisingly, zinc showed no toxicity signs, like iron, even though the concentrations tested were up to twenty times higher than those reported by Wataha et al.

3.2.3 Electrospun fibers for microgel immobilization

The first attempt at fiber-modification with laser generated nanoparticles was achieved by a simple method in which particles were ablated within an organic solution which contained dissolved polymer. The approach included nanoparticle synthesis and mixing with polymer. Afterwards, the nanoparticles were stabilized by evaporating the organic solvent and inclusion of the particles within the polymer matrix. The composites were subsequently resolved in a THF-DMF mixture and processed by means of electrospinning [46]. As a result, non-wovens with homogeneously distributed nanoparticles were achieved. This method is simple but it only assures homogeneously mixed fiber-particle composites. The location of the particles, i.e. assembly on or within the fibers, cannot be controlled. As a consequence, incorporated nanoparticles would only be available for the healing process once the fiber-matrix degrades (a very time consuming process in the case of PCL). Conversely, a certain amount of inorganic material would not be available immediately after contact with the wound. It has to be assumed that the nanoparticles are statistically distributed within all layers of the fibers, as well as on top of the surface. Moreover, there are no additional forces except for Van-der-Waals interactions linking the nanoparticles on the surface hence this method was only valuable for composites with limited relevance for biomedical applications.

Figure 3.3 shows PCL-microfibers after electrospinning in the presence of various nanoparticles from THF-DMF mixtures. THF was chosen as the solvent in which laser ablation was performed due to its solubility and optical permeability. Since the cavitation bubble causes high temperature and pressure gradients, pyrolysis of THF was investigated. It was found that pyrolysis leads to ring opening of the cyclic ether as observed by means of FTIR spectroscopy. Due to the high partial pressure of the solvent and by-products, quantifying the pyrolysis was not possible. Qualitatively, FTIR spectroscopy confirmed the destructive influence of laser light on THF [46]. THF therefore had to be replaced by another solvent and we switched to an aqueous system.

The next step of nanoparticle utilization on microfibers was to introduce a carrier-system capable of providing two features: first as a surfactant, supporting the dispersibility and colloidal stability of the nanoparticles in an aqueous medium second as an adherence surface, anchoring the nanoparticles exclusively on the fiber

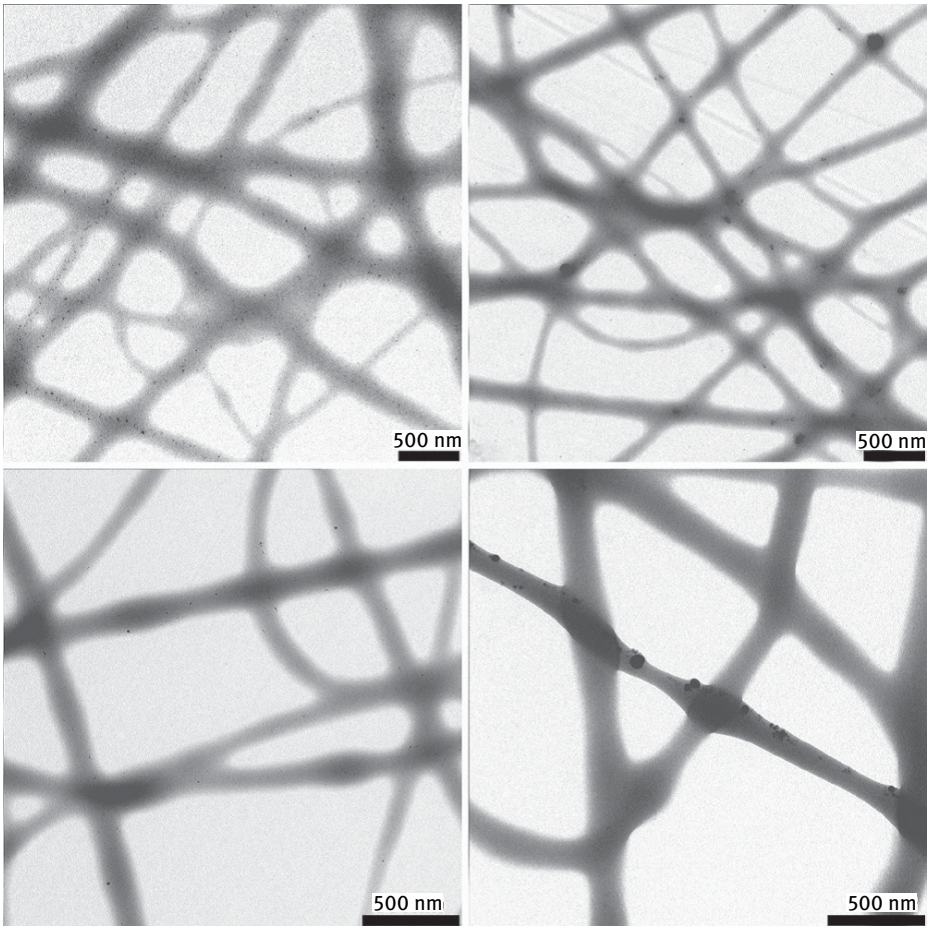

Fig. 3.3: Electrospun PCL-fibers including metal nanoparticles of different metals: zinc (top left), magnesium (top right), iron (bottom left) and tantalum (bottom right). [46]

surfaces in order to allow metal ions to be released into wound media with therapeutic properties. As mentioned above, the fiber acts as a carrier for soft containers. These containers were chosen to be hydrogels in colloidal state, so-called microgels. Like their macro-scaled relatives, microgels react to external stimuli, e.g. temperature change, change of pH and so on. In contrast, the reaction time is lower, ranging from milliseconds up to few seconds [51, 52]. Due to surface charges, the colloids can persist as a colloidal dispersion usually dispersed in water or alcohols. Most of the literature therefore describes microgels as useful systems for the transport of therapeutical agents through biological environments. In this work, microgels were utilized as coating agents containing drugs, releasing them from the fiber surface. Hence, here the microgels still fulfill their purposes as drug-delivery agents containing metal-

nanoparticles, and as fiber coatings. After adhesion on the fiber surfaces, metal-ions are released while nanoparticles are detained from diffusing into the wound at the same time.

The standard system established over the last decades is poly(N-iso-proylacrylate) (PNIPAM). In this work, another microgel system was used as a carrier system, namely poly(vinyl-N-caprolactam) (PVCL). This system is commonly preferred for biomedical applications due to the relatively low toxicity of its monomer (VCL), especially in comparison with NIPAM [53]. The typical hydrogel-like properties are still available and PVCL shows great water stability and the possibility of nanoparticle-inclusion. PVCL-based microgels are usually prepared by co-polymerization in the presence of other monomers. Co-polymerization of microgels offers a simple strategy of adding additional properties by choosing an appropriate monomer, e.g. dicetonic, acids, PEG, amines, etc. Besides the chemical-based functionality, choosing an additional monomer will also influence particle composition.

This fact is linked to the very unique synthesis mechanism. Microgel preparation is generally called “precipitation polymerization”. This term describes the formation of a water-insoluble polymer in water which is formed from water-soluble monomers. Shortly after initiation, larger fractions of polymers will precipitate due to the synthesis conditions. Further chain growth occurs by consumption of monomers from the aqueous phase and addition to the suspended polymer chains. The spatial composition of the microgel is driven by the behavior of the different polymers in water. The more hydrophilic the character of the polymer, the more probable is the assembly in the shell regions and vice versa [51, 52, 54].

The preparation of a novel wound dressing including microfibers which release metal ions from their corresponding nanoparticles, requires the hosting microgels to be able to adhere to the fiber surfaces. Moreover, the microgel components have to be chosen to be biocompatible but still be capable of fulfilling the application-related requirements. First experiments were done by converting typical microgel synthesis approaches into the laser-chamber where microgel synthesis was accomplished simultaneously to the laser ablation process [47]. The first system used consisted of PVCL-based microgel which was copolymerized with AAEM, a well-known system already successfully used for ZnO encapsulation [55, 56]. In situ preparation led to low zinc masses while processing the microgels was suitable for fiber preparation.

Works of Pich and Winnik introduced a novel microgel system consisting of three different polymers [57]: PVCL, PAAEM and additional PEG. It was shown that increased PEG content leads to increased water-polymer interactions and hence loss of the spherical morphology. SEM experiments showed that microgels with increased PEG content showed a shape shift towards a more distorted shape. Furthermore, microgels with higher PEG content lost their sensitivity to temperature, meaning the hydrodynamic radii remained constant for temperatures below and above typical VPTT of PVCL, 32 °C. Once more, the microgels were based on PVCL and included PAAEM- and PEG-copolymers with a PEG content of up to 1.6 mol %.

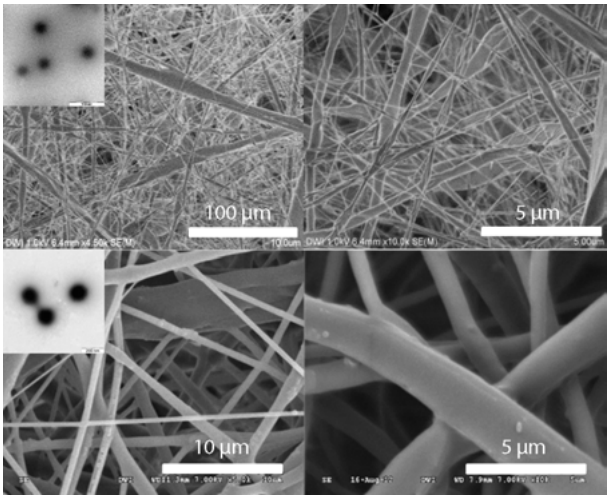

Fig. 3.4: Electrospun fibers including PVCL microgels (top) and PVCL-AAEM microgels (bottom), respectively. All microgels were gained during laser ablation of zinc nanoparticles. Insets show microgels used for electrospinning process.

A derivative had been developed for the laser ablation process consisting only of PVCL and PEG, omitting AAEM. In contrast to the PVCL-PAAEM-PEG system mentioned before, this novel system was investigated for PEG contents up to 10 mol %. Furthermore, the overall concentration of the reaction approach was reduced by a factor of 4 in order to reduce the particle diameter. Diameter reduction was preferred due to lower turbidity of the microgel dispersion. Turbidity is not favored when laser beams have to transit the suspension unhindered in order to hit the metal target. First tests revealed that microgel formation under standard concentration led to quenched ablation process due to the intense turbidity. After reducing the concentration, low turbidity enabled preparation of sufficient amounts of inorganic material from metal foils.

The synthesis of sufficient PEG-containing microgels was accomplished by precipitation polymerization of VCL and methylmethacrylate (MMA)modified PEG of low molecular mass (Mn 526 g/mol). The synthesis was performed at two different concentrations: 0.1 mol/L and 0.25 mol/L related to VCL. The first approach led to formation of a turbid suspension while lower concentration led to the formation of transparent dispersions. Light-scattering of the dialyzed products revealed a ten-times lower hydrodynamic diameter in the case of four-fold lower starting concentration. Even though the diameters were increased by the wet-chemical approach in the absence of particles, after the laser ablation process the metal nanoparticles were sufficiently encapsulated. This gives evidence that *in situ* polymerization of the PVCL-PEG at c(VCL) of 0.25 mol/L is still suitable for the encapsulation process. At the same time, formation of microgels which were not involved in the particle-encapsulation process did not influence the ablation process by increasing turbidity.

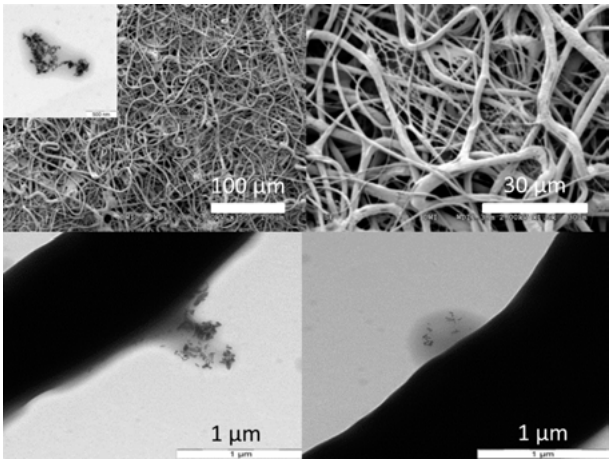

Fig. 3.5: Electrospun fibers including PVCL-PEG microgels. TEM images (bottom) prove the surface modification of fibers with microgels encapsulating zinc nanoparticles gained by laser ablation. Inset shows microgel-zinc composite used for fiber modification.

TEM characterization of the PVCL-PEG-zinc oxide systems before and after electrospinning proved the successful encapsulation and coating of microfibers (Fig. 3.5). Subsequent release tests were performed by adding non-wovens into buffered medium at pH 7.5 and 37 °C, the standard conditions for investigation of bioactive material. Release tests were accomplished by means of cumulative release, i.e. total volume exchange at given times, and characterization by ICP-MS. The tests clearly showed that release takes place as expected, showing a fast increase within the first 24 hours, a decreasing rate at around 48 hours and slow rates during the following three days. After a total of five days release tests were aborted (Fig. 3.6).

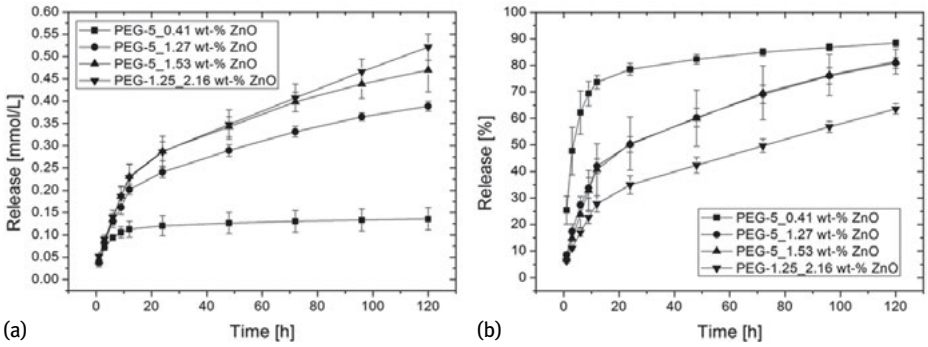

Fig. 3.6: Zinc ion release plots achieved by cumulative release studies. First plot shows absolute concentrations (a), second shows relative release rates (b).

3.2.4 Microfiber biotesting

The microfibers were tested following the same biocompatibility protocols previously used for the microgels. Here also, we could not see any differences in the LDH release between the control culture and the different concentrations of microfiber's eluate (Fig. 3.7 (a)). Nevertheless, the proliferation assay performed showed a statistically increased cell activity compared to the control culture at concentrations higher than 1 mg/ml (Fig. 3.7 (b)). When 10 % (w/w) microgel was added to the microfibers this enhancement was observed starting with 400 µg/ml, but we could not find statistically significanct differences between the proliferation values of the two microfiber groups. The electrospinning process aiming to immobilize microgels reduced the beneficial

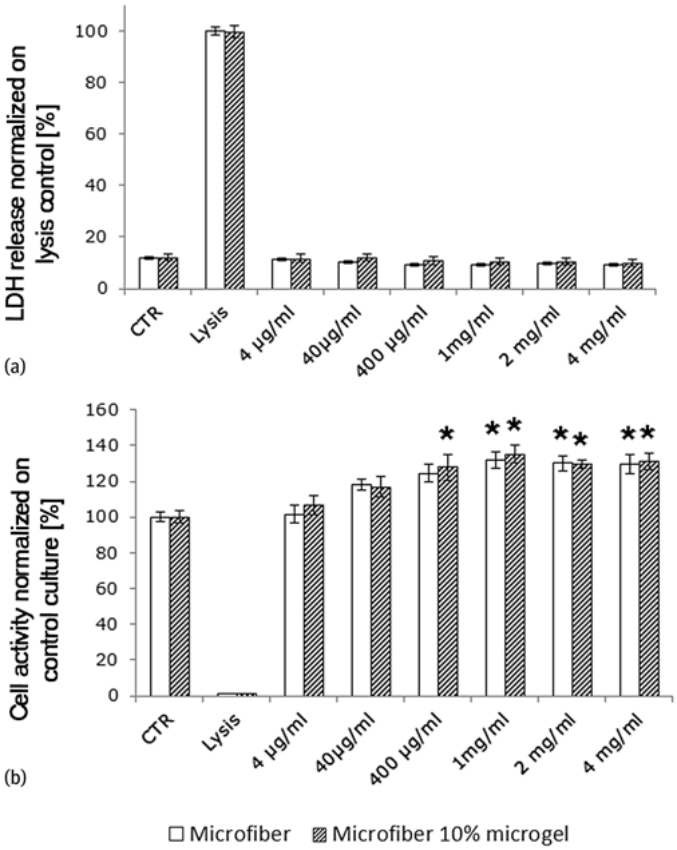

Fig. 3.7: Effect of different microfiber eluate concentrations and contents on L929 cell line culture. (a) cytotoxicity assay and (b) proliferation assay performed with elutions of the different microfibers. Values are normalized on lysis control for (a) and control culture (CTR) for (b). Results expressed as means of three independent experiments ± standard error of the mean; Bonferroni analysis of variance, * $p < 0.05$.

effect previously observed of the microgel on cell proliferation. The eluates of the microfibers themselves enhance proliferation, however, although all particles were removed by centrifugation and filtration.

3.3 Conclusion

We established a totally water-based synthesis routine for the fabrication of metal nanoparticle loaded microgels. Therefore, we investigated the laser ablation process and gain new insights into the processes during nanoparticle generation. By switching the PVCL-based microgels to the PEG-system, we circumvented the turbidity increase, due to microgel polymerization, which otherwise could have handicapped the laser ablation process. This routine allows production of a high variety of ion release systems, and adjustment of the element released to any stage of wound healing. By combining this laser ablated metal nanoparticle encapsulation with electrospinning methods and variation of the compound amount used, we were able to adjust the ion release. We were also able to define each compound as biocompatible and ions released from these materials remained in the subtoxic concentration regime. In addition microgels tend to enhance cell proliferation indirectly, an effect that could be further increased when the hydrogels were loaded with zinc nanoparticles. This also needs to be tested *in vivo*, after further *in vitro* complementary experiments, as we cannot rule out systemic effects in the context of wound healing. In summary the combination of laser ablated metal nanoparticles, *in situ* microgel encapsulation and electrospinning immobilization may be well-suited for the establishment of controlled, programmed and adaptive multiple ion release wound dressings.

References

[1] Lindahl M, Leanderson P, Tagesson C. Novel aspect on metal fume fever: zinc stimulates oxygen radical formation in human neutrophils. Human & experimental toxicology 1998; 17: 105–110.

[2] Feng Y, Likos JJ, Zhu L, et al. Solution structure and backbone dynamics of the catalytic domain of matrix metalloproteinase-2 complexed with a hydroxamic acid inhibitor. Biochimica et biophysica acta 2002; 1598: 10–23.

[3] Lorente L, Martin MM, Labarta L, et al. Matrix metalloproteinase-9, -10, and tissue inhibitor of matrix metalloproteinases-1 blood levels as biomarkers of severity and mortality in sepsis. Critical care 2009; 13: R158.

[4] Williams KE, Olsen DR. Matrix metalloproteinase-1 cleavage site recognition and binding in full-length human type III collagen. Matrix Biol 2009; 28: 373–379.

[5] Mantri M, Krojer T, Bagg EA, et al. Crystal Structure of the 2-Oxoglutarate- and Fe(II)-Dependent Lysyl Hydroxylase JMJD6. Journal of molecular biology 2010; 401: 211–222.

[6] Inoue Y, Hasegawa S, Ban S, et al. ZIP2 protein, a zinc transporter, is associated with keratinocyte differentiation. The Journal of biological chemistry 2014; 289: 21451–21462.

[7] Husslein H, Haider S, Meinhardt G, Prast J, Sonderegger S, Knofler M. Expression, regulation and functional characterization of matrix metalloproteinase-3 of human trophoblast. Placenta 2009; 30: 284–291.
[8] Nagase H, Woessner JF. Matrix Metalloproteinases. Journal of Biological Chemistry 1999; 274: 21491–21494.
[9] Page-McCaw A, Ewald AJ, Werb Z. Matrix metalloproteinases and the regulation of tissue remodelling. Nature reviews Molecular cell biology 2007; 8: 221–233.
[10] Hahn A, Günther S, Wagener P, Barcikowski S. Electrochemistry-controlled metal ion release from silicone elastomer nanocomposites through combination of different metal nanoparticles. Journal of Materials Chemistry 2011; 21: 10287.
[11] Leite-Silva VR, Lamer ML, Sanchez WY, et al. The effect of formulation on the penetration of coated and uncoated zinc oxide nanoparticles into the viable epidermis of human skin in vivo. European Journal of Pharmaceutics and Biopharmaceutics 2013; 84: 297–308.
[12] Kocbek P, Teskac K, Kreft ME, Kristl J. Toxicological aspects of long-term treatment of keratinocytes with ZnO and TiO2 nanoparticles. Small 2010; 6: 1908–1917.
[13] Roy R, Das M, Dwivedi PD. Toxicological mode of action of ZnO nanoparticles: Impact on immune cells. Molecular immunology 2014; 63: 184–192.
[14] Sowa-Söhle EN, Schwenke A, Wagener P, et al. Antimicrobial efficacy, cytotoxicity, and ion release of mixed metal (Ag, Cu, Zn, Mg) nanoparticle polymer composite implant material. BioNanoMaterials 2013; 14: 217–227.
[15] Hahn A, Brandes G, Wagener P, Barcikowski S. Metal ion release kinetics from nanoparticle silicone composites. Journal of controlled release : official journal of the Controlled Release Society 2011; 154: 164–170.
[16] Meneìndez-Manjoìn A, Wagener P, Barcikowski S. Transfer-Matrix Method for Efficient Ablation by Pulsed Laser Ablation and Nanoparticle Generation in Liquids. The Journal of Physical Chemistry C 2011; 115: 5108–5114.
[17] Shiro Kobayashi KM. Encyclopedia of Polymeric Nanomaterials: Springer Berlin Heidelberg; 2014.
[18] Jiang Y, Liu P, Liang Y, Li HB, Yang GW. Promoting the yield of nanoparticles from laser ablation in liquid. Applied Physics A 2011; 105: 903–907.
[19] Tsuji T, Thang DH, Okazaki Y, Nakanishi M, Tsuboi Y, Tsuji M. Preparation of silver nanoparticles by laser ablation in polyvinylpyrrolidone solutions. Appl Surf Sci 2008; 254: 5224–5230.
[20] Liu L, Guo CC, Li SC, Wang LY, Dong QY, Li W. Improved H-2 sensing properties of Co-doped SnO2 nanofibers. Sensor Actuat B-Chem 2010; 150: 806–810.
[21] Xu L, Dong BA, Wang Y, et al. Porous In2O3:RE (RE = Gd, Tb, Dy, Ho, Er, Tm, Yb) Nanotubes: Electrospinning Preparation and Room Gas-Sensing Properties. J Phys Chem C 2010; 114: 9089–9095.
[22] Zhao MG, Wang XC, Ning LL, Jia JF, Li XJ, Cao LL. Electrospun Cu-doped ZnO nanofibers for H(2)S sensing. Sensor Actuat B-Chem 2011; 156: 588–592.
[23] Kim ID, Rothschild A. Nanostructured metal oxide gas sensors prepared by electrospinning. Polym Advan Technol 2011; 22: 318–325.
[24] Mu JB, Shao CL, Guo ZC, et al. High Photocatalytic Activity of ZnO-Carbon Nanofiber Heteroarchitectures. ACS applied materials & interfaces 2011; 3: 590–596.
[25] Kanjwal MA, Barakat NAM, Sheikh FA, Park SJ, Kim HY. Photocatalytic activity of ZnO-TiO2 hierarchical nanostructure prepared by combined electrospinning and hydrothermal techniques. Macromol Res 2010; 18: 233–240.
[26] Sahay R, Sundaramurthy J, Kumar PS, Thavasi V, Mhaisalkar SG, Ramakrishna S. Synthesis and characterization of CuO nanofibers, and investigation for its suitability as blocking layer

in ZnO NPs based dye sensitized solar cell and as photocatalyst in organic dye degradation. J Solid State Chem 2012; 186: 261–267.
[27] Liu HQ, Yang JX, Liang JH, Huang YX, Tangz CY. ZnO nanofiber and nanoparticle synthesized through electrospinning and their photocatalytic activity under visible light. J Am Ceram Soc 2008; 91: 1287–1291.
[28] Amna T, Hassan MS, Barakat NAM, et al. Antibacterial activity and interaction mechanism of electrospun zinc-doped titania nanofibers. Appl Microbiol Biot 2012; 93: 743–751.
[29] Hwang SH, Song J, Jung Y, Kweon OY, Song H, Jang J. Electrospun ZnO/TiO2 composite nanofibers as a bactericidal agent. Chemical communications 2011; 47: 9164–9166.
[30] Shalumon KT, Anulekha KH, Nair SV, Nair SV, Chennazhi KP, Jayakumar R. Sodium alginate/poly(vinyl alcohol)/nano ZnO composite nanofibers for antibacterial wound dressings. Int J Biol Macromol 2011; 49: 247–254.
[31] Lee S. Multifunctionality of Layered Fabric Systems Based on Electrospun Polyurethane/Zinc Oxide Nanocomposite Fibers. J Appl Polym Sci 2009; 114: 3652–3658.
[32] Horzum N, Tascioglu D, Okur S, Demir MM. Humidity sensing properties of ZnO-based fibers by electrospinning. Talanta 2011; 85: 1105–1111.
[33] Greiner A, Wendorff JH. Electrospinning: A fascinating method for the preparation of ultrathin fibres. Angew Chem Int Edit 2007; 46: 5670–5703.
[34] Pitt CG, Chasalow FI, Hibionada YM, Klimas DM, Schindler A. Aliphatic Polyesters .1. The Degradation of Poly(Epsilon-Caprolactone) Invivo. J Appl Polym Sci 1981; 26: 3779–3787.
[35] Khatiwala VK, Shekhar N, Aggarwal S, Mandal UK. Biodegradation of Poly(epsilon-caprolactone) (PCL) Film by Alcaligenes faecalis. J Polym Environ 2008; 16: 61–67.
[36] Tokiwa Y, Suzuki T. Hydrolysis of Polyesters by Lipases. Nature 1977; 270: 76–78.
[37] Schwenke A, Wagener P, Nolte S, Barcikowski S. Influence of processing time on nanoparticle generation during picosecond-pulsed fundamental and second harmonic laser ablation of metals in tetrahydrofuran. Appl Phys A, Springer 2011; 104: 77–82.
[38] Bärsch N, Jakobi J, Weiler S, Barcikowski S. Pure colloidal metal and ceramic nanoparticles from high-power picosecond laser ablation in water and acetone. Nanotechnology 2009; 20: 445603.
[39] Liu W, Kosareva O, Golubtsov I, et al. Femtosecond laser pulse filamentation versus optical breakdown in H2O. Appl Phys B, Springer 2003; 76: 215–229.
[40] Wagener P, Schwenke A, Chichkov BN, Barcikowski S. Pulsed Laser Ablation of Zinc in Tetrahydrofuran: Bypassing the Cavitation Bubble. J Phys Chem C 2010; 114: 7618–7625.
[41] De Giacomo A, Dell'Aglio M, Santagata A, et al. Cavitation dynamics of laser ablation of bulk and wire-shaped metals in water during nanoparticles production. Physical chemistry chemical physics : PCCP 2013; 15: 3083–3092.
[42] Ibrahimkutty S, Wagener P, Menzel A, Plech A, Barcikowski S. Nanoparticle formation in a cavitation bubble after pulsed laser ablation in liquid studied with high time resolution small angle x-ray scattering. Appl Phys Letters 2012; 101: 103104.
[43] Wagener P, Ibrahimkutty S, Menzel A, Plech A, Barcikowski S. Dynamics of silver nanoparticle formation and agglomeration inside the cavitation bubble after pulsed laser ablation in liquid. Physical Chemistry Chemical Physics 2013; 15: 3068–3074.
[44] Wagener P, Faramarzi S, Schwenke A, Rosenfeld R, Barcikowski S. Photoluminescent zinc oxide polymer nanocomposites fabricated using picosecond laser ablation in organic solvent. Appl Surf Sci 2011; 257: 7231–7237.
[45] Wagener P, Brandes G, Schwenke A, Barcikowski S. Impact of in situ polymer coating on particle dispersion into solid laser-generated nanocomposites. Phys Chem Chem Phys 2011; 13: 5120–5126.

[46] van 't Zand DD, Nachev P, Rosenfeld R, et al. Nanocomposite Fibre Fabrication via in situ Monomer Grafting and Bonding on Laser-generated Nanoparticles. J Laser Micro Nanoen 2012; 7: 21–27.
[47] Nachev P, van 't Zand DD, Coger V, et al. Synthesis of hybrid microgels by coupling of laser ablation and polymerization in aqueous medium. J Laser Appl 2012; 24: 042012-1–042012-7.
[48] Wataha JC, Hanks CT, Sun Z. Effect of cell line on in vitro metal ion cytotoxicity. Dental materials : official publication of the Academy of Dental Materials 1994; 10: 156–161.
[49] Wataha JC, Hanks CT, Craig RG. The effect of cell monolayer density on the cytotoxicity of metal ions which are released from dental alloys. Dental materials : official publication of the Academy of Dental Materials 1993; 9: 172–176.
[50] Jenkins W, Perone P, Walker K, et al. Fibroblast response to lanthanoid metal ion stimulation: potential contribution to fibrotic tissue injury. Biological trace element research 2011; 144: 621–635.
[51] Pelton R. Temperature-sensitive aqueous microgels. Advances in colloid and interface science 2000; 85: 1–33.
[52] Pich A, Richtering W. Microgels by Precipitation Polymerization: Synthesis, Characterization, and Functionalization. Adv Polym Sci 2010; 234: 1–37.
[53] Saunders BR, Laajam N, Daly E, Teow S, Hu XH, Stepto R. Microgels: From responsive polymer colloids to biomaterials. Advances in colloid and interface science 2009; 147–48: 251–262.
[54] Saunders BR, Vincent B. Microgel particles as model colloids: theory, properties and applications. Advances in colloid and interface science 1999; 80: 1–25.
[55] Boyko V, Pich A, Lu Y, Richter S, Arndt KF, Adler HJP. Thermo-sensitive poly(N-vinylcaprolactam-co-acetoacetoxyethyl methacrylate) microgels: 1 - synthesis and characterization. Polymer 2003; 44: 7821–7827.
[56] Agrawal M, Pich A, Gupta S, et al. Temperature sensitive hybrid microgels loaded with ZnO nanoparticles. Journal of Materials Chemistry 2008; 18: 2581–2586.
[57] Pich A, Berger S, Ornatsky O, Baranov V, Winnik MA. The influence of PEG macromonomers on the size and properties of thermosensitive aqueous microgels. Colloid Polym Sci 2009; 287: 269–275.

K. Wallat, M. M. Gepp, S. Berger, R. Le Harzic, J. C. Neubauer,
H. Zimmermann, F. Stracke, and M. Epple

4 Nanoparticle-loaded bioactive hydrogels

Abstract: Laser-induced sub 100 nm structures were prepared on silicon, thoroughly characterized, and the process of their formation was elucidated. They were used as substrates for a controlled deposition of calcium phosphate nanoparticles by electrophoretic deposition. Calcium phosphate nanoparticles are used as carriers for biomolecules such as nucleic acid for transfection or gene silencing in the context of gene therapy. It is important to apply only a defined quantity of nanoparticles and nucleic acids to a given cell culture or tissue. A defined number of nanoparticles were deposited onto a ripple structured silicon surface by electrophoretic deposition Alginate beads were then rolled on this surface allowing the nanoparticles to adsorb onto the surface of the alginate bead. This resulted in alginate beads with a defined quantity of particles and biomolecules on their surface. The effect of calcium phosphate nanoparticle-coated alginate beads on cells was studied by the hanging drop method.

4.1 Introduction

There is great interest in the genetic manipulation of living cells by the administration of nucleic acids (DNA or RNA) in experimental medicine, e.g. for the integration of fluorescent reporter genes [1]. It can additionally enable the induction of pluripotency in patient-derived cells using epigenetic reprogramming methods, opening up new possibilities for personalized medicine and disease-specific drug discovery. While these artificially generated cells do not exist in the human body, comparable to embryonic stem cells, human induced pluripotent stem cells (hiPSC) have the ability to differentiate into every cell type of the human body and to renew themselves by mitotic cell division [2].

Due to the fact that nucleic acids alone are not able to enter a cell, suitable carriers are needed. Currently, a retrovirus-mediated gene transduction is often used, but non-viral systems are becoming increasingly important [3]. Nanoparticles can be used for the transport of nucleic acids because they can easily be taken up by cells and no further transport vectors are necessary [4]. In order to standardize this process, the exposure of cells to a defined number of nanoparticles is necessary. Note that with dispersed nanoparticles, it is difficult to clearly define the dose of nanoparticles in direct cell contact. As most cell types, including fibroblasts and hiPSCs, grow in adherent culture, a homogeneous immobilization of nanoparticles on a surface is one possible method of controlling nanoparticle exposure [5]. The cultivation of a defined num-

ber of cells on specified growth areas homogeneously loaded with DNA-containing nanoparticles can lead to a reproducible gene transfection [5].

Different inorganic nanoparticles have been used for the transport of nucleic acids into cells [6, 7]. In comparison to organic particles, inorganic particles are often easier to synthesize, less toxic, not sensitive to microbial degradation and easier to store. In this case, we used calcium phosphate nanoparticles as drug carriers [8, 9]. Calcium phosphate is a biomineral found in mammalian bone and teeth, leading to high biocompatibility [10]. We used the cationic polymer poly(ethyleneimine) (PEI) to stabilize the calcium phosphate nanoparticles. This led to a positive zeta potential and colloidal stability. Note that the particles need to carry a surface charge for electrophoretic deposition. Electrophoretic deposition was used to coat silicon, both smooth and ripple-nanostructured [11, 12]. In general, the coating of implants is an interesting area in medicine to increase their bioactivity [13]. These deposited nanoparticles were then transferred to alginate beads by rolling the beads over the nanoparticle-coated surface. In earlier work we have shown that laser-structured surfaces are ideally suited for controlled deposition of calcium phosphate nanoparticles [12] and that cells show distinct behavior towards such coated surfaces [11].

Alginate, a hydrogel derived from marine brown algae, is a highly suitable matrix for immobilization of nanoparticles. Alginate is often used for cell encapsulation and is easy to modify according to specific cell characteristics and applications [14]. Ultrapure alginates can be used for cell-based assays, due to the low risk of contamination (in the case of in vitro application), inflammation and immune response (in case of in vivo application). Gel formation from fluid alginates to gelled alginate hydrogels takes place by ionotropic crosslinking with alkaline-earth metal cations (e.g. Ca^{2+}, Ba^{2+}) under gentle conditions (neutral pH, room temperature). This allows the encapsulation of cells into alginate without significantly damaging the cells [15]. Several methods for dispensing [16] and modification have been published in the last decades ranging between coatings [17], physical modifications [18], and covalent coupling of bioactive molecules [19].

A method of studying the interaction of cells and dispersed particles is the hanging drop cultivation method [20]. Here, cells are cultivated in a small drop (20–40 µL) of culture medium which is placed in the inner lid of a cell culture dish. Due to gravitation, all cells in the droplet are forced to form one homogeneous aggregate in the lower part of the droplet. In combination with alginate microcarriers loaded with nanoparticles containing nucleic acids, this method is highly suitable for the transfection of cells due to the enforced cell-surface contact within the drop. The defined and homogeneous spatial arrangement of nanoparticles with transcription factors for cell reprogramming on the growth surface of cells will increase reproducibility and standardization. Using the advantages of automation, this cell culture method additionally permits almost complete control of the microenvironment as well as a significantly increased reproducibility of the results by volume miniaturization and parallelization.

4.2 Material and methods

4.2.1 Laser-induced sub 100 nm structures

Periodic pattern formation on surfaces under laser irradiation in a certain fluency range has long been known and is termed laser induced periodic surface structures (LIPSS) [21, 22]. Depending on the illumination parameters and the material properties, a variety of topologies and scales can be realized. A basic classification of these structures is made by the spatial frequency of the pattern in relation to the wavelength of the generating laser light: patterns with structural dimensions comparable to the laser wavelength are called low spatial frequency LIPSS (LSFL) [23, 24], those with subdiffractive structural dimensions are accordingly called high spatial frequency LIPSS (HSFL) [23, 25, 26].

By the application of appropriate irradiation and material parameters, HSFLs can have periodicities of around 100 nm and below. This is of the order of typical diameters of nanoparticles for biomedical and pharmaceutic use [27–29]. Hence it is promising to study the potential of HSFL-patterned surfaces for biomedical nanoparticle arrangement and transfer. To this end, extended areas of HSFL patterns are needed in contrast to the single focal spot structures widely produced for mechanistic elucidation of the structure generation [27]. This was achieved by scanning the laser focus along the substrate surface. In order to have better process control during patterning, low energy ultra-short pulses (nJ) were utilized at a high repetition rate (MHz) in contrast to the usual high energy pulses at low repetition rate (Hz–kHz) used by amplified laser systems. A compact ultra-fast Ti:sapphire tunable laser system (80 MHz, $E_{max} \approx 40$ nJ/pulse, $\tau = 140$ fs (FWHM), $\lambda = 800$ nm) coupled to a laser workstation specially designed and developed for accurate micro- and nanoprocessing was used to generate these periodical ripples on large areas. The surface patterns were created by pulse trains of some 150 000 pulses in a quasi-continuous fashion in contrast to mostly single pulse evoked structures known from the literature [23, 26]. Since a quasi-continuous evolution of HSFL in spatial contact to already formed HSFL (due to scanning) may have very specific mechanisms of formation, this was the subject of extensive studies [30–33]. The results of these studies now help to understand, control and predict periodicities and orientation of our large area HSFL upon irradiation and material parameters.

In order to achieve a defined orientation and surface density, the calcium phosphate nanoparticles were deposited onto reusable stamps, consisting of silicon wafers patterned with HSFL. These high spatial frequency ripples were generated in air on standard one-side-polished, boron-doped p-type 525 µm thick Si wafers with a crystallographic orientation of 100. The low energy femtosecond laser pulses were focused by a 20× focusing objective with a relatively high numerical aperture (NA) of 0.75 to reach the fluency threshold of HSFL generation. The focus diameter was about 1.3 µm at the surface of the sample. More details on the experimental setup can be found

in [34]. A peculiarity of laterally extended, pulse train-generated HSFLs is the necessity of removing expelled material via an adapted etching step. For silicon, this was accomplished by treatment with aqueous ammonium fluoride solution.

4.2.2 Production of alginate beads and hydrogels

Alginate beads were produced using an air-jet droplet generator (Fig 4.1) as described in [15], [35] and [14]. Liquid Na-alginate solution or Na-alginate/cell suspensions were supplied in 1 mL syringes. The solution was transported with constant feed through a disposable nozzle (Fig. 4.1 (b) and (c)), producing homogeneous droplets using an

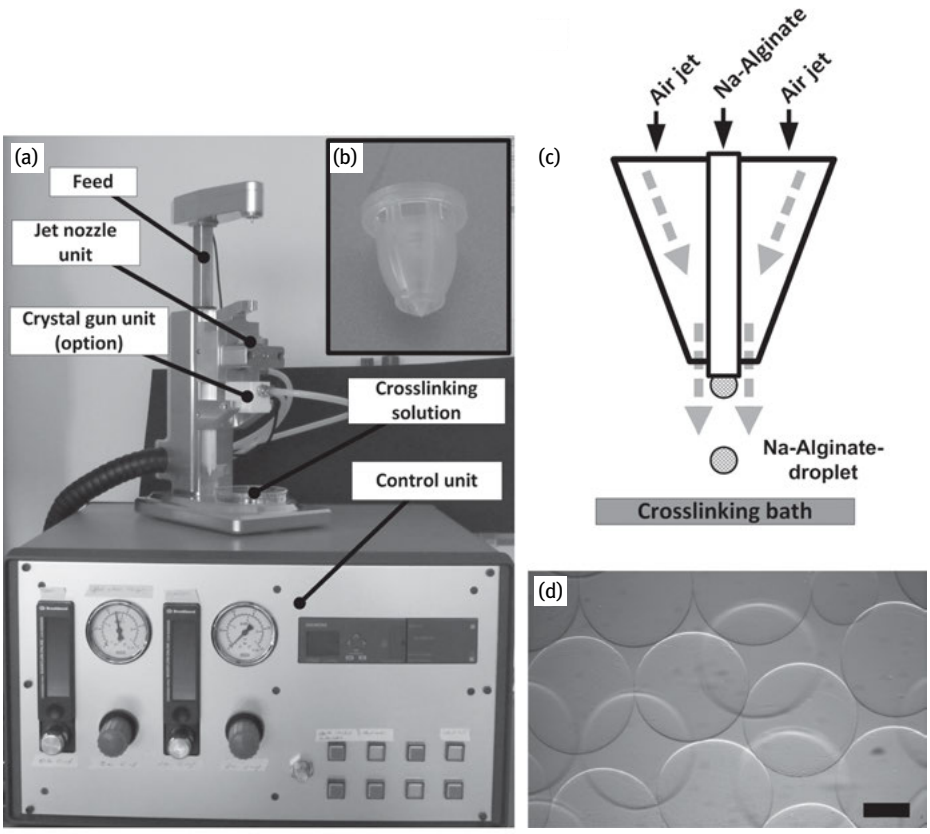

Fig. 4.1: Alginate air-jet droplet generator. (a) Alginate bead generator for fully sterile bead production. Na-alginate was supplied in a 1 mL syringe and pressed through the jet nozzle unit for air-jet driven droplet formation. Alginate droplets were internally crosslinked by barium chloride crystals and the crystal gun. Final crosslinking occurred after free fall of alginate droplets into the crosslinking solution. (b) Detailed view on jet nozzle unit. (c) Schematic drawing of jet nozzle unit. (d) Typical alginate beads produced from ultra-high viscous alginates (scale bar 250 µm).

air flow of 1.5 L min^{-1}. The geometry of the disposable nozzle was optimized for the production of alginate beads with a diameter of 500 µm. The droplet generator allowed adjustment of the bead size by increasing air flow. After droplet break-off and during freefall, alginate droplets were internally gelled by bombardment with $BaCl_2$ crystals.

External gelling of alginate usually takes place with a 20 mM $BaCl_2$ iso-osmolar solution, producing perfectly round alginate beads (Fig. 4.1 (d)). Alginate beads were usually gelled for 15 min at room temperature and intensively washed in iso-osmolar NaCl solution to remove excess Ba^{2+} ions. Due to low mechanical stress and physiological conditions of all media used, excellent cell viability was achieved [36].

4.2.3 Synthesis of calcium phosphate nanoparticles

4.2.3.1 Calcium phosphate nanoparticles, dispersed in ethanol

The calcium phosphate nanoparticles in ethanol were prepared by precipitation in the presence of poly(ethylenimine) (PEI) [5]. Aqueous solutions of calcium-*L*-lactate (c = 18 mmol L^{-1}) and di-ammonium hydrogen phosphate (c = 10.8 mmol L^{-1}) were pumped into a beaker by a peristaltic pump. A PEI solution (c = 2 g L^{-1}) was added by a second peristaltic pump. The volume flow rate was adjusted to a ratio of 1 : 1 : 2 (Ca^{2+} : PO_4^{3-} : PEI). Labelled PEI was used for the fluorescently labelled particles, fluorescein or tetramethylrhodamine isothioacyanate (FITC or TRITC, respectively). The calcium phosphate nanoparticles were isolated by centrifugation for 1 h at 1500 g, washed with water and freeze-dried. After freeze-drying, the particles were redispersed in ethanol by ultrasonication to achieve a stable colloidal dispersion.

4.2.3.2 Calcium phosphate nanoparticles, dispersed in water

The water-dispersed calcium phosphate nanoparticles were prepared by precipitation. Aqueous solutions of calcium-*L*-lactate (c = 6 mmol L^{-1}) and di-ammonium hydrogen phosphate (c = 3.6 mmol L^{-1}) were pumped together into a 5 cm tube with a volume flow rate of 25 mL min^{-1}. After nucleation in the tube, PEI (c = 2 g L^{-1}) was added with a flow rate of 12.5 mL min^{-1}. After stabilization the particles were isolated by centrifugation (20 min, 1100 g) and redispersed in water by ultrasonication (50 % amplitude, 0.8 pulse). Different amounts of EGFP-DNA (50 µg mL^{-1}, 25 µg mL^{-1} and 15 µg mL^{-1}) were added to the positively charged calcium phosphate-PEI nanoparticles [37]. A stable colloidal dispersion was obtained.

4.2.3.3 Calcium phosphate nanorods, dispersed in water

PEI-functionalized calcium phosphate nanorods were synthesized by adding a 6 % Ostim®-suspension to 6 mL water and 3 mL PEI-solution (c = 10 g L^{-1}). Ostim® is a commercially available bone substitution material and consists of water-dispersed

nanoscopic hydroxyapatite, $Ca_{10}(PO_4)_6(OH)_2$ [38]. These calcium phosphate nanorods can be functionalized by nucleic acids and used for transfection and gene silencing [38]. The mixture was dispersed by ultrasonic treatment. The particles were then isolated by centrifugation for 30 min at 4700 g and redispersed in water by ultrasonication. A stable colloidal dispersion of calcium phosphate nanorods was obtained with a concentration of 6 mg mL^{-1} calcium phosphate. For electrophoretic deposition the dispersion was diluted to 1 mg mL^{-1} calcium phosphate.

All nanoparticles were characterized by dynamic light scattering (DLS), zeta potential measurements and scanning electron microscopy (SEM). Dynamic light scattering and zeta potential measurements were carried out with the Zetasizer Nano ZS instrument from Malvern. The SEM images were recorded with an ESEM Quanta 400 FEG instrument from FEI.

4.2.4 Electrophoretic deposition

Electrophoretic deposition was carried out with ethanol and water as dispersion media. The medium is important for the choice of voltage and deposition time. The calcium phosphate nanoparticles in ethanol were deposited at 50 V DC. The deposition time varied between 30 s and 2 min. The water-dispersed calcium phosphate nanoparticles and nanorods were deposited at 2 V DC. The deposition time was between 30 min and 5 h. Voltage is limited in water to avoid the electrolysis of water. All electrophoretic depositions were carried out at room temperature. Silicon, indium-doped tin oxide (ITO) and silicon with ripple structures were used as substrates. All substrates were dried in air after deposition. The apparatus for electrophoretic deposition is shown in Fig. 4.2.

4.3 Results

4.3.1 Characterization of laser-induced sub 100 nm structures

Investigations were performed to characterize the HSFL structures in terms of morphology, periodicity, depth profile, aspect ratio and the influence of varying parameters such as energy per pulse, number of applied pulses (scan speed), wavelength, polarization, NA of the focusing optics and incident angle of the laser beam. For these purposes, the resulting irradiated surface morphologies were examined with scanning electronic microscopy (SEM). Fine cross-sectional cuts of structured fields recovered with HSFL were performed by focused ion beam (FIB) milling to analyse the depth profiles. An example of HSFL generated in Si is shown in Fig. 4.3. The periodicity of the ripples was measured in two ways: Classically by directly measuring the distances between two rims at several locations on the SEM image with the help of image analysis

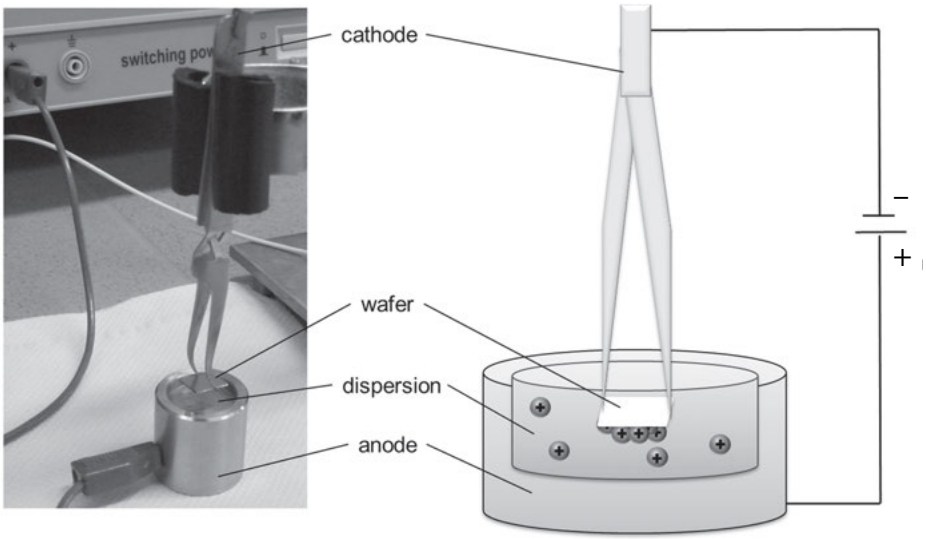

Fig. 4.2: Setup for the electrophoretic deposition (EPD) of nanoparticles on structured surfaces.

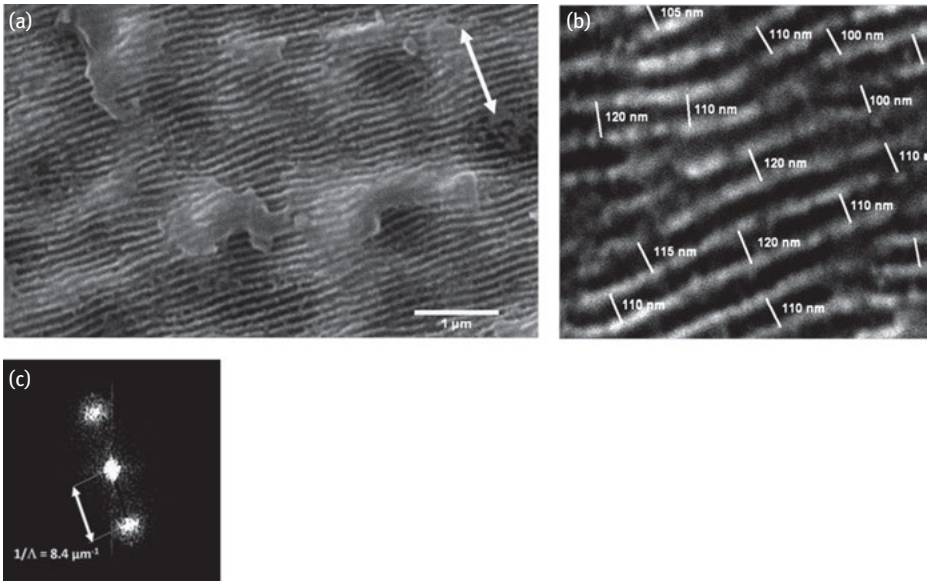

Fig. 4.3: (a) SEM image of HSFL generated in Si at 700 nm at an energy per pulse of 3 nJ and at a scan speed of 1 mm s^{-1}. (b) Details of the HSFL with direct measurements. (c) 2D-FT of image (b). The double arrow represents the polarization of the laser irradiation.

software as seen in the magnified image of Fig. 4.3 (b). The average periodicity based on limited measurements was $\Lambda_{\text{average}} \approx 111\,\text{nm} \pm 10\,\text{nm}$ This method is relatively accurate but limited to a very small area. The other method which is not limited to the size of the area and directly gives the quantitative averaged result consists of taking the discrete two-dimensional Fourier transformation (2D-FT) of the whole SEM image of Fig. 4.3 (b), as shown in Fig. 4.3 (c). The quantitative periodicity obtained by 2D-FT was $\Lambda \approx 119\,\text{nm}$.

The FIB cross-section procedure includes firstly the deposition of a protective platinum layer on the surface, and secondly the successive removal of the silicon layer in the depth, using gallium ions with a continuously decreasing energy down to 30 keV for ultimate fine removal and polishing. An example of a cross-section ($15\times5\,\mu\text{m}^2$) performed on the silicon-surface covered with HSFL generated at 800 nm, at an energy of 4.5 nJ/pulse and a scan speed of $1\,\text{mm}\,\text{s}^{-1}$ is shown in Fig. 4.4. Comparatively homogeneous ripples in morphology, periodicity and depth with a repeatable sinusoidal-like profile can be observed in Fig. 4.4 (b). The depth of the crater (~ 135 nm) is close to the distance between two rims (~ 125 nm). This leads to an aspect ratio of about 1 : 1 which was deduced from the magnified image of a ripple in Fig. 4.4 (c).

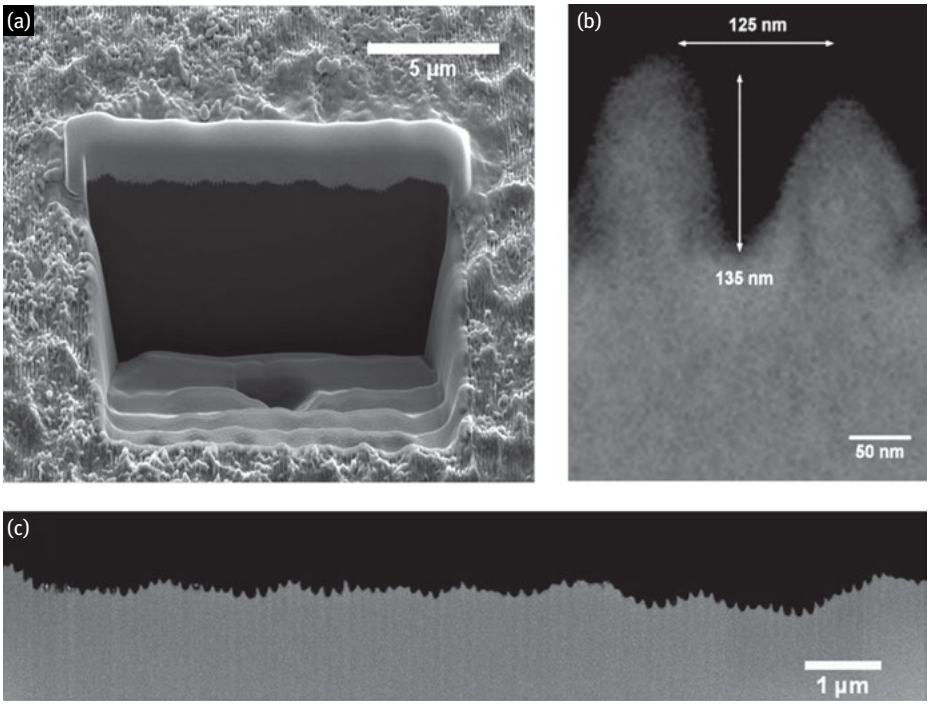

Fig. 4.4: SEM images of the crosssectional profile of HSFL in Si. (a) FIB section overview. (b) High magnification of HSFL profile. (c) Crosssectional profile overview of the HSFL.

The influence of the various parameters listed above was systematically studied by SEM and FIB. It was shown that HSFL initiation, formation, and arrangement in silicon under ultra-short pulses with low energy at high repetition rates combine the structural modification of the surface, initiated by heat accumulation of successive pulses with second harmonic generation (SHG). The periodicity of HSFL is wavelength-dependent and increases with a wavelength between 700 nm and 950 nm [25, 26]. At a first approximation, the periodicity of the HSFL tends to follow the equation $\Lambda = \lambda/2n_\lambda$ satisfactorily [39]. A revisited and refined model of the SHG ripple spacing theory taking the modified femtosecond laser excited silicon refractive index n_λ^* as a function of the wavelength for Si into account was proposed. It matched the experimental data very well [32, 39]. These results are summarized in Fig. 4.5.

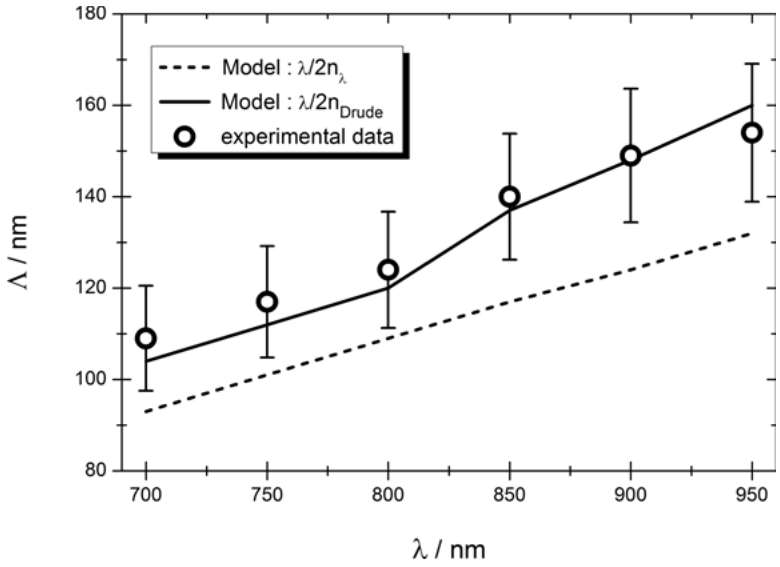

Fig. 4.5: HSFL periodicity as a function of the wavelength. Comparison of experimental data and theoretical models of HSFL spacing.

The orientation of the HSFL is dependent on the direction of polarization and perpendicular to this, but no influence of the direction of polarization was observed on periodicity, profile and aspect ratio of the crosssections of HSFL [24, 30]. The periodicity, morphology, depth and aspect ratio of the HSFL are quite independent from the energy, the number of pulses applied, the focusing geometry and the incidence angle of the laser beam [34, 40].

4.3.2 Electrophoretic deposition of nanoparticles

Unstructured silicon wafers were coated with TRITC- or FITC-PEI-labelled fluorescing spherical cationic calcium phosphate nanoparticles. The nanoparticles were redispersed in ethanol, and electrophoretic deposition was carried out at 50 V DC for 1 min. After deposition, the surface showed a multilayer of spherical nanoparticles (Fig. 4.6 (a)). These coated wafers were subsequently used to coat the alginate beads. Anionic DNA-functionalized spherical nanoparticles in water were also used for electrophoretic deposition. The surface showed a nanoparticle monolayer after electrophoretic deposition at 2 V for 30 min (Fig. 4.6 (b)). The electrically conducting glass indium-doped tin oxide (ITO) was coated with cationic PEI-stabilized calcium phosphate nanorods in water. After deposition for 5 h at 2 V, the surface showed a nanorod multilayer with about 17 layers (Fig. 4.6 (c)).

The dose of nanoparticles both on the silicon substrate and on the alginate beads is important to judge the biological effect. A length of 159 nm and a diameter of 35 nm of the calcium phosphate nanorods were assumed for the calculation of the number of nanorod layers on the substrate [37]. The volume was calculated assuming a cylindrical shape of the particles with $1.33 \cdot 10^{-22}$ m^3 per particle. The mass of one nanorod was calculated with the density of hydroxyapatite (3160 kg m^{-3}), giving $4.20 \cdot 10^{-19}$ kg per particle.

The amount of calcium was measured by elemental analysis (dissolution of the calcium phosphate nanorod layer with nitric acid, followed by atomic absorption spectroscopic determination of the calcium concentration in the acid). A mass of 0.0565 mg calcium per cm^2 was determined. This corresponds to a mass of 0.14 mg hydroxyapatite, assuming the stoichiometry of hydroxyapatite, $Ca_5(PO_4)_3OH$. Consequently, $3.33 \cdot 10^{11}$ nanorods were deposited on 1 cm^2 of the substrate.

The layer thickness of the calcium phosphate nanorods was 599 nm assuming the spheres were closepacked (74 vol %) as approximation. It was assumed that the nanorods were lying on the long edge of the substrate on calculation of the number of layers.

$$\delta_{\text{layers}} = \frac{N \cdot V_{\text{NR}}}{A \cdot 0.74} = \frac{3.33 \cdot 10^{11} \cdot 1.33 \cdot 10^{-22}\ \text{m}^{-3}}{10^{-4}\ \text{m}^2 \cdot 0.74} = 5.99 \cdot 10^{-7}\ \text{m} = 599\ \text{nm}$$

$$N_{\text{layers}} = \frac{\delta_{\text{layers}}}{d} = \frac{599\ \text{nm}}{35\ \text{nm}} = 17$$

N: number of nanoparticles on the substrate
A: area of the substrate (10^{-4} m^2)
δ_{layers}: layer thickness assuming close-packed spheres
d: one nanorod thick
N_{layers}: number of layers on the substrate

This gives 17 nanorod layers, with an estimated error of ± 20 %.

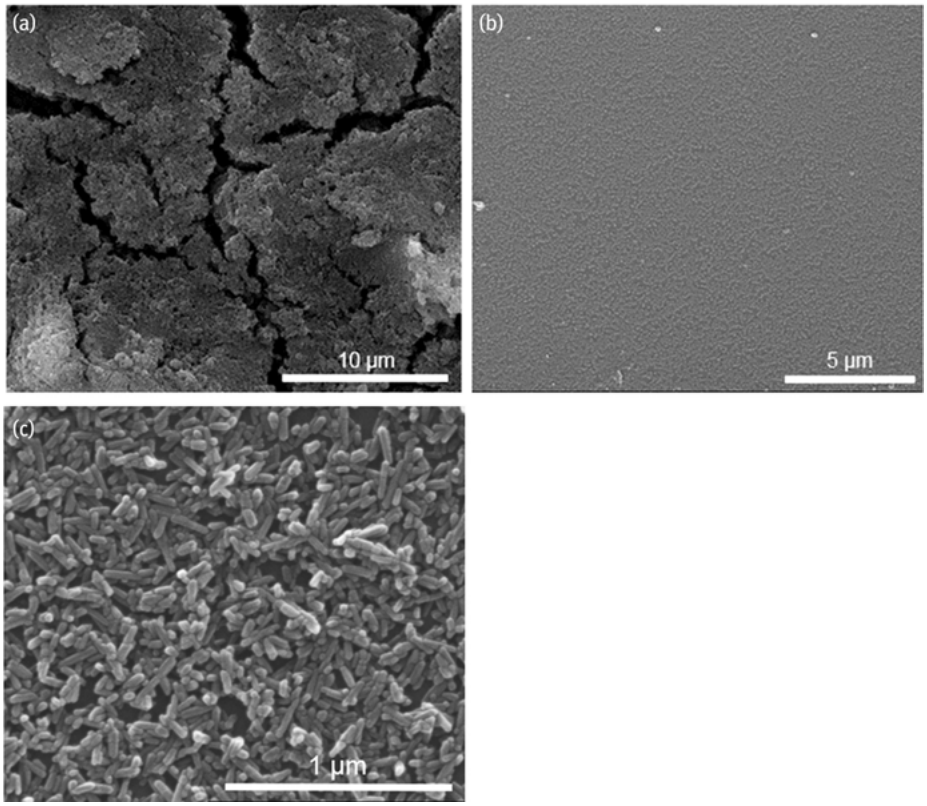

Fig. 4.6: SEM images of substrates coated with different calcium phosphate nanoparticles after electrophoretic deposition (EPD). (a) PEI-labelled calcium phosphate nanoparticles in ethanol, $U = 50$ V, $t = 1$ min. (b) DNA-functionalized calcium phosphate nanoparticles in water, $U = 2$ V, $t = 30$ min. (c) PEI-functionalized calcium phosphate nanorods in water, $U = 2$ V, $t = 300$ min.

4.3.3 Combination of bead production and coating of dispersed calcium phosphate nanoparticles

Nanoparticle-coated alginate beads can be realized in two different ways. On the one hand, the gelled alginate beads can be coated with nanoparticles by incubation in a nanoparticle dispersion. On the other hand, alginate bead production and coating with nanoparticles can be combined during bead production as described above.

The nanoparticles for deposition were supplied in the crosslinking bath. The contact of liquid alginate drops with the crosslinking bath containing nanoparticles affected the accumulation of calcium phosphate nanoparticles on the bead surface and, at the same time, gelation of alginate resulted in stable alginate beads. Bead preparation using different crosslinking baths containing 20 mM $BaCl_2$, 10 mM $BaCl_2$ and 0.15 mg mL^{-1} calcium phosphate nanoparticles as well as a pure calcium phosphate

nanoparticle dispersion with 0.1 mg mL^{-1}, 0.2 mg mL^{-1} and 0.3 mg mL^{-1} (mass refers to calcium phosphate) showed that nanoparticle dispersions alone are not sufficient for the production of stable alginate beads, underscoring the need for other procedures.

PEI-TRITC-functionalized calcium phosphate nanoparticles were used for better analysis of the loading procedure from dispersion. A pure nanoparticle dispersion with 0.1 mg mL^{-1} and 0.2 mg mL^{-1} alginate tended to form large agglomerates on the bead surface (Fig 4.7 (a) and (b)). At a concentration of 0.3 mg mL^{-1}, partial bead formation, and large agglomerates of alginate beads and unshaped hydrogel were observed (Fig 4.7 (c) and (d)). In contrast, a mixture of calcium phosphate nanoparticle dispersion with $BaCl_2$ crosslinking solution (final concentration 0.15 mg mL^{-1} calcium phosphate nanoparticles in 10 mM $BaCl_2$) resulted in stable alginate beads (Fig. 4.7 (e)), comparable to beads produced with standard crosslinking solution (Fig. 4.7 (f)). Calcium phosphate nanoparticle-loaded alginate beads can be distinguished by increased surface contrast and are also generally darker in comparison to standard alginate beads.

The stability of standard and calcium phosphate nanoparticle-loaded alginate beads was monitored over 4 days and analyzed with respect to their diameter. Standard alginate beads at day 0 and day 4 and calcium phosphate-loaded beads at day 0 showed comparable equivalent diameters of about 600 µm (Fig. 4.7 (g)). Alginate beads loaded with calcium phosphate nanoparticles showed a slight decrease in diameter of approximately 50 µm after storage for 4 days. Differences were significant between standard alginate beads and calcium phosphate-loaded beads on day 0 as well as between calcium phosphate-loaded alginate beads on day 0 and day 4. The differences between standard and calcium phosphate-loaded beads can be explained by additional particles in the crosslinking solution, influencing bead shape, whereas differences of calcium phosphate-loaded beads on day 0 and day 4 are probably caused by further crosslinking by calcium and thus shrinking of alginate beads over time. Nevertheless, calcium phosphate nanoparticle-loaded alginate beads were intact after 4 days and showed no signs of disintegration. The reproducible shape, as well as the stability over several days, gave the basis for integrating these beads into the cell-based hanging drop cultivation assay. Future studies must also focus on long-term stability with additional mechanical stress to evaluate the applicability of calcium phosphate nanoparticle-loaded alginate beads in stirred bioreactor systems.

4.3.4 Coating of alginate beads from solution

The alginate beads were coated with PEI-TRITC-functionalized calcium phosphate nanoparticles. Nanoparticle dispersion was used after precipitation without purification. 1.5 mg alginate beads were added to 30 mL nanoparticle dispersion and the dispersion was stirred for 1 h. The beads were isolated from the dispersion by sedi-

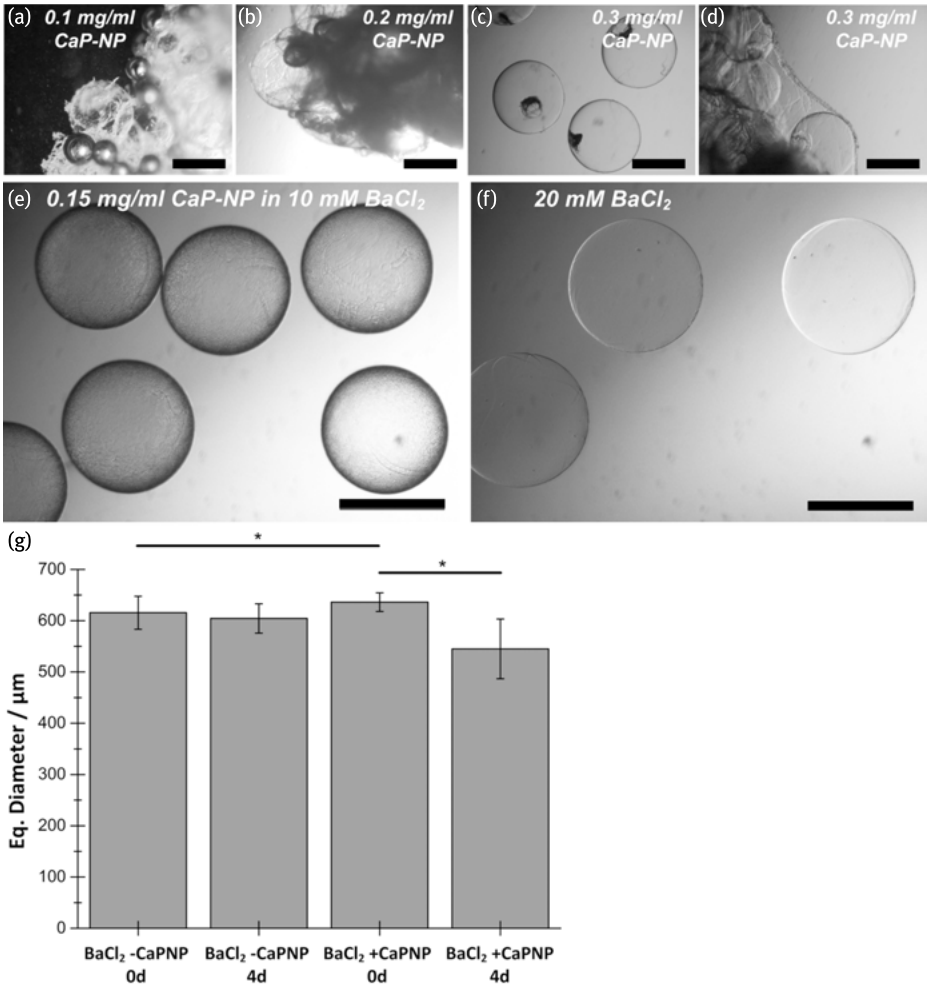

Fig. 4.7: Alginate beads which were modified with PEI-functionalized calcium phosphate nanoparticles (labelled TRITC) from solution. (a)–(d) Alginate beads were modified with pure calcium phosphate nanoparticle dispersion with concentrations of (a) 0.1 mg mL^{-1}, (b) 0.2 mg mL^{-1}, (c) and (d) 0.3 mg mL^{-1}. (e) Alginate beads with 0.15 mg mL^{-1} nanoparticles in 10 mM $BaCl_2$. Stable modified alginate beads could only be produced reproducibly with a mixture of calcium phosphate and $BaCl_2$. (f) Unmodified native alginate beads. (g) Dimensional properties of alginate beads quantified by equivalent diameter after day 0 and day 4. Data are presented as mean ± standard deviation (SD, $n = 3$), (*) indicates statistical significance ($p < 0.05$, t-test). Scale bar: 500 µm.

mentation and subsequent washing with water. The coated alginate beads are shown in Fig. 4.8 (a). The calcium phosphate nanoparticles (red) formed a homogeneous coating on the beads. However, the alginate beads lost their round shape after coating. This may be due to free calcium ions in the dispersion.

Experiments were carried out with the purified nanoparticle dispersion to check whether the calcium ions have an effect on bead shape. The experiments were performed as described above. The beads were washed with water after 1 h of stirring. Figure 4.8 (b) shows the coated beads. Notably, the beads did not lose their shape during coating.

The calcium concentration of the beads was measured with elemental analysis (atomic absorption spectroscopy of the calcium concentration; computation according to the example given above). With these results, it was possible to estimate the number of calcium phosphate nanoparticles from 10^{10} to 10^{11} on each alginate bead.

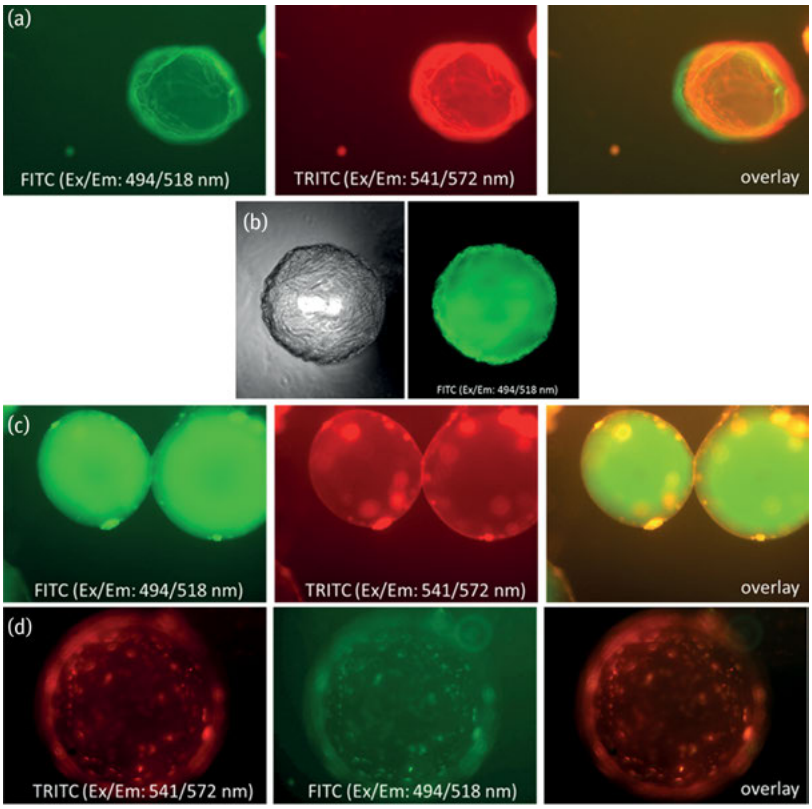

Fig. 4.8: Fluorescence microscopic images of alginate beads (a) with a coating of PEI-TRITC-functionalized calcium phosphate nanoparticles with free Ca^{2+} in dispersion; (b) with a coating of calcium phosphate nanoparticles without free Ca^{2+} in dispersion; (c), (d) with a coating of calcium phosphate nanoparticles. (c) For this coating, the alginate beads were rolled over an electrophoretically coated surface with PEI-TRITC-functionalized calcium phosphate nanoparticles. (d) For this coating, the alginate beads were sequentially rolled over electrophoretically coated surfaces with PEI-FITC- and PEI-TRITC-functionalized calcium phosphate nanoparticles.

4.3.5 Coating from substrates

Unstructured silicon substrates were coated with calcium phosphate nanoparticles by electrophoretic deposition. A multilayer with fluorescent calcium phosphate nanoparticles was used for the coating. The first coating was carried out with PEI-FITC-functionalized alginate beads and PEI-TRITC-functionalized calcium phosphate nanoparticles. PEI-TRITC-functionalized calcium phosphate nanoparticles were deposited on a silicon surface with a layer thickness of about 400 nm. The alginate beads were then rolled over the surface. The coated alginate beads are shown in Fig. 4.8 (c). The surface coating was clearly inhomogeneous and patchy. The particles were agglomerated (red) on the surface and there were gaps with no particles. However, the particles adhered to the bead surface very well.

The second coating procedure was carried out with two different colored fluorescent calcium phosphate nanoparticles. For this coating, two different silicon wafers were coated, each with one kind of fluorescent nanoparticles (PEI-TRITC- or PEI-FITC-functionalized calcium phosphate nanoparticles). The alginate beads were rolled over the first surface and then over the second surface. The first layer on the alginate beads consisted of PEI-TRITC-functionalized calcium phosphate nanoparticles (red). Some free patches were then coated with PEI-FITC-functionalized calcium phosphate nanoparticles (green). Figure 4.8 (d) shows alginate beads which were coated with two kinds of fluorescent calcium phosphate nanoparticles in the way described.

4.3.6 Cell reactions to calcium phosphate nanoparticle-coated alginate membranes

Alginate membranes coated with calcium phosphate nanoparticles were used to study the effects of the physicochemical surface properties and thus the changed cellular behaviour. Native and calcium phosphate-coated alginate membranes and a tissue culture-treated polystyrene surface were inoculated with L929 fibroblasts and monitored over 24 hours in automated microscopes (Biostation IM, Nikon). As an indicator of the changed surface properties of alginate introduced by coating with calcium phosphate nanoparticles, the attachment of fibroblasts was quantified after 24 h.

Visual inspection of the cells showed cells attached to standard tissue culture polystyrene surface (TCPS; Fig. 4.9 (a)) and no fibroblasts attached to native alginate hydrogel surfaces (Fig. 4.9 (b)). Cells on native alginate hydrogels tended to agglomerate due to the absence of integrin binding sites. In contrast, fibroblasts were able to attach and spread on calcium phosphate nanoparticle-loaded alginate hydrogel surfaces (Fig. 4.9 (c)). Compared to cells attached to rigid TCPS, cells on nanoparticle-coated alginate hydrogel surfaces appeared to be less flat and spread due to different substrate stiffness. Overall, 94 % ± 2 % cells were attached to the TCPS surface after 24 h, whereas 76 % ± 21 % cells were attached to calcium phosphate nanoparticle-coated alginate hydrogels. Only 2 % ± 2 % of the cells were attached to native alginate

hydrogel surfaces (Fig. 4.9 (d)). These data lead to the conclusion that calcium phosphate nanoparticles, stabilized with TRITC-PEI, trigger an integrin-mediated adhesion of anchorage-dependent cells like fibroblasts. Positive surface charges introduced by PEI as well as probably an increased roughness of the hydrogel surface by deposited nanoparticles further enhanced the cytocompatibility for cells like fibroblasts. Future studies should focus on the modification of nanoparticles with extracellular matrix (ECM) proteins like collagen or laminin to engineer more specific cellular environments for multipotent or pluripotent stem cells.

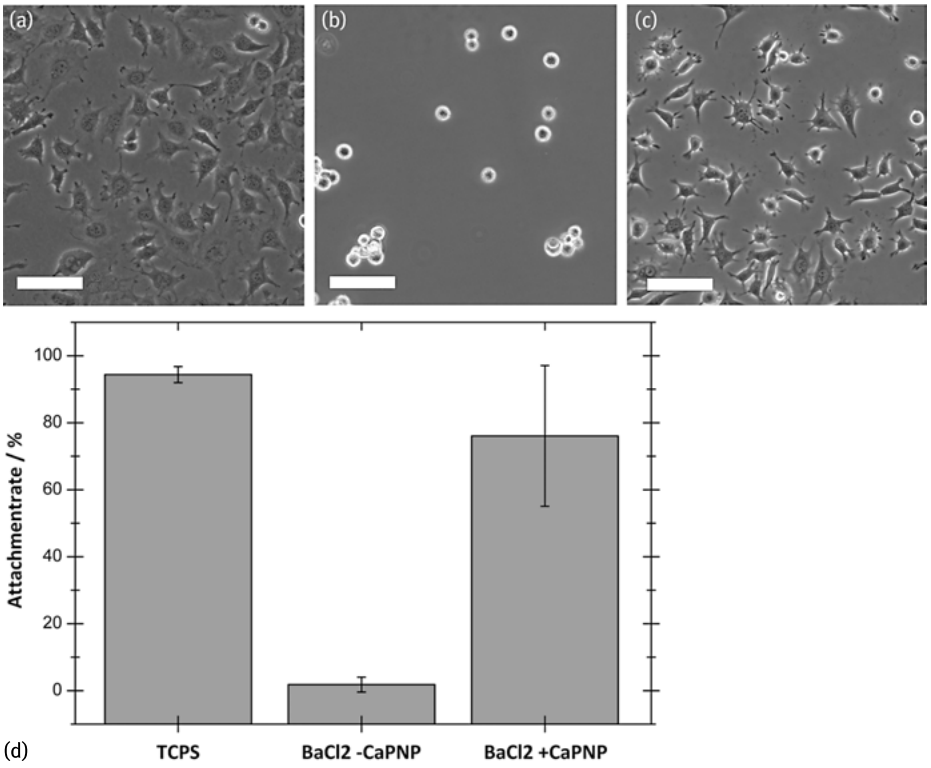

Fig. 4.9: Reactions of L929 fibroblasts, cultured on different surfaces. (a) Fibroblasts attached to rigid tissue culture-treated polystyrene surface. (b) Fibroblasts attached to native Ba-alginate membranes forming multicellular agglomerates indicating low cell-matrix interactions. (c) Fibroblasts attached to a nanoparticle-coated Ba-alginate membrane. (d) Overall attachment rate of L929 fibroblasts on the surfaces shown in (a)–(c). The modification of native Ba-alginate significantly increased the attachment rate, presented as average with SD ($n = 3$ independent experiments). The highest attachment rate was observed on the TCPS surface. The scale bars in (a), (b) and (c) indicate 200 µm.

4.3.7 Robotic coating of alginate beads with calcium phosphate nanoparticles from substrates

The coating from nanostructured, two-dimensional templates requires an adjustable robotic stage for moving and loading alginate beads at the same time. On the basis of a commercially available xyz-table (Nano-Plotter, GeSiM mbH, Grosserkmannsdorf, Germany) and its passive tip holder, we mounted an aluminum endplate for collection and moving of alginate beads to be coated (Fig. 4.10 (a)). Alginate beads interacted with the aluminum endplate due to a thin layer of liquid around the beads (Fig. 4.10 (b)). To load the alginate beads with calcium phosphate nanoparticles, the endplate with adhered beads was contacted with the surface and moved in the *x*- and *y*-directions in order to roll the beads over the deposited nanoparticles (Fig. 4.10 (c)). A rectangular moving pattern was implemented where the head was moved for 3 mm in the *x*- and *y*-directions. The moving pattern was repeated four times. Unloaded native alginate beads (Fig. 4.10 (d)) were coated with nanoparticles by this procedure. Figure 4.10 (e) shows calcium phosphate nanoparticle-coated alginate beads after the robotic loading procedure was performed, as indicated by the red fluorescence of TRITC. Figure 4.10 (f) illustrates alginate beads being loaded with calcium phosphate nanoparticles by intensity histograms of fluorescence channels before and after the loading procedure. Small deformations observed on alginate beads after the loading procedure had to be overcome, e.g. by spring-loaded surfaces. The successful transfer of nanoparticles using this prototype gave the basis for further studies with the focus on electrophoretically deposited nanoparticles on structured surfaces as shown in Fig. 4.3 (a).

4.3.8 Hanging drop technology with calcium phosphate nanoparticle-coated alginate beads

After alginate beads had been successfully loaded with nanoparticles as shown in Fig. 4.7 and the first promising results with respect to the increased cytocompatibility of alginate hydrogels (Fig. 4.9) were achieved, calcium phosphate nanoparticle-coated alginate beads were used as microcarriers for human mesenchymal stem cells (hMSCs) in the hanging drop cultivation technique. hMSCs (PromoCell GmbH, Heidelberg, Germany) were cultivated in hanging drop cultivation substrates in volumes of 40 µL. A schematic drawing of the hanging drop principle is shown in Fig. 4.10 (g). Microcarriers and cells cultivated in hanging drops accumulated in the drop meniscus and were allowed to interact by cell-cell or cell-matrix interactions. In our experiments, microcarriers, native alginate beads, calcium phosphate nanoparticle-coated alginate beads (both produced as described in Section 4.3) were cultivated with 4000 cells per droplet (40 µL) in commercially available hanging drop plates (GravityPLUS™, InSphero AG, Schlieren, Switzerland). Cells and microcarriers were harvested after

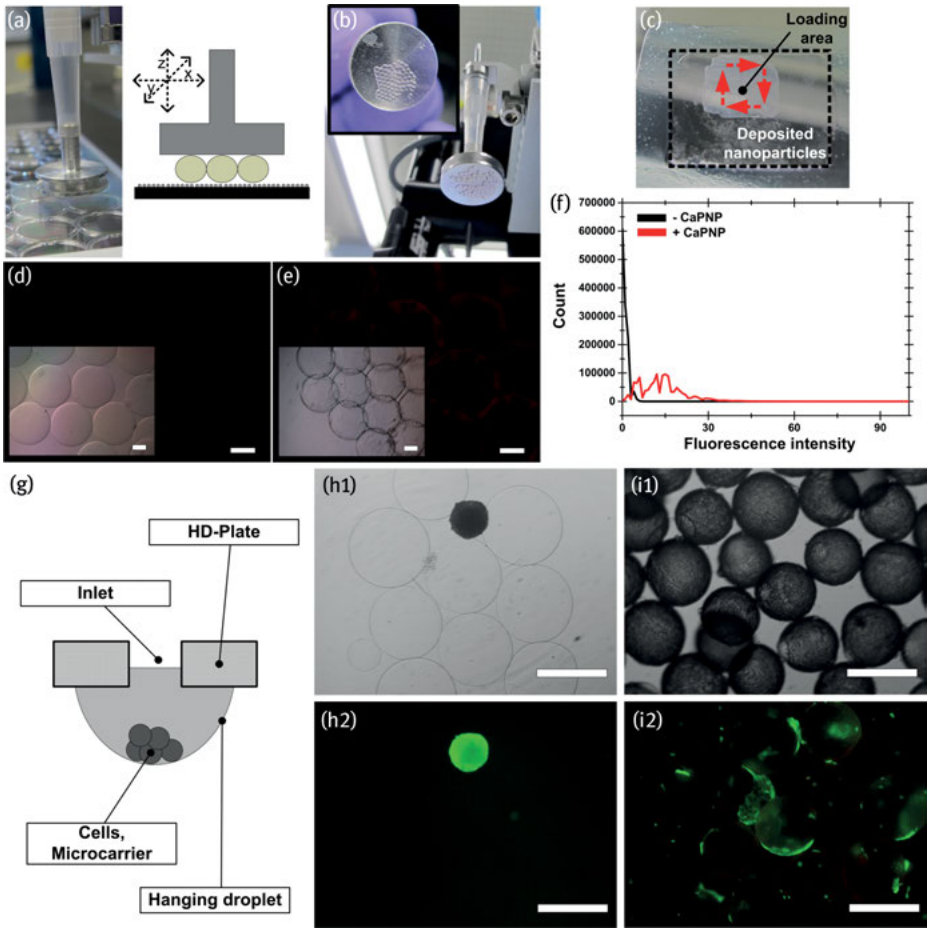

Fig. 4.10: (a)–(f) Prototype for the coating of alginate beads with nanoparticles from surfaces. (a) Holder for the coating of alginate beads from two-dimensional surfaces. (b) Tool with sticky alginate beads before (inset) and after (large image) coating. (c) Two-dimensional coating template, loaded with calcium phosphate nanoparticles, after the coating procedure. The coating area is clearly identifiable (red arrows indicate moving direction of xy robot). (d) Native alginate beads before the coating procedure: bright field image (inset) and fluorescence image (large image). (e) Modified alginate beads after coating procedure: bright field image (inset) and fluorescence image (large image). (f) Histograms of the red channel from fluorescence images in (d) and (e). The increased intensity of the red channel shows the loading of alginate beads with calcium phosphate nanoparticles (TRITC modified). Scale bars in (d) and (e): 200 µm. (g)–(i) Hanging drop technology. (g) Schematic drawing of the hanging drop principle. Small volumes of medium with cells and microcarrier are placed on compatible surfaces for droplet formation and cell cultivation. Cells and microcarrier were located in the droplet's meniscus. (h) hMSCs after cultivation in HD with native alginate beads. (i) hMSCs after cultivation in HD with calcium phosphate nanoparticle modified alginate beads. (h), (i): Image 1: bright field microscopic; Image 2: fluorescence image (triple band filter). Scale bars: 500 µm.

5 days, stained with fluorescein diacetate and ethidium bromide and analyzed by bright field and fluorescence microscopy.

Human mesenchymal stem cells showed no cell-matrix interaction with native alginate as expected. The cells interacted mainly with other cells and built agglomerates (Fig. 4.10 (h)). An increased cell-matrix interaction was observed on calcium phosphate nanoparticle-coated alginate beads. Cells tended to adhere and spread or to build smaller agglomerates on modified alginate beads (Fig. 4.10 (i)). These results indicate that cells were able to interact with nanoparticles on the alginate surface, providing the basis for future gene transfer and drug delivery studies.

4.4 Conclusions

Characterization of the laser-induced sub 100 nm structures was performed by SEM and FIB measurements. Here, the HSFL structures were investigated in terms of morphology, periodicity, depth profile, aspect ratio and how various parameters such as energy per pulse, number of applied pulses (scan speed), wavelength, polarization, NA of the focusing optics and incident angle of the laser beam, influence them. The results show that the periodicity of HSFL is wavelength-dependent and increases with wavelengths between 700 and 950 nm. The resulting structures were relatively homogeneous ripples with a crater depth of 135 nm. This is close to the distance between two rims (~ 125 nm) which gives an aspect ratio of about 1 : 1.

Silicon wafers with and without ripple structures were used for electrophoretic deposition. Calcium phosphate nanoparticles redispersed in ethanol were deposited and gave a particle multilayer. The electrophoretic deposition with biofunctionalized calcium phosphate nanoparticles from water led to a monolayer. Calcium phosphate nanorods were deposited from water, forming a multilayer with about 17 layers.

Different ways of loading alginate beads with calcium phosphate nanoparticles were investigated. One of these was incubation in a nanoparticle dispersion. The second was loading from the crosslinking bath. The nanoparticle dispersion alone was not sufficient to produce stable alginate beads. Calcium phosphate nanoparticle-coated alginate beads were distinguished by increased surface contrast and were generally darker in comparison to standard alginate beads. The calcium phosphate-coated alginate beads remained intact for at least 4 days and showed no signs of disintegration. Coating with solution gave the best results with a calcium-free dispersion. Nanoparticle coating on the alginate beads was very efficient, and the beads did not lose their shape. The coating of the nanoparticles on the beads was homogeneous in this case.

Coating with a nanoparticle-loaded substrate was also elaborated. The final coating was applied with fluorescent PEI-functionalized calcium phosphate nanoparticles. Fluorescence microscopy pictures showed an inhomogeneous coating. The nanoparticles were agglomerated on the alginate surface. However, it was possible to

coat the surface of the beads with different kinds of fluorescent calcium phosphate nanoparticles.

The best method of coating alginate beads with calcium phosphate nanoparticles from a substrate was using a robot. Electrophoretically coated structured surfaces carrying nanoparticles were used as substrates.

After loading the alginate with calcium phosphate nanoparticles, the effects on the surface properties and the subsequent cellular behavior were studied. Three different samples were examined: native alginate, calcium phosphate-coated alginate and tissue culture-treated polystyrene. The surfaces were colonized with L929 fibroblasts. The nanoparticle-coated alginate surfaces triggered the integrin-mediated adhesion of anchorage-dependent cells like fibroblasts. Finally, calcium phosphate nanoparticle-coated alginate beads were used as microcarriers for human mesenchymal stem cells in the hanging drop cultivation technique. hMSCs showed no cell-matrix interaction on native alginate, whereas the cell-matrix interaction was significantly increased on calcium phosphate-loaded alginate beads.

Overall, the electrophoretic deposition of calcium phosphate nanoparticles on laser-structured surfaces, followed by transfer to alginate beads is a promising method of preparing microcarriers to influence the behavior of cells.

Acknowledgments

This work was supported by the German National Science Foundation (DFG, priority programme SPP 1327). The FIB profiles were prepared by M. Menzel, S. Henning and A. Heilmann at the Fraunhofer Institute for Mechanics of Materials (IWM) in Halle (Saale), Germany.

References

[1] Kesharwani P, Gajbhiye V, Jain NK. A review of nanocarriers for the delivery of small interfering RNA. Biomaterials 2012, 33, 7138–7150.
[2] Chen C, Dubin R, Kim MC. Emerging trends and new developments in regenerative medicine: a scientometric update (20002014). Expert Opin Biol Ther 2014, 14, 1295–1317.
[3] Guo X, Huang L. Recent advances in nonviral vectors for gene delivery. Acc Chem Res 2012, 45, 971–979.
[4] Sokolova V, Epple M. Inorganic nanoparticles as carriers of nucleic acids into cells. Angew Chem Int Ed 2008, 47, 1382–1395.
[5] Kovtun A, Neumann S, Neumeier M, et al. Nanoparticle-mediated gene transfer from electrophoretically coated metal surfaces. J Phys Chem B 2013, 117, 1550–1555.
[6] Xu ZP, Zeng QH, Lu GQ, Yu AB. Inorganic nanoparticles as carriers for efficient cellular delivery. Chem Eng Sci 2006, 61, 1027–1040.
[7] Cai Y, Tang R. Calcium phosphate nanoparticles in biomineralization and biomaterials. J Mater Chem 2008, 18, 3775–3787.

[8] Olton D, Li J, Wilson ME, et al. Nanostructured calcium phosphates (NanoCaPs) for non-viral gene delivery: Influence of the synthesis parameters on transfection efficiency. Biomaterials 2007, 28, 1267–1279.
[9] Epple M, Ganesan K, Heumann R, et al. Application of calcium phosphate nanoparticles in biomedicine. J Mater Chem 2010, 20, 18–23.
[10] Dorozhkin SV, Epple M. Biological and medical significance of calcium phosphates. Angew Chem Int Ed 2002, 41, 3130–3146.
[11] Wallat K, Dörr D, Le Harzic R, et al. Cellular reactions toward nanostructured silicon surfaces created by laser ablation. J Laser Appl 2012, 24, 042016.
[12] Epple M, Neumeier M, Doerr D, et al. Electrophoretic deposition of calcium phosphate nanoparticles on a nanostructured silicon surface. Materialwiss Werkstofftech 2011, 42, 50–54.
[13] Boccaccini AR, Keim S, Ma R, Li Y, Zhitomirsky I. Electrophoretic deposition of biomaterials. J Royal Soc Interface 2010, 7, S581-S613.
[14] Zimmermann H, Shirley SG, Zimmermann U. Alginate-based encapsulation of cells: Past, present, and future. Curr Diab Rep 2007, 7, 314–320.
[15] Zimmermann H, Ehrhart F, Zimmermann D, et al. Hydrogel-based encapsulation of biological, functional tissue: fundamentals, technologies and applications. Appl Phys A 2007, 89, 909–922.
[16] Gepp MM, Ehrhart F, Shirley SG, Howitz S, Zimmermann H. Dispensing of very low volumes of ultra high viscosity alginate gels: a new tool for encapsulation of adherent cells and rapid prototyping of scaffolds and implants. Biotechniques 2009, 46, 31–43.
[17] Gröhn P, Klöck G, Zimmermann U. Collagen-coated Ba(2+)-alginate microcarriers for the culture of anchorage-dependent mammalian cells. Biotechniques 1997, 22, 970–975.
[18] Morra M, Cassinelli C. Cell adhesion micropatterning by plasma treatment of alginate coated surfaces. Plasmas Polym 2002, 7, 89–101.
[19] Rowley JA, Madlambayan G, Mooney DJ. Alginate hydrogels as synthetic extracellular matrix materials. Biomaterials 1999, 20, 45–53.
[20] Schulz JC, Stumpf PS, Katsen-Globa A, Sachinidis A, Hescheler J, Zimmermann H. First steps towards the successful surface-based cultivation of human embryonic stem cells in hanging drop systems. Eng Life Sci 2012, 12, 584–587.
[21] Birnbaum M. Semiconductor surface damage produced by ruby lasers. J Appl Phys 1965, 36, 3688–3689.
[22] Sipe JE, Young JF, Preston J, van Driel H. Laser-induced periodic surface structure I Theory Phys Rev B 1983, 27, 1141–1154.
[23] Borowiec A, Haugen HK. Subwavelength ripple formation on the surfaces of compound semiconductors irradiated with femtosecond laser pulses. Appl Phys Lett 2003, 82, 4462–4464.
[24] Bonse J, Rosenfeld A, Krüger J. On the role of surface plasmon polaritons in the formation of laser induced periodic surface structures upon irradiation of silicon by femtosecond laser pulse. J Appl Phys 2009, 106, 104910.
[25] Le Harzic R, Schuck H, Sauer D, Anhut T, Riemann I, König K. Sub-100 nm nanostructuring of silicon by ultrashort laser pulses. Optics Express 2005, 13, 6651–6656.
[26] Dufft D, Rosenfeld A, Das SK, Grunwald R, Bonse J. Femtosecond laser-induced periodic surface structures revisited: a comparative study on ZnO. J Appl Phys 2009, 105, 034908.
[27] Doane TL, Burda C. The unique role of nanoparticles in nanomedicine: imaging, drug delivery and therapy. Chem Soc Rev 2012, 41, 2885–2911.
[28] Thanh NKT, Green LAW. Functionalisation of nanoparticles for biomedical applications. Nano Today 2010, 5, 213–230.

[29] Kamaly N, Xiao Z, Valenca PM, Radovic-Moreno AF, Farokhzad OC. Targeted polymeric therapeutic nanoparticles: design, development and clinical translation. Chem Soc Rev 2012, 41, 2971–3010.
[30] Jia TQ, Chen HX, Huang M, et al. Formation of nanogratings on the surface of a ZnSe crystal irradiated by femtosecond laser pulses. Phys Rev B 2005, 72, 125429.
[31] Miyaji G, Miyazaki K. Origin of periodicity in nanostructuring on thin film surfaces ablated with femtosecond laser pulses. Opt Express 2008, 16, 16265–16271.
[32] Le Harzic R, Stracke F, Zimmermann H. Formation mechanism of femtosecond laser-induced high spatial frequency ripples on semiconductors at low fluence and high repetition rate. J Appl Phys 2013, 113, 183503.
[33] Le Harzic R, Dörr D, Sauer D, et al. Formation of periodic nanoripples on silicon and germanium induced by femtosecond laser pulses. Phys Proc 2011, 12, 29–36.
[34] Le Harzic R, Dörr D, Sauer D, et al. Large-area, uniform, high-spatial-frequency ripples generated on silicon using a nanojoule-femtosecond laser at high repetition rate. Opt Lett 2011, 36, 229–231.
[35] Zimmermann H, Zimmermann D, Reuss R, et al. Towards a medically approved technology for alginate-based microcapsules allowing long-term immunoisolated transplantation. J Mater Sci Mater Med 2005, 16, 491–501.
[36] Zimmermann H, Hillgärtner M, Manz B, et al. Fabrication of homogeneously cross-linked, functional alginate microcapsules validated by NMR-, CLSM-and AFM-imaging. Biomaterials 2003, 24, 2083–2096.
[37] Klesing J, Chernousova S, Epple M. Freeze-dried cationic calcium phosphate nanorods as versatile carriers of nucleic acids (DNA, siRNA). J Mater Chem 2012, 22, 199–204.
[38] Klesing J, Chernousova S, Kovtun A, et al. An injectable paste of calcium phosphate nanorods, functionalized with nucleic acids, for cell transfection and gene silencing. J Mater Chem 2010, 20, 6144–6148.
[39] Le Harzic R, Dörr D, Sauer D, Stracke F, Zimmermann H. Generation of high spatial frequency ripples on silicon under ultrashort laser pulses irradiation. Appl Phys Lett 2011, 98, 211905.
[40] Le Harzic R, Menzel M, Henning S, Heilmann A, Stracke F, Zimmermann H. Cross-sectional study of high spatial frequency ripples performed on silicon using nanojoule femtosecond laser pulses at high repetition rate. Appl Surf Sci 2014, 305, 670–6733.

F. Burmeister, S. Steenhusen, R. Houbertz, T. S. Asche, J. Nickel,
S. Nolte, N. Tucher, P. Josten, K. Obel, H. Wolter, S. Fessel,
A. M. Schneider, K.-H. Gärtner, C. Beck, P. Behrens,
A. Tünnermann, and H. Walles

5 Two-photon polymerization of inorganic-organic polymers for biomedical and microoptical applications

Abstract: Two-photon polymerization (2PP) is an attractive technique for the fabrication of arbitrary three-dimensional structures with feature sizes down to 100 nm. In this chapter, the potential of subwavelength structures for biomedical and microoptical applications is studied. We optimized the focusing of ultrashort laser pulses and developed new materials. Specially adapted refractive-diffractive hybrid optics were designed and constructed to maintain the sub-micrometer resolution of the fabrication process for the complete height of large-scale structures. New inorganic-organic polymers were synthesized and characterized with respect to their biocompatibility and biodegradability. Additionally, molecular modeling of inorganic-organic polymers was carried out to understand the structure and dynamics of monomers and polymerization products on a molecular level. 2PP-fabricated structures for the controlled growth of human endothelia in 2D and 3D cells are presented. Finally, microlenses, diffractive optical elements, and a diaphragm array for multi-aperture camera modules were fabricated and characterized with respect to their optical performance.

5.1 Introduction

Two-photon polymerization is a lithography technology capable of producing arbitrary three-dimensional structures with feature sizes as small as 100 nm [1, 2]. This is achieved by focusing ultrashort laser pulses into a UV-light curable resin, which is transparent for the applied laser wavelength. A polymerization reaction is initiated by two-photon absorption exclusively within the focal region, where the intensities are sufficiently high. By scanning the focus through the resin, arbitrary geometries can be fabricated with a resolution exceeding the diffraction limit of the applied wavelength. This unique property facilitates a wide range of applications such as photonic crystals [3–5], microoptical elements [6–8] and also biomedical devices, i.e. scaffolds for three-dimensional cell growth [9–11].

Modern applications impose challenging requirements on geometries and material properties of the structures fabricated. The desired structures should not only have sub-micrometer feature sizes but also large overall sizes. The materials should

additionally be biocompatible and biodegradable for biomedical applications. Therefore, investigating illumination and applied materials is crucial for the fabrication of functionalized structures for biomedical and microoptical applications of 2PP.

In present state-of-the-art setups, the laser pulses are focused with oil immersion microscope objectives into the polymer. These objectives suffer from structuring-depth-dependent aberrations, due to the refractive index mismatch of polymer, immersion oil, and coverslip. As a consequence correction of these aberrations is required to maintain the intensity distribution (and consequently the resulting structure sizes) for different structuring depths. Inorganic-organic hybrid polymers such as ORMOCER®s[1] have proven to be suitable materials for 2PP. However, on a molecular level the structure and polymerization reactions of these materials are not yet understood. Improved knowledge might enable synthesis of novel materials with smaller structure sizes.

In Section 5.2 the influence of aberrations on focal intensity distribution is investigated and a specially designed hybrid objective is introduced. Synthesis and properties of the applied inorganic-organic polymers, including the modeling of their molecular structures are discussed in Section 5.3. Finally, biomedical and microoptical applications are described in Section 5.4.

5.2 Hybrid optics

In the structuring process of 2PP, the polymerization reaction is triggered by the interaction of the polymer with the ultrashort laser pulses inside the focal volume of the optics. Thus, feature size and stability of the resulting structure is defined by the focal intensity distribution of the focusing optics employed. Since severe problems arise from the use of conventional microscope objectives, specially adapted focusing optics were constructed which might offer a solution to these problems.

5.2.1 Conventional focusing with microscope objectives

In typical setups for 2PP, the laser pulses are focused by an oil immersion microscope objective with a numerical aperture (NA) of around 1.4 to achieve a minimized focal spot inside the polymer. These objectives are designed for a fixed setup determined by (1) the refractive index of the immersion oil ($n_d = 1.527$) and (2) the thickness ($d = 170\,\mu m$) and refractive index of the coverslip. Due to the large angles appearing in the beam path, even small deviations from these design conditions will result in

1 ORMOCER®: registered by the Fraunhofer-Gesellschaft zur Förderung der Angewandten Forschung in Deutschland e. V.

additional aberrations thus significantly increasing the focal spot size. In the case of 2PP, the most critical factor concerning aberrations is the refractive index mismatch between the polymer and the immersion oil. Additionally, standard microscope objectives are designed to focus on the back of the coverslip. If the focus is moved deeper into the volume of the polymer strong spherical aberrations will occur depending on the refractive index mismatch and focusing depth. These aberrations lead to decreased intensity with increasing structuring depth, changing the resulting structure sizes.

Several strategies have been proposed to compensate index-mismatch-induced aberrations in recent years. One method is to increase the applied laser power according to the focusing depth in order to compensate for the drop of peak intensity caused by the aberrations [12]. However, this method does not prevent focal spot enlargement and is cumbersome to implement experimentally. A more sophisticated technique uses a combination of a spatial light modulator (SLM) and an adaptive mirror [13]. This combination allows for the compensation of a large amount of aberrations, but requires the integration of additional devices into the setup. Another approach is to remove immersion oil and coverslip, and to dip the objective directly into the liquid polymer [14, 15]. In this configuration, the optical path will not change when the focus is scanned through the polymer and consequently the focal intensity distribution remains constant. However, it is challenging to achieve a diffraction limited focal spot, since the design conditions of the objective are not met. This can be achieved by using objectives with an integrated correction ring for spherical aberrations and the choice of a polymer with an appropriate refractive index.

Another major drawback of conventional microscope objectives is their limited working distance which is usually around 100 µm and sets a fixed limit on the maximum structure height realizable. To overcome these drawbacks, specially adapted optics for focusing ultrashort laser pulses into a polymer were designed and assembled. These are corrected for refractive index mismatched induced aberrations and are not limited in the achievable structure height by the working distance.

5.2.2 Optical design

The layout of the optical design of the hybrid optics is shown in Fig. 5.1 (a) [16, 17]. The optics are optimized to focus 300 fs pulses with a central wavelength $\lambda = 515$ nm into the ORMOCER® OC-I. The centerpiece is an aspherical lens with NA = 0.66 (Edmund Optics, Stock No. #49-097). A half-ball lens is added as a solid immersion lens (ASIL) to further increase the NA without generating additional aberrations [18, 19]. An ASIL increases the NA of a lens by a factor of n^2, with n being the refractive index of the ASIL [20]. The upper limit for the total NA is given by n. When looking at the optical layout (Fig. 5.1 (a)), the ASIL not only consists of the half-ball lens alone, but also the immersion liquid and the coverslip. The polymer without photoinitiator is used as the

immersion liquid. When the focus is moved deeper into the polymer, the thickness of the immersion oil is reduced by exactly the same distance. Consequently, the total thickness of the ASIL and the optical path remain constant. The final NA of asphere and ASIL is 1.30.

So far however, the optical design has only been discussed regarding monochromatic light without considering chromatic aberration. The optics work well at the central wavelength of the laser pulses (λ = 515 nm) but show strong chromatic aberration for wavelengths at the edge of the spectrum. An approach to correct chromatic aberrations with as few optical elements as possible relies on the concept of refractive-diffractive hybrid optics. The basic idea is to exploit the reciprocal dependency on the wavelength to correct the chromatic aberration of a refractive lens with the diffractive power of a diffractive optical element (DOE) [21]. The phase function of the DOE was optimized using the commercial optical design software OpticStudio [22]. The resulting phase profile quantized by 2π was manufactured by means of laser lithography onto a 1.1 mm thick glass substrate (Borofloat, Schott). Figure 5.1 (b) shows the optical path difference for the hybrid optics including the DOE. The final optics have a diffraction-limited performance for the complete spectrum of laser pulses.

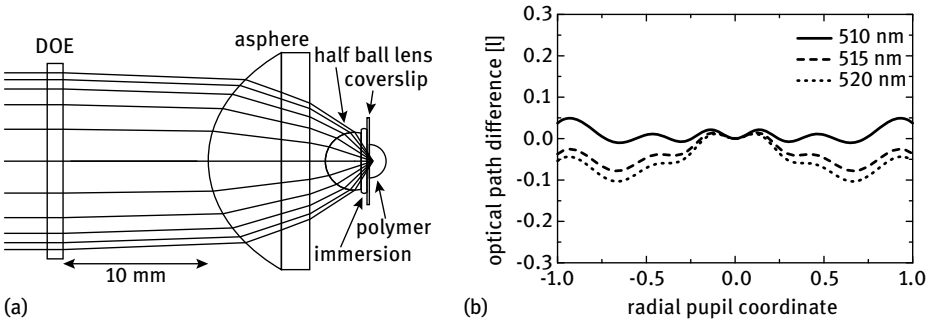

Fig. 5.1: (a) Layout of the optical design of the hybrid optics. The DOE (diffractive optical element), asphere and half-ball lens are mounted as a fixed unit. The optics focuses on the back of the coverslip, where the polymer is drop casted. From [17]. (b) Optical path difference for the focusing optics. The DOE corrects the chromatic aberration for the complete spectrum of the laser pulses.

This first prototype was still limited by its working distance of 630 µm in achievable structure heights. To eliminate this restriction, a second design was realized where the coverslip was removed, as suggested by Bückmann et al. [14]. The hybrid optics are dipped directly into the polymer which can now be drop casted onto an arbitrary substrate.

Due to the aberration correction the hybrid objective enables structuring of submicron feature sizes with constant process parameters over the entire working distance range.

5.2.3 Experimental results

Prism-shaped structures with different heights were fabricated to demonstrate the improvements of the hybrid optics for three-dimensional structuring, using hybrid optics and an oil immersion microscope objective (Plan-Apochromat NA = 1.4, Zeiss MicroImaging GmbH, Germany) for focusing. The process parameters (average power, writing speed) were kept constant for all prisms. Scanning electron microscopy (SEM) pictures of the resulting structures are shown in Fig. 5.2. When focusing with the microscope objective, the prisms become more and more unstable with increasing heights, due to the writing-depth-dependent aberration. When hybrid optics are used for focusing, all prisms are stable and show sharp edges independent of their height. However, to verify diffraction-limited focusing of the hybrid optics direct measurement of either the point spread function or the wavefront of the optics is required, which is currently experimentally implemented.

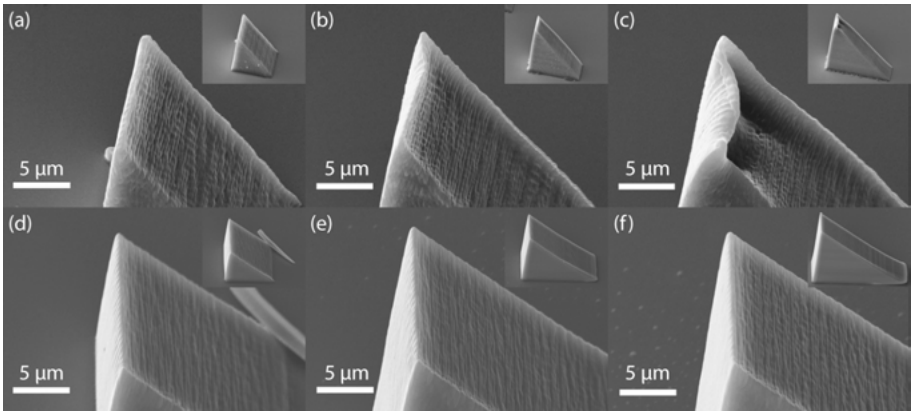

Fig. 5.2: Prism-shaped structures of different heights, fabricated with constant process parameters, for focusing with (a)–(c) microscope objective and (d)–(f) hybrid optics. The heights are (from left to right) 20 µm, 40 µm, and 60 µm, respectively. The surface qualities of the prism structures could be improved by applying adapted process parameters, e.g. smaller hatch distances.

5.3 Inorganic-organic polymers

Inorganic-organic hybrid polymers such as ORMOCER®s are particularly suited for photonic and biomedical applications [23]. Their chemical and physical properties can be widely tailored to the specific application by the use of special alkoxysilane precursors and by control of the synthesis conditions [24]. The materials synergistically combine material properties of inorganic materials such as glass with those of polymer materials, typically resulting in thermally and chemically very stable materials which can be processed like classical photoresists via lithography methods in 2D and 3D.

Additionally, specific material compositions allow the control of the materials' mechanical properties and surface functionalities which make them particularly suitable for cell growth investigations [25]. A completely new material feature makes it possible to physiologically degrade the materials [26] which can be processed analog to the classical ORMOCER® materials via one- or two-photon processes.

5.3.1 Synthesis and properties

A variety of ORMOCER®-materials were synthesized and specially adapted to the 2PP process in order to broaden the processing window for individual material formulations. The materials were chosen for optical and/or biomedical applications, and allow the generation of structures from sub100 nm [17] up to mm dimensions [23] which is a prerequisite for certain optical and biomedical applications. The synthesized ORMOCER®s differ strongly in their chemical composition, their reaction kinetics, and their potential level of crosslinking behavior.

Table 5.1 summarizes some properties of the ORMOCER®s used for 3D 2PP lithography.

Tab. 5.1: Synthesized ORMOCER® materials for optical (OPT) and biomedical (BIO) applications.

Material	$-[SiO]_n$ (%)	Crosslinkable group	Degradable	Application	
				OPT	BIO
OC-I	25.5	methacrylate	—	✓	✓
OC-27sc	27.2	styryl	—	✓	n. a.
OC-DIM01	21.8	methacrylate	—	✓	n. a.
OC-IV	8.9	acrylate	—	✓	✓
OC-V	13.9	acrylate	—	✓	✓
OC-GM	8.8	methacrylate	✓	n. a.	✓
OC-SVI	6.5	methacrylate	✓	n. a.	✓
OC-SVII	7.5	methacrylate	✓	n. a.	✓
OC-SVIII	14.7	methacrylate	✓	n. a.	✓

Synthesis follows a general scheme of hydrolysis and polycondensation reactions, often referred to as a sol-gel reaction [24]. However, for the present material synthesis, gelation is often prevented by controlling the polycondensation reactions, thus providing materials which can be used analog to conventional negative tone resist materials [27, 28] with shelf lives of up to several years, depending on the material modification. Optical properties can be widely varied, yielding inorganic-organic hybrid polymer materials with low or high refractive indexes [29, 30], or low absorption losses at data and telecom wavelengths [27, 31]. In addition other material properties such as mechanical and thermal properties and surface functionalization can be

modified [24, 32]. Particularly with respect to applications in biomedicine, controlled variation of the mechanical properties (see Tab. 5.2) or the materials' surface functionalization is a prerequisite for cell adhesion.

As shown in Tab. 5.1, most of the materials are suitable for photonic and/or biomedical applications. These materials are nonbiodegradable and extremely stable regarding their thermal, chemical, or mechanical properties. The materials' inorganic content strongly varies, and is highest for the materials OC-I, OC-27sc, and OC-DIM01. OC-I and OC-27sc were also chosen for molecular modeling [33] (see Section 5.3.2) due to the fact that their still complicated chemical structure is the simplest of the synthesized material formulations and that their properties were thoroughly characterized. In addition, OC-I and OC-27sc are synthesized using identical synthesis conditions except for the exchange of the alkoysilane precursor 3-methacryloxypropyltrimethoxysilane for p-styryl trimethoxysilane, thus changing the organic functional group for crosslinking.

OC-27sc in particular has yielded the smallest structure sizes via TPA patterning [17], making it an ideal candidate for molecular modeling. This is probably due to the styryl group which reacts slower than the methacrylate group in OC-I preventing a strong spatial propagation of the polymerization reaction. Figure 5.3 depicts fabrication results of a voxel size study (a) and photonic crystal structure (b) in OC-27sc revealing feature sizes of approx. 100 nm. Using μ-Raman spectroscopy, it was demonstrated that organic crosslinking in 2PP-fabricated structures can be as high as in UV-exposed layers (depending on the particular 2PP parameters). A C=C bond conversion of up to 75 % was found for OC-I [17].

In the past, some ORMOCER®s have been reported to be biocompatible despite being typically nondegradable [23, 25, 34]. Since the latter feature is essential for certain tissue engineering and long-term biomedical applications, a new class of 2PP convenient ORMOCER®s was developed which contains biodegradable parts (see Tab. 5.1). Starting from a base material (OC-GM), the amount of organically crosslinkable groups, the spacer length connecting the inorganic and organic parts, the inorganic content, and the degree of polycondensation were modified in order to control the materials' mechanical properties. In Tab. 5.2, the tensile strengths and Young's moduli of the biodegradable hybrid polymer materials, henceforth referred to as RENACER®[2], are compared to those of natural tissue. The data clearly show that RENACER®s' mechanical properties can be adjusted via their chemical composition and structure to meet those of natural tissue.

In order to investigate the degradation rate, a procedure was established to determine the mass loss of test samples prepared from the RENACER® modifications OC-GM, OC-SVI and OC-SVIII. The mass loss was determined using disks of about 200 mg which where incubated in different aqueous media at 37 °C. The medium was

2 RENACER®: registered by the Fraunhofer Gesellschaft für Angewandte Forschung e. V.

Tab. 5.2: Mechanical data of RENACER® materials compared to natural tissue.

Synthesized materials	Tensile strength (MPa)	Young's modulus (MPa)
OC-GM	4.3 ± 0.2	43.5 ± 2.6
OC-SVI	1.8 ± 0.2	18.9 ± 1.1
OC-SVII	30.3 ± 3.1	615 ± 116
OC-SVIII	12.5 ± 0.6	109 ± 11.1
Natural tissue		
Bladder [35, 36]	0.27 ± 0.14	n. a.
Vessel [37]	1.4 to 11.1	n. a.
Aorta [35, 38]	1.72 ± 0.89	n. a.
Cartilage [39]	≈ 5	n. a.
Hard tissue [40]	n. a.	10 to 1500
Soft tissue [40]	n. a.	0.4 to 350

changed every week, and three disks were removed after one week, four weeks and four months, respectively. The disks were dried to constant weight using silica gel, and their mass loss was determined. Figure 5.3 (c) shows the mass loss of the base material in various buffer solutions. As the hydrolytic cleavage of most degradable groups is known to be pH-dependent [41, 42], buffers were chosen whose pH values differed significantly ranging from pH 4.5 (acetate buffer) to 9.5 (carbonate buffer). According to the literature physiological pH values also vary in a similar range, depending on specific body regions [43]. Thus, the influence of catalytically active ions like H_3O^+ or OH^- on the mass loss was investigated.

As demonstrated in Fig. 5.3 (c) the samples show a pH-dependent mass loss with a maximum of 40 % being observed for samples incubated in carbonate buffer (pH 9.5). This high mass loss is attributed to the presence of hydroxide ions in the setup.

In order to investigate the crosslinking behavior which is a prerequisite for further patterning by 2PP lithography, samples of the base material OC-GM formulated with a suitable photoinitiator were prepared between two cover slips separated by a 100 µm thick spacer to ensure a preferably similar film thickness. Samples were light-irradiated in the range 380–520 nm, and subsequently analyzed by µ-Raman spectroscopy (WITEC Alpha 300). Since γ irradiation was used to sterilize these samples, spectra were taken from samples which had been irradiated, and also samples which hadn't. The results are displayed in Fig. 5.3 (d), where a close-up of the µ-Raman spectra is shown displaying just the stretching vibrations from the C=C bond at 1640 cm^{-1}, and from the C=O bond at 1740 cm^{-1}. Peak structure and shift of the C=O peak is a byproduct of the C=C conversion due to a lack of conjugation in the hybrid polymer compared to the former resin. These data indicate that the material is highly crosslinked. The material has a low residual monomer content which is required to achieve a high degree of biocompatibility. In addition, γ irradiation does not significantly impact the material's structure, thus allowing the sterilization of the

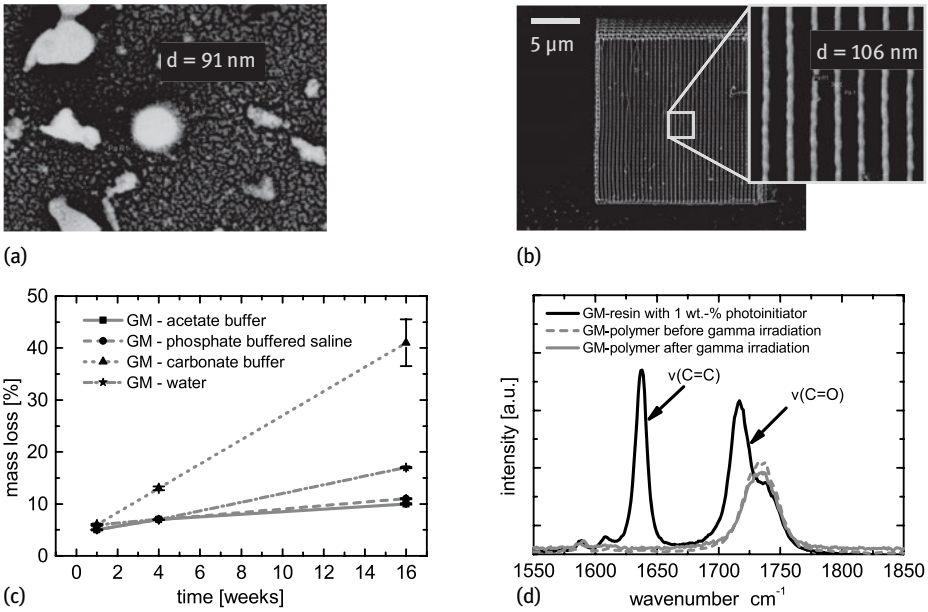

Fig. 5.3: (a) 91 nm voxel fabricated in OC-27sc. (b) Photonic crystal structures with approx. 100 nm line width fabricated in OC-27sc. (c) Mass loss of the base RENACER®material in different buffer solutions in dependence of the immersion time. (d) µ-Raman spectra of the base material before and after γ sterilization.

samples prior to cell culture applications, for example which is a superior feature compared to the behavior of conventional ORMOCER®s which can only be sterilized in ethanol (cf. Section 5.4.1).

5.3.2 Molecular modeling

Considering structure sizes below 100 nm one of the most promising ORMOCER® materials is OC-27sc (see Tab. 5.1). Due to the large size of the molecules used in the polymerization reaction, the high molar masses, and the amorphous nature, the possibilities for experimental gathering of structural information are highly limited. However, an enhanced understanding of the underlying molecular structures is essential for a further reduction of possible structure sizes. Therefore, a modeling approach was applied, as described below.

Atomistic modeling of ORMOCER® materials is only feasible with force field methods for two main reasons: firstly, the resin consists of very large molecules; secondly, a proper description of the amorphous structure of the material itself demands large simulation cells containing more than one molecule. This results in simulation cells

with up to a few thousand atoms, which can only be described with force field methods employing acceptable CPU time.

In force fields, molecules are built up by hard spheres connected by springs, corresponding chemically to atoms and bonds between them. Typically, changes in bond lengths and bonding angles can be treated with harmonic potentials or with a combination of quadratic, cubic and quartic terms for increased accuracy. Other multi-body terms like torsions can be handled with different cosine-type functions. Cross-terms are added for a better description of vibrational modes. These allow for interactions between changes in bond lengths, bond angles and torsions. Intermolecular interactions are incorporated in terms of van der Waals and Coulomb forces. Any further influence of the electrons or the electronic structure is neglected. For this reason, only the different stages of a material during its synthesis can be modeled, excluding the reactions from one stage to another.

Experimental procedure

The chosen force field is crucial for the simulation, especially when complex systems like ORMOCER® materials are considered. The applicability of the COMPASS force field employed (Accelrys, BioVia) [44, 45] has already been proven in previous studies [33]. However, further validation procedures may be necessary if the system differs strongly from those previously treated (see below).

In contrast to [33], the models of the fluid phases and the resin were constructed using the "Amorphous Cell" module within Materials Studio, which uses a Monte Carlo search for the position of individual, in vacuo energy minimized molecules in the simulation cell under periodic boundary conditions (PBCs). For every model, 100 structures were generated and their energy was minimized. The structure with the lowest potential energy was chosen for the molecular dynamics simulations.

Molecular dynamics simulations for density calculation were performed under ambient conditions for 1 ns, the second half of the trajectory was used for analysis. All parameters used in the modeling can be found in the supplementary material (Section 5.6).

The synthesis of ORMOCER® materials is – as mentioned above – usually a two-step procedure: First, precursor molecules undergo condensation reactions between silanol groups forming siloxane bonds; the resulting product is called a resin, the resulting siloxane oligomers are designated as monomers for the following polymerization reaction. In the second step, the resin is polymerized via irradiation to the final material, the polymer. Molecular modeling methods may give valuable insight into the process at an atomistic level at each stage.

Results: precursors

At first, the precursors were modeled as pure condensed phases, either as crystals (diphenylsilanediol, DPD) or as liquids (p-styryltrimethoxysilane, pSTMS; see Fig. 5.4). The density is expected to be overestimated at small cell sizes, since in small cells only a few different orientations may be considered, leading to remaining ordered arrangements in the model. On the other hand, models comprising large cell sizes are computationally expensive. Therefore, it is necessary to find a suitable cell size which allows to use the density as a benchmark parameter for all models. In addition, these models may show the general suitability of the employed force field for density prediction and the use of molecular dynamics techniques for the compounds of the material.

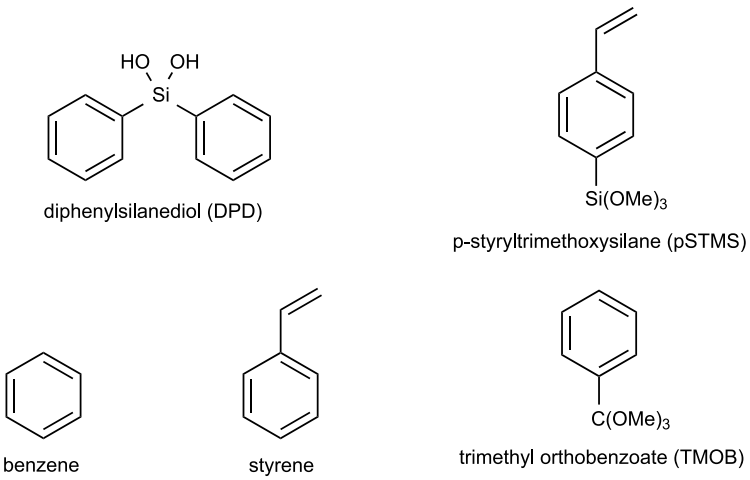

Fig. 5.4: Structures of the molecules modeled as pure phases; the precursors of the material OC-27sc are shown in the top row.

For the precursors, models containing more than 1000 atoms lead to stable results for the density (Fig. 5.5 (a)). While the experimental value can be verified for DPD, the density of pSTMS is overestimated by about 1–2 %. It was assumed that this effect might be attributed to the functional groups of pSTMS. In order to clarify this assumption the densities of three organic substances; trimethyl orthobenzoate (TMOB), benzene and styrene, were calculated in the same way. TMOB, a molecule with a structure comparable to pSTMS (the silicon atom is replaced by a carbon atom and the styryl functionality is missing; Fig. 5.4) shows similar behavior. In contrast, the calculated densities for benzene and styrene match the experimental ones (Fig. 5.5). However, very large models are needed in the case of benzene. It can therefore be assumed that the methoxy groups of pSTMS and TMOB cause higher densities for fluids showing low viscosities.

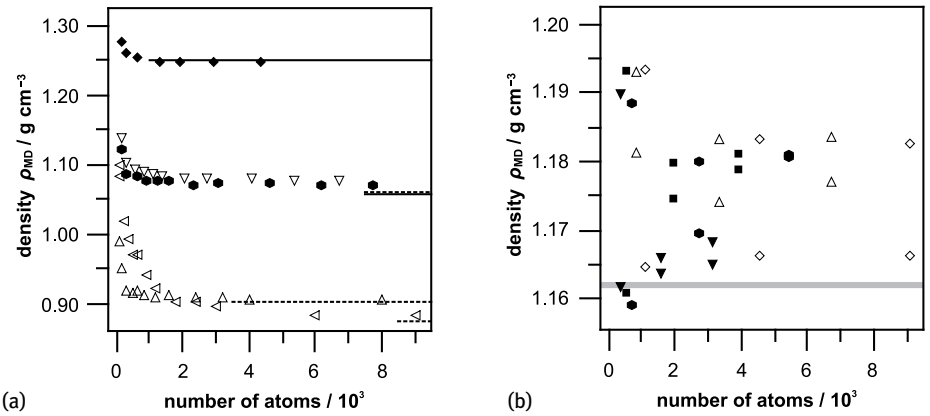

Fig. 5.5: (a) Densities obtained from molecular dynamics simulations for the precursors DPD (filled diamonds) and pSTMS (filled hexagons) versus the number of atoms in the simulation cell. Experimental values are shown as lines. For DPD, the experimental value is reached for cell sizes larger than 1000 atoms; for pSTMS, the predicted densities are overestimated by 1–2 % even for very large simulation cells. Results for the test substance trimethyl orthobenzoate (triangle, pointing down) obtained in a similar manner, show analog behavior to pSTMS, whereas for styrene (triangles, pointing up) and benzene (triangles, pointing left) the density calculations gave reasonable results. (b) For resin models with the same composition (designated by one symbol each), large deviations of the calculated densities can be observed at small cell sizes. In most cases, enlargement of the cells by the construction of supercells of the starting structure led to a more precise prediction of the density (filled symbols).

Results: resins

A similar approach has already been published for another ORMOCER® system for the resin models [33]: forty resin cells were constructed from four different monomers, which were composed of four to fifteen precursor units each. Different types of monomers, containing rings, branched rings as well as linear and branched chains were considered. The deviations in density observed for the precursor models of pSTMS will influence the density calculations of the resin models as well. However, the effect is minimized since the number of methoxy groups is reduced in these mixed resins compared to the pure compound. The resin models typically contain only about 0.5–0.7 methoxy groups per silicon atom.

Differences in density between two different models with the same monomer composition can be observed for a few resin models (less than 10 %; Fig. 5.5 (b)). The precision of the density prediction can be increased by building supercells, i.e. increasing the cell size to a few thousand atoms to circumvent this effect. Nevertheless, these models are too large to gain results in reasonable CPU time if performed for all resin cells.

Most of the resin models resulted in densities which deviated from the experimental value by less than 3 %. There are no observable trends for special types of

monomers yielding better results. For example, models containing only linear chains exhibit similar deviations to models with branched chains or branched rings. This stands in contrast to the results of modeling of ORMOCER®-I, where the consideration of octaphenylcyclotetrasiloxane as a major condensation product led to a better description of the properties of the resin [33]. An analog behavior cannot be observed for OC-27sc, i.e. no preferred combination of the considered monomers was detected, each of the resin models led to reasonable results.

Results: polymers

The polymer models were obtained from all resin models by manually inserting bonds between two polymerizable groups and adding protons when needed until a conversion degree close to the experimental value of approximately 35–40 % was reached. The deviation of the calculated densities from the experimental value is again mostly below 3 % and even below 2 % for 80 % of the models. Typically, shrinkages of around 0.5–2.5 % in volume can be observed (Fig. 5.6 (a)).

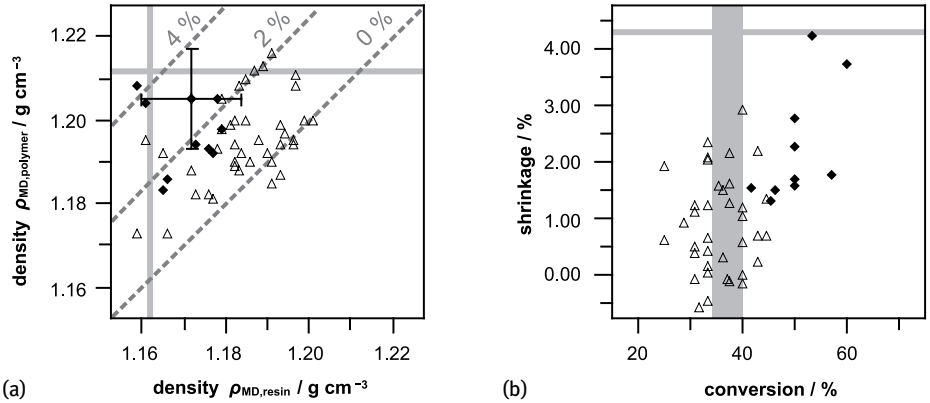

Fig. 5.6: (a) Average densities from molecular dynamics calculations (0.5–1.0 ns) for polymerized models of OC-27sc versus equally computed densities of the corresponding resins. The styrene conversion was set near (triangles) or above (filled diamonds) the experimental value. The experimental densities are shown as grey bars, while the dark grey dotted lines illustrate the shrinkage during polymerization. Only two models with a high degree of conversion (i.e. the two diamonds in the upper left corner) of the resin and polymer models came close to the experimental density values. The estimated error for density prediction is calculated from the standard deviation and only plotted for one data point. (b) Shrinkage versus conversion degree for the models presented in (a). The experimental values are again shown as gray bars. The experimentally determined shrinkage can only be achieved at higher conversion degrees, while the shrinkage is underestimated at the expected conversion.

The shrinkage is underestimated in all models. Using higher conversion degrees than the experimentally determined ones can increase observed shrinkage (i.e. increase the polymer density; Fig. 5.6 (b)). However, with regard to the standard deviation calculated for density prediction, the results lead to a valuable conclusion: the models which are close to the experimental polymer density and exhibit good representation of behavior during polymerization are composed of monomers with less than ten precursor units and usually contain at least two branched monomers and rings. Therefore, it can be expected that such combinations of monomers lead to a good representation of the material OC-27sc.

A general drawback of the polymer model employed is the resulting polymer structure, which is only built up by very small units. This can result in an underestimation of polymer density and observed shrinkage. With more CPU time becoming available, the resin models may be enlarged and a more suitable polymer model with longer hydrocarbon backbones could be developed. On the other hand, the fact that a reasonable description of the polymer structure (as judged by the generally fair to good agreement of predicted experimental densities) is possible with small polymer building units suggests that the size of these units (mainly below 2 nm) will not influence the photochemical structuring process.

The studies published in [33] and in this section are the first serious approaches to the computational treatment of such complicated materials as ORMOCER®s. The complications arise from the generally amorphous state of the materials (as in all polymers), from their two step generation (different to many polymers), and especially from their organic-inorganic nature. Future work will concentrate on other ORMOCER® systems and will try to predict additional properties such as the Young's modulus.

5.4 Applications

5.4.1 Biomedicine

Restoration of diseased or damaged tissue remains one of the great challenges in regenerative medicine. The growth of cells on 3D porous scaffolds for tissue engineering (TE) is a promising approach for the generation of autologous tissue.

In addition, to understand the interactions between cells and their microenvironment, new tools have to be created by combining surface chemistry, material sciences and microfabrication techniques. Since many cellular responses are the result of intracellular signaling events being triggered by the interaction of cell surface receptors with particular components of their environment [46] diverse aspects of cellular processes, such as proliferation, migration, differentiation or apoptosis cannot be analyzed correctly using standard cell-based assays. An interaction with appropriate surfaces is a general prerequisite for the survival of adherent cells in that it allows

the formation of adhesive forces required for subsequent cell spreading. Aside from the plain surface chemistry characterized by the types of interacting partners (like extracellular matrix (ECM) proteins) their density, spatial distribution and conformation have also been reported to be important surface features [46–50]. Thus, it could already be demonstrated that certain cellular responses depend on the mechanical compliance of cell-adhering substrates as well as on their local distributions [51, 52]. The ability to control the spatial chemistry, geometrical patterning and stiffness of the desired substrate might therefore provide important insights into the fundamental aspects of cell-scaffold interactions [53, 54]. This might be translated into tissue engineering approaches focusing on a precise control of cell adhesion, spreading, growth, and differentiation provided by chemically and spatially designed surfaces created by 2PP lithography. In particular, sub-micron feature sizes at the surface of 3D scaffolds are assumed to promote cell adhesion and growth.

The preparation of biological samples follows different routines, depending on which type of cells will be seeded onto the structures. The cells used for these investigations were primary endothelial cells, i.e. human microvascular endothelial cells (mvECs). These cells first have to be isolated from tissue samples as previously described [55].

Cells were cultured at 37 °C, 5 % CO_2, and 95 % relative humidity in standard cell culture incubators. Cells were propagated up to a maximum of 4 passages or unless they were transferred onto ORMOCER® structures. In order to evaluate the cell cultivation on 2PP patterned samples, different geometries (circular structures, crossed lines, parallel lines, etc.; see Fig. 5.7) with varying lattice sizes were fabricated in OC-I.

Cell viability was analyzed using the WST-1 (water soluble tetrazolium-1) reagent (Roche Diagnostics, Mannheim, Germany) according to the supplier's instructions. Due to metabolic activities, WST-1 is reduced by cellular hydrogenases forming a fromazan which can be photometrically analyzed at 450 nm. To visualize the cells in microscopy, HE (Hematoxilin/Eosin) stainings were performed according to standard protocols. The samples were mounted with DAPI-Fluoromount-G® in order to stain their nuclei (SouthernBiotech, Burningham, AL, USA).

To initially determine whether residual compounds derived from ORMOCER® production processes might be cytotoxic, glass slides were covered with OC-I without having been structured by 2PP. After incubation, a development step was carried out analog to the development after 2PP patterning. As control samples, untreated glass slides were used. The glass slides were transferred into 6-well-plates and incubated with VascuLife® ECGMmv medium for 24 h at 37 °C, 5 % CO_2 in a water-saturated atmosphere in a CO_2 incubator. After incubation, the medium was removed and hmvECs were seeded at a density of 2×10^5 cells per well. After the cells were grown to confluence, the slides were removed from the 6-well plates, gently washed with PBS, fixed using a 4 % para-formaldehyde solution, and afterwards stained with hematoxylin and eosin (HE).

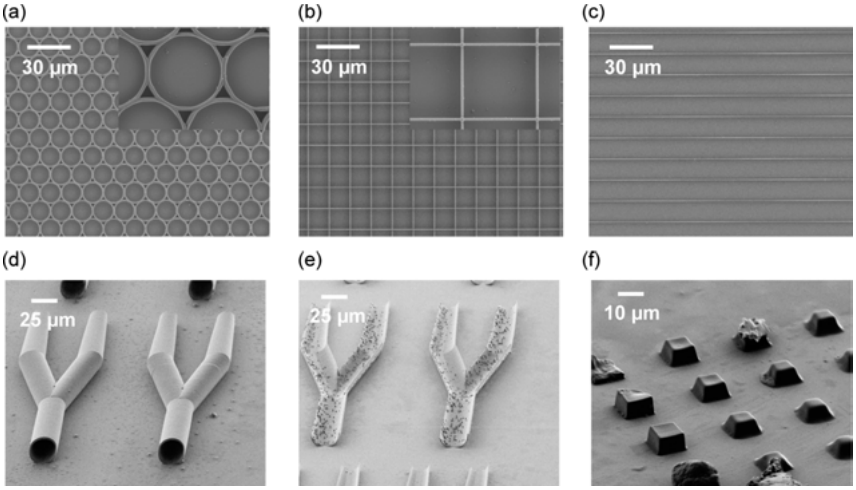

Fig. 5.7: SEM images of structures on glass substrates fabricated for biomedical applications. (a)–(c) Test patterns for cell cultivation experiments fabricated from OC-I. (d)–(e) Tubular structures for cell cultivation with anchor points for promotion of cell adhesion (OC-V). (f) Test pattern to demonstrate applicability of OC-SVII for 2PP patterning.

The cells grew as a monolayer to confluence on both surfaces, indicating that the substrates used are not cytotoxic. However, cells detached partially from the untreated glass slides during the fixation process, which was not observed in case of the OC-I treated surfaces. Additionally, the cells grown on OC-I treated glass slides reveal slight differences in their overall morphology in that they appear more spread compared to those grown on the untreated controls (data not shown). This might indicate that more and/or stronger adhesion contacts were formed between the hmvECs and OC-I coated substrates, for example.

However, in cell biology interactions between adherent cells and their non-cellular environment (e.g. the extracellular matrix) are typically facilitated by the formation of so-called focal adhesions (FAs) which represent specific types of large macromolecular assemblies through which both, mechanical force and regulatory signals are transmitted to the cellular interior [56]. FAs resemble dynamic protein complexes which are in in a state of constant flux in that they continuously associate and dissociate from the substrate. These interactions are limited to a clearly defined distance of 15 nm between the the plasma mebrane and the particular substrates, however [57]. The first experiments shown earlier did not answer the question of whether the observed adhesion is solely dependent on altered surface chemistry, a spatial topological distribution of the substrate, or on both parameters.

In order to test topological effects on cell adhesion or cell morphology, a variety of structures (linear, circular, or quadratic structures) fabricated by 2PP of OC-I on glass slides (Fig. 5.8 (a)–(d)) were used as substrates for hmvECs. The structures were fabri-

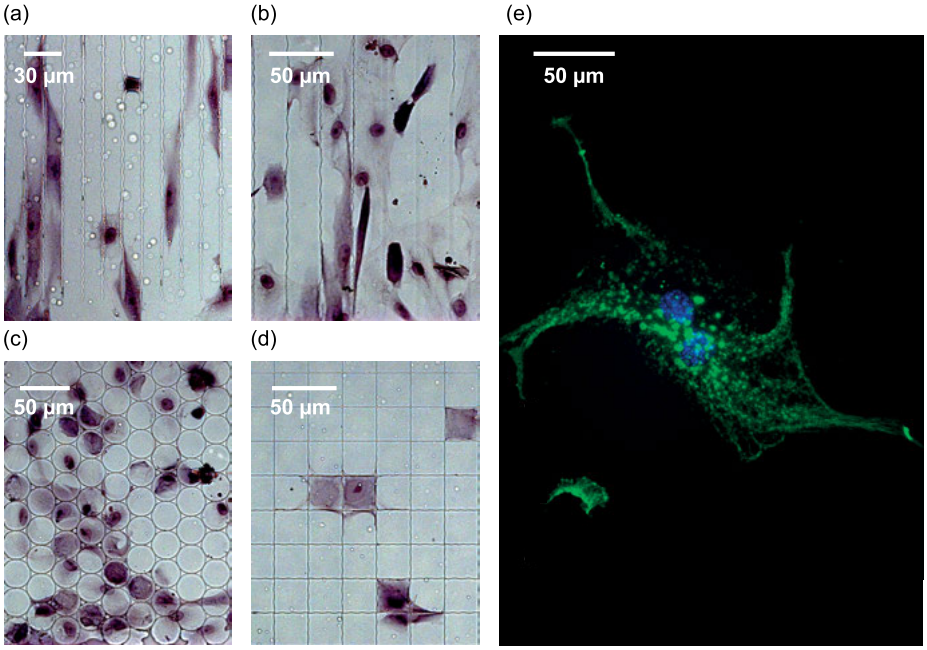

Fig. 5.8: Cultivation of hmvECs on 2PP patterned OC-I. (a)–(d) HE-stained cells grown on glass slides decorated with different OC-I structures. (e) Microvascular endothelial cell (Upcyte® HDMECs, Medicyte GmbH, Heidelberg) grown on OC-GM structures. Nuclei appear blue due to DAPI staining. Immunohistological staining of β-tubulin (filaments) appears green.

cated using a high NA objective (Zeiss Plan-Apochromat NA = 1.4), a writing velocity of $v = 1$ mm/s and an average laser power of $P = 4.25$ W (amplitude systems t-pulse: wavelength $\lambda = 515$ nm, repetition rate $\nu = 10.1$ MHz, pulse duration $\tau = 350$ fs).

In order to visualize the overall morphology of the endothelial cells used, the samples were fixed and stained with HE. In general, cells grown on linear patterns show a more spindle-shaped morphology (see Fig. 5.8 (a) and (b)) compared to those grown on circular (Fig. 5.8 (c)) or quadratic patterns (Fig. 5.8 (d)). Also, the distance between 2PP-written ORMOCER® structures significantly influences cell growth and morphology. In the case of linear structures, the majority of cells grew within the structures if those were separated by 15 µm. Increasing the distances to 25 µm clearly resulted in altered cell growth and cell morphology. Using these distances, the cells seemed to grow – at least partially – on top of the structures. These phenotypological differences were further analyzed by immunhistological stainings of actin filaments, which are essential components of the cytoskeleton. These stainings clearly revealed that the actin filaments were oriented parallel to the linear OC-I structures only if those were separated by 15 µm. In all other cases, the actin filaments were found to be in a random orientation (data not shown). Astonishingly, using quadratic or circular struc-

tures the cells grew within the structures if separated by 25 µm, whearas they grew on top of structures with 15 µm distances, the opposite behavior to linear structures.

Alongside biocompatibility, scaffolds used for TE approaches should also be biodegradable. First 2PP patternings were therefore carried out using a RENACER® as biodegradable material. 2PP-written cubes were created in SV-II, and the first results are shown in Fig. 5.7 (f). The programmed cube dimensions are $10 \times 10 \times 7.5\,\mu m^3$ fabricated with a variation in process parameters such as the average laser power (decreasing from top to bottom) and hatching distance (decreasing from left to right). It can be seen that only a certain set of laser power and hatching distance yielded well-shaped cubes. It turned out that a hatching distance of $\Delta x = 0.1\,\mu m$ and laser power of $P = 1800\,\mu W$ are suitable for structuring SV-II material. As for any other hybrid material synthesized so far (see Tab. 5.1), this material modification also shows promising patterning results for further scaffold fabrication to be used for cell growth. Primary endothelial cells (Upcyte®, Medicyte GmbH, Heidelberg, Germany) were grown on these as described above (see Fig. 5.8 (e)). The cells adhere well to the substrate, and show a typical cellular morphology. Cell division can be observed by immunostaining using DAPI and anti-Tubulin β antibodies.

In summary, the ORMOCER® structures obtained by 2PP fulfill all criteria of substrates which can be used in standard 2D cell culture sytems as well as in innovative 3D tissue engineering approaches. First results, depicted in Fig. 5.7 (d) and (e), using conventional microscope objectives demonstrate the general feasibility of small tubular structures with varying diameters, randomly distributed pores, and tiny (≈ 100 nm) anchor points, which might promote cell adhesion (the results of these experiments will be published elsewhere). Current work focuses on the application of the hybrid objective (see Section 5.2) in order to produce large (> 1 cm in length and > 500 µm in diameter) artificial vessels possessing sub-micrometer anchor points which can subsequently be used as scaffolds for vascularization.

5.4.2 Microoptics

Microoptical applications can benefit from 2PP fabrication in multiple ways. Due to the intrinsic ability to fabricate arbitrarily shaped surfaces, new designs with complex topologies for microoptical structures can be implemented. Furthermore, 2PP can trigger refractive index modifications which enable the fabrication of three-dimensional waveguides [58]. In order to obtain microoptical elements with good optical performance, the roughness and waviness of the surfaces must be smaller than 100 nm.

2PP fabrication of diffractive optical elements

The fabrication of diffractive optical elements (DOEs) for laser beam manipulation is typically carried out using state-of-the-art lithography techniques such as electron

beam lithography [59, 60]. As these methods are two-dimensional processes, the DOE topographies realized are binary which affects the achievable diffraction efficiency. The conventional 2D processes must be repeated several times in order to fabricate multilevel DOEs, which significantly increases the price of fabrication and decreases the yield [61]. Jia et al. proposed 2PP for DOE fabrication in 2007 [62]. However, their strategy of fabrication is limited in throughput. Also the shape of the pixels, which make up the entire DOE, is aberrant.

In this study a new strategy for DOE fabrication was developed: instead of scanning the laser focus in 3D pixel by pixel, the entire DOE area is scanned with high velocity scan stages. The "position synchronized output" (PSO) feature of the positioning system controller is used to trigger the laser rapidly and accurately whenever the scanning path intersects with a DOE pixel. Thus, the feed rate can be increased to around 10 mm/s in contrast to commonly used techniques [7, 62]. The procedure is repeated for each of the desired DOE height levels – typically 16. Figure 5.9 (a) depicts a $640 \times 640\,\mu m^2$ DOE fabricated from OC-V with very accurate reproduction of lateral pixel geometries. Here, a total interval between the lowest and highest pixels of 1.29 µm, corresponding to a 2π phase shift at the design wavelength $\lambda = 632.8$ nm was used. Topography characterization was carried out using laser scanning microscopy (LSM). The results shown in the inset of Fig. 5.9 (a) reveal good agreement between DOE design and the fabricated structure. As the entire height of the DOE is of the order of a micron, it is obvious that sub 100 nm height control is mandatory for the fabrication of functional DOEs. This could be accomplished by the choice of illumination and hatching strategy as well as by an appropriate choice of laser parameters and optical material. Despite the well-defined topography, the optical performance still has to be optimized. When observing the resulting diffraction image on a screen (Fig. 5.9 (b)), the Statue of Liberty can be identified as calculated by the design. However, the zeroth order is still dominant and pronounced speckles occur over the entire image. For this reason, the influence of the structuring parameters on the resulting pixel heights is to be investigated in more detail in the future. Furthermore, the effect of the pixels' edges on the diffracted intensity distribution will be taken into account.

Microlenses

The fabrication of microscopic beam steering or focusing elements applying 2PP is well-known in the literature [7]. Applications as collimators on fiber tips and as micro-Fresnel lenses have been demonstrated [59, 63]. Despite the impressive proof-of-principle in these papers, it is important to increase the throughput and to validate the performance of 2PP-fabricated microoptical components for real-life applications.

In the following section, 2PP-fabricated microlenses which were created with a new hatching strategy are demonstrated. In contrast to conventional 3D scanning of the entire lens volume, only the shells of the microlenses are polymerized by 2PP and the liquid core is solidified after the development process using conventional UV

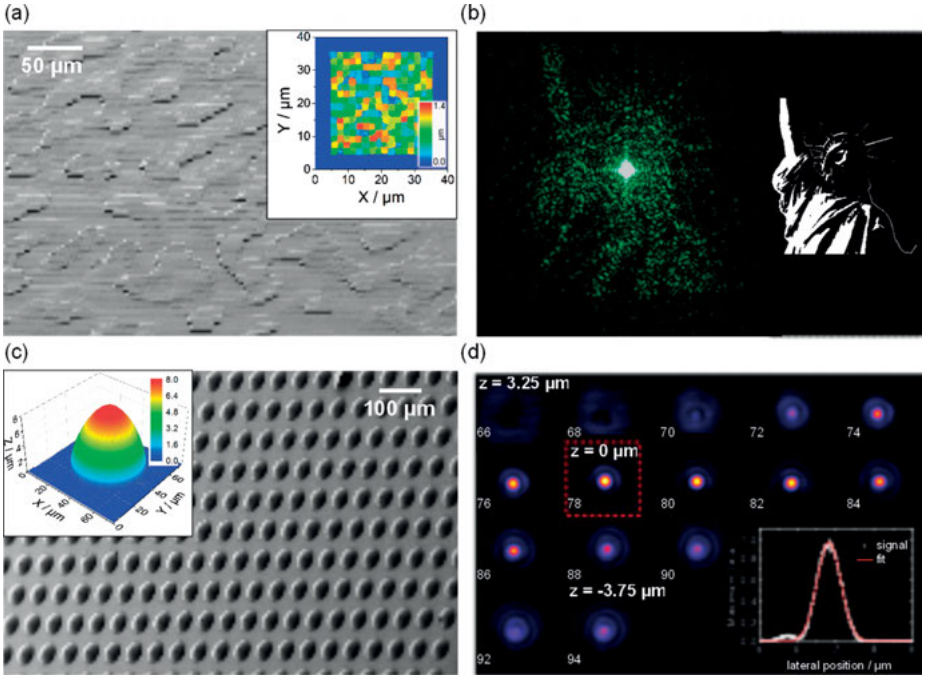

Fig. 5.9: 2PP-written microoptical elements in OC-V (SEM): (a) Diffractive optical element. The inset depicts the height characterization of DOE pixels by means of LSM. (b) Diffracted Statue of Liberty (532 nm light) with strong zeroth order. (c) Array of microlenses. The inset shows an AFM scan of an individual microlens. (d) Slices of focal intensity distribution and lateral focal intensity ($z = 0$).

illumination. In addition, the shell of the surface of the lens was hatched using an annular scanning strategy. This allowed for the fabrication of very smooth surfaces with low surface roughness. In order to achieve this goal, the beginning and end of each hatching circle was distributed randomly on the lens surface. Tangential lines for acceleration and deceleration were introduced to compensate for the mass inertia of the positioning system. Figure 5.9 (c) depicts an SEM image of lenses fabricated from OC-V using this strategy. Without additional measures, our fabrication strategy reduces the duration for the fabrication of a single lens to between one and two minutes (depending on the lens radius). This is still subject to further improvements as the axis feed rate was only set to 500 µm/s. As a result of this increase in throughput, microlens arrays can be rapidly fabricated with high surface finishes.

The characterization of lens topography was carried out using atomic force microscopy (AFM) and LSM, and both methods deliver consistent results. A typical surface scan is depicted in the inset of Fig. 5.9 (c). Both AFM and LSM topography characterization reveal negligible deviations from the design geometry and very low surface roughness.

As in 2PP the photon dose (feed rate and pulse energy) determines the resulting voxel size and as a result voxel size combined with hatching distance during structure formation impact surface topography. It is important to understand the impact of these parameters on the surface roughness. It was possible to show for example, that by using 1 mW of average power, a hatching distance of 0.4 µm at a feed rate of 500 µm/s resulted in an rms-roughness of 29 nm on planar surfaces. In comparison, the roughness resulting from 4 mW, 0.1 µm at the same feed rate is below 4 nm. However, the rms-roughness of the microlenses fabricated applying these parameters was considerably higher with 67 nm. In addition to the roughness investigation, AFM/LSM measurements also revealed that shrinkage after UV light polymerization is negligibly small.

The focusing behavior of the fabricated microlenses was investigated using a modified confocal microscope. The lens is illuminated by a collimated and spatially homogeneous laser intensity distribution and the focused intensity is then probed in 3D by a high-NA microscope objective. Figure 5.9 (d) illustrates the characterization by means of several slices of the focal intensity distribution and a fit through the lateral intensity in the focal plane ($z = 0$). It could be demonstrated that focal distance, beam waist ($w_0 = 0.63$ µm), and the Rayleigh length corresponded well with theory.

Current work focuses on the implementation of custom-designed aspherical surfaces, particularly designed for aberration-free focusing. Moreover, the positioning system can provide feed rates higher than the 500 µm/s finally employed. Decreasing the fabrication time of a single microlens down to only some tens of seconds is conceivable in the future. This advance in process acceleration has to be accompanied by further material research as the ORMOCER®'s polymerization rate has to keep pace with increasing scanning speeds.

Diaphragm array for multi-aperture cameras

A multi-aperture approach relying on microlens arrays is a promising candidate to further miniaturize digital real-time vision systems [64–66]. In these multi-aperture camera modules, individual optical channels capture different portions of the overall field of view (FOV). A super resolution imaging approach in combination with the segmentation of the FOV allows for a reduction of the focal length of the microlenses and consequently leads to modules with shorter total track lengths. Furthermore, the fabrication is based on wafer-level process technology allowing the parallel and cost effective fabrication of several hundred modules at once.

Figure 5.10 (a) shows a schematic crosssection of the optical layout of a multi-aperture camera module. An important issue of these modules is optical cross talk, which appears when light is imaged from one microlens onto the sensor area of a neighboring channel and causes so called "ghost images". To prevent this cross talk a special diaphragm array is necessary (Fig. 5.10 (a)). These diaphragm arrays consist of 600 µm high tubes with a tapered profile, a diameter of 38 µm at the top and

34 µm at the bottom (Fig. 5.10 (b)). Additionally, these tubes are undercut with angles up to 30 degrees depending on their position over the sensor. These challenging geometries are impossible to fabricate with conventional lithographic technologies. However, two-photon polymerization allows the direct structuring of these tilted tubes into the polymer. Because of the large height (600 µm) of these tubes, hybrid optics (see Section 5.2) are applied to focus the laser pulses during the structuring process. The feasible structure heights are not restricted by the working distance when using the hybrid optics which, furthermore, are corrected for structuring-depth-dependent aberrations. Figure 5.10 (c) shows a microscope image of the structured diaphragm array. It consists of 135 channels and its total size is 7 mm × 4 mm × 0.6 mm.

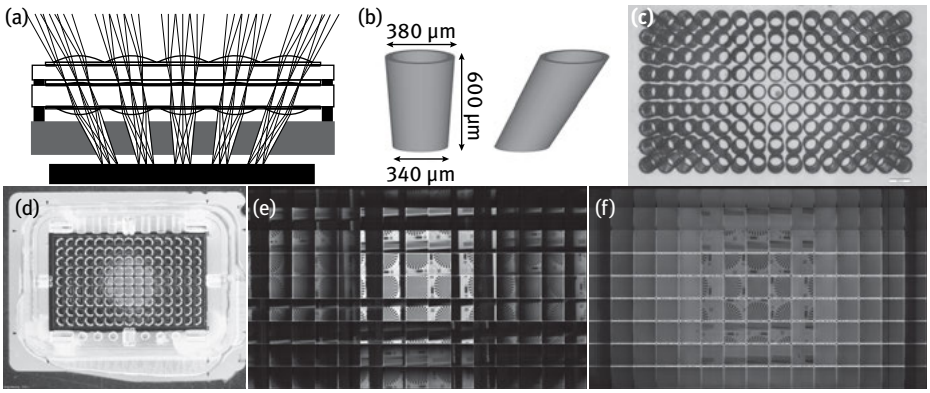

Fig. 5.10: (a) Schematic cross-section of the optical layout of a multi-aperture camera module. Special diaphragm arrays (gray) are necessary to prevent optical cross talk. (b) Schematic of the tubes with a tapered profile which depends on their position over the image sensor. (c) Fabricated diaphragm array consisting of 135 channels. (d) Black epoxy resin replicated diaphragm array mounted on the imaging sensor. (e) Segmented image of a test chart without the diaphragm array. The central object reappears in ghost images in the outer channels. (f) Segmented image of a test chart with the diaphragm array. No ghost images are visible in the outer channels.

The intermediate spaces of the fabricated diaphragm array were subsequently filled with an epoxy resin, and then replicated into silicon. This silicon master structure was used as a mold to replicate the diaphragm arrays with a black epoxy resin as the final material. This process chain allows fast fabrication of the diaphragm arrays suitable for mass production, since only the master structure of the mold is fabricated using two-photon polymerization with its long writing times. Figure 5.10 (d) shows a replicated diaphragm array mounted on the imaging sensor. The segmented image of a test chart taken with the multi-aperture camera module without the diaphragm array is depicted in Fig. 5.10 (e). The central object reappears as ghost images in the outer channels. When the diaphragm array is integrated into the module, these ghost images are suppressed and the object only appears in the central channels (Fig. 5.10 (f)).

5.5 Conclusion

In order to utilize 2PP for applications in microoptics and biomedicine, illumination for the structuring process as well as the synthesis and properties of the applied materials were investigated. For the fabrication of structures combining smallest feature sizes with heights up to the mm range, a specially adapted refractive-diffractive hybrid objective was designed and assembled. This objective is corrected for structuring-depth-dependent aberrations and is not restricted by a working distance in achievable structure heights. Due to the aberration correction of the objective the sub-micrometer resolution of the structuring process can be maintained even for structures with heights in the mm range.

ORMOCER®s were investigated with respect to their mechanical and optical properties, their suitability for structuring with 2PP, and possible applications. With ORMOCER® OC-27sc, smallest structure sizes below 100 nm were obtained. In order to understand this complex material on a molecular level, molecular modeling simulations were carried out for its precursors, the resin, and the polymerization products. The results obtained are a first step towards prediction of material properties, thereby facilitating the synthesis of novel functionalized materials.

The novel biodegradable material class RENACER® was developed especially for biomedical applications. These polymers show good crosslinking behavior for patterning with 2PP and the mechanical properties of the solidified structures are similar to those of natural tissue, making them an excellent material choice for tissue engineering.

It was also shown for the first time that the ORMOCER® OC-I is biocompatible for the growth of primary human endothelial cells. These cells are crucial for the artificial creation of human blood vessels. A combination of suitable materials and 2PP structuring techniques might provide scaffolds e.g. for artificial vessels with all required pores and anchor points. Future work will focus on upscaling 3D structures towards the mm range and applying the newly synthesized RENACER® material.

Fabrication time and accuracy of microoptical elements fabricated with 2PP were improved with adapted structuring strategies demonstrated by a DOE with 16 levels and a writing speed of 10 mm/s. Microlenses with a surface roughness of 67 nm (RMS) were fabricated by applying an angular scanning method. Furthermore the focusing behavior of the microlenses was characterized. A large-area diaphragm array was fabricated to further improve the imaging quality of multi-aperture camera modules. The array consists of 135 diaphragms with heights of 600 µm and suppresses ghost images, which appear due to optical cross talk between neighboring channels.

In conclusion, combined with the use of existing and newly synthesized inorganic-organic polymers the novel focusing concept enabled the fabrication of structures featuring demanding geometries and adapted properties for biomedical and microoptical applications, using 2PP.

5.6 Supplementary material

Tab. 5.3: Molecular modeling – experimental parameters.

Parameter	Value
General:	
– Software	– Materials Studio 7.0
– Force field	– COMPASS
Energy summation:	
– van der Waals interactions	– cut-off, 15.5 Å, cubic spline truncated
– Coulomb interactions	– Ewald summation, accuracy 10^{-5} kcal mol^{-1}
Energy minimization:	used for all structures
– minimizer	– "smart" cascade, 5000 steps
Quenched dynamics:	used for in vacuo structures and polymers
– Ensemble	– NVT
– Temperature	– 800 ± 10 K (velocity-scaling)
– Time, time step	– 100 ps, 1 fs
– minimized every	– 100 steps
Molecular dynamics:	used for density calculations
– Ensemble	– *NpT*
– Integration scheme	– Velocity-Verlet
– Temperature	– 298 K (Berendsen, decay c. = 0.1 ps)
– Pressure	– 0.1 MPa (Berendsen, decay c. = 0.1 ps)
– Time, time step	– 1 ns, 1 fs (second 500 ps used for production)
– Output every	– 100 steps
Hardware:	4 identical nodes
– Processors	– 2 Xeon E5620 (Quad-Core, 2.4 GHz)
– RAM	– 24 GB per node

References

[1] Maruo S, Nakamura O, Kawata S. Three-dimensional microfabrication with two-photon-absorbed photopolymerization. Opt. Lett. 1997, 22, 132–134.
[2] Serbin J, Egbert A, Ostendorf A, et al. Femtosecond laser-induced two-photon polymerization of inorganic–organic hybrid materials for applications in photonics. Opt. Lett. 2003, 28, 301–303.
[3] Ergin T, Stenger N, Brenner P, Pendry JB, Wegener M. Three-Dimensional Invisibility Cloak at Optical Wavelengths. Science 2010, 328, 337-339.
[4] Straub M, Gu M. Near-infrared photonic crysals with higher-order bandgaps generated by two-photon photopolymerization. Opt. Lett. 2002, 27, 1824.

[5] Sun H-B, Matsuo S, Misawa H. Three-dimensional photonic crystal structures achieved with two-photon-absorption photopolymerization of resin. Appl. Phys. Lett. 1999, 74, 786–788.
[6] Brasselet E, Malinauskas M, Žukauskas A, Juodkazis S. Photopolymerized microscopic vortex beam generators: Precise delivery of optical orbital angular momentum. Appl. Phys. Lett. 2010, 97, 211108.
[7] Malinauskas M, Žukauskas A, Purlys V, et al. Femtosecond laser polymerization of hybrid/integrated micro-optical elements and their characterization. J. Opt. 2010, 12, 124010.
[8] Wu D, Wu S-Z, Niu L-G, et al. High numerical aperture microlens arrays of close packing. Appl. Phys. Lett. 2010, 97, 031109.
[9] Klein F, Richter B, Striebel T, et al. Two-Component Polymer Scaffolds for Controlled Three-Dimensional Cell Culture. Adv. Mater. 2011, 23, 1341–1345.
[10] Malinauskas M, Baltriukiene D, Kraniauskas A, et al. In vitro and in vivo biocompatibility study on laser 3D microstructurable polymers. Appl. Phys. A 2012, 108, 751-759.
[11] Melissinaki V, Gill AA, Ortega I, et al. Direct laser writing of 3D scaffolds for neural tissue engineering applications. Biofabrication 2011, 3, 045005.
[12] Zhou G, Gu M. Direct optical fabrication of three-dimensional photonic crystals in a high refractive index LiNbO3 crystal. Opt. Lett. 2006, 31, 2783–2785.
[13] Simmonds RD, Salter PS, Jesacher A, Booth MJ. Three dimensional laser microfabrication in diamond using a dual adaptive optics system. Opt. Express 2011, 19, 24122–24128.
[14] Bückmann T, Stenger N, Kadic M, et al. Tailored 3D Mechanical Metamaterials Made by Dip-in Direct-Laser-Writing Optical Lithography. Adv. Mater. 2012, 24, 2710–2714.
[15] Houbertz R, Stichel T, Steenhusen S, inventors; Device and method for producing three-dimensional structures. patent WO2011141521.
[16] Burmeister F, Zeitner UD, Nolte S, Tünnermann A. High numerical aperture hybrid optics for two-photon polymerization. Opt. Express 2012, 20, 7994.
[17] Burmeister F, Steenhusen S, Houbertz R, Zeitner UD, Nolte S, Tünnermann A. Materials and technologies for fabrication of three-dimensional microstructures with sub-100 nm feature sizes by two-photon polymerization. J. Laser Appl. 2012, 24, 042014.
[18] Lang M, Aspnes E, Milster TD. Geometrical analysis of third-order aberrations for a solid immersion lens. Opt. Express 2008, 16, 20008–200028.
[19] Mansfield SM, Kino GS. Solid immersion microscope. Appl. Phys. Lett. 1990, 57, 2615–2616.
[20] Ippolito SB, Goldberg BB, Ünlü MS. Theoretical analysis of numerical aperture increasing lens microscopy. J. Appl. Phys. 2005, 97, 053105.
[21] Fuchs U, Zeitner UD, Tünnermann A. Hybrid optics for focusing ultrashort laser pulses. Opt. Lett. 2006, 31, 1516–1518.
[22] OpticStudio 14. March 2014. Zemax. Redmond, USA.
[23] Houbertz R, Steenhusen S, Stichel T, Sext G. Two-Photon Polymerization of Inorganic-Organic Hybrid Polymers as Scalable Technology Using Ultra-Short Laser Pulses. In: Duarte FJ, ed. Coherence and Ultrashort Pulse Laser Emission: InTech; 2010: 583–608.
[24] Sanchez C, Julian B, Belleville P, Popall M. Applications of hybrid organic-inorganic nanocomposites. J. Mater. Chem. 2005, 15, 3559–3592.
[25] Doraiswamy A, Patz T, Narayan R, et al. Biocompatibility of CAD/CAM ORMOCER polymer scaffold structures. MRS Proc. 2004, 845.
[26] Obel K, Steenhusen S, Hümmer J, et al. Novel partially degradable hybrid polymers for biomedical applications. In: European Symposium of Polymer Science; 2014; Wien; 2014.
[27] Houbertz R, Domann G, Cronauer C, et al. Inorganic-organic hybrid materials for application in optical devices. Thin Solid Films 2003, 442, 194–200.

[28] Viheriaelae J, Niemi T, Kontio J, Pess M. Nanoimprint Lithography - Next Generation Nanopatterning Methods for Nanophotonics Fabrication. In: Young K, ed. Recent Optical and Photonic Technologies: InTech; 2010.
[29] Houbertz R, Wolter H, Dannberg P, Serbin J, Uhlig S. Advanced packaging materials for optical applications: bridging the gap between nm-size structures and large-area panel processing. Proc. SPIE 2006, 61265.
[30] Uhlig S, Frohlich L, Chen MX, et al. Polymer optical interconnects - A scalable large-area panel processing approach. Ieee Transactions on Advanced Packaging 2006, 29, 158–170.
[31] Buestrich R, Kahlenberg F, Popall M, Dannberg P, Müller-Fiedler R, Rösch O. ORMOCERs for Optical Interconnection Technology. J.Sol.-Gel. Sci. Techn. 2001, 20, 181–186.
[32] Haas KH, Wolter H. Synthesis, properties and applications of inorganic-organic copolymers (ORMOCER\textsuperscript\textregistered s). Curr. Opin. Solid St. M. 1999, 4, 571–580.
[33] Fessel S, Schneider AM, Steenhusen S, Houbertz R, Behrens P. Towards an atomistic model for ORMOCER®-I: application of forcefield methods. J.Sol.-Gel. Sci. Techn. 2012, 63, 356–365.
[34] Doraiswamy A, Jin C, Narayan RJ, et al. Two photon induced polymerization of organic-inorganic hybrid biomaterials for microstructured medical devices. Acta Biomater. 2006, 2, 267–275.
[35] Caves JM, Cui W, Wen J, Kumar VA, Haller CA, Chaikof EL. Elastin-like protein matrix reinforced with collagen microfibers for soft tissue repair. Biomaterials 2011, 32, 5371–5379.
[36] Dahms, Piechota, Dahiya, Lue, Tanagho. Composition and biomechanical properties of the bladder acellular matrix graft: comparative analysis in rat, pig and human. Brit. J. Urol. 1998, 82, 411–419.
[37] Kumar VA, Caves JM, Haller CA, et al. Acellular vascular grafts generated from collagen and elastin analogs. Acta Biomater. 2013, 9, 8067–8074.
[38] Mohan D, Melvin JW. Failure properties of passive human aortic tissue. I – Uniaxial tension tests. J.Biomech. 1982, 15, 887–902.
[39] Williamson AK, Chen AC, Masuda K, Thonar EJ-MA, Sah RL. Tensile mechanical properties of bovine articular cartilage: Variations with growth and relationships to collagen network components. J. Orthop. Res. 2003, 21, 872–880.
[40] Mallick K. Biomaterial scaffolds for tissue engineering. Front. Biosci. 2013, 5, 341.
[41] Iordanskii AL, Rudakova TE, Zaikov GE. Interaction of polymers with bioactive and corrosive media. VSP Utrecht, The Netherlands; 994.
[42] Wintermantel E, Ha S-W. Medizintechnik: Life Science Engineering. 5. ed. Berlin, Springer Berlin Heidelberg; 2009.
[43] Zaikov GE. Quantitative aspects of polymer degradation in the living body. J. Macromol. Sci. C 2007, 25, 551–597.
[44] Sun H. COMPASS: An ab Initio Force-Field Optimized for Condensed-Phase Applications – Overview with Details on Alkane and Benzene Compounds. J. Phys. Chem. C 1998, 102, 7338–7364.
[45] Materials Studio 7.0. San Diego; CA: Accelrys Software Inc.; 2014.
[46] Hynes RO. Integrins: bidirectional, allosteric signaling machines. Cell 2002, 110, 673–687.
[47] Healy KE, Thomas CH, Rezania A, et al. Kinetics of bone cell organization and mineralization on materials with patterned surface chemistry. Biomaterials 1996, 17, 195-208.
[48] Maheshwari G, Brown G, Lauffenburger DA, Wells A, Griffith LG. Cell adhesion and motility depend on nanoscale RGD clustering. J. Cell. Sci. 2000, 113, 1677–1686.
[49] Keselowsky BG, Collard DM, Garcia AJ. Surface chemistry modulates fibronectin conformation and directs integrin binding and specificity to control cell adhesion. J. Biomed. Mater. Res. A 2003, 66, 247–259.

[50] Rajagopalan P, Marganski WA, Brown XQ, Wong JY. Direct comparison of the spread area, contractility, and migration of balb/c 3T3 fibroblasts adhered to fibronectin- and RGD-modified substrata. Biophys. J. 2004, 87, 2818–2827.
[51] Chen CS, Mrksich M, Huang S, Whitesides GM, Ingber DE. Geometric control of cell life and death. Science 1997, 276, 1425–1428.
[52] McBeath R, Pirone DM, Nelson CM, Bhadriraju K, Chen CS. Cell shape, cytoskeletal tension, and RhoA regulate stem cell lineage commitment. Dev. Cell 2004, 6, 483–495.
[53] Engler AJ, Griffin MA, Sen S, Bonnemann CG, Sweeney HL, Discher DE. Myotubes differentiate optimally on substrates with tissue-like stiffness: pathological implications for soft or stiff microenvironments. J. Cell. Biol. 2004, 166, 877–887.
[54] Wong JY, Leach JB, Brown XQ. Balance of chemistry, topography, and mechanics at the cell-biomaterial interface: Issues and challenges for assessing the role of substrate mechanics on cell response. Surf. Sci. 2004, 570, 119–133.
[55] Schanz J, Pusch J, Hansmann J, Walles H. Vascularised human tissue models: a new approach for the refinement of biomedical research. J. Biotechnol. 2010, 148, 56–63.
[56] Chen CS, Alonso JL, Ostuni E, Whitesides GM, Ingber DE. Cell shape provides global control of focal adhesion assembly. Biochem. Bioph. Res. Co. 2003, 307, 355–361.
[57] Zaidel-Bar R, Cohen M, Addadi L, Geiger B. Hierarchical assembly of cell-matrix adhesion complexes. Biochem. Soc. T. 2004, 32, 416–420.
[58] Schmidt V, Kuna L, Satzinger V, Jakopic G, Leising G. Two-photon 3D lithography: A Versatile Fabrication Method for Complex 3D Shapes and Optical Interconnects within the Scope of Innovative Industrial Applications. JLMN 2007, 2, 170–177.
[59] Prasciolu M, Cojoc D, Cabrini S, et al. Design and fabrication of on-fiber diffractive elements for fiber-waveguide coupling by means of e-beam lithography. Microelectron. Eng. 2003, 67–68, 169–174.
[60] Vieu C, Carcenac F, Pépin A, et al. Electron beam lithography: resolution limits and applications. Surface Science in Micro & Nanotechnology 2000, 164, 111–117.
[61] Swanson GJ. Binary optics technology: Theoretical limits on the diffraction efficiency of multilevel diffractive optical elements. Technical Report. Massachusetts Institue of Technology 1991.
[62] Jia BH, Serbin J, Kim H, Lee B, Li JF, Gu M. Use of two-photon polymerization for continuous gray-level encoding of diffractive optical elements. Appl. Phys. Lett. 2007, 90, 073503.
[63] Cojoc G, Liberale C, Candeloro P, et al. Optical micro-structures fabricated on top of optical fibers by means of two-photon photopolymerization. Microelectron. Eng. 2010, 87, 876–879.
[64] Brückner A. Multi-aperture optics for wafer-level cameras. J. Micro-Nanolith. Mem. 2011, 10, 043010.
[65] Brückner A, Duparré J, Leitel R, Dannberg P, Bräuer A, Tünnermann A. Thin wafer-level camera lenses inspired by insect compound eyes. Opt. Express 2010, 18, 24379–24394.
[66] Meyer J, Brückner A, Leitel R, Dannberg P, Bräuer A, Tünnermann A. Optical Cluster Eye fabricated on wafer-level. Opt. Express 2011, 19, 17506–17519.

P. Reichenbach, U. Georgi, U. Oertel, T. Kämpfe, B. Nitzsche,
B. Voit, and L. M. Eng

6 Optical antennae for near-field induced nonlinear photochemical reactions of photolabile azo- and amine groups

Abstract: We performed a series of nonlinear-optical, photochemically-induced experiments using different copolymers which were UV-sensitized at around 400 nm through various chemical side groups (e.g. NVOC-protected amines). Our approach focuses on inducing very localized photoreactions on an area much smaller than the diffraction-limited optical spot, using nonlinear optical effects in the near-fields of metallic nanoparticle (NP) antennae embedded in the polymer thin film. We thus illuminated the copolymers with 100 fs pulses at a 790 nm exciting wavelength in order to trigger photoreactions through nonlinear optical effects at around 400 nm. Spin coating the copolymers onto both y-cut lithium niobate (LNO) sample surfaces (which is an excellent SHG amplifier) and onto bare glass surfaces (no SHG) and then comparing the as-induced nonlinear optical photoreactions showed a direct two-photon absorption to be the dominant photoreaction mechanism, while SHG radiation (as emitted by LNO) did not show any significant influence. High efficiency of this process can be achieved by the near-field enhancement close to metallic NPs present in the polymer thin film. First evidence is given here with protected amine side groups when spin coating the copolymer over sharp gold edges as obtained from triangular metallic NPs (i.e. so-called Fischer pattern); after laser exposure at 790 nm, the photochemically deprotected amines were successfully photo-labeled and then imaged by STORM microscopy.

6.1 Introduction

Photolithographic structuring has developed into one of the most important tools of nanostructuring to date. The most prominent example is the nanostructuring of silicon [1]. Combining photolithographic techniques with photochemistry allows inclusion of the vast variety of chemical structuring and functionalization into the repertoire of photolithography. Examples are the photoreactions of protected amine-terpolymers under UV illumination [2, 3] for instance. In this case the illuminated and deprotected parts of the amines are easily functionalized with fluorescence markers or other molecules for further use or monitoring purposes.

An important milestone in the research into photochemistry at the nanometer length scale is the use of metallic nanoparticles (NPs) which concentrate light in their near-fields. One example is photoreactions of resist thin films in the near-field

of metallic nanorods [4] or bow-tie antennae [5]. Such photoresist reactions in the vicinity of the NP's near-fields were also shown to be successful when triggered via nonlinear optical absorption [6–8] rather than in the linear optical regime.

The goal of our work was thus to trigger photochemical reactions in polymer matrices on the nanometer length scale [9–12]. Furthermore, as indicated by the examples above we also intended to induce such processes in the near-fields of metallic nanoparticles. Our primary idea was to embed these metallic (e.g. gold) nanoparticles into a photosensitive polymer and illuminate them with focused 100 fs pulses at an infrared (IR) wavelength of about 790 nm. The localized photoreaction would then take place at around 395 nm, profiting from the NP's plasmonic amplification.

We did not concentrate on photoresists as photosensitive material but rather developed copolymers mainly consisting of MMA and a comonomer add-on which carries the photosensitive group such as the protected amine side groups already mentioned above [2, 3]. These polymer matrices are optically transparent at 790 nm; thus no photoreaction occurs over the whole diffraction-limited optical spot of the exciting IR beam. Instead, the polymer is photosensitive in the range of 395 nm.

We intended to use the second harmonic radiation (SHG) from the nanoparticles to induce the photoreaction at 395 nm primarily, as many investigations demonstrated that metallic nanostructures with strong field enhancement must also constitute good SHG sources [13–17], and investigations in our group also comprised nanoparticle SHG [9, 18].

However, the question had to be solved whether SHG or multiphoton absorption processes are actually the dominant reaction mechanisms. Experiments with polymer matrices on lithium niobate single crystals (sc-LNO) as a good SHG source showed the dominance of a two-photon absorption. This two-photon absorption also profits from high absorbance at the SHG wavelength of 395 nm, being equivalent to a single-photon absorption at this wavelength.

Metallic nanoparticles can be joined with the polymer in many ways, mostly by NP embedding (Fig. 6.1) or overcoating the NP array sitting on a substrate with a polymer thin film. As nonlinear optical processes are much stronger in the near-fields of

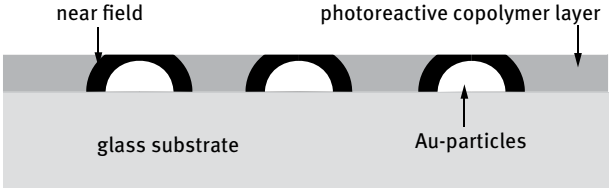

Fig. 6.1: Sketch of the principal idea of our experiments: a photoreactive copolymer layer (dark gray) is spin coated onto a glass substrate (light gray) carrying Au nanoparticles (NPs; white). Upon pulsed laser irradiation at ~ 790 nm, the NPs produce a considerable enhanced near-field (black zones around NPs) where the photochemical reaction concentrates to a sub-100-nm spatial area.

the particles than in the far fields, photochemical reactions triggered by these processes can be confined to volumes in the sub-100-nm regime. The outcome of such a photochemical reaction and its localization can in turn be monitored through several different methods, depending solely on the type of chemicals used for the photolabile group as will be described below.

6.2 Experimental design

Our experiments were conducted with the following setup.

The femtosecond laser beam (~ 100 fs at 790 nm at a repetition rate of 75 MHz) passes an upright standing 40× air objective and is focused onto the sample surface positioned via a xyz piezo stage. For each writing process the focus is moved about 7 µm away from the sample surface in order to broaden the area of photoreaction and include more nanoparticles. Typically, the sample consists of a cover glass carrying a spin-coated photosensitive polymer matrix layer about 100 nm thick which may also include embedded metallic nanoparticles.

Using the piezo stage we are also able to photochemically "write" any arbitrary pattern onto these films: While illuminating the sample surface with the focused laser beam, the photosensitive polymer layer is scanned laterally through the focus, thus resulting in lines of a few µm in length where the photoreaction has taken place. These experiments were carried out on pure polymer substrates spin coated onto glass as well as with embedded nanoparticles.

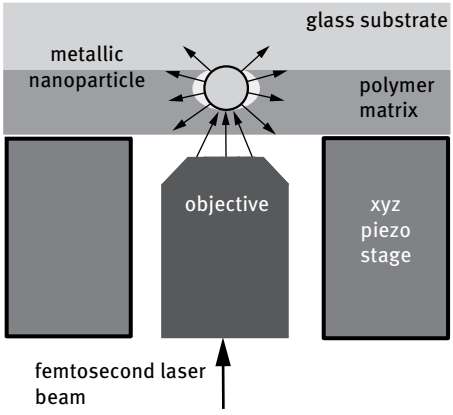

Fig. 6.2: Sketch of the experimental setup used in these studies. The sample structure (described in Fig. 6.1) is inserted upside down into the setup with the polymer film facing the objective. The femtosecond laser beam is focused onto the sample surface and excites the plasmonic NPs to produce a strong near-field both at the fundamental and the second harmonic (SHG) field (see arrows emitted from the NP). The xyz piezo stage is used to adjust the focus to the sample surface as well as to initiate xy-sample structuring.

Three kinds of copolymers were used for our experiments:

(a) Copolymers with azobenzene side groups which photochemically react with a trans-cis isomerization; this process may be tracked optically through a pronounced change in absorbance [12].

(b) Copolymers with azosulfonate side groups which decay with subsequent cross-linking; the resulting local changes of elasticity are detectable with AFM [11, 19].
(c) Copolymers with protected amine side groups using NVOC. After photochemical separation of the NVOC molecules, different dyes such as fluorescent markers may be chemically attached to the deprotected amines, highlighting the reaction sites. This enables detection by different kinds of fluorescence microscopy [2].

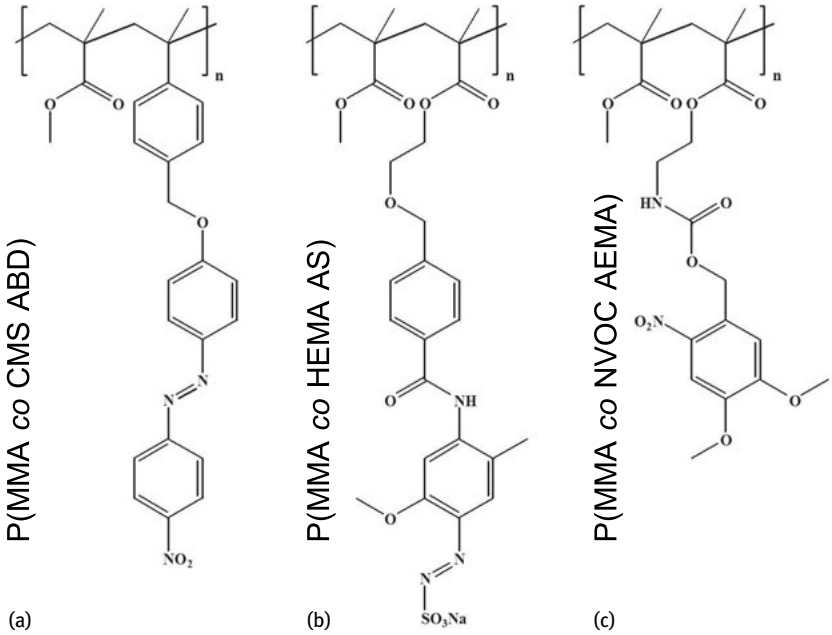

Fig. 6.3: Chemical structures of the copolymers used in this work Several different polymer side-chains were synthesized to the backbone, i.e. (a) azobenzene derivatives (ABD), (b) azosulfonates (AS), and (c) NVOC-protected amines (AEMA).

As stated in the introduction, we intended to trigger the photochemical reactions by SHG radiation from the embedded nanoparticles. However, the question arose whether or not the photoreaction may also be induced by direct two-photon absorption. To clarify the impact of these different reaction mechanisms on the localization of the photoreaction, we modeled the particle near-fields at the fundamental and second-harmonic frequency by evaluating the near-fields $\boldsymbol{E}^{\omega}$ (fundamental) and $\boldsymbol{E}^{2\omega}$ (SHG) for a Hertzian dipole emitter. The calculated photoreaction density thus turns out to be proportional to $|\boldsymbol{E}^{\omega}|^4$ and $|\boldsymbol{E}^{2\omega}|^2$ for the two-photon and SHG absorption processes, respectively. Hence, photoreactions triggered by a two-photon absorption process were found to be more effective and even to be much more localized than SHG-induced photoreactions.

To find out which of the two mechanisms in our experiments is dominant we spin coated the polymer matrix both onto glass samples and onto a y-cut lithium niobate (LNO) surface without using any nanoparticles. Moving the polymer matrix in the xy plane through the femtosecond laser focus (100 fs, 790 nm) then allowed the writing of several lines of a variable exposure by altering the laser power density. We then tried to observe and monitor the as-induced photochemical reactions. While lithium niobate is a strong second harmonic source (for light polarized along the extraordinary optical axes), glass does not show any SHG radiation at all, thus allowing a fair comparison of the two photoreactions.

In the subsequent experiments including embedded nanoparticles we used metallic nanostructures known as Fischer patterns (Fig. 6.4) [20]. They constitute flat hexagonally arranged, triangular gold islands. They are fabricated by evaporating gold onto the (glass) substrate surface through a mask built up by a monolayer of hexagonally dense-packed polystyrene beads with a diameter of about 600 nm [20–22]. The beads are then removed and the copolymer spin-coated over the antennae structures. The use of such Fischer patterns has three advantages: Firstly, Fischer patterns are prepared easily; secondly, their low height allows for good polymer spin-coating and spreading, while thirdly their tips and edges are very sharp hence promoting strong near-field enhancement due to the lightning rod effect.

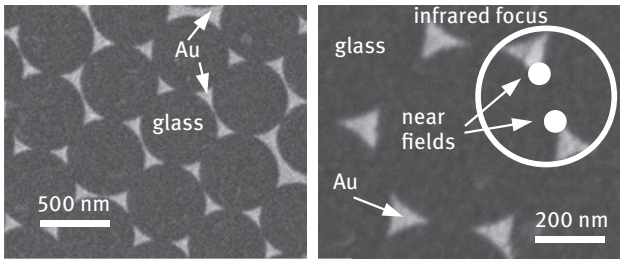

Fig. 6.4: Fischer patterns result in hexagonally arranged Au triangles grown by evaporating Au through a mask of close-packed polystyrene beads (not shown). The dark area in this SEM image represents the bare glass surface while the bright areas are the 20 nm high Au NPs. (a) SEM overview, and (b) close up with the white circle denoting the optical focus of the objective as used for excitation; note the two asperities at the triangular corners emitting the near-field at both the fundamental and SHG wavelength.

6.3 Photochemical experiments using a copolymer carrying azobenzene side groups

The first photosensitive polymer matrix is a PMMA-type copolymer containing an azobenzene derivative with an NO_2 molecular group (Fig. 6.2 (a)) [11, 12]. Azobenzenes are already widely used for writable data carriers [23] and in volume holography

[24]. The photochemical reaction of the azobenzene derivative selected for our work is a reversible trans-cis isomerization. This photoreaction leads to a change in absorbance of the substrate, which allows direct optical detection and monitoring. The azobenzene derivative possesses two main advantages: Firstly, it absorbs in the range of 400 nm, while secondly the thermally induced back-reaction of the reversible trans-cis isomerization is comparably slow and proceeds over several hours [12].

The copolymer contains 80 % methylmethacrylate (MMA) and 20 % chloromethylstyrene (CMS) and has been synthesized using the RAFT polymerization method (reversible addition fragmentation chain transfer polymerization) [25–27] known to show minimal side reactions. The azobenzene derivative was linked covalently to the CMS parts of the copolymer [12]. The copolymer was dissolved in methylethylketone (MEK) and then spin-coated onto the glass or lithium niobate (LNO) sample surfaces to form a dense and uniform layer 70 nm thick. The covalent binding of the azobenzene derivative to the copolymer ensures there is no segregation of the azobenzene from the MMA/CMS-copolymer.

The photochemical experiments on glass and LNO were carried out as outlined below. The glass and LNO substrates carrying the 70 nm thin polymer matrix layers were inserted upside down into the measurement setup (Fig. 6.3) with the photosensitive polymer film facing the objective directly. The optical focus was adjusted to sit at the substrate sample surface. The LNO used was a y-cut crystal oriented in such a way that the linearly polarized beam yielded a maximum SHG intensity when focused onto the LNO surface. Using the piezo stage, 5 µm long lines were then written onto the polymer films using different average laser powers tuned from 2 to 15 mW. Here and in all experiments to follow, a stepwise sample motion was employed with individual steps measuring 167 nm in size (i.e. 5 µm divided by 300 steps) and dwelling times of 50 ms per step.

After photochemical writing, the optical transmission of these lines was measured in-situ using the focused light of a 405 nm diode laser for illumination and a fiber coupling mounted above objective and sample. This in-situ measurement has the advantage that changes in the optical transmission can be monitored immediately and even before any back-reaction sets in. The 405 nm light was reduced to a power of a few µW before being focused through the same objective onto the sample surface, thus not inducing any further sample reaction at all. The light transmitted through the photosensitive layer was collected with an optical fiber fed into a fiber spectrometer (Maya 2000 Pro from Ocean Optics). On scanning the exposed area with the written lines through the blue laser focus we obtained images of these lines since the photoreaction considerably increased optical transmission (i.e. less absorption in the exposed areas as shown in Fig. 6.5).

As an outcome, we found that increased transmission of the lines became visible for “writing” laser power densities of 6 mW or above, both on the glass and LNO substrate. The absence of a significant difference between glass and LNO shows that the SHG from the LNO substrate does not significantly contribute to the photoreaction, but

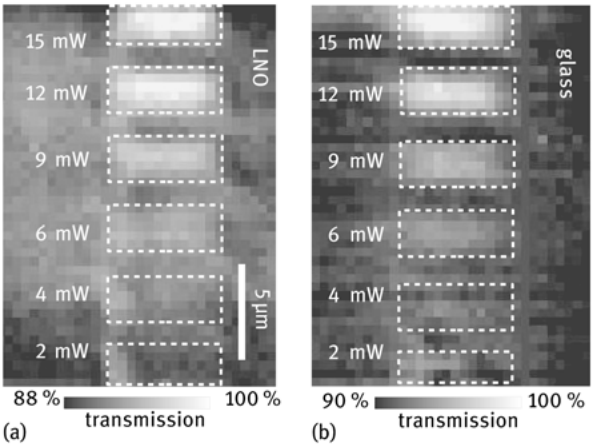

Fig. 6.5: Optically recorded transmission scans of the 70 nm thick azobenzene-containing copolymer spin coated onto (a) LNO and (b) glass substrates. Note the different lines (dashed frames) and their varying transmission cross-sections resulting from exposure to the focused femtosecond beam at different average power densities; notably, the higher the power, the lower the absorbance.

that the photoreaction is triggered by direct absorption of the IR light. Photochemical writing with the infrared laser radiation in cw mode and at the same power density did not result in detectable transmission changes – an indication that the photoreaction is mainly triggered by a nonlinear optical effect, namely a two-photon absorption process of the femtosecond light.[1]

When we compared the photon density of blue light from a monochromator used to trigger a photoreaction directly with the SHG photon density on lithium niobate, we found that the SHG photon density from the lithium niobate at 6 mW incident power is about three orders of magnitude lower than for the blue light from the monochromator. As SHG from nanoparticles is typically not stronger than from the y-cut LNO surface, we can expect that nanoparticle SHG also does not contribute significantly to photoreactions. Of course, SHG light is more concentrated in the particle near-fields, however, the same is the case for the near-fields at the fundamental frequency.

1 At this point the question arises whether or not the reaction might be thermally induced as well, by simple laser heating of the substrate. As cw irradiation did not trigger photoreactions, we carried out some model calculations investigating the difference in the time development of the sample temperature when hit either by pulsed or cw illumination. These calculations showed that the maximum temperature did not differ at all in both cases, which excludes sample heating as the source of the reported photoreactions.

6.4 Photochemical experiment with azosulfonate-carrying copolymers

Optical detection of the photoreactions in the azobenzene-containing copolymer has a diffraction-limited resolution, so we did not carry out experiments including gold nanostructures. However, the next copolymer used was designed to change its elasticity due to the photoreaction, and such a change can be detected with AFM at a resolution of around 50 nm. The copolymer consisted of 75 % MMA and 25 % HEMA (hydroxyethylmethacrylate) and was polymerized with the RAFT method. On the hydroxyl groups of the HEMA an azosulfonate group (Fig. 6.2 (b)) was bound covalently in a polymer-analog reaction [12]. Again, this azosulfonate derivative was selected for its optimal absorption at 395 nm. However, the absorption of that derivative still strongly decays between 380 and 400 nm and is about one order of magnitude smaller than azobenzene. The chosen azosulfonate does not isomerize reversibly but isomerization leads to a decay into SO_3Na radicals and phenyl radical residuals under nitrogen evolution [28, 29]. A crosslinking reaction between the residual phenyl radicals and the polymer chains causes increased elasticity of the polymer matrix in the reaction volume, an effect which can also be used for photoresins [29]. On scanning the as-exposed area with AFM, this change of elasticity can be readily detected via phase contrast imaging. The preparation of these layers is again done by spin-coating, but this copolymer is dissolved in dimethylformamide.

This proof-of-principle was carried out by illuminating the polymer substrate through a TEM grid (Fig. 6.6 (a)) using a white-light beam (UV extended spectrum) followed by AFM scans over the polymer surface. The AFM scan (Fig. 6.6 (b)) shows no topographic pattern which corresponds to the TEM grid, but the phase image (Fig. 6.6 (c)) clearly shows a phase contrast pattern in accordance with exposure through the TEM grid. The phase contrast is of the order of 1°. Experiments including Fischer patterns should thus clearly show this phase change in the surroundings (i.e. in the near-field range) of the gold triangles.

However, before doing so we again compare the behavior of a pure polymer matrix layer on glass and on LNO. As absorbance drops strongly below 400 nm, the exciting wavelength was shifted to 780 nm to achieve a two-photon wavelength of 390 nm. The polymer substrates (70 nm thick) were irradiated for different laser powers and then scanned with AFM. In contrast to the azobenzene-carrying copolymer, average powers of 20 mW and higher had to be applied to yield lines that could be detected by AFM at all. However, these lines were not only detectable via phase contrast, but were also always accompanied by the formation of topographic swales with comparably huge depths measuring tens of nm in height. Similar to the azobenzenes, no differences were obtained between glass and LNO surface (indicating again the dominance of two-photon absorption), while these effects were absent for cw illumination. However, on comparing these results with the reaction of a pure PMMA layer, we found the same results even for these layers. At the high powers above 20 mW, not only azosulfonate

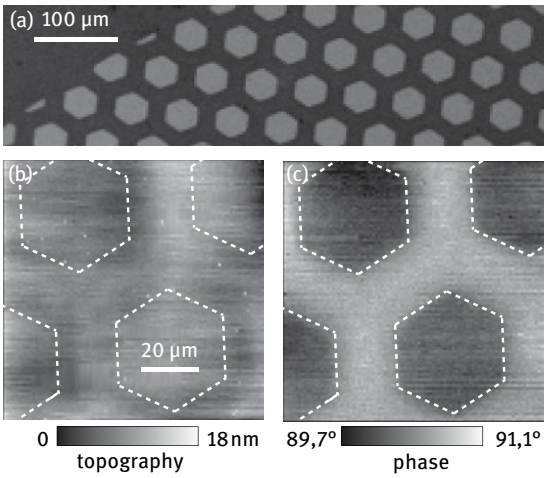

Fig. 6.6: (a) SEM image of the TEM grid structure used. (b) AFM topographic image of the azosulfonate-carrying copolymer exposed through the TEM grid using a UV-extended white light source. (c) AFM phase image of the same area showing enhanced stiffness at exposed areas (white). The border of the TEM grid structure is indicated by dashed lines in the AFM pictures for clarity.

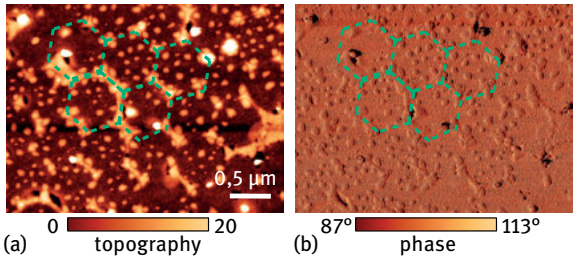

Fig. 6.7: AFM topography (a) and phase (b) scans of the azosulfonate-containing copolymer spin coated over Fischer patterns. These scans were taken well inside a line that had previously been written by pulsed illumination with an average power of 0.2 mW. We clearly differentiate these Fischer patterns in (a), marked by dashed lines, together with a fine-pitched quasi-regular arrangement of polymer debris blisters, the latter stemming from the initial exposure and insufficient dissolving of the copolymer.

decay sets in but also quite different reactions of the PMMA itself will be triggered through multiphoton absorption. This makes it difficult to detect the specific photochemical reaction of the azosulfonates unambiguously solely by AFM phase contrast.

Furthermore, the azosulfonate-carrying polymer was also spin-coated over the glass substrates carrying 10 nm high Fischer patterns. The topography of these triangles was also visible on the upper side of the 70 nm thick copolymer layer, a well-known effect in polymer layer overstructuring. With these embedded nanostructures the polymer already bursts at 5 mW illumination and shows topographic deformations

already for 0.2 mW. At this small power density, small blisters appeared around the nanotriangles. However, they appeared not only along the boundaries of the triangles, but were distributed over the whole viewing field (Fig. 6.7). Due to these topographical features, phase contrasts in the order of about 20° appeared which superpose possible phase contrasts in the order of 1° which could stem from crosslinking. In this case, clear detection of photochemical induced decay and crosslinking is also not possible.

6.5 Photochemical experiment with copolymers carrying protected amines

After these experiments using photolabile copolymers we now concentrate on copolymers with protected amine side groups. Protected amine groups have a large variety of applications in synthesis [30] and in surface patterning [2, 3, 31, 32]. Photochemistry allows for selective deprotection of the amines and subsequent binding of many different kinds of molecules or particles. For our purposes, we synthesized a copolymer P(MMA-co-Nvoc-AEMA) with RAFT consisting of 2/3 MMA and 1/3 aminoethylmethacrylate (AEMA). The AEMA is protected by nitroveratryloxycarbonyl (NVOC) groups (Fig. 6.2 (c)). The photoreaction causes removal of the NVOC groups; the deprotected amines are then accessible to bind to different kinds of molecules, such as fluorescence markers to label the reaction volume as shown here for fluorescein (Fig. 6.8). Monitoring with sub-wavelength resolution is then possible using specialized super-resolution fluorescence microscopy techniques such as stochastic optical reconstruction microscopy (STORM) [33, 34], stimulated emission depletion (STED) microscopy [35, 36] or photoactivated localization microscopy (PALM) [37, 38]; notably these techniques were honored with the 2014 Nobel Prize in Chemistry.

The block copolymer was dissolved in MEK and spin-coated over glass and LNO surfaces resulting in dense polymer layers with a now reduced thickness of 30 nm. After writing lines at different power densities, all samples were immersed into a solution containing fluorescein isothiocyanate (FITC) molecules in order to fluorescently label the deprotected amine groups (Fig. 6.8). The written lines became visible in fluorescence images for power densities around 1–2 mW (Fig. 6.9 (a)). Similar to the above-reported experiments, no difference was found for this copolymer when using glass and LNO substrates, and no photoreaction took place under cw illumination. Again, two-photon absorption turns out to be the dominant reaction mechanism here. Besides the lines, a homogeneous background of non-specifically bound fluorophores, which could not washed away, appeared over the whole area.

The same experiment carried out with 10 nm high Fischer patterns on the glass substrate is shown in (Fig. 6.9 (b)). In comparison to the pure glass surface, the photoreaction takes place already for a power threshold around 0.5 mW (as opposed to the 1–2 mW before) indicating that the particle near-fields increased the photoreaction.

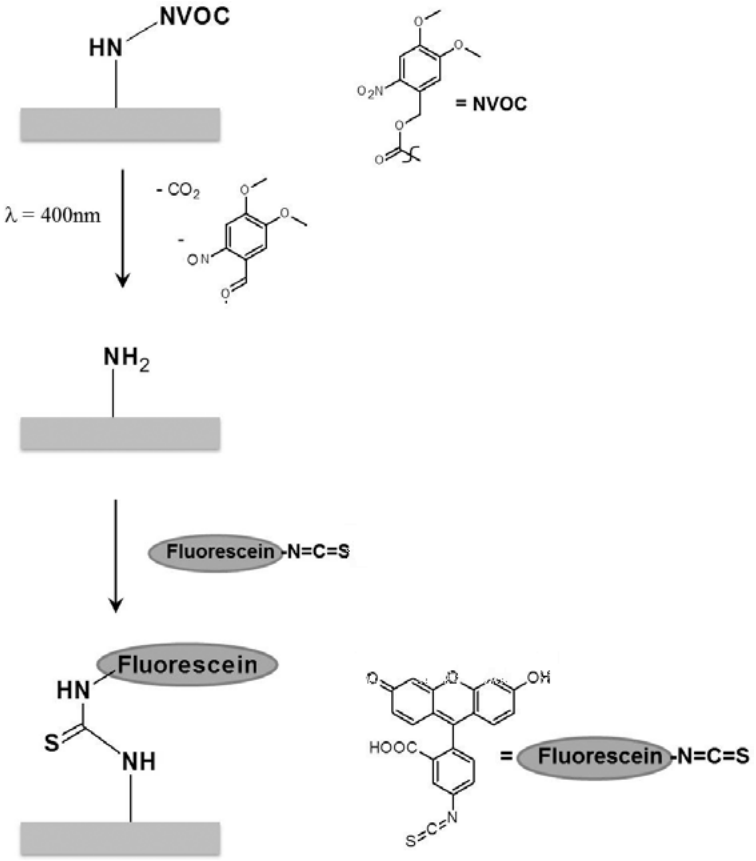

Fig. 6.8: Sketch of the chemical method of deprotecting the NVOC functionalized amines and subsequently binding the fluorescein (FITC) molecules. Note that the same route can also be applied successfully with a variety of other markers.

However, the confocal fluorescence microscope used for monitoring so far is not able to provide any sub-wavelength resolution. For that reason we investigated the same kind of samples by STORM [33, 34], a method which allows imaging of the bound fluorescence markers with a resolution well below the 100 nm threshold. The more stable fluorescence marker Alexa 647 was used for the STORM measurements. After photochemical writing, the samples were immersed for 2 h in a solution containing the marker in methanol. Note that the methanol causes a slight swelling of the polymer matrix so that the marker molecules may also penetrate the whole polymer matrix and non-specifically bind to the reaction volumes in the neighborhood of the gold triangles inside the matrix, not only to their surface. This penetration is facilitated by the reduced layer thickness of 30 nm. As the Fischer patterns are buried under the polymer matrix, their near-fields and the resulting photoreaction volumes are mainly

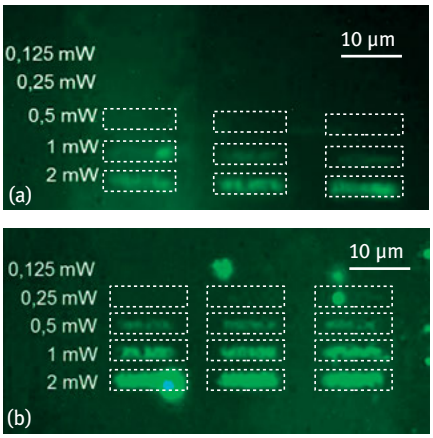

Fig. 6.9: Confocal fluorescence images of lines photochemically written into the 70 nm thick copolymer layer with protected amine side groups (a) on pure glass and (b) on glass carrying a 10 nm thick Au Fischer pattern. The deprotected amines were labeled with FITC (Fig. 6.8) after photochemical writing in order to render the free amine side groups visible by confocal fluorescence microscopy. As shown, the Fischer-patterns considerably enhance the photochemical processing.

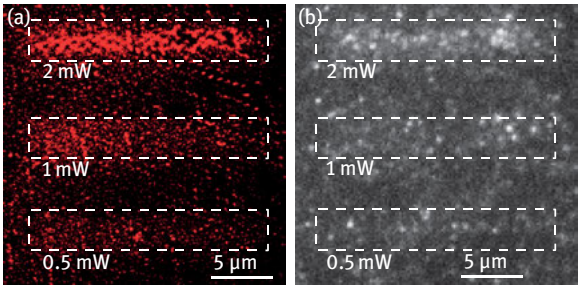

Fig. 6.10: STORM images of Alexa 647 fluorescence markers attached to amine side groups following the same recipe illustrated in Fig. 6.8 for FITC attachment. Amines were deprotected photochemically by writing lines at different power densities into the 30 nm thick copolymer layer sitting on glass with a 10 nm high Fischer pattern. (a) Evaluated STORM image exhibiting a finer structure, indicating the influence of the periodic Fischer patterns on the photoreaction In contrast, (b) shows a single fluorescence image from the raw data. The written lines are marked by dashed boxes. Again, the Fischer patterns considerably enhance the photochemical processes.

located in the interior of the polymer matrix, well below its surface. After incubation with markers, the samples were immersed in pure methanol for 1h in order to wash off any non-bound residuals.

The STORM image (Fig. 6.10 (a)) and a corresponding single fluorescence image (Fig. 6.10 (b)) shows a photoreaction at powers of the order of 1 mW in the shape of stripes of increased fluorophore density. Periodic substructures of these stripes with a periodicity below 1 µm correspond to periodic Fischer pattern structures. They

clearly indicate the influence of the nanoparticles' near-field distribution on the local photoreactions. Further experiments trying to increase the quality and resolution of these images are in progress. In this image, the lines are also accompanied by non-specifically bound fluorophores around the written lines.

6.6 Conclusions

We triggered nonlinear optically induced photoreactions in several MMA-based copolymers using three different photolabile groups. We focused on proving photochemical reactions in the near-field of metallic nanoparticles embedded in the polymer matrix. Basic tests were carried out in order to demonstrate whether or not such photoreactions may be selectively triggered through second harmonic generation (SHG) from nanoparticles as opposed to multiphoton absorption processes. Our experiments showed that direct two-photon absorption is the dominant photoreaction mechanism in all cases.

Nevertheless, good localization and enhancement of the photoreaction in the near-fields of metallic nanoparticles can always be expected. However, for the azobenzenes and azosulfonates, no localized photoreactions were found, as the azobenzene reaction only changes absorbance, and the elasticity change due to azosulfonate decay is superposed to topographic changes due to side reactions in the polymer thin film. The only promising way of proving such near-field enhanced reactions turned out to be the deprotection of NVOC-protected amines which in turn allowed labeling of the reaction volume for high-resolving fluorescence microscopy. In principle, the advantage of this deprotection reaction is the wide variety of molecules (or even nanostructures) which exist and are ready to bind site-specifically to the deprotected amines for further applications. This type of photoactive unit has now been implemented into the membrane of polymersomes, a class of artificial vesicles. Photochemical experiments using near-field effects with integrated gold nanoparticles at those polymersomes are in progress. A site-specific modification of the polymersomes induced by a biologically harmless irradiation is envisioned.

Acknowledgments

P. R., U. G. and T. K. acknowledge financial support from the German Science Foundation (DFG) through the DFG priority program SPP 1327 and the Cluster of Excellence "Center of Advancing Electronics Dresden", as well as support from the European Social Funds through the ESF-NFG project "Mind Nano".

References

[1] Levinson HJ, Arnold WH. Optical Lithography. In: Rai-Choudhury P, ed. Handbook of Microlithography, Micromachining, and Microfabrication. Bellingham, USA, SPIE Press, 1997.
[2] Braun F, Eng L, Trogisch S, Voit B. Novel labile protected amine terpolymers for the preparation of patterned functionalized surfaces: Synthesis and characterization. Macromol. Chem. Phys. 2003, 204, 1486–1496.
[3] Opitz J, Braun F, Seidel R, Pompe W, Voit B, Mertig M. Site-specific binding and stretching of DNA molecules at UV-light-patterned aminoterpolymer films. Nanotech. 2004, 15, 717–723.
[4] Deeb C, Zhou X, Gerard D et al. Off-resonant optical excitation of gold nanorods: Nanoscale imprint of polarization surface charge distribution. J. Phys. Chem. Lett. 2011, 2, 7–11.
[5] Wang L, Uppuluri SM, Jin EX, Xu X. Nanolithography using high transmission nanoscale bowtie apertures Nano Lett. 2006, 6, 361–364.
[6] Ueno K, Juodkazis S, Shibuya T et al. Nanoparticle plasmon-assisted two-photon polymerization induced by incoherent excitation source. J. Am. Chem. Soc. 2008, 130, 6928–6929.
[7] Murazawa N, Ueno K, Mizeikis V, Juodkazis S, Misawa H. Spatially selective nonlinear photopolymerization induced by the near-field of surface plasmons localized on rectangular gold nanorods. J. Phys. Chem. C 2009, 113, 1147–1149.
[8] Sundaramurthy A, Schuck PJ, Conley NR, Fromm DP, Kino GS, Moerner WE. Toward Nanometer-Scale optical photolithography: Utilizing the Near-Field of bowtie optical nanoantennas. Nano Lett. 2006, 6, 355–360.
[9] Reichenbach P, Horneber A, Gollmer D et al. Nonlinear-optical point light sources through field enhancement at metallic nanocones. Opt. Expr. 2014, 22, 15484–15501.
[10] Reichenbach P. Metallische Nanoantennen: Frequenzverdopplung und photochemische Reaktionen auf kleinen Skalen. PhD thesis. Dresden, Germany, Technische Universität Dresden, 2012.
[11] Georgi U. Synthese photoreaktiver Polymere zur optischen Strukturierung dünner Schichten. PhD thesis. Dresden, Germany, Technische Universität Dresden, 2014.
[12] Georgi U, Reichenbach P, Oertel U, Eng LM, Voit B. Synthesis of azobenzene-containing polymers and investigation of their substituent-dependent isomerisation behaviour. Reac. Funct. Polymer 2012, 72, 242–251.
[13] Aussenegg FR, Leitner A, Gold H. Optical second-harmonic generation of metal-island films. Appl. Phys. A 1995, 60, 97–101.
[14] Bozhevolnyi SI, Beermann J, Coello V. Direct observation of localized second-harmonic enhancement in random metal nanostructures. Phys. Rev. Lett. 2003, 90, 197403-1-4.
[15] Danckwerts M, Novotny L. Optical frequency mixing at coupled gold nanoparticles. Phys. Rev. Lett. 2007, 98, 026104-1–4.
[16] Lesuffleur A, Kumar LKS, Gordon R. Enhanced second harmonic generation from nanoscale double-hole arrays in a gold film. Appl. Phys. Lett. 2006, 88, 261104-1–3.
[17] Eftekhari F, Gordon R. Enhanced second harmonic generation from noncentrosymmetric nanohole arrays in a gold film. IEEE J. Sel. Top. in Quant. 2008, 14, 1552–1558.
[18] Reichenbach P, Eng LM, Georgi U, Voit B. 3D-steering and superfocusing of second-harmonic radiation through plasmonic nano antenna arrays. J. Laser Appl. 2012, 24, 042005-1–8.
[19] Braun F, Eng LM, Loppacher C, Trogisch S, Voit B: Novel Diazosulfonate terpolymers for the preparation of structured functionalized surfaces: Synthesis and characterization. Macromol. Chem. Phys. 2002, 203, 1781–1789.
[20] Fischer UC, Zingsheim H. Submicroscopic pattern replication with visible light. J. Vac. Sci. Technol. 1981, 19, 881–885.

[21] Kosiorek A, Kandulski W, Chudzinski P, Kempa K, Giersig M. Shadow nanosphere lithography: simulation and experiment. Nano Lett. 2004, 4, 1359–363.
[22] Li H, Low J, Brown KS, Wu N. Large-area well-ordered nanodot array pattern fabricated with self-assembled nanosphere template. IEEE Sens. J. 2008, 8, 880–884.
[23] Nuyken O, Scherer C, Baindl A, Brenner AR, Dahn U. Azo-group-containing polymers for use in communications technologies. Prog. Polym. Sci. 1997, 22, 93–183.
[24] Hvilsted S, Sanchez C, Alcala R. The volume holographic optical storage potential in azobenzene containing polymers. J. Mater. Chem. 2009, 19, 6641–6648.
[25] Chiefari J, Chong YK, Ercole F et al. Living Free-Radical Polymerization by Reversible Addition – Fragmentation Chain Transfer: The RAFT Process. Macromolecules 1998, 31, 5559–5562.
[26] Feldermann A, Ah Toy A, Phan H, Stenzel MH, Davis TP, Barner-Kowollik C. Reversible addition fragmentation chain transfer copolymerization: influence of the RAFT process on the copolymer composition, Polymer 2004, 45, 3997–4007.
[27] Favier A, Charreyre MT, Experimental Requirements for an Efficient Control of Free-Radical Polymerizations via the Reversible Addition-Fragmentation Chain Transfer (RAFT) Process. Macromol. Rapid Commun. 2006, 27, 653–692.
[28] Nuyken O, Voit B. Water-soluble and photosensitive copolymers from methyl methacrylate and sodium 3-vinylphenylazosulfonate. Makromol. Chem. 1989, 190, 1325–1332.
[29] Nuyken O, Voit B. The photoactive diazosulfonate group and its role in polymer chemistry. Makromol. Chem. Phys. 1997, 198, 2337–2372.
[30] Pillai VNR. Photoremovable protecting groups in organic synthesis. Synthesis 1980, 1, 1–26.
[31] Millaruelo M, Eng LM, Mertig M et al. Photolabile Carboxylic Acid Protected Terpolymers for Surface Patterning. Part 2: Photocleavage and Film Patterning, Langmuir 2006, 22, 9446–9452.
[32] Sieczkowska B, Millaruelo M, Messerschmidt M, Voit B. New Photolabile Functional Polymers for Patterning onto Gold Obtained by Click Chemistry. Macromolecules 2007, 40, 2361–2370.
[33] Rust MJ, Bates M, Zhuang X. Sub-diffraction-limit imaging by stochastic optical reconstruction microscopy (STORM). Nature Methods 2006, 3, 793–796.
[34] Hess ST, Girirajan TPK, Mason MD. Ultra-High Resolution Imaging by Fluorescence Photoactivation Localization Microscopy. Biophys. J. 2006, 91, 4258–4272.
[35] Hell SW, Wichmann J. Breaking the diffraction resolution limit by stimulated emission: stimulated-emission-depletion fluorescence microscopy. Opt. Lett. 1994, 18, 780–782.
[36] Klar TA, Hell SW. Subdiffraction resolution in far-field fluorescence microscopy. Opt. Lett. 1999, 24, 954–956.
[37] Betzig E. Proposed Method for molecular optical imaging, Opt. Lett. 1995, 20, 237–239.
[38] Betzig E, Patterson GH, Sougrat R et al. Imaging Intracellular Fluorescent Proteins at Nanometer Resolution. Science 2006, 313, 1642–1645.

I. Alexeev, U. Quentin, K.-H. Leitz, J. Strauß, M. Baum, F. Stelzle, and M. Schmidt

7 Optical trap assisted sub diffraction limited laser structuring

Abstract: The ability to structure surfaces on a submicron scale is becoming increasingly important for a broad range of technical and biological applications. Such structures can be produced via irradiating micron sized transparent particles placed over a substrate of interest with ultrafast laser pulses. To enhance the structuring flexibility of this method particles can be optically trapped and spatially manipulated relative to the structured surface in order to achieve arbitrary patterns. In this contribution the authors describe the principle of optical trap assisted nanostructuring and present simulated and experimental results demonstrating the potential and limitations of this innovative nanoscale optical material processing technology.

7.1 Introduction

Optical and especially laser based fabrication methods are commonly used to produce structures with characteristic dimensions on a micron and submicron spatial scale. Submicron structuring is often performed using photolithographic methods and although extremely capable (currently achieving spatial feature sizes of 22 nm and targeting 14 nm in the near future [1]) they have wellknown drawbacks of complexity and high cost. Alternatively, nonphotolithographic direct write laser processing [2, 3] can be relatively straightforward, inexpensive, and flexible but the achievable minimum structural feature size of such methods remains to be investigated. As a first approximation the feature size of a direct write technique is assumed to be limited by optical diffraction and determined by the size of the focused laser beam (Fig. 7.1 (a)). In the case of an ideal Gaussian beam the focal spot radius is given by (7.1) [4]

$$r_{\mathrm{fG}} = \frac{\lambda f}{\pi r_{\mathrm{beam}}}, \tag{7.1}$$

where λ is the laser wavelength, f is the focal length of the focusing lens, and r_{beam} is $1/e^2$ radius of the incident beam. The equation inexplicitly assumes that the incident laser beam diameter is small compared to the size of the focusing optics and the diffraction effects from the lens edges are negligible. This is typically not the case when a short focal length microscope objective is used for focusing since its entrance pupil is commonly overfilled by the incident laser beam to utilize the full lens aperture (although overfilling leads to a significant portion of laser beam energy being wasted it, however, permits achievement of smaller focal spots). Overfilling is achieved via spatial magnification of the incident laser beam to a size larger than the lens entrance

aperture and use of the central beam area only effectively reducing the beam intensity variation across the pupil. Hence the incident laser beam can be approximated by a plane wave and the focal radius is calculated using (7.2) which gives a distance from the central maximum to the first intensity zero of the Airy disk in the focal plane [4]

$$r_{\mathrm{fA}} = \frac{0.61\lambda}{\mathrm{NA}}, \tag{7.2}$$

where NA is the numerical aperture of the lens (it should be kept in mind that equations (7.1) and (7.2) define beam radii at different intensity levels and cannot be compared directly). Although equation (7.2) effectively states that a laser beam cannot be focused to a size smaller than half of its wavelength (in air NA $<$ 1), there are a number of methods of circumventing its effect on the achievable minimum structural feature size in the case of laser material processing applications allowing fabrication of structures with characteristic dimensions below the stated value. Some of these approaches are based on the specifics of light-matter interaction processes and take advantage of various material effects to achieve feature sizes below the diffraction limit. The nonlinear (power) dependence of the multiphoton absorption process on electric field intensity allows subfocal confinement of the laser-matter interaction zone. This is exploited for example in the two-photon polymerization technique [5–7] or glass structuring with ultrafast lasers [8]. The threshold-like behavior of ultrafast laser ablation permits removal of material from an area smaller than the laser beam focal spot via careful adjustment of the peak fluence (Fig. 7.1 (b)) [9, 10]. Fabrication of nanostructures has also been attained using near-field techniques incorporating inhomogeneous evanescent waves present at the boundaries to achieve subdiffraction resolution. Here small apertures [11], tips [12], and particles [13] have been used to focus laser beams onto substrates positioned in close proximity to the focusing element (Fig. 7.1 (c)). A combination of near-field and threshold based methods can lead to even smaller structural feature sizes (Fig. 7.1 (d)).

Focusing a laser beam with microscopic dielectric spheres has been extensively investigated both theoretically and experimentally successfully demonstrating its nanostructuring capabilities [14–17]. The approach appears to be particularly efficient for large surface area nanopatterning via deposition of a monolayer of microspheres which acts as an array of microlenses and irradiating them with a large area laser beam [18]. Although such coatings also known as contacting particle lens arrays (CPLA) are of interest for a number of applications [19, 20] variability of the achievable patterns is quite low due to the self-organizing behavior of the colloidal particles which tend to settle into highly periodic hexagonlike shapes. In order to address the issue of CPLA structuring inflexibility while preserving its ability to produce nanoscale structures a sequential patterning method which attempts to combine near-field focusing with optical trapping has been investigated by a number of research groups [21, 22]. Here, a micron size transparent dielectric bead is confined using established principles of optical tweezing and spatially manipulated in 2D or 3D space using

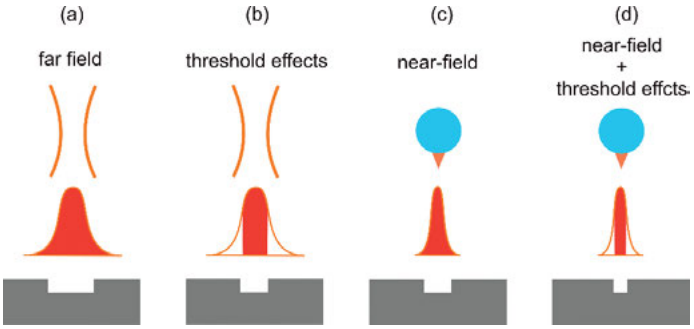

Fig. 7.1: Feature size reduction in laser based structuring: (a) restriction of feature size by diffraction in the far-field; (b) reduction of feature size by utilization of threshold effects; (c) reduction of feature size by utilization of near-field effects; and (d) further reduction of feature size via combination of near-field and threshold effects. Adopted with permission from [42].

either high precision positioning equipment or adaptive optics integrated into the trapping laser beam path. By displacing the bead with respect to the surface of interest and simultaneously irradiating it with an additional structuring laser beam, almost arbitrary surface patterns can be produced with feature sizes below the diffraction limit. In this work the authors present their findings in the field of optical trap assisted laser nanopatterning (OTAN) obtained within the scope of the DFG priority program SPP1327. In the following sections we will present numerical modeling of laser beam focusing with an optically trapped microsphere, experimental investigations of the beadassisted structuring processes, and demonstrate several applications.

7.2 Optical trapping

The key point of the approach investigated is application of optical trapping for precise spatial manipulation of the structuring bead(s). In general, the technique of optical trapping (also known as optical tweezing) is a well-established method which allows noncontact manipulation of micron or submicron sized objects of various origins [23–25]. Optical tweezers are commonly built around a relatively low power continuous wave laser emitting a high quality light beam. The beam is tightly focused with a high numerical aperture microscope objective (typically NA > 1) forming a potential well deep enough to spatially confine a small particle (typically under 10 microns in diameter) [26]. Lens numerical aperture can exceed a value of 1 for immersion objectives since NA $= n \sin\theta$, where n is the index of refraction of the lens working medium. Optical trapping is typically performed in a liquid medium with water being the most common ambient environment. For the relatively large dielectric beads ($d \geq \lambda$) used in this research the trapping mechanism can be understood based on the geometrical optics considerations. In the ray optics model, the trapping force originates from the

light refraction as the laser beam enters and exits the dielectric bead. Except for the on axis ray, the light ray propagation direction changes due to refraction. Since light (or rather photons) has momentum, the deviation in the light direction leads to its momentum change while the bead experiences an equal but opposite momentum change according to the law of conservation. If the sphere is displaced from the center of a symmetrical laser beam focus it will experience a net force turning it back. This net force is due to the light intensity variation across the bead: more intense beams impart a larger momentum change towards the focus than less intense beams which impart a smaller momentum change away from the focus. As a result, if the bead is located on the laser beam axis the lateral forces cancel out due to the symmetry while the scattering force in the longitudinal direction is compensated by the axial gradient force leading to a stable trapping of the particle slightly downstream of the beam waist. While a Gaussian optical trap (formed with a tightly focused Gaussian laser beam) restricts particle movement in all spatial directions other beam types which effectively do not possess an intensity gradient along the longitudinal axis, such as Bessel beams for example, can achieve particle confinement only in the lateral plane [27]. Both 3D and 2D tweezing have been used in OTAN applications [21, 28] but here we concentrate on the former approach only since it permits more defined positioning of the structuring bead although it is also more susceptible to surface irregularities such as tilt and roughness. Depending on the medium used to suspend the focusing bead either oil or water immersion objectives with NA $>$ 1 can be used to form the optical trap. If the medium is aqueous then a water immersion lens would form a trap with almost constant stiffness across various depths [22]. On the other hand if the index of refraction of the ambient medium is high, as for the liquid photopolymer NOA84 (Norland Products) $n_{\mathrm{NOA84}} \approx 1.46$ used for the twophoton polymerization studies described later in the chapter, then switching to an oil immersion lens will be beneficial due to a closer match ($n_{\mathrm{oil}} \approx 1.51$ and n_{NOA84}) of the refractive indices. It should be mentioned that the immersion and trapping media are separated by a thin glass slide and do not mix. For this reason both lens types have been used depending on the process being investigated If a non-aqueous medium is used attention should be paid to its viscosity since the drag forces can exceed the trapping force effectively preventing the bead from being manipulated. High viscosity, for example, restricts the number of photopolymers which can be used in combination with the OTAN technique. Additionally, beads of materials with a relatively low index of refraction, such as silica ($n_{\mathrm{SiO2}} \approx 1.45$) may not be trapped if n_{medium} is noticeably higher than n_{water} due to drastically reduced refraction at the bead surface requiring use of a material with a higher n such as polystyrene ($n_{\mathrm{PS}} \approx 1.58$). Simultaneous trapping of several particles is possible, for example, with holographic optical tweezers [29] or by splitting the trapping beam into multiple arms, allowing parallelization of the OTAN technique [30–32].

7.3 Microsphere focusing in liquid media – numerical simulations

7.3.1 General considerations

In order to understand the capabilities and limitations of the OTAN technique it is important to investigate focusing properties of the microbead used for structuring. Compared to the extensively studied case of dielectric microspheres dispersed on dry surfaces there are several important differences for the technique presented which must be considered. The first and most obvious is that the microparticle is surrounded by an optical medium with a much larger index of refraction than air ($n_{\text{air}} = 1$), strongly affecting the bead's focusing properties.

The second difference is rather technical but should still be carefully analyzed. In the optical tweezers setup the final optical element is a high NA microscope objective which tightly focuses the trapping laser beam. Due to the short working distance of such lenses (less than a few mm) the structuring laser beam has to be launched into the experimental sample through the same microscope objective resulting in its (structuring beam) strong focusing. Although sharing this optical element does not necessarily ensure exact overlap of the bead position and the structuring beam focus, it may be incorrect to treat the (structuring) laser beam as a plane or quasi plane wave as is commonly done. Additionally, a lateral displacement of the pre-focused structuring beam may result in a strong asymmetrical distortion of the bead focus. An apparent alternative solution of using counterpropagating laser beams (for trapping and structuring respectively) will likely result in focusing the structuring beam inside the trapping objective lens and its damage effectively making this approach impractical.

The third difference to be considered is that optical trapping permits a nonzero gap between the microsphere and the substrate to be structured meaning that the longitudinal intensity profile of the particle focus should be taken into consideration too.

In order to investigate these differences and the effects of process parameters a numerical simulation model has been developed using the optical module of the COMSOL Multiphysics software. The model calculates a stationary solution of the 3D wave propagation equation (7.3) while ignoring the temporal behavior of the structuring laser pulse. This simplification is justified since the spatial length of even the shortest pulse used in this work (~ 100 fs or 30 µm) is significantly longer than the typical bead size.

$$\nabla \times \mu_r(\nabla \times \vec{E}) - k_0^2 \left(\varepsilon_r - \frac{j\sigma}{\omega \varepsilon_0} \right) \vec{E} = 0 \tag{7.3}$$

Here, E is the electric field, k is the free space wave number, ω is the wave frequency, ε_0 is the vacuum permittivity ε_r and μ_r are the relative permittivity and permeability respectively, and σ is the electrical conductivity. In the model the relative permittivity ε_r is expressed as $\varepsilon_r(\omega) = \hat{n}^2(\omega)$, with the frequency dependent refractive index taken from published sources [33–37]. For polystyrene and water the refractive indices are taken to be complex, for fused silica glass the index is assumed to be real due to

low absorption for the wavelengths of interest, and for photo polymer NOA84 only the real part of the refractive index is used due to a lack of information about its absorption at 800 nm wavelength. The electrical conductivity σ for each material is taken from the database supplied with COMSOL. In the model the electromagnetic wave is assumed to be linearly polarized in the *x-z* plane with the negative *z* axis being the direction of propagation. Boundary conditions have been defined as "perfect electric conductor" for *y-z* planes and "perfect magnetic conductor" for *x-z* planes. The top and bottom boundaries have been described as "scattering boundary conditions" with the incident electric field being defined as a plane wave or a Gaussian beam respectively. Incident electric field geometrical symmetry in the *x-z* and *y-z* planes is assumed to reduce computational efforts (Fig. 7.2). The process parameters which can be varied in the model are the wavelength of the incident laser beam, bead size and material (refractive index), ambient trapping medium (refractive index), and curvature of the incident laser beam front. The wavelength set investigated was 1064 nm, 800 nm, 532 nm, 400 nm, 355 nm, and 266 nm to match wavelengths of the most common ultrafast lasers. The sizes of the silica (SiO_2) and polystyrene (PS) spheres varied between 0.5 µm and 5 µm in diameter – these bead sizes are readily available. Two trapping media have been considered: water and liquid photopolymer NOA84 (both were used in the experimental part of the program). The structured substrate if mentioned, is always assumed to be a common optical glass such as BK-7 to mimic the experimental arrangements described later. In air the bead and the substrate always contact each other while in the liquid media the simulations are effectively done in two steps – first, the presence of the substrate is ignored and the longitudinal position of the field enhancement peak is determined. Second, the substrate surface is aligned with the plane defined in the previous step and the intensity distribution is recalculated (Fig. 7.2). This two-step approach is adopted to consider the influence of the substrate on bead focusing. Figure 7.2 shows exemplary focal intensity distributions formed by silica and polystyrene spherical beads of 2 µm in diameter in air (a), water (b), and photopolymer NOA84 (c). The incident electric field is a linearly polarized plane wave with an amplitude of $E_x = 1$ V/m and a wavelength of 800 nm. In this chapter we define the intensity as the *z*-component of the Poynting vector $S_z = [\vec{E}\,\vec{H}]_z$, since it has been found to be responsible for structure formation in pulsed laser nanofabrication [38]. In the case of the PS bead immersed in photopolymer NAO84 (Fig. 7.2 (c)) the presence of the substrate is not considered since this setup is of primary interest for 3D additive applications where the particle-substrate separation is likely to be non-constant.

For the dry environment (air) peak intensity enhancement occurs almost immediately underneath the bead permitting the use of contacting particles for surface structuring. The focal spots in the substrate surface plane are slightly asymmetrical for both bead types (SiO_2 and PS) with the orthogonal full width at half maximum (FWHM) diameters given in Tab. 7.1. For comparison the size of a diffraction limited focal spot is also redefined at 50 % intensity drop in the principal maximum of the

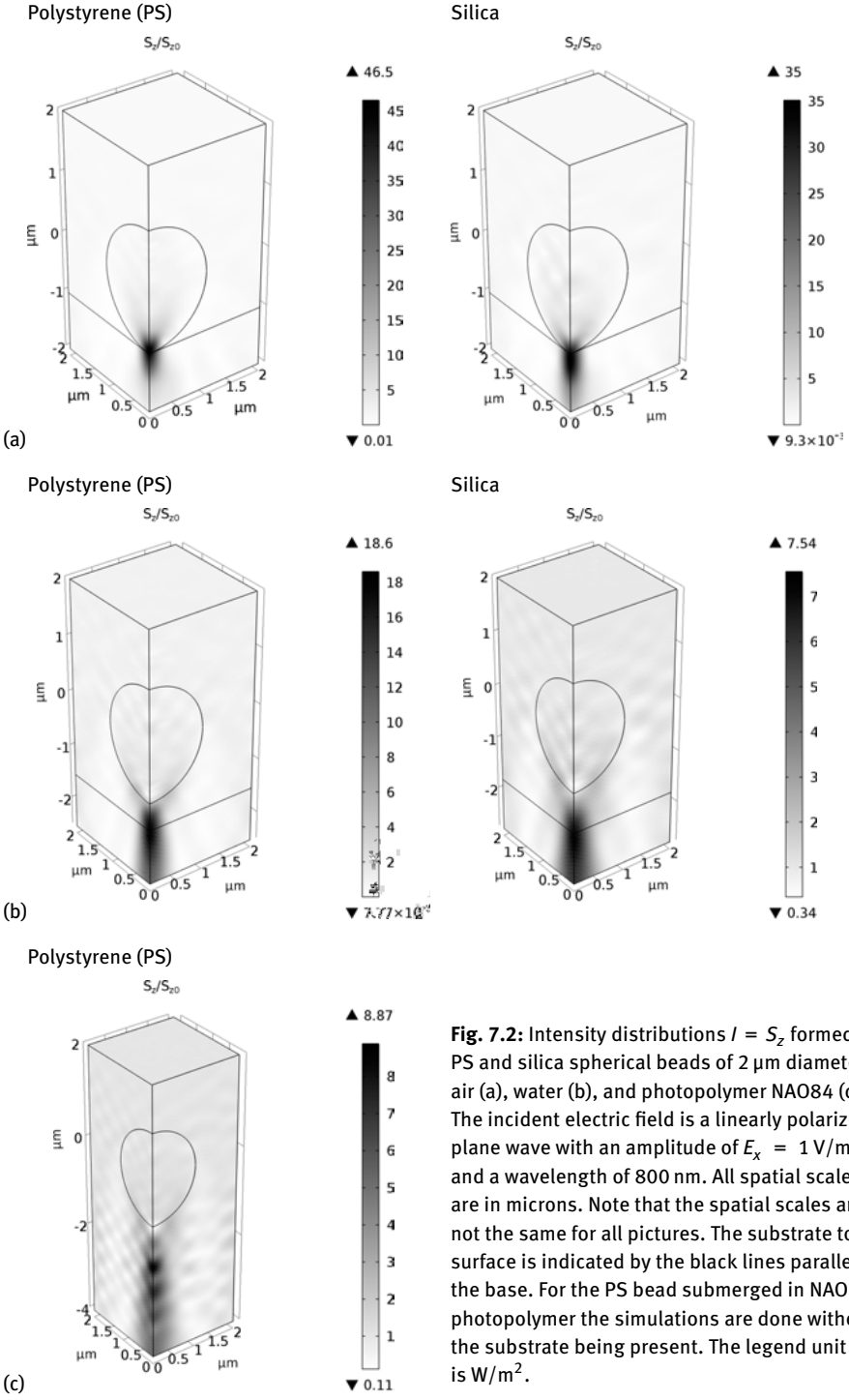

Fig. 7.2: Intensity distributions $I = S_z$ formed by PS and silica spherical beads of 2 μm diameter in air (a), water (b), and photopolymer NAO84 (c). The incident electric field is a linearly polarized plane wave with an amplitude of $E_x = 1$ V/m and a wavelength of 800 nm. All spatial scales are in microns. Note that the spatial scales are not the same for all pictures. The substrate top surface is indicated by the black lines parallel to the base. For the PS bead submerged in NAO84 photopolymer the simulations are done without the substrate being present. The legend unit is W/m^2.

Airy disk resulting in a modified equation (7.2)

$$\mathrm{FWHM}_{\mathrm{fA}} = \frac{0.52\lambda}{\mathrm{NA}}, \tag{7.2'}$$

or $\mathrm{FWHM}_{\mathrm{fA}} \geq 420\,\mathrm{nm/NA}$ at 800 nm wavelength. Based on the simulation results it can be seen that in a dry environment (NA < 1) both bead types focus the incident wave below the diffraction limit promoting contact particle based nanopatterning. Also the results shown in Tab. 7.1 indicate that presence of the substrate should be taken into consideration since it leads to a slight but observable variation of the focal spot size compared to the situation when the particle is levitated in air. A likely reason for such an enlargement is the reduction of the bead focusing power at the contacting area since the index of refraction of the particle is quite close to that of the substrate. The factor of laser intensity enhancement $S_{z\,\mathrm{substrate}}/S_{z0}$ is relatively high for both bead types ensuring that for a broad range of incident intensities only the surface under the particle will be affected.

When the beads are submerged in water (Fig. 7.2 (b)) their focusing power is reduced due to a smaller refractive index difference $n_{\mathrm{bead}} - n_{\mathrm{medium}}$, which becomes apparent in the simulations with the results being less univocal. In the case of the silica bead focusing with the particle becomes equivalent to using a relatively modest 0.75 NA objective, while the PS bead focus still remains smaller than the diffraction limit in air (Tab. 7.1). In this case the threshold effect should be carefully utilized to achieve the desired goal of sub 100 nm minimum feature size. Actually the manifold reduced intensity enhancement factor may favor this approach since a smaller area within the bead focus will exceed the ablation threshold – although care should be taken to avoid structuring with the unfocused beam. Additionally beads made out of optically denser material such as sapphire ($n_{\mathrm{sapphire}} \sim 1.76$) can make the focus tighter with simulations predicting the FWHM diameter to be approximately 340 nm for a 2 µm bead and 800 nm incident beam. Also the longitudinal extent of the focus formed by the sapphire bead is reduced to about 1 µm with the peak intensity formed approximately 150 nm beyond the bead surface. Those focal parameters can make sapphire beads efficient for applications such as biological cell membrane perforation which can be achieved via controllably placing particles with the optical tweezers and irradiating with a structuring laser.

Another important difference compared to the case of dry processing is the existence of a sizable gap between the focusing bead and the substrate (Fig. 7.2 (b)); its formation is consistent with elongation of the bead focal length in water. On the one hand the gap prevents the bead from being damaged or removed after a single pulse irradiation as commonly occurs for the contacting particles permitting reuse of the same microsphere during the structuring process. But on the other hand, the same gap adds an extra degree of complexity namely longitudinal bead position which has to be dealt with. The simulations also show that the influence of the substrate on the beam focusing (when a gap is present) is quite marginal compared to the dry envi-

ronment implying that the experimental procedure can remain the same for different substrate types. Interestingly, the existence of the bead–focus gap allows not only surface patterning but also intramaterial structuring to be performed if the particle is positioned directly on the substrate surface. The proper choice of laser fluence permitted experimental performance of subsurface structuring while preserving the surface integrity, although pulse energies which were too high resulted in both intramaterial modification and surface damage. The latter is likely to occur due to rapid expansion and contraction of glass in the bead focus volume subsequently leading to mechanical microfragmentation.

In the case of the liquid photopolymer NOA84 only PS beads can be used for focusing as silica particles are not capable of light gathering in this environment ($n_{SiO2} < n_{NOA84}$). Here, the PS bead acts as a ball lens with extreme spherical aberrations forming a relatively large focal spot (Fig. 7.2(c)) although the affected zone will be much smaller due to the quadratic intensity dependence of the light-polymer interaction process. Although the bead does not form a very tight focus in the polymer its use may still be preferable to a conventional objective if the lens immersion environment is not optimized for this type of medium.

Tab. 7.1: Simulation results for 2 micron bead focusing of 800 nm wavelength plane wave.

Model configuration	**FWHMx, nm**	**FWHMy, nm**	$S_{z\,\text{substrate}}/S_{z\,0}$	***Bead–Substrate* separation, nm**
SiO2 bead levitated in air	360	330	38	0
PS bead levitated in air	330	390	47	0
SiO2 bead on glass substrate in air	400	340	33	0
PS bead on glass substrate in air	380	320	45	0
SiO2 bead in water with glass substrate	590	580	7.3	900
PS bead in water with glass substrate	420	420	18	500
PS bead in polymer NOA84	460	400	8.7	1000 (bead–$S_{z\,\text{peak}}$ separation)
Sapphire bead in water	330	340	28	150 (bead–$S_{z\,\text{peak}}$ separation)

7.3.2 Variation of structuring wavelength and bead size

The other two process parameters which will strongly influence the structuring process are laser wavelength and bead size (the interaction process itself is not considered in the model) [12] Although they can both assume only discrete values they vary in relatively broad ranges allowing their use in process optimization/control. Figure 7.3 shows the variation of the focal spot FWHM diameter (a) and the enhancement factor (b) beneath a bead submerged in water as a function of its size for both SiO_2 and PS particle types at the laser wavelength of 800 nm. The diameters are measured in the planes of highest enhancement.

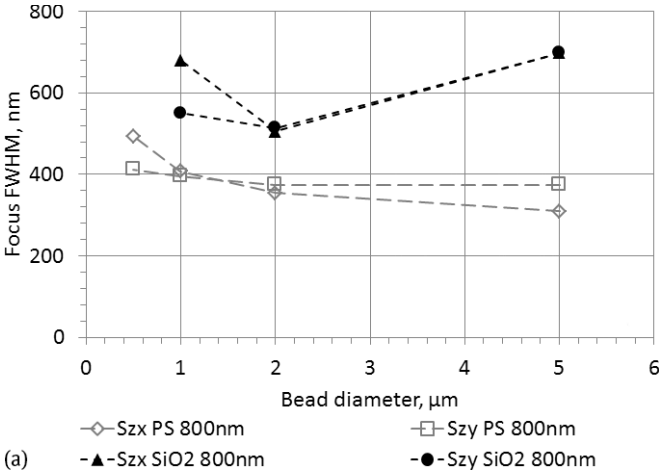

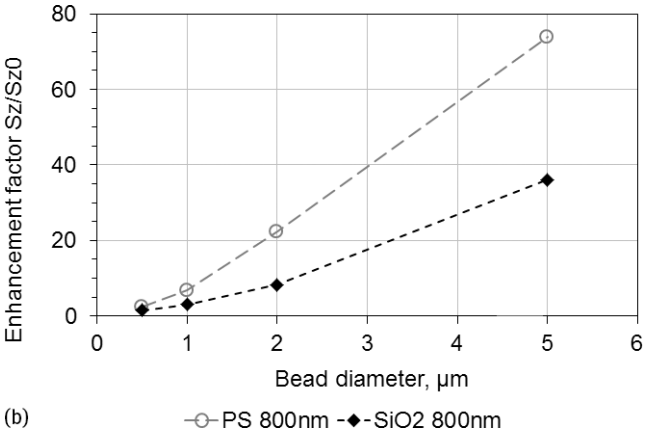

Fig. 7.3: Focus FWHM diameter (a) and enhancement factor (b) beneath a microsphere particle submerged in water vs. particle size (wavelength $\lambda = 800$ nm). The focal diameters are determined in the planes of highest enhancement. The connecting lines are a visual aid only.

As expected, the use of PS particles appears preferable since they always form a smaller focus compared to fused silica. A larger PS bead collects more light to a tighter spot resulting in a higher enhancement factor, but interestingly, it also makes the use of threshold effect more challenging so the size of 2 microns appears to be a good compromise from practical considerations. Figure 7.4 shows the dependence of the focal FWHM diameter on the irradiating laser wavelength. As expected the focal spot gets bigger as the wavelength increases but the focus enlargement is actually more dramatic as linear λ dependence due to the dispersion effect and the corresponding reduction of the refractive indices difference ($n_{\text{bead}} - n_{\text{medium}}$) at longer wavelengths This can be clearly seen as the focal spot size effectively doubles when the wavelength changes from 800 to 1064 nm. Use of short (in the UV region) wavelengths becomes preferable to achieve the targeted feature size of 100 nm and below.

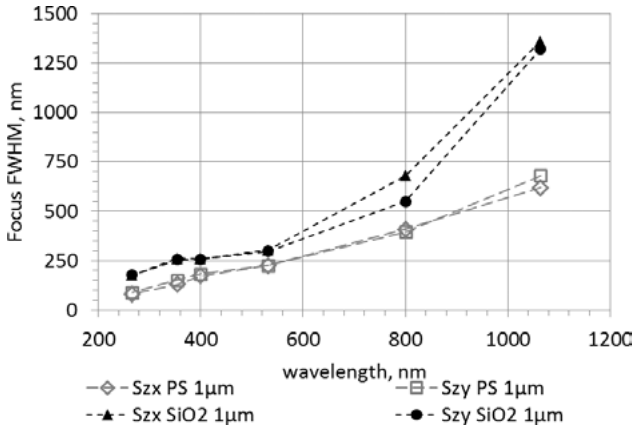

Fig. 7.4: Focus FWHM diameter vs. laser wavelength (particle size $d = 1$ µm), the ambient medium is water. The connecting lines are a visual aid only.

7.3.3 Bead irradiation with a non-plane wave

In general, the structuring laser beam shall not be treated as an infinite plane wave if its focus is located in the proximity of the particle but this scenario can happen since both trapping and structuring beams are focused with the same objective lens (see "Experimental procedure" for more details). To qualitatively illustrate the effect of non-plane wave bead focusing Fig. 7.5 shows an extreme case when the structuring laser beam focal plane is situated on top of a polystyrene bead (of 2 micron diameter) submerged in water. The laser beam focal spot is taken to be 1.5 micron in diameter ($1/e^2$), which is a realistic estimation for the experimental setup described later in the chapter. Since the structuring beam focus is smaller than the particle itself the bead effective NA is decreased leading to weakening of its focusing power and poten-

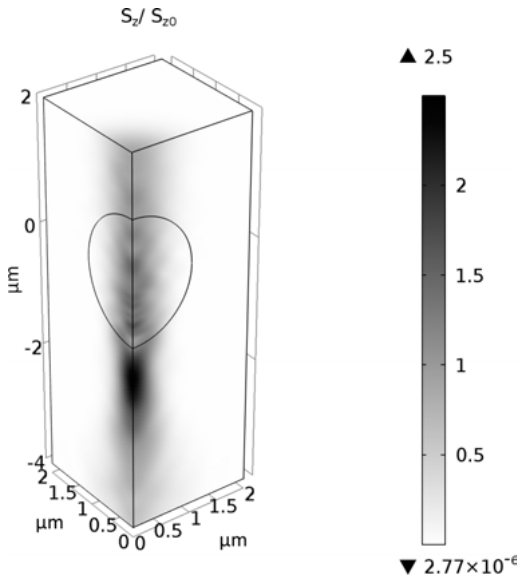

Fig. 7.5: Focusing of a Gaussian beam with $1/e^2$ diameter of 1.5 μm by a 2 μm PS bead in water. The beam focal plane overlaps the top of the bead.

tially defeating the purpose of using the microbead for sub-diffraction focusing. In the example given, the focal FWHM diameters are 540 nm and 580 nm for the x and y direction respectively with the maximum enhancement factor being below 3.

To avoid this scenario the particle should remain irradiated with a fairly uniform laser beam which can be attained by displacing the structuring beam focus downstream. In practice such decoupling of the trapping and structuring beam focal planes is achieved by adjusting the divergence of those beams although the resulting separation may remain fairly small in absolute terms of the order of tens of microns. Nevertheless it is significantly longer than the corresponding Rayleigh range of the structuring beam which is ~ 5 μm, ensuring relatively uniform irradiation of the bead and complete use of its aperture. The structuring beam must be focused beyond the bead; otherwise the particle collimates the beam rather than focuses it. Care should be taken here, however, to avoid surface/volume patterning with the structuring laser beam focus instead of the bead's.

7.4 Experimental procedure

The experimental investigation of the OTAN capabilities was performed using the apparatus described below. While the hardware setup remained pretty much the same for almost all experiments different test samples and process parameters were applied. A typical sample consists of a glass coverslip and an uncoated or polyimide coated soda lime glass slide (to be structured) which seal a volume of aqueous or photopolymer solution of microspheres of constant size and type (a test sample is

schematically shown in Fig. 7.6). Different samples must be used if a variation of partial size or material is desired. The sealed volume is approximately 5 mm × 5 mm × 90 µm with typical bead concentration of $1.7 \cdot 10^5$ particles/ml. This concentration is high enough to ensure the presence of several particles in the field of view of the process monitoring imaging system and sufficiently low to avoid the trapping of multiple beads in the tweezing laser beam focus at the same time The schematic of the OTAN setup is depicted in Fig. 7.6 and can be effectively split into three subsystems. The first subsystem (green) is the trapping arm which consists of either a frequency doubled cw Nd:YAG laser with a wavelength of 532 nm focused through a water immersion objective with NA of 1.2 (used for aqueous bead solutions) or a 1064 nm Nd:YAG laser focused by a 1.25 NA oil immersion objective (used for experiments with the photopolymer). The structuring arm (purple) can employ either an 800 nm/400 nm laser beam from a Ti:Sapphire femtosecond laser (100 fs pulse duration) or a 532 nm beam from a 10 ps high repetition rate Nd:YVO_4 laser. Magnifying telescopes are introduced in both subsystems to control size and divergence of the beams with the latter being necessary to introduce proper separation of the trapping and structuring beam foci. The third subsystem (light orange) is used for imaging of the trapped bead and monitoring of its displacement. The resolution of this subsystem is not sufficient for detailed real time examination of the structures produced; that has to be done later using optical and electron microscopes. For structuring the test sample mounted on a high precision 3D linear translation stage is displaced with respect to the stationary trapping and structuring beams.

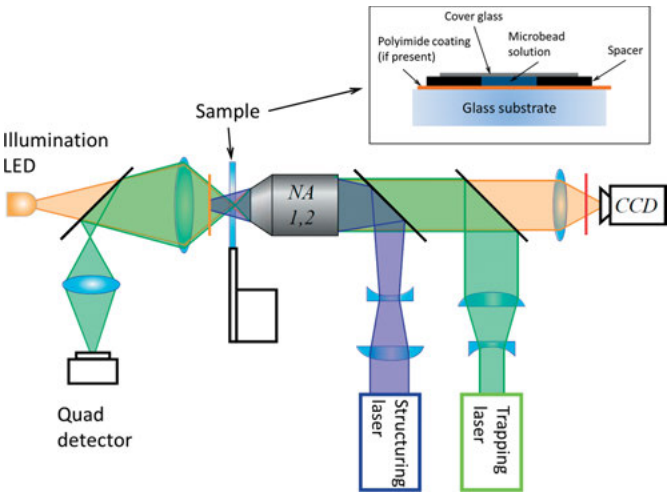

Fig. 7.6: Experimental setup of OTAN. Green path – optical trapping subsystem incorporating either 532 nm or 1064 nm cw laser; purple path – structuring arm which can employ either 800 nm 100 fs, 400 nm 100 fs, or 532 nm 10 ps laser pulses; light orange path – imaging subsystem used for structuring process visualization A typical test sample is schematically shown in the insert.

As discussed earlier in order to perform surface structuring using the OTAN approach the bead must be properly spaced with the sample surface and a correct gap must be maintained during the patterning process. Although the bead longitudinal position can be optimized by performing surface structuring at different particle-substrate separations, effectively using the trial and error approach a more accurate method of axial beam positioning is based on correlating the size of the imaged diffraction pattern of a reference particle with its longitudinal position. As the particle is moved in the axial direction, its diffraction pattern changes and the apparent diameter increases the further it is displaced away from the object plane of the imaging system (Fig. 7.7). Since the change in diameter varies linearly with the distance, this effect can be used to determine the particle position assuming proper calibration coefficients have been established: Gap = Linear Function(Bead Image Size). Such coefficients can be determined based on quantization of a sequence of bead images taken at different particle displacements away from the imaging plane. Quantization is done using multistep image processing analysis which includes denoising, intensity gradient determination, and wavelet thresholding with the sizes of the resulting particle binary images being easily extractable [39]. In practice such surface positioning is done not with a bead that will be used for structuring later on (its position and appearance remain constant in the imaging setup) but with a particle attached to the surface of interest. Such a bead(s) appears to always be present in every sample.

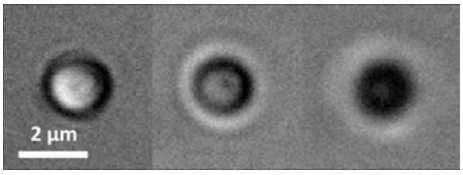

Fig. 7.7: Different axial particle position relative to the object plane leads to different diffraction patterns Adopted with permission from [39].

7.5 Nanostructuring results

7.5.1 Surface nanopatterning

The initial surface nanopatterning was performed on polyimide coated glass substrates using an SiO_2 particle of 2 µm diameter irradiated with 532 nm wavelength 10 ps laser pulses (Fig. 7.8). The pulse fluence (F = 8 mJ/cm^2), feed rate (5 µm/s), and pulse repetition rate (500 Hz) were adjusted to stably produce welldefined structures. In general the laser pulse rate represents a tradeoff between structuring speed and process stability. At high pulse frequencies the structuring bead cannot resettle at the equilibrium position after being displaced by the ablation process thus the pulse frequency is typically kept below 2 kHz to ensure process stability.

The image presented clearly demonstrates the feasibility of surface nanostructuring using optical microbeads trapped with Gaussian tweezers although the achieved

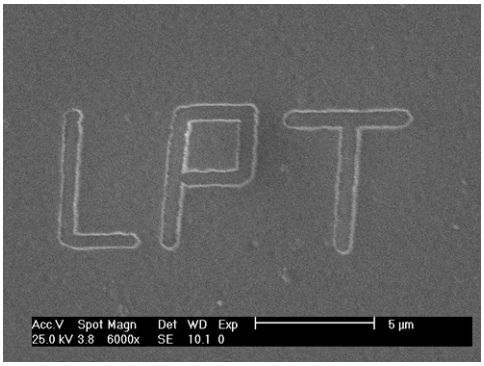

Fig. 7.8: SEM microphotograph of nanostructures on polyimide (EPO-Tek P1011). Process parameters: 2 µm SiO2 microsphere irradiated with $\lambda = 532$ nm, $\tau = 10$ ps, pulse frequency $f = 500$ Hz and fluence $F = 8\,\mathrm{mJ/cm^2}$ laser beam. Image adopted with permission from [28].

characteristic dimensions of the pattern appear to be relatively large – approximately 500 nm line width and 150 nm depth wise. Simulations performed for a matching microsphere irradiated with a 532 nm plane wave predict the bead focal size to be 460 nm FWHM pointing out that surface structuring was performed by the entire focus without using the thresholding effect. Use of 400 nm 100 fs laser pulses and 1 micron beads made it possible to achieve narrower structures (approximately 200 nm wide). It should be pointed out that further reduction of the line width can be limited not only by the size of the bead focus and laser fluence (threshold effect), but also by jitter of the structuring particle around its equilibrium position. Since any nonpoint line-like structure is produced by overlapping multiple shots its characteristic width will be broadened on the level of the average bead position deviation from its mean value: Line Broadening $\sim 2\sigma_{\text{Bead Deviation}}$. Such deviations depend on the properties of the optical trap and have been shown to vary between 30 and 100 nm under typical experimental conditions making line broadening an important limiting factor for structuring processes [39]. This variation can be reduced by the use of stiffer traps (care should be taken not to damage the bead with the trapping beam) and lowering the pulse repetition frequency (unfortunately the latter will also reduce the structuring speed) but ultimately it will still be limited by pointing stability of the trapping laser and Brownian motion (the latter is on the level of 5 nm). In this case single shot point-like surface structuring can provide more accurate information on the potentially achievable minimum feature size. In these experiments PS particles irradiated with 800 nm laser pulses of different energies were used to make dot-like structures on different test substrates (soda lime glass, fused silica glass, and polyimide coated glass) with the results being presented in Fig. 7.9. The laser pulse energy appears to be the most important "tuning knob" for the structure size utilizing the threshold effect. The smallest feature size achieved remains fairly similar for different particle sizes and substrate materials and appears to be of the order of 200 nm. Further feature size reduction is achievable by shortening the structuring wavelength to 400 nm. This has enabled production of point pattern on polyimide coated substrate with a diameter of 80 nm [40].

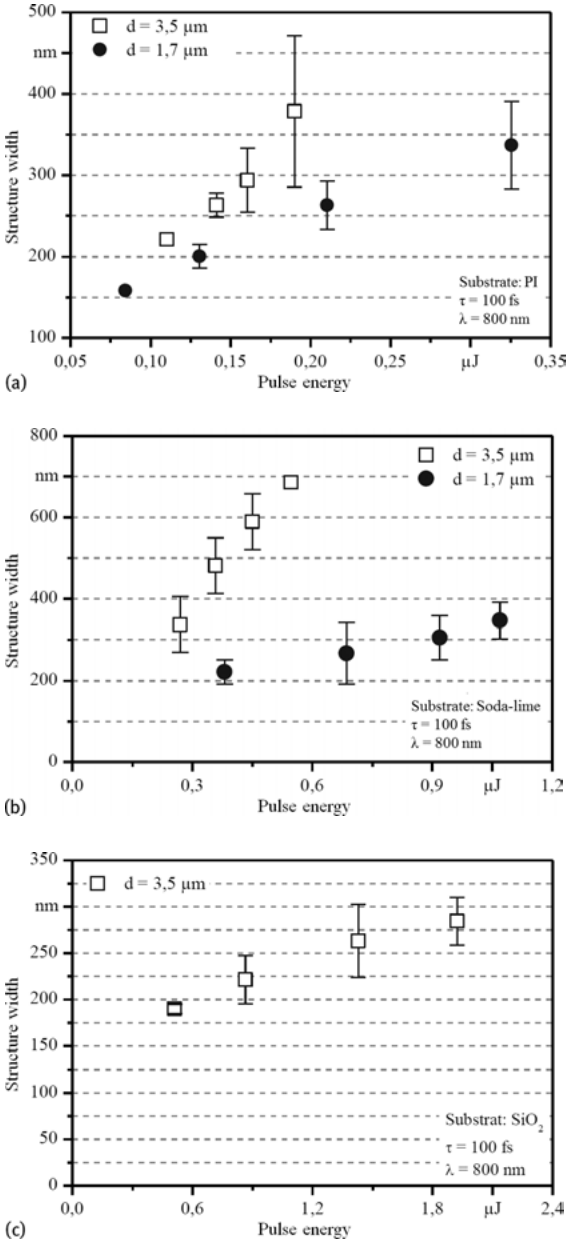

Fig. 7.9: Variation of dot-like structure size on polyimide coating (a), soda lime glass (b), fused silica glass (c) for different laser pulse energies. The laser wavelength is 800 nm and the pulse duration 100 fs. The focusing polystyrene particle sizes are 1.7 µm and 3.5 µm in diameter except for the fused silica substrate; here only 3.5 µm beads have been used.

7.5.2 Multiphoton polymerization

Besides surface and subsurface patterning applications the OTAN technique can be used to create structures via multiphoton material processing. Multiphoton polymerization is based on simultaneous absorption of two or more photons with the total energy sufficient to initiate a photo-polymerization reaction. Since the probability of simultaneous absorption of several photons is a nonlinear function of light intensity polymerization occurs only within the laser beam focus. NOA84 liquid photopolymer is effectively transparent for 800 nm wavelength since its absorption starts below $\lambda = 450$ nm but light intensity can be sufficiently enhanced in the bead focus (Fig. 7.2 (c)) to cause the nonlinear effect. PS particles can be successfully trapped and displaced in NOA84 polymer using the setup described above. When the trapped bead is irradiated with ultrafast laser pulses (100 fs) at fluence levels 5–20 mJ/cm^2 then tracks of polymerized voxels (volumetric pixel) are created on a glass substrate surface. The size of the structures generated is strongly influenced by the process parameters primarily the incident laser fluence with the smallest achieved size being 83 ± 11 nm in diameter (Fig. 7.10) [41].

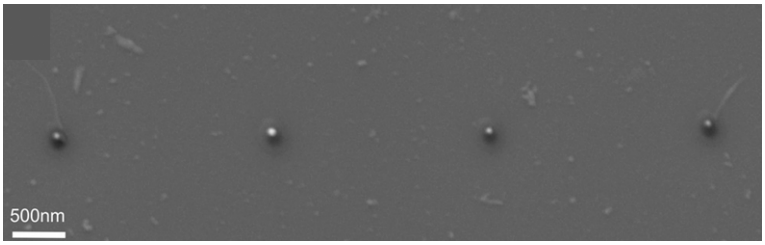

Fig. 7.10: Line of voxel generated by irradiating a 3.5 µm polystyrene microbead in NOA84 photopolymer. Average voxel diameter is 83 ± 11 nm. Image adopted with permission from [41].

7.6 Conclusion

The research conducted has demonstrated the feasibility of using optical trap assisted nanopatterning for surface and subsurface laser structuring. The achievable patterns have flexible geometries with the minimum structural feature size being determined by a number of process parameters. In order to achieve the targeted feature size of 100 nm careful combination of short laser wavelengths with threshold-like ultrafast laser ablation must be utilized simultaneously since the bead focus on its own appears to be larger than the targeted value. Although fabrication of sub 100 nm dot-like structures has been successfully demonstrated the minimal feature size of more complex line-like structures tends to be noticeably larger, at around 200 nm. This increase in feature size can be attributed to the jitter of the structuring bead around the equilib-

rium position due to Brownian motion and the pointing stability of the trapping laser in combination with shot-to-shot energy variation of the structuring laser pulses.

Accurate use of the thresholding effect is a complex task since not only the pulse energy but also the beam focal position must be maintained with a very high degree of accuracy to ensure the same laser intensity during the structuring process. The OTAN technique can provide an advantage for intensity threshold based processing since the position of the bead focus with respect to the particle remains constant while the positioning of the sphere itself can be a simpler task owing to its ease of visualization and tracking. Another exemplary application of the OTAN technique can be for two-photon polymerization since the bead focus should remain constant at different immersion depths compared to conventional microscope objectives which are not designed for such an ambient medium (photopolymer).

References

[1] Bohr M, Mistry K. Intel's revolutionary 22 nm transistor technology. Intel website 2011.
[2] Arnold CB, Piqué A. Laser direct-write processing. MRS bulletin 2007; 32: 9–15.
[3] Gattass RR, Mazur E. Femtosecond laser micromachining in transparent materials. Nature Photon 2008; 2: 219–25.
[4] Saleh BEA, Teich MC. Fundamentals of photonics: John Wiley and Sons, New York, 1991.
[5] Kawata S, Sun H, Tanaka T, Takada K. Finer features for functional microdevices. Nature 2001; 412: 697–8.
[6] Li L, Fourkas JT. Multiphoton polymerization. Materials Today 2007; 10: 30–37.
[7] LaFratta CN, Fourkas JT, Baldacchini T, Farrer RA. Multiphoton Fabrication. Angew. Chem. Int. Ed. 2007; 46: 6238–6258.
[8] Bhuyan MK, Courvoisier F, Lacourt PA, et al. High aspect ratio nanochannel machining using single shot femtosecond Bessel beams. Applied Physics Letters 2010; 97: 081102–081102-3.
[9] Pronko PP, Dutta SK, Squier J, Rudd JV, Du D, Mourou G. Machining of sub-micron holes using a femtosecond laser at 800 nm. Optics communications 1995; 114: 106–110.
[10] Korte F, Serbin J, Koch J, et al. Towards nanostructuring with femtosecond laser pulses. Applied Physics A 2003; 77: 229–235.
[11] Hecht B, Sick B, Wild UP, et al. Scanning near-field optical microscopy with aperture probes: Fundamentals and applications. J. Chem. Phys. 2000; 112: 7761.
[12] Dickmann K, Jersch J, Demming F. Focusing of Laser Radiation in the Near-field of a Tip (FOLANT) for Applications in Nanostructuring. Surface and interface analysis 1997; 25: 500–504.
[13] Huang SM, Hong MH, Lukiyanchuk B, Chong TC. Nanostructures fabricated on metal surfaces assisted by laser with optical near-field effects. Applied Physics A 2003; 77: 293–296.
[14] Luk'yanchuk BS, Arnold N, Huang SM, Wang ZB, Hong MH. Three-dimensional effects in dry laser cleaning. Applied Physics A 2003; 77: 209–215.
[15] Devilez A, Bonod N, Wenger J, et al. Three-dimensional subwavelength confinement of light with dielectric microspheres. Opt. Express 2009; 17: 2089.
[16] Zhou Y, Hong MH, Fuh JY, et al. Direct femtosecond laser nanopatterning of glass substrate by particle-assisted near-field enhancement. Applied Physics Letters 2006; 88: 23110.

[17] Huang SM, Sun Z, Luk'yanchuk BS, Hong MH, Shi LP. Nanobump arrays fabricated by laser irradiation of polystyrene particle layers on silicon. Appl. Phys. Lett. 2005; 86: 161911.
[18] Guo W, Wang ZB, Li L, Whitehead DJ, Luk'yanchuk BS, Liu Z. Near-field laser parallel nanofabrication of arbitrary-shaped patterns. Appl. Phys. Lett. 2007; 90: 243101.
[19] Barnes WL, Dereux A, Ebbesen TW. Surface plasmon subwavelength optics. Nature 2003; 424: 824–830.
[20] Liu K, Cao M, Fujishima A, Jiang L. Bio-Inspired Titanium Dioxide Materials with Special Wettability and Their Applications. Chemical reviews 2014.
[21] McLeod E, Arnold CB. Subwavelength direct-write nanopatterning using optically trapped microspheres. Nat Nanotechnol 2008; 3: 413–417.
[22] Quentin U, Leitz K, Deichmann L, Alexeev I, Schmidt M. Optical trap assisted laser nanostructuring in the near-field of microparticles. J. Laser Appl. 2012; 24: 42003.
[23] Ashkin A, Dziedzic JM, Yamane T. Optical trapping and manipulation of single cells using infrared laser beams. Nature 1987; 330: 769–771.
[24] Svoboda K, Block SM. Optical trapping of metallic Rayleigh particles. Opt. Lett. 1994; 19: 930.
[25] Ashkin A, Dziedzic JM, Bjorkholm JE, Chu S. Observation of a single-beam gradient force optical trap for dielectric particles. Opt. Lett. 1986; 11: 288.
[26] Neuman KC, Block SM. Optical trapping. Review of scientific instruments 2004; 75: 2787–809.
[27] Arlt J, Garces-Chavez V, Sibbett W, Dholakia K. Optical micromanipulation using a Bessel light beam. Optics communications 2001; 197: 239–245.
[28] Quentin U, Leitz K, Alexeev I, Schmidt M. Application of Gaussian optical tweezers for ultrafast laser assisted direct-write nanostructuring. Journal of Laser Micro/Nanoengineering 2012: 7
[29] Curtis JE, Koss BA, Grier DG. Dynamic holographic optical tweezers. Optics communications 2002; 207: 169–175.
[30] McLeod E, Arnold CB. Array-based optical nanolithography using optically trapped microlenses. Opt. Express 2009; 17: 3640.
[31] Tsai Y, Fardel R, Arnold CB. Nanopatterning on rough surfaces using optically trapped microspheres. Appl. Phys. Lett. 2011; 98: 233110.
[32] Tsai Y, Leitz K, Fardel R, Otto A, Schmidt M, Arnold CB. Parallel optical trap assisted nanopatterning on rough surfaces. Nanotechnology 2012; 23: 165304.
[33] Thormählen I, Straub J, Grigull U. Refractive index of water and its dependence on wavelength, temperature, and density. J. Phys. Chem. Ref. Data 1985; 14: 933.
[34] Hale GM, Querry MA. Optical constants of water in the 200-nm to 200-µm wavelength region. Appl. Opt. 1973; 12: 555.
[35] French RH, Winey KI, Yang MK, Qiu W. Optical properties and van der Waals-London dispersion interactions of polystyrene determined by vacuum ultraviolet spectroscopy and spectroscopic ellipsometry. Australian Journal of Chemistry 2007; 60: 251.
[36] Ma X, Lu JQ, Brock RS, Jacobs KM, Yang P. Determination of complex refractive index of polystyrene microspheres from 370 to 1610 nm. Phys. Med. Biol. 2003; 48: 4165.
[37] RefractiveIndex.info (http://refractiveindex.info/). Norland Optical Adhesive 84 (http://www.norlandprod.com/adhesives/NOA%2084.html).
[38] Wang ZB, Joseph N, Li L, Luk'Yanchuk BS. A review of optical near-fields in particle/tip-assisted laser nanofabrication. Proceedings of the Institution of Mechanical Engineers, Part C: Journal of Mechanical Engineering Science 2010; 224: 1113–1127.
[39] Quentin U, Leitz K, Paulus J, Alexeev I, Schmidt M. Positioning Accuracy in Optical Trap Assisted Nanostructuring. Journal of Laser Micro/Nanoengineering 2013; 8.
[40] Quentin U, Berg B, Alexeev I, Schmidt M Optical Trap Assisted Nanostructuring of Glasses and Polymers, Proceedings of LAMP2013 – the 6th International symposium on Laser Advanced Material Processing 2013.

[41] Leitz K, Tsai Y, Flad F, et al. Multiphoton polymerization using optical trap assisted nano-patterning. Appl. Phys. Lett. 2013; 102: 243108.
[42] Leitz K, Quentin U, Alexeev I, Schmidt M. Process investigations of optical trap assisted direct-write microsphere near-field nanostructuring. CIRP Annals-Manufacturing Technology 2012; 61: 207–210.

T. A. Klar

8 STED lithography and protein nanoanchors

Abstract: Two-photon lithography (or, more general, multiphoton lithography) is apt to produce three-dimensional structures with feature sizes below the diffraction limit set out by Abbe. This is due to chemical nonlinearities which are intrinsic to polymerization. However, if one wants to write two nanometric structures close together yet prevent those structures from merging, two-photon lithography basically turns out to be bound to the diffraction limit unless some specific tricks are applied, such as the use of "forgetting starters" which require, however, particularly slow scanning speeds. An appealing means of working around this problem is provided by STED lithography, where STimulated Emission is used to Deplete (STED) the polymerization starters in the outer rim of the point spread function, very similar to the way in which it is used in STED microscopy. After reviewing STED microscopy and introducing STED lithography and its current state-of-the-art in terms of minimal structure size (54 nm) and resolution (120 nm), and after touching on photo-optical switching techniques alternative to STED, the following application for biological and physiological research will be outlined. Using STED lithography, it is possible to write nanoanchors for antibodies which carry only one antibody per nanoanchor. This allows proteins to be displayed on a substrate surface in any arbitrary pattern and with utmost control over the surface density. A discussion of some current problems and possible further directions of research will conclude this chapter.

8.1 Introduction

In 1931, Maria Göppert-Mayer proposed that two photons could be simultaneously absorbed in order to excite a molecule from its ground state to the first excited state [1]. However, it took almost 60 years until this effect was utilized by Denk, Strickler, and Webb in fluorescence microscopy in order to achieve axial resolution without confocalization being necessary [2]. The latter feature comes from the fact that the optical transfer function provides a finite value for the axial k-vector in cases of two-photon absorption, unlike the situation in one photon fluorescence microscopy [3]. Shortly after the publication of their landmark paper on two-photon microscopy, Strickler and Webb showed that two-photon excitation of a photopolymer allows high density data storage [4]. In 1997, Maruo et al. from the Kawata group adapted the method for three-dimensional, two-photon-induced polymerization lithography (2PPL) [5]. Meanwhile, 2PPL facilitates writing features with lateral sizes of 90 [6], 80 [7, 8], and 65 nm [9] when pulsed lasers are used for two-photon excitation with wavelengths of 1030, 800, and 520 nm, respectively. Due to a chemical nonlinearity [10], these feature sizes are already below the diffraction limit given by Abbe [11]. We will discuss this below

in more detail. Further, a line width of 50 nm has been achieved by post deposition shrinking [12]. Importantly, the dimensions of isolated structures must not be confused with resolution. The latter is defined by the minimal spacing of two adjacent yet separated structures and is currently in the range of 200 nm (lateral resolution) for 2PPL [13]. This is obviously much larger than the resolution typically achieved in e-beam or ion beam lithography or with far-UV mask-based lithography. Both techniques approach a resolution of 20 nm. However, they show two decisive drawbacks: First, both use high energetic particles or photons which can be tolerated by robust solids such as semiconductor wafers, but are detrimental for biological tissue or soft plastic electronics. Second, they are intrinsically bound to structuring of surfaces, while 2PPL comprises an intrinsic three-dimensional capability. Hence, opportunities for decreasing feature size to, say, 20 nm and increasing resolution to the sub 100 nm range are highly sought after in 2PPL using low energetic visible photons and featuring intrinsic 3D capability.

In 1994, Hell and Wichmann [14] came up with an idea to break the restrictions set to resolution in optical microscopy by Abbe's diffraction limit [11]. They proposed that the resolution in fluorescence microscopy will not be bound to diffraction if one switches off the fluorescence in the outer rim of a diffraction-limited point spread function (PSF) of the excitation beam quick enough so that the fluorophores cannot emit a photon. Depletion after excitation but before emission is actually possible because the average fluorescence lifetime of a typical fluorophore is in the range of 1 nanosecond, which leaves plenty of time to bring the molecule from the excited state down to the ground state [14]. One possibility (but by far not the only one) to inhibit spontaneous emission is depletion of the excited state via stimulated emission. After initial experimental corroboration of the idea, which showed a resolution in all three directions in the range of 100 nm [15, 16], an effective PSF with a lateral width of 8 nm was realized using far field fluorescence STED microscopy [17], a value which was unimaginable 20 years ago. In consequence, Stefan Hell received the Nobel Prize for Chemistry for his achievements in the year 2014. The original method of de-exciting the molecules in the outer rim of the excitation focus, stimulated emission depletion (STED), gave the name to a whole field of sub-Abbe resolution microscopy. Many applications have been shown within the last decade, most of them in the field of nanoscopic physiology and cell biology [18–28], but some applications in materials science were also reported [29–31].

Similar to the further development of two-photon microscopy [2] into 2PPL [4, 5], it was already postulated in the first experimental reports of STED microscopy that a confined effective excitation volume can also be applied to spatially control photochemical reactions on the nanometer scale [15, 16]. STED and STED-inspired 2PPL have been reported experimentally recently [13, 32–37].

8.2 STED microscopy

Before turning to STED lithography, one should briefly recall what is required to build a STED microscope. In the traditional STED configuration (Fig. 8.1 (a)) [16], an excitation laser is required in the UV-Vis range, which matches the excitation spectrum of the fluorophores. Commonly, a pulsed laser in the nano- to femtosecond regime is applied in order to guarantee a temporally defined excitation, although STED microscopy with continuous wave (CW) excitation and CW STED have been reported [38], though with some compromise in resolution. A typical choice for a pulsed excitation laser is the tunable output of an optical parametric oscillator (OPO) with built-in second harmonic generation, or simply a suitable picosecond semiconductor laser [39, 40]. Traditionally, the STED beam stems from a Ti:Sa femtosecond laser. In this case, the STED pulse needs to be stretched to some tens of picoseconds at least in order to achieve effective depletion of the excited singlet state via STED, because a femtosecond pulse would only lead to a 50/50 equal distribution between the effective emission level and a higher vibronic level of the ground state due to reabsorption [41]. Alternatives to Ti:Sa lasers for the STED beam are Raman lasers [42], fiber lasers [40], or even pulsed laser diodes [43]. CW lasers have been used as STED lasers, as well, with some compromise in resolution [38]. Nevertheless, full resolution can be regained by temporal gating of the detection of fluorescence if at least the excitation is pulsed [44, 45].

The excitation pulse must be expanded in a telescope and the transversal mode profile is cleaned (if necessary) by a pinhole in order to illuminate the rear aperture with a plane wave. This is mandatory to achieve the smallest possible diffraction limited excitation-PSF. The mode of the STED laser is cleaned by a pinhole and expanded as well. In order to produce a high-quality donut shaped STED-PSF in the focus, a phase pattern needs to be imprinted on the wave front of the STED beam, which is then Fourier-transformed by the objective lens into a hole-shaped STED-PSF in the focus. When only a lateral improvement of the resolution is desired (specifically if all fluorophores of interest are in one plane only, such as in total internal reflection (TIRF) STED microscopy [46]), the 2π spiral phase mask is superior [19]. When a three-dimensional improvement is desired, an annular phase mask is the choice, as shown in Fig. 8.1 (a) [16]. Instead of these static phase masks where the phase is imprinted onto the wave front of the STED beam via varying optical path length, dynamic phase control using spatial phase modulators has recently been applied in some STED setups [18, 47, 48]. This dynamic phase control bears the advantage that aberrations can be corrected which could otherwise deteriorate the central zero of intensity of the STED-PSF. However, dynamic phase control systems are more complicated to handle and more expensive than static phase masks.

Figure 8.1 (b) shows, as a historic example, the first ever published effective PSF of a three-dimensional STED microscope [16]. A 48 nm bead, doped with the dye LDS 751, was imaged, whereby each forward and backward scanning line was sorted into two different images. While the STED beam was switched off during one scan direction

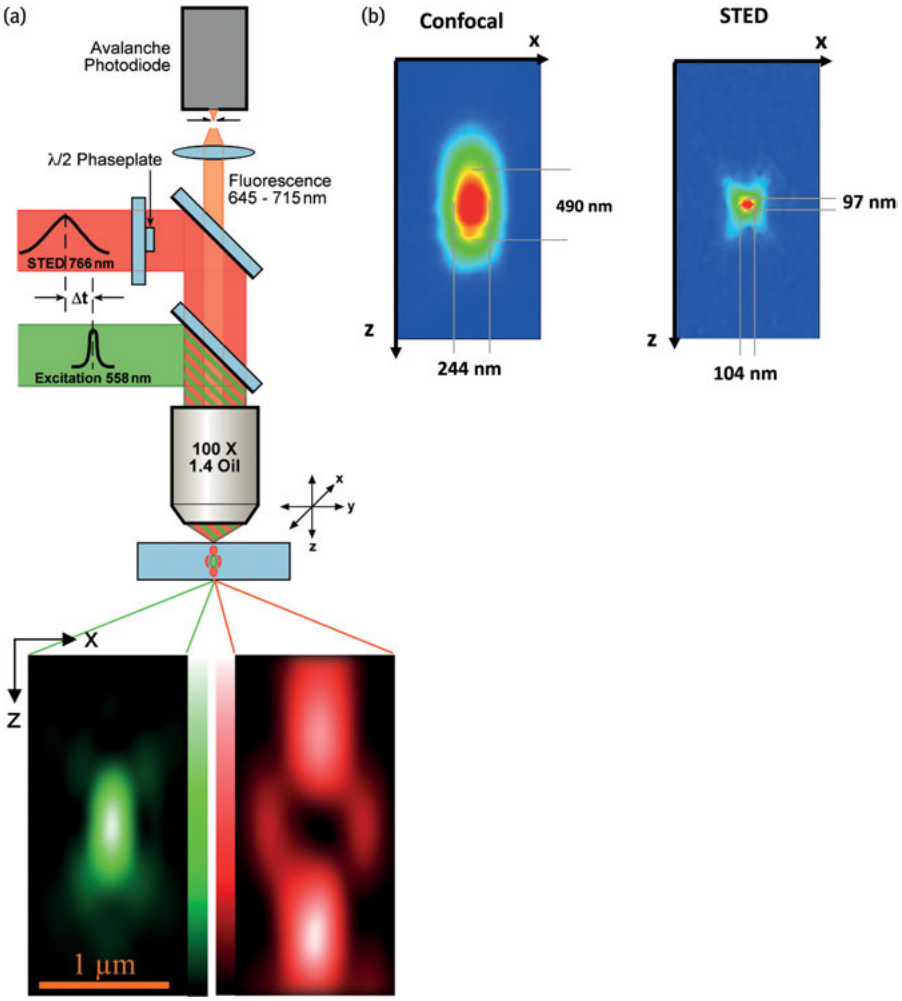

Fig. 8.1: (a) First ever realization of a 3D STED microscope. A normal shaped green PSF excites the fluorophores, while a hole shaped red PSF depletes the fluorophores in the outer rim. The hole shaped STED PSF is realized by an annularly shaped $\lambda/2$ plate in the STED beam path. (b) A dye doped bead imaged in confocal (left) and in STED-confocal mode (right). In 2000, effective STED PSF measured approximately 100 nm in all 3 directions. Meanwhile, sub 10 nm PSFs are realized in STED microscopy. Taken from [16]. Copyright 2000, National Academy of Sciences, USA.

(hence detecting a "classical" confocal image), it was switched on in the other scan direction. This way, both images shown in Fig. 8.1 (b) were taken, line by line, at the same time, excluding bleaching. In those days (around the year 2000), STED microscopy showed an effective PSF of 100 nm in all three directions, which was clearly below the Abbe limit. Due to systematic improvements, modern STED microscopy has now reached sub 10 nm effective PSFs and resolution [17].

8.3 STED lithography

Figure 8.2 (a) shows a typical setup for STED-2PPL lithography. Femtosecond laser pulses of 780 nm are used for multiphoton excitation of the photostarters, and STED is performed via a continuous wave (CW) 532 nm laser. Similar to a STED microscope, both beams are expanded by a telescope and pinholes in the foci of the telescopes are used to clean the transversal modes. A phase plate is used to produce the donut shaped STED beam. If only a mere lateral improvement of feature sizes and resolution is desired, a 2π phase spiral is used as a phase plate (PP) and a $\lambda/4$ wave plate is applied to match the helicity of the polarization to the orientation of the phase spiral. In order to start with the utmost resolution already without STED, a high-end alpha-Plan Apochromat, 100×, NA = 1.46 oil immersion lens is applied. Stage scanning is performed via a capacitively coupled three axes piezo stage which is mounted on top of a mechanical three axes micrometer driven stage. An avalanche photo diode (APD) is used to monitor the (weak) back-reflected beams transmitting the two dichroic mirrors before the objective lens in order to adjust and properly overlap the two beams.

A 40/60 mixture of the acrylates pentaerythritol tetraacrylate (PETTA) and pentaerythritol triacrylate (PETA), including 300–400 ppm monomethyl ether hydroquinone, was used as a photoresist [37]. 0.25 wt % of 7-Diethylamino-3-thenoylcoumarin (DETC) was added as a photosensitive starter of radical polymerization. It has recently been shown that at least one more photon seems to be required to start radical polymerization when DETC is used as a starter, although two 780 nm photons are needed to excite fluorescence of DETC [49]. Despite this fact of an effective multiphoton excitation of DETC, the more common term "2PPL" will be used instead of "MPPL" as an acronym for multiphoton polymerization. Whatever the excitation mechanism might be, DETC can be readily depleted by 532 nm photons from a CW laser via STED [50]. The wavelength of the depleting STED laser is in the red wing of the fluorescence emission spectrum of DETC as shown in Fig. 8.2 (b). Figure 8.2 (c) and (d) show the lateral point spread functions of the multiphoton excitation beam and the STED beam, respectively, imaged by back reflection from a gold nanoparticle. Figure 8.2 (e) shows a line written by 2PPL only (without STED). Due to an intrinsic chemical nonlinearity [10], this line already shows a line width of 87 nm, below the diffraction limit. Applying the STED beam in addition, the line width shrinks to 54 nm, as shown in the SEM image of Fig. 8.2 (f).

As we will discuss in more detail in Section 8.5, the feature size (in this case: line width) must not be confused with resolution. As shown in Fig. 8.2 (e), it is easily possible to write individual lines with sub-Abbe line widths using 2PPL, however, to the best of our knowledge, a true resolution below the Abbe diffraction limit is not expected using 2PPL unless a photoresist is "completely forgetting" as outlined by Fischer and Wegener [51]. In order to determine the lateral resolution of STED-2PPL, double lines with a nominal distance of δ were written on a glass substrate. The AFM images of such double lines are shown in Fig. 8.3 [37]. One clearly sees that double lines with

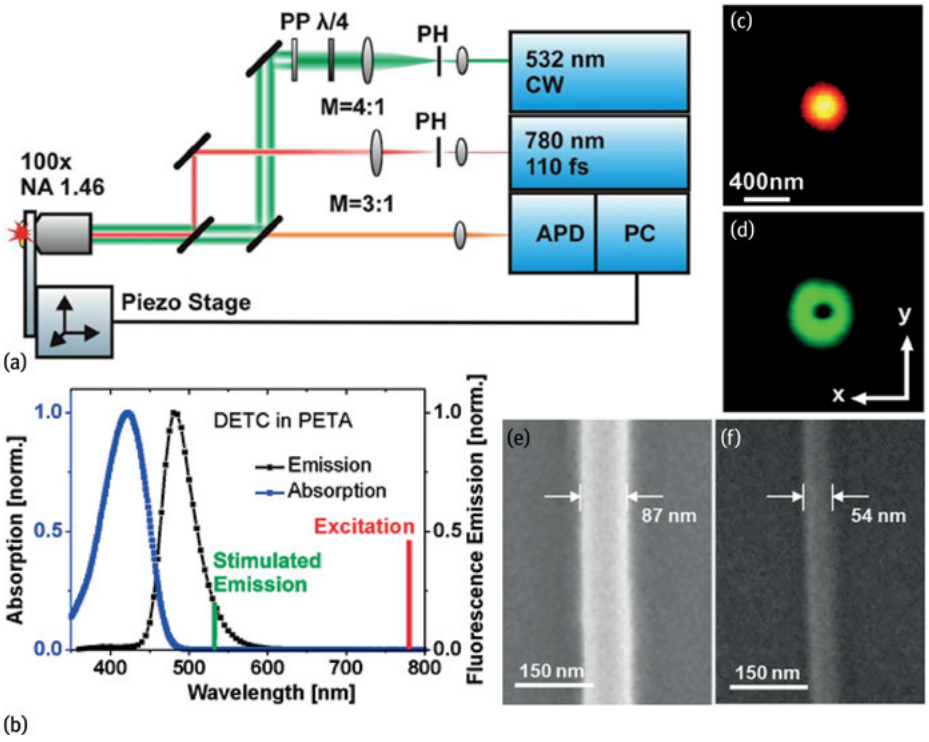

Fig. 8.2: (a) Setup for STED-lithography. Two-photon excitation at 780 nm and depletion at 532 nm. PH: pinholes for mode purification; PP: 2π spiral phase plate to create a donut beam; objective lens: 100×, NA = 1.46; APD: avalanche photodiode. (b) Spectra of the photoinitiator DETC in PETA. (c) Measured excitation PSF and (d) depletion PSF, lateral (*x*-, *y*-) cross-sections in the focal plane (measured via back-reflection from a gold nanoparticle, diameter 50 nm). (e), (f) SEM images of solitary polymerized lines written with (e) ordinary 2PPL, and (f) STED-2PPL. Taken from [37] with permission. Copyright 2013 The Optical Society of America.

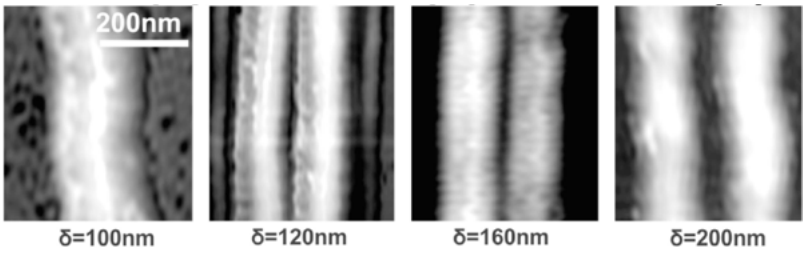

Fig. 8.3: AFM images of double lines, written at nominal distances δ of 100, 120, 160, and 200 nm. Adjacent lines with 120 nm line distance are clearly resolved. Reprinted with permission from [37]. Copyright 2013 The Optical Society of America.

distances down to $\delta = 120$ nm can be written and appear as double lines with clear spacing in between, while the double lines with a nominal distance of $\delta = 100$ nm have merged into one thick line. It was therefore concluded in 2013 that the lateral resolution of STED lithography was 120 nm [37]. This is clearly below the diffraction limit considering the writing wavelength of 780 nm and the depleting wavelength of 532 nm, however, one should think about further improvements. Nevertheless, there is justified hope that resolution in STED lithography will further improve, in the same way that resolution in STED microscopy has improved from the 100 nm range in its earliest experimental reports [15, 16] down to below 10 nm [17].

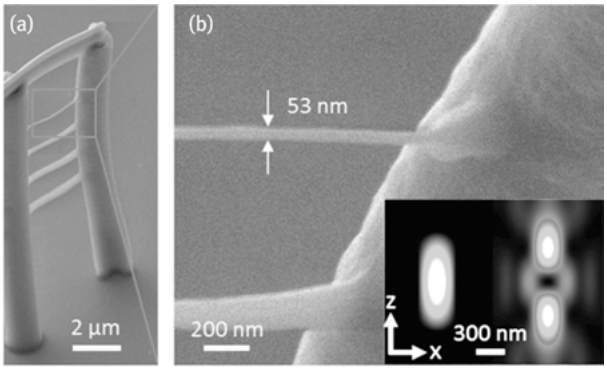

Fig. 8.4: (a) Scanning electron microscopy (SEM) image showing two vertical poles and a horizontal bar on top written with 2PPL to provide a frame for STED-2PPL written horizontal rungs using different STED-intensities. (b) Close-up of the rung written with 4.24 mW excitation and 6.27 mW STED power, showing a thickness of 53 nm. Inset: calculated ordinary shaped two-photon excitation PSF (780 nm) and hole shaped STED PSF (532 nm). From [52]; The Royal Swedish Academy of Sciences. Reproduced by permission of IOP Publishing. All rights reserved.

In order to achieve a three-dimensionally improved structure size with STED, an annular phase mask needs to be applied. This creates a "bottle" shaped STED PSF, as shown in the inset of Fig. 8.4 [52]. Again, a 40/60 mixture of PETTA and PETA, including 300–400 ppm monomethyl ether hydroquinone was used as a photoresist, and 0.25 % of DETC was added as a photosensitive starter. Figure 8.4 (a) shows two vertical poles and one horizontal bar on top written with 2PPL to provide a frame for STED-2PPL structures. Between the two poles, it was intended to write five thin rungs applying STED-intensities of 0 to 8.4 mW in steps of 2.1 mW. The diameters of the rungs continuously decrease with increasing STED power from bottom to top for the first four rungs. The fifth rung did not appear, possibly because the STED power became too large and/or because the zero in the center of the hole-shaped STED-PSF became distorted when the focus was scanned deeper into the resist. Figure 8.4 (b) shows a close-up of the fourth rung, which displays a thickness of only 53 nm. Assuming a

circular cross-section of the rung, it can be concluded that the axial feature size is also in the range of 53 nm. This is clearly below the diffraction limit, when using 780 nm for two-photon excitation and 532 nm for STED.

8.4 STED related lithography

Figure 8.5 compares several methods of improving resolution in 2PPL via optical switching. The upper panel shows the "true" STED method, where an intense STED beam is spectrally tuned to the red side of the fluorescence emission line in order to quench the excited molecules of the photostarter back down to the ground state before they undergo intersystem crossing (ISC). Hence, the population of the triplet system is avoided and the triggering of the polymerization consequently hindered as this triggering is supposed to be initiated by molecules in the triplet state (in the case of radical polymerization). The middle panel of Fig. 8.5 shows an alternative: one could actually allow for ISC if the radical polymerization is hindered by a further excitation within the triplet system, the so-called up-conversion quenching [53]. This is effectively the case if the polymerization starter ITX is used [50, 54], or if the starter DETC is quenched by yellow or red light [54] (instead of 532 nm which predominantly causes STED in the case of DETC [50]). Nevertheless, the exact mechanism is not yet fully understood. For instance, it could as well be the case that an excited state absorption within the singlet system takes place and a higher lying singlet state S_n is not effective for polymerization. It is, however, probable that this kind of excited state absorption is responsible for the early observation of sub-Abbe sized features using malachite green carbinol base as photostarter [33, 55]. In this case, volume elements (voxels) axially confined down to 40 nm have been reported, but without lateral improvement of the feature size and resolution was not quantified. As the triplet states are rather long-lived [55], it has been speculated that this technique is less suitable for fast patterning using a donut shaped depletion PSF [51].

The lower panel in Fig. 8.5 shows another idea of how to improve structure size and resolution in 2PPL lithography. In this technique, the photostarter is not manipulated by a second laser beam. Instead, a second type of photoactivatable molecule is mixed into the resist which, once photo-excited by another wavelength than that used for the starter, may either de-excite the starter molecules directly or stop chain growth of the polymer in the outer rim of the starter-PSF. In a radical polymerization resist, a photoactivatable radical scavenger would be suitable. Two groups claim to have experimentally achieved sub-Abbe feature size and resolution based on this start/stop technique [32, 35, 56]. However, these publications have recently been deeply questioned [57] by some of the authors who were also in the original claims. They raised deep doubts on the effectiveness of photo-excited stoppers which ideally should only be present in the donut shaped ring around the excitation focus but not within the hole of the STED PSF. The authors of [57], however, argued that the stoppers, activated in

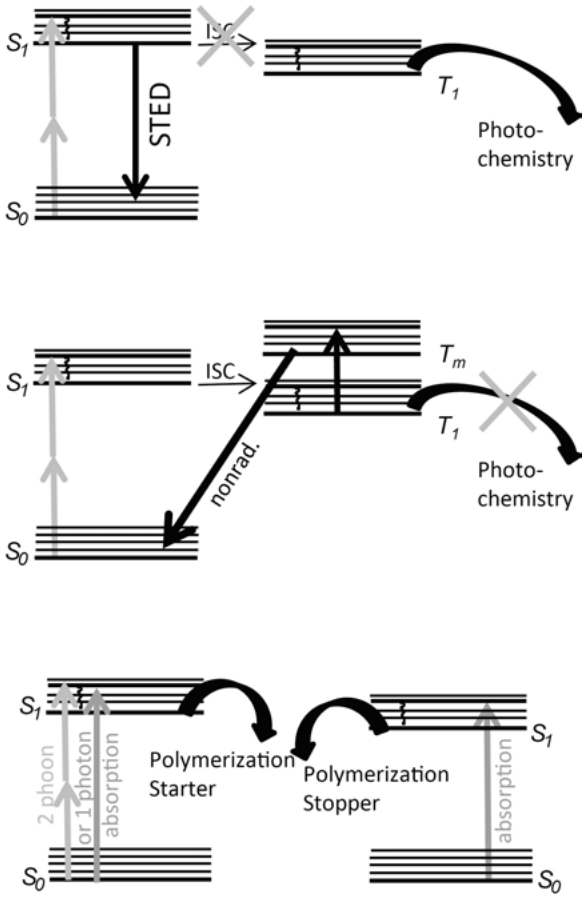

Fig. 8.5: Photo switching techniques in 2PPL. Upper panel: "True STED". A STED beam deactivates the S1 level, thus preventing intersystem crossing (ISC) and hence population of the triplet state, from which radical polymerization is started. Middle: ISC is allowed, but a second (red) laser beam excites the fluorophore into some higher triplet state from which nonradiative de-excitation is favored. Bottom: One- or two-photon excitation excites a photostarter. A second type of molecule which inhibits polymerization once excited by another wavelength is also present in the resist.

the donut, diffuse into the hole of the STED PSF very quickly, in fact in a shorter time than it is supposed to take for the polymer to solidify. Nevertheless, very recent work shows that the voxels solidify within less than a millisecond [58]. This, in turn, questions the basic assumption of a slow (1 second) time scale for solidification assumed by the authors who scrutinized the start/stop technique. More research is definitely needed in order to find out why, indeed, sub-Abbe feature sizes and resolutions could be reported in [32, 35, 56].

Tab. 8.1: Overview of STED and STED-inspired 2PPL results for structure size and resolution. Note that the results for "starter & stopper" are currently under discussion [57, 58].

Technique	Group	Structure Size	Resolution
true STED	Wegener[1]	170 nm axial	175 nm lateral 375 nm axial
	Klar[2]	55 nm lateral 53 nm axial[8]	120 nm lateral
excited state absorption	Fourkas[3]	40 nm axial	—
	Wegener[4]	65 nm lateral	—
polymer. starter & stopper	Scott[5]	110 nm lateral	—
	Gu[6,7]	10 nm lat. (2 Phot. Start) 40 nm lat. (1 Phot. Start)	52 nm lateral 80 nm axial (2 Phot. Start)

1 Opt. Mat. Express, 1, 614 (2011)
2 Opt. Exp. 21, 10831 (2013)
3 Science 324, 910 (2009)
4 Adv. Mat. 22, 3578 (2010)
5 Science 324, 913 (2009)
6 Nature Comm. 4, 2061 (2013)
7 Opt. Exp. 19, 19486 (2011)
8 Phys. Scr., T162, 014049 (2014)

An overview of the values of feature sizes and resolutions so far achieved is given in Tab. 8.1. The start/stop technique using two-photon absorption to excite the starter and one-photon absorption to excite the stopper seems to be superior; however, as mentioned above, these results need to be taken with care.

8.5 Resolution in microscopy and lithography

Let us briefly review the terms "localization" and "resolution" in microscopy and compare them to "feature size" and "resolution" in two-photon lithography. See Fig. 8.6 for some illustrations to help distinguish these terms. Suppose the observer has prior knowledge that only one observable entity (such as a single fluorophore) is located within the PSF. It can then be located with infinite precision, provided the total number N_{Phot} of detected photons is infinite, because the localization accuracy of a PSF is proportional to $1/\sqrt{N_{\mathrm{Phot}}}$ (Fig. 8.6, upper row left). This fact is used in stochastically blinking microscopy techniques such as PALM, STORM, dSTORM, and the like [59–64]. In contrast to localization, resolution deals with the question of whether two objects with identical physical properties (same emission wavelength, same or random polarization etc.) can be distinguished. Two typical situations are frequently addressed, the Rayleigh criterion[65], with a pronounced minimum in the intensity distribution of the image (Fig. 8.6 upper row right), or the Sparrow criterion[66], where the minimum is just about to appear (Fig. 8.6 upper row middle).

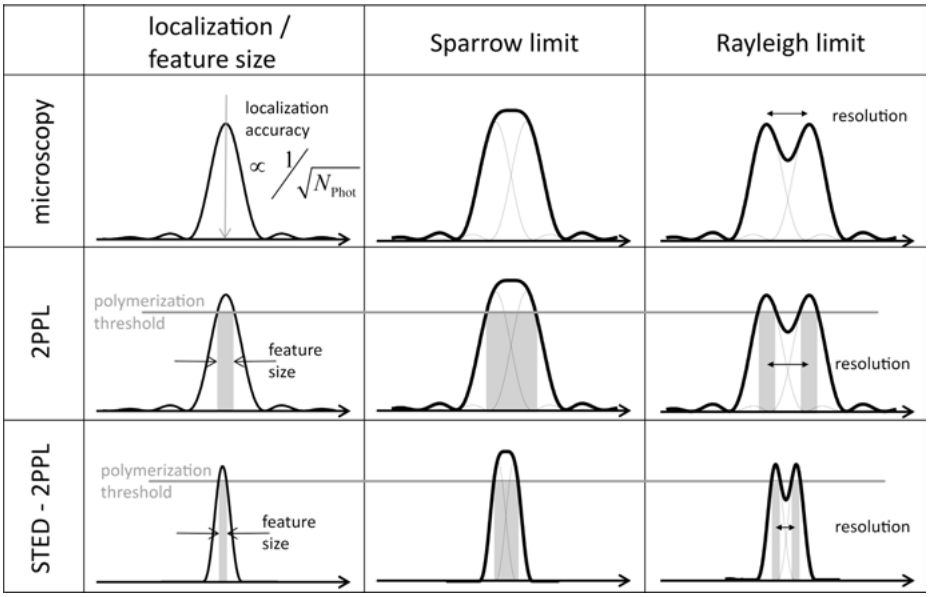

Fig. 8.6: Localization, feature size and resolution in microscopy and lithography. Upper row: if just one entity (e.g. a single dye molecule) is imaged, it can in principle be localized exactly. If two entities are separated according to the Sparrow limit, they can just not be resolved any more. In the Rayleigh limit, a clear dip is visible in the image. Middle row: in 2PPL, a certain threshold of polymerization (say, 80 %) needs to be overcome in order to crosslink the resist to such an extent that it withstands washing. Only where illumination exceeds this threshold will a feature appear showing a half width smaller than the FWHM of the PSF. In the Sparrow limit, only a thick line will polymerize. In the Rayleigh limit, two lines will appear with an unpolymerized region in between. Resolution in 2PPL will hence be similar to that of two-photon microscopy. Bottom row: STED-2PPL starts with a substantially narrower effective PSF, leading to narrower feature size. The full power of STED-2PPL is achieved in resolution where, in the Rayleigh limit, sub-Abbe resolution is possible.

In the case of two-photon lithography (2PPL), the size of a solitary feature plays a similar role to that of the localization accuracy in microscopy; compare the left column in Fig. 8.6, upper and middle panels. “Solitary” means that the next neighboring features are well separated by several wavelengths at least. An infinitely small feature size could in principle be attained if the threshold of polymerization (gray horizontal line) is close to the peak of the PSF [10, 67]. The polymerization threshold is defined as the illumination intensity which causes just enough polymerization (say 80 %), such that the written structure withstands the development (washing) steps. Indeed, this resembles a strong chemical type of nonlinearity because of the binary distinction between areas polymerized sufficiently to withstand washing and the minor exposed areas which do not withstand washing. Strictly speaking, this is a “yes or no” function, the most nonlinear function possible and clearly, this is apt to provide sub-Abbe feature sizes. In reality, however, an infinitely thin feature size is hard to reach, because

this would require pushing the polymerization threshold to the upmost tip of the PSF, or in turn lowering the illumination intensity such that it just exceeds the polymerization threshold. In practice, a solitary line written in such conditions would not be continuous if the threshold was pushed too close to the limit of the PSF [51]. This can be easily understood because both the top of the PSF and the polymerization threshold fluctuate. The intensity of the PSF fluctuates because, for instance, the excitation laser fluctuates or because there are differently absorbing species between the objective lens and the focus while scanning. The polymerization threshold fluctuates as well because it depends, for instance, on the local density of polymerization starters, which in practice will show spatial inhomogeneity. For these reasons, feature sizes below 100 nm are difficult to achieve using 2PPL.

But let's now turn to the term "resolution" in 2PPL: in the case of the Sparrow criterion (Fig. 8.6, middle row, central panel), the polymerized structures are broader compared to the solitary lines (assuming an "non-forgetting" resist [51]). When a minimum develops in the sum of both PSFs by further separating them, e.g. up to the Rayleigh limit (Fig. 8.6, middle row, right), it becomes possible for the polymerization threshold to lie in between the two maxima and the central minimum of the summed illumination intensity. Both polymerized features (grey shaded areas) are now fully separated due to the binary nonlinearity of polymerization while the optical image in microscopy would not show a zero of intensity in the center (Fig. 8.6 upper row).

The lower row of Fig. 8.6 depicts the situation of STED–assisted 2PPL. In comparison to ordinary 2PPL, STED-2PPL shows a substantially narrowed effective PSF. Obviously, the sharpened effective PSF leads to an improvement of the minimal feature size (Fig. 8.6, lowest row, left), as compared to the feature size achievable by 2PPL. The reason is that due to the sharper effective PSF in the case of STED-2PPL, the requirement to push the polymerization threshold to the upmost tip of the PSF is relaxed. Mathematically speaking, the bending or the second derivative of the effective PSF of STED-2PPL is larger. Finally, STED-2PPL allows for true sub-Abbe resolution of two neighboring features as depicted in the lower right panel of Fig. 8.6.

8.6 Nanoanchors for single antibody display

We have used STED-2PPL in order to write arrays for proteins as a first application in biological and physiological research. This is a first step towards templates for proteins which could mimic the native surroundings and stimulate specific cell responses. Such templates may help study cellular dynamics and interactions, though ex vivo, in an environment similar to the natural habitat [68–70]. For instance, micropatterned substrates have been used to investigate cell proliferation, differentiation, and migration [68, 71–74]. Nanoconfined, specific ligand display serves as an important tool for such studies [75–77]. Templates or scaffolds have been written for proteins using different techniques. Nanoparticle self-assembly [69, 70, 78], dip-pen nanolitho-

graphy [79–81], nanoimprint lithography [82], or electron beam lithography [83, 84] were used to construct two-dimensional nanostructures, which serve as binding sites for proteins. Although all these techniques have their advantages, they also have distinct limitations, for example high cost (e-beam) or restrictions in structure geometry, specifically in self-assembled structures where only periodic patterns are possible, and all of them are hardly extendable into the third dimension. In contrast, 2PPL allows free-form patterning of docking sites for proteins even in 3D. And of course, STED is apt to reduce structure size and enhance resolution also in the case of protein scaffolds as outlined below.

In a pilot study we used a (80/20) mix of the two acrylate monomers SR499 (Sartomer, Colombes Cedex, France) and PETA, including 300–400 ppm monomethyl ether hydroquinone, and again added 0.25 wt % of DETC as a photosensitive starter [85]. Two-photon excitation powers of 4.85 mW and depletion powers of 25 mW (entering the objective lens) were applied to write the smallest features.

Figure 8.7 summarizes the results [85]. We wrote periodic arrays of 32×32 patches with a spacing of 5 µm between the patches, some written with low resolution using conventional 2PP lithography and some written with high resolution using STED-2PP lithography. The protein-adherent acrylate patches were written on glass slides which were passivated with PEG-silan prior to writing. This ensured that the substrate was inert against protein adhesion while the acrylate patches (due to the content of SR499) adhered proteins. Figure 8.7 (a) shows, from left to right, an SEM image of one such array, a fluorescence image of another array in the green channel of a fluorescence microscope, and an image taken with the red channel after incubation of the patches with anti-CD59 antibodies (αCD59), stained with Atto655. The patches are visible in the green channel because the photostarter DETC is a coumarin dye molecule and hence the patches show auto-fluorescence. However, the patches are invisible in the red channel prior to incubation with the stained antibodies. Hence, auto-fluorescence can be used to find the arrays in the fluorescence microscope quickly, while the red channel can be used to monitor protein loading.

The sketch on the left of Fig. 8.7 (b) shows two situations whereby the larger patches, written with ordinary 2PPL carry several αCD59, while the patches written by STED-2PPL are supposed to carry only one αCD59 each. The fluorescence strength per patch, averaged over one array and normalized to the fluorescence strength of single αCD59 antibodies, shows quick saturation after only a few incubation steps (right graph in Fig. 8.7 (b)). In the case of the 2PPL written patches, an average of 8.28 ± 1.22 antibodies per 2PP fabricated patch is found (blue line). In contrast, the STED-2PPL patches carry on average only 1.16 ± 0.11 antibodies (red line) [85]. Hence, the STED-2PPL patches were termed nanoanchors.

As a further proof that there was only one antibody per nanoanchor in most cases, we performed dSTORM measurements [86]. Figure 8.7 (c) shows two nanoanchors, one of which displays only one fluorescing spot (with 26 nm localization diameter), while the other nanoanchor shows two such spots. On approx. 80 % of the dots we

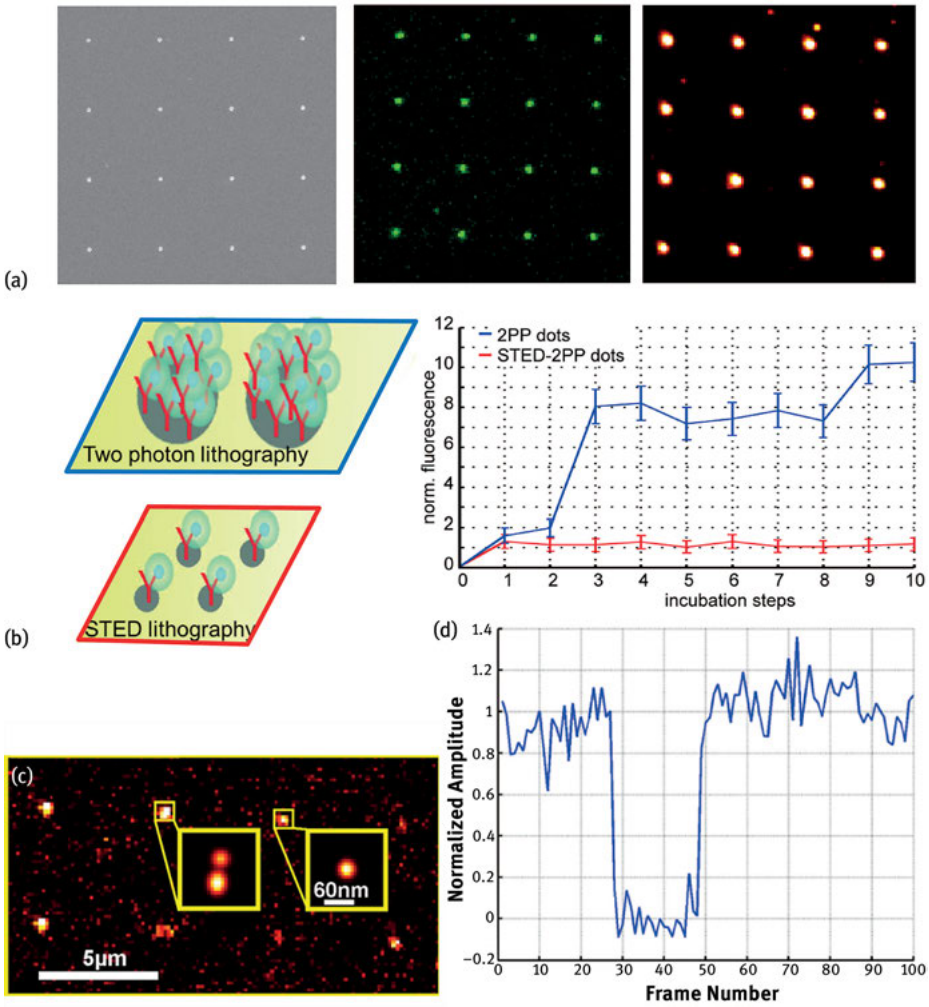

Fig. 8.7: (a) Rectangular array of STED-2PPL fabricated nanoanchors, spaced 5 µm apart. Left: SEM image; middle: auto-fluorescence of the DETC polymerization starter in the green channel of a fluorescence microscope; right: Atto655 fluorescence of the labeled IgG antibodies attached to the nanoanchors, imaged by the red channel of a fluorescence microscope. (b) Left: sketch of many IgGs on 2PPL-written islands and single IgGs on STED-2PPL-written nanoanchors. Right: Fluorescence signal per island, normalized to the fluorescence strength of a single IgG as a function of incubation steps. 2PPL-written islands carry 8 to 9 IgG, while STED-2PPL written nanoanchors carry only 1.2 IgGs on average. (c) Zoomed out are two typical dSTORM images of nanoanchors. In about 20 % of all cases, two fluorescence spots are detected, in about 80 % of all cases, only a single localized spot is detected. (d) On/off blinking of a spot containing only one IgG. Parts (b)–(d) reprinted and adapted with permission from [85]. Copyright 2013 American Chemical Society.

observed single fluorescent spots. Still, as the localization accuracy was 26 nm, several fluorophores could be hidden inside this spot. However, on-off blinking experiments showed unambiguously that only single fluorophores were present in most cases (Fig. 8.7 (d)). We further know [85], that more than 90 % of the antibodies are loaded with fluorophores, so we can safely conclude that about 80 % of the nanoanchors are loaded with only one antibody. Additional evidence was achieved by applying a probability density fit algorithm [87, 88] estimating the average number of fluorescing species per patch. Details can be found in Wiesbauer et al. [85].

8.7 Conclusion/Further directions

Since its proposition 20 years ago, STED nanoscopy has become a routine technique in bio-imaging. A multitude of physiological questions has been addressed using STED microscopy, specifically in the fields of neurophysiology and the physiology of membrane-based proteins, and the Nobel Prize in Chemistry was co-awarded for these achievements in 2014. One can safely say that the diffraction limit implied by Abbe lost its significance in fluorescence microscopy and a resolution below 10 nm has been achieved using visible light. The transformation of STED microscopy toward STED lithography has been illustrated in this chapter. Similar to STED-microscopy, STED is not the only way to deplete photostarters of polymerization. In the family of STED-related microscopy, stimulated emission, ground state depletion, optical activation of fluorescence-quenchers, and photochromic switching are techniques which can be utilized to force dye molecules into an off-state. In STED inspired lithography, stimulated emission, up-conversion from excited states or, potentially, optically activatable polymerization-stoppers can be applied. STED nanoscopy has meanwhile reached sub 10 nm resolution. Until now, the resolution in STED- and STED-inspired-lithography is an order of magnitude worse, though clearly below the diffraction limit. However, it should be recognized that STED microscopy took 10 years to come down from 100 nm resolution in the early experimental reports to sub 10 nm resolution. STED lithography and its relatives are only 4 years old and should still be considered in its infancy. Above, one field of applications, producing nanoscale patterns for protein adhesion down to the single protein level [85], has been outlined.

Other applications, shown by the Wegener group, are in the field of photonic devices: photonic crystals with stop bands in the visible range [13, 89, 90], including polarization sensitive devices [91], and a carpet cloak [36, 92]. Further, the Min Gu group reported ultra-high density data storage [93, 94].

Some challenges need to be tackled in the future. In order to push resolution further down in STED and STED related lithography, materials need to be discovered which allow for nanoscale structuring on the one hand but are stiff enough to withstand the washing process on the other. Most importantly, photoresists must not shrink during the washing or drying process. Only negative tone resists have

been used in STED- and STED-inspired lithography so far. A positive tone resist will certainly open new fields of applications. Further, STED lithography has merely been restricted to radical polymerization. Finding alternative classes of polymerization and alternative polymerization starters is top on the agenda for further development of STED lithography.

Acknowledgments

At this point I would like to cordially thank my PhD supervisor, Stefan Hell, who proposed to me the topic of STED microscopy in 1997, and all the colleagues from those days in Göttingen with whom I had the pleasure of collaborating while STED was in its infancy.

The more recent work on STED lithography would not have been possible without the help of several colleagues at TU Ilmenau until 2010 and at the Johannes Kepler University in Linz during the last four years. Specifically, I would like to thank (in alphabetical order) Bianca Buchegger, Bernhard Fragner, Habed Habibzadeh, Florian Hartmann, Johannes Heitz, Jaroslaw Jacak, Julia Katzmann, Alois Mühlbachler, Alfred Nimmervoll, Heidi Piglmayer-Brezina, Kurt Schilcher, Moritz Wiesbauer, Clemens Wolfesberger, and Richard Wollhofen. The work would also not have been possible without the financial support of the Deutsche Forschungsgemeinschaft (DFG) via grant KL1432/5-1 within the priority programme SPP 1327. Recent support has been provided by the Austrian Science Fund (FWF) via grant number P 26461-N20.

References

[1] Göppert-Mayer M. Über Elementarakte mit zwei Quantensprüngen. Annalen der Physik 1931, 401(3), 273–94.

[2] Denk W, Strickler JH, Webb WW. Two-photon laser scanning fluorescence microscopy. Science 1990, 248(4951), 73–76.

[3] Gu M. Principles of three dimensional imaging in confocal microscopes. Singapore, World Scientific Publishing Co. 1996.

[4] Strickler JH, Webb WW. Three-dimensional optical data storage in refractive media by two-photon point excitation. Optics Letters 1991, 16(22), 1780–1782.

[5] Maruo S, Nakamura O, Kawata S. Three-dimensional microfabrication with two-photon-absorbed photopolymerization. Optics Letters 1997, 22(2), 132–134.

[6] Burmeister F, Steenhusen S, Houbertz R, Zeitner UD, Nolte S, Tünnermann A. Materials and technologies for fabrication of three-dimensional microstructures with sub-100 nm feature sizes by two-photon polymerization. Journal of Laser Applications 2012, 24(4), 042014.

[7] Xing JF, Dong XZ, Chen WQ, Duan XM, Takeyasu N, Tanaka T, *et al.* Improving spatial resolution of two-photon microfabrication by using photoinitiator with high initiating efficiency. Applied Physics Letters 2007, 90(13), 131106.

[8] Ferreras Paz V, Emons M, Obata K, Ovsianikov A, Peterhänsel S, Frenner K, *et al.* Development of functional sub-100nm structures with 3D two-photon polymerization technique and optical methods for characterization. Journal of Laser Applications 2012, 24(4), 042004.
[9] Haske W, Chen VW, Hales JM, Dong WT, Barlow S, Marder SR, *et al.* 65 nm feature sizes using visible wavelength 3-D multiphoton lithography. Optics Express 2007, 15(6), 3426–3436.
[10] Kawata S, Sun HB, Tanaka T, Takada K. Finer features for functional microdevices. Nature 2001, 412(6848), 697–698.
[11] Abbe E. Beiträge zur Theorie des Mikroskops und der mikroskopischen Wahrnehmung. Archiv für Mikroskopische Anatomie 1873, 9, 413–468.
[12] Dong XZ, Zhao ZS, Duan XM. Improving spatial resolution and reducing aspect ratio in multi-photon polymerization nanofabrication. Applied Physics Letters 2008, 92(9), 091113.
[13] Fischer J, Wegener M. Three-dimensional direct laser writing inspired by stimulated-emission-depletion microscopy. Optical Materials Express 2011, 1(4), 614–624.
[14] Hell SW, Wichmann J. Breaking the diffraction resolution limit by stimulated emission: stimulated-emission-depletion fluorescence microscopy. Optics Letters 1994, 19(11), 780–782.
[15] Klar TA, Hell SW. Subdiffraction resolution in far-field fluorescence microscopy. Optics Letters 1999, 24(14), 954–956.
[16] Klar TA, Jakobs S, Dyba M, Egner A, Hell SW. Fluorescence microscopy with diffraction resolution barrier broken by stimulated emission. Proceedings of the National Academy of Sciences of the United States of America 2000, 97(15), 8206–8210.
[17] Rittweger E, Han KY, Irvine SE, Eggeling C, Hell SW. STED microscopy reveals crystal colour centres with nanometric resolution. Nature Photonics 2009, 3(3), 144–147.
[18] Willig KI, Kellner RR, Medda R, Hein B, Jakobs S, Hell SW. Nanoscale resolution in GFP-based microscopy. Nature Methods 2006, 3(9), 721–723.
[19] Willig KI, Rizzoli SO, Westphal V, Jahn R, Hell SW. STED microscopy reveals that synaptotagmin remains clustered after synaptic vesicle exocytosis. Nature 2006, 440(7086), 935–939.
[20] Kittel RJ, Wichmann C, Rasse TM, Fouquet W, Schmidt M, Schmid A, *et al.* Bruchpilot Promotes Active Zone Assembly, Ca^{2+} Channel Clustering, and Vesicle Release Science 2006, 312(5776), 1051–1054.
[21] Sieber JJ, Willig KI, Kutzner C, Gerding-Reimers C, Harke B, Donnert G, *et al.* Anatomy and Dynamics of a Supramolecular Membrane Protein Cluster Science 2007, 317(5841), 1072–1076.
[22] Westphal V, Rizzoli SO, Lauterbach MA, Kamin D, Jahn R, Hell SW. Video-Rate Far-Field Optical Nanoscopy Dissects Synaptic Vesicle Movement. Science 2008, 320(5873), 246–249.
[23] Eggeling C, Ringemann C, Medda R, Schwarzmann G, Sandhoff K, Polyakova S, *et al.* Direct observation of the nanoscale dynamics of membrane lipids in a living cell. Nature 2009, 457(7233), 1159–1163.
[24] Pellett PA, Sun XL, Gould TJ, Rothman JE, Xu MQ, Correa IR, Jr., *et al.* Two-color STED microscopy in living cells. Biomedical Optics Express 2011, 2(8), 2364–2371.
[25] van den Bogaart G, Meyenberg K, Risselada HJ, Amin H, Willig KI, Hubrich BE, *et al.* Membrane protein sequestering by ionic protein–lipid interactions. Nature 2011, 479(7374), 552–525.
[26] Liu KSY, Siebert M, Mertel S, Knoche E, Wegener S, Wichmann C, *et al.* RIM-Binding Protein, a Central Part of the Active Zone, Is Essential for Neurotransmitter Release. Science 2011, 334(6062), 1565–1569.
[27] Berning S, Willig KI, Steffens H, Dibaj P, Hell SW. Nanoscopy in a Living Mouse Brain. Science 2012, 335(6068), 551.
[28] Chojnacki J, Staudt T, Glass B, Bingen P, Engelhardt J, Anders M, *et al.* Maturation-Dependent HIV-1 Surface Protein Redistribution Revealed by Fluorescence Nanoscopy. Science 2012, 338(6106), 524–528.

[29] Westphal V, Seeger J, Salditt T, Hell SW. Stimulated emission depletion microscopy on lithographic nanostructures. Journal of Physics B 2005, 38(9), S695-S705.
[30] Harke B, Ullal CK, Keller J, Hell SW. Three-dimensional nanoscopy of colloidal crystals. Nano Letters 2008, 8(5), 1309–1313.
[31] Friedemann K, Turshatov A, Landfester K, Crespy D. Characterization via Two-Color STED Microscopy of Nanostructured Materials Synthesized by Colloid Electrospinning. Langmuir 2011, 27(11), 7132–7139.
[32] Scott TF, Kowalski BA, Sullivan AC, Bowman CN, McLeod RR. Two-Color Single-Photon Photoinitiation and Photoinhibition for Subdiffraction Photolithography. Science 2009, 324(5929), 913–917.
[33] Li L, Gattass RR, Gershgoren E, Hwang H, Fourkas JT. Achieving $\lambda/20$ Resolution by One-Color Initiation and Deactivation of Polymerization. Science 2009, 324(5929), 910–913.
[34] Fischer J, von Freymann G, Wegener M. The Materials Challenge in Diffraction-Unlimited Direct-Laser-Writing Optical Lithography. Advanced Materials 2010, 22(32), 3578–3582.
[35] Cao YY, Gan Z, Jia B, Evans RA, Gu M. High-photosensitive resin for super-resolution direct-laser-writing based on photoinhibited polymerization. Optics Express 2011, 19(20), 19486–19494.
[36] Fischer J, Ergin T, Wegener M. Three-dimensional polarization-independent visible-frequency carpet invisibility cloak. Optics Letters 2011, 36(11), 2059–2061.
[37] Wollhofen R, Katzmann J, Hrelescu C, Jacak J, Klar TA. 120 nm resolution and 55 nm structure size in STED-lithography. Optics Express 2013, 21(9), 10831–10840.
[38] Willig KI, Harke B, Medda R, Hell SW. STED microscopy with continuous wave beams. Nature Methods 2007, 4(11), 915–918.
[39] Han KY, Willig KI, Rittweger E, Jelezko F, Eggeling C, Hell SW. Three-Dimensional Stimulated Emission Depletion Microscopy of Nitrogen-Vacancy Centers in Diamond Using Continuous-Wave Light. Nano Letters 2009, 9(9), 3323–3329.
[40] Göttfert F, Wurm CA, Mueller V, Berning S, Cordes VC, Honigmann A, *et al.* Coaligned Dual-Channel STED Nanoscopy and Molecular Diffusion Analysis at 20 nm Resolution. Biophysical Journal 2013, 105(1), L01-L3.
[41] Schrader M, Meinecke F, Bahlmann K, Kroug M, Cremer C, Soini E, *et al.* Monitoring the excited state of a fluorophore in a microscope by stimulated emission. Bioimaging 1995, 3(4), 147–153.
[42] Rankin BR, Kellner RR, Hell SW. Stimulated-emission-depletion microscopy with a multicolor stimulated-Raman-scattering light source. Optics Letters 2008, 33(21), 2491–2493.
[43] Schrof S, Staudt T, Rittweger E, Wittenmayer N, Dresbach T, Engelhardt J, *et al.* STED nanoscopy with mass-produced laser diodes. Optics Express 2011, 19(9), 8066–8072.
[44] Moffitt JR, Osseforth C, Michaelis J. Time-gating improves the spatial resolution of STED microscopy. Opt Express 2011, 19(5), 4242–4254.
[45] Vicidomini G, Moneron G, Han KY, Westphal V, Ta H, Reuss M, *et al.* Sharper low-power STED nanoscopy by time gating. Nature Methods 2011, 8(7), 571–573.
[46] Gould TJ, Myers JR, Bewersdorf J. Total internal reflection STED microscopy. Optics Express 2011, 19(14), 13351–13357.
[47] Auksorius E, Boruah BR, Dunsby C, Lanigan PMP, Kennedy G, Neil MAA, *et al.* Stimulated emission depletion microscopy with a supercontinuum source and fluorescence lifetime imaging. Optics Letters 2008, 33(2), 113–115.
[48] Gould TJ, Burke D, Bewersdorf J, Booth MJ. Adaptive optics enables 3D STED microscopy in aberrating specimens. Optics Express 2012, 20(19), 20998–21009.

[49] Fischer J, Mueller JB, Kaschke J, Wolf TJA, Unterreiner AN, Wegener M. Three-dimensional multi-photon direct laser writing with variable repetition rate. Optics Express 2013, 21(22), 26244–26260.
[50] Wolf TJA, Fischer J, Wegener M, Unterreiner AN. Pump-probe spectroscopy on photoinitiators for stimulated-emission-depletion optical lithography. Optics Letters 2011, 36(16), 3188–3190.
[51] Fischer J, Wegener M. Three-dimensional optical laser lithography beyond the diffraction limit. Laser Photonics Review 2013, 7(1), 22–44.
[52] Klar TA, Wollhofen R, Jacak J. Sub-Abbe resolution: from STED microscopy to STED lithography. Physica Scripta 2014, T162, 014049.
[53] Rittweger E, Rankin BR, Westphal V, Hell SW. Fluorescence depletion mechanisms in super-resolving STED miscroscopy. Chemical Physics Letters 2007, 442(4–6), 483–487.
[54] Harke B, Bianchini P, Brandi F, Diaspro A. Photopolymerization Inhibition Dynamics for Sub-Diffraction Direct Laser Writing Lithography. ChemPhysChem 2012, 13(6), 1429–1434.
[55] Stocker MP, Li L, Gattass RR, Fourkas JT. Multiphoton photoresists giving nanoscale resolution that is inversely dependent on exposure time. Nature Chemistry 2011, 3(3), 223–227.
[56] Gan Z, Cao Y, Evans RA, Gu M. Three-dimensional deep sub-diffraction optical beam lithography with 9 nm feature size. Nature Communications 2013, 4, 2061.
[57] Forman DL, Cole MC, McLeod RR. Radical diffusion limits to photoinhibited superresolution lithography. Phys Chem Chem Phys 2013, 15(36), 14862–14867.
[58] Mueller JB, Fischer J, Mayer F, Kadic M, Wegener M. Polymerization Kinetics in Three-Dimensional Direct Laser Writing. Advanced Materials 2014, 26(38), 6566–6571.
[59] Betzig E, Patterson GH, Sougrat R, Lindwasser OW, Olenych S, Bonifacino JS, *et al.* Imaging intracellular fluorescent proteins at nanometer resolution. Science 2006, 313(5793), 1642–1645.
[60] Rust MJ, Bates M, Zhuang XW. Sub-diffraction-limit imaging by stochastic optical reconstruction microscopy (STORM). Nature Methods 2006, 3(10), 793–795.
[61] Hess ST, Girirajan TPK, Mason MD. Ultra-high resolution imaging by fluorescence photoactivation localization microscopy. Biophysical Journal 2006, 91(11), 4258–4272.
[62] Fölling J, Bossi M, Bock H, Medda R, Wurm CA, Hein B, *et al.* Fluorescence nanoscopy by ground-state depletion and single-molecule return Nature Methods 2008, 5(11), 943–945.
[63] Heilemann M, Van de Linde S, Schuttpelz M, Kasper R, Seefeldt B, Mukherjee A, *et al.* Subdiffraction-Resolution Fluorescence Imaging with Conventional Fluorescent Probes. Angewandte Chemie International Edition 2008, 47(33), 6172–6176.
[64] Biteen JS, Thompson MA, Tselentis NK, Bowmann GR, Shapiro L, Moerner WE. Super-resolution imaging in live caulobacter crescentus cells using photoswitchable EYFP. Nature Methods 2008, 5(11), 947–949.
[65] Lord Rayleigh JWS. On the Theory of Optical Images, with special Reference to the Microscope. Philosophical Magazine and Journal of Science 1896, 42, 167–195.
[66] Sparrow CM. On spectroscopic resolving power. Astrophysical Journal 1916, 44(2), 76–86.
[67] Kawata S, Sun HB, Tanaka T, Takada K. Finer structures for functional microdevices. Nature 2001, 412(6848), 697–698.
[68] Thakar RG, Ho F, Huang NF, Liepmann D, Li S. Regulation of vascular smooth muscle cells by micropatterning. Biochemical and Biophysical Research Communications 2003, 307(4), 883–890.
[69] Cavalcanti-Adam EA, Micoulet A, Blummel J, Auernheimer J, Kessler H, Spatz JP. Lateral spacing of integrin ligands influences cell spreading and focal adhesion assembly. European Journal of Cell Biology 2006, 85(3–4), 219–224.
[70] Lohmüller T, Triffo S, O'Donoghue GP, Xu Q, Coyle MP, Groves JT. Supported membranes embedded with fixed arrays of gold nanoparticles. Nano Letters 2011, 11(11), 4912–4918.

[71] Chien FC, Kuo CW, Yang ZH, Chueh DY, Chen PL. Exploring the formation of focal adhesions on patterned surfaces using super-resolution imaging. Small 2011, 7(20), 2906–2913.
[72] Thery M. Micropatterning as a tool to decipher cell morphogenesis and functions. Journal of Cell Science 2010, 123(24), 4201–4213.
[73] Tang X, Ali MY, Saif MTA. A Novel Technique for Micro-patterning Proteins and Cells on Polyacrylamide Gels. Soft Matter 2012, 8(27), 7197–7206.
[74] Beduer A, Vieu C, Arnauduc F, Sol JC, Loubinoux I, Vaysse L. Engineering of adult human neural stem cells differentiation through surface micropatterning. Biomaterials 2012, 33(2), 504–514.
[75] Wingren C, Borrebaeck CAK. Progress in miniaturization of protein arrays-a step closer to high-density nanoarrays. Drug Discovery Today 2007, 12(19–20), 813–819.
[76] Huang S, Schopf E, Chen Y. Dynamically configurable biomolecular nanoarrays. Nano Letters 2007, 7(10), 3116–3121.
[77] Wang S, Ota S, Guo B, Ryu J, Rhodes C, Xiong Y, *et al.* Subcellular resolution mapping of endogenous cytokine secretion by nano-plasmonic-resonator sensor array. Nano Letters 2011, 11(8), 3431–3434.
[78] Arnold M, Schwieder M, Blummel J, Cavalcanti-Adam EA, Lopez-Garcia M, Kessler H, *et al.* Cell interactions with hierarchically structured nano-patterned adhesive surfaces. Soft Matter 2009, 5(1), 72–77.
[79] Chai JA, Wong LS, Giam L, Mirkin CA. Single-molecule protein arrays enabled by scanning probe block copolymer lithography. Proc Natl Acad Sci U S A 2011, 108(49), 19521–19525.
[80] Mirkin CA. The power of the pen: development of massively parallel dip-pen nanolithography. ACS Nano 2007, 1(2), 79–83.
[81] Curran JM, Stokes R, Irvine E, Graham D, Amro NA, Sanedrin RG, *et al.* Introducing dip pen nanolithography as a tool for controlling stem cell behaviour: unlocking the potential of the next generation of smart materials in regenerative medicine. Lab on a Chip 2010, 10(13), 1662–1670.
[82] Pla-Roca M, Fernandez JG, Mills CA, Martinez E, Samitier J. Micro/nanopatterning of proteins via contact printing using high aspect ratio PMMA stamps and nanoimprint apparatus. Langmuir 2007, 23(16), 8614–8618.
[83] Christman KL, Schopf E, Broyer RM, Li RC, Chen Y, Maynard HD. Positioning Multiple Proteins at the Nanoscale with Electron Beam Cross-Linked Functional Polymers. Journal of the American Chemical Society 2009, 131(2), 521–527.
[84] Schlapak R, Danzberger J, Haselgrübler T, Hinterdorfer P, Schäffler F, Howorka S. Painting with Biomolecules at the Nanoscale: Biofunctionalization with Tunable Surface Densities. Nano Letters 2012, 12(4), 1983–1989.
[85] Wiesbauer M, Wollhofen R, Vasic B, Schilcher K, Jacak J, Klar TA. Nano-Anchors with Single Protein Capacity Produced with STED Lithography. Nano Letters 2013, 13(11), 5672–5678.
[86] Van de Linde S, Sauer M, Heilemann M. Subdiffraction-resolution fluorescence imaging of proteins in the mitochondrial inner membrane with photoswitchable fluorophores. Journal of Structural Biology 2008, 164(3), 250–254.
[87] Schmidt T, Schütz GJ, Gruber HJ, Schindler H. Local Stoichiometries Determined by Counting Individual Molecules. Analytical Chemistry 1996, 68(24), 4397–4401
[88] Brameshuber M, Weghuber J, Ruprecht V, Gombos I, Horvath I, Vigh L, *et al.* Imaging of mobile long-lived nanoplatforms in the live cell plasma membrane. J Biol Chem 2010, 285(53), 41765–41771.
[89] Frölich A, Fischer J, Zebrowski T, Busch K, Wegener M. Titania Woodpiles with Complete Three-Dimensional Photonic Bandgaps in the Visible. Advanced Materials 2013, 25(26), 3588–3592.

[90] Frölich A, Fischer J, Wolff C, Busch K, Wegener M. Frequency-Resolved Reciprocal-Space Mapping of Visible Spontaneous Emission from 3D Photonic Crystals. Advanced Optical Materials 2014, 2(9), 849–853.
[91] Thiel M, Ott J, Radke A, Kaschke J, Wegener M. Dip-in depletion optical lithography of three-dimensional chiral polarizers. Optics Letters 2013, 38(20), 4252–4255.
[92] Ergin T, Fischer J, Wegener M. Optical Phase Cloaking of 700 nm Light Waves in the Far Field by a Three-Dimensional Carpet Cloak. Physical Review Letters 2011, 107(17), 173901.
[93] Gu M. Optical Data Storage with Diffraction-Unlimited Resolution. Conference on Lasers and Electro-Optics Europe: Munich; 2013.
[94] Gu M, Li X, Cao Y. Optical storage arrays: a perspective for future big data storage. Light: Science and Applications 2014, 3, e177.

Index